



## KÖSZÖNTŐ

Borbás Lajos  
a Magyar Biomechanikai Társaság elnöke  
[borbas@kege.bme.hu](mailto:borbas@kege.bme.hu)

---

Immár ötödik alkalommal rendezzük Magyarországon konferenciánkat a Biomechanika tárgykörében.

Az életminőség javítása az orvos társadalom számára esküjünkben megfogalmazott alapvetés, amely a 21. században, a korszerű műszaki ismeretek alkalmazása nélkül megvalósíthatatlan célkitűzés.

Kutatók és fejlesztők a mérnökök és orvosok táborában azért dolgoznak, hogy élhetőbbé tegyék a betegek mindennapjait, segítséget nyújtsanak abban, hogy javítsák életminőségüket, könnyebbé tegyék mindennapjaikat, egyben reményt adjanak egy élhetőbb világ eléréséhez. Ebben a tekintetben a biomechanika napjaink megkerülhetetlen tudományága, amely az inter-, és multidiszciplinaritás elvén épít úgy az orvosi, biológiai, mind a mérnöki tudományok ismereteinek és eredményeinek humán gyógyászati felhasználására.

A biomechanika tárgyköre nem pusztán mechanikai szemléletet takar, magában foglalja mindazokat a törekvéseket, eljárásokat és gondolkodomódot, ami hozzásegíti a potenciális rászorultakat életvitelük könnyítéséhez, egyszersmind reményt ad a ma még megoldatlannak tűnő orvos-biológiai kérdések jövőbeni megoldására.

Jelen rendezvényünk mind az orvosok, mind a mérnökök szemszögéből arra törekszik, hogy bemutassa tudományterületének legújabb eljárásait, megoldásait és elképzeléseit, előrevetítve egy élhetőbb, reménytelibb élet megvalósítását.

Tudományterületünk meghatározó személyiségei jól körülhatárolt iskolákhoz köthetők, melyekben az egyik legfontosabb feladat az utánpótlás nevelése, a fiatal oktatók, kutatók munkáinak megismertetése a széles tudományos közvéleménnyel. Ebben a tekintetben kifejezetten jelentősnek érzem, hogy rendezvényünk résztvevőinek többsége fiatal, Ph.D. hallgató, ill. nemrégén végzett orvos, vagy mérnök doktor. Jelen rendezvényünk lehetőséget biztosít munkájuk széles közvéleménnyel való megismertetésre, ami hozzásegít eredményeik lehetőség szerinti leggyorsabb megvalósításra.

Konferenciánk szervezőinek elsődleges célja mindezek alapján nem lehet más, mint rendszeres fórumot biztosítani az orvosok, mérnökök, a szakmában dolgozó szakalkalmazottak számára eljárásaik, kutatási eredményeik bemutatására, annak érdekében, hogy azok minél előbbi bevezetésre kerülhessenek a humán gyógyászat legkülönbözőbb területein.

## TOMOGRAPHIC RECONSTRUCTION OF MICRO-VASCULAR NETWORK IN CEREBRAL CORTICAL SAMPLES

Kristóf Kapitány<sup>1</sup>, László Négyessy<sup>2,3</sup>, Árpád Barsi<sup>1</sup>

<sup>1</sup>Department of Photogrammetry and Geoinformatics, Budapest University of Technology and Economics

<sup>2</sup>Wigner Research Centre for Physics, Hungarian Academy of Science

<sup>3</sup>Department of Anatomy, Histology and Embryology, Semmelweis University

[kapitany@eik.bme.hu](mailto:kapitany@eik.bme.hu)

---

### **Abstract**

#### Objectives

The purpose of the research is the automatic processing and analysis of high-amount (nearly 1500) and high-resolution synchrotron based tomography images of mammalian cerebral cortical tissues. The objective was to acquire quantitative data allowing future blood flow modeling based on the structure of cerebral vessel network. The brain samples were processed with histological method compatible with synchrotron x-ray microtomography. The method developed performs automated extraction of the relevant parameters of the vessel network on a standard personal computer using previously set parameters.

#### Method

The method implemented on the image series performs automatic segmentation by using determined intensity values. The procedure finds the boundary of the vessels and provides quantitative measures of the segments, and it also creates the topology of the vessel network.

#### Results

Our method produces topologically correct network of continuous, branching micro blood vessels of the sample studied. We present multiple options for the visualization of the detected vessels. The data structure also contains the statistics of each detected cross-section, in addition with the numerical quality statistics of the continuous vessel branches (e. g. vessel length or mean diameter). The algorithm resulted in highly accurate fitting at micrometer geometric resolution.

#### Conclusion

The reconstructed vessel network is the geometrically accurate description of the blood vessels in the tissue. The data acquired could be the base of a blood vessel surface reconstruction, and by adding physiological information it could be used for simulations in normal and pathological conditions (e. g. arteriosclerosis). The precise vascular geometry and the distance distribution provides information about the barely understood neurovascular coupling, which is the basis of such modern diagnostic and research tools as the fMRI. After analyzing samples from multiple species or brain regions the difference could be determined objectively.

---

### **Introduction**

To understand brain functioning, we have to know precisely the inner structure of the cerebral tissue, the connection network of the blood vessels and the neurons.<sup>1,2</sup> The conventional method of medical imagery is to analyze the tissues (after special pretreatment) with the use of optical- or

electron microscope depending on the object of examination. Traditional microscopic methods cannot detect overlapping structures which are small relative to the thickness of the tissue. Therefore the tissue must be cut for ultra-thin slices, and each thin section be analyzed separately. If vessels are the object of research the slices should be 1-2  $\mu\text{m}$  thick, but in case of dendrites 50-70 nm thin sections must be cut,<sup>3</sup> but sometimes even 15-40 nm thin cuts are needed.<sup>4</sup> This process is extremely labor-intensive and inefficient, and as the sample is sliced, it can't be used for other analyses. X-ray micro tomography enables non-destructive tests on the tissue samples. Computer tomography (CT) creates series of projections with the radiology of the rotated sample; hence CT enables thorough introspection inside the examined material. By analyzing tissues using this method, after special pretreatment, various objects or materials could be detected in a sample.<sup>5,6</sup> This article presents the process of an image series, showing and discussing the results.

The purpose of this study is to detect the micro blood vessels of the cerebral cortex of mammalian species on series of microtomographic images, and to acquire information from the image data in order to create a geometrically accurate vessel network.

## Materials

X-ray micro-tomography images were obtained from samples of the mammalian cerebral cortex. The present study is focused on the examination of the rat cortical tissue. Animals were treated in accordance with the Guide for the Care and Use of Laboratory Animals (National Research Council 1996), European Directive 86/609 and the guidelines of the local institutional animal care and use committee. Histological pre-treatment was started with transcardial perfusion of an aldehyde solution to preserve brain structure. Blocks including the region of interest were removed from the fixed brain and sections were cut at 20-60  $\mu\text{m}$  thickness, then washed and stained. In our case the sections were stained with phosphotungstic acid (PTA), which enhances the contrast of the tissue by binding to proteins and nucleotides. Consequently, the lumen of the blood vessels remained unstained in the background of the labeled tissue. The following step was the dehydration, before embedding into resin. Embedded tissues can be further cut into very thin, so called ultra-thin sections. Using a micropunch tool we cut a cylinder-shaped sample from the embedded section with dimensions of 500  $\mu\text{m}$  in diameter and 60  $\mu\text{m}$  in height.<sup>7</sup>

The samples were imaged at the Swiss Light Source (SLS) at the Paul Scherrer Institute in Switzerland, in a third-generation synchrotron light source, which provides photon beams of high brightness. The X-ray tomography images were created with a beamline, called TOMCAT (TOMographic Microscopy and Coherent rAdiology experimenT's), which is a special experimental instrument of the SLS. The samples were analyzed by a monochromatic beam with 10keV energy using the TOMCAT application, which is designed to rotate the samples therefore to provide three-dimensional data.<sup>8</sup> By the rotation of the sample holder 1401 X-ray tomography images were captured about one sample with the dimension of 2048 $\times$ 1356 pixels. The nominal pixel size of the images is 0.38  $\mu\text{m}$ , which provides high-resolution images of the sample. They were transformed into 2048 $\times$ 2048 pixel wide cross-section images using inverse Radon-transformation (*Figure 1*). Because the sample is transparent to the X-ray radiation (although anisotropically as the result of PTA staining) raw images include information of the whole sample

from different rotation angles. Radon-transformation, which needs powerful computational resources, is used to create series of digital cross sections of the sample, similar to that seen in regular CT examinations. Our methods are designed for simple personal computers and so this transformation optimizes the input data, without the loss of valuable information.

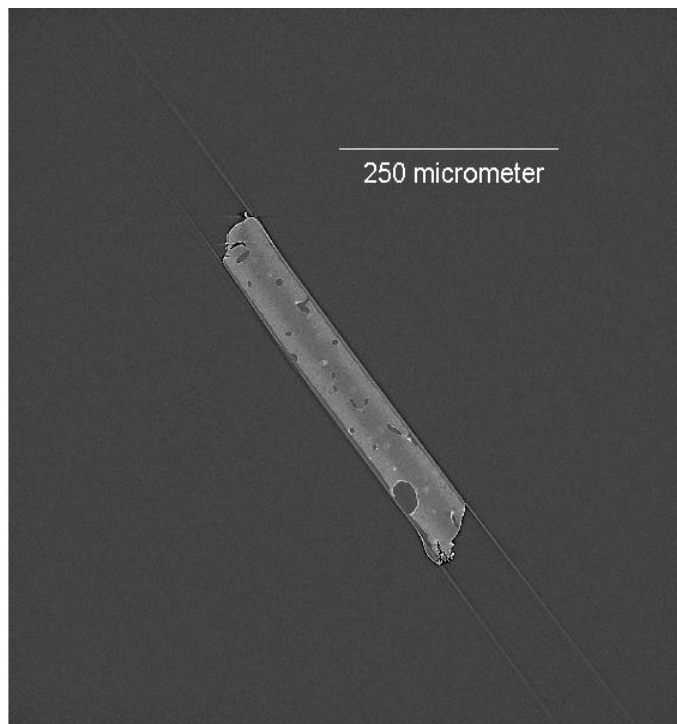


*Figure 1.* A single image after inverse Radon transformation

## **Method**

### **Detection of the vessels**

The images are of high-resolution, the color depth is 16-bit, so because of the huge data amount it is hard to work with the whole series of a block on a standard personal computer. Our method analyzes each image in the series one-by-one and creates the segments of the vessels. To reduce processing time the sample was segmented from the image, with an algorithm that finds the bounding box of the sample's cross section on each image, and trims out the union of the bounding boxes from the images. This reduced the image size from  $2048 \times 2048$  to  $859 \times 1096$  pixels resulting considerable less process time and memory consumption. The algorithm was written in MATLAB.

To reconstruct a blood vessel model, we have to find the vessels first. The vessels' cross-sections were segmented using a threshold value, and were saved in a stacked image format, where a layer was created for each projection as a binary image. The threshold values were determined using the Java-based, open source image processing software ImageJ.<sup>9</sup> Using this software the image series could be loaded into one group and the threshold of the blood vessels could be determined with the stack histogram of the image group. The segmented image of *Figure 1* is shown in *Figure 2*. During the segmentation false regions were also detected e. g. interior noisy blobs or tissue shreds on the outer surface of the sample. The surface of the sample is rough because the sampling method can't provide perfect cylinder-shaped blocks due to the soft and ductile

biological material. As part of the procedure the sampling was repeated digitally to eliminate the shreds on the tissue's periphery.<sup>10</sup>

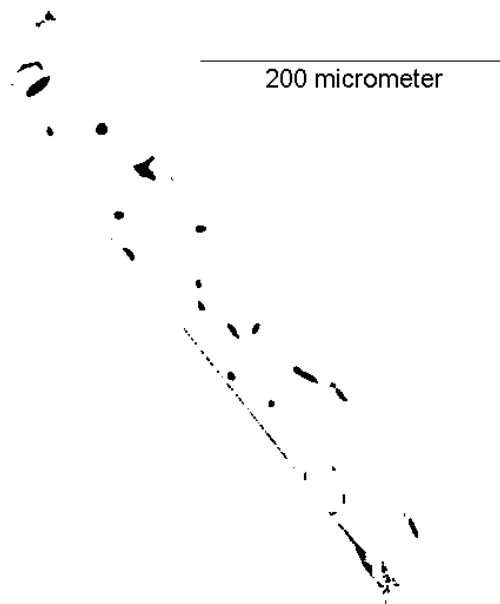


Figure 2. Segmented vessel regions of Figure 1

After the digital punch approach statistical data was gathered about the detected regions. By this process the centroids' coordinates of the detected vessel cross-sections were collected with the matching area parameter, semi-major and semi-minor axis length, the orientation of the major axis and the pixels composing the region's boundary. The statistics of each region were stored uniquely labeled.

After obtaining this information about the regions, the transformed digital images are not required any more in the object reconstruction process, since each region could be represented by the coordinates of its centroid and the collected data. Using this method there is no more need for the original image series during the analysis, the data is stored in a tabular format, and it is much easier to work with the derived results.

### Reconstruction of the vessels

The reconstruction of the blood vessel network was designed as a pipe-work composed by connected, ungula-shaped elements. The unguulas consist of two parallel, circle-shaped planes, and a surface which connects them. The radiuses of the two planes are usually different, and they are derived from the statistics of the detected regions with the centroids' coordinates. To reconstruct the vessel network first the connection has to be established between the discrete elements. This was carried out with an additional identification number. Each region was projected to the image below, and the regions near by the projected centroid were analyzed. If the projected centroid was inside another region the two detected elements were joint and both got the same identification number (linking step). If there was no connecting element on the image below, the region got a new identification number. Each region was identified using this method. In case of a bifurcation, the cross-section of the blood vessels has amorphous shape and the statistics about major/minor axis lengths do not describe the geometry of the vessels. These cases must be handled separately, therefore bifurcation detection algorithm was developed. Double

identification were initiated (a) to enable separate vessel segment handling and (b) to manage them in a complex representation. This method is shown in *Figure 3*.

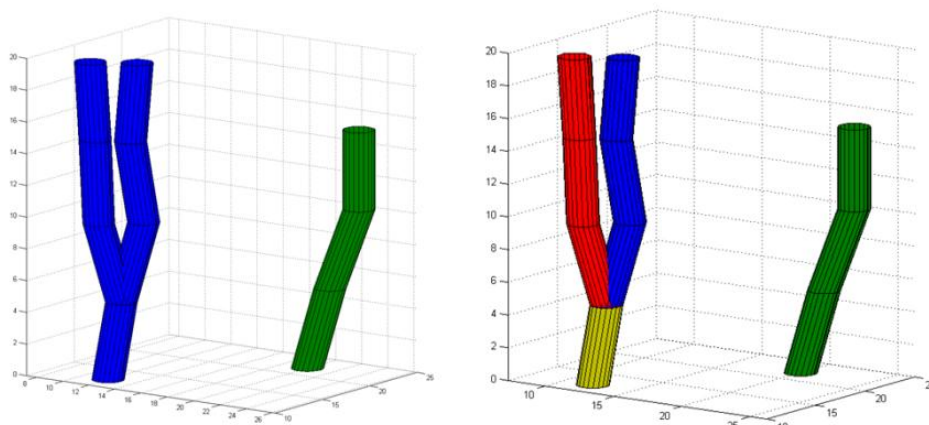


*Figure 3.* The double element identification: color-code represents unique identifiers for complex structures (left) and separate vessel segments (right)

To reconstruct a blood vessel, the semi-minor axis length and the coordinate of the centroid were used from the statistics of the detected regions. Our method conceives blood vessels as tubular objects. The captured synchrotron images aren't usually perpendicular to vessel axis, so the shape of the section boundaries differs from circle. One can prove, that the semi-minor axis length is the invariant feature which can be taken as the vessels' radius, even if the vessel crosses the image plane almost horizontally. This is shown in *Figure 4* where *A* is the horizontal plane, *B* is the tilted cross-section, and *R* means the radius of the vessel.

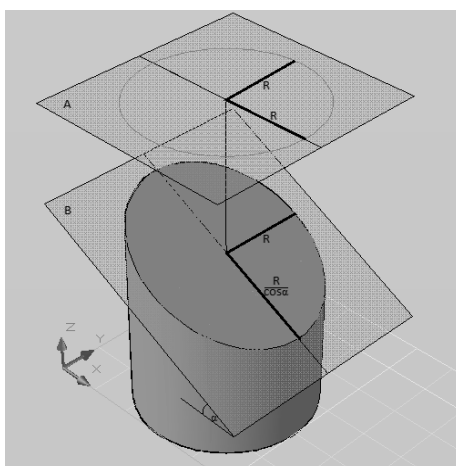


*Figure 4.* Horizontal and tilted cross-section of a cylinder

### Examining the density of vascular structures

The reconstructed vessel network presented before, enables vascularity analysis. For this the volume of the sample was divided into voxels, and for each voxel the Euclidian distance was calculated to every detected vessel. The minimum of the calculated distances was stored in a three-dimensional array form and to visualize the result, a color tone was attached to each computed distance. Using this method the vascularity of the tissue could be examined in different resolutions, and in every cross-section (in arbitrary directions). Three perpendicular cross-sections are shown in *Figure 5*, where the voxel size is  $0.76\mu\text{m} \times 0.76\mu\text{m} \times 0.76\mu\text{m}$ ,  $200 \times 200 \times 200$

voxels are represented. The gray scale shows the normalized distance from the vessels in the examined part of the tissue and the yellow color shows the vessels.

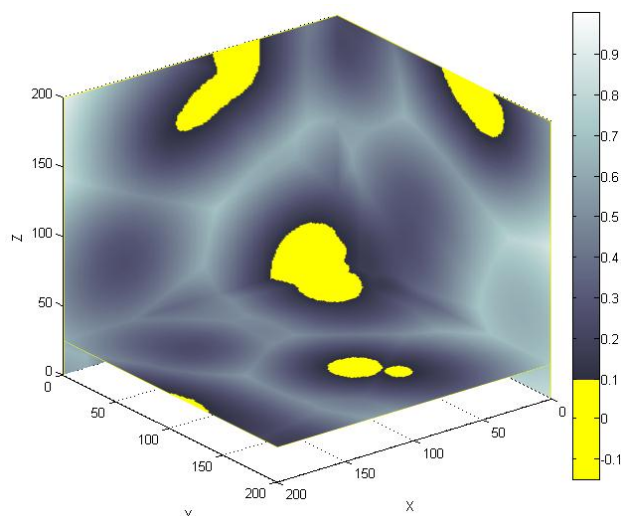


Figure 5. Vascularity in the tissue

## Results & Discussion

The raw data were transformed into two dimensional images, which could be handled easily by a standard personal computer. The images were segmented and statistics were gathered from the cross-sections of the vessels. The topology of the vessel network was built based on the derived statistical data. The collected data were stored in a structured format to handle each vessel separately. The quality measure of the examined sample is shown in *Table 1*.

|  |                                      |
|--|--------------------------------------|
| Number of detected vessel cross-sections:                  | 12 209                               |
| Number of detected separate vessels:                       | 2 390                                |
| Number of elements in the longest vessel:                  | 271                                  |
| Mean number of vessel elements:                            | 5.11                                 |
| Global length of detected vessels:                         | 4 639.42 $\mu\text{m}$               |
| Length of the longest vessel:                              | 102.98 $\mu\text{m}$                 |
| Mean length of the vessels:                                | 1.94 $\mu\text{m}$                   |
| Diameter of the greatest vessel:                           | 43.76 $\mu\text{m}$                  |
| Mean diameter of the vessels:                              | 4.02 $\mu\text{m}$                   |
| Volume of the examined sample:                             | 8 082 723.82 $\mu\text{m}^3$         |
| Total vessel volume:                                       | 58 818.57 $\mu\text{m}^3$            |
| Tissue supply (blood supply of the sample per vessel unit) | 1 742.18 $\mu\text{m}^3/\mu\text{m}$ |

Table 1. Basic statistics of the analyzed sample

Using the acquired statistics data, the blood vessels could be visualized. Vessels composed from more than nine elements, are plotted using the ungula-based model in *Figure 6*.



Figure 6. Model of the vessel network using ungula elements

In *Figure 7* spheres were plotted instead of ungulas to the centroids with the adherent semi-minor axis length as the radius of the sphere. Significantly larger spheres indicate vessel bifurcations.



Figure 7. Model of vessel network using sphere elements

## Conclusion

Our method produces the object-model of the micro blood vessel network inside cerebral cortical samples using synchrotron-based tomography. The algorithm detects the vessel sections on two-dimensional tomography images and finds the connection between the separate elements. The algorithm could be used to visualize the micro blood vessels inside the sample, to derive quality measures or to perform quantitative analysis on the vessels. The method needs minimal pre-processing on the biological tissues, and it could provide enough information for the object reconstruction including vessel surface network. An important modification of the present study as compared to previous studies<sup>2</sup> is that the vessels were not directly stained with contrast agents. The efficacy of perfusing the vascular system with barium-sulfate (standard contrast agent in x-ray examination) or other contrast solutions<sup>2</sup> is unknown. Here we enhanced the contrast by a non-specific staining of the tissue (proteins and nucleic acids), which leaves the vessel lumen



completely transparent. Consequently, our procedure is free of labeling artifacts. The data acquired could be the base of a blood vessel surface reconstruction, and by adding physiological information it could be used for simulations of normal and pathological conditions (e. g. arteriosclerosis). After analyzing samples from multiple species the difference could be determined automatically by the statistics of the tissues.

---

## REFERENCES

1. Logothetis NK, Pfeuffer J. On the nature of the BOLD fMRI contrast mechanism. *Magnetic Resonance Imaging* 2004 Dec;22(10):1517-31.
2. Guibert R, Fonta C, Plouraboué F. Cerebral blood flow modeling in primate cortex. *Journal of Cerebral Blood Flow & Metabolism* 2010 Nov;30(11):1860-73.
3. Denk W, Horstmann H. Serial block-face scanning electron microscopy to reconstruct three-dimensional tissue nanostructure. *PLoS biology* 2004 Nov;2(11):e329.
4. Knott G, Marchman H, Wall D, Lich B. Serial section scanning electron microscopy of adult brain tissue using focused ion beam milling. *The Journal of Neuroscience* 2008 Mar 19;28(12):2959-64.
5. Mizutani R, Takeuchi A, Akamatsu G, Uesugi K, Suzuki Y. Element-specific microtomographic imaging of *Drosophila* brain stained with high-Z probes. *Journal of synchrotron radiation* 2008 Jul;15(Pt 4):374-7.
6. Plouraboué F, Cloetens P, Fonta C, Steyer A, Lauwers F, et al. X-ray high-resolution vascular network imaging. *Journal of microscopy* 2004 Aug;215(Pt 2):139-48.
7. Kapitány K. Object-reconstruction from high-resolution X-ray images (In Hungarian) 2012.
8. Stampanoni M, Groso A, Isenegger A, Mikuljan G, Henein S, Betemps R. Trends in synchrotron-based tomographic imaging: the SLS experience. *SPIE Proceedings "Developments in X-ray Tomography V"*; 2006; San Diego, CA.
9. ImageJ website. [cited 2013 4. 5.]; <http://rsb.info.nih.gov/ij/>.
10. Kapitány K. Geometric reduction of high amount histological image data. *Conference of Junior Researchers in Civil Engineering*; 2012; Budapest.

***This study was supported in the framework of the project „Talent care and cultivation in the scientific workshops of BME" project by the grant TÁMOP – 4.2.2.B-10/1—2010-0009 as well by the SLS (proposal ID 20090952 and 20100156).***

## MODERN WOUND TREATMENT WITH DEVICES WORKING ACCORDING TO VARIOUS PHYSICAL PRINCIPLES

Miklós Szokoly<sup>1</sup>, Petra Aradi<sup>2</sup>

<sup>1</sup> Péterfy Hospital and Trauma Center

<sup>2</sup> Department of Mechatronics, Optics and Engineering Informatics, Budapest University of Technology and Economics

[orvig@peterfykh.hu](mailto:orvig@peterfykh.hu)

---

### **Abstract**

The prevalence of venous diseases in Europe is 25.2%. According to studies of the University of Bonn this number can be as high as 90%. Optimistic estimates suggest this number to be 27.5% in Hungary, 21.5% in Germany. Treatment costs of varicosis and its complications are covered by 2% of the annual healthcare expenditure in Western countries. Chronic venous insufficiency (CVI, or chronic venous disease, CVD) affects 1.7% of European population, and can lead to venous ulcers. In Hungary 0.5-1% of the population suffers from venous ulcers, which is a result of primary or secondary varicosity.

Although an increasing number of modern wound dressings have appeared during the last decade, the treatment of ulcerous wounds in necrotic and exudative phases requires additional methods, either conventional or surgical. Infrared light is used to discover pathologic veins. Beside sclerotherapy and surgical treatment external and internal (so called intraluminal) methods are used. Leg ulcers of venous origin in various phases can be cleaned with ultrasound devices, vacuum therapy or high pressure water. Hyperbaric oxygen treatment, keratinocytes, magnetic treatment, laser wound care and skin transplantation can be used as adjuvant.

Authors present the aforementioned procedures with examples. New devices and methods help to reduce healing time and to avoid amputation in cases that are often considered hopeless.

Technical advancement and modern wound dressings permit successful treatment and healing of wounds that earlier were untreatable, however monetary shortage and the current status of healthcare.

**Keywords:** chronic wound, venous leg ulcer, treatment, wound care technologies.

---

### **Introduction**

The prevalence of venous diseases in Europe is 25.2%. According to studies of the University of Bonn this number can be as high as 90%. Optimistic estimates suggest this number to be 27.5% in Hungary, 21.5% in Germany. Treatment costs of varicosity and its complications are covered by 2% of the annual healthcare expenditure in Western countries. Chronic venous insufficiency (CVI, or chronic venous disease, CVD) affects 1.7% of European population, and can lead to venous ulcers. In Hungary 0.5-1% of the population suffers from venous ulcers, which is a result of primary or secondary varicosity.

In Hungary the majority is leg ulcers is detected in population around 70 years of age. Female-male ratio is 3:1. It is unfortunate that only 29% of patients reports for treatment. The situation is

---

much direr for diabetic patients. in 2003 the number of diabetes patients was 194 million worldwide, 5.1% of population. The predicted number of patients for 2025 is 333 million, 6.3% of population. In people suffering from diabetes wounds form 40 times more often, than in healthy population. Micro- and macroangiopathic complications reduce life expectancy by 6-10 years. 50% of the total of 5,000 non-traumatic amputations are performed on diabetics. During the first year after amputation 10% of patients die, in the fifth year mortality is 70%.

Another category is the wounds that appear in connection with various types of peripheral artery occlusive disease.

If treatment of wounds of leg ulcers is started immediately after their formation, healing chances are far better, than treatments started at a later phase. This paper focuses on treatment equipment and methods of previously untreated wounds, with the threat of amputation.

## Method

Ulcers are classified according to Wagner<sup>1</sup> (*Table 1*). This primary classification is the basis of selecting treatment method and the type of wound dressing.

|                |   |
|----------------|---|
| <b>Grade 1</b> | No ulcer in a high risk foot.   |
| <b>Grade 1</b> | Superficial ulcer involving the full skin thickness, but not underlying tissues.                    |
| <b>Grade 2</b> | Deep ulcer, penetrating down to ligaments and muscle, but no bone involvement or abscess formation. |
| <b>Grade 3</b> | Deep ulcer with cellulitis or abscess formation, often with osteomyelitis.                          |
| <b>Grade 4</b> | Localized gangrene.   |
| <b>Grade 5</b> | Extensive gangrene involving the whole foot.  |

*Table 1.* Wagner's Foot Ulcer Grading System<sup>1</sup>

General principles concerning chronic wounds are as follows

- wounds are considered septic and treated accordingly
- treatment principle depends of stage
- wounds are kept open
- modern wound treatment is based on bacteriological tests
- alginates, silver-containing ointment dressings, hydrocolloids and hydrogels are used to keep wounds moist
- wound surroundings have to be protected, however iodine, mercurochrome (merbromin) and antiseptic wound powders have to be avoided
- load relief

Phases of chronic wounds are necrotic, exudative, granulation, and ephitelisation. Description and treatment are summarized in *Table 2*.

Wound debridement devices working along various physical principles are used in exudative phase. Exudative or infected phase wounds are painful and tender, have ample purulent exudates on the wound base, redness, warmth and induration appears in adjacent tissues. Exudative wounds need to be cleaned to the basis, resulting in a bleeding fresh wound. Then as in acute wounds, wound healing can commence.

| Phase          | Treatment   | Dressing   |
|----------------|---|--|
| necrotic       | necrectomy, debridement<br>mechanic<br>surgical<br>enzymatic<br>protection of peri-ulcer area   | washing with disinfectants<br>alginate<br>active carbon compresses<br>enzymatic dressings<br>hydrogel<br>absorbents<br>daily dressing change             |
| exudative      | mechanic<br>surgical<br><b>hydrosurgical cleaning</b><br><b>ultrasound assisted cleaning</b><br>enzymatic<br>negative pressure wound therapy<br>protection of peri-ulcer area | washing with disinfectants<br>alginate<br>active carbon compresses<br>enzymatic dressings<br>absorbents<br>silver nanoparticles<br>daily dressing change |
| granulation    | protection of peri-ulcer area<br>dressing change every 2-3 days   | hydrogel<br>hydrocolloid<br>impregnated compresses<br>absorbents   |
| epithelisation | dressing change every 3-4 days  | hydrogel<br>impregnated compresses   |

Table 2. Phases of chronic ulcers

### Hydrosurgical wound debridement

Hydrosurgery means the use of high speed concentrated fluid flow instead of traditional mechanical devices. Necrotic tissue, bacteria and other contamination can be removed with high precision, while creating a smooth wound bed and preserving as much viable tissue as possible.

Smith & Nephew's Versajet Hydrosurgery System (Figure 1), winner of the Wall Street Journal's 2006 Technology Innovation Award was tested in ulcer patients, details are presented later in Results.



Figure 1. Versajet Hydrosurgery System<sup>2</sup>

VersaJet's operating principle is the Venturi effect. A high velocity sterile saline stream jets across the operating window, where Venturi effects creates a localized vacuum. This is how removed tissue is simultaneously aspirated from the site. Various settings allow the use of a device for controlling the amount of removed tissue, e.g. at low power levels, it is almost like a vacuum-only cleaner, which removes little or no tissue. With the increase of power tissue ablation increases, too, so tissues with harder consistency get removed.

### Ultrasonic Assisted Wound Treatment (UAW)

UAW is a non-invasive method using ultrasound energy combined with irrigation solution to clean wounds and promote wound healing.

Söring's ultrasonic assisted wound treatment system<sup>3</sup> (*Figure 3*) was tested in ulcer patients, details are presented later in Results.



*Figure 2.* Söring Ultrasonic Assisted Wound Treatment System<sup>3</sup>

The ultrasound generating device is connected to a handpiece that applies 25 kHz low-frequency ultrasound directly to the wound surface with simultaneous saline flow that acts a coupling medium, coolant and wound lavage. The handpiece have three interchangeable tips for different wound surfaces (flat, concave and convex).

Wound debridement is performed via mechanical and cavitation processes with simultaneous intensive flushing of the wound. Necrotic tissue, cell debris, fibrin layer and bacteria are flushed from the wound while healthy granulation tissue is preserved and microvascular circulation is promoted. The method does not destroy granulation tissue, blood vessels, or nerves due to their higher tensile strength.

### Other wound treatment methods

Other promising treatment methods, which hopefully will be widely available in the near future, are hyperbaric oxygen treatment, Bemer magnetotherapy, and various methods of skin replacement. These methods require adequate wound cleaning, and their main purpose is to be adjuvant to the definite therapy.

### The importance of modern wound dressings

Phase-specific wound management of venous leg ulcer needs different types of wound dressings. Quite a number of manufacturers produce such dressings. Alginates, silver-ions, active carbon, hydrocolloids and hydrogels are the most used in wound treatment; however the emphasis has to be placed on wound debridement, preferably with the use of previously mentioned methods, to retain as much of viable tissue as possible.

### Results

The results presented below are direct experience of the first author. One of the patients whose case is presented here had a spontaneous varix rupture (left side of *Figure 3*), which was followed by skin necrosis. Necrosis progressed rapidly already on the next day (right side of *Figure 3*).



Figure 3. Spontaneous varix rupture and progressive skin necrosis on the next day

Angiography showed a severely narrowed and occluded major blood vessel (Figure 4).



Figure 4. Occluded blood vessel on angiogram

Blood thinning by LMWH treatment had been commenced and the wound was cleaned with Versajet (Figure 5). Wound base was a little bit bloody the next day; however on the third day granulation phase already begun.

Later on Reverdin-grafting was performed (Figure 6). During the whole duration of treatment appropriately chosen modern wound dressings were applied (Figure 6).



Figure 5. Hydro-surgical wound debridement with Versajet



Figure 6. Reverdin-grafting and the use of modern wound dressings



Figure 7. Results of Reverdin-grafting after one month

The second patient, whose case is presented had been given an appointment for urgent amputation, because of the consequences of an infection. Snapshots from the treatment are shown in Figure 8.



Figure 8. Instead of amputation wound was systematically treated with modern debridement methods and dressings

## **Conclusion**

Modern wound cleaning methods have proven their grounds, as one can see in the presented cases. Even in situations considered hopeless and untreatable by conventional wound management, amputation being the only possible outcome; hydrosurgical and ultrasonic wound cleaning together with modern wound dressings helped to save the limb and quality of life.

---

## **REFERENCES**

1. Wagner FW, Jr. The diabetic foot. *Orthopedics* 1987 Jan;10(1):163-72.
2. VERSAJET II Hydrosurgery System.  
<http://www.smith-nephew.com/key-products/advanced-woundmanagement/versajet/>.
3. Söring Ultrasonic Assisted Wound Treatment.  
[http://www.soering.com/applications/wound\\_treatment/](http://www.soering.com/applications/wound_treatment/).

*Authors would like to thank Hungarian vendors of VersaJet wound debridement system and that of Söring's ultrasonic-assisted wound treatment device for providing devices for evaluation.*



## EFFECT OF PRELOADING ON LOWER JAW IMPLANT

János Simonovics<sup>1</sup>, Péter Bujtár<sup>2</sup>, Károly Váradi<sup>1</sup>

<sup>1</sup> Department of Machine and Product Design, Budapest University of Technology and Economics

<sup>2</sup> Department of Maxillofacial Surgery, University Hospitals of Leicester

[janos@simonovics.hu](mailto:janos@simonovics.hu)

---

### **Abstract**

The procedure of mandible resection is basically unavoidable in case of cancer in the field of oral surgery. The reinforcement and the reconstruction of the jaw closest to its original condition is very challenging. Considering the load properties the examination of the plates used in the reconstruction is highly important. The cadaver examination procedure however is very difficult to execute, therefore the use of the Finite Element Analysis proves rather supportive. Fast recovery can be achieved by applying the implants correctly. Furthermore brakeage resulting from high loads in the plates can be avoided. The goal is to examine and understand the Non-locking screwing technique used with plate implants in different mandible resections and reconstructions, focusing on the preloaded force. Furthermore the study and comparison of different stress that arise in different cases.

A toothless mandible was used for the creation of the Finite Element Analysis model. The data was provided for the model by CBCT. During the creation of the model we separated four different resection areas to which we used the plates with the Non-Locking screwing technique, also used in clinical reconstructions. For the preload of the plates we used different preloaded forces on the screws. We considered and used boundary conditions complying with the anatomical structure. The muscles required for chewing were transferred to the model and used as main loads. The bone structure is heterogenic and the bone density is based on CBCT.

The preloaded forces have a major role in the stresses arising in the bone during the use of Non-locking technique. The comparison of the resection techniques can provide valuable information regarding the preloaded condition and the following chewing load condition connected to the main loads in the bone.

Those measurements that are important from biomechanical point of view and would prove difficult or impossible with in vivo or in vitro load measurements to be examined can be compared with the Finite Element Analysis method.

**Keywords:** mandible, implant, finite element analysis, resection.

---

### **Introduction**

In case of cancer and more closely oral cavity cancer in Hungary takes a very high number within the European Union. Considering the diagnosed oral cavity cancer, the male to female patient ratio is 5.3:1. The number of cancer patients from 1970 is constantly increasing. Nowadays 1700 patients die out of the 3000 diagnosed cases. Oral cavity cancers are however the easiest to detect. The doctors even in a regular dentist examination can detect and diagnose the cancer, in which case the illness can be cured with high success rate. This rate however radically decreases with time. In case of advanced state cancers the recovery is only possible with drastic measures

---

and surgeries. The main factor of oral cavity cancer development is the inadequate oral hygiene, extent use of alcohol and tobacco products.

It is important to point out that cancers would cause metastasis in the bone as the third most common place after the lung and liver, in which case the jaw is also affected.

In case of mandible cancer resection is performed to remove it. During the surgery the affected area is determined by Computer Tomography and that specific part is than removed. The surgeon usually removes a larger area to ensure that there is no bone with cancer left. The complete resection method results in a loss of mechanical load carrying function and continuity of the mandible. Furthermore the self-picture of the patient is also affected, which can cause serious and overwhelming mental stress.

In the earlier times to gain more knowledge regarding the arising stresses in the bone and the connected implants, cadaver and bone ribbon examinations very conducted in laboratory settings. These examinations however are restricted by permissions, hence performing them is quite complicated.<sup>2,7</sup> Because of this fact and the development of the technical science, the finite element analysis is becoming the more preferred solution. In the area of biomechanics the more complicated clinical cases become possible to be examined, this way supporting the creation of more optimal implants and the faster and more successful recovery of patients.<sup>3-5</sup> In this thesis the different solutions of reconstruction in connection with the mandible resection is examined.

## Methods

Implants are used in the reconstruction of resections. The implant manufacturers possess a large palette of implants that can be used for reconstruction. One of these is a regularly used so called reconstruction plate, which can be found in most of the manufacturers' catalogue with almost the same geometry. To fasten these plates commonly screws are used.

The mandible resections in clinical practice although not easily, but can be categorized into different groups. In reality the same case never occurs twice, however similarities can be found. In this current research the different sections where the cutting planes mostly occur are examined. 4 were highlighted and they were modeled with the help of the cutting planes (*Figure 1*).

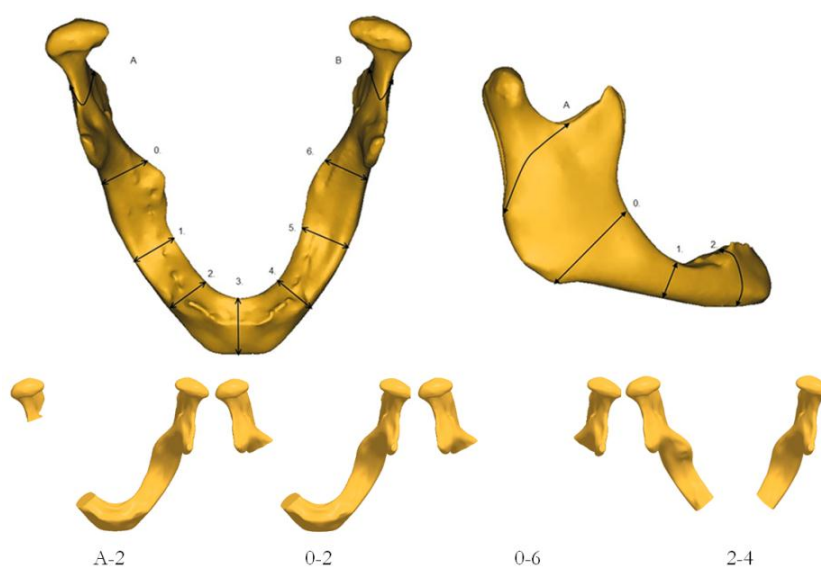


Figure 1. Different resections

Regular reconstruction plates, which can be found at almost every manufacturer, were used with the prepared model in the mechanical reconstruction of the mandible. The plate thickness was set to be 3 mm. The plate lengths used for the resection are always unique to conform to the surgery and to the length of the removed bone section. The plates during the examination were fixed with 3-3 bicortical screws on each resection side. The diameters were 2 mm. The screws were examined with non-lock technology, which is secured by the traditional force-locking connection. In this current research the screws were not examined with the shape-locking lock technology. The material properties of the implants can be seen in the following table (*Table 1*). In case of the examined non-lock technique the pretention of the screws before the chewing load was also considered. Two different screw pretentions were examined in this study.

| MATERIALS             |                     |                                 |         |
|-----------------------|---------------------|---------------------------------|---------|
| Name                  | Young modulus [GPa] | Ultimate Tensile Strength [MPa] | Poisson |
| Plate - pure Titanium | 102                 | 680                             | 0.3     |
| Screws - Ti6Al7Nb     | 105                 | 900                             | 0.33    |

Table 1. Material properties

Realistic geometry was used during the construction of the jaw geometrical model. No simplification was applied. The model was created by the use of CBCT point cloud after the performed layer segmentation. The resection cuts on the mandible that were wished to be examined and the implant models to each case (reconstruction plates and the bicortical screws) were developed and positioned by CAD software (*Figure 2*).

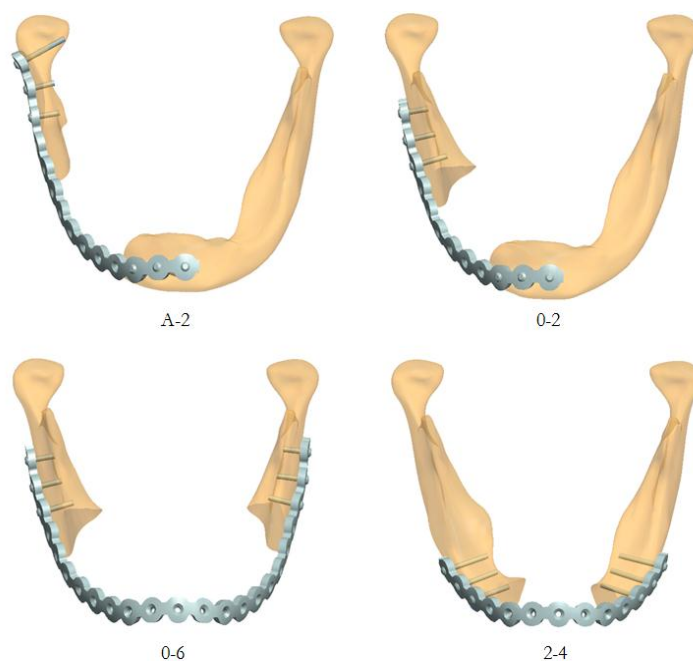


Figure 2. Different cases with implants

The necessary simulation mesh was created by using finite element software. During the mesh 10-node tetra elements were selected. Sub models were created in the area of the screws within the global model to support the refinement of the mesh and the examination of the different

screw geometries. The mandible in the finite element model was applied with heterogeneous material properties to which the CBCT provided the necessary information. From the CBCT density results a mathematical formula was created to connect the material properties. Unique cylinders were made of selected materials and assembled into a plate for validation. Linear regression analysis was used to get correlation between HU value of the cylinders and relative density of the bone. The values of the Hounsfield Unit are known for the different commonly occurring materials in nature, for example distilled water (zero at standard temperature and pressure) and air (-1024 HU). The real material density was determined by the Hounsfield Unit (Equation 1).

$$\text{density } \rho = 1.14264 \cdot \text{HU} + 309.4935 \text{ [g/cm}^3\text{]} \quad (1)$$

According to the written literature there is a connection between the linear elastic modulus and the density, hence the linear elastic modulus scale that reflects the bone structure can be covered (Equation 2). This change between 0-23000MPa.<sup>1,7</sup>

$$E = 0.024 \cdot \rho^{1,777} \text{ [MPa]} \quad (2)$$

The complete range was divided into 100 sections considering the material heterogeneous structure, where the material property can be changed by each tetra element. Next to the heterogeneous structure linearly elastic isotropic material properties were applied. The Poisson coefficient was set to 0.3 in case of the bone.

A cortical layer thickness was possible to be created with this model structure that is closer to reality. It was also very important to create a punctual model in the area of the screws which are used to fasten the reconstruction plates.

During the examination anatomically correct chewing muscle forces were used to describe the load on the mandible. These forces were used in earlier biomechanical researches. The three main applied muscle groups were the masseter, the temporalis and the medial pterygoid (Figure 3, Figure 4).

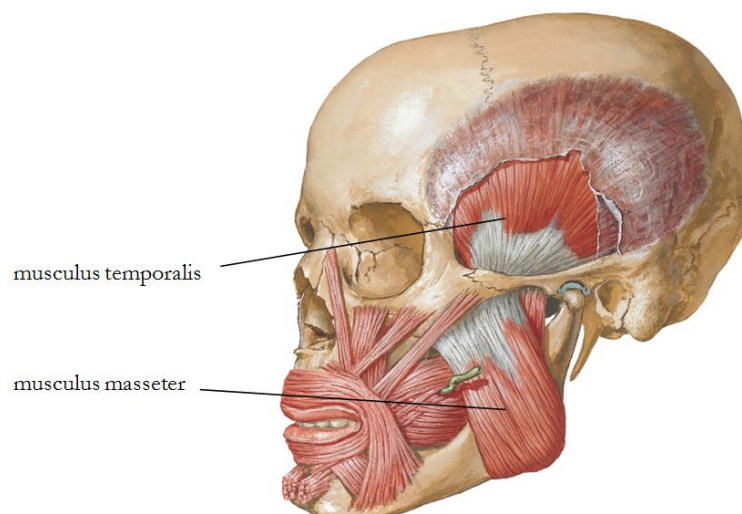


Figure 2. Temporalis and masseter muscles

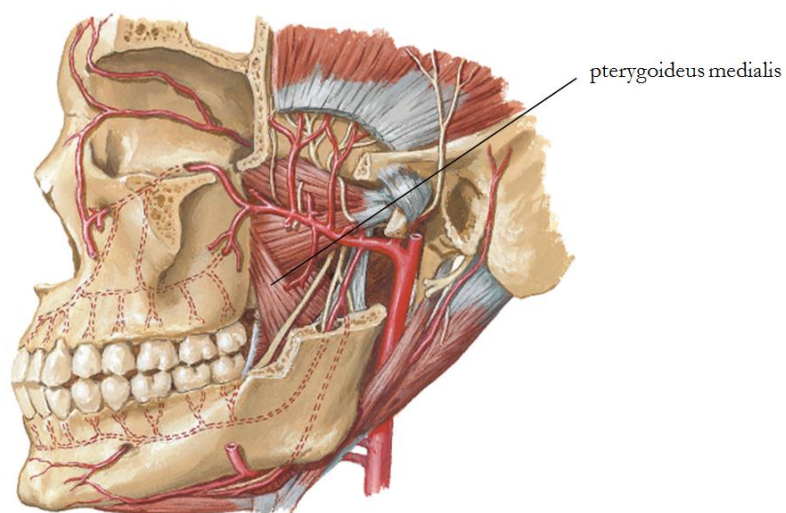


Figure 3. Medial pterygoid muscle

The loads and boundary conditions can be found on the following picture (Figure 5). The load cases in connection with each muscle group can be found in the Table 2.

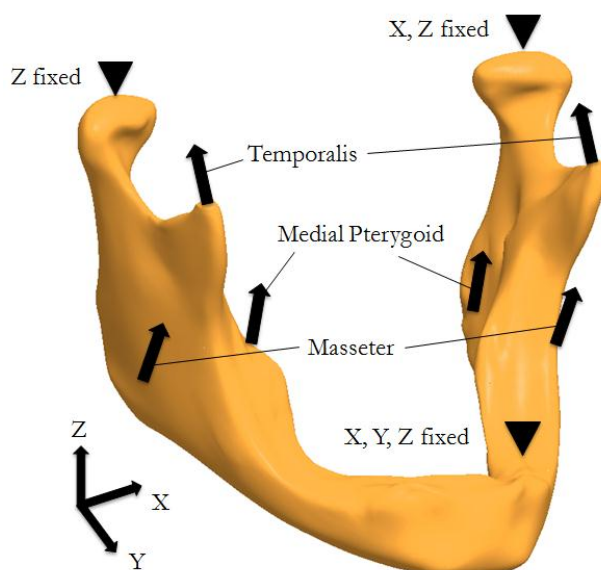


Figure 4. Boundary conditions and loads

| Loads in different directions [N] |     |      |     |
|-----------------------------------|-----|------|-----|
|                                   | X   | Y    | Z   |
| Masseter                          | 50* | 50   | 200 |
| Medial Pterygoid                  | 0   | 50   | 100 |
| Temporalis                        | 0   | -100 | 200 |

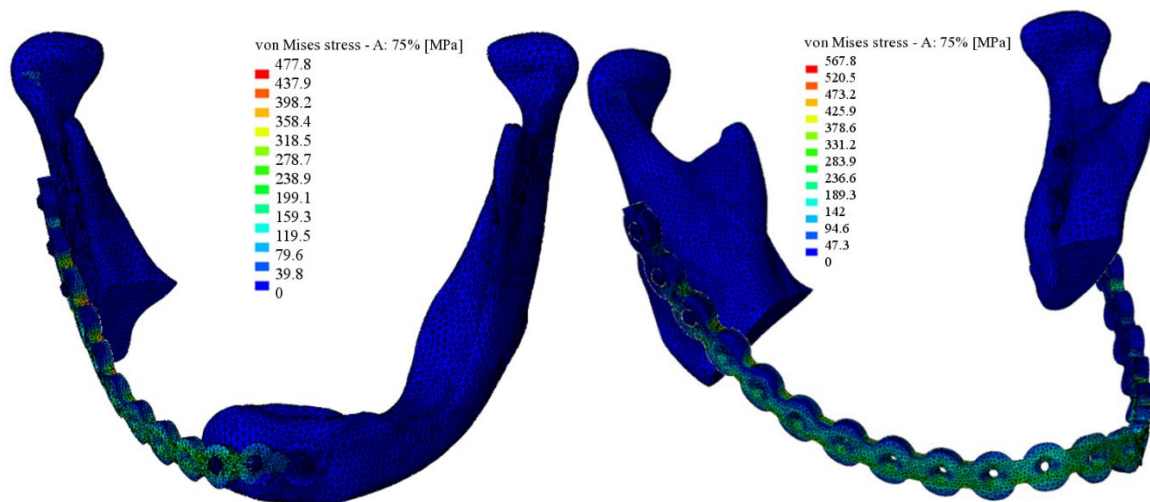
\*The X component is directed away from the mid-sagittal plane.

Table 1. Muscle forces on mandible

In every case between the bone and plates and between the screws and plates friction connections were defined because in the finite element analysis the non-lock cases were modeled. The coefficient is 0.3. [6] Shape-lock method was unable to use because of non-locking system. Force-locking connection was built with pretention force. One of the main focuses of the examination was the evaluation of the pretention force, therefore the finite element model was built up from two steps. In the first step the pretention of the plate is realized. Pretention was built by screw preloading. In the second step the chewing main load is applied. During the pretention of the plate in one case 50N, in the other case 100N preload was defined for every screws in same time. The plate was pushed to the bone by these screws preloading. The pretention was provided this way. Bonded connection was defined between the bone and screws.

## Results

During the evaluation of the results the clinical practice and the previous examination results were also considered. Based on this the bone area of screw number 3 and 4 were specifically alerting. These screws are located closest to the resection. In previous examinations the highest stress arose in these areas, which proves quite convincingly that the screw tear-out effect also occurs there. First step was to collect the stress data while using the pretention forces. In the second step the values while applying the main chewing load were gathered. The von Mises stress of the 0-2 and the 0-6 resection cases can be seen on the next figure (*Figure 6*).



*Figure 5.* 0-2 and 0-6 resection cases, von Mises stress

The selected von Mises stresses were considered with nodal values on each element. The stresses are summarized in the following table (*Table 3*).

| Maximal stress in mandible at 3rd and 4th screwplace |          | 50N PRELOAD |         |         |         | 100N PRELOAD |         |         |         |
|--|----------|-------------|---------|---------|---------|--------------|---------|---------|---------|
|  |          | Step 1      |         | Step 2  |         | Step 1       |         | Step 2  |         |
|  |          | Screw 3     | Screw 4 | Screw 3 | Screw 4 | Screw 3      | Screw 4 | Screw 3 | Screw 4 |
| A-2  | vM [MPa] | 18,3        | 49,1    | 66,7    | 300,1   | 25,6         | 58,9    | 60,5    | 246,2   |
|  | S1 [MPa] | 23,7        | 55,8    | -12,5   | 344     | 32,1         | 67,2    | 73,9    | 281,4   |
|  | S3 [MPa] | 3,9         | 2,5     | -84,38  | 17,37   | 4            | 3,1     | 7,7     | 14,1    |
| 0-2  | vM [MPa] | 16,3        | 53,9    | 109,7   | 70,9    | 23,1         | 65,1    | 128,7   | 45,3    |
|  | S1 [MPa] | 19,6        | 60,6    | 126,9   | 80,4    | 27,7         | 73,6    | 148     | 49,4    |
|  | S3 [MPa] | 2           | 2       | 8,2     | 3,9     | 2,5          | 2,5     | 8,4     | 0,1     |
| 0-6  | vM [MPa] | 11,9        | 10,9    | 97,4    | 136     | 17,3         | 18,8    | 93,3    | 142,1   |
|  | S1 [MPa] | 13,6        | 15,3    | 112,9   | -42,3   | 19,8         | 26,6    | 108,1   | -44     |
|  | S3 [MPa] | 0,5         | 3,7     | 7,6     | -118,4  | 1            | 6,5     | 6,9     | -196,6  |
| 2-4  | vM [MPa] | 13,2        | 17,2    | 78,7    | 75,7    | 21,3         | 24,9    | 63,4    | 59,3    |
|  | S1 [MPa] | 15,2        | 19,5    | -6,8    | 86,6    | 23,6         | 27,7    | 71,3    | 67      |
|  | S3 [MPa] | 0,6         | 0,7     | -90,7   | 4,7     | 0,1          | 0,3     | 2,3     | 2,5     |

Table 2. Stress values

The results are also shown on diagrams (Figure 7 and 8), where the stress difference in case of the use of 50N and 100N pretention force can be seen in each screw position case. It can be observed that in each case of screw number 3, for example A-2 and 0-6, the difference is minimal between the stresses while using the pretention force in the second chewing load. Considering screw number 3 in 0-2 and 2-4 cases the previous statement does not apply as there is a real difference between the arising von Mises stresses. After the main load a significant difference can only be seen in the A-2 case. Further it can be stated that during the main chewing load between 0-2 and 2-4 cases there is no significant stress elevation compared to the pretention. In case of the chewing load the chance of implant tear-out is higher at screw number 3 in 0-2 case and at screw number 4 in A-2 case. This can be concluded from diagrams.

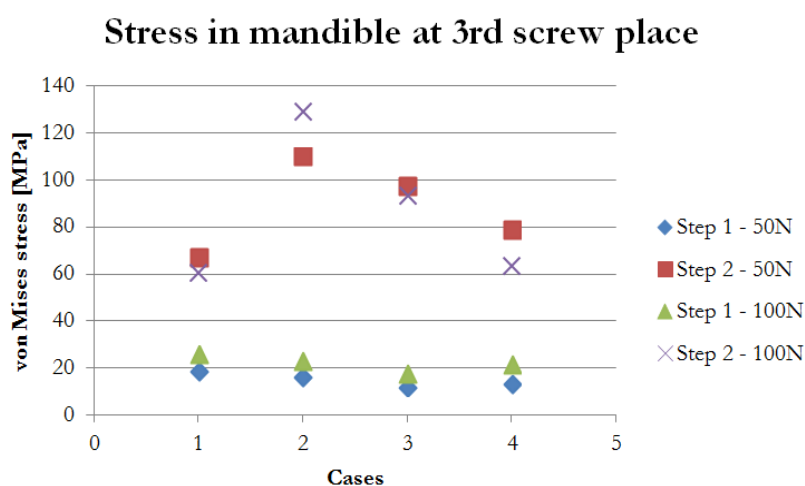


Figure 6. Different von Mises stress values at 3rd screw place

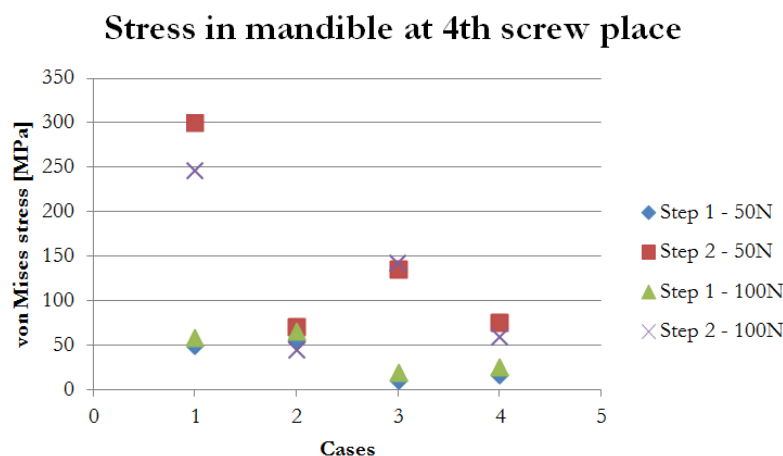


Figure 7. Different von Mises stress values at 4th screw place

The concluded finite element analysis gave the chance to estimate the stress in the areas of the screws in case of bicortical non-lock fastening technique during different resections. The results reflect which are the cases where the chance of screw tear-out is more likely to occur, furthermore in which cases the pretention forces have a higher effect in the arising stresses.

## REFERENCES

1. Bujtar P, Avery C, Simonovics J, Sandor KG, Pan J. Refinements in osteotomy design to improve structural integrity: a finite element analysis study. *The British Journal of Oral & Maxillofacial Surgery* 10/2012; DOI:10.1016/j.bjoms.2012.09.015
2. Avery CME, Best A, Patterson P, Rolton J, Ponter ARS. Biomechanical study of prophylactic internal fixation of the radial osteocutaneous donor site using the sheep tibia model. *Brit J Oral Maxillofac Surg.* 2007;45:441-6.
3. Simonovics J, Bodzay T, Váradi K. Study and examination of the implements used for securing pelvis bone. *Biomechanica Hungarica III* 2010;(1):215-23.
4. Bagi I. Finite element study of some parameters of bone fractures fixed with screws. *Periodica Polytechnica – Mechanical Engineering* 2011;55(1):57-61.
5. Lakatos É, Bojtár I. Stochastically Generated Finite Element Beam Model for Dental Research, *Periodica Polytechnica Ser. Civ. Eng.*, 2009;53(1):3–8.
6. Shirazi Adl A, Dammak M, and Paiement G, Experimental determination of friction characteristics at the trabecular bone/porous coated metal interface in cementless implants. *Journal of biomedical materials research*, 1993;27(2):167-75.
7. Keller, T.S., Predicting the compressive mechanical behavior of bone. *Journal of Biomechanics*, 1994;27(9):1159-68.

*I would like to thank Péter Mészáros for his help and support.*



## THE NEW PROCESSING OF THE RESULTS OF EXAMINATIONS MADE WITH ZEBRIS WIN-SPINE SPINE-MEASURING METHOD AND ITS VALIDATION

Mária Takács<sup>1</sup>, Ervin Rudner<sup>1</sup>, Ildikó Nagy<sup>1</sup>, Mihály Jurák<sup>2</sup>, Rita M. Kiss<sup>3</sup>, László Kocsis<sup>4</sup>

<sup>1</sup>MÁV Hospital Department of Orthopaedics

<sup>2</sup>Budapest University of Technology and Economics

<sup>3</sup>Department of Structural Engineering, Budapest University of Technology and Economics

<sup>4</sup>EDUTUS College

[drtakacsmaria@freemail.hu](mailto:drtakacsmaria@freemail.hu)

---

### Abstract

**Aim:** The Zebris spine-examination system and the associated measurement control program determine the spatial coordinates of processus spinosus. Our processing program calculates kyphosis, lordosis and scoliosis values from the measurement data similarly to Cobb method. The aim of our research is to clarify whether the angle values determined from the X-ray results of young schoolchildren suffering from scoliosis by Cobb method differ from the values calculated from the spatial coordinates of processus spinosus.

**Methods:** In the case of 25 children suffering from scoliosis two-way full spine X-rays in standing position on 31 occasions were taken, in accordance with the professional standards. On the basis of the photographs the thoracic kyphosis, lumbar lordosis and scoliosis values were determined with Cobb method. While the children were in standing position, ultrasound-based spine examinations were performed with a WINSPINE measuring software developed specially for the Zebris CMS-HS measuring system.

From the spatial coordinates of processus spinosus the same angle values with our self-developed Excel processing program according to the principles of Cobb method were calculated. The degree of scoliosis was evaluated in the dorsal and in the lumbar section separately. The relationship between the two measurements was indicated by the Pearson correlation.

**Results:** From the comparison of the results of the two different measurement methods it was concluded that the correlation was strong between the values of the dorsal kyphosis and the lumbar lordosis ( $r_{\text{kyphosis}}=0.80$   $r_{\text{lordosis}}=0.94$ ) while the correlation between the scoliosis values of the dorsal and lumbar sections was moderate ( $r_{\text{thoracic scoliosis}}=0.67$   $r_{\text{lumbar scoliosis}}=0.73$ ).

**Conclusion:** The sagittal curvatures calculated with our self-developed software from the spatial coordinates of processus spinosus which were determined with the CMS-HS ultrasound-based motion analysing system, show a strong correlation with the values calculated from X-rays using Cobb technique. The accurate assessment of the degree of scoliosis can only be done with an X-ray. Values defined with motion analysing measurements without exposure to radiation in the terms between X-rays performed regularly as specified in the professional recommendations can give satisfactory information about the possible trend of changes.

**Keywords:** children, spine, posture, ultrasound-based motion analysing system, Zebris.

---

## **Introduction**

A frequently asked question in paediatric orthopaedics is how can be evaluated the spinal curvatures quantitatively in children who suffer from postural disorders or scoliosis. To determine the shape and the curves of the spine an X-ray is required. It is a priority to protect the young, growing organism against X-ray radiation<sup>1</sup>. Many efforts have been made to use low radiation to follow the changes in the shape of the spine, such as the ultra-low dose 2D/3D digital X-ray system<sup>2</sup> or the 3D freehand ultrasound system<sup>3</sup> developed from the traditional ultrasound measuring system. The biggest disadvantage of the latter is that the examined subject is in a lying position so the examination does not provide information about the posture in a natural standing position. Vrtovec and his colleagues examined devices suitable for taking X-rays with exposure to low radiation and they discovered that their accuracy is not worse than the accuracy of the traditional devices<sup>4</sup>. To reduce or to completely avoid X-ray radiation, the use of various motion analysing systems is becoming more and more common. They are used to determine the curvatures of the spine and to monitor the effectiveness of the therapy. During the measurement procedures the processus sensors are placed on the skin above the processus spinosus to determine their spatial position (Fastrack, CA6000)<sup>5,6</sup>. From these spatial coordinates the curvatures of the spine can be seen and also the mobility of each spine section can be calculated<sup>7,8</sup>. The advantage of these examination methods is that they can be used in motion, too. Their disadvantage, however, is that the sensors on the body also record the skin movements, the sensors can move away when the skin is sweaty and they can influence or alter the motion as well. Today sensing systems which are not attached to the spine but scrolled over or touched to the processus spinosus (Spinal Mouse, kyphometer, goniometer and inclinometer)<sup>9,10,11,12,13,14,15</sup> are also available. One of the disadvantages of these systems and of their softwares is that the curvatures of the spine are not calculated according to the radiological Cobb method used in routine medical practice. The Zebris CMS-HS system and the WINSPINE software which was specially developed for this system fall into this category. Scoliosis is one of the most complex spinal deformities, as it can cause pathological curvatures in all three planes (sagittal, frontal and horizontal). The treatment is mostly conservative therapy which includes long-term physiotherapy, Schroth exercises and the wearing of a corset. If the curvature is severe (over 45-50 Cobb degrees), corrective surgery with conservative therapy before and after the operation may be needed. Concerning spinal deformities the rapid growth period in puberty requires special attention. In females between the ages of 10-14 years and males between the ages of 12-16 years the progression of scoliosis may be expected<sup>16</sup>. When the bone growth is complete there is little chance for deterioration. To set up a diagnosis we use X-ray (Rissel sign). Besides a lateral X-ray, which is used nowadays to diagnose scoliosis, also antero-posterior X-ray photographs help to determine the Cobb degree of lordosis and kyphosis. For screening mild cases, however, X-ray can be used for very strong professional reasons only, but in case of bad posture where there is no frontal deformity it cannot be used at all. After the diagnosis of scoliosis, during the monitoring of the effectiveness of the therapy it is necessary to make an effort to use non-invasive devices. The aim of our study was to define how much the spinal curvatures – which were calculated with our self-developed software from the spatial coordinates of the processus spinosus measured with Zebris ultrasound-based motion analysing system – differ from the curvature values determined with the Cobb method on X-rays. In this research the correlation of dorsal kyphosis, lumbar lordosis and scoliosis determined in a standing position was calculated.

## Material and methods

### Subjects

In the Orthopaedic Department of MÁV Hospital, Szolnok several children suffering from spine deformities were examined but the ultrasound based and X-ray examinations were carried out only in 25 scoliosis cases at the same time. Comparative examinations were made after half a year and after one year in 6 further cases in the group. The patients' parents had always received detailed verbal and written information before they filled the consent form. The average age of the 12 male subjects was  $9.2 \pm 1.4$  years, the average height was  $135.8 \pm 7.1$  cm and the average weight was  $30.1 \pm 4.2$  kg. The average age of the 19 female subjects was  $9.5 \pm 1.3$  years, the average height was  $140.1 \pm 8.5$  cm and the average weight was  $33.5 \pm 6.6$  kg.

### Methods

#### 1. X-ray examination

The traditional X-ray images were taken in a natural standing position. Antero-Posterior (A-P) and lateral radiographs were taken about the whole spine.

#### 2. Zebris Ultrasound-based spinal examination

In the Biomechanics Laboratory of MÁV Hospital, Szolnok the shape of the spine in a natural standing position was measured with a Zebris CMS-HS ultrasound-based motion analysing system (Zebris Medizintechnik GmbH, Isny, Germany). The system consists of

- a head which emits ultrasound pulses from three transmitters,
- a triplet consisting of three ultrasound microphones to screen the movements of the spine
- a pointer stick with two ultrasound microphones

The three transmitters of the head send ultrasound pulses at regular intervals which are recorded by the microphones (the measurement frequency is 100 Hz). If the temperature is known, from the speed and running time of the ultrasound the distance from the microphones to the transmitters can be calculated. By triangulation the spatial coordinates of the microphones can be determined in every minute during the measurement from the spatial coordinates of the head's markers and from the distance between the markers and the microphones. This calculation can be performed for every microphone. The WINSPINE measuring software (Zebris Medizintechnik GmbH, Isny, Germany) records and stores the spatial coordinates of the microphones numerically and the spatial coordinates of the processus spinosus are calculated from these coordinates.

The steps of the examination (*Figure 1*):

1. Placing the triplet consisting of three miniature ultrasound microphones on the patient's pelvis. Connecting the triplet and the pointer stick to the central unit with special cables (a).

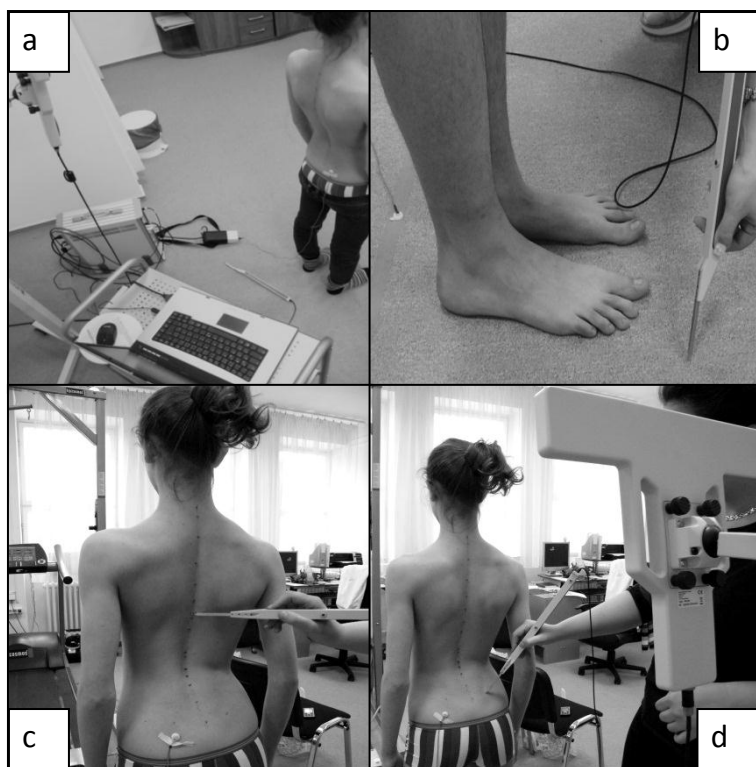


Figure 1. The steps of the examination

2. Placing the subject in front of the measuring head with his back towards the machine. It is necessary to pay special attention to the correct posture when children are the subjects: shoulders must be lowered, flat scapulas must be held close to each other.
3. Calibration: measuring of the global coordinate system with the pointer (b).
4. Marking of certain anatomic points on both sides of the body (acromion, angulus inferior scapulae, spina iliaca posterior superior) and the determination of the point between the thoracic XII. and the lumbar I. vertebrae.
5. Recording the shape of the spine: guiding the pointer over the processus spinosus from the cervical VII. vertebrae to the sacral I. vertebrae.

### Characteristics and statistical analysis

#### 1. X-ray characteristics

Cobb method was used to evaluate the A-P and lateral curvatures. On the lateral radiographs the degree of the thoracic kyphosis was calculated as the supplementary angle of the perpendicular lines placed on the upper closing membrane of the thoracic I. and on the lower closing membrane of the thoracic XII. vertebrae. The lordosis between L1 and L5 was also determined using Cobb angles with the same method. On antero-posterior X-ray images the supplementary angles of the perpendicular lines placed on the two closing membranes of the vertebrae at the ends of the curvature which gave both the degree of the thoracic and that of the lumbar scoliosis was determined.

#### 2. Data of Zebris ultrasound-based motion analysing system

The spatial position of the processus spinosus was calculated with the Zebris CMS-HS ultrasound-based measuring system and its WINSPINE measurement control program. The further processing was made with the self-developed Excel-based processing program.

To determine the thoracic and lumbar curvature we used coordinates from the sagittal plane (x-z plane) (Figure 2):

- the angle of thoracic kyphosis in the sagittal plane is the differences between the angle formed by the straight line placed on the processus spinosus of the thoracic vertebrae I. and II. and the vertical line and the angle formed by the straight line placed on the processus spinosus of the thoracic vertebrae XI. and XII. and the vertical line.
- the angle of lumbar lordosis in the sagittal plane is the difference between the angle formed by the straight line placed on the processus spinosus of the lumbar vertebrae I. and II. and the vertical line and the angle formed by the straight line placed on the processus spinosus of the lumbar vertebrae IV. and V. and the vertical line

The angle of the scoliosis was determined in the frontal plane (y-z plane) and so we used only coordinates of this plane (Figure 3):

- The degree of thoracic scoliosis is the angle formed by the straight line placed on the processus spinosus of the thoracic vertebrae I. and II. and by the straight line placed on the processus spinosus of the thoracic vertebrae XI. and XII.
- The degree of lumbal scoliosis: the angle formed by the straight line placed on the processus spinosus of the lumbar vertebrae I. and II. and by the straight line placed on the processus spinosus of the lumbar vertebrae IV. and V.

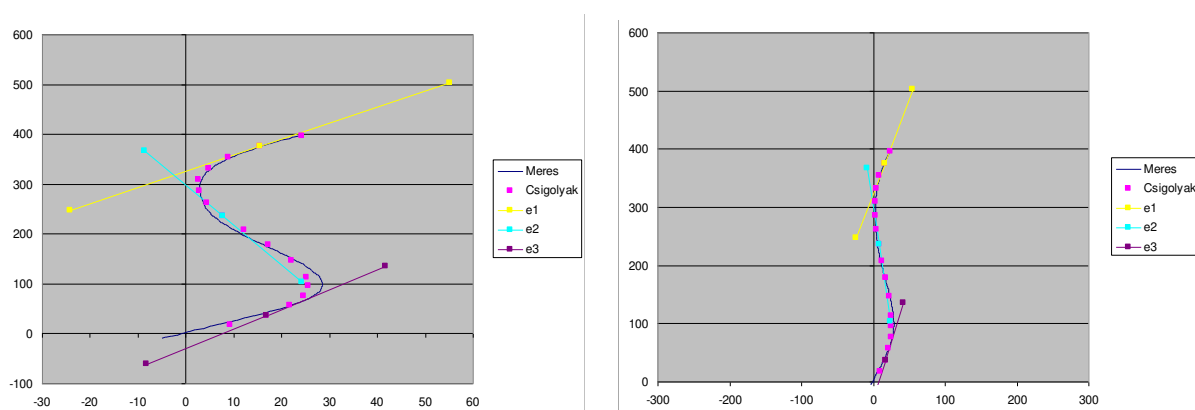


Figure 2. Spine posture in the sagittal plane non-scaled (left) and scaled (right)

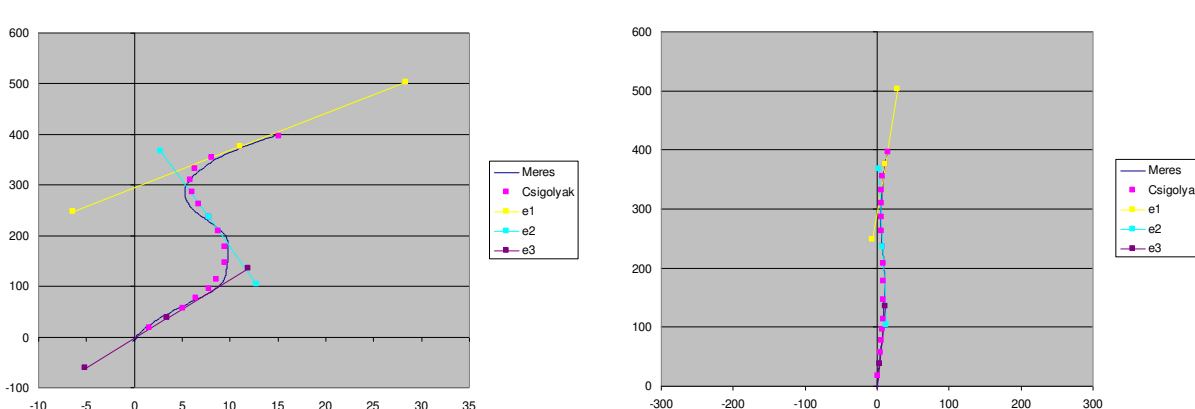


Figure 3. Spine posture in the frontal plane non-scaled (left) and scaled (right)

## Statistical analysis

In the case of every subject the thoracic kyphosis, lumbar lordosis, thoracic and lumbar scoliosis were determined by both methods. From the results the means, standard deviations (SD) and the maximum and minimum values of the groups were calculated. From the calculated data the Pearson correlation coefficient ( $r$ ), the gradient of the regression line ( $m$ ) were determined with linear regression and the significance level was calculated by one-sample t-test. The statistical analysis was made with Microsoft Excel 2003.

## Results

From the spatial coordinates of the subjects' processus spinosus which were measured on the radiographs and were determined with the WINSPINE with Excel processing software we calculated the angles' means, standard deviations, minimum and maximum values as it is shown in *Table 1*. The results of the statistical analysis are shown in *Table 2*.

|                    |                   | mean $\pm$ SD     | minimum | Maximum |
|--------------------|-------------------|-------------------|---------|---------|
| Thoracic kyphosis  | X-ray Cobb degree | 34.58 $\pm$ 6.76  | 20.0    | 50.0    |
|                    | Excel             | 33.48 $\pm$ 5.45  | 21.9    | 42.9    |
| Lumbar lordosis    | X-ray Cobb degree | 32.84 $\pm$ 10.17 | 10.0    | 50.0    |
|                    | Excel             | 27.75 $\pm$ 8.95  | 12.2    | 45.5    |
| Scoliosis Thoracic | X-ray Cobb degree | 6.55 $\pm$ 4.41   | 0.0     | 15.0    |
|                    | Excel             | 5.35 $\pm$ 3.88   | 0.1     | 16.1    |
| Scoliosis Lumbar   | X-ray Cobb degree | 7.81 $\pm$ 4.87   | 0.0     | 20.0    |
|                    | Excel             | 7.43 $\pm$ 5.28   | 0.5     | 22.0    |

*Table 1.* The mean $\pm$ standard deviation (SD), minimum and maximum values were calculated with the two different methods in sagittal (thoracic kyphosis, lumbar lordosis) and in frontal plane (scoliosis thoracic, scoliosis lumbar)

|          | Thoracic Kyphosis<br>(Cobb degree-<br>Excel) | Lumbar Lordosis<br>(Cobb degree-<br>Excel) | Scoliosis<br>deformation<br>(Thoracic)<br>(Cobb degree-<br>Excel) | Scoliosis<br>deformation<br>(Lumbar)<br>(Cobb degree-<br>Excel) |
|----------|--|--|---|---|
| <b>r</b> | 0.80   | 0.94                                       | 0.67  | 0.73  |
| <b>m</b> | 1.00   | 1.07                                       | 0.77  | 0.67  |
| <b>p</b> | 0.07   | 0.00                                       | 0.03  | 0.29  |

*Table 2.* The values of the correlation coefficient ( $r$ ), the gradient of the regression line ( $m$ ) and the significance level ( $p$ ) at kyphosis, lordosis, thoracic scoliosis and lumbar scoliosis, calculated with the two measuring methods

By comparing the results of the two measuring methods the conclusion is that the correlations between the thoracic kyphosis and the lumbar lordosis values are good ( $r_{\text{kyphosis}}=0.80$ ;  $r_{\text{lordosis}}=0.94$ ) which is confirmed by the gradients of the regression lines ( $m_{\text{kyphosis}}=1.00$ ;  $m_{\text{lordosis}}=1.07$ ). The correlations between thoracic scoliosis and lumbar scoliosis values are

medium ( $r_{\text{thoracic scoliosis}} = 0.67$ ;  $r_{\text{lumbar scoliosis}} = 0.73$ ) (Table 1. and 2.), which is confirmed by the gradients of the regression lines ( $m_{\text{kyphosis}} = 1.00$ ;  $m_{\text{lordosis}} = 1.07$ ).

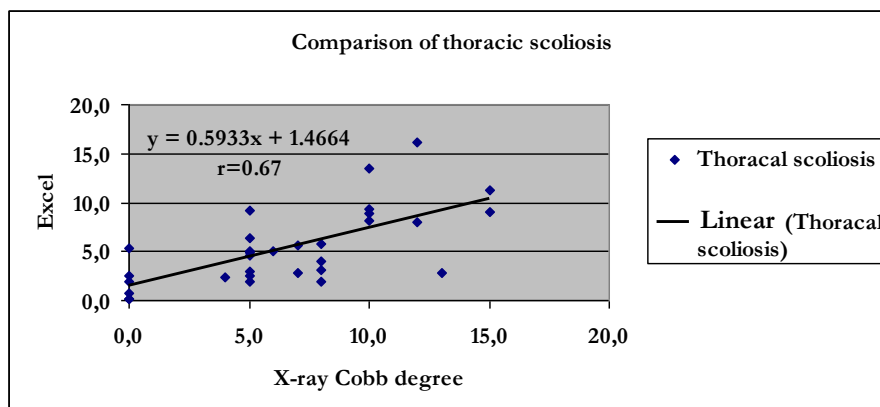


Figure 4. Comparing the thoracic scoliosis values of the two methods

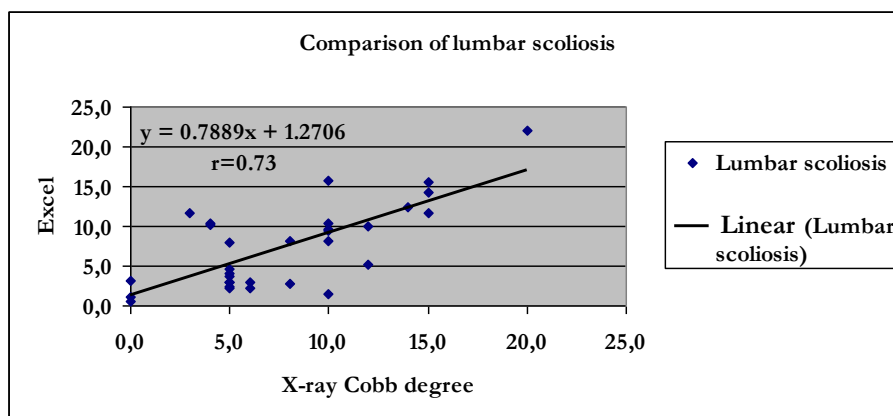


Figure 5. Comparing the lumbar scoliosis values of the two methods

## Discussion

Viola and his colleagues<sup>18</sup> concluded from an examination of 25 girls suffering from AIS (Adolescent Idiopathic Scoliosis) that the Cobb degree for measuring the degree of scoliosis and the angle formed by the processus spinosus and defined by Zebris WIN-SPINE show a strong correlation in the frontal plane both in the thoracic and at the lumbar sections. When they evaluated the results, however, they did not mention the sagittal curvatures<sup>18</sup>. In our study we were able to assess the degree of thoracic kyphosis and lumbar lordosis on lateral radiographs of children suffering from scoliosis. In our study the angles set by the Cobb method on radiographs with the angles determined with the self-developed Excel software from the processus spinosus defined with Zebris WINSPINE were compared. The results of the two measurement methods are close to identical in the sagittal plane in kyphosis and lordosis because the correlation is strong and the gradient of the regression line is around 0.7 (Figure 4 and 5). The comparison of X-ray images was only possible in patients suffering from scoliosis. The results showed that scoliosis induces deformities of the spine in all three dimensions but still the curvatures measured in the different dimensions are almost identical when we compare the results of the two methods.

Therefore, we assumed that in daily orthopaedic practice the Zebris motion analyzing system and our self-developed Excel processing software together are useful for the follow-up of the effectiveness of conservative therapy in children with bad posture and in children suffering from deformities in the sagittal plane caused by Scheuermann's disease. Because of the medium correlation found in frontal curvatures the diagnosis of scoliosis and the annual health check must be based on X-ray in the future too, in accordance with the recommendations of the Orthopaedic Advisory Board, but in the intervals the Zebris motion analysing system with the self-developed Excel processing software can be used to estimate the degree of scoliosis.

---

## REFERENCES

1. Doody MM, Lonstein JE, Stovall M, Hacker DG, Luckyanov N, Land CE. Breast cancer mortality after diagnostic radiography: findings from the U.S. Scoliosis Cohort Study. *Spine* 2000;25(16):2052-63.
2. Somoskeöy S, Tunyogi-Csapó M, Bogyó C, Illés T. Accuracy and reliability of coronal and sagittal spinal curvature data based on patient-specific three-dimensional models created by the EOS 2D/3D imaging system. *Spine J.* 2012;12(11):1052-9.
3. Purnama KE, Wilkinson MH, Veldhuizen AG, van Ooijen PM, Lubbers J, Burgerhof JG, Sardjono TA, Verkerke GJ. A framework for human spine imaging using a freehand 3D ultrasound system. *Technol Health Care* 2010;18(1):1-17.
4. Vrtovec T, Pernus F, Likar B. A review of methods for quantitative evaluation of spinal curvature. *Eur Spine J.* 2009;18(5):593-607.
5. Mannion A, Troke M. A comparison of two motion analysis devices used in the measurement of lumbar spinal mobility. *Clin Biomech* 1999;14(9):612-9.
6. Petersen CM, Johnson RD, Schuit D, Hayes KW. Intraobserver and interobserver reliability of asymptomatic subjects' thoracolumbar range of motion using the OSI CA 6000 Spine Motion Analyzer. *J Orthop Sports Phys Ther.* 1994;20(4):207-12.
7. Schuit D, Petersen C, Johnson R, Levine P, Knecht H, Goldberg D. Validity and reliability of measures obtained from the OSI CA-6000 Spine Motion Analyzer for lumbar spinal motion. *Man Ther.* 1997;2(4):206-215.
8. Troke M, Moore AP, Maillardet FJ, Hough A, Cheek E. A new, comprehensive normative database of lumbar spine ranges of motion. *Clin Rehabil.* 2001;15(4):371-9.
9. Mannion AF, Knecht K, Balaban G, Dvorak J, Grob D. A new skin-surface device for measuring the curvature and global and segmental ranges of motion of the spine: reliability of measurements and comparison with data reviewed from the literature. *Eur Spine J.* 2004;13(2):122-36.
10. Ripani M, Di Cesare A, Giombini A, Agnello L, Fagnani F, Pigozzi F. Spinal curvature: comparison of frontal measurements with the Spinal Mouse and radiographic assessment. *J Sports Med Phys Fitness.* 2008;48(4):488-94.
11. Van Herp G, Rowe P, Salter P, Paul JP. Three-dimensional lumbar spinal kinematics: a study of range of movement in 100 healthy subjects aged 20 to 60+ years. *Rheumatology (Oxford).* 2000;39(12):1337-40.
12. Salisbury PJ, Porter RW. Measurement of lumbar sagittal mobility. A comparison of methods. *Spine* 1987;12(2):190-3.



13. Stokes IA, Bevins TM, Lunn RA. Back surface curvature and measurement of lumbar spinal motion. *Spine* 1987;12(4):355-61.
14. Tillotson KM, Burton AK. Noninvasive measurement of lumbar sagittal mobility. An assessment of the flexicurve technique. *Spine* 1991;16(1):29-33.
15. Zuberbier OA, Kozlowski AJ, Hunt DG, Berkowitz J, Schultz IZ, Crook JM, Milner RA. Analysis of the convergent and discriminant validity of published lumbar flexion, extension, and lateral flexion scores. *Spine* 2001;26(20):E472-8.
16. Busscher I, Wapstra FH, Veldhuizen AG. Predicting growth and curve progression in the individual patient with adolescent idiopathic scoliosis: design of a prospective longitudinal cohort study. *BMC Musculoskelet Disord.* 2010;11:93.
17. Tanure MC, Pinheiro AP, Oliveira AS. Reliability assessment of Cobb angle measurements using manual and digital methods. *Spine J.* 2010;10(9):769-74.
18. Viola S, Szoke G, Kocsis L, Körmendi Z, Zsidai A. Kinesiological examination in AIS. *Orv Hetil.* 2007;148(6):259-63.

***The authors gratefully acknowledge the Hungarian Scientific Research Fund OTKA for providing financial support in the frame of the grant K-075018.***

## THE FIRST STEPS TO THE DEVELOPMENT OF THE KNEE PROSTHESIS RATING METHOD

Béla M. Csizmadia, Gábor Péter Balassa, Gábor Katona

Department of Mechanics and Engineering Design, Faculty of Mechanical Engineering, Szent István University

[csizmadia.bela@gek.szie.hu](mailto:csizmadia.bela@gek.szie.hu)

### Abstract

During prosthesis implantation, the surgeon can choose from replacements of a wide variety of manufacturers and sizes. So far, no specific coefficient has been introduced that determines the suitability, or goodness of these prostheses. In this paper an apparatus is presented for the qualification of knee prostheses. This apparatus is able to measure the rotation of any prosthesis, therefore the obtained results can be compared with the measured values on human cadaver knees. The prostheses are classified by the rate of their conformity. In addition, the first experimental results are reported as well.

**Keywords:** biomechanics, knee, prosthesis.

### Introduction: when is a prosthesis suitable?

Surgeons have a wide range of choice regarding the brands and sizes of knee replacements, although there are no specific numbers indicating the quality or goodness of the applicable prostheses. However, what factors determine the quality of prosthesis? Definitely not the similarity of the prosthesis surfaces compared to the physiological surfaces, but the ability of the replacement to ensure closely the same kinematics compared to the original, physiological knee joint.

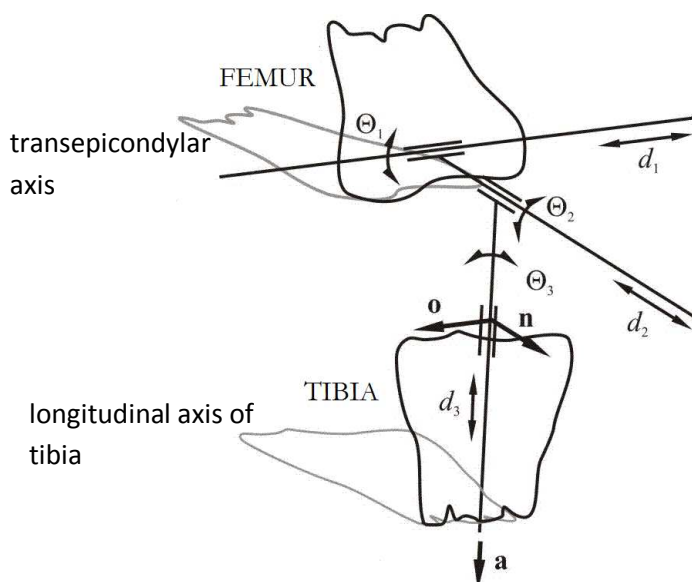


Figure 1. Three-cylindrical mechanism<sup>1</sup>

Naturally, the wear due to the sliding-rolling relationship<sup>2</sup> between the condyles along with the material properties of the prostheses are also essential, but this article deals exclusively with the

qualification of the reproduced movement. During the movement of the knee joint, the flexion can be controlled while the other movements (rotation, abduction, etc) *are constrained by the connection of the condyles*. Among the constrained movements the main emphasis is set on the magnitude and trend of the rotation, since its correspondence between the original and reproduced motion has the most importance.

## Methods and materials

In order to estimate the goodness of the obtained rotation-functions regarding the prostheses, a basis rotation has to be defined. The research group carried out several experiments on cadavers in the past years. For these experiments, a special test rig has been designed<sup>3</sup> and manufactured which allows carrying out measurements on multiple kinematical quantities. Among others, the rotation of the tibia – carried out by its self-weight – was measured as a function of flexion angle. Taking into consideration the numerous measurements carried out on human cadavers and the results found in the literature<sup>4</sup> (with significant deviations), it has been concluded that the flexion-rotation functions depend on several parameters. They naturally depend on the investigated person (we examined in each case non-pathological knees), the type of the movement, the test rig, the examination method, the data acquisition system and significantly on the processing method. In case of the latest one, the positioning of the model and the reference system has crucial significance. The model was described by a three-cylindrical mechanism, with six degrees of freedom (*Figure 1*). In our case, the movements were related to an anatomical coordinate-system<sup>4</sup>.

On the basis of our experiments, which were carried out on 28-60 years old male subjects according to the same protocol<sup>5</sup>, an averaged flexion-rotation curve has been determined (*Figure 2*). The protocol included the processing method as well. This function was considered as a *reference function*. As it is seen in *Figure 2*, the function was approximated with a tri-linear function. The segments of the function – with moderate freedom – were determined based on the carried out movement. In the first 25° segment, the movement is constrained, while the following 25° segment is considered as a transition towards unconstrained rotation (presumed from the trend of the measurements), which is definitely possible above 50° of flexion angle.

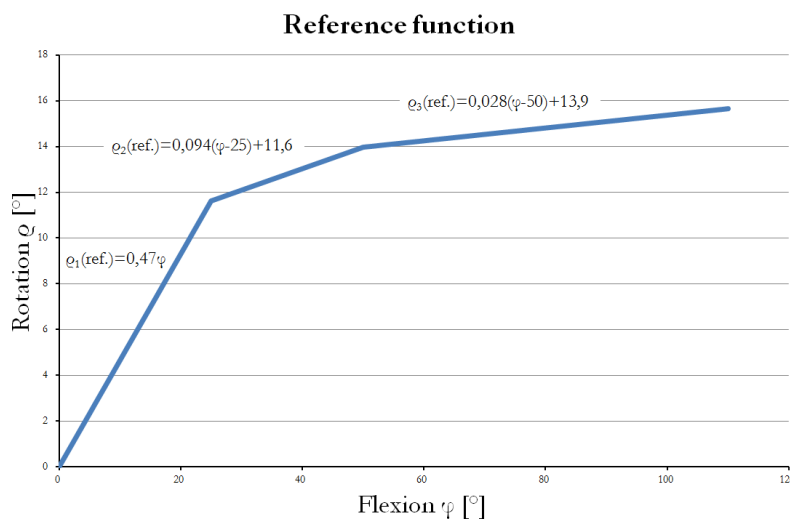


*Figure 2.* The reference function

The aim of the research is to create a test rig which is able to qualify the kinematics of prostheses, based on the above mentioned reference-function comparison. For this reason the concept of the design was carried out in a way that the test rig, together with the measuring – and processing method – for the sake of an adequate comparison – would be identical with the reference-function determined by cadaver and prosthesis experiments.

## Results and discussion

### Description of the test rig

The first condition is that the qualification device has to be the part of the test rig (*Figure 3*). This ensures that during the flexion of the knee joint, which is controlled by the quadriceps under the effect of self-weight, the same type of movement can be compared. The magnitude and the change of load (1) alongside with the bending mechanism of the joint is the same regarding the test rig for cadaver- or prosthesis measurements. The load is transmitted through a rubber-muscle model<sup>3</sup>, while the movement is exerted by a force applied on the end of the tibial bone. The test rig has been complemented by a stepper motor (2), which allows the knee to be flexed beyond 70-80° of flexion angle. The test rig is designed in a way that the tibial shaft (or cadaver) can carry out unconstrained movement. This feature is in essential since the movement has to be controlled only by the quadriceps, the self-weight and the condyle surfaces. The unconstrained movement was secured by the use of bushing- and planar bearings (3). The flexion was controlled by a curved rail (4) and the movement was performed along with it.

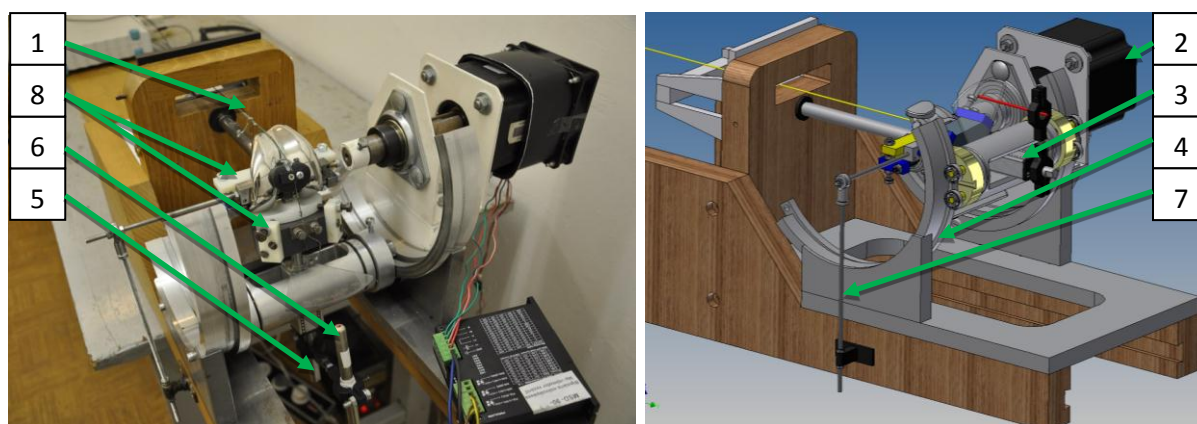
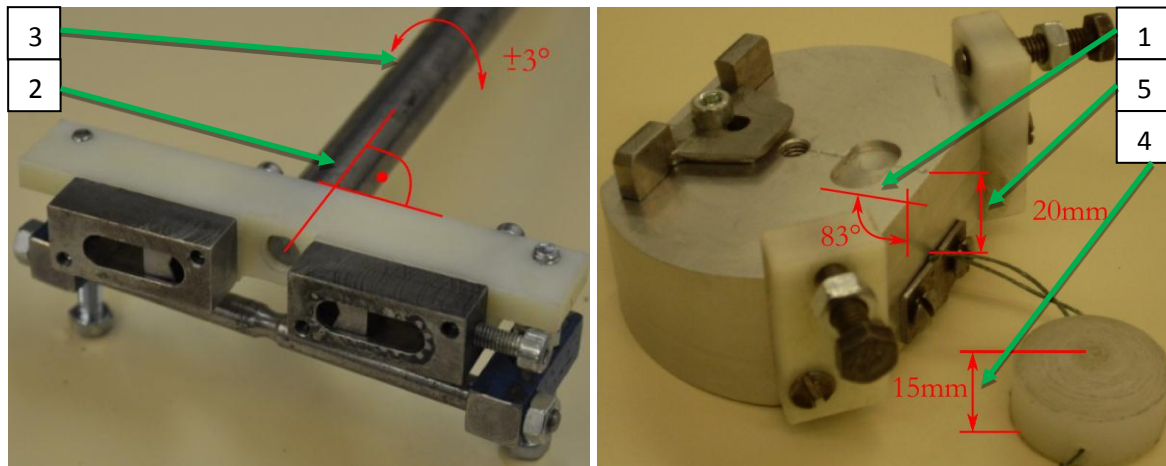


Figure 3. Test rig for prosthesis qualification

In order to make a fair comparison between the cadaver and prosthesis movement, the measuring device and the processing method has to be identical respectively to the aims. The rotation was directly measured on the test rig by a laser (6). The tibia plateau part of the prosthesis was attached to the tibial model (5), which represents the direction of the medullary cavity or canal (contains bone marrow). In the interest of having identical rotation measurements with respect to the cadaver results, the reference-system has to be also identical in both cases. The anatomical coordinate system can only be determined in case of cadavers by a rather complex method<sup>5</sup>. With regard to prostheses, the surgeon performs the prosthesis implantation in way that the replacement condyles would precisely connect to the patient's anatomical system. This process is supported by certain assisting tools and a strict protocol. Based on the analysis of this certain protocol, and the consultation of Dr. Kristóf Andrónyi surgeon, the prostheses were

inserted into the test rig that their „condyles” would be correctly positioned with respect to the anatomical coordinate-system. This ability of the test rig is provided by a special fixture system (8), which ensures the upcoming new conditions during the insertion as well (*Figure 4*).



*Figure 4.* The special fixture system

During our investigations, a condition-system had to be fulfilled which was pre-defined during the insertion of the prosthesis. This process was ensured by a universal fixture system (*Figure 4*) and the correctly set test rig, as follows:

- Tilt of tibia plateau to  $7^\circ$  (*Figure 4*) (1). This is secured by the tibial fixture of the test rig,
- The femoral component of the prosthesis fixed into the test rig is at a  $90^\circ$  angle relative to the axis of femur (*Figure 4*) (2), therefore the anatomical angle is ensured. As the prosthesis is inserted into the test rig, the femur is adjusted from the mechanical axis to the anatomical axis by performing  $5^\circ$  of tilt and creating perpendicularity between the femoral component and the anatomical axis,
- Setting the adequate rotation (*Figure 4*) (3).  $3^\circ$  of femoral component tilt in the lateral direction respectively to the left or right leg.

Additional settings on the test rig with regard to the anatomy of the leg:

- The point of action of the quadriceps force is approximately situated at 15 mm (4) of height (*Figure 4*),
- Line of action of quadriceps: the line of action has  $5^\circ$  of lateral difference compared to the femoral axis with regard to a right-legged or left-legged prosthesis (*Figure 3*) (1),
- Quadriceps tendon attachment on the tibia is situated 20 mm away from the resection (*Figure 4*) (5).

An additional calibrating device (*Figure 3*) (7) had to be designed and manufactured as well, to adjust the rotation to zero with the use of a hinge-type, „cylindrical” prosthesis.

The test rig is able to qualify prostheses in different size, brand, independently from additional features such as cruciate-retaining (CR) or posterior-stabilizer (PS). As initial steps in this research, measurements were performed on seven prostheses of different size, brand and type (*Figure 5*).

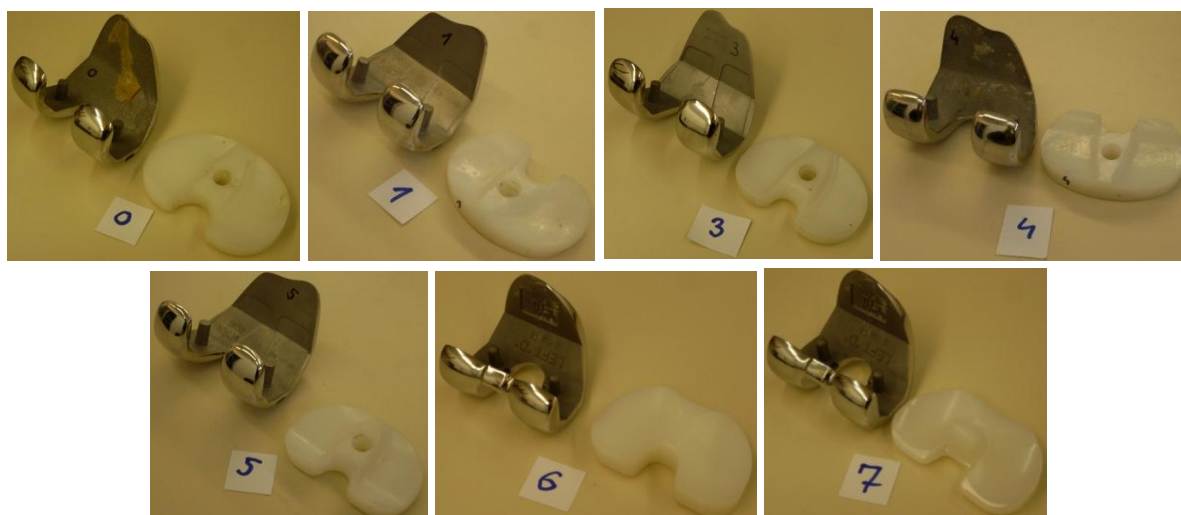


Figure 5. Examined prostheses

Table 1 includes the parameters of the examined prostheses. Prostheses of four different designs from three different manufacturers were investigated: left, right, cruciate-retaining and posterior-stabilizer.

| Number | Manufacturer | Femur size        | Tibia size   | Femur Ref. num.  | Tibia Ref. num. | Leg   | Type |
|--------|--------------|-------------------|--------------|------------------|-----------------|-------|------|
| 0      | Unknown      | L-L ARGE          | XLGE 12      | KA 0017 12-00-74 | -               | Left  | CR   |
| 1      | Biotech      | Medium Right B140 | B105 M10     | 051-1311-3070    | -               | Right | CR   |
| 3      | Biotech      | B102 XL-L         | B106 L10     | 051-1712-5078    | -               | Left  | CR   |
| 4      | Unknown      | M-L ARGE          | MED 10       | KA 0432 12-00-70 | -               | Left  | CR   |
| 5      | Biotech      | Medium Right B146 | B104 S10     | 051-1311-3070    | -               | Right | CR   |
| 6      | Sanatmetal   | „D”               | GRN-17PE     | -                | (z) 60158134    | Left  | CR   |
| 7      | Sanatmetal   | „D”               | EF 5-6 10 PE | -                | (z) FE 61878361 | Left  | PS   |

Table 1. Examined prostheses

### First experimental results, qualification method

When the prosthesis was secured in the test rig, the rotation was measured as a function of flexion angle (Figure 6). Each prosthesis was measured six times, and the average of these six measurements are plotted in the diagram. Prostheses – selected for qualification – were removed from patients due to the need of new replacements. In Figure 6, all the measured average values are plotted together with the reference-function. The difference between the measured and the reference values is quite significant.

In order to qualify the movement, carried out by the prostheses, a *goodness-function* has been introduced ( $\kappa$ ), which provides a percentile value about the performed prosthesis rotation compared to the reference-function:

$$\kappa(\varphi) = \frac{\rho_{pr}(\varphi)}{\rho_{ref}(\varphi)} 100 \quad (1)$$

where:

$\rho_{pr}(\varphi)$ : rotation of the prosthesis as a function of flexion angle,

$\rho_{ref}(\varphi)$ : reference-function of the cadaver knee joint as a function of flexion angle.

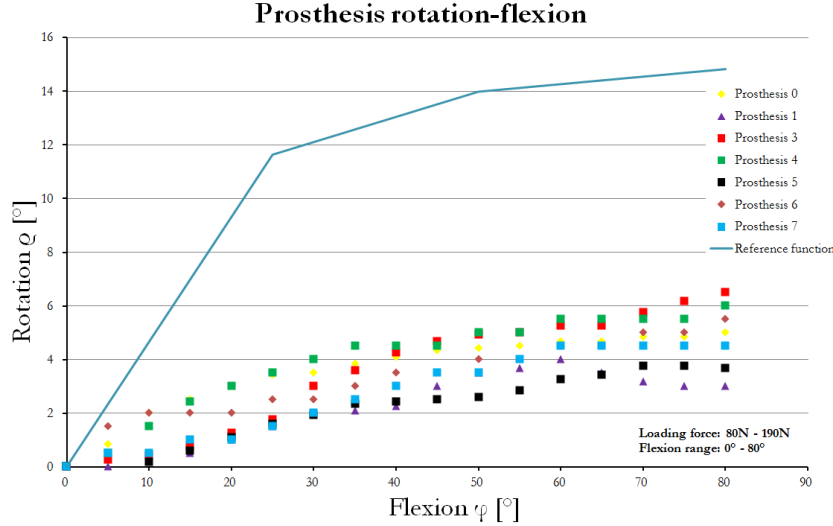


Figure 6. Rotational function on prostheses

Since the reference-function (the averaged change of rotation as a function of flexion angle) was approximated by tri-linear function, the same function was fitted on the measured prosthesis rotations as well. The equations of the fitted approximation-function on each segment:

$$\rho_{1pr} = a_1 \varphi \quad [^\circ] \quad (2)$$

$$\rho_{2pr} = a_2(\varphi - 25) + \rho_{10} \quad [^\circ] \quad (3)$$

$$\rho_{3pr} = a_3(\varphi - 50) + \rho_{20} \quad [^\circ] \quad (4)$$

The constants were summarized in Table 2, along with the values of the goodness-function, obtained in the boundary points. In Figure 7, the change of the goodness-grade of the seven prostheses is plotted as a function of flexion angle.

| $i$   | $a_1$<br>[-] | $a_2$<br>[-] | $a_3$<br>[-] | $\rho_{10}$<br>[°] | $\rho_{20}$<br>[°] | $\rho_{3(\varphi=80^\circ)}$<br>[°] | $\kappa(25^\circ)$<br>[%] | $\kappa(50^\circ)$<br>[%] | $\kappa(80^\circ)$<br>[%] |
|-------|--------------|--------------|--------------|--------------------|--------------------|-------------------------------------|---------------------------|---------------------------|---------------------------|
| Pr. 0 | 0,1506       | 0,02311      | 0,02227      | 3,765              | 4,342              | 5,01                                | <b>32,4</b>               | <b>31,1</b>               | <b>34,1</b>               |
| Pr. 1 | 0,0509       | 0,08482      | -0,00753     | 1,272              | 3,393              | 3,167                               | <b>10,9</b>               | <b>24,3</b>               | <b>21,6</b>               |
| Pr. 3 | 0,06212      | 0,15589      | 0,02115      | 1,553              | 5,450              | 6,085                               | <b>13,3</b>               | <b>39</b>                 | <b>41,3</b>               |
| Pr. 4 | 0,14636      | 0,05314      | 0,02914      | 3,659              | 4,98               | 5,861                               | <b>31,5</b>               | <b>35,7</b>               | <b>39,9</b>               |
| Pr.5  | 0,0509       | 0,06422      | 0,03273      | 1,272              | 2,878              | 3,86                                | <b>10,9</b>               | <b>20,6</b>               | <b>26,2</b>               |
| Pr.6  | 0,11575      | 0,04192      | 0,04792      | 2,893              | 3,941              | 5,379                               | <b>24,9</b>               | <b>28,2</b>               | <b>36,6</b>               |
| Pr. 7 | 0,05818      | 0,09339      | 0,03024      | 1,454              | 3,789              | 4,696                               | <b>12,5</b>               | <b>27,1</b>               | <b>31,9</b>               |
| Ref.  | 0,47         | 0,094        | 0,028        | 11,6               | 13,9               | 14,7                                | -                         | -                         | -                         |

Table 2. Fitting parameters of the experiment

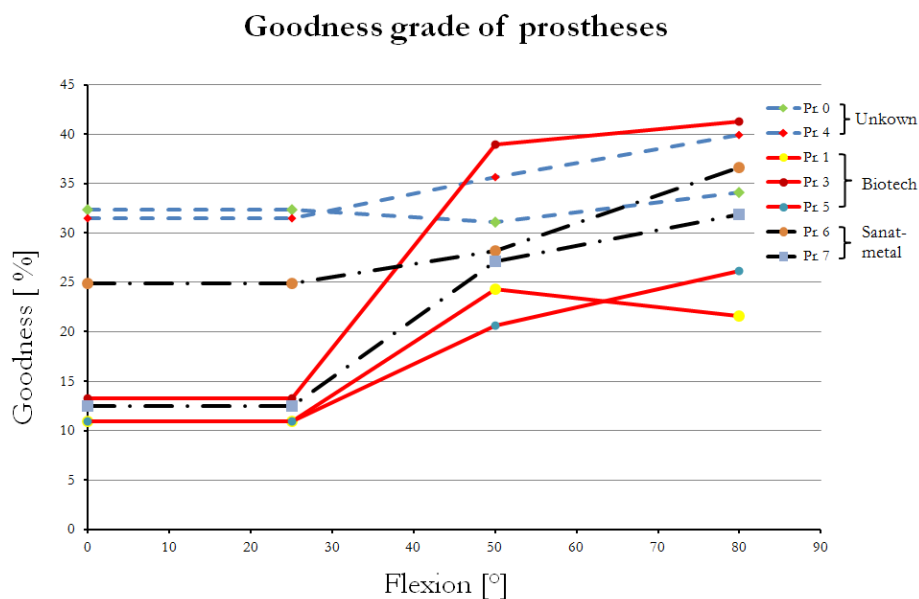


Figure 7. Goodness function of different prostheses

## Conclusion

As a summary, we can conclude that:

- A test rig has been designed and assembled which is capable to measure and qualify the performed rotation of any prosthesis,
- A qualification-method has been elaborated,
- Measurements were carried out on seven commercial prostheses. The results showed that the prostheses can only achieve the 10-30% of the appointed rotation.

Our investigations with respect to the qualification of prostheses are followed by the examination of factors and their effect on the rotation.

## REFERENCES

1. Bíró I, Csizmadia BM, Katona G. Determination of instantaneous axis of rotation of tibia and its role in the kinematical investigation of human knee joint. In: L. Borbás editor. Proceedings of the Third Hungarian Conference on Biomechanics; 2008. July 4-5. Budapest: 2008:57-62.
2. Fekete G, De Baets P, Wahab MA, Csizmadia MB, Katona G, Vanegas-Useche LV, Solanilla JA. Sliding-rolling ratio during deep squat with regard to different knee prostheses. Acta Polytechnica Hungarica 2012; 9(5): 5-24.
3. Szakál Z. Mérőberendezés térdízület mozgásvizsgálatához. GÉP 2006; LVII(1):37-40.
4. Katona G, Csizmadia BM, Bíró I, Andrónyi K, Krakovits G. Motion analysis of human cadaver knee-joints using anatomical coordinate system. Biomechanica Hungarica 2010; 3(1):93-100.
5. Katona G, Csizmadia BM, Andrónyi K. Determination of reference function to knee prosthesis rating. In: L. Borbás editor. Proceedings of the Fifth Hungarian Conference on Biomechanics; 2013. May 24-25; Budapest



## MECHANICAL SCANNER OF VERTEBRAL COLUMN

László Danka<sup>1</sup>, Gabriella Träger<sup>2</sup>, Annamária Paróczy<sup>3</sup>, Péter Tamás<sup>3</sup>, József Molnár<sup>3</sup>, Norbert Szakály<sup>3</sup>

<sup>1</sup>Hospital of Brothers Hospitallers of St. John of God at Buda

<sup>2</sup>Gold Sanitas Ltd.

<sup>3</sup>Department of Mechatronics Optics and Information Engineering, Faculty of Mechanical Engineering, Budapest University of Technology and Economics

[laszlo.danka@osteoporosis.hu](mailto:laszlo.danka@osteoporosis.hu)

---

**Keywords:** vertebral column, 3D model, scoliosis, Cobb angle, vertebral scanner.

---

### 1. Introduction

It is very important to know the geometry of vertebral spine for diagnosis and treatment of spinal deformation. There is no equipment to reproduce the shape of vertebral column, except for very expensive EOS systems.<sup>1</sup> Patients lie in CT-s, X-ray images from two sides are not exact enough. The world-wide used Spinal Mouse<sup>2</sup> measures only the curve of vertebral column, but there is no information about the torsion. In the neck it is not useable because of the sizes. The aim of the development was an equipment measuring the torsion and useable at the neck.

### 2. Methods

First version was based on the mobile phone. There is an accelerometer in the phone, and moving the phone the position can be integrated from the acceleration.

#### 2.1. Mobile phone application

The working principle is the same as the Spinal mouse. The phone application integrates the acceleration and store data in its own memory. If it was needed the data can be sent to PC via Bluetooth®. The phone was a Nokia N97 type with Symbian S60v5 operating system. Programming language was Python and program needs 3.5 Mbyte free memory.<sup>3</sup> The program calculates positions of vertebra sections upon the values of acceleration: Starting the application the program search for Bluetooth connection. It is possible to use it or store data inside and transfer them later. The vertebral spine can be shown on the phone (*Figure 1*) as well as the on the PC (*Figure 2*).

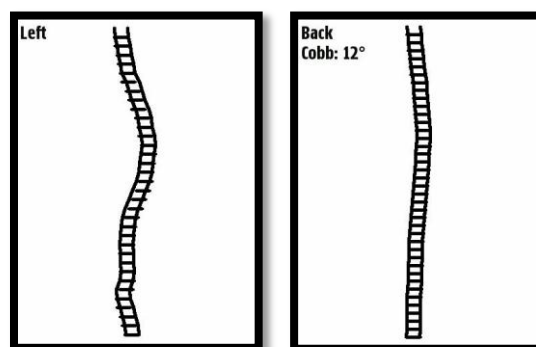


Figure 1. Left and Back view of a vertebral column

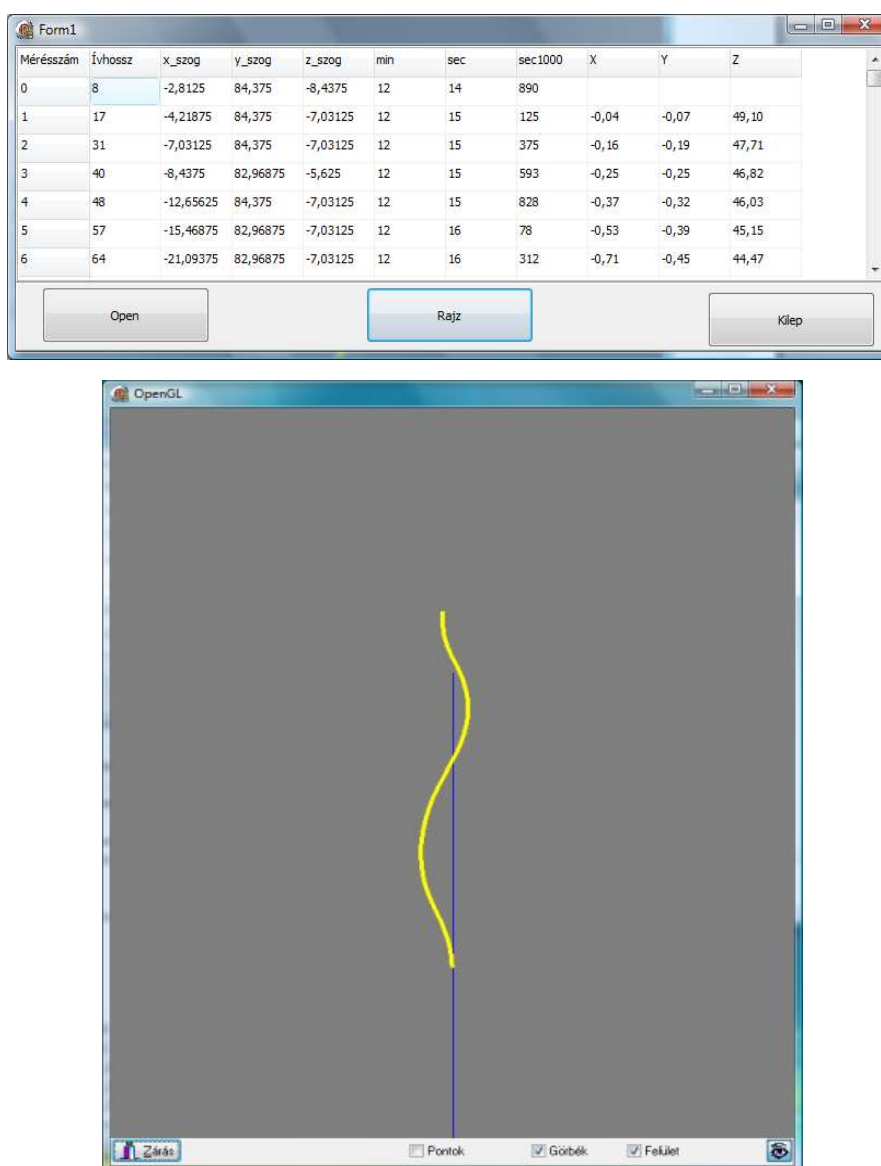


Figure 1. Vertebral spine data on PC

The fluent and frictionless driving the equipment is a basic requirement, so with help of an old mouse and a phone console, a new docking equipment was built (Figure 3).

Later with help of 3D prototyping a new docking equipment was developed (Figure 4).



Figure 3. Docking equipment



Figure 4. 3D printed docking equipment

## 2.2. Cobb angle

In case of C-shape scoliosis the maximum and minimum of angles on the back-view can be defined and Cobb angle is defined. In case of S-shape scoliosis, the program search for inflexion point if any. After the upon 3 point the two Cobb angles can be calculated numerically.<sup>4</sup>

## 2.3. New version of vertebral scanner

The traditional Spinal Mouse<sup>2</sup> measures only the curve position of spine and it is not able to track the torsion of vertebral spine because of its wheels are arranged as it was a bicycle. It is not able to measure on neck part of spine because of its geometry. Phone based equipment did not solve these problems. We have created a brand new version. The new construction is based on an MMA 3D accelerator sensor (Figure 5) and an encoder (Figure 6).

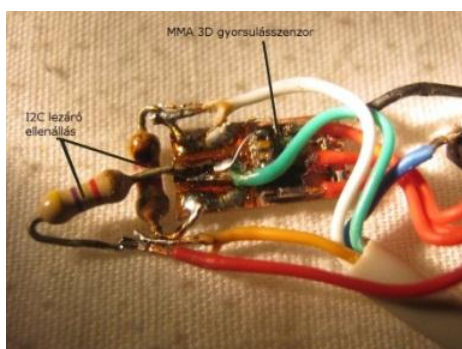


Figure 5. The MMA 3D accelerometer



Figure 6. The encoder

While the encoder moves along the spine arc length is continuously measured. The accelerator sensor and encoder built on a printed circuit board (PCB). Data from this equipments are processed a central processing unit (CPU). Mouse is controlled by user so a button is on the PCB. The outer voltage is 5V. The accelerator sensor works on 3.3V so a level interface was needed. We can connect to the PCB trough Inter Integrated Circuit (I2C) bus or program loader connector. Connection to PC-s is solved by USB interface. The PCB is shown on Figure 7 and the scheme is on the Figure 8.

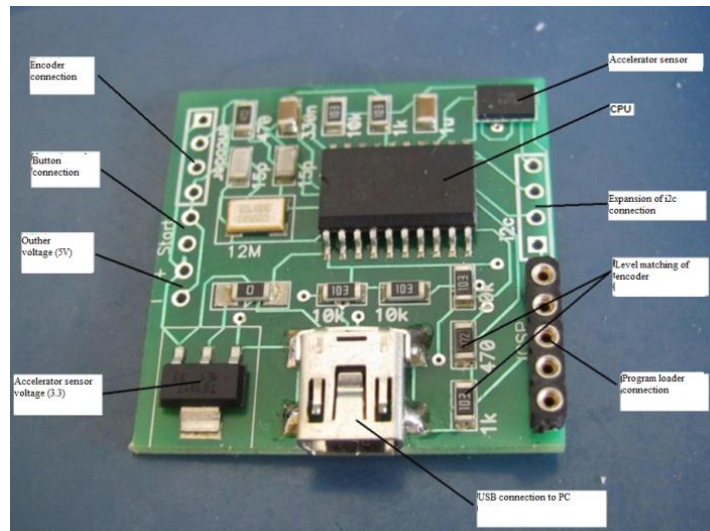


Figure 7. The electronics

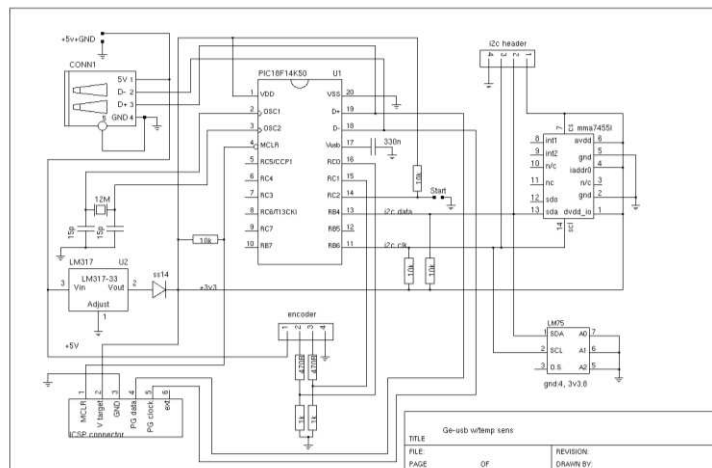


Figure 8. The scheme of electronics

There are two supporting wheel to measure the rotation. The encoder built in the instrument such a way that the mouse can follow even the curvature of neck (Figure 9).

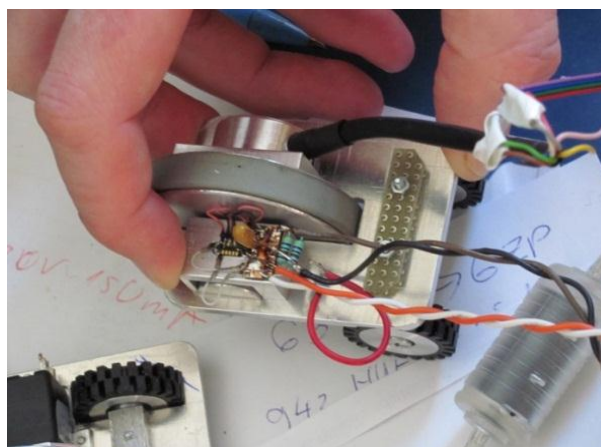


Figure 9. The supporting wheels

A rapid prototyped aesthetic housing was manufactured (Figure 10).

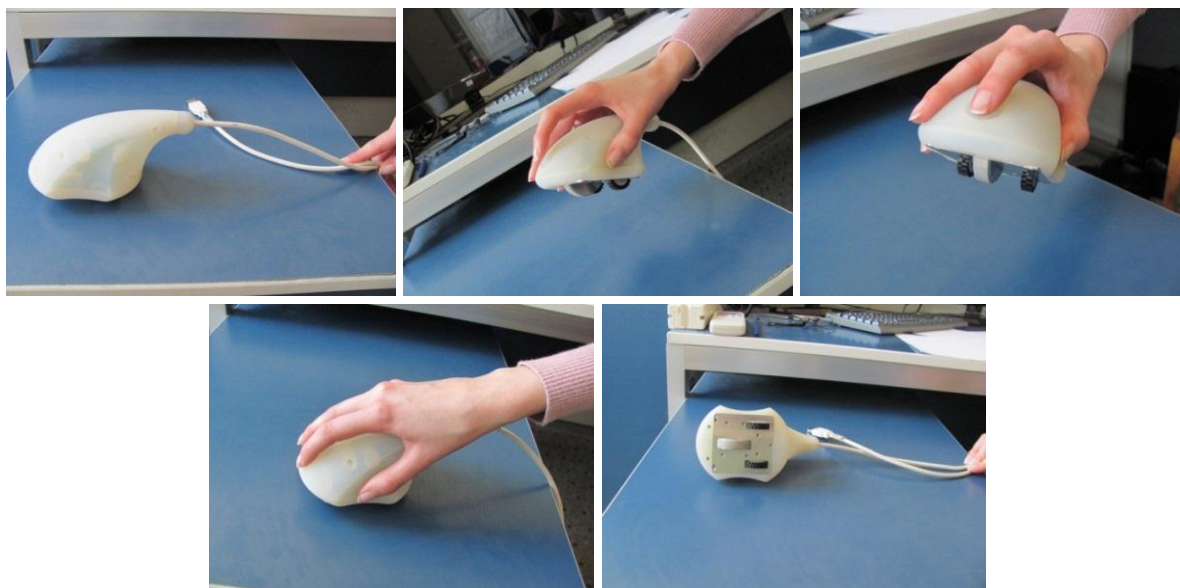


Figure 10. The product

## 2.4. Mathematical background of measuring

Direction is acceleration is registered in the coordinate  $(x, y, z)$  system of PCB (Figure 11). Z axe of global coordinate system points to centrum of Earth. X and Y axes are in the perpendicular plane. The gravity vector measured in  $(x, y, z)$  system is  $(g_x, g_y, g_z)$ . The encoder gives the movement  $\Delta s$  in direction  $z$  (Figure 11).

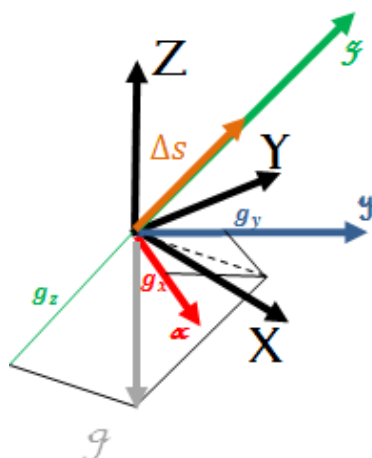


Figure 11. The gravity vector defines the global coordinate system

When the momentary  $g$  vector in the  $i$ . moment is measured there is an average computing because the sensitivity of the instrument (1).

$$\begin{aligned}\bar{g}_{x,i} &= \sum_{k=0}^n \frac{g_{x,k}}{2 * n + 1} \\ \bar{g}_{y,i} &= \sum_{k=0}^n \frac{g_{y,k}}{2 * n + 1} \\ \bar{g}_{z,i} &= \sum_{k=0}^n \frac{g_{z,k}}{2 * n + 1}\end{aligned}\tag{1}$$

The unit vector point to direction of gravity at the  $i$ . moment

$$\begin{aligned}e_{x,i} &= \frac{\bar{g}_{x,i}}{|g_i|} \\ e_{y,i} &= \frac{\bar{g}_{y,i}}{|g_i|} \\ e_{z,i} &= \frac{\bar{g}_{z,i}}{|g_i|}\end{aligned}\tag{2}$$

The resultant movement is the sum of movements of the  $i$ . moments<sup>5</sup>

$$\begin{aligned}x(s) &\cong \sum \Delta s_i * e_{x,i} \\ y(s) &\cong \sum \Delta s_i * e_{y,i} \\ z(s) &\cong \sum -\Delta s_i * e_{z,i}\end{aligned}\tag{3}$$

The equations of curve

$$\underline{p}(s) = \begin{bmatrix} x(s) \\ y(s) \\ z(s) \end{bmatrix} = \begin{bmatrix} \int_0^s x(s) ds \\ \int_0^s y(s) ds \\ \int_0^s z(s) ds \end{bmatrix}\tag{4}$$

Frenet frame of curve is defined by tangent curvature and torsion directions (reference<sup>6</sup>). We have measured  $\Delta s$  movement, so the curve parameterized by curve length. The tangent unit vector is:

$$\underline{t}(s) = \frac{\frac{d\underline{p}(s)}{ds}}{\left| \frac{d\underline{p}(s)}{ds} \right|}\tag{5}$$

The normal unit vector is

$$\underline{n}(s) = \frac{\frac{d^2 \underline{p}(s)}{ds^2}}{\left| \frac{d^2 \underline{p}(s)}{ds^2} \right|} \quad (6)$$

and the binormal unit vector is

$$\underline{b}(s) = \frac{\frac{d\underline{p}(s)}{ds} \times \frac{d^2 \underline{p}(s)}{ds^2}}{\left| \frac{d\underline{p}(s)}{ds} \times \frac{d^2 \underline{p}(s)}{ds^2} \right|} \quad (7)$$

The *Figure 12* shows the directions of Frenet frame vectors.

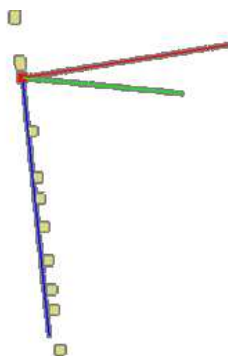


Figure 12. The Frenet frame

### 3. Model of vertebral column

The curve and the direction of curvature define the situation of vertebra and it shown on *Figure 13*.

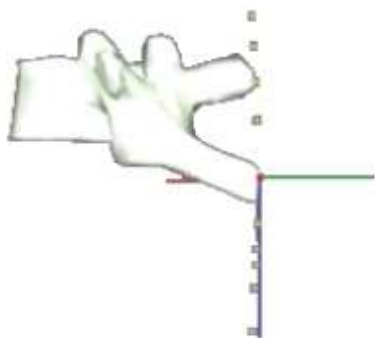


Figure 13. Position of vertebra

Because the encoder gives the curve length, from (4) we can compute the coordinates and derivatives of  $\underline{g}(s)$  curve. We know the lengths at  $s_i$  points. The reparameterization (8) helps to define the correct positions of vertebrae.

$$h = s_i - s_{i-1} \quad \text{for every } i \quad (8)$$

We suppose that the vertebrae divide the length upon the original model<sup>7</sup>. The reconstructed model is shown on *Figure 14*.



Figure 14. Model of vertebral column

#### 4. Results

For every coordinate function (9), (10) and (11) we can write equations like for  $x$ .

$$\left. \frac{dx(s)}{ds} \right|_{s=s_i} \cong \frac{x(s_{i+1}) - x(s_i)}{s_{i+1} - s_i} = \frac{x(s_i + h) - x(s_i)}{h} \quad \text{for every } i \quad (9)$$

$$\begin{aligned} \left. \frac{d^2x(s)}{ds^2} \right|_{s=s_i} &\cong \frac{\left. \frac{dx(s)}{ds} \right|_{s=s_i} - \left. \frac{dx(s)}{ds} \right|_{s=s_{i-1}}}{h} = \\ &= \frac{x(s_i + h) - 2 * x(s_i) + x(s_i - h)}{h^2} \quad \text{for every } i \end{aligned} \quad (10)$$

$$\begin{aligned} \left. \frac{d^3x(s)}{ds^3} \right|_{s=s_i} &\cong \frac{\left. \frac{d^2x(s)}{ds^2} \right|_{s=s_i} - \left. \frac{d^2x(s)}{ds^2} \right|_{s=s_{i-1}}}{h} = \\ &= \frac{x(s_i + h) - 3 * x(s_i) + 3 * x(s_i - h) - x(s_i - 2 * h)}{h^3} \quad \text{for every } i \end{aligned} \quad (11)$$



We can compute the curvature ( $g$ ) and torsion of curve ( $c$ ) substituted (9), (10) and (11) into (12) and (13).

$$g = \left| \frac{d^2 g(s)}{ds^2} \right| \quad (12)$$

and

$$c = \frac{\frac{dg(s)}{ds} \frac{d^2 g(s)}{ds^2} \frac{d^3 g(s)}{ds^3}}{\left| \frac{dg(s)}{ds} \times \frac{d^2 g(s)}{ds^2} \right|^2} \quad (13)$$

---

## REFERENCES

1. Az EOST<sup>TM</sup> röntgengép elve és gyakorlati használata a mindennapi ortopédiai gyakorlatban. Orvosi Hetilap 2012;812:289-95.
2. <http://www.spinalmousesolutions.com/index.html> 2012.12.10
3. [www.nokia.com](http://www.nokia.com)
4. Negrini S, Atanasio S, Fusco C, Zaina F. Effectiveness of complete conservative treatment for adolescent idiopathic scoliosis (bracing and exercises) based on SOSORT management criteria: results according to the SRS criteria for bracing studies. SOSORT Award 2009 Winner.
5. Bajcsay P. Numerikus analízis. Budapest: Tankönyvkiadó, 1978.
6. Szőkefalvi NG, Gehér L, Nagy Péter. Differenciálgeometria. Budapest: Műszaki Könyvkiadó, 1979.
7. <http://www.anatomia-creations.com>.

*National Office for Research and Technology (NKTH) of Hungarian Government for their support since this study has been carried out commonly as part of the project GERINCO2*

## INTELLIGENT CORSETTE FOR TREATMENT OF SCOLIOSIS

Péter Tamás, József Molnár, Norbert Szakály

Budapest University of Technology and Economics, Mechanical Engineering Faculty, Department of Mechatronics, Optics and Engineering Informatics

[tamas@mogi.bme.hu](mailto:tamas@mogi.bme.hu)

---

**Keywords:** scoliosis, corsette, force resisting sensor, accelerometer, thermometer, calibration

---

### 1. Introduction

Spinal disorder (*Figure 1.*) is dangerous and widespread disease for young girls, nowadays. Spinal disorders may be corrected by gymnastic, corsets and operations. Every case is individual. It is very important that the disorder should be detected as early as possible.<sup>1</sup> After computer aided diagnostics (CADM Computer Aided Diagnostic in Medicine) if necessary an automatic custom-made corset could be realized to make corrections and avoid operations. The primary information for CAD/CAM system is obtained from the special 3D modelling of humans body<sup>2</sup> and after the measuring the influence of device. We want to reform the shape of corsets, and the efficiency of treatment. Corsets are made in practical way, patients wear them, health staff asks the patients about wearing the corset is comfortable or not, first when making corset, after a periodic wearing time. No exact force and wearing information day-after-day. We created a wearable microcontroller-based measuring system to get and collect information forces between patient and corset, moving and temperature data to determine a wearing time interval.



*Figure 1.* 2D EOS AP spinal rtg.<sup>3</sup>

## 2. Method, the measuring equipments

### 2.1 Using FSR sensors

We were looking for a useable sensor between the patient and corset. Main requirements are: lightweight, thin enough, plastic, electrically connectable sensor. We do not want too precise force measurement, because in this application we wanted to create categories on display: “not touching”, “too small force”, “normal force”, “too much force”. Nobody wants the exact force measurement or more digits. The metal force sensors found in kitchen or bathroom scales are too big, and hard to fix on the back side of the corset. Interlink Electronics’ FSR sensors seemed applicable in corsets (*Figure 2*). FSR stand for “Force Sensing Resistor”, made from thin polymer film and conductive material. They are changing resistance when applying a force its area, so we can detect a force, and pressure too. FSR sensors are plastic, 0.55 mm thin, and fixable with adhesive material to a corset. However, because the polymer material’s properties, the sensor’s resistance is near exponential, and has an elastic, time-dependent change (*Figure 3*). These problems can be handling by long-time calibration process.



Figure 2. FSR sensor<sup>4</sup>

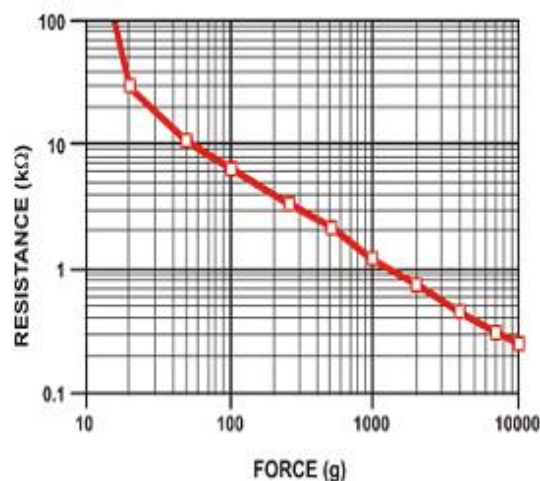


Figure 3. FSR sensor characteristic<sup>4</sup>



Figure 4. The voltage divider

We can use an FSR sensor in a simple voltage divider, output voltage equation:

$$V_{out} = \frac{R_M}{R_M + R_{FSR}} \cdot V + \quad (1)$$

By changing resistor  $R_M$  we can set the output characteristic, and force amplitude. (Figure 5).<sup>4</sup>

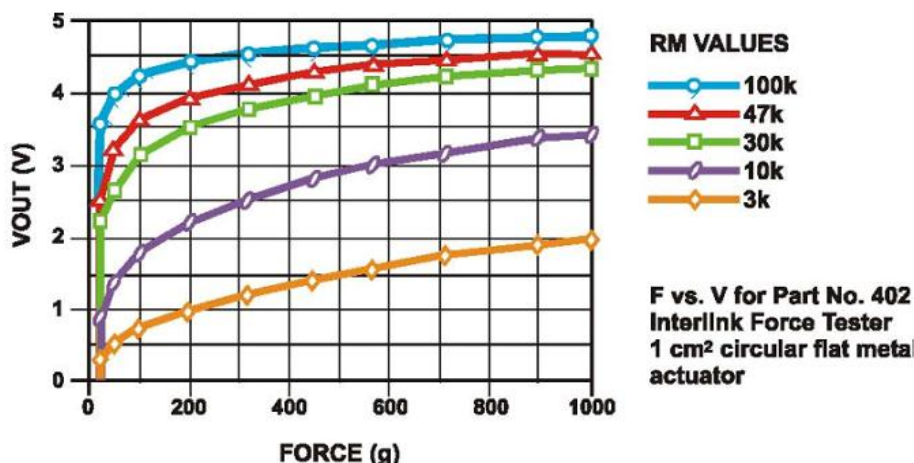


Figure 5. Output characteristic of sensors v4

## 2.2 Thermometer specification

In addition to force sensors, we measure other parameters in a corset: temperature and patient's moving situation. Thermometer is the simplest ic with readable digital output via i2c bus, type is NXP LM78A.

## 2.3 Accelerometer specification

Moving situation measure can be made with accelerometer, or gyroscope. We designed a low-cost 3 axis accelerometer into the hardware. Accelerometer type is Freescale MMA7455, readable via i2c bus.

The equipment is connected to the corsette. The iCorsette manages sensors and stores data. It has its own memory and it works by battery or by USB.

## 2.4 iCorset 1.0 – first version to testing subsystems

The scheme of the equipment is show non Figure 6. Digital parts work on 3.3V and analogue parts on stabilized 5V. Voltage converters are needed because of switching between the working modes.

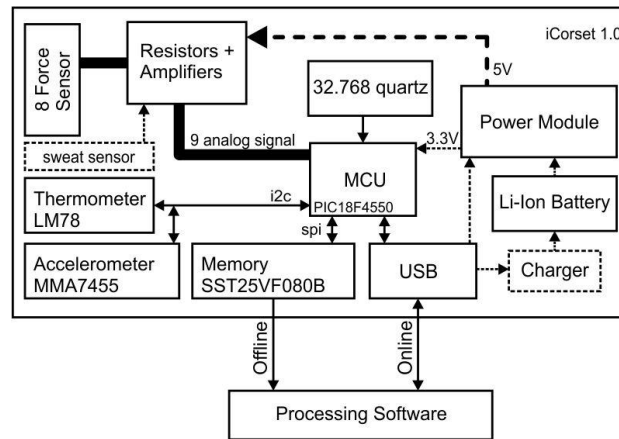


Figure .6 iCorset 1.0 block diagram

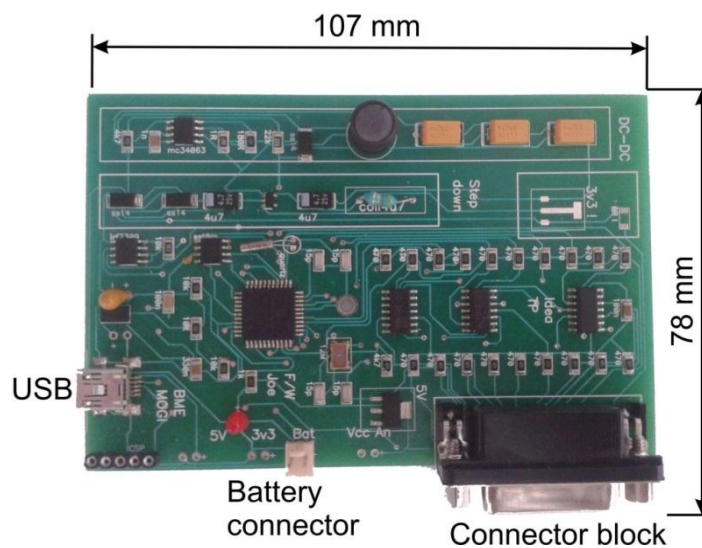


Figure 7 iCorset 1.0

Because this device is battery operated, the analogue part's power supply enabled only the measurement time. FSRs attached to test corset with adhesive, pcb attached with screw M3.

## 2.5 Second version based on users opinion: iCorset 2.0

The first version pcb size was too big: it contains two dc-dc converters, hot-swappable between battery power and USB power, analogue part works from +5V stabilized, digital part works from +3.3V converted supply. The redesigned version works from single +3.3V power supply, stabilized by smd size linear stabilizer, not hot power swappable. Voltage followers were eliminated: sensors connected directly to cpu, creating a small error. New, 2.0 pcb size 40x36 mm, easier to put on the corset's surface.

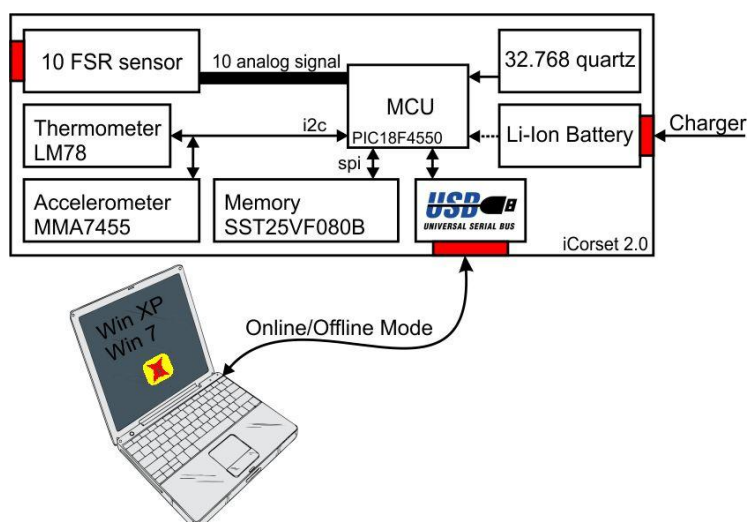


Figure.7. iCorset 2.0 block diagram

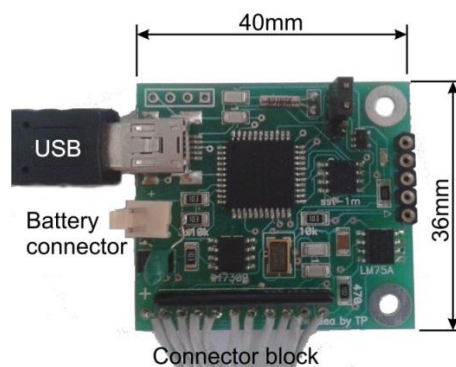


Fig.8. iCorset 2.0 pcb

## 2.6 Storage capacity of iCorset

Table 1. shows the data in the memory of the corsette.

| Name         | Type   | Size (byte)       |
|--------------|--------|-------------------|
| Time         | Long   | 4                 |
| Pressure     | 10*Int | 20                |
| Acceleration | 3*Int  | 6                 |
| Temperature  | Int    | 2                 |
| Summ         |        | 32 byte/measuring |

Table 1. Data in iCorset

32 byte memory stores data of one measure. The SST25VF080B EEPROM memory has 1Mbyte memory. It is able to store data of 32768 measures. This means more than 22 days capacity if the

measures follow one after the other in one every minute. It needs to charge the battery in every 2 days. There are nine hours capacity if we make measuring in every second.

### 3. Discussion Calibration of FSR sensors

Measuring interval of selected sensors is 0.1N-100N domain. The forces in the corsette are in this interval. Calibration of sensors<sup>5</sup> was done by a standard range of weights (*Figure 9*).

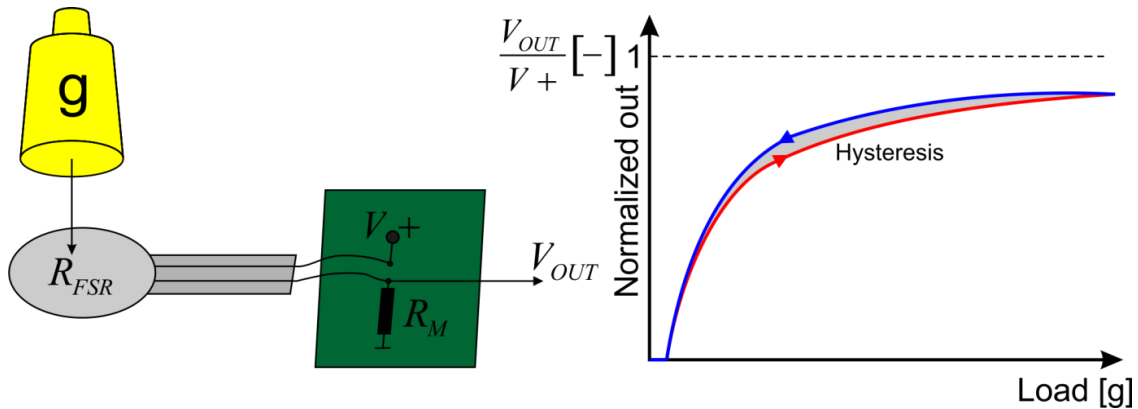


Figure 9. Calibration

There were two problems to solve.<sup>6</sup> The measured values were functions of time, and there were a hysteresis between the upload and download. Not the output voltage was measure, but the quotient of the output voltage and the input voltage.<sup>7</sup> In this way the measure is independent from the input voltage. The characteristic is correct even in case of input voltage fluctuation. There is an RM resistance of 470 Ohm (*Figure 4*). The measured values are shown in *Figure 10*. The logarithmic curve follows the measured points well.

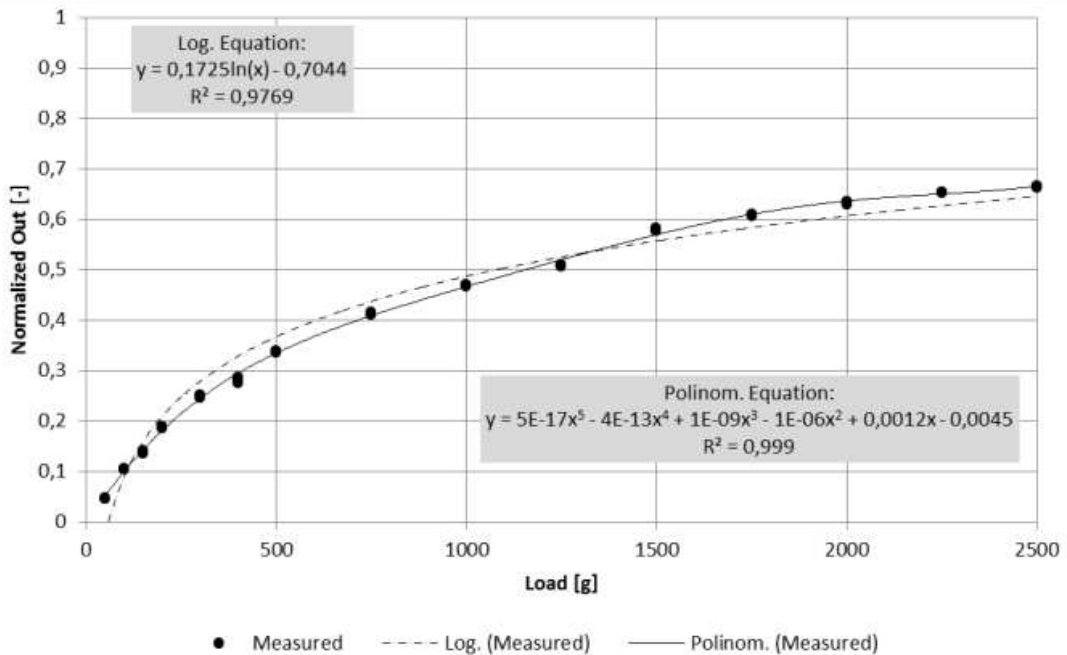


Figure 10. Normalized output as a function of pressure

Unfortunately if we want exact values than all of the sensor should be calibrated. If we need only approximate value, it is enough to use the normalized values.

### 3.1 Software of iCorsette

There is no display in iCorsette, so we developed a Window application for visualization and processing the data. The *Figure 11* shows the actual positions of FSR sensor (left side) and the forces as the function of time.

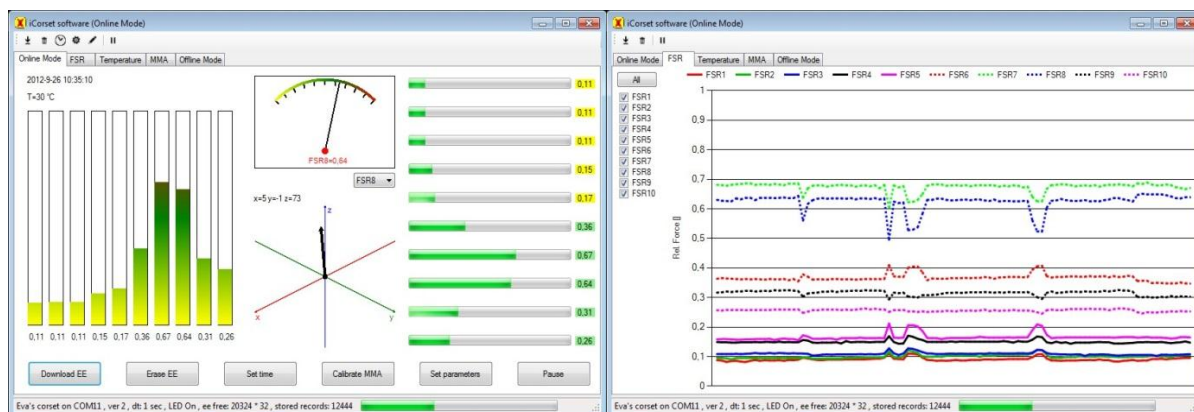


Figure 11. The iCorsette software

iCorsette connected to the computer can solve special tasks. For example it is able to measure of forces along a line. In the left side of *Figure 11* we can see the distribution of forces in curve on corsette surface. Acceleration vector is shown too. The downloaded data can be visualized and analyzed (in right side of *Figure 11*)

### 4. Result, test of iCorsette

The electronics of version I. is connected to the corsette (*Figure 12*). The iCorsette was tested many times for a week. There were periods of workdays weekend, sport relax and nights also. All activity were traceable on records.

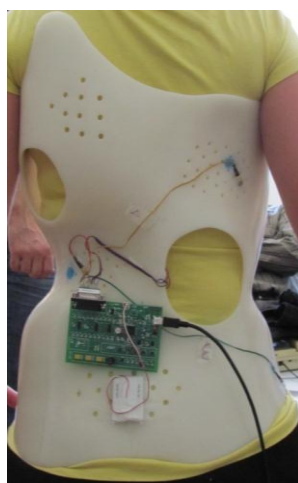
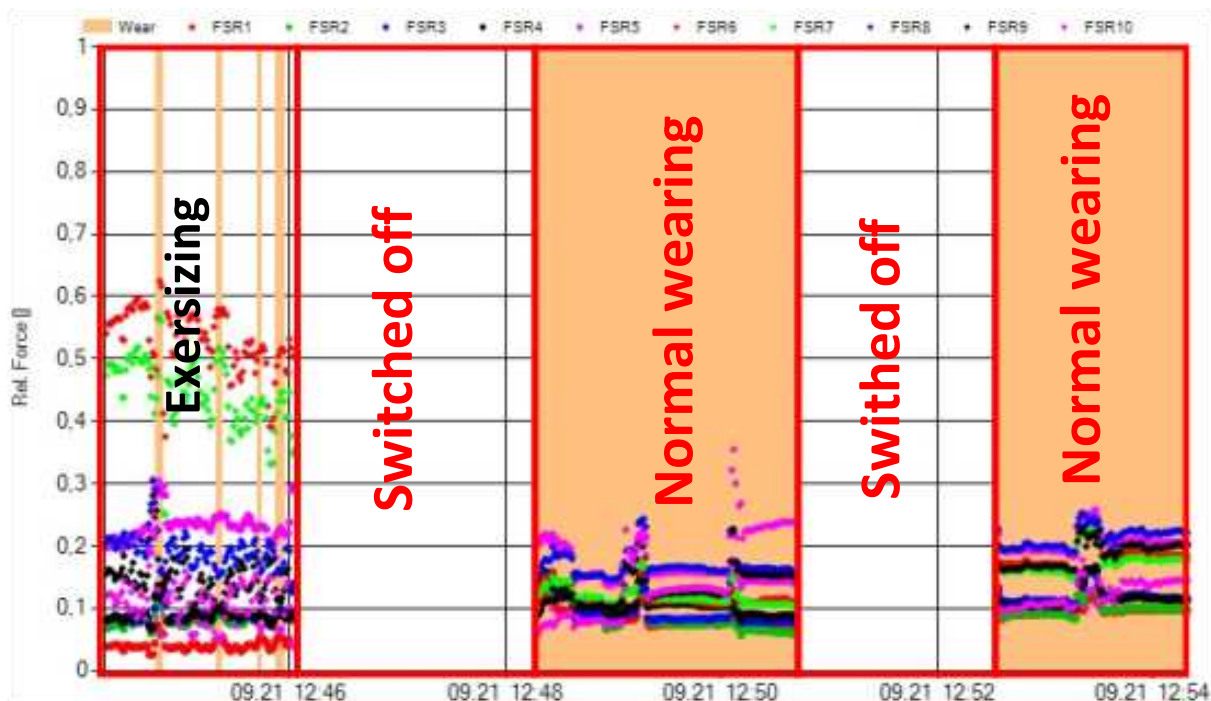


Figure 12. The iCorsette 1.0



There is the result of a measuring in *Figure 13*. There are a lot of different periods. The monitored person exercised in the first period. Because of leaning on left and right there is high pressure on some sensors (red and green). On the second and fourth period the equipment was off. The third and fifth period show normal wearing of corsette.



*Figure 13.* Results of long time measuring

## 5. Future work

After successful testing, some hardware and software modifications can be made. Communication needs to change to wireless, write a mobile phone application, which can send downloaded data over internet to central database.

## REFERENCES

1. Wenzel K, Ábrahám Gy. Measurement of Distortion Using the Moire Method. *Experimentelle Technik der Physik* 36. 1988.6:429-34.
2. Tamas P, Halasz M, Somló J. 3D Measuring of the Human Body by Robots 5th International Conference Innovation and Modelling of Clothing Engineering Processes – IMCEP 2007, University of Maribor, Faculty of Mechanical Engineering, 2007. October 10-12; Moravske Toplice, Slovenia p 109-115 ISBN 978-961-248-047-9.
3. Martinns PAF, Kwiatkowski L, Franzen V, Tekkaya AE, Kleiner M. Single Point Incremental Forming of Polymers, *CIRP Annals – Manufacturing Technology*. CIRP 396 2009 Articles in Press
4. Interlink Electronics FSR - Force Sensing Resistor Inrtegration Guide and Evaluation Parts Catalog. Version 1.0, Revision D.
5. Flórez JA, Velásquez A. Calibration of Force sensing resistors (fsr) for static and dynamic applications

6. Hollinger A, Wanderley MM. Evaluation of Commercial Force-Sensing Resistors, NIME06, Paris, France
7. Barnea A, Oprisan C, Olaru D. Force Sensitive Resistors Calibration for the Usage in Gripping Devices, Diagnosis and Prediction in Mechanical Engineering Szstems, DIPRE 12

***National Office for Research and Technology (NKTH) of Hungarian Government for their support since this study has been carried out commonly as part of the project GERINCO2 TECH\_08-A1/2-2008-0121.***

## GARMENTS UNDER BRACE LIFE QUALITY IMPROVE AFFECT EXPERIMENT OF TECHNOLOGY AND PHYSIOLOGY

Orsolya Nagy Szabó, András Koleszár  
Óbuda University, Faculty of Light Industry and Environmental Engineering  
[szabo.orsolya@rkk.uni-obuda.hu](mailto:szabo.orsolya@rkk.uni-obuda.hu)

---

### **Abstract**

Scoliosis is a spinal deformity that most commonly appears in girls and makes itself apparent at puberty during the early teenage years. Living with scoliosis can be especially difficult for children, particularly when a brace is required to stop its progression. The context of clothing physiology help a clothing system of air, vapor permeable insulation and opportunities. These same characteristics are changed when brace wearing, but also help the right materials and design concepts for the development. In view of the currently available properties of fabrics during the test and we see clothing physiology using different raw materials and functional textiles, as well as the solution for improving the body's microclimate. In our research achieve an optimal physiological state of body with a corver on the brace, that improves the body's microclimate, reduce the unpleasant effects of the brace at high temperatures, but the basic function of the medical device support.

**Keywords:** Scoliosis, brace, underwear, clothing physiology.

---

### **1. Introduction**

12 million people suffer some form of scoliosis all over the world.<sup>1</sup>

There are 450 new scoliosis cases each year in our country, but among them 150 patients need orthopedic help, but the number is steadily increasing.<sup>2</sup>

There are many types of scoliosis. Depend on the disease type and severity of various types were made brace in custom size.

Orthopedic surgeon diagnose spinal disease and prescription a brace, according to the type of the spine disease, and the brace is made of by the orthopedic technician.

Conservative treatment of diseases the 5 mm thick plastic "armor" should be weared, which can only be effective if the 24-hour of a day at least 18-20 hour wear the child until they beome adult.

Our goal is to develop a system of clothing that is worn under brace and in addition to improving the level of comfort in wearing and reduced uncomfortable feeling of brace.

The brace is not only caused a physical hardship but also it has very negative effect on young people.

The proper set up and wearable of brace associated with comfort feeling the clothing which is worn under, the comfort and aesthetic properties should be improved.

The fabrics currently available, taking into account the properties of the test during the brace worn which cause a variety of clothing physiology problems based on functional textile underwear. Our research will seek a solution to improve the body's microclimate.

The aim is to achieve an optimal physiological conditions with underwear or a special pulled coating product development that improves the body's microclimate, reduce unpleasant effects of the device, but the basic function of a medical device supports.

We desiged some underwear products based on children needs: T-shirts, bras, panties, pulled clothes to brace and with construction, modeling, technology implementation we have tried to satisfy all those requirements, which are adapted to this special wearability.

We have developed some modell variation and we selected functional fabrics with special properties, eg. Antibacterial Coolmax, Outlast PCM and flexible cotton, and we tested this t-shirts from tis special textiles.

The underwear design process greatly affect the wearing comfort. The material properties are taken into account - which are based on various textile testing - we tried to identify additional opportunities with which to improve our children's wellbeing.

## **2. Methods and materials**

### **2.1. The commercially available underwear products**

Commercial cotton shirts do not follow the body shape, and thus under the brace crinkles in which prolonged skin irritation. There are variety of sportswear specifically designed and made of special textile T-shirt, underwear available. These are not suitable because:

- The location of cutlines are depend on fashion, it does not take into account the pressure points of the brace,
- T-shirts are typically in the form of body shape but they have too many cutlines
- The seams are not always lapped seam
- Construction of the T-shirts is not precisely follow the body shape
- For many of the brace wearer the cutline through the armpits specific irritant
- From functional materials fashion sportswear products are expensive
- Seamless, form knitted T-shirts are also available but these textiles made of polyester, which is in is not comfortable to wear, and the knitted pattern is pressed into the skin.
- The operating instructions and the size designation is designed for comfortable

### **2.2. Problems under wearing brace**

Upper body movement is very limited in brace it can not bend down, turn right and left is limited.

The two most important features of the clothing are the thermal insulation and water vapor permeability. They affect thermoregulation of human body.

The tests are performed in some various designs and textiles underwear, and the brace had and old and an improved version was performed in which the air and leak tightness can be improved by means of perforation.

We had a survey among children who carried out brace. Based on the answers to most of their distractions while they were wearing brace.

- There is the pressure in armpit
- Rub the skin in pressure points
- Crumpled shirt, slide up underneath the dress
- Do not wear when in a less visible from the outerwear
- Placing bra clips

### **2.3. Physiological effect**

The context of clothing physiologic give help a clothing system air and vapor permeable insulation and optimum adjustment possibilities. Problem is that these same indicators change when the brace is worn. The method helps to select the appropriate materials and design concepts and develop the textile selection. The clothing thermal insulation and in the brace composition of the material to be tested due to the different temperatures of the body "comfort". Materials is to look at under brace in which improve the physiological conditions, and a built-in intelligent systems to be develop and improve comfort feeling.

Two most important characteristics of the clothing thermal insulation and water vapor permeability. They affect human thermoregulation. We make various tests based on underwear design and tailoring, as well as at present and in an improved version of brace wich has air through perforations and features of brace can be improved.

It should be noted the problem at the pressure points of the brace and the body relationship which may affect the size of the holes in the skin bulges, which can cause permanent damage.

### **2.4. Criteria for selection of appropriate materials**

A functional and smart textiles, which are due to their composition, or as a result suitable for a finish to protect health, improve quality of life. In our study, we were looking for answers to the new generation of commercially available materials which parameters in test conditions, which best meet the needs of customers physiology.

Our basic requirements from textiles:

- Good air permeability
- Antibacterial
- Moisture-wicking
- Good abrasion resistance
- Washable
- Good to be processed.

Many different compositions materials were tested and tried in sports activities / walking, running, ice- hockey, / and wearing brace.

A further studies of the best properties of materials continued.

The wearing of cotton-type tests based on the subjective evaluation of Outlast and Coolmax functional fabrics selected from the raw material of T-shirts.

## 2.5. Major features of materials

### Cotton

Cotton is a soft, fluffy staple fiber that grows in a boll, or protective capsule, around the seeds of cotton plants of the genus *Gossypium*.

The cotton fabrics have soft and high breathability properties. Good hygroscopic, deep in water it can be taken 25 to 27 times up their own weight. It is difficult to dry and does not charge electrostatically. The fabric quality depends on the quality of the cotton fibers.<sup>3</sup>

### Outlast

At the textiles also used special particles in the liquid-crystalline materials, changes in the physical state of the unusual phenomena can be observed:

- The melting of solid phases at the first one for liquid, dense, confusing, "liquid crystal" state,
- Followed by further heating the isotropic liquid and gaseous materials.

A "normal" liquids isotropic property of the liquid-crystalline state, however, the material coming from different directions and respond differently influences ("anisotropic" phase). The "Phase Change Material," the phrase in English PCM-agent spread after phase-alternating phase-changing, state-set exchange properties. The PCM-s ability to absorb a significant amount of heat energy, temporarily stored and then adapting to the changes in the environment of this latent heat is utilized. If temperatures in the range of their physical state change request:

- Solid phase near liquid state is cooling,
- Liquid cooling states of matter has an external effect, e.g. heat loss. The PCM is stopped before the melting point of the heating cycle.<sup>4</sup>

That Outlast technology, the company was first developed for astronauts the basic materials of everyday life can be used in many fields, especially for clothing.

### Coolmax

COOLMAX fabric with a specially designed polyester fiber made from elemental that wicks away perspiration from the body, and through the material quickly evaporates, so the clothing wearer comfort improvement. *Figure 5* has shown 4 and 6-channel fibers develop. The increased fiber surface due to the tissue surface of the water quickly evaporates.<sup>5</sup>

## **Results and discussion**

### **3.1. Underwear design point of view**

The design takes into account the material properties and the specific physiological needs, which arise for the corset wearers. Primary consideration when designing products in the seam, relocation, removal armpit seam, and the less cutline longitudinal design. A "hard armor" is one feature of the wearer's armpits to push, helping to maintain proper spine.

Problems during wearing brace:

- The pressure points at the skin becomes red,
- Underwear seams deeply press in the skin
- In armpit strong pressure and rubbing occurs,
- Commercially available products underwear cause wrapping problem and t-shirt slide up under brace
- The body sweat more strongly especially during movement
- Summer weather conditions, the wearing comfort is extremely bad.

### **3.2. T-shirt design**

- |                                   |  |
|-----------------------------------|--|
| 1. Brace pressure in armpit       | cutline delete in armpit                 |
| 2. T-shirt don't wrap under brace | t-shirt construction with special method |
| 3. Neck curve                     | don't see from upper clothes             |

Taken into account the area of the most commonly used pressure points of the brace, which was specifically designed for the T-shirt.

The t-shirt is made of a flexible textile, depending on the body size, and in the construction need 5-25% below in the wrap direction and 5-10% rod direction to prevent the formation of wrinkles on wearing, which rub the skin. This greatly increases the comfort feeling.

Taking into account we designed the cut lines of the t-shirt most ideal locations different way of usual cut lines.

First of all 3 kinds of cutlines placement was planned, taking into account the development of medical devices typical pressure points consultation with orthopedic technician, so the shirts are comfortable in wearing the seam widths pressed in the skin minimal.

Take into account a variety of cutline shirt was designed everyone can find right in which the seam pressure does not irritate the skin.

The pattern size can be made manually, based on the purchase, preparation of computer manufacturing system and 3D body scanners. The pattern should be considered in the design of pressure

### 3.3. T-shirt description

T-shirt is tight, closely following the body. The length of it is ending in hip line, but it is variable. Slives can be made of short and long, raglan, Japanese and normal version. Neck curve can be round or "V"-cut. Cutlines primarily depends on pressure points on, at girls / women / it is formatting breast.

Some of the possible types of product plan (Figure 1):

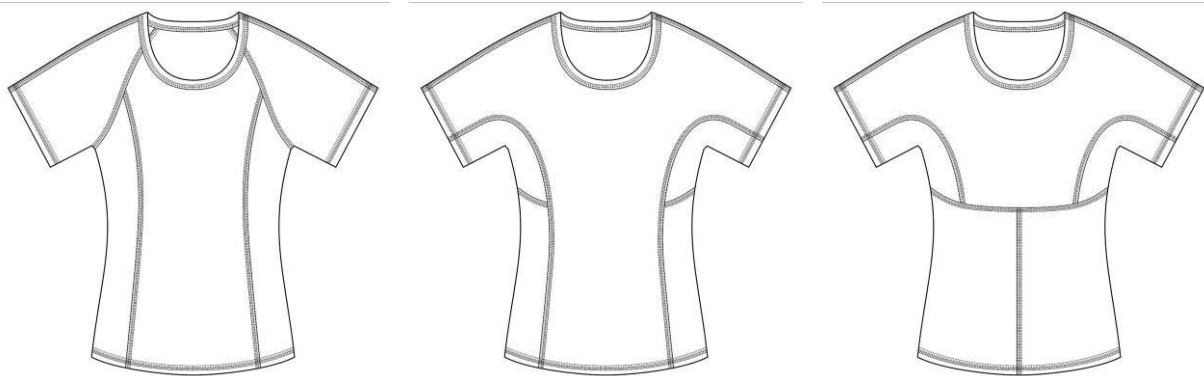


Figure 1:T-shirts

### 3.4. T-shirt technology

The technology is making 3 or 4 pin coverstich sewing machine with lapped seam. One possible solution is that all cutlines use this kind of seam technology and decorations can result in the use of colored thread.(Figure 2)

The assembly sequence of operations depends on the location of the cut lines.



Figure 2: 3 or 4 pin coverstich sewing



### 3.5. Bra and slip design

The wearer of brace is a higher percentage of young women who are already wearing a bra. This is a problem for many people because of one pressure points is definitely a place where the brace has a pressure point and bra back buckle or adjuster is located.

We designed a bra that buckle is at the front, and the special rubber does not cause skin irritation under brace. The cups of bra can be made of cut lines (see *Figure 3*), but without cut lines thermoforming and foam version. The bra can be made of underwire if it is not cause pressure in skin. If this solution does not work, be prepared for a variation of built-shirt bra.



*Figure 3:* Bra and slip design

The slip, thongs, panties and French as well formed. They different only in the shape of the cut lines to minimize the skin is pressed seam width. Each product shows the selection of the rubber should be carefully followed. The rubber width, thickness and elasticity, and sew technology affect the level of comfort while wearing products.

### 3.6. Textilcover design

The brace material properties take over from the temperature outside, cold in winter, hot in summer. In order to improve the comfort feeling, we make a textile coat to the brace. This solution eliminates the underwear layer. The inside layer of coat is very flexible with good physiological properties, the outer layer is not flexible, insulating properties dimensionally stable, which is assembled and washable.

Only in individual size can be made, taking into account the brace form and design. The coat can be open by zip, easily pulled and removable to brace and easy to wash. (*Figure 4*)



*Figure 4:* Brace with cover

#### 4. Conclusion

Subjective tests were performed among children who is wearing brace. They tested 5 kinds of raw material sample collections. Their views can be stated that the types of cotton fabrics in certain weather conditions are appropriate in terms of comfort, the PCM-enabled products proved to be the most appropriate in the tested temperature. The brace coated textiles give esthetic and physiological characteristics of the device which can be improved and the vital functions and in the healing effect to devices.

---

#### REFERENCES

1. <http://idiopathic scoliosis.com/the-bracing-experience/protocol-of-care>.
2. [http://www2.sci.u-szeged.hu/fokozatok/PDF/Czibula\\_Agnes/Czibula\\_Agnes\\_PhD\\_disszertacio.pdf](http://www2.sci.u-szeged.hu/fokozatok/PDF/Czibula_Agnes/Czibula_Agnes_PhD_disszertacio.pdf) p. 11.
3. Gyimesi S. Textilipari kézikönyv. 1979. p. 53.
4. Árokszállási K. Hőtárolás. A jövő technológiája Roxa Kft. 2002. p. 84.
5. <http://www.advancedfibres.eu/coolmax-2/what-is-coolmax/coolmax-comfort-system>.

*Felina Hungary Rt. give technical assistance to the products preparation.*

*This work was supported by the project GERINCO2 (TECH\_08-A1/2-2008-0121, NDA) respectively.*

## DEPTH SENSORS IN SCREENING OF SCOLIOSIS

Péter Major, Dániel Ayhan, Péter Tamás

Budapest University of Technology and Economics Mechanical Engineering Faculty

[axadox@outlook.com](mailto:axadox@outlook.com)

### 1. Introduction

The aim of the presented project was to develop equipment for screening and early recognizing of scoliosis. The Moiré method is generally used in practice, but the correct processing of Moiré images is not currently solved. Depth sensors capture images which describe the distances of the observed surfaces from the camera. With the help of these sensors a 2.5 D model of the human back can be created. This model can be used to create an automatic or semi-automatic scoliosis diagnosis system. The paper describes the development, structure and internal mechanisms of such a measurement method.

### 2. The theoretical background of the Kinect sensor

The Kinect has four main parts: an infrared projector, an infrared camera, a color camera and a signal processor. The infrared projector projects a structured pattern of points to the environment.<sup>1</sup> It uses a special pattern of points (lower left corner of *Figure 1*) to provide local position information on the infrared image which is captured by the infrared camera. This type of structured light depth mapping is patented by PrimeSense.<sup>2</sup> Because infrared light is utilized the effect of external lighting usually does not disturb the measurement. However, the device cannot be used in direct sunlight as the infrared light of the projector is not bright enough to give the necessary amount of contrast. If the reflectivity of the observed surfaces is too strong or weak, the Kinect may not be able to calculate their true distance from the camera. The depth map is calculated by triangulation, as the position of the emitted and captured rays of IR light is known, the position of their intersections can be determined. For this method it is necessary to have enough distance between the IR projector and detector, which causes shadows on the depth image. The optical zoom equipped depth camera achieves a working distance of 0.6 to 8 meters.

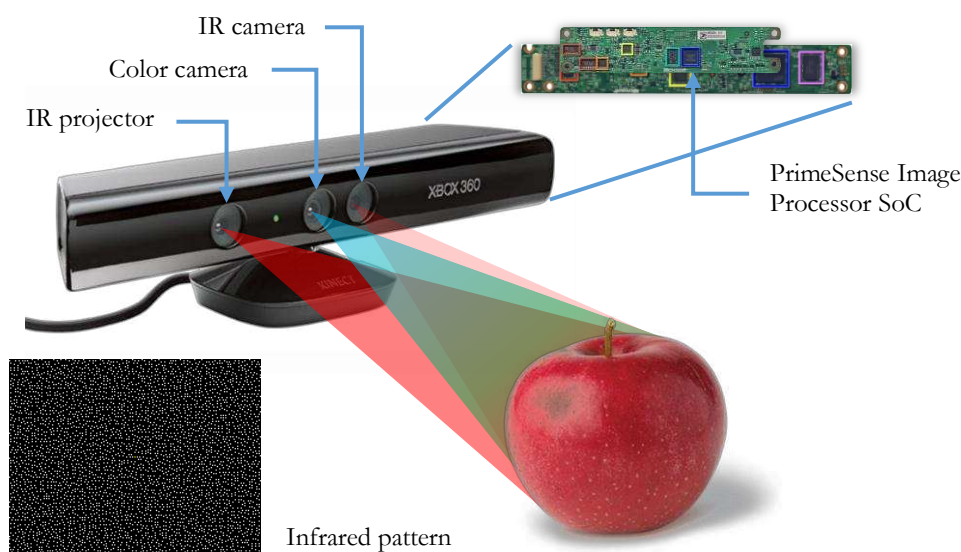


Figure 1. The Kinect sensor

The third main part of the Kinect is a color camera. The color images may be used to create textured models. The resolution of cameras is  $1280 \times 1024$  pixels, but the bandwidth of the USB 2 connection limits the video to 30 frame per second at  $640 \times 480$  pixels while transmitting the depth and color images simultaneously (Figure 2.). Because the projected grid of points cannot be used to calculate the depth for every pixel, the Kinect uses interpolation to fill the gaps. The distance measurement has a bit depth of 11 bits.



Figure 2. The color and IR images created with the Kinect

All cameras are calibrated during the manufacturing, but this calibration is not precise enough for 3D scanning. We have created an original calibration method to solve this problem.

### 3. Calibration

Before performing the measurements we had to calibrate the Kinect, for this the theoretical model of the measurement had to be established.

#### 3.1 The mathematical model of the Kinect

The Kinect was modeled as a pinhole camera and the distortion was described by the Brown model. Let a 3D point be on the surface of an observed surface ( $\mathbf{P}$ )! Let assume that we know the position of  $\mathbf{P}$  in the world coordinate system ( $P_w(x_w, y_w, z_w)$ )! The origin of camera is at the aperture of the lens,  $X$  is the horizontal axis,  $Y$  is the vertical axis of the picture plane and  $Z$  is perpendicular to  $X$  and  $Y$ . In this coordinate system every point has three coordinates  $(x, y, z)$ . From this we create  $Z$ -normalized coordinates ( $\mathbf{P}_n(x_n, y_n)$ ). After this the non-linear distortion of the cameras is applied.<sup>2-3</sup> The radial distortion is represented by (1) and (2) equations.

$$r_n^2 = x_n^2 + y_n^2 \quad (1)$$

$$\mathbf{P}_d = \begin{bmatrix} x_d \\ y_d \end{bmatrix} = (1 + k_1 r_n^2 + k_2 r_n^4 + k_3 r_n^6) \begin{bmatrix} x_n \\ y_n \end{bmatrix} + \mathbf{d}_t \quad (2)$$

Where  $\mathbf{P}_d(x_d, y_d)$  is the vector of the distorted point,  $P_n(x_n, y_n)$  is the Z-normalized vector,  $k_1..k_i$  are the coefficients of radial distortion and  $\mathbf{d}_t$  is the tangential distortion vector. Usually only the first two or three coefficients are used in practice. The tangential distortion is defined by (3).

$$\mathbf{d}_t = \begin{bmatrix} 2t_1x_ny_n + t_2(r_n^2 + 2x_n^2) \\ t_1(r_n^2 + 2y_n^2) + 2t_2x_ny_n \end{bmatrix} \quad (3)$$

Where  $t_1, t_2$  are the coefficients of tangential distortion. The perspective projection of the camera has to be applied to the distorted vectors. The projection is defined with the help homogenous coordinates by (4) and (5) equations.

$$\mathbf{A} = \begin{bmatrix} f_x & s & c_x \\ 0 & f_y & c_y \\ 0 & 0 & 1 \end{bmatrix} \quad (4)$$

$$\begin{bmatrix} x_i \\ y_i \\ 1 \end{bmatrix} = \mathbf{A} \begin{bmatrix} x_d \\ y_d \\ 1 \end{bmatrix} \quad (5)$$

Where  $\mathbf{A}$  is the camera matrix,  $f_x$  and  $f_y$  are the focal lengths in the direction of  $X$  and  $Y$  axes,  $c_x$  and  $c_y$  are the coordinates of the intersection point of the optical axis and the picture plane. The skew factor ( $s$ ) describes the bias of axes from perpendicular case ( $0$ ). With this transformation the projected point ( $\mathbf{P}_i(x_i, y_i)$ ) in the picture plane is defined. The flowchart of the projection model is shown on *Figure 3*. The projection is unambiguous in the direction of arrows in *Figure 3*. However, in the other direction it is non-linear and has multiple solutions due to the non-linear distortion. Fortunately with the GPU (Graphical Processor Unit) we can remove the non-linear distortion form the image, so a distortion free, linear model can be used.

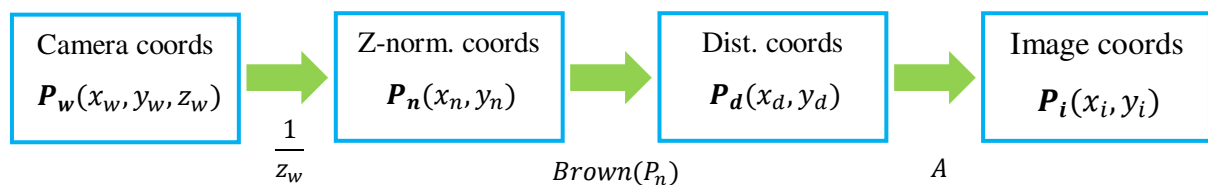


Figure 3. The projection model

This model was used for the color and the IR (depth) camera too, but first we had to estimate the parameters in the transformation matrices and distortion equations.

### 3.2 The calibration process

There are a lot of different methods for the calibration of the Kinect.<sup>4,6</sup> The calibration of IR and color camera is based on Zhang's method, which is implemented by the Camera Calibration Toolbox in MATLAB.<sup>7</sup> In this method multiple images are taken from different positions from a known sized chessboard pattern. Using the known relative positions of the corners of the

pattern and their position on the image an over constrained equation system can be defined, from which the value of parameters can be approximated by numerical optimization.

To simplify the capture of the necessary depth, color and IR images, we have created an easy to use interface, as shown on *Figure 4*. The captured images are processed automatically by our MATLAB script. First the corners of the checkerboard pattern are extracted with human assistance from the IR and color images (see *Figure 5*). After that the first approximation of the camera matrix, the distortion parameters, and the position of the pattern is calculated. The 3D positions of the corners are projected back to the image plane, and a new, automatic corner selection is performed. Than the approximation is repeated, to achieve better results. The reprojection errors also show the quality of the calibration (*Figure 6*.) After this we perform the stereo calibration of IR and depth cameras, the results are used for texturing the models.

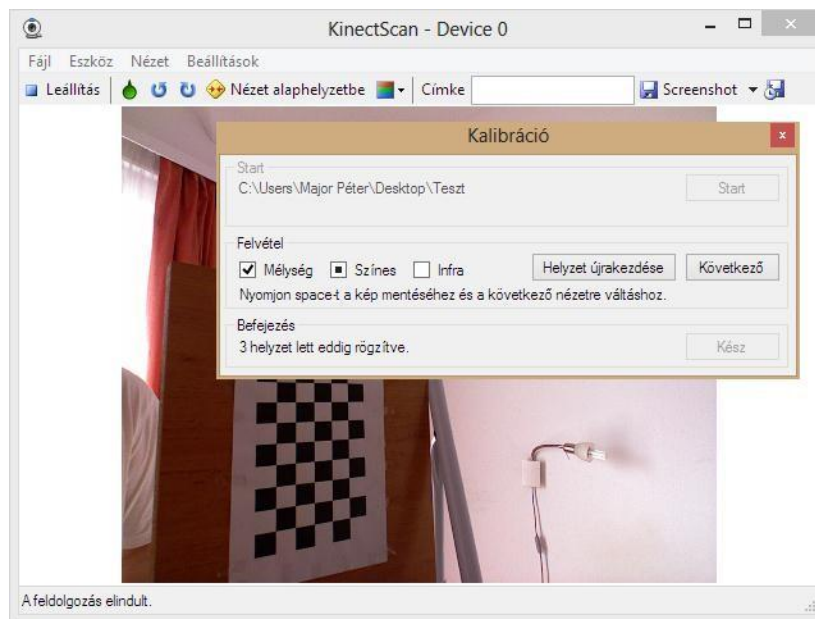


*Figure 4.* The calibration process

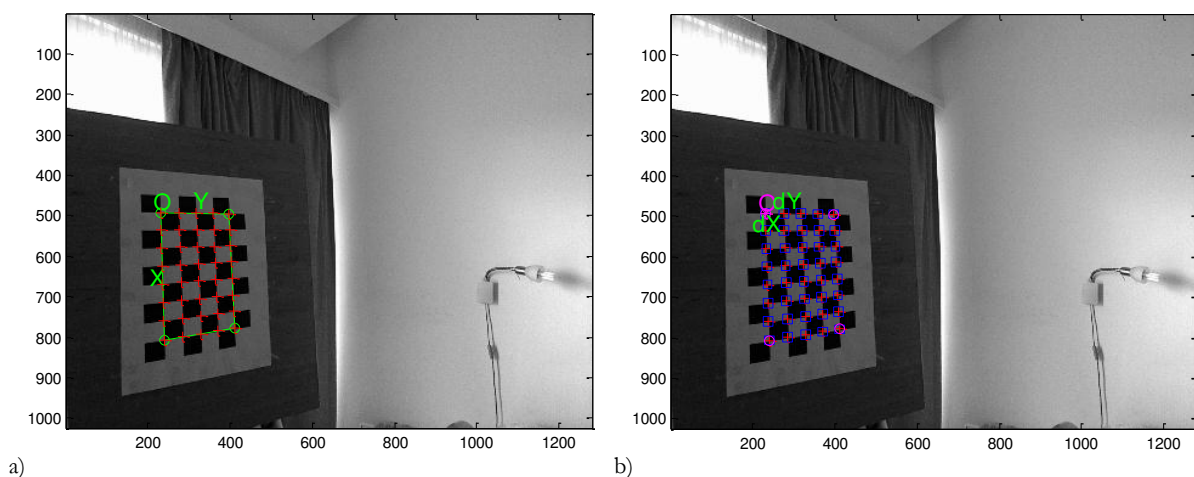


*Figure 5.* Corner extraction

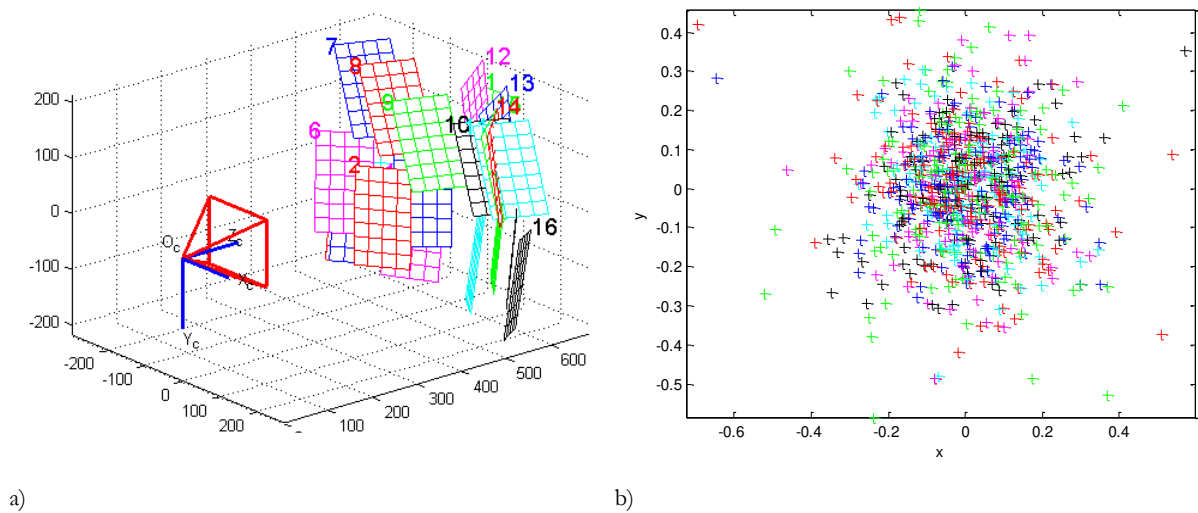


Figure 6. The backprojection

For the depth calibration of Kinect we have used the estimated position of the pattern and compared it to the measured depth values. Figure 7 shows the measured values. We have used non-linear curve fitting to approximate the depth function, and we have found the following formula:

$$h(x) = -2.33458 - \frac{35498.8}{x - 1093.09} \quad (6)$$

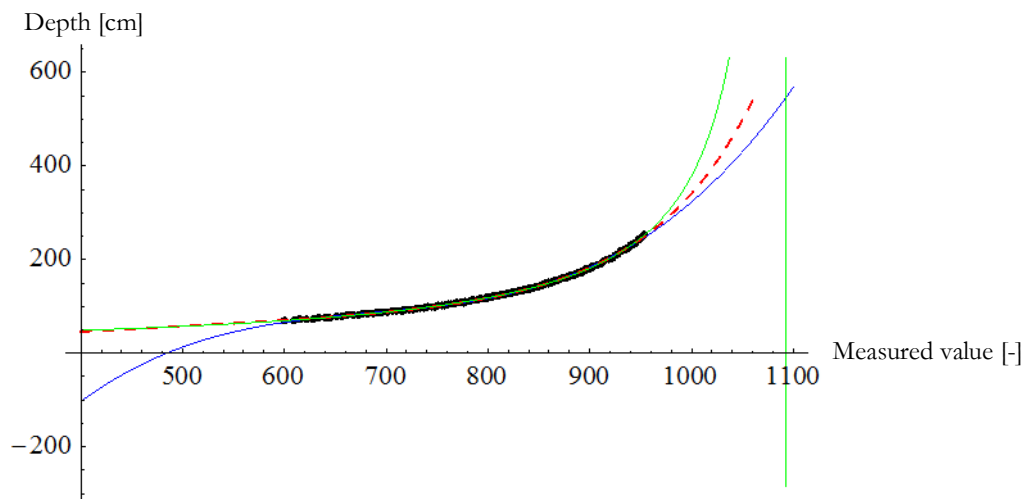


Figure 7. The depth values

#### 4. The image processing pipeline

The result of following process is the textured 3D model of the observed environment. The process is entirely hardware accelerated by the GPU, so it works in real-time.

#### 4.1 Control of processing

We have used the OpenKinect driver<sup>8</sup> because of its functionality and small resource usage. The structure of the image processing pipeline is shown on *Figure 8*.

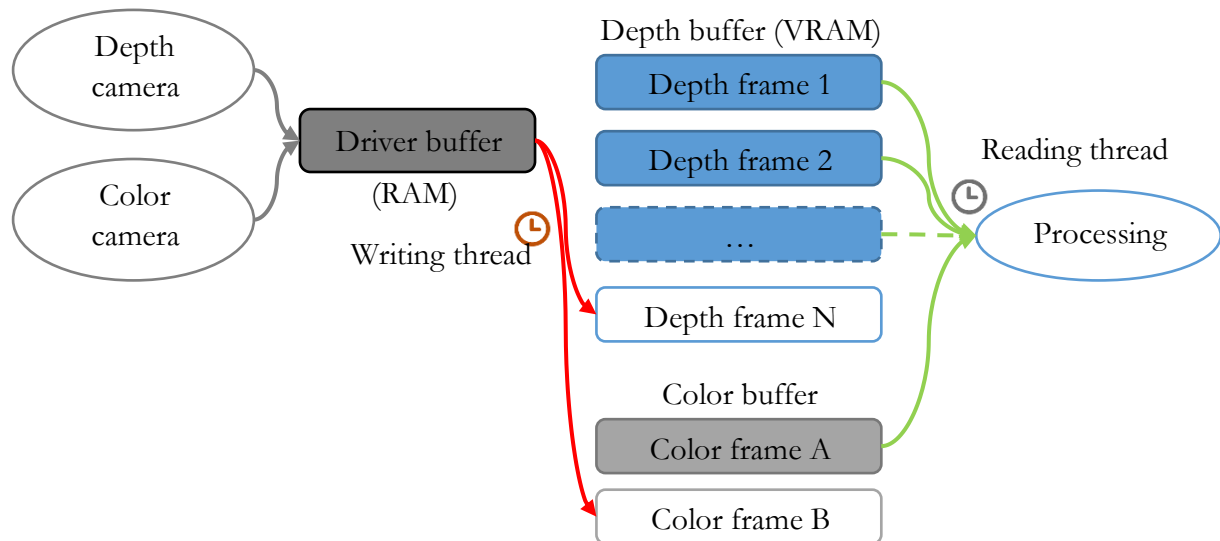


*Figure 8.* The image processing pipeline

As the depth and color images are captured asynchronously, first the depth and color images are uploaded to a double buffer in the video memory, where they stand ready for further processing. From this point every image processing related calculation is performed by the GPU, while the CPU controls the processing.

#### 4.2 Hardware accelerated image processing

The application development has been done with Microsoft DirectX in the .Net environment by using the XNA framework. This allowed us to utilize the raw power of the graphics card by writing every image processing function as a HLSL shader, and achieving rapid development with the help of the .Net framework.

As depth images are rather noisy, we have applied filtering on depth images. For static and quasi-static measurements we have used temporal averaging. For dynamic measurements averaging cannot be used, so we have also implemented Gaussian filtering for spatial averaging.

From the distortion parameters we have created distortion maps for depth and color images. With these maps we remove the distortion of the images by a special shader in real time. After removing distortion the color image is ready to use as a texture.

We calculate the vector of the represented light ray for each pixel of the depth image using the inverted camera matrix of the depth camera, with the constant depth coordinate of 1. After that the real depth for every pixel is calculated using the hyperbolic formula. Then the vectors are multiplied with the associated depth values, and we get the position of the points in the coordinate system of the depth camera.



These points can be projected on the screen using Z-normalization and a virtual camera matrix. Before that the user can also define a variety of transformations by the world matrix. With this the user can rotate, scale and translate the created model. The points can also be projected to the color image. This way the texture coordinates for each vertex are defined. The whole scheme of these calculations is shown on *Figure 9*.

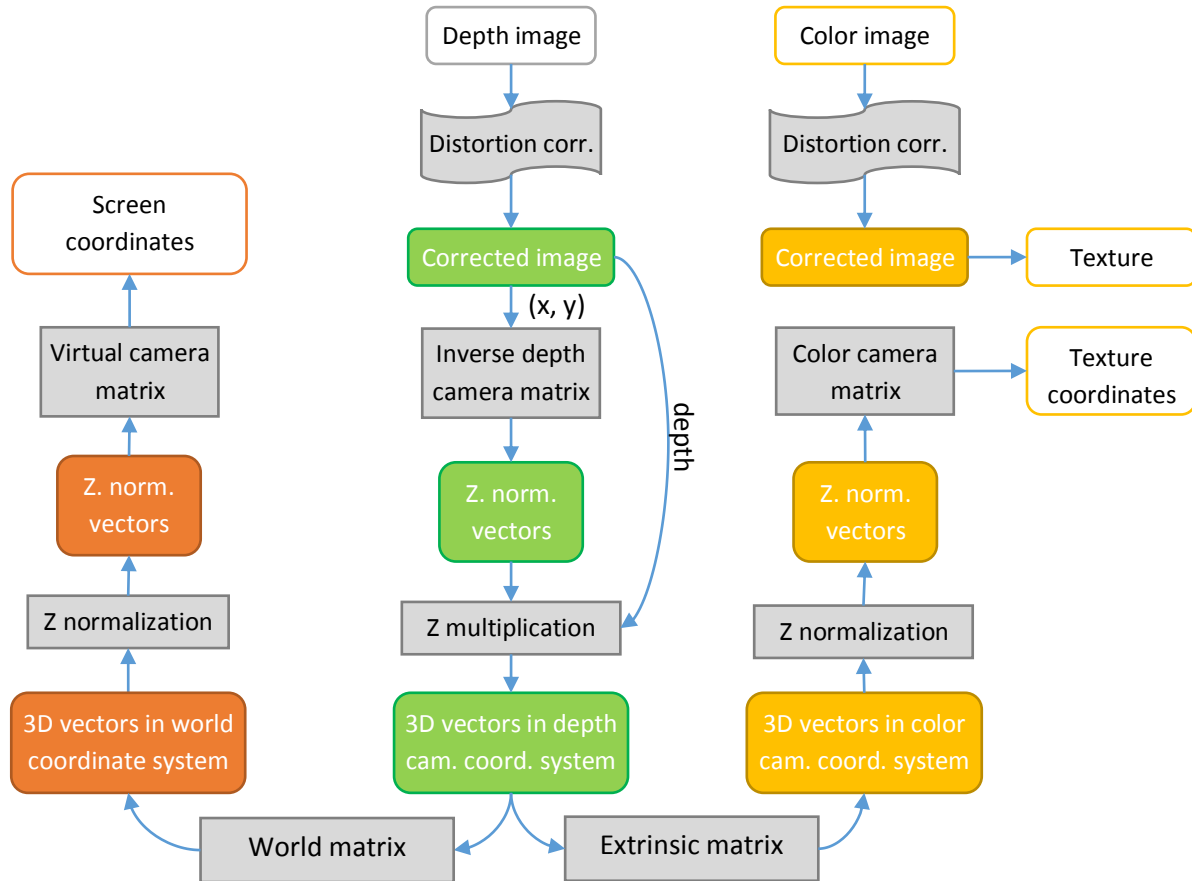


Figure 9. The flowchart of modelling

To show the 3D model we use the depth image as a displacement map for a grid of triangles. As the Kinect cannot see behind objects, it is necessary to remove some of the triangles which are facing nearly perpendicular to the depth camera. For this purpose the surface normals are also estimated, these can be used for visualization too.

## 5. Visualization

After the vertex processing numerous visualization modes are possible by applying different pixel shaders. It is possible to put the original texture on the model (first picture on *Figure 10*). The surface can be also colored by using the depth from the depth or the virtual camera. By applying a sinusoidal function to the depth we get false-Moiré images (second picture on *Figure 10*), which can be used for traditional diagnostic methods. We can specify a color scale for depth as shown on the third picture in *Figure 10*. By using the depth as the hue value in HSL color space we get rainbow shading (fourth picture on *Figure 10*).

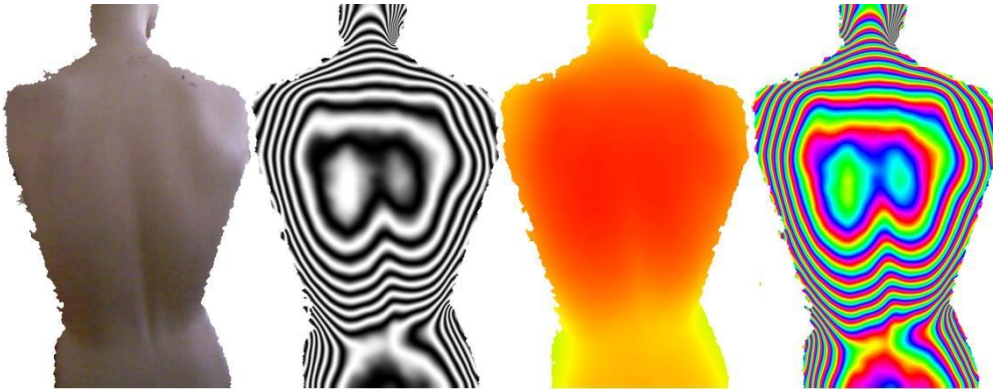


Figure 10. The visualization of the model

## 6. Position of vertebral column on the model

There is a hypothesis that the curve of the vertebral column can be estimated on a 3D model. In this case the 3D scanning works as a spinal mouse. In the first step we have to find the symmetry line of the back. This is computed by checking the cross sections of the back. The numerical model is based on the difference between the two parts as it shown in *Figure 11*. The minimum of the difference as a function of the position defines the symmetry point in every level.

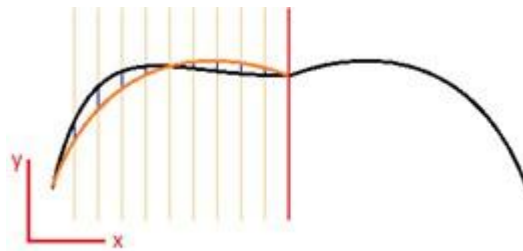


Figure 11. Searching for the symmetry curve

According to the hypothesis the symmetry point defines the position of the spine. (*Figure 12*.)

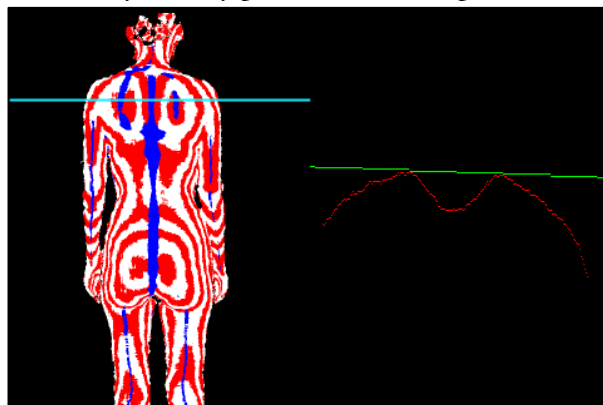


Figure 12. The estimation of the spine's position

## **7. Future work**

The presented method can be a good basis of the following tests to prove the possibilities of the method.

---

## REFERENCES

1. Freedman B, Shpunt A, Machline M, Arieli Y. „Depth mapping using projected patterns”, United States Patent Application Publication, Pub. No.: US 2010/0118123, 2010
2. Brown DC. „Close-Range Camera Calibration”, *Photogrammetric Engineering* 1971; 37(8): p. 855-66
3. Vassy G, Perlaki T. „Applying and removing lens distortion in post production”, *The Second Hungarian Conference on Computer Graphics and Geometry 2003*, Budapest, 2nd best speech.
4. Khoshelham K. „Accuracy Analysis of Kinect Depth Data”, *International Archives of the Photogrammetry, Remote Sensing and Spatial Information Sciences*, Volume XXXVIII-5/W12, 2011, ISPRS Calgary 2011 Workshop, 2011 Aug 29-31; Calgary, Canada. p. 133-38.
5. Smisek J, Jancosek M, Pajdla T. „3D with Kinect”, *2011 IEEE International Conference on Computer Vision Workshops, Proceedings*; p. 1154-60.
6. Herrera C. D, Kannala J, Heikkilä J. „Accurate and Practical Calibration of a Depth and Color Camera Pair”, *CAIP 2011, Part II, LNCS 6855*; p. 437–45.
7. Zhang Z „A flexible new technique for camera calibration”, *IEEE Transactions on Pattern Analysis and Machine Intelligence*, 2000; 22(11): p. 1330-34.
8. „The OpenKinect project”, [http://openkinect.org/wiki/Main\\_Page](http://openkinect.org/wiki/Main_Page), date of access: 2012. 09. 28.

**We would like to thank to the National Office for Research and Technology (NKTH) of the Hungarian Government for their support since this study has been carried out commonly as part of the project GERINCO2 TECH\_08-A1/2-2008-0121.**

## COMPUTER AIDED PROCESSING OF CERVICAL SPINE RADIOGRAPHS

Petra Aradi<sup>1</sup>, László Danka<sup>2</sup>, György Lipovszki<sup>1</sup>, Ildikó Németh<sup>3</sup>

<sup>1</sup>Budapest University of Technology and Economics, Faculty of Mechanical Engineering, Department of Mechatronics, Optics and Engineering Informatics

<sup>2</sup>Policlinic of Hospitaller Brothers of St. John of God, Department of Orthopedics

<sup>3</sup>Dr. Rose Kft.

[aradi.petra.bme@gmail.com](mailto:aradi.petra.bme@gmail.com)

---

### **Abstract**

Quite a number of medical specialties require distance and angle measurements on x-ray images. Drafting and measurement on traditional x-ray films can be done with marker pens, rulers and protractor, but this method is time consuming and often inaccurate. Authors present a computer aided drafting and measurement method for both digitized and digital x-rays.

Evaluation of cervical spine x-rays is especially important for patients suffering from rheumatoid arthritis. Our computer program helps users to mark necessary points and draw lines on x-rays interactively on the computer screen, then the program calculates relevant angles and distances based on literature data.

Manual drafting on traditional x-ray films is time consuming, and it is usually impossible or at least difficult to repeat. When one wants to try drafting more than once, previous lines have to be erased from the film, or a separate transparent film can be used. Reading distance and angle values requires a ruler and a protractor. The tip size of the marker pen and the precision of ruler, protractor positioning can result in measurement errors of multiple millimeters and degrees.

Contrarily, computer based drafting allows arbitrary number of users arbitrary number of attempts to define necessary points on x-rays, and then predefined algorithms calculate the results.

Computer aided drafting can be performed by many persons, a number of times. Accuracy can be improved by using image processing capabilities such as zooming, contrast correction, etc. Results can be superimposed on x-ray images, making follow-up easier.

Compared to „traditional” drafting, the computer-aided method’s repeatability and reliability is a great advantage. It is easier to learn computer-based drafting, especially when a large number of points have to be marked and complicated measurements are involved. With an appropriate drafting and evaluation protocol, processing of x-rays provides added diagnostic value, e.g. further examinations can be ordered based on the results, scheduling of follow-ups can be optimized.

**Keywords:** functional radiograph, rheumatoid arthritis, digital processing, distances and angles.

---

### **Introduction**

As stated in the reference<sup>1</sup> joint destruction in rheumatoid arthritis patients’ cervical spine may lead to progressive vertebral instability. The consequences of this condition can lead to sudden death under certain conditions, e.g. during anaesthesia. Physical symptoms are not always in

correlation with joint destruction, meaning symptomless patients might very well be endangered. Cervical spine deformities can be visualized on radiographs. Five standard x-ray settings are used: conventional bidirectional (anteroposterior and lateral), transoral dens and functional (performed in flexion and extension) lateral images are taken. This study discusses the importance of such radiographic examinations, both as preoperative evaluation and as follow-up examination. Based on the results of such examinations, patients can be directed to other imaging tests, such as x-rays in other directions, CT, MRI, to decide on eventual operative fixation.

In order to uniformly evaluate this radiograph series, various methods are to be found in international literature. Common in these methods is the use of lines directed through certain anatomical points. Distances and angles are calculated from these lines, providing the possibility of diagnostic classification. Traditional drafting methods involve the use of marker pens, rulers, a protractor and a traditional x-ray film. Manual drafting on traditional x-ray films is time consuming on the one hand, and it is usually impossible or at least difficult to repeat on the other hand. Difficulties come up if drafting has to be performed more than once, or the original radiograph without pen lines has to be kept as well. Further errors can occur from too wide tip size of the marker pen, precision of measurement devices, and reading errors. Another problem arises from the use of digital x-rays, when the image is normally not printed, so that drafting can be performed.

Physicians evaluating such series of radiographs require thorough training in this relatively time (and resource) consuming drafting process and in determining required distances and angles.

To get around these difficulties, a computer program is developed. The program can use digital x-ray images natively, while traditional x-ray films have to be digitized. Another advantage is the systematic onscreen “drafting”, where the evaluation protocol is to be followed, minimizing the chances of error from incorrectly marked points and lines. A further asset is that the use of the program requires less experience, than “traditional” drafting. Other advantages of computer processing include automated calculation of distances and angles, as well as the opportunity of evaluation by multiple users, more than once, and digital storage of images, drafted lines and results.

## **Methods and materials**

### **X-ray protocol**

The method<sup>1</sup> developed at Policlinic of Hospitaller Brothers of St. John of God is systematically covers screening, measuring and grading of cervical subluxations and instability. The protocol specifies how x-rays have to be made (*Table 1* and *Figure 1*).<sup>1</sup>

| # | Description   | Sample    |
|---|---|-----------|
| 1 | Anteroposterior axis, 100 cm focus-film distance, 10° caudocranial tilt, centered to C3   | Figure 1a |
| 2 | Lateral direction, 150 cm focus-film distance, horizontal primary beam, centered to C2  | Figure 1b |
| 3 | Lateral direction, flexion with chin pressed down, 150 cm focus-film distance, horizontal primary beam, centered to C3          | Figure 1c |
| 4 | Lateral direction, extension with head tilted back, 150 cm focus-film distance, horizontal primary beam, centered to C3         | Figure 1d |
| 5 | Anteroposterior axis, transoral dens image, 50 cm focus-film distance, perpendicular primary beam, centered to dens epistrophei | Figure 1e |

Table 1. X-ray protocol for rheumatoid arthritis<sup>1</sup>

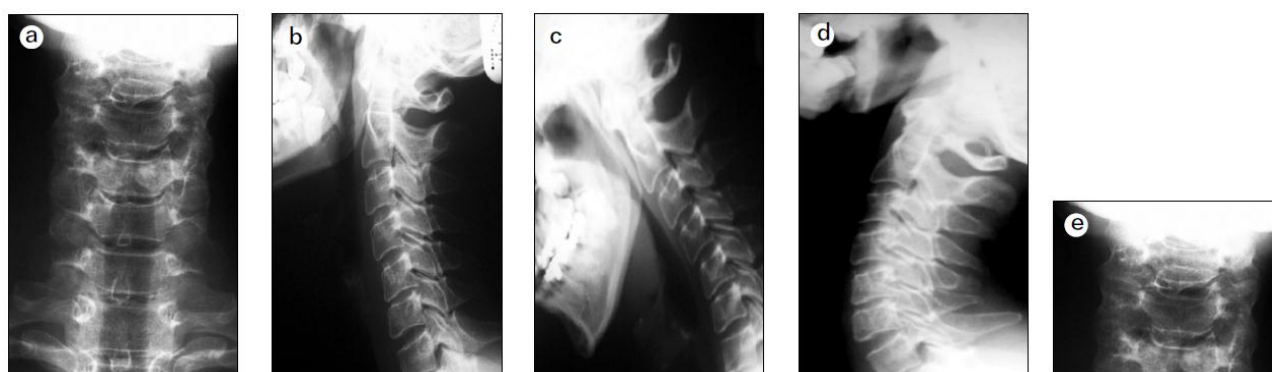


Figure 1. Sample images<sup>1</sup> prepared according to x-ray protocol for patients with rheumatoid arthritis

a: Anteroposterior, b: Lateral, c: Functional lateral (flexion), d: Functional lateral (extension), e: Transoral anteroposterior dens

### Drafting protocol

Drafting protocol, e.g. specific points and lines, developed at Policlinic of Hospitaller Brothers of St. John of God is composed of a number of evaluation methods from international literature.

There are two types of x-rays, anteroposterior (normal and transoral dens), and lateral (neutral, fully flexed and extended). The points, lines and distances needed in evaluation of transoral dens images are shown in Table 2 and Figure 2.

| Object id | Description  |
|-----------|--|
| 1         | intervertebular line   |
| 2         | bimastoid line   |
| 3         | transspinous-transdental line going through the central line of dens |
| 4         | distance from dens to lateral mass of atlas on both sides            |

Table 2. Objects to be marked on anteroposterior transoral dens radiograph<sup>1</sup>

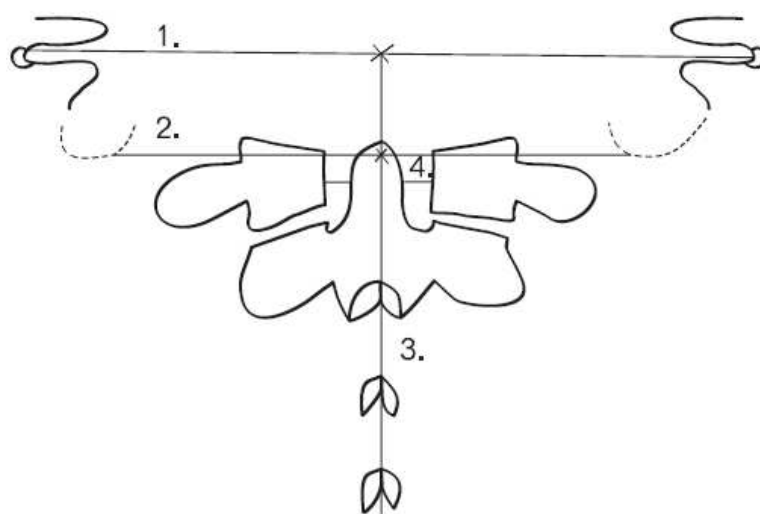


Figure 2. Lines to be drawn on anteroposterior transoral dens radiograph<sup>1</sup>

Lateral radiographs are evaluated with the use of points, lines and angles specified in the above mentioned protocol, and are presented in *Table 3* and *Figure 3*.

| Object id | Description   |
|-----------|---|
| 1         | atlantodental interval (ADI) is measured between the line drawn over the dorsal contour of C1's anterior tubercle and the ventral surface of dens                   |
| 2         | posterior atlantodental interval (PADI) is the retrodental space  |
| 3a        | lower atlas line in Sakaguchi–Kauppi method   |
| 3b        | tangential line of upper arc of C2's pedicle in Sakaguchi–Kauppi method   |
| 4         | subaxial central canal (sAC) is the shortest distance between dorsal vertebral line (8) and spinolaminar line (7) on a given level                                  |
| 5         | line in McGregor method connects dorsal endpoint of os palatum with outer contour of occiput, and the relative position of the dens' tip is compared to it          |
| 6         | in Wackenheim method a line is drawn down the posterior surface of the clivus and its position is compared to the posterior aspect of dens                          |
| 7         | spinolaminar line is an arc connecting the inner contours of spinous processes from the posterior margin of foramen magnum  |
| 8         | posterior vertebral line is an arc above the dorsal contours of vertebral bodies  |
| 9         | processus spinosus relation is the distance between two neighboring spinous processes (lower arch of the upper one and the upper arch of the spinous process below) |
| 10        | angle of lines drawn at the lower surfaces of two neighboring vertebrae   |

Table 3. Objects to be marked on lateral radiographs (neutral, flexed, extended)<sup>1</sup>

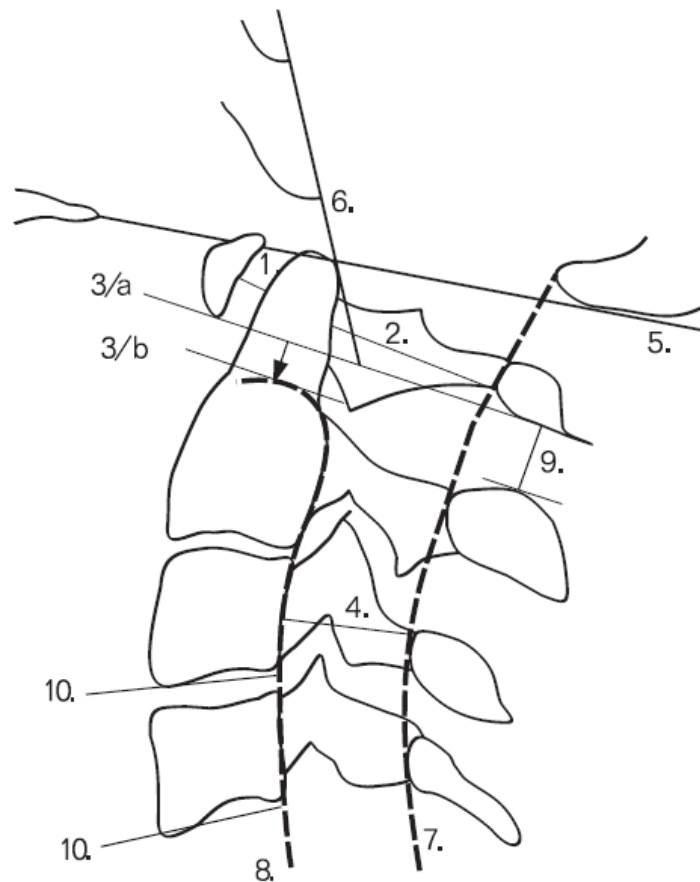


Figure 3. Objects to be marked on lateral radiographs<sup>1</sup>

## Results

### Drafting and evaluation program

2009 versions of National Instruments LabVIEW<sup>2</sup> and NI Vision<sup>3</sup> were used to implement computer based drafting and for calculating relevant distances and angles.

The program has a main window (*Figure 3*), to control execution. Each function (selecting radiographs, evaluating various images and finally displaying results) can be accessed with a button. At the moment everything (button labels, instructions, etc.) are bilingual.

Functions have to be performed in a certain order, so it is not possible to press the five drafting buttons, until the first task, namely selecting radiographs has not been completed. The completion of each task is indicated by a round LED next to the button (e.g. the first task is completed in *Figure 3*). Similarly, it is not possible to press the Results button, until at least one evaluation has not been completed. When the user presses a button, a new window opens, and after finishing the selected task it is closed, and the user is returned to the main window. The



Stop button in the lower right corner of the main program window allows stopping the program; however without performing the saving of results, each and every drawn line and calculated value will be lost. To avoid accidental data loss, pressing Stop pops up a confirmation dialog.

Traditional x-ray films have to be digitized (into JPG format), DICOM digital images has to be converted to JPG. When the program asks the user for the five images, user has to select the one that is specified in the title row of each File Open dialog box (Figure 4).

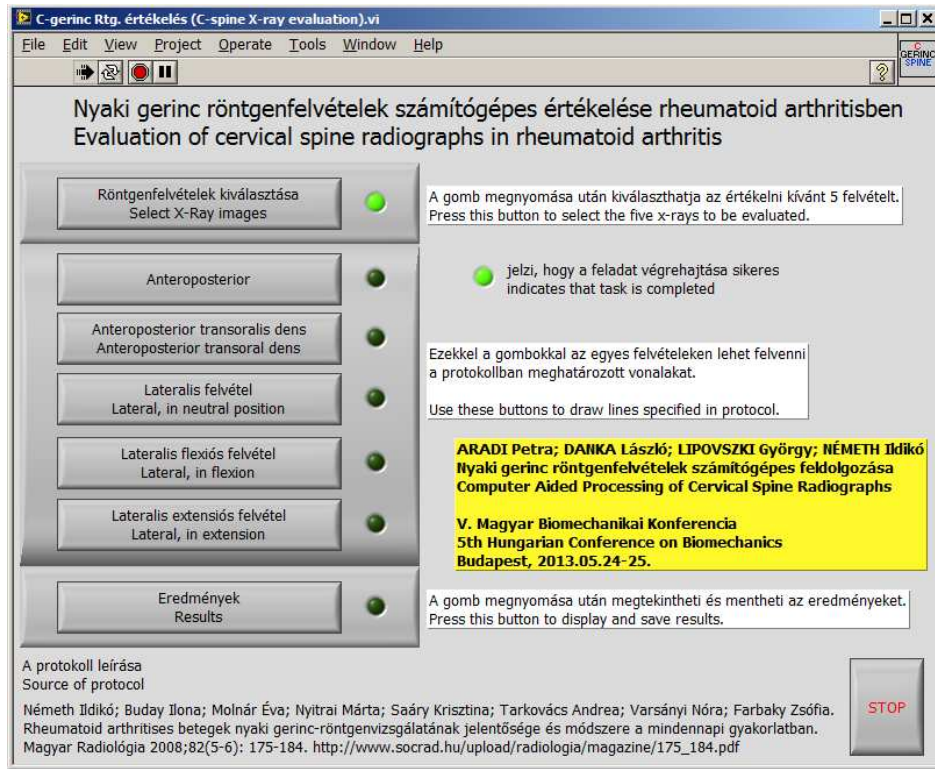


Figure 3. Main program window

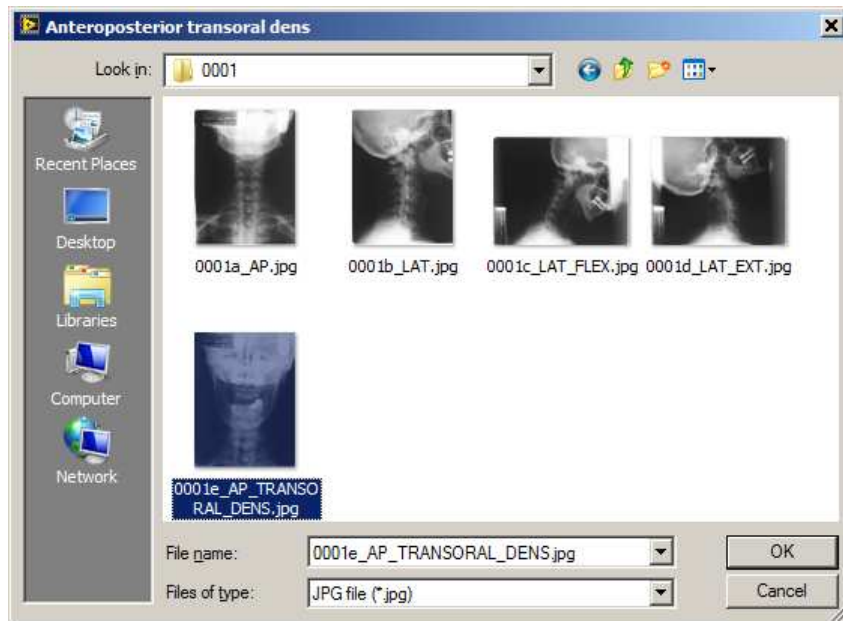


Figure 4. Selecting and opening JPG format radiographs one by one

The user interface in each of the drafting tasks shows the graphics (Figures 2,3) and bilingual text guides (Tables 2,3) from the protocol as a help for users. In Figure 5 evaluation steps for the anteroposterior transoral dens radiograph are presented, showing that step 3 is already completed. In the small image in the lower left part of the window the already drawn transspinous-transdental line is visible. When the user presses one of the numbered buttons, a new window opens up with the image sized to the maximal vertical screen resolution, in order to make drawing not too difficult and as precise as possible. Until this image window is open, the line can be modified by its endpoints or moved as a unit. Each numbered drawing step can be redone as many times, as it suits the user. Stop button can be pressed anytime, without even performing any drawing; however it has no use, because it does not produce any lines and consequently nothing can be calculated.

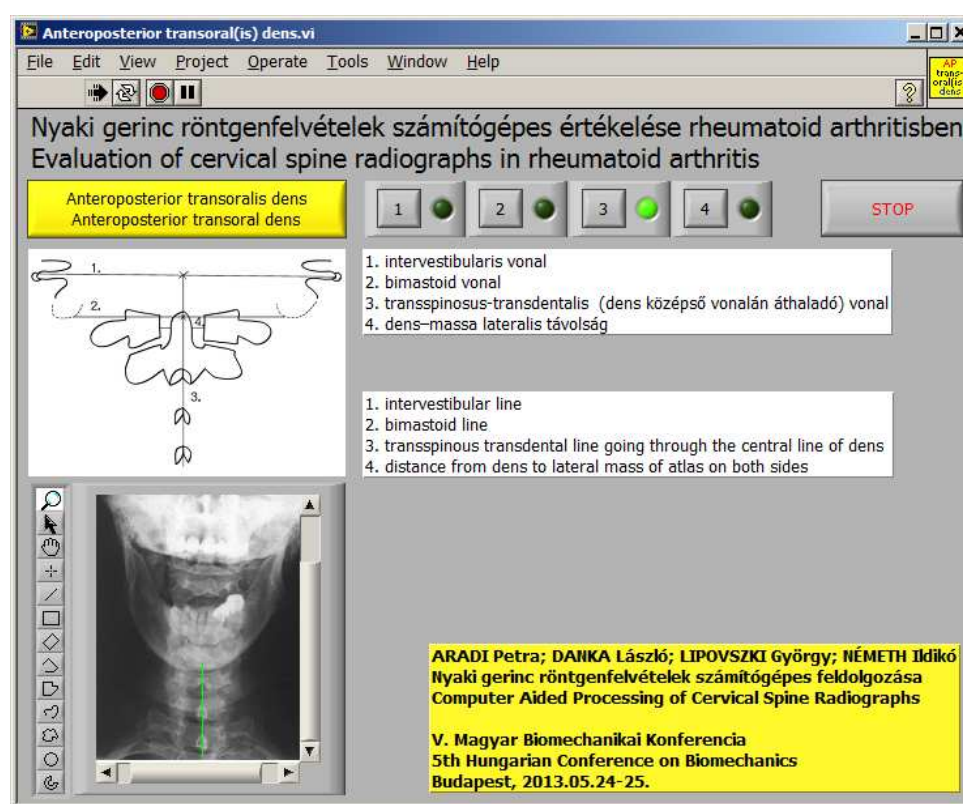


Figure 5. Drafting on anteroposterior transoral dens radiograph with step-by-step instructions

Windows similar to the one in Figure 5 are available for all the other images. Because of the interdependency of elements drawn on lateral images (as shown in Table 3), e.g. step 4 requires lines 7 and 8, user have to draw these two lines first, to enable button 4.

When drafting tasks are completed and Results button is pressed, first patient's data can be set, as well as the evaluating person and other relevant data. The program then performs the necessary calculations to provide results needed to determine patient's status. Pathologic values and the

recommended diagnostic procedures from the referenced article<sup>1</sup> are included in the program, so that it can mark them and classify the type and degree of atlantoaxial subluxation accordingly.

For the time being, the possibility of drawing other widely used auxiliary lines for methods, which are not part of the protocol, such as Ranawat, or Redlung–Johnell-method, a button is set in the Results section. By pressing this button similar drafting windows appear, and results can be obtained, too.

### **Conclusion**

The program is still under extensive testing and development, according to users' needs; however one can immediately see the positive difference it brings, compared to traditional manual drafting. Among the advantages one has to mention that drafting and evaluation can be repeated, results as numbers, text and lines superimposed on radiographs can be stored.

Further development might include some kind of automation in recognizing points to be used to draw the lines, true multilingual user interface, etc.

---

### REFERENCES

1. BÍRÓ I, CSIZMADIA BM, KATONA G. Determination of instantaneous axis of rotation of tibia and its role in the kinematical investigation of human knee joint. In: L. Borbás editor. Proceedings of the Third Hungarian Conference on Biomechanics; 2008. July 4-5. Budapest; 2008:57-62.
2. Fekete G, De Baets P, Wahab MA, Csizmadia BM, Katona G, Vanegas-Useche LV, Solanilla JA. Sliding-rolling ratio during deep squat with regard to different knee prostheses. Acta Polytechnica Hungarica 2012; 9(5): 5-24.
3. Szakál Z. Mérőberendezés térdízület mozgásvizsgálatához. GÉP 2006; LVII(1): 37-40.

*The authors would like to thank National Development Agency (NDA) of Hungarian Government for its support since this study has been carried out commonly as part of project GERINCO2 TECH\_08-A1/2-2008-0121.*

## TRACKING MOVEMENT OF BODY-MOUNTED MARKERS THROUGH OPAQUE ORTHOTICS

Petra Aradi<sup>1</sup>, Gábor István Horváth<sup>1</sup>, András Czmerk<sup>1</sup>, Tamás Terebessy<sup>2</sup>, Péter Tamás<sup>1</sup>

<sup>1</sup>Budapest University of Technology and Economics, Faculty of Mechanical Engineering, Department of Mechatronics, Optics and Engineering Informatics

<sup>2</sup>Semmelweis University, Department of Orthopedics

[aradi.petra.bme@gmail.com](mailto:aradi.petra.bme@gmail.com)

---

### **Abstract**

It is very important in marker-based motion capture systems that cameras can follow markers attached to anatomical points without any obstruction. Based on marker positions the computer program can reconstruct movement of the body's biomechanical model by calculating typical distances, angles and trajectories.

Analysis becomes complicated when the person wears a rigid and opaque orthotic device (e.g. a plastic corset), through which cameras can not see markers attached to the body surface.

We had to find a marker attachment method, so that infrared motion capture cameras can follow movement of markers attached to certain anatomical points on scoliosis patients wearing their corsets, when analyzing the effects of corsets on posture and movement.

Infrared cameras in the Gait Analysis Laboratory of Semmelweis University's Department of Orthopedics can not „see through” polyethylene corsets. Markers have to be attached directly to the body surface, because a corset is a rigid body, therefore it moves differently, than the human body under it. Multiple considerations have to be made, when choosing markers. There is limited room between body and corset, markers can not affect wearer's movement and can not cause discomfort. The chosen method uses magnets attached to the skin with medical tape. Size and properties of magnets were verified by simulation. Infrared cameras can follow the painted magnet counterparts on the outer surface of the corset.

Magnets attached to the corset's outer surface follow the movement of magnets taped to the body, so cameras can follow movement of anatomical points under the opaque corset, without the need of providing direct visibility by destructing corset material. Holes larger than the size of markers would be required, to avoid the shading effects of the corset resulting from body-corset and body-camera distance and angle.

According to measurement results of patients with and without corsets, magnetic markers sufficiently follow the body's movement under the corset. In the meantime with markers attached immovably to the corset's outer surface, movement of the corset as a rigid body can be tracked, as well.

The presented method allows further detailed investigation, concerning the movement altering effects of not just corsets, but other orthotics, too.

**Keywords:** biomechatronics, spinal disorders, magnetic sensors, corset, motion capture system

## Introduction

The number of juvenile scoliosis patients is increasing worldwide. Part of conservative treatment is the use of rigid orthotic devices, called corsets<sup>1</sup>. It is important to analyze the effects of corsets, which can be done with gait analysis<sup>2</sup>, since the spine plays a central role in posture and movement.

The infrared marker based motion capture system of Semmelweis University's Department of Orthopedics was used to test various sensor configurations. Markers are attached to the person's body in specific anatomical points, which the motion capture system uses for computer reconstruction of movement. Markers to be used by persons wearing a corset have to:

- be small enough to fit between corset and body surface
- weigh little, so that movement is not notably affected
- be detectable through the corset's polyethylene material
- be as small as possible, so that they can be considered point wise
- be easily attachable and eliminate skin motion
- be safe to wear and be of no health risk

A number of trials showed, that widely used polyethylene corsets do not allow infrared cameras to „see through” them, that is “regular” markers attached to the body under the corset are invisible for cameras. Various methods were tested, and finally magnetically attached markers provided satisfactory results. Magnetic attachment properties were tested and simulated, than evaluated with the motion capture system.

The basis of work presented in this paper was carried out in the frame of Gerincőr (SpineGuard) Project, as a thesis<sup>3</sup> project submitted as partial fulfillment of BSc in Mechatronic Engineering degree, by the second author, under the supervision of the other authors.

## Methods

### Motion capture system setup

Motion capture systems use markers attached to anatomically relevant body points. The above mentioned motion capture system uses six static infrared cameras. Markers that these cameras can detect are attached to certain body points with medical adhesive as shown in *Figure 1*. The test person walks along a predefined path, meanwhile cameras record position of markers. After that the software processes the acquired data and shows reconstructed 3D movement on screen. Wavy lines on *Figure 1* show the position of markers during walking.

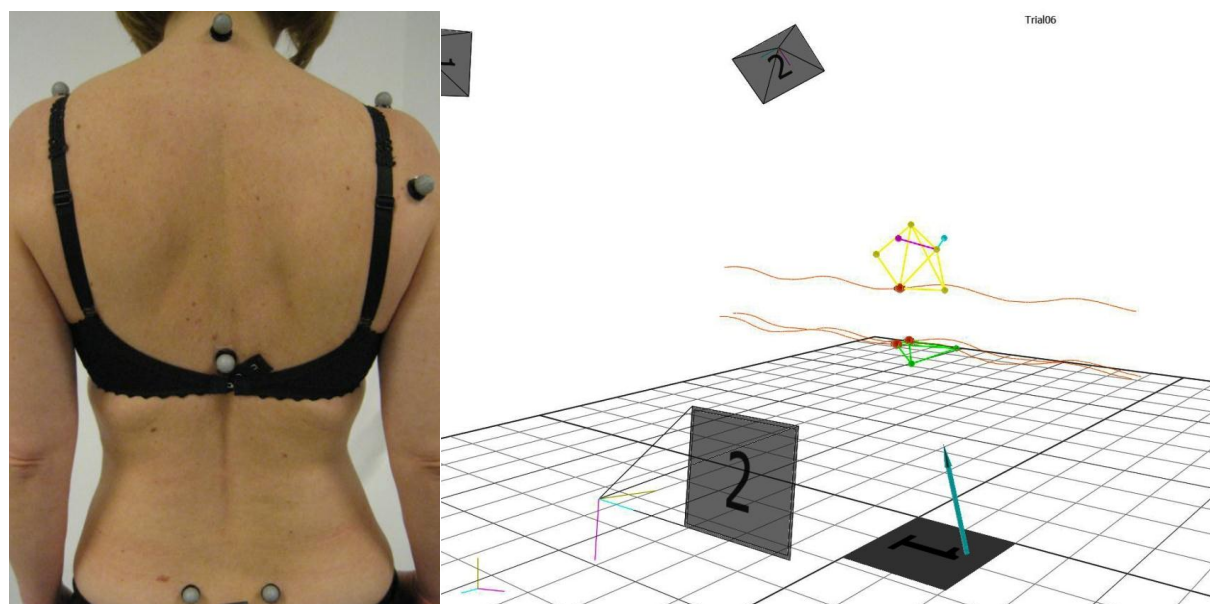


Figure 1. Infrared markers attached to skin and their recorded movement

The effects of wearing a corset appear not just in static posture, but during movement, as well. An important aspect would be the possibility to compare movement with and without corset. Infrared markers under the corsets are not just invisible for cameras, but as one can see in *Figure 1*, in most cases are too big to fit under the corset. The conclusion is that this measurement system can not be used for testing patients wearing an opaque corset.

The very first idea, namely attaching the markers normally used on skin, onto the corset, above the predetermined points is of no practical use. It can surely show the corset's movement, however the important aspect would be to follow the body's movement under the rigid corset.

### Cutting holes on the corset

One possibility is to cut holes on the corset where markers need to be placed. It is not optimal, because holes destruct corset material, and they might even be large enough to endanger corset's structural integrity. Holes do have to be of larger diameter than markers, to allow the minimal movement of markers together with skin movement and to avoid the shading effects of the corset resulting from variable body-corset and body-camera distance and angle, especially during movement.

### Infrared LEDs as markers

Another option is the use of infrared LEDs attached to the skin as markers. This option has quite a number of drawbacks. However LEDs and the necessary electronics including batteries can be small enough (well under a square centimeter), so size is not a problem, but it requires quite high power to light through the corset, which means a large amount of dissipated heat, making it uncomfortable to wear.

Still, there were experiments made with LED panels, after the most appropriate components were selected and simulated with SPEOS program (Figure 2).

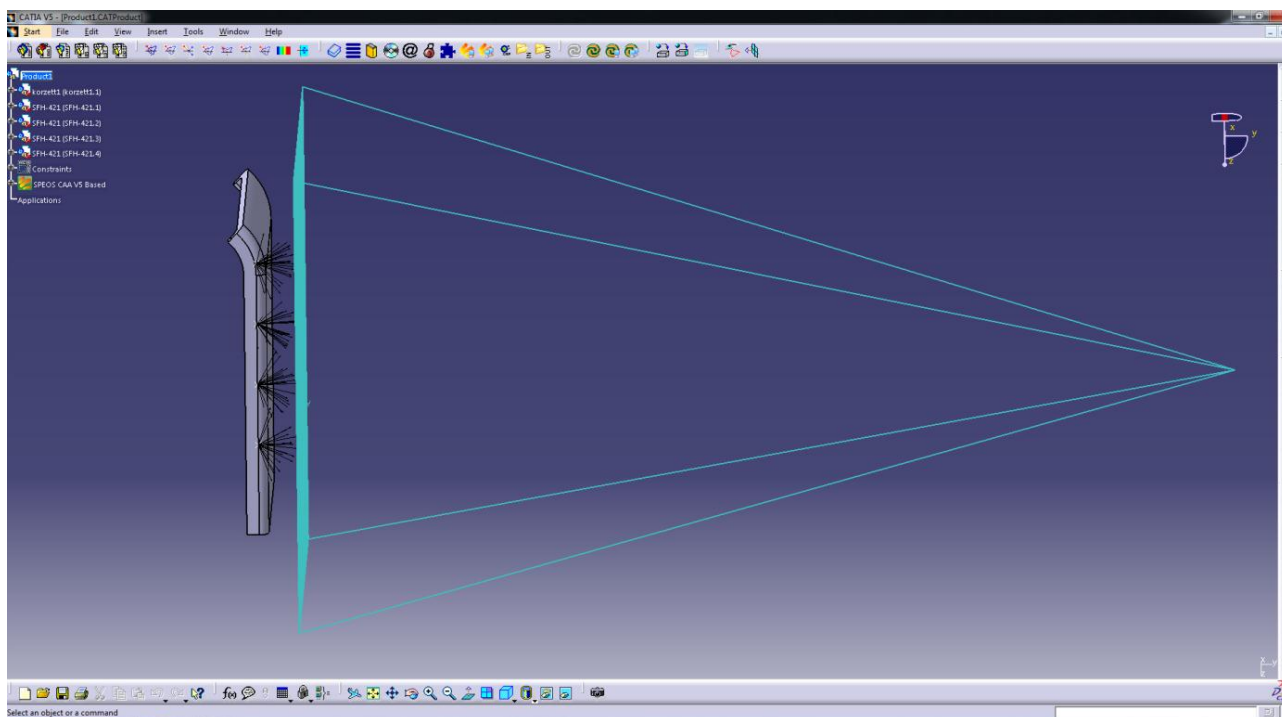


Figure 2. SPEOS light intensity simulation of chosen infrared LEDs placed on the body under the corset

After obtaining the convincing simulation results, an experimental setup was built and tested with the motion capture system. LEDs were mounted under a corset and placed into the laboratory. The results showed that the selected setup is not applicable, because cameras could not detect infrared light from LEDs hidden behind the corset. Without the opaque corset, infrared LED markers were perfectly detectable with the cameras, even during movement.

The contradictive results of simulation and measurement might be traced back to the too simplified corset model geometry, which does not take into account light scattering on the real corset surface.

### **Magnets as bridges between skin and corset**

The idea of magnetic motion capture systems is already present in literature<sup>4</sup>, but because of the limited range of the mentioned system and the need to use the available infrared motion capture system, another approach had to be evaluated.

The basic idea is the use of permanent magnet pairs, one of which is attached to the skin in desired anatomical points, while the other magnet is on the outer side of the corset. The latter

magnet is covered with special dye that makes it visible for infrared cameras. When the marker magnet on the body moves, its pair also changes position, what cameras can follow.

Magnets have to satisfy the six requirements specified in Introduction. So, magnet pairs have to be lightweight, small in size, but have to provide sufficient cohesion. The chosen magnets are made of rare earth elements, and are usually nickel plated. Nickel is a metal that often causes allergic skin reactions, so magnets can not be covered with nickel to avoid health risks.

Cylindrical magnets were chosen, and their geometric model and material properties were introduced in finite element simulation (*Figure 3*), to optimize magnet dimensions that provide appropriate cohesion.

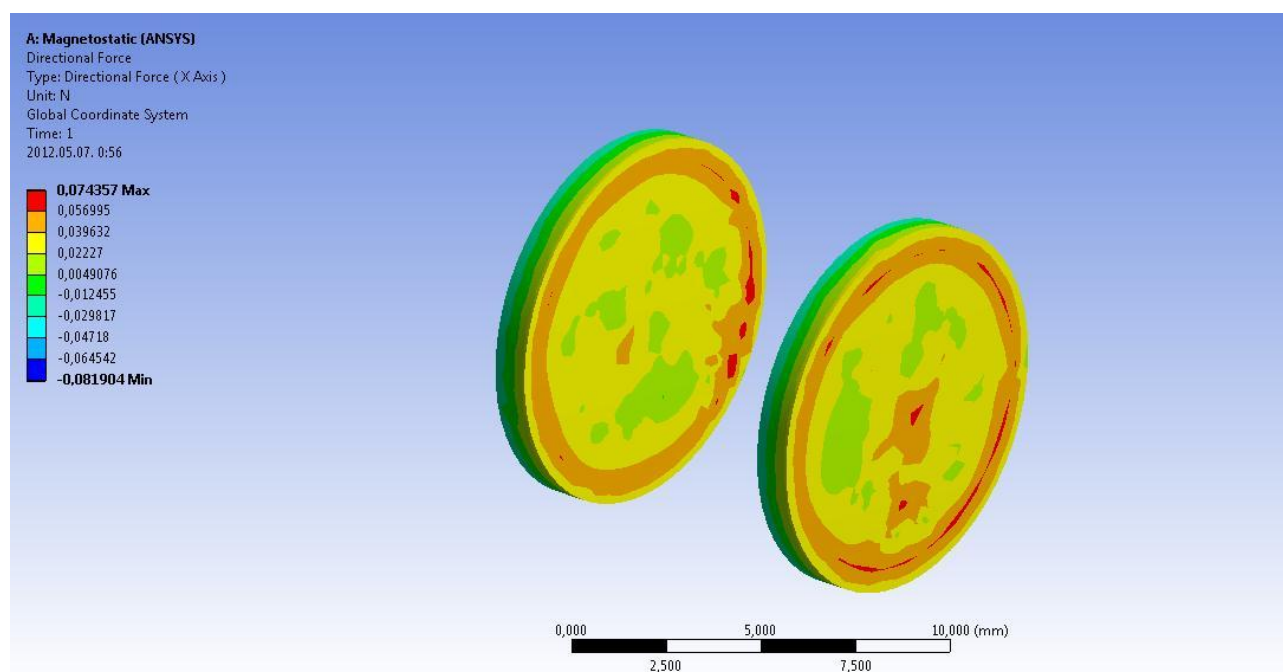


*Figure 3.* Finite element simulation of magnet pair

Further tests were carried out with parametric models to determine relationship among magnet size (radius and height), distance between magnets and forces. One of the results among three of four parameters, magnet radius, (half the) distance and force between magnets is shown in *Figure 4*. Similar graphs were obtained for the other two available parameter combinations.

Constraints had to be defined for magnet height, because 4 mm high magnets can be placed on the skin without touching the corset from inside. The other limit (1 mm) is the height of commercially available disk shaped magnets.

A parameter sensitivity diagram (*Figure 5*) was also obtained from the program, showing that force between magnets is mostly affected by distance (távolság), the negative sign meaning inverse proportionality. The second affecting parameter is magnet height (vastagság), where the positive sign represents direct proportionality.



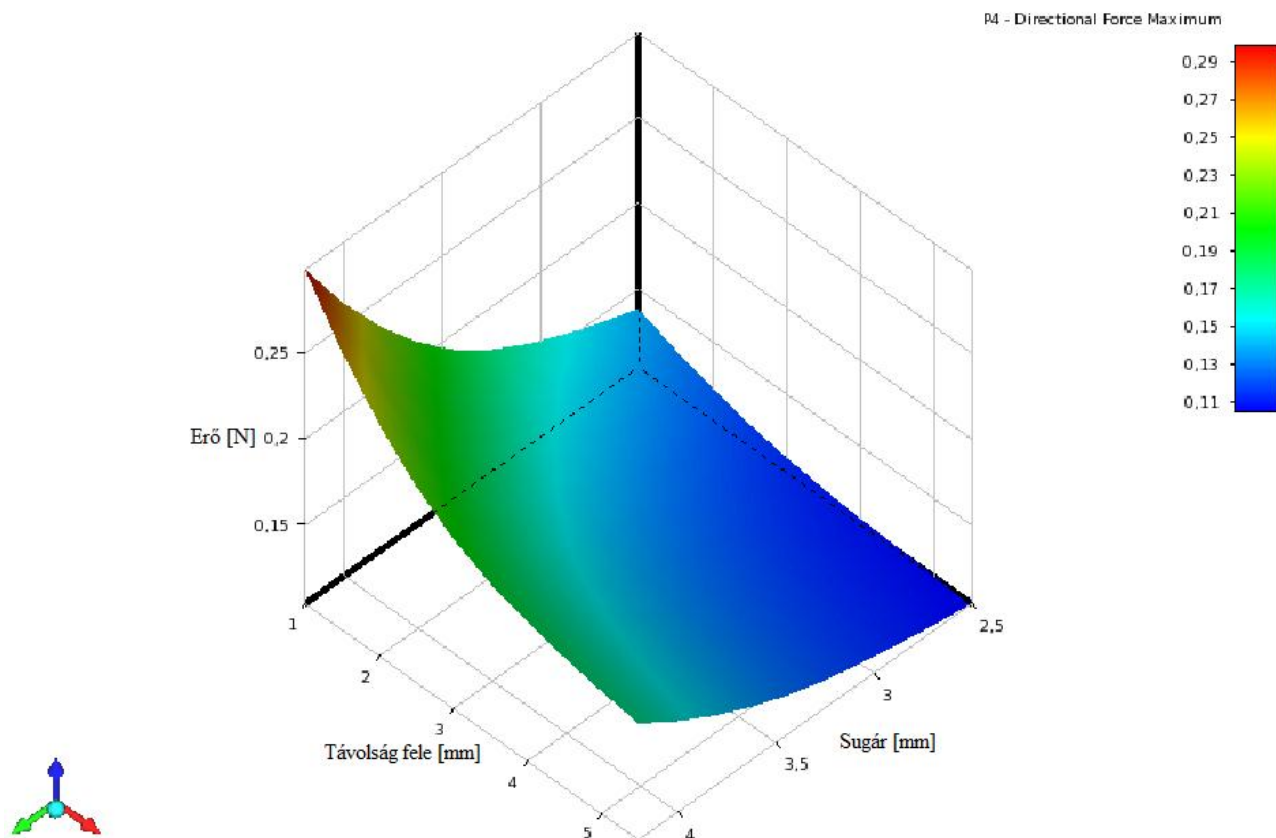


Figure 4. Results of parametric tests among magnet radial size (sugár), distance (távolság) and force (erő)

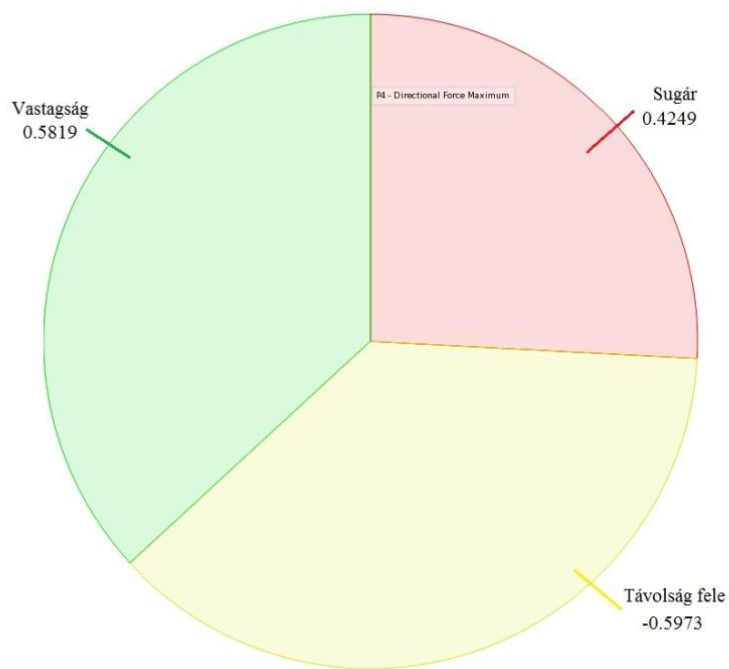
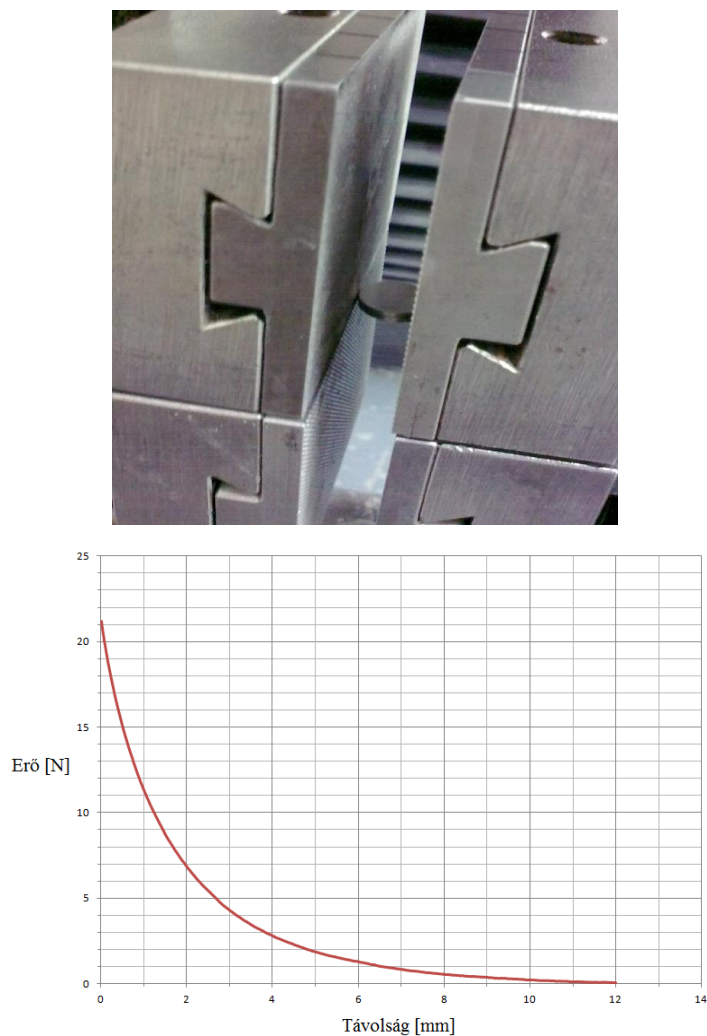


Figure 5. Parameter sensitivity diagram of force, effects of height (vastagság), radius (sugár), (half the distance (távolság))

After simulation results were evaluated and magnets were obtained, tensile strength tests were performed to create a mathematical model of force as a function of distance (*Figure 6*).



*Figure 6.* Magnet in tensile strength tester and measurement result, distance (távolság)-force (erő) diagram

Tensile strength tests confirmed simulation results; however simulation results have a great numerical deviation from measurement results, caused probably by model simplifications.

Another test was performed to determine dead band that is when a magnet moves just a little, the other magnet might not start to move (*Figure 7*).

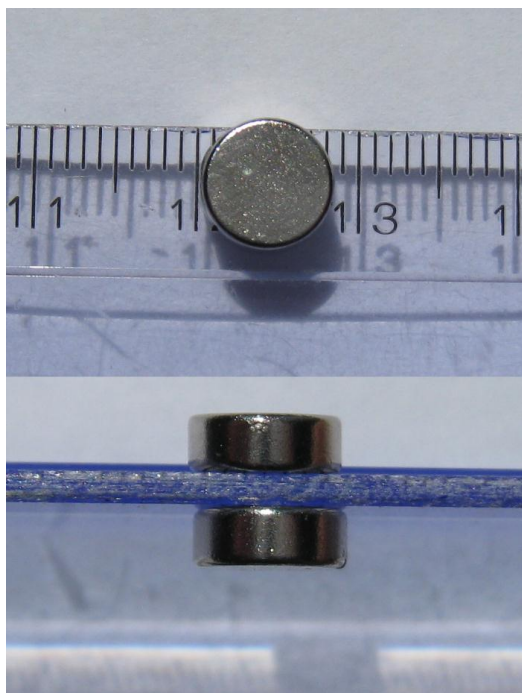


Figure 7. Determination of dead band

Magnet pair interaction also had to be examined, to avoid the unwanted interaction of two magnets on the outside of the corset. It can happen, when the predefined anatomical points are so near to one another that their outside magnets start to draw each other, instead of reacting to the movement of their respective pairs on the body surface. A minimal distance was determined for magnets on the body surface, as well as one for the outer ones.

When the first corset tests were performed with three magnet pairs, the anatomical points used were lumbar spinous processes, another problem surfaced. At two of the three points, the distance between the magnet on the skin and the corset was too big, so various sized spacers had to be created. Spacers have to be lightweight, and have to be magnetically connectable on both ends.

## Results

After tests without corset and with the original markers (*Figure 1*), magnets (and where needed spacers) were attached to the body and their counterparts were put to the corset outside. Results shown in *Figure 8* justify the presented magnetic marker motion capture principle.

Spacers introduce some uncertainty in measurement, so further analysis is necessary to eliminate it.

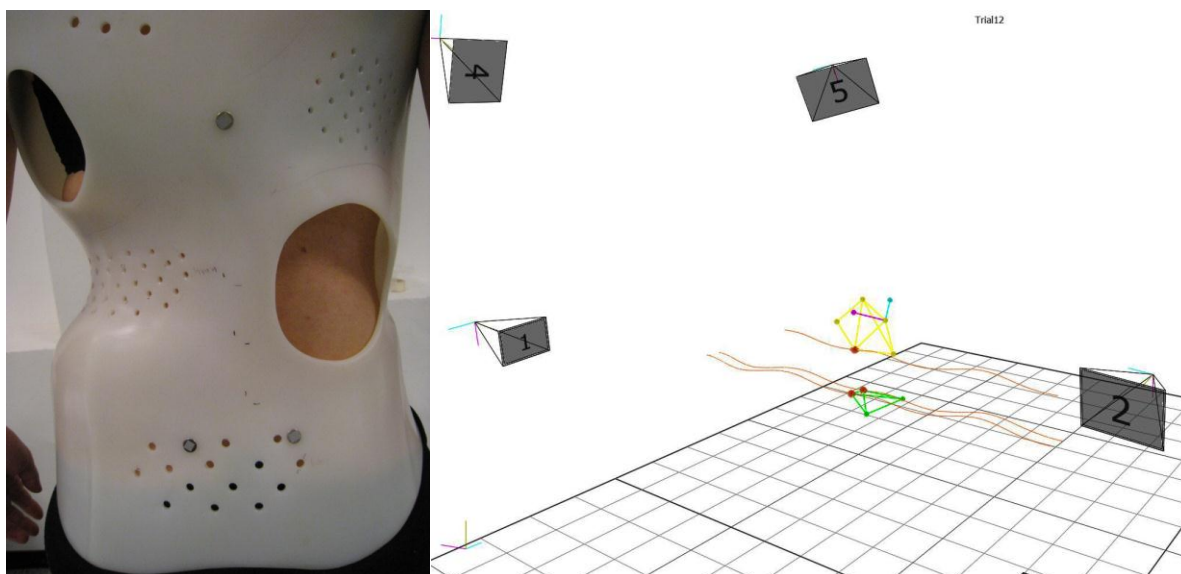


Figure 8. Magnetic marker pairs and their recorded movement

## Conclusion

A method with such inexpensive accessories deserves further tests and investigations, which are under way, to validate this promising measurement principle. Other types of plastic orthotic devices can be tested with the method, too. Different tests can be designed and examination protocols written, so that not just the effects of corsets on walking could be tested.

---

## REFERENCES

1. Szendrői M (editor). Ortopédia. Budapest: Semmelweis Kiadó, 2009. ISBN: 978 963 9879 49 2
2. Kocsis L, Kiss RM, Illyés Á. Mozgásszervek biomechanikája. Budapest: Terc Kiadó, 2007. ISBN: 978 963 9535 64 0
3. Horváth GI. Motion capture through non-transparent material, BSc thesis in Mechatronics (major in Biomechatronics), Budapest university of Technology and Economics, Department of Mechatronics, Optics and Engineering Informatics, 2012.
4. Hashi S, Toyoda M, Yabukami S, Ishiyama K, Okazaki Y, Arai KI, Kanetaka H. Wireless magnetic motion capture system using multiple LC resonant magnetic markers with high accuracy. Sensors and Actuators A 142 – 2008: 520-27.

*The authors would like to thank National Development Agency (NDA) of Hungarian Government for its support since this study has been carried out commonly as part of project GERINCO2 TECH\_08-A1/2-2008-0121.*

## INTERNET DATABASE OF SCOLIOSIS SCREENING

Norbert Szakály<sup>1</sup>, Péter Tamás<sup>1</sup>, Tamás Terebessy<sup>2</sup>, Dóra Végvári<sup>2</sup>, Péter Marschalkó<sup>3</sup>, László Basch<sup>4</sup>

<sup>1</sup>Budapest University of Technology and Economics Mechanical engineering Faculty

<sup>2</sup>Semmelweis University Orthopedic Department

<sup>3</sup>Heim Pál Children Hospital, Orthopedic Department

<sup>4</sup>Sensitiv Ltd.

szakaly@mogi.bme.hu

### Abstract

In Gerinco2 project there are a lot of examinations. To store data of examination a new database created with Internet technology. The aim of database is to screen to explore of scoliosis and follow treatment ill of children.

**Keywords:** scoliosis screening, Internet, MySQL, artificial intelligence

### 1. Method, the structure of database

There are two main parts of database. One of them is the database with its defined structure of a server. The other is a client program for doctors and assistants. The data structure is realized in MySQL<sup>1</sup> system which is free of charge and it is able to serve more users in one time. The structure of database is shown on the *Figure 1*.

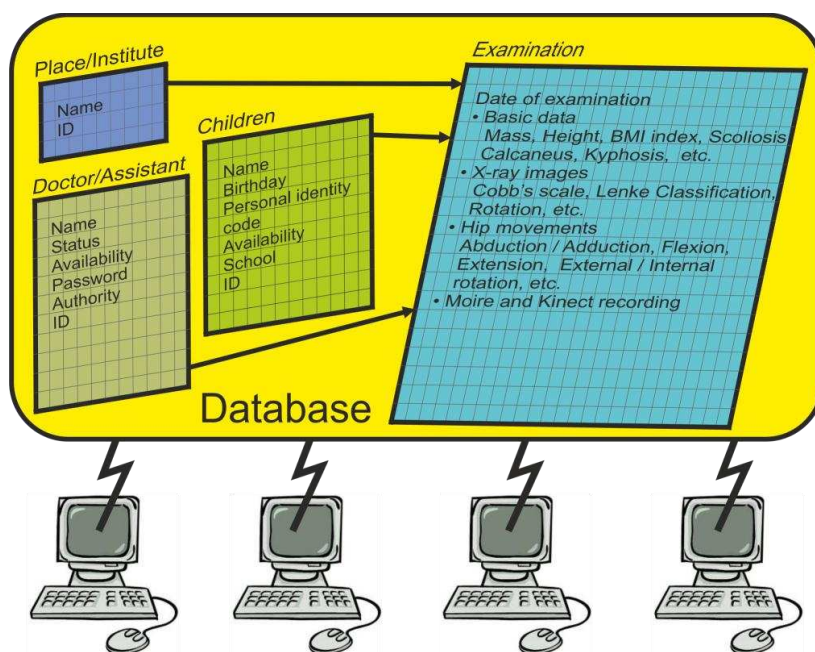


Figure 1. Structure of the database

Structure of the database ensures that the data traffic is as low as possible. Because of the used method the system is usable even on a weak Internet connection. The pictures are stored on the

server machine. Users download only the needed pictures. The downloaded pictures are stored in the client machine and they downloaded again only the case of changing.

There are four tables in database there. Data institutes and examiners authorized to use the system are stored two separate tables. The system uses different levels of authority and password so everybody can use only his own information.

The data of patients and the examinations are stored in the other two tables. In case of pupils the data of school and the class are stored. There are special identification numbers in the system so the personal identification data are not used. Results of all examinations are in the examination table.


## 2. Result, the database management software

### System specification

|                             |  |
|-----------------------------|--|
| Supported operating system: | Windows XP<br>Windows 7  |
| Needed software:            | MySQL ODBC Connector 5.1   |
| Processor:                  | 1GHz Pentium processor   |
| RAM:                        | 256 MB   |
| Hard disk:                  | 50 MB free space (suggested plus 500 MB for the downloaded pictures) |
| Display:                    | 1024 x 768 high color, 32-bit  |

Internet connection is needed for usage of the system.

### 2.1 Setup and upgrade

*GDB\_setup.exe* (  *GDB\_setup.exe* ) program installs the software in an interactive way. The user can define the position of the program in the machine and the Start menu. Default position of the program is C:\Program Files (x86)\GDB\. (Figure 2.)

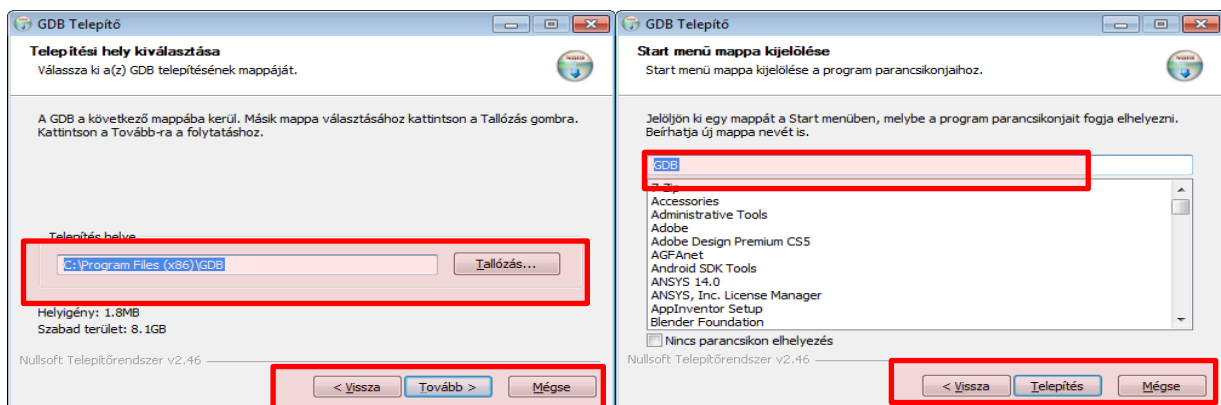


Figure 2. The setup dialog

After setup there is an icon in the Desktop and the Start menu to start the program. The login panel of the program is shown in *Figure 3*.



*Figure 3.* The login panel of GDB

The program is able to upgrade itself. After every ten usage the application searches for the newer version on the server. The needed version of MySQL ODBC driver also can be downloaded. After the log in we can use the software. The language of the communication is Hungarian.

## 2.2 Data of examiners

Data of examiners are username, name, qualification, status, address, phone number, e-mail, authorization, status (*Figure 4*). Examiners are able to change their own data (*Figure 5*).

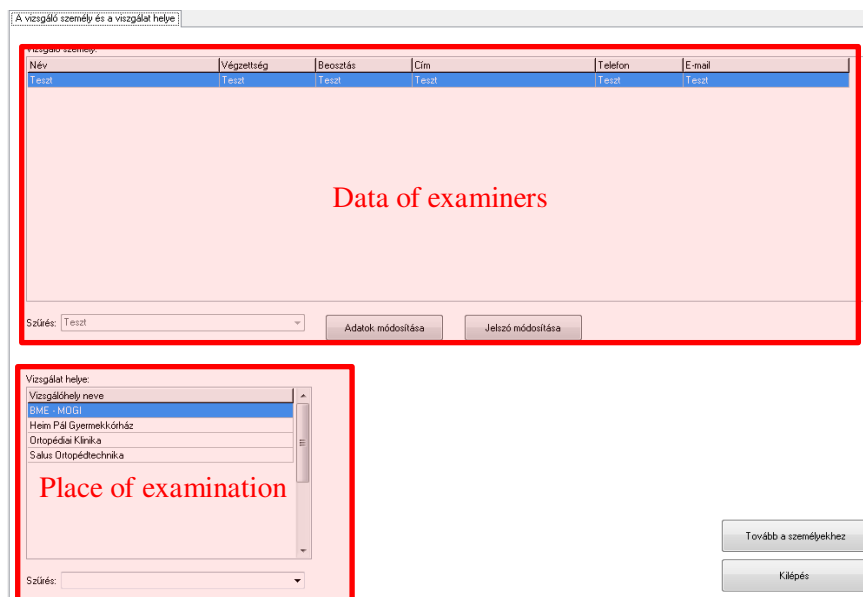


*Figure 4.* Data of examiners

Figure 5. Modification of personal data of examiners

We can continue with the patient data.

### 2.3 Data of patients

Panel of patients data has three parts. Name of patients are in the left side. There is a filtering possibility to help the searching process. (Figure 6.)

Figure 6. Patients' panel

Data of the selected patient (name, date of birth, name of mother, phone number, address, school, class) are shown in right side on the panel. There are possibilities to change or delete the patients.



User name and place of the examination are the user information as they were defined at login phase.

## 2.4 Data of examinations

In the right side of dialog we can see the examinations. There is a possibility to choose an examination or create a new one. The selected examination data are shown in the dialog and we are able to modify or delete the data if we have enough rights. (Figure 7.)

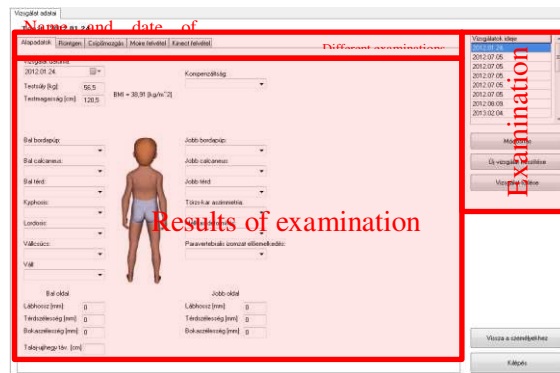


Figure 7. Results of examination

There are a lot of examination can be stored on database: the main data of the patient, X-Ray pictures, moving the hip, moiré and Kinect pictures.

### 2.4.1 Main data of examinations

The data can be stored are data of left rib hump, right rib hump, left calcaneus, right calcaneus, left knee, right knee, kyphosis, lordosis, shoulder, shoulder point, asymmetry of body-hand, deformity of chest paravertebralis muscle protrusion, left compensation, right compensation, data of legs

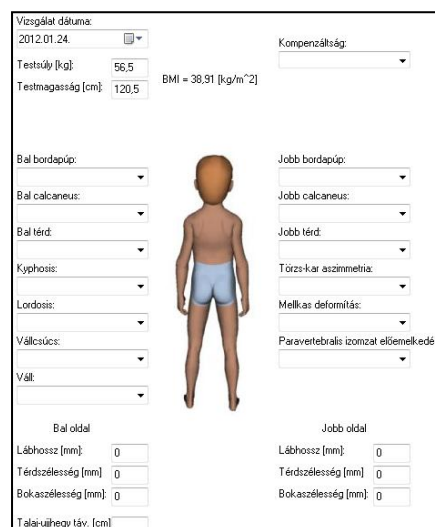


Figure 8. Main data

## 2.4.2 xRay pictures

Panel of X-Ray there is a possibility to store and analyze the recorded pictures. (Figure 9.)

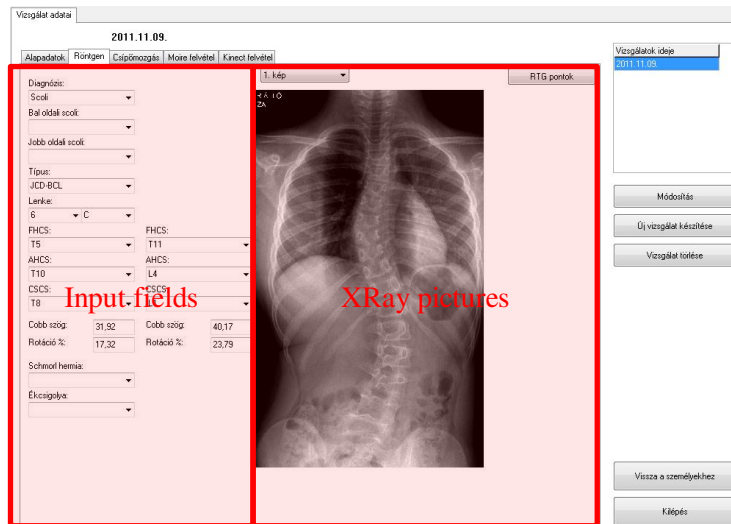


Figure 9. The X-Ray panel

In the left side there are some input field to store the diagnosis (Scoliosis, Scheuermann), the type of illness the Lenke classification<sup>2</sup> factor and other data of vertebrae (Cobb angle, rotation<sup>3</sup>).

With help of a special function there is a possibility to analyze X-Ray pictures. On the Figure 10 there are some moveable line segments there with moveable endpoint of A, B, C, D, E, F and G. Of course the picture can be zoomed and rezoomed.

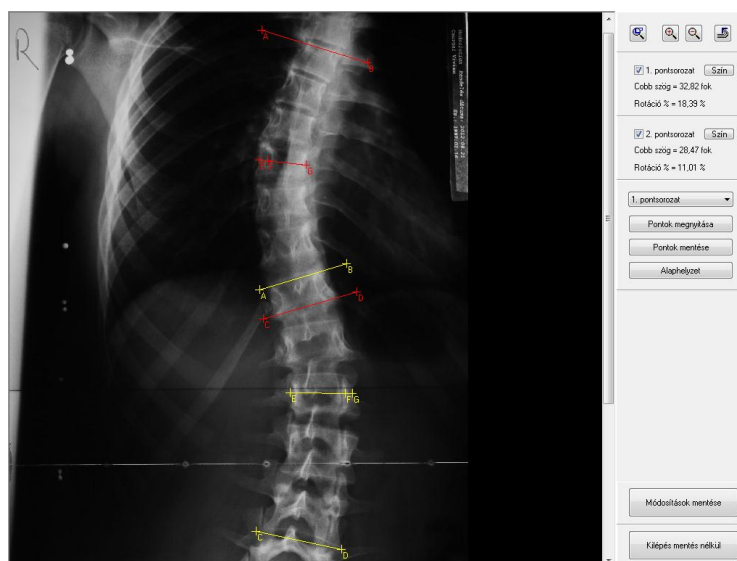


Figure 10. Analysis of X-Ray picture

The angle between the AB and CD sections defines the Cobb angle, and E, F and G sections defines the rotation, depend on the F (Figure 11).

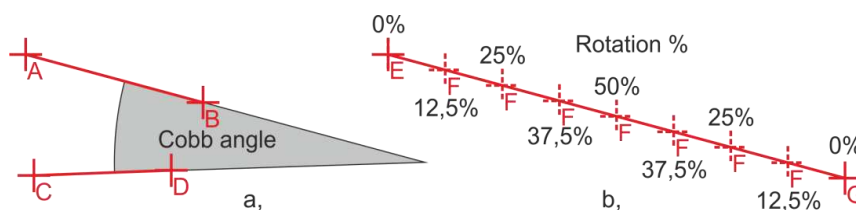


Figure 11. The Cobb angle (a,) and the rotation % (b,)

### 2.4.3 Hip movement

On the Hip movement panel the user can define a lot of test data as we can see on the Figure 12.

|                | Left Site |   |     | Right Site |   |     |
|----------------|-----------|---|-----|------------|---|-----|
| Ext/Flexio:    | 10        | 0 | 110 | 10         | 0 | 125 |
| Thomas test:   | 0         |   |     | 0          |   |     |
| Abd (90°):     | 35        |   |     | 35         |   |     |
| Abd/Add (0°):  | 40        | 0 | 30  | 40         | 0 | 30  |
| BRo/KRo (90°): | 20        | 0 | 30  | 25         | 0 | 30  |
| BRo/KRo (0°):  | 25        | 0 | 10  | 40         | 0 | 15  |
| Antetorsio:    | 5         |   |     | 5          |   |     |

Figure 12. Hip movement data

### 2.4.4 Moiré (Kinect) analysis

Either on the traditional moiré<sup>4</sup> pictures or Kinect procedure<sup>5</sup> there is a possibility to measure POTSI (POsterior TrunkSymmetry Index<sup>6</sup>) visible in Figure 13. or the Gerinco2 project evaluated Prediag method<sup>7</sup> visible on Figure 14.

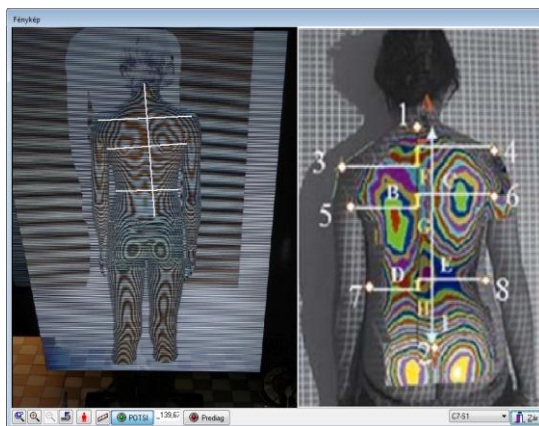


Figure 13. POTSI analysis

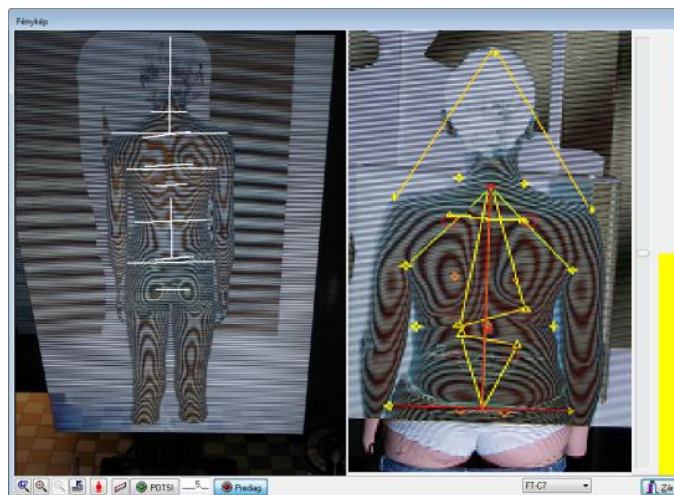


Figure 14. *The Prediag analysis*

## REFERENCES

1. MySQL : [www.mysql.com](http://www.mysql.com) 2013
2. King HA. Analysis and treatment of type II idiopathic scoliosis. *Orthop Clin North Am.* 1994;25:225-37.
3. Cobb JR. Outline for the study of scoliosis. *The American Academy of Orthopedic Surgeons Instructional Course Lectures. Vol. 5.* Ann Arbor, MI: Edwards; 1948.
4. Jain AK, Figueiredo M, Zerubia J (editors) 2001. *Energy Minimization Methods in Computer Vision and Pattern Recognition.* Springer Verlag Berlin 2011.
5. Kinect – [www.microsoft.com](http://www.microsoft.com) 2013.
6. Kinect- Mínguez MF, Buendía M, Cibrián RM, Salvador R, Laguía M, Martín A, Gomar F. Quantifier variables of the back surface deformity obtained with a noninvasive structured light method: evaluation of their usefulness in idiopathic scoliosis diagnosis. *Eur Spine J* 2007;16:73–82.
7. Tamás P, Szakály N. Decision Help System Supported Data-mining Method. V. Magyar Biomechatronika Konferencia, Budapest 2013.

***National Office for Research and Technology (NKTH) of Hungarian Government for their support since this study has been carried out commonly as part of the project GERINCO2 TECH\_08-A1/2-2008-0121.***

## INTEGRATION OF DATA RESULTING FROM VARIOUS TYPES OF LUMBAR SPINE EXAMINATIONS

Petra Aradi<sup>1</sup>; László Danka<sup>2</sup>; Gabriella Träger<sup>3</sup>; György Lipovszki<sup>1</sup>; Barbara Abonyi<sup>4</sup>

<sup>1</sup>Budapest University of Technology and Economics, Faculty of Mechanical Engineering, Department of Mechatronics, Optics and Engineering Informatics

<sup>2</sup>Policlinic of Hospitaller Brothers of St. John of God, Department of Orthopedics

<sup>3</sup>Gold Sanitas Kft.

<sup>4</sup>Semmelweis University, Faculty of Physical Education and Sport Sciences, Department of Psychology

[aradi.petra.bme@gmail.com](mailto:aradi.petra.bme@gmail.com)

---

### **Abstract**

Lower back region and lumbar spine in particular can be measured and evaluated with a number of methods and from a number of viewpoints. Measurement method depends essentially on the objective. Tests can be static or dynamic, can target detection of pathological conditions or just evaluate persons with no specific complaints, can be performed once or repeatedly (as follow-up series).

Authors present the development of a complex system that records and stores examination data of various types and formats (image, video, numeric, text, etc.).

Moiré-based virtual imaging method and a mechano-optical handheld scanning device, developed at the Department of Mechatronics, Optics and Engineering Informatics, Budapest University of Technology and Economics (BME MOGI) are used for static examinations. Dynamic tests can be performed with the system (developed also at BME MOGI) that gives 3D information with the help of depth sensors. Conventional examination results, such as static pressure maps obtained with a podoscope, x-ray images, and results of manual measurements (distances, angles, muscle ductility) provide useful information one by one. Measurement protocols help systematic data collection.

Integrating measurement results from previously mentioned methods, and utilizing 3D visualization, data storage and processing, increases the amount of information compared to individual pieces of data, and previously unknown connections can be revealed.

The integrated data acquisition and processing system helps organization and systematic processing of data stored in various (file) formats, type (text, image, numerical, etc.) and information content.

**Keywords:** lumbar spine, lower back, measurement and evaluation, integrated data acquisition, storage and processing

---

### **Introduction**

Large parts of the population in so called civilized countries lead an inactive, sedentary lifestyle. This lack of movement, especially that of physical training often results in different illnesses, a number of those involving the musculoskeletal system. Prominent among musculoskeletal ailments is backache, actually it is said to be the second most common type of pain in adults (the most common being headaches). It would also be worthwhile to investigate causes of headaches,

---

as some types of them have musculoskeletal origin, like muscle spasms in the upper back and neck. The human back can be divided into three large parts according to the segments of the vertebral column. In this paper authors focus on the bottommost of these parts, the lumbar fragment or lower back.

When any pain, e.g. lower back pain presents, the possible causes have to be explored thoroughly. Tests performed by physicians are complemented by those of physical therapists and other healthcare and sports professionals. There are quite many examination protocols in everyday use, and a large number of supplementary measurement methods are in use as well. Examination or measurement method depends essentially on the objective. Tests can be static or dynamic, can be used to discover suspected pathological conditions, or just evaluate a person who has no specific complaints, and to follow and map results of therapy. One time and repeated tests or measurements are performed, according again to the purpose of the examination.

Evolving methods and measurement devices can very well add information and provide new insights to tests and measurements considered traditional. Authors summarize traditional methods in examining the lower back and present the use of equipment developed in the frame of Gerincőr (SpineGuard) Project at the Department of Mechatronics, Optics and Engineering Informatics. The paper provides insight into the development process of an integrated data storage and processing system for collecting data from tests and measurements that can be related to lower back complaints.

## **Methods and results**

There are many examinations, tests and measurements involving the evaluation of lumbar spine, and those that aim to map effects of this region on other parts of the body. In our information technology and computer penetrated era, an increasing number of results of such methods are in one of the many digital formats. Traditional methods, such as the use of tape-measures and goniometers also allow some kind of digitalization, the most simple being the use of a computer program like a spreadsheet to manually record data. Various image formats are the result of the use of imaging equipment from medical systems like x-ray, to not yet so widely spread methods (e.g. moiré-based virtual imaging, the use of 3D scanners, depth sensors, just to mention some). Large amounts of numerical data from other measurement devices such as the mechano-optical handheld scanning device is transformed to visual information.

It is a challenge to integrate the ever increasing types and amount of data into a uniform system that provides access to each and every piece of relevant data without bombarding the user with unnecessary information like rows and rows of numbers. When all these data is stored and human-friendly visualization is provided, a further question and task to be solved arises. Would it be possible to explore connections in this diversified multitude of information?

### **“Conventional” measurements and tests<sup>1-3</sup>**

Each and every measurement method has criteria of reliability, precision and validity, which is extended by the requirement of repeatability, when measurements have to be repeated frequently.

The lumbar fraction of the spine can be measured in quite a number of ways. To facilitate collection of objective data, such as numbers, images, motion pictures, everything that is relevant in evaluation of lumbar spine and low back status should be given as “objective” data. So, physical examination can give results as distances and angles. Tests can be static, such as the measurement of the length of extremities, length of muscles in different postures, angle of joints. X-rays both in neutral position and in specific postures belong to the group of static tests, too. Ultrasound, CT and MRI give more detailed views and can focus on more aspects, the latter two methods provide additional information with 3D image reconstruction. Foot pressure maps can be recorded either in standing position, or during walking, when the test is dynamic.

The large number of muscles in the pelvic region is responsible not just for the lumbar region, but can cause symptoms in body parts relatively far from this area. Incorrect pelvis position, is not always visible, one has to measure several parameters to confirm it. To explore the effects of incorrect pelvis position, first the direction in which the pelvis left its anatomical place has to be determined. Forward or backward tilt can affect the sagittal curvature of the whole spine, with emphasis on the lumbar section of course, besides it can modify the position of the hip joint. Causes of pelvic tilt have to be examined, too, to determine whether it is caused by pathological issues or stress related posture problems. For example even in healthy people stress can cause unilateral increase of the muscle tone of tensor fasciae latae, thus causing sideward pelvic tilt. Its further consequences are the shortening of quadratus lumborum muscle on the other side as a result of fatigue, with additional muscle reactions that can lead to knee pain as well.

Dynamic tests are used to test movement. Two different examination techniques have to be mentioned, active and passive movement. Range of motion (ROM) compared to other body parts can directly give numerical data, or result can be classified in a manner used in fuzzy rule based systems. Fuzzy membership functions are defined over the possible domain of ROM, and movement can be classified verbally, using qualifiers like normal, less than normal, extremely small, etc. Experts have to define the numerical mapping of these verbal classifiers by setting up a fuzzy rule base system. The presence and intensity of pain can be given by the widely used verbal 0(1)-10 scale, where zero means no pain and 10 is the worst pain the patient has ever experienced, or graphical scales, like the Wong-Baker FACES Pain Rating Scale can be used. Muscles in different spinal ranges can be tested by control exercises, to evaluate their resistance to certain force and their ductility. These tests can be focused on movement, time-span and number of repetitions. Marker based motion capture systems of various physical principles (like infrared imaging) can also be part of the evaluation.

### **Recently developed equipment**

Measurement devices shown below were developed as part of Gerincőr (SpineGuard) Project as stated in Introduction. One aim is this project is to develop new measurement methods for the human spine, so results can be applied to lower back.

Moiré-imaging is a well-known and quite old optical method. It is used on the human back as a non-invasive method to obtain information on the inner musculoskeletal structure. Modern moiré equipment, such as the one developed at MOGI, use video projectors, digital cameras and a computer integrated into a portable test system. An improvement and derivation from traditional moiré imaging is the use of projected stripes with different colors. This system is

dubbed as rainbow scanner and after processing images (*Figure 1*) provides a 2.5D model of the human back (*Figure 2*).

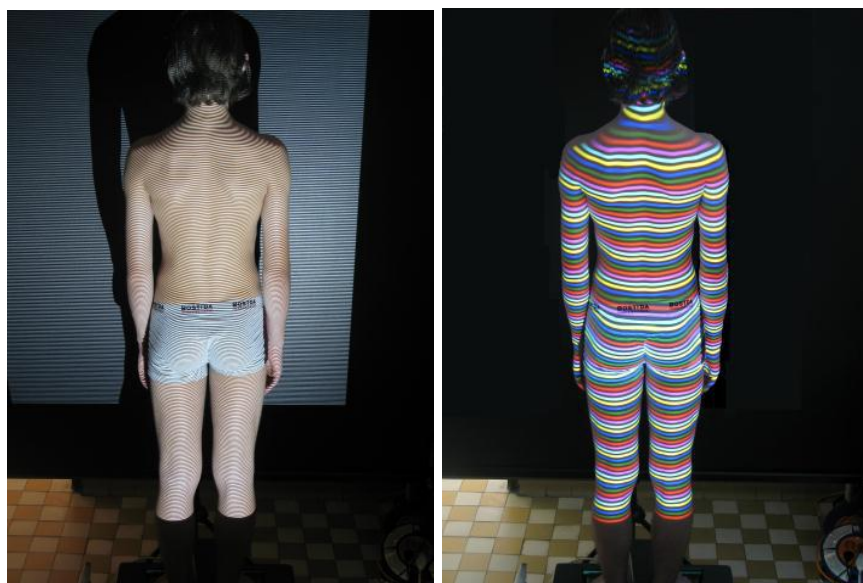


*Figure 1.* Traditional and rainbow (moiré) scanner setup with stripes projected onto the back

The use of any moiré body scanner requires calibration and standardized measurement conditions, so that results could be compared and evaluated. Methods for scanning and calibration with the rainbow scanner are specified and the processing program was written with these considerations in mind. A large number of school age children were screened for scoliosis at various sites with the rainbow scanner setup, which is equipped with another imaging equipment to simultaneously record foot pressure distribution. Moiré images belong to static measurement, and rely heavily on correct positioning and posture. People using moiré scanners, therefore need to be trained in calibration and examination protocol.

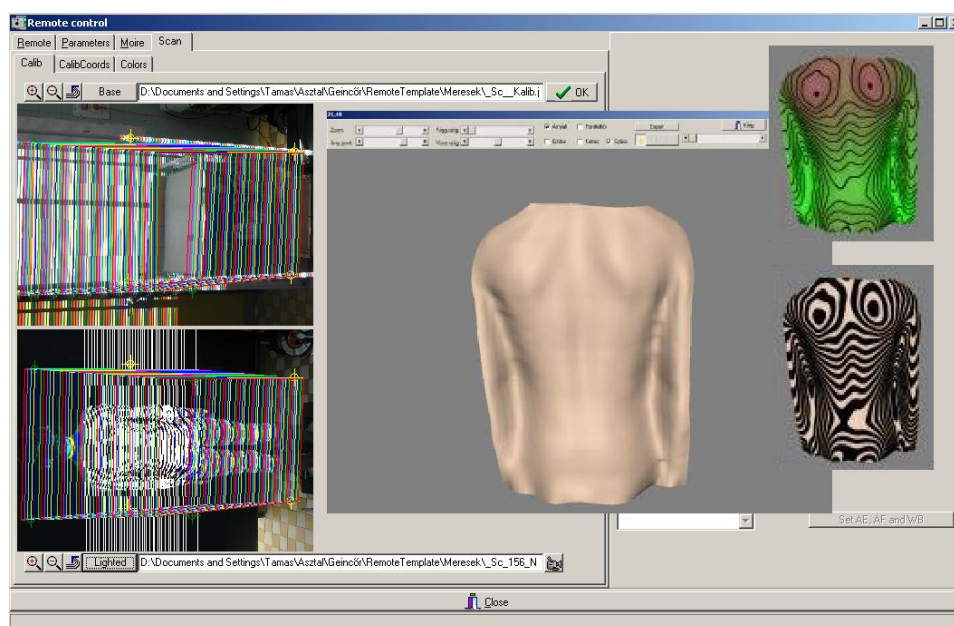


*Figure 2.* Rainbow (moiré) scanner software with raw image, reconstructed body model and moiré images



A mechano-optical handheld scanning device, or vertebral scanner for short, has also been developed. The device shows some minimal resemblance to the commercially available SpinalMouse, but has significant differences in measurement principle, measured region and data. After experimenting with various measurement principles, constructions, hardware and software solutions, the device shown in *Figure 3* is used now. Data collected along the spine is processed and a 3D geometrical spine model shows the measured position and rotation of each vertebra. The use of this device requires training and the precise following of the measurement protocol, too.

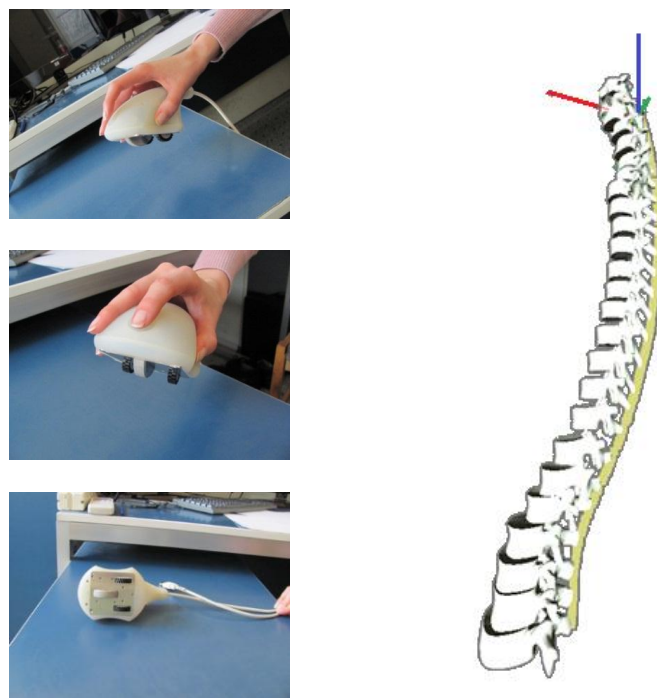


*Figure 3.* Vertebral scanner, a mechano-optical handheld scanning device and a spine model based on scanned data

The third apparatus uses the depth sensor and cameras built into Microsoft's Kinect. The combination of cameras and depth sensors map 3D objects to 2D with additional distance information for each pixel. Various graphical representations obtained by the software driving Kinect and processing its data are shown in *Figure 4*. Depth information also helps create a 3D model of the human body surface.

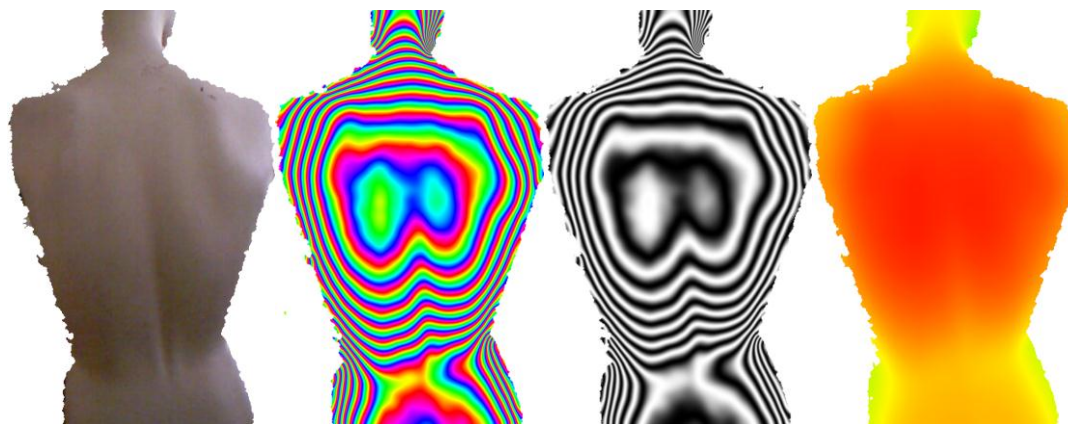


*Figure 4.* Various representations of the back produced with depth sensors

The last measurement equipment to be mentioned is the 3D laser body scanner. Person to be scanned has to stand motionless inside a special frame that allows simultaneous movement of laser line sources and taking of multidirectional digital photographs. The associated computer program processes data from these photographs: first it creates the body's point-cloud model, from which it produces a 3D body model with parametric features. *Figure 4* shows the point-cloud result of a body scan and two views of the body surface model.

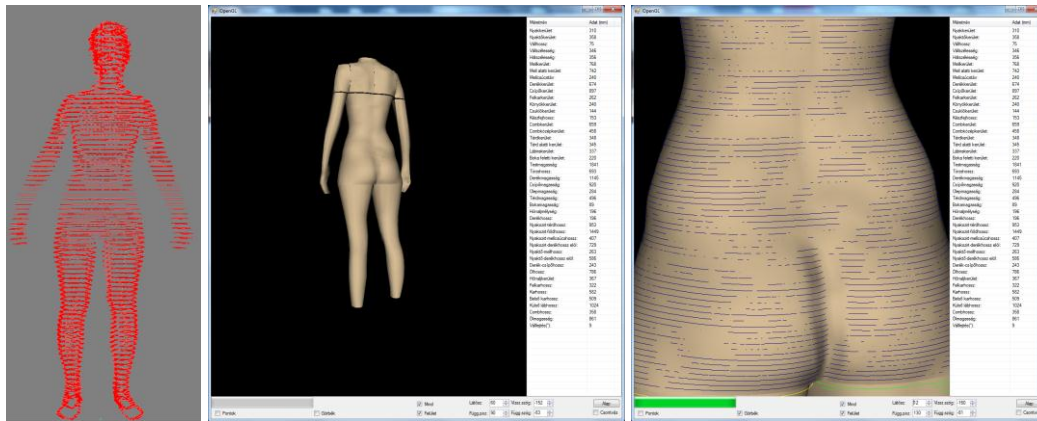


Figure 5. Point-cloud and reconstructed body surface based on data from 3D laser body scanner

### Data integration – software structure

The amount of data is huge in itself. Defining connection among various types of test results require the specification of some (in the magnitude of 100) specific parameters, that represent each data type. These parameters are then used to define connections. Relevant parameters have to be selected by experts, like physicians, physical therapists, etc.

At the time of this writing an XML specification is being created to store relevant data and provide a common connective frame. As various software produce results in different file formats, each program has to be equipped with a data export module. The framework program uses exported XML data from individual software sources and allows users to specify connections. Based on consequences drawn by experts a complex database is under development, enabling access to individual results, and provide follow-up.

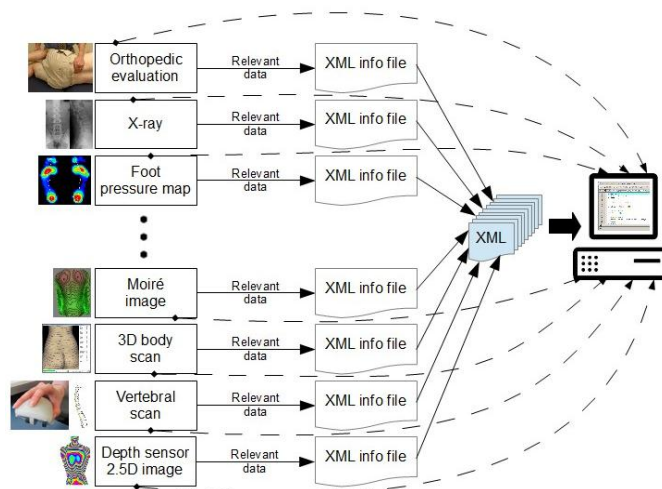


Figure 6. Schematics of collected data, XML info files and program

## **Conclusion**

The ever increasing number of tests requires a careful selection; which tests are relevant for the evaluation task in mind. It is also important to check the availability of measurement methods and equipment and their relevance in connecting symptoms, measured data and eventual consequences. When meaningful tests have been chosen, they are repeated, so that progress could be monitored. The amount of gathered data can quite suddenly require adequate storage, which is not the main problem, but it is the platform interconnecting the various results. The developed software aims to provide such a system, focusing to data involving the lower back, at the moment. As more and more data becomes available, the program has to be tuned accordingly; this process is well under way, too.

---

## **REFERENCES**

1. Szendrői M (editor). Ortopédia. Budapest: Semmelweis Kiadó, 2009. ISBN: 978 963 9879 49 2
2. Kocsis L, Kiss RM, Illyés Á. Mozgásszervek biomechanikája. Budapest: Terc Kiadó, 2007. ISBN: 978 963 9535 64 0
3. Eston R, Reilly T. Kinanthropometry Laboratory Manual, Anthropometry and Exercise Physiology. Routledge, New York, 2008. ISBN 978-0-415-46671-4

***The authors would like to thank National Development Agency (NDA) of Hungarian Government for its support since this study has been carried out commonly as part of project GERINCO2 TECH\_08-A1/2-2008-0121***

## DECISION HELP SYSTEM SUPPORTED DATA-MINING METHOD

Péter Tamás, Norbert Szakály

Budapest University of Technology and Economics Mechanical engineering Faculty Department of Mechatronics, Optics and Engineering Informatics

[tamas@mogi.bme.hu](mailto:tamas@mogi.bme.hu)

---

### Abstract

Database of scoliosis examination stores a lot of data of patients. The exact numbers and the written opinion of doctors are useable in decision about the resolution of screening process. The moiré method and results of depth scanning are pictures. The conclusions are subjective. The paper is about a data mining based method for qualification of case to help of diagnosis.

**Keywords:** scoliosis, screening, moiré method, POTSI, computer aided decision

---

### 1. Introduction

The aim of the project was to develop a teachable system which is able to store all data of examinations and it is able to suggest a conclusion or a diagnosis to doctors based on the database stored cases.

### 2. Methods

The heart of the system a database and selection of the nearest data and the interpolation.

#### 2.1 Database of the system

The method of decision making is the known data mining method named n-nearest neighbor<sup>1</sup> and the interpolation technics.<sup>2</sup> Data of examination is stored in database and upon the vector of actual parameters of examination is compared with all of the stored exams data vector and select the k nearest examinations. The nearest examination that where the difference between the stored data vectors and the actual data vector is the minimal one. Conclusion can be defined on the subset with k element, where the known conclusions interpolated with a polynomial as the function of the known parameters. The actual parameters are substituted into the interpolated function value will be the suggested conclusion.

There is a frame system teachable with measured data and accepted decisions. The aim to find the closest cases to actual examination data set (green in the *Figure 1*). Based this data the system evaluates the conclusion upon the known cases (red in *Figure 1*).

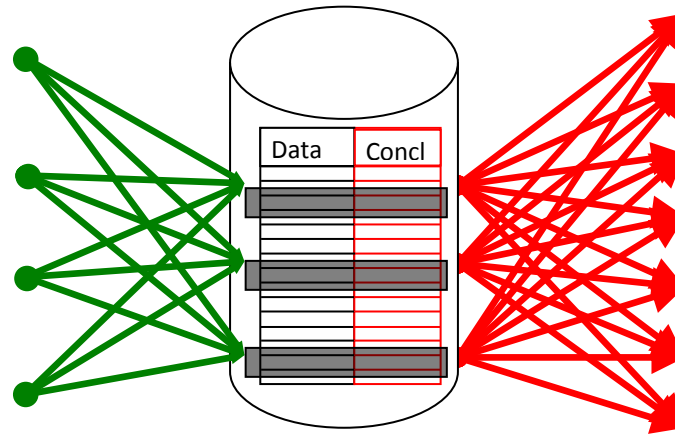


Figure 1. Schema of the system

## 2.2 Working of the system

The data of all examination are stored in numerical form in database. Concluded data are numerical too. The applied method is a multidimensional interpolation. The first step is to define the set of closest data with help of a query. Let us imagine the decision data of the known cases as the multidimensional function of the known data!

## 2.3 The developed mathematical background

Data of examinations are defined as elements of intervals. Limits of intervals defined by the possible maximum and minimum of these values  $[x_i^{\min}, x_i^{\max}]$  where  $i=1, \dots, N$  and  $N$  is the number of known and accepted cases. That means data are in an interval of  $N$  dimension.

$$[x_1^{\min}, x_1^{\max}] \times [x_2^{\min}, x_2^{\max}] \times \dots \times [x_N^{\min}, x_N^{\max}] = X \quad (1)$$

Similarly the accepted conclusions are in an interval of  $P$  dimension.

$$[y_1^{\min}, y_1^{\max}] \times [y_2^{\min}, y_2^{\max}] \times \dots \times [y_P^{\min}, y_P^{\max}] = Y \quad (2)$$

The basis of work is to find the function  $\Phi$  mapping the known data to known conclusions.

$$\Phi : X \rightarrow Y ; \Phi(\underline{x}) = \underline{y}; \quad \underline{x} \in X \text{ and } \underline{y} \in Y \quad (3)$$

If  $\phi$  function is known we can substitute the questionable examination data in it and the suggestion will be the function values. Because of numerical stability it is worth to project all interval into  $[0,1]$ . Let the  $\alpha_i$  and  $\beta_j$  the normalizer functions.

$$\begin{aligned} \alpha_i : [x_i^{\min}, x_i^{\max}] &\rightarrow [0,1] ; \alpha_i(\underline{x}) = \xi ; & i=1 \dots N \text{ and } j=1 \dots P \\ \beta_j : [y_j^{\min}, y_j^{\max}] &\rightarrow [0,1] ; \beta_j(\underline{y}) = \eta ; & \underline{x} \in X \text{ and } \underline{y} \in Y \\ & & \xi \in [0,1]^N \text{ and } \eta \in [0,1]^P \end{aligned} \quad (4)$$

Using the normalized data we search for the  $\phi^*$  function. It can be computed from (3) and (4).

$$\phi^* : [0,1]^N \rightarrow [0,1]^P ; \phi^*(\underline{\xi}) = \eta ; \quad \xi \in [0,1]^N \text{ and } \eta \in [0,1]^P \quad (5)$$

The following shows the definition of  $\phi^*$  function.

In the first step we search for the function in third order:

$$\phi^*_{j}(\underline{x}^*) = \sum_{i=1}^N (a_{i,j} \xi_i^3 + b_{i,j} \xi_i^2 + c_{i,j} \xi_i + d_{i,j}) \quad j = 1 \dots P \quad (6)$$

We can select the  $4*N$  closest records to the questionable one based on the Euclidian norm. The interpolation function of  $\phi^*$  is defined with the  $4*N$  equations for  $4*N$  unknown  $a_{i,p}$ ,  $b_{i,p}$ ,  $c_{i,p}$ ,  $d_{i,j}$  coefficient. If the equation system is solvable then we are ready. We can substitute the questionable data end we get the suggestions.

If it is not possible to solve the equation system (there is no enough data or there is a singularity), than the  $\phi^*$  function can be searched for the following form

$$\phi^*_{j}(\underline{x}^*) = \sum_{i=1}^N (a_{i,j} \xi_i^2 + b_{i,j} \xi_i + c_{i,j}) \quad j = 1 \dots P \quad (7)$$

In this case we have to select the closest  $3*N$  records from the database. If the interpolation  $\phi^*$  function in second order successful, the coefficients  $a_{i,p}$ ,  $b_{i,p}$ ,  $c_{i,j}$  can be defined we are ready and  $\phi^*$  function is defined.

If it was not successful because of there is no enough data or there is a singularity, than we search for the  $\phi^*$  function upon the  $2*N$  closest records in form of (8).

$$\phi^*_j(\underline{x}^*) = \sum_{i=1}^N (a_{i,j}\xi_i + b_{i,j}) \quad j = 1 \dots P \quad (8)$$

When there are  $2*N$  closest records and it is successful to compute  $a_{i,j}$ ,  $b_{i,j}$  coefficients ( $i=1 \dots N$ ), then  $\phi^*$  defines  $\phi$ .

If it was unsuccessful then it is enough to search the closest record to the actual data. The conclusion part of it will define  $\phi^*$  function and the  $\phi$  function and the suggestion.

### 3. Used data

There are two special examination included in the system.

#### 3.1 A POTSI (POsterior TrunkSymmetry Index)

Upon POTSI - posterior trunk symmetry index<sup>3</sup> we are able to conclude the deformity of back surface and so the curvature of vertebral in the vertical plane. There are eight points on the back we have to define. It is easy to do however on a photo or on the moiré picture. In a symmetric back surface the POTSI index is zero. The higher POTSI index is the worse. The index under 27.5 it is normal. Upon the experiences POTSI classification is good for asymmetry, but it show a lot of cases of the scoliosis to be healthy. The experiences shows that the POTSI is the function of Cobb angle in 44.6% and the rotation in 26.8%. The POTSI is defined by equation of (9) based on *Figure 2*.

$$POTSI = FAI + HAI \quad (9)$$

where definitions of FAI: is the Frontal Asymmetry Index and HAI: Height Asymmetry Index  
There are the follows:

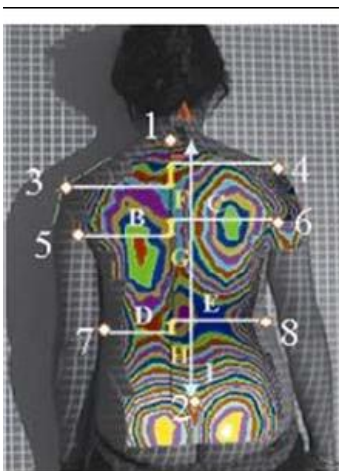


*Figure 2.* Definition of POTSI

The eight anatomic points are:

1. C7 vertebra
2. upon point of back-end
3. intersection point of tangent of left shoulder and tangent of left hand
4. intersection point of tangent of right shoulder and tangent of right hand
5. left armpit
6. right armpit
7. left waist point
8. right waist point

Upon these

- I:** distance between **1.** and **2.** points
- A:** length of vertical projection of **I** (this is the reference line of following calculations.
- B:** distance of point **5.** from **A** section
- C:** distance of point **6.** from **A** section
- D:** distance of point **7.** from **A** section
- E:** distance of point **8.** from **A** section
- F:** vertical projection of distance from **3.** to **4.**
- G:** vertical projection of distance from **5.** to **6.**
- H:** vertical projection of distance from **7.** to **8.**

From these

$$FAI = FAI_{C7} + FAI_{armpit} + FAI_{waist} \quad (10)$$

where

$$FAI_{C7} = A * 100 / I \quad (11)$$

and

$$FAI_{armpit} = |B - C| * 100 / I \quad (12)$$

and

$$FAI_{waist} = |D - E| * 100 / I \quad (13)$$

and

$$HAI = HAI_{shoulder} + HAI_{armpit} + HAI_{waist} \quad (14)$$

where

$$HAI_{shoulder} = F * 100 / I \quad (15)$$

$$HAI_{armpit} = G * 100 / I \quad (16)$$

$$HAI_{waist} = H * 100 / I \quad (17)$$

### 3.2 Prediag method

There was a survey made in frame of Gerinco2 project with more than 300 examinations of students. Upon the test doctors created a new estimation method named prediag.<sup>4</sup>



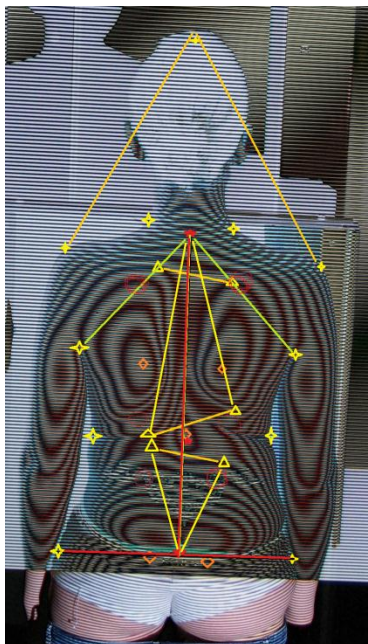


Figure 3. The estimation data

On Figure 3 the definitions of estimation data are shown. The main contour points are signed with four sided yellow stars.

|            |                                |
|------------|--------------------------------|
| KFT        | maximum height of head,        |
| KNYB, KNYJ | contour points on the neck,    |
| KVB, KVJ   | contour on the shoulder,       |
| KHB, KHJ   | contour points on the armpits, |
| KDB, KDJ   | contour points on the waist,   |
| KTB, KTJ   | contour points on the hams.    |

The special main points are signed by red pentangular.

|    |                                      |
|----|--------------------------------------|
| C7 | vertebra C7                          |
| S1 | spinal process of vertebra           |
| L  | the lower point of the lumbar sector |

Other point on the moiré picture signed by yellow triangle

|                  |  |
|------------------|--|
| ISOTHPB, ISOTHPJ | proximal iso-lines on left and right thoracic region |
| ISOTHDB, ISOTHDJ | distal iso-lines on left and right thoracic region   |
| ISOLPB, ISOLPJ   | proximal iso-lines on left and right lumbar region   |

Estimated centrum points of iso curves are signed by orange rectangles. t

|     |                      |
|-----|----------------------|
| BDC | Left dorsal centrum  |
| JDC | Right dorsal centrum |
| LC  | Lumbar centrum       |

|     |                                   |
|-----|-----------------------------------|
| BGC | Left gluteal centrum              |
| JGC | Right gluteal centrum (same as L) |

From the above mentioned the healthy case when the C7-S1 line is the same than the VL - vertical line (the sagittal plane) (Vertical Line) and the KTB-KTJ line is the same as the (HL - horizontal line). The measure of compensation is the angle of C7-S1 and the vertical line.

#### 4. Results, Processing of moiré picture

In the software system there is a panel of moiré picture (Figure 4). On the panel we are able to show and to analyze the stored moiré picture.

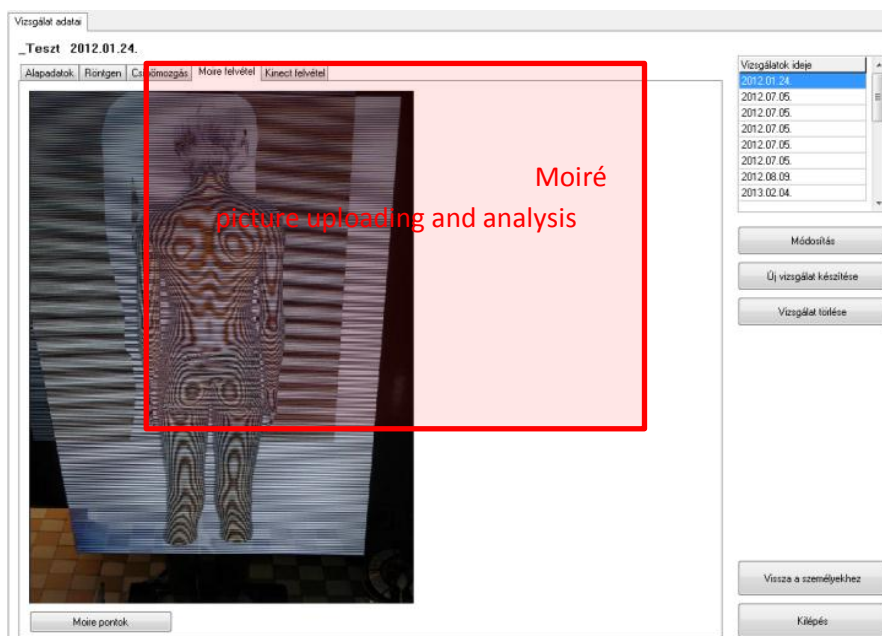




Figure 4. Moiré panel

If we have a new examination or we want to modify an old one we show the dialog of moiré examination (Figure 4). There is the possibility to zoom and re-zoom the picture by buttons. With  button we select the POTSI examination. After selection the button  and the selection one element on list of Figure 5. (Hungarian software) we can select a distance to define in the picture Figure 6.

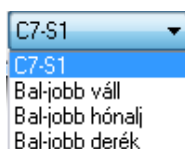


Figure 5. Selection of the POTSI distance

After defining the POTSI panel shows the POTSI value.

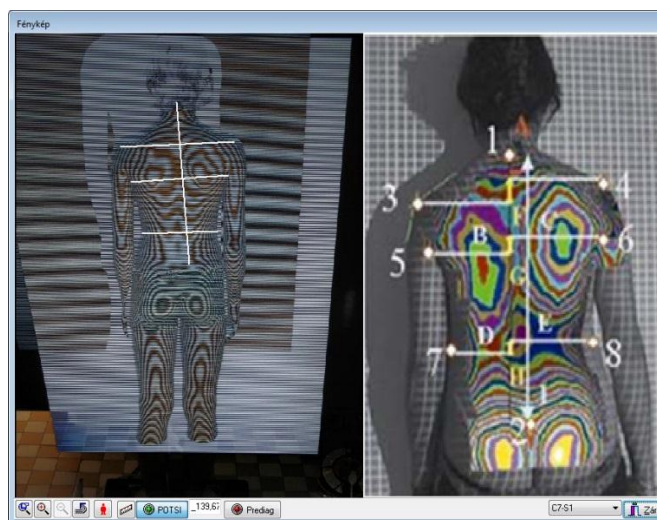



Figure 6. The POTSI panel

If we choose the  **Prediag** button we will get the Prediag dialog (Figure 7).

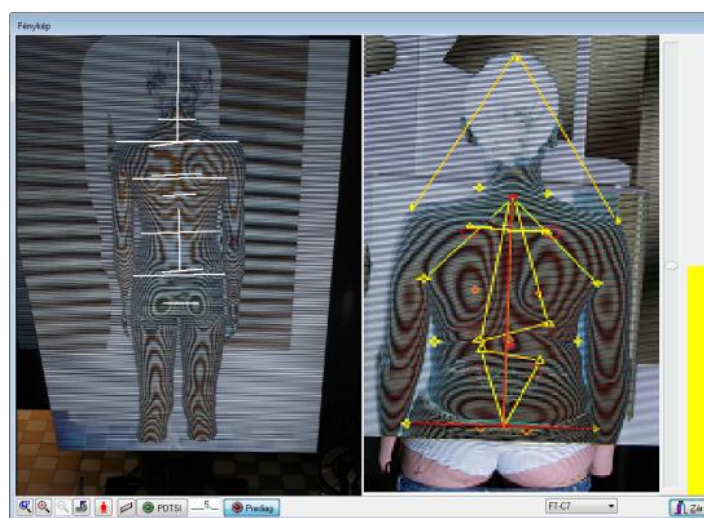


Figure 7. The Prediag panel

Like in the case demonstrated above we can choose a distance by a list shown in Figure 8.



*Figure 8. The distances of Prediag*

In the case of new examination or modified examination in the right scrollbar of the panel doctor is able to qualify the patient. The healthy case is colored green, the problematic is yellow and the dangerous is red. The system helps to decide in way written in 2. In the case of old examinations the system automatically shows the qualification of the case.

## **5. Discussion**

The presented method worked well in test phase. The next step is the verification in real screening processes. Tuning of setting parameters can be made after the processing of results.

---

## REFERENCES

1. Abonyi J. Adatbányászat a hatékonyság eszköze , ComputerBooks Kiadó Budapest 2006.
2. Dr. Bajcsay P. Numerikus analízis, Tankönyvkiadó, Budapest, 1978
3. Minguez MF, Buendia M, Cibrián RM, Salvador R, Laguia M, Martin A, Gomar F. Quantifier variables of the back surface deformity obtained with a noninvasive structured light method: evaluation of their usefulness in idiopathic scoliosis diagnosis. *Eur Spine J* 2007;16:73–82.
4. Report of Gerinco2 project

***National Office for Research and Technology (NKTH) of Hungarian Government for their support since this study has been carried out commonly as part of the project GERINCO2 TECH\_08-A1/2-2008-0121.***

## TAILOR-MADE CRANIOPLASTY USING CAD-CAM TECHNOLOGIES

László Lovas<sup>1</sup>, Dusán Vitanovics<sup>2</sup>

<sup>1</sup>Department of Vehicle elements and Vehicle structure analysis, Budapest University of Technology and Economics

<sup>2</sup>National Institute of Neurosciences, Budapest

lovas@kege.bme.hu

---

### Abstract

Treatment of traumatic head injuries and various neurosurgical conditions sometimes includes a removal of a large part of the cranial bone. Later on, the formed crane window must be closed with an implant. In this paper we present a method that allows producing implants of any size and complexity, with accurate fit and relatively low manufacturing cost. The implants are finalized upon virtual verification and need short operations to built in the cranial bone. The method can be used also for changing existing implants.

**Keywords:** crane, reconstruction, CAD

---

### Introduction

In case of certain diseases or injuries of the head it is necessary to remove a part from the cranial bone. The cranial defect is closed either with autogenous bone or with alloplastic material. Theoretically the use of autogenous bone should be better for the patient. However, in the practice various problems (bone necrosis, bone absorption) may occur in this case. When alloplastic material is used, the cranial defect is closed with metal (ex.: titan) or plastic material (polymer). One of these mentioned polymers is the polymethyl-metacrylate (PMMA). This material is not only cheap, but also easy to model with thus implants of various shape can be realized. Upon the literature, infection type post operational complications appear in 13,3-13,8% of the cases.<sup>1</sup> Removal of the implant is necessary in 4,4-12,5% of the cases.<sup>1</sup>

### Methods

In the early 80's the implant was realized by melting the half polymerized PMMA directly on the bone window during the operation. The polymerization of plastic material finished in situ on the crane. The heat produced by the process was removed through continuous cooling of the implant.<sup>2</sup>

A typical implant making method used by Hungarian surgeons is shown in *Figure 1*. Here a rough implant model is realized by melting PMMA on the hairy skin. From this model a negative mould is made. A raw implant model is mould in the negative during operation. When the access to the bone window is free, the surgeon takes the half-polymerized implant, and forms it so to fit the window. The final implant shape and precision depend on the skills of the surgeon, and can not be predicted.

Later, more developed methods used series of CT images. From these image series CAD model of the cranial bone was constructed. From the crane model the CAD model of the implant has

been created either using mathematical logical operations, or using a large database of CT-extracted CAD crane models. Precise fit of the implant model has been verified by comparison to the original CT images. Then a rough implant was realized using CAM techniques. After finishing, a casting mould was made from the rough implant. The final implant was melt in the mould and implanted after polymerization.<sup>3</sup> Often, even the crane model has been manufactured with CAM technology for easier operation planning and implant shape verification.<sup>4</sup>

One of the first papers in Hungarian medical literature treating of the CAD-CAM method application in implant realization has appeared in 1995.<sup>5</sup> In the late 1990's researchers have developed the possible methods for realizing a CAD implant model, and advantages and disadvantages of such methods have been shown. Such research results are summed up for example in the 2003 paper of Hieu et al.<sup>6</sup> In case of small implants, model is realized using the principle of symmetry, while in case of large implants, model is based on a crane of similar shaped crane extracted from a database. These methods are easy to algorithmize. With an appropriate software based on such algorithms a simple implant model can be realized in 6-8 hours. If the implant is larger than the half of the cranial bone, or it passes through the symmetry plane of the crane, or it covers irregularly placed crane windows, then modeling still needs large quantity of manual work.<sup>6</sup> In such cases the skills of the implant model maker, and the cooperation among the medical doctor, the model maker (CAD) and the manufacturer (CAM) are of great importance.

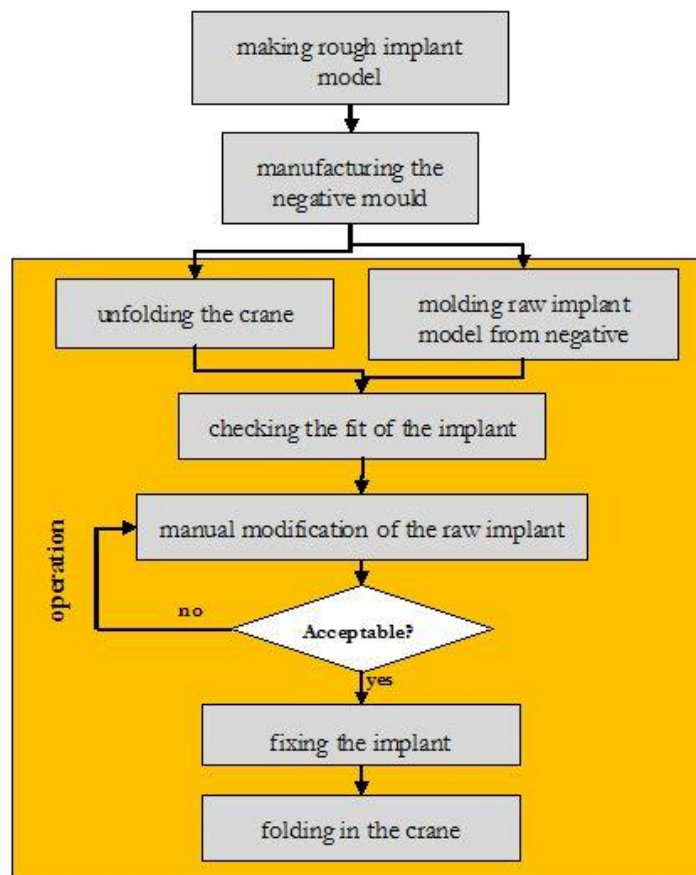


Figure 1. A traditional method for making PMMA implants

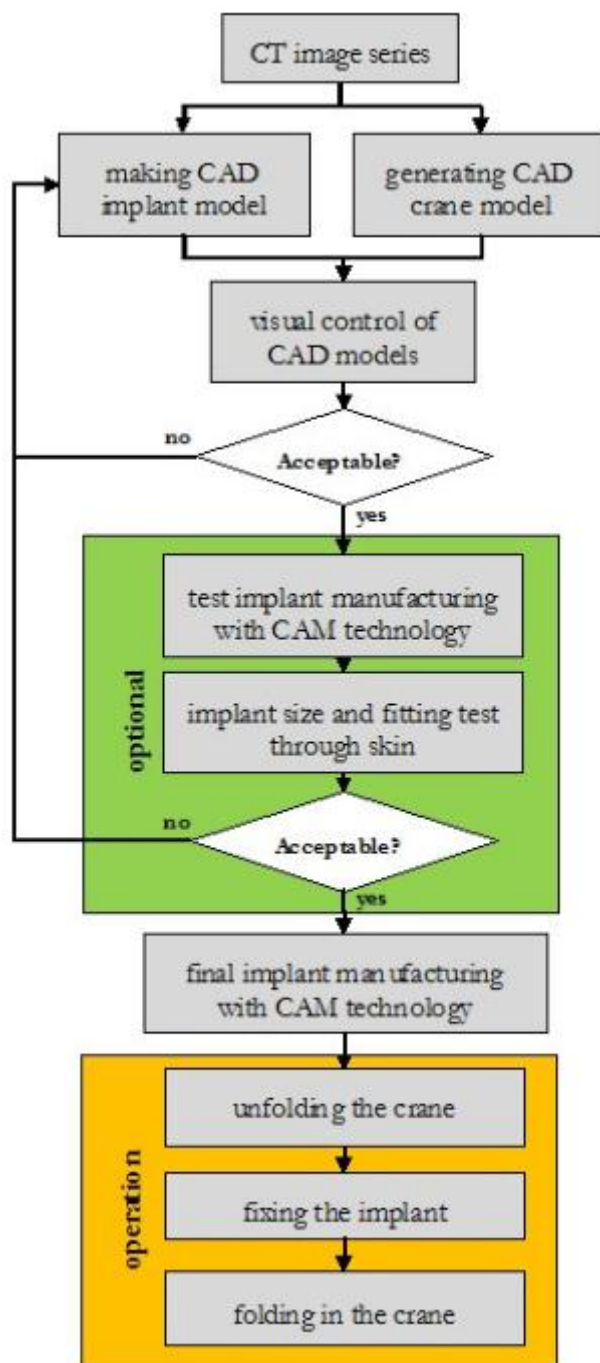


Figure 2. The developed CAD-CAM implant manufacturing process

All of the procedures using CAD designed implants are well proven, and there is large practical experience behind them. We wanted to develop such design process that is more precise and more cost efficient. Our priorities were the following:

- implant design based directly on the CT images (precision)
- implant model control directly in CAD environment (cost efficiency)

- minimal use of CAM technology (cost efficiency)
- minimal operation time (cost efficiency, patient less exposed to surgery)

Instead of PMMA, ultra high molecule-weight polyethylene (UHMW-PE) was chosen as implant material. This material is a very rigid, non corrosive, non toxic thermoplastic. It is relatively cheap and has good radiological transparency.

The steps of the developed implant manufacturing process are shown in *Figure 2*. Implant models are built manually, in cooperation of the CAD engineer and the medical doctor. The implant limit surface follow closely the real cranial bone window contour. Example of generated crane model is shown on *Figure 3*. The taylor-made implant can be seen in *Figure 4*. Note that optional verification loop can be added to the algorithm if the CAD engineer is beginner or the implant shape is too complex. For simpler implants or with professional engineer the optional loop can be omitted. Example of implant fixation is shown in *Figure 5*. The implant and the crane are linked with small titanium sheets fixed by screws both on the crane and the implant.

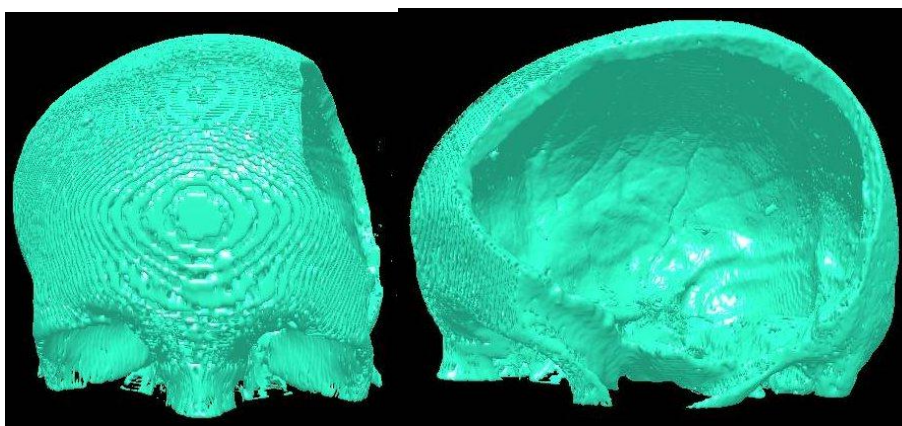


*Figure 3.* Crane model

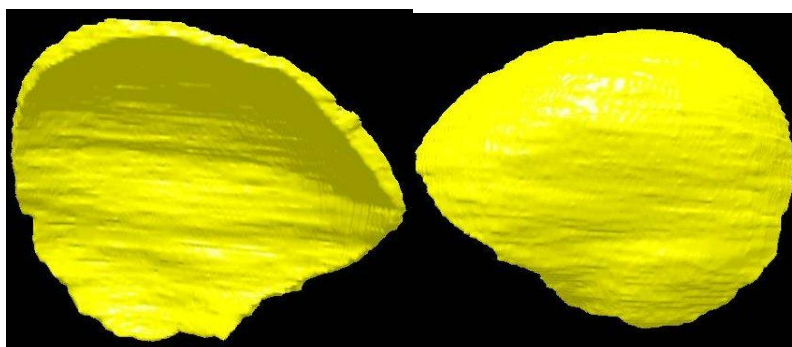


*Figure 4.* Implant model





Figure 5. Fixing the implant

The advantage of the manual method is that implant models of any shape, size or complexity can be realized in good quality. The disadvantage of the method is that the time needed for building a model is always more than building a model automatically by software.

### Discussion

22 implants realized with the developed CAD-CAM manufacturing procedure were applied in 19 patients in the last 8 years. None of the implants had to be modified during the operation, all fit perfectly the bone window. Short time post operational complications appeared at 2 patient (9%). Long time post operational complications appeared at only 1 patient, where one of the two implants had to be removed (4,5%).

After recovery, the presence of implant on the crane is not perceptible (Figure 6). Aesthetical problems were not signaled by the patients.



Figure 6. Head shape before and after cranioplasty

The developed CAD-CAM implant manufacturing procedure can also be applied when a previous implant is not convenient, is damaged, moved away or broken. Changing of a previous damaged polymer implant can be realized in one operation: the old implant is removed, and the

tailor made new is implanted (Figures 7-8). The procedure was successfully applied also for changing problematic, infected old implants.

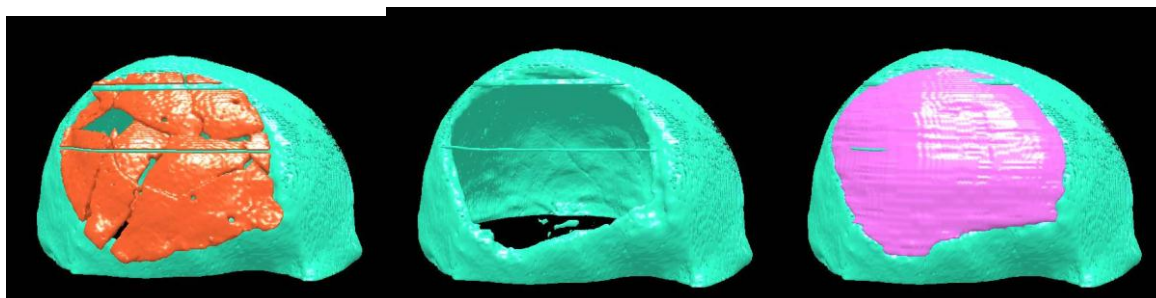


Figure 7. Steps of CAD correction: broken old implant, clean crane window, new implant fit



Figure 8. Broken old implant and head shape with new implant

## Conclusion

The elaborated procedure allow to realize tailor made precise implants at relatively low cost. As manual method is used, it is better applied for implants of complicated shape or big size. Upon the experiences, the risk of post-operative problems is not higher than the usual.

## REFERENCES

1. Cabraja M, Klein M, Lehmann TN. Long-term results following titanium cranioplasty of large skull defects. *Neurosurgical Focus* 2009;26(6):E10,1-7.
2. Marchac D, Greensmith A. Long-term experience with methylmethacrylate cranioplasty in craniofacial surgery. *Journal of Plastic, Reconstructive & Aesthetic Surgery* 2008;61:744-52.
3. Goh RCW, Chang CN, Lin CL, Lo LJ. Customised fabricated implants after previous failed cranioplasty. *Journal of Plastic, Reconstructive & Aesthetic Surgery* 2010;63:1479-84.
4. Hieu LC, Zlatov N, Vander Sloten J, Bohez E, Khanh L, Binh PH, Oris P, Toshev Y. Medical rapid prototyping applications and methods. *Assembly Automation* 2005; 25(4):284-92.

5. Gulyás G, Pulay Gy, Volant M, Bárdosi Tné, Farkas G, Juharosi Z. Koponyacsontpótlás számítógép segítségével készített implantátummal. Orvosi Hetilap 1995;136:2393-97.
6. Hieu LC, Bohez E, Vander Sloten J, Phien HN, Vatcharaporn E, Binh PH, An PV, Oris P. Design for medical rapid prototyping of cranioplasty implants. Rapid Prototyping Journal 2003;9(3):175-86.

## PROCESSING OF DIGITAL MOIRÉ IMAGES IN SALUS ORTOPÉDTECHNIKA KFT.

Petra Balla, Ferenc Marlok, Katalin Prommer, Szilvia Nagy, Orsolya Schulcz, Gyula Kocsis,  
Benjamin Magocsi

Salus Ortopédtechnika Kft.

[petra.balla@mogi.bme.hu](mailto:petra.balla@mogi.bme.hu)

---

### **Abstract**

More and more children and youngsters are affected by spinal deformities these days. These diseases can be well cured if they are detected and filtered out in time. We wanted to set up an objective and safe method with which we can diagnose wide spectrum of school-aged youngsters without harmful side-effects. Creating moiré images was one way to solve this problem, that is the reason why we started to test this method in filtering and following the condition of our young patients. Patients measured by us were going through a general examination method where their physical status was examined by physiotherapists, and relief images were taken of their back.

The initial aim to make the moiré image use an objective method to filter and follow the patient's condition in case of weed curvature of the spine could not be totally fulfilled. The reason is that the evaluation of the images is still a subjective method done by our vision. A possible solution could be to find an objective evaluation method where we can process, evaluate and compare the images with the same conditions. The programming and use of a proper image processing algorithm could be a great help for us.

**Keywords:** digital moiré, moiré evaluation, Kamal's method, moiré method

---

### **1. Introduction**

In the Salus Kft. the digital, computer-aid moiré device is being tested for a few years. We use it especially to follow patients' conditions, but it can be used also for screening healthy patients. Originally this method would have been a substitution instead of manual examination. Unfortunately this system has not been developed yet, but we would like to improve a method.

In every 3 months children have to get their braces checked. They have to visit our company to let us take a moiré picture/image of their bodies. In this way the improvement or deterioration will be visible. Sometimes this picture can be eye-catching for children, in many cases they face their backs' condition. If somebody wears the brace carelessly and the moiré picture shows decadence the experience causes the patient to wear the brace properly. If somebody wears this device properly, 20-22 hours daily, the moiré picture generally shows some improvement. This experience could help to follow the treatment dedicated to reach the best results.

In a few cases the moiré image is not in balance with the X-ray images. Sometimes improvement was detected, however the X-ray showed unequivocal decadence. This phenomenon is attributed to the physiotherapy led by us. We have experienced the opposite way as well.

The back is left untouched by the examination, so it does not cause any exposure for young and teenage children. Moreover the number of examinations of the patient's back could be increased

using this method. The examination is fast and quite cheap, so it can be performed any number of times.

## **2. The Moiré Effect**

Optical measurement methods of three-dimensional surface metrology became rapid and effective tools especially in the field of orthopedics,<sup>1-5,7,17-19</sup> where moiré imaging (used mostly in spinal deformities) is considered to be capable of measuring and graphically displaying whole surfaces instantaneously.<sup>23</sup>

By the superimposition of two similar periodic structures translated, or rotated relative to each other, a new structure arises with longer periods. This one is called moiré pattern and it consists of the moiré fringes.

During the moiré surface measurement a grating (or its shadow) is projected to the surface of the model, where this grating will take a distorted form due to the model's shape. Another grating (which can be the same) is located between the model and the observer (that can be for example a camera or a person's eye). As the second grating remains unchanged, it can be considered as a reference grating. The axis of the observer encloses a certain angle with the axis of the projection by intersecting each other on the surface.<sup>30-32</sup>

We can find several points on the moiré pattern that have the same distance from the reference surface (or base plane). By connecting these points, contours can be created, just as at the topographical maps, in this way the test surface can be described with these lines.

By superimposing two periodic or quasi-periodic structures, the moiré phenomenon can be observed. When the two structures have the same or slightly different line spacing and their lines are set approximately parallel, a new coarse pattern appears. This pattern is known as the moiré fringe pattern. The spacing and orientation of the moiré fringes depend on the spacing and orientation of the structures being overlapped whereas the visibility of fringes is related to the width of transparent or black lines with respect to the line spacing of the structures. Moiré topographical methods can be distinguished as: the basic grating-shadow, the grating-projection, the grating-TV and the synthetic, computer generated grating methods. Shadow moiré is a contour mapping technique that involves positioning a grating close to an object and observing its shadow on the object through the grating. Thus, the basic grating-shadow method offers the best accuracy and the simplest arrangement because the projected grating and the master grating are identical, so they have the highest degree of binding. The disadvantage of the shadow moiré technique is that the master grating must have similar size as the measured object.

The moiré method has several advantages, such as being fast, relatively cheap, highly sensitive, and has graphical results. It is also essential that the method offers a non-contact surface measurement<sup>20</sup> which does not burden the patient with radiation, unlike x-ray analysis. Moiré measurement can be a supplementary method for determining the necessary further examinations and treatments of patients.

The main advantages of the moiré technique during the quantification of spinal deformities are the simple assembly and cheap construction of the measuring device. It offers a fast and easy way

to interpret the content of the moiré picture towards the user. The moiré fringes formed on the human back allows the examiner to find the characteristic points of the spine easily.

The measurement method can be applied in several other areas, as it offers the chance to determine deformations caused by pressure or temperature change in cases where mechanical measurement methods are not an option. The dimensional accuracy of mass production or products in robotics can also be measured with this method.

### **3. The moiré equipment**

This equipment is used in the gym of Salus Ltd., it is designed and developed with help of orthopedic medicals. Actually it is a classical projection moiré equipment,<sup>21-22</sup> but we use video projector instead of the traditional projector. We have to take a picture from the reference area first, then the patient's back appears in the examined area. The pattern and the settings are left without change. Because of the examined object the pattern will be strained. Another photo is taken of this, and the computer<sup>24</sup> produce a moiré picture from these data.<sup>33</sup> The image can be evaluated with one of the previously described algorithms. In this picture the contours are visible, subjective evaluation also can be applied.<sup>27-28</sup>

### **4. Spinal Deformity Types**

Scoliosis is a weed deformity on the spine it can be visible mostly in the frontal plane. It has two different types, functional and structural scoliosis. In both cases there are weed lateral deformities on the spine, but in case of funtional scoliosis there isn't any rotation. Rib deformations cannot be observed with stoop instead of structural scoliosis, as it is hard to remark. Mostly angle of that deformity will stagnate. Physiotherapy can be the suitable method to cure it. Asymmetrical strengthening of the back muscles is a good solution to pull weed curvatures into the right position.

It can be divided into primer and secunder scoliosis. If patients has difference between their legs, weakness in their muscles, it can be diagnosed as a secunder scoliosis. It is very important to find and cure cases for the successful treatment. Without any visible cases can be diagnosed as a primer scoliosis.

By structural scoliosis there are weed lateral deformities on the spine with torsion. Cases has not been found yet to complain the development of the disease. Dispersion is not equal between the two genders. Young girls are more often concerned compared to boys. It could be discovered in rapid growth phase of the bones, mostly at teenagers. Sadly we meet 3-4 years old little children with large deformities who have to wear the brace until the end of ossification.

Rib or chest deformations can be observed, as the result of vertebrae torsion. Patients handled by us the physiological sagittal curvatures seems to be reduced. Patients have to wear brace until the end of ossification, without this the disease will deteriorate. For teenage girls the ossification ends two years after the first menstruation. To verify it X-ray images are needed, that can show the developed Rissel mark on the pelvis. Scoliosis without treatment can cause pain, aesthetic problems, diasbility and even failures in blood circulation.

The Cobb angle is measured on plane radiographs by drawing a line through the superior endplate of the superior end vertebra of a scoliotic curve, and another line through the inferior endplate of the inferiormost vertebra of the same scoliotic curve, and then measuring the angle between these lines.<sup>6,26</sup>

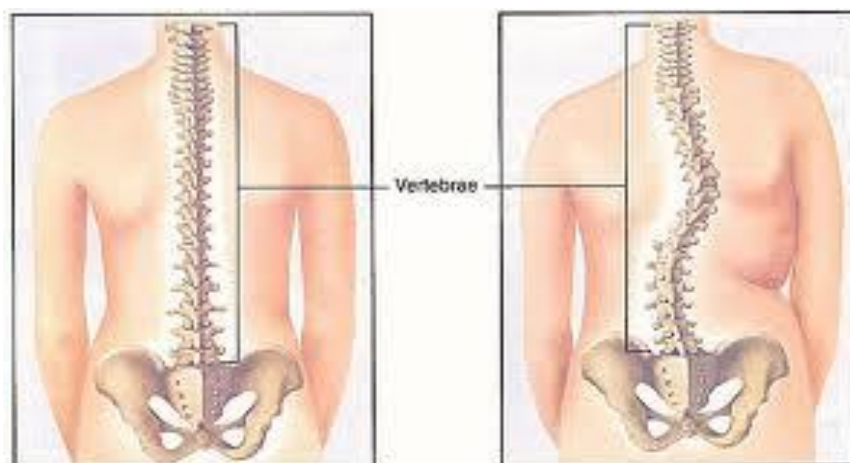


Figure 1. Scoliosis<sup>8</sup>

The second type of spine deformity is the Scheuermann disease. At this disease the spine is straight in the frontal plane, but the kyphosis is much rounder than at healthy people. Nowadays the lumbar kyphosis is also very frequent. Often negligent posture is diagnosed instead of Scheuermann disease, and it remains without a brace and a suitable treatment. In general, shapes of vertebrae change on the inner side of spine. In case of the disease vertebrae are lower in the inner side and the collagen combination is changed in the endplates, so the cartilage rift becomes tight between vertebrae.

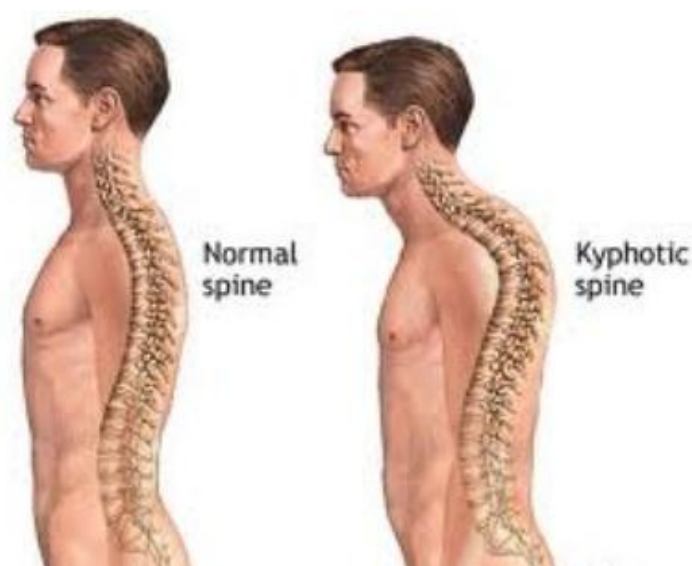


Figure 2. Scheuermann disease<sup>29</sup>

## **5. Treatment of The Spinal Deformations**

The treatment method has to be chosen according to the condition of the disease.

Under 20 Cobb degree physiotherapy can be sufficient. During the tournament muscles are strengthen asymmetrically, so they can keep the weed curvatures in the normal position. A few special exercises have to be practiced 5 to 7 times a week to get improvement.

Between 20 and 50 Cobbs special Schroth physiotherapy have to be combined with brace treatment. The brace is a rigid, uncomfortable device. It puts pressure on the trunk to upright carriage. Opposite of this there have to be moving areas, it's because of the movement needs of the trunk. It stimulates patients to use their own muscles, as they try to get into a position where they don't feel pain. It is important to do also physiotherapy. Doing other sports (swimming for example) while wearing brace could be also effective, as muscles of the spine get stronger asymmetrically, just like with physiotherapy.<sup>10-15</sup>



*Figure 3. Gschwend brace* <sup>9</sup>

Above 50 degree surgical consultation shall be needed. In case of a considerable deformity with large rotation the spine has to be stretched a few weeks before the operation. Under the operation surgeon lay a metal device onto vertebrae and connect it with the spine. This device removes weed curvatures and keep the spine in a fixed position. It is only suggested in case of a very serious disease.



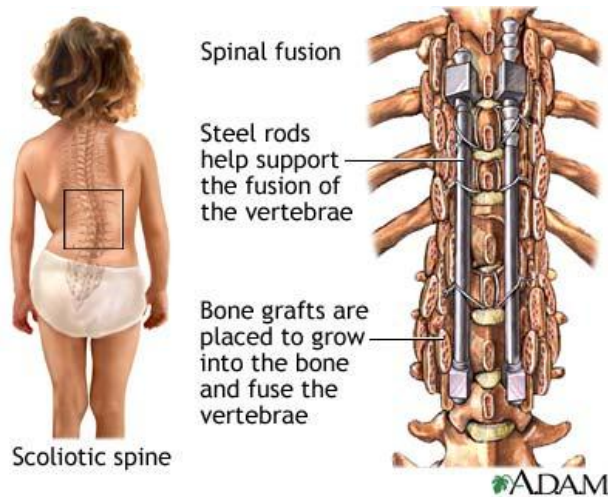


Figure 4. Spinal surgery <sup>16</sup>

## 6. Evaluating method

With Kamal's method<sup>25</sup> we can calculate the  $\theta$  angle of the spinal curvature from moiré images which correlates to Cobb angle in case of single curve scoliosis. The following points have to be used by this mathematical method (according to Figure 5.):

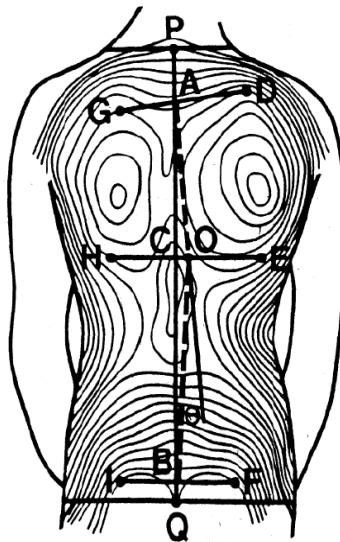


Figure 5. Measurement of the angle of spinal curvature by moiré topographs <sup>18</sup>

$$\theta = \sphericalangle CAO + \sphericalangle CBO = Y1 + Y2$$

The d1, d2 and d3 sections show the minimum asymmetry and can be given with the following equations where left to right direction is positive while right to left is negative:

$$d1 = \frac{1}{2} * (CH+CE)$$

$$d2 = \frac{1}{2} * (AD+AG)$$

$$d3 = \frac{1}{2} * (BF+BI)$$

$$\tan Y1 = \frac{|\square|d1-d2|\square|}{CA}$$

$$\tan Y2 = \frac{|\square|d1 - d3|\square|}{BC}$$

Kamal's algorithm to determine the points necessary for the calculations according to *Figure 5*. is as follows:

1. The midpoint of the neck (P) have to be joined to the midpoint of the pelvis (Q).
2. Find the moiré fringe on the scapula, which shows the most significant asymmetry, and intersect it with a line perpendicular to line PQ. So we can get points H, C and E.
3. Draw an upper tangent to the moiré fringe, which has been intersected by HE. This way we get points G, A and D.
4. Finally, find a moiré fringe on the lumbar part of the spine, which is not significantly distorted, and intersect it with a line perpendicular to PQ. Points G, A and D can be defined this way.

Moiré images taken by us are used mostly to detect changes of patients' backs. The subjective evaluation by eyes can also show the changes. It is important to give psychical help for young children. Showing the result is always a good experience for them. This can give them willpower to continue the treatment. Otherwise decadence can be also challenging.

We found some conflicted cases, where the moiré picture showed improvement, but X-ray images showed reverse results. It is planned to examine this problem, but at first very simple problems were chosen to be evaluated. Patients were selected with long thoracic curvature and minor rotation. The most often type of weed curvatures is a curve with right convex, long thoracic and left convex short lumbar part. Four patients were selected by us with similar deformity. We paid special attention to the perfect selection, the selected children's curves are very similar.

## 7. Examinations

The 4 selected children have at least two different X-ray photos, and two or more moiré pictures. 12 moiré pictures were evaluated. From moiré pictures approximate results were calculated. These results were compared with the Cobb angles calculated by orthopedic medicals from X-ray pictures.

The evaluation and the measurements were done using RapidformXOR software. The height of the children and the zoom of the pictures were taken into consideration. The height of the patients were measured in the picture, and the measured height was scaled with the original height.



Figure 6. The first examined patient's moiré and X-ray images

The pictures were imported into the program, and the mentioned points were marked. Between the neck (P) and the hips (Q) a line was drawn to show the gradient of the spine. G, A, D, H, C, E and I, B, F points were designated also.

The distances were measured and summarized in a table. The angles were calculated using Kamal's method and mathematical equations.

We wanted to try Kamal's method in use. The easiest deformity is the mentioned right convex long thoracic and left convex lumbar curvatures. It is easy to be perceived on the back. Kamal's method can be used, as the effect of the disease can be visible mostly in the middle of the back, under the scapulae.

## 8. Results

Every selected patient has 3 moiré pictures. The first and the 3th images were taken at the same time as the X-rays, while middle moiré picture was compared to whichever X-ray image was taken at closer time to it.

The original Cobb angles – measured by orthopedic medicals – were compared with the calculated angles using the Kamal algorithm. I paired the results to be able to prepare a statistical evaluation.<sup>34-36</sup>

Average of medical measured Cobb angles was 30.4°. The average using the Kamal algorithm turned up 28.58°.

The standard deviation in the first case was 10.66, in the second case it was 10.95.

Standard error was 3.078, after the evaluation of moiré pictures 3.161.

The original and the measured angles were stand in pairs, and paired t-test<sup>37</sup> was applied. The P value was 0.2642. It can be declared that there is no significant difference between the two methods, the evaluation of moiré images can give similar results as the other method.

The normal dispersion was checked with the Shapiro-Wilk test, p is not significant.

## **9. Recommended Modification**

The first problem is that Cobb angles are measured on every weed curvature. If there is 2 or 3 weed curvatures on the spine, medicals measure 2 or 3 different values of them. Kamal algorithm is good for thoracic curvatures, but we haven't got data for other types of deformities. It is planned to examine other types of curvatures, like lumbar curvature and Scheuermann disease.

It is very important to have correct calibration and right settings before the measurement. The camera and the projector have to be perpendicular to the patient's back.

It is important to warn patient to stand in the right position, the picture has to be taken in time of total exhalation. We plane to use a handrail during taking the pictures to eliminate movement of the patients. It is important to have the pelvis in the correct position, length of legs have to be checked if it is necessary.

During the evaluation we have to pay attention to use the same contour lines, if it is possible.

---

## REFERENCES

1. Theocaris PS. Moiré Fringe in Strain Analysis, Pergamon Press 1969.
2. Patorski K, Kujawinska M. Handbook of the Moire Fringe Technique, Elsevier, Amsterdam; 1993.
3. Durelli AJ, Parks VJ. Moiré Analysis of Strain, Prentice-Hall, Englewood Cliffs, New Jersey; 1970.
4. Parks VJ. Geometric Moiré, SEM Handbook of Experimental Mechanics, Prentice-Hall, Englewood Cliffs, New Jersey; 1987.
5. Parks VJ. Strain measurement using grids, Optical Engineering 1982;21::633-39.
6. Orosz M. Conservative treatment of the idiopathic scoliosis, Pediatrics 2005;56(6):651-57.
7. Adir IV, Wijk MC, Armstong WD. Moiré topography in scoliosis screening. Clin. Orthop., Clin. Orthop. 1977;129:165-71.
8. [www.qualshare.com](http://www.qualshare.com)
9. <http://korzetteselet.blogspot.com>
10. Chêneau J. Ein Weg zur richtigen Skoliosebehandlung. Orth. Tech., 4, 222, 1990.
11. Chêneau J. Das „original“ Chêneau-Skoliosen-Korsett. Orth. Tech. Dortmund 1997.
12. Cobb JR. Outline for study of scoliosis. Am. Acad. Orthop. Surg. 5; 1948:261-6.
13. Orosz M. About the idiopathic scoliosis. Movement Therapy. 1; 2000:3-8.
14. Orosz M., Marlok F. The Chêneau brace. Rehabilitation. 1; 1997:10-11.
15. Orosz M. Structural failure of incorrectly prepared and used Cheneau braces in the treatment of scoliosis. Magyar Traumat. 2; 2000:83-90.

16. [www.healthcentral.com](http://www.healthcentral.com)
17. Batouche M, Benlamri R, Kholadi MK. A computer vision system for diagnosing scoliosis using moiré images, *Computers in Biology and Medicine*, 1996;26(4):339-53.
18. Ruggerone M, Austin JHM. Moiré Topography in Scoliosis, Correlations with Vertebral Lateral Curvature as Determined by Radiography, *Physical Therapy*, 1986;66(7):1072-77.
19. Laulund T, Søjbjerg JO, Hørlyck E. Moiré Topography in School Screening for Structural Scoliosis, *Acta Orthopaedica*, 1982;53(5):765-68.
20. Windischbauer G. Survey on application of moire-techniques in medicine and biology. In *Optics in Biomedical Sciences, Proceedings of the International Conference*; Springer-Verlag Berlin; 1981:244-9
21. Takasaki H. Moiré Topography, *Applied Optics*, 1970;9(6):1467-72.
22. Takasaki H. Moiré Topography, *Applied Optics*, 1973;12(4):845-50.
23. Laulund T, Søjbjerg JO, Hørlyck E. Moiré Topography in School Screening for Structural Scoliosis, *Acta Orthopaedica*, 1982;53(5):765-8.
24. Wenzel K, Antal Á, Molnár J, Tóth B, Tamás P. New Optical Equipment in 3D Surface Measuring, *Journal of Automation Mobile Robotics & Intelligent Systems* 2009;3(4):29-32.
25. Kamal SA. Determination of degree of correction of spinal deformity by moiré topographs, In: *Moiré Fringe Topography and Spinal Deformity, Proceedings of the 2nd. International Symposium*, Gustav Fischer Verlag, Stuttgart 1983. p. 117-26.
26. Neugebauer H. The different methods of measuring the curvature of scoliotic spine. In: *Moiré Fringe Topography and Spinal Deformity, Proceedings of the 2nd. International Symposium*, Gustav Fischer Verlag; Stuttgart 1983. p. 17-26.
27. Frontino G, Negri V, Rinaldi E. Photographic moiré method for preliminary diagnosis of spine deformity, *Ateneo Parmense Acta Biomed.* 1980;51(1):33-8.
28. Kim SH, Ishida K, Ishikawa S, Ohtsuka Y, Shimizu H. Discriminating spinal deformity employing centroids difference on the moiré images, *Systems and Computers in Japan* 32(7): 20-28.
29. [www.healthtap.com](http://www.healthtap.com)
30. Gaal Zs, Antal Á, Péter T. Scoliosis testing features on the basis of electronically generated Moire patterns, *Biomechanica Hungarica* 2010;III(1):84-92.
31. Gaál Zs, Antal Á, Tamás P. Statistical Analysis of Determining the Rate of Scoliosis from Electronically Generated Moire Patterns, In: *Proceedings of Seventh Conference on Mechanical Engineering*. Budapest; Hungary; 2010.05.25-2010.05.26 Budapest; 796-803.
32. Gaál Zs, Antal Á, Tamás P. Scoliosis Testing Features on the Basis of Electronically Generated Moire Patterns, In: *8th IEEE International Symposium on Applied Machine Intelligence and Informatics*. 2010.01.28-2010.01.3; Herlany, Slovakia; 335-40.
33. Gaál Zs, Tamás P, Antal Á. Calibration and Measurement Test of Medical Moiré Equipment, In: *XXIV. microCAD International Scientific Conference*. Miskolc, Hungary; 2010.03.18-2010.03.20 Miskolc: Miskolci Egyetem Innovációs és Technológia Transzfer Centruma; ISBN: 978-963-661-919-0 ; 41-46.
34. Gaál Zs, Antal Á, Tamás P. Statistical Analysis of Scoliosis Rate of Electronically Generated Moiré Images, In: *IV. Hungarian Biomechanical Conference*. Pécs, Hungary; 2010.05.07-2010.05.08; Paper A-0062.
35. Vincze I. *Mathematical Statistics With Industrial Applications*, Műszaki Kiadó; Budapest; 1968
36. Varga L. *Introduction of the methods of didactic research*, Tankönyvkiadó; Budapest; 1986
37. Kemény S, Deák A. *Planning and evaluation of examinations*, Műszaki Könyvkiadó; Bp.; 2000

***Conducting The research part of the tender called “Research of an intelligent device and method for observing and nursing orthopaedic deformities” (TECH\_08-A1/2-2008-0121), specified by the Hungarian National Bureau of Research and Technology.***

## TECHNOLOGICAL INNOVATION AT SALUS ORTOPÉDTECHNIKA KFT. REGARDING THE GERINCOR PROJECT

Petra Balla, Ferenc Marlok, Katalin Prommer, Gyula Kocsis

Salus Ortopédtechnika Kft.

[petra.balla@mogi.bme.hu](mailto:petra.balla@mogi.bme.hu)

---

### Abstract

In this article we tried to introduce our renewed technology regarding the Gerincor project. Instead of the old technology the new provides much cleaner, more accurate, and more comfortable procedure for our young patients. Moreover data could be archived much easier.

**Keywords:** Imageware, RapidformXOR, plastering, milling, spinal deformity

---

### 1. Introduction

The GERINCO2 project – started in 2009, with 5 different company and Research Institute – got a problem to solve: how to simplify manufacturing of the aid for spinal deformities, and how to improve the brace. Our company, Salus Orthopedic Ltd. is one of the leading hungarian orthopedic companies, medicating thousands of patients in Hungary and beyond the borders.

Wearing a brace is not easy. It is a firm, rigid device, that has to be worn from the detection of spinal deformity until the end of the ossification. Our company is leader of manufacturing these devices in Hungary, Europe and even in the whole World.

Spinal deformities are diseases, which are weed variation of physiological spinal curvatures. Weed variations could be: *scoliosis*, and *Scheuermann disease*.

### 2. Spinal Deformity Types

Scoliosis means spinal weed deformity mostly in the frontal plane. It could be divided into functional and structural scoliosis. In both cases there are weed lateral deformities on the spine, but in case of funtional scoliosis there are problems only in two dimensions, so there isn't any rotation. Therefore no rib deformations can be observed with stoop, as it is hard to remark. In general angle of that deformity won't deteriorate. In most cases it can be cured with special physiotherapy. With asymmetrical strengthening of the back muscles the curvatures could get better. If there is not a simple reason, it is a primer scoliosis. In case of secondary scoliosis a cause could be found, for example difference between the length of the legs, muscles weakness. Liquidation of cases is very important for an effective treatment.<sup>1-2</sup>

By structural scoliosis there are weed lateral deformities on the spine with minor or large torsion. Researchers has not found any cases to complain the development of the disease. Young girls are more often affected than boys by this disease. It could be discovered in rapid growth phase of the bones, mostly at teenagers. Rarely it has appeared by younger 3-4 years old kids, where the opportunity of recovery is less.

As a result of vertebrae torsion, rib or chest deformations can be observed. The physiological sagittal curvatures seems to be reduced. Without treatment structural scoliosis could be even worse until the end of ossification. For teenage girls the ossification ends two years after the first menstruation. To verify it X-ray photographs are needed, that can show the developed Rissel mark on the pelvis. Scoliosis without treatment can cause pain, aesthetic problems, diability and even failures in blood circulation.

The Cobb angle is measured on plane radiographs by drawing a line through the superior endplate of the superior end vertebra of a scoliotic curve, and another line through the inferior endplate of the inferiormost vertebra of the same scoliotic curve, and then measuring the angle between these lines.<sup>3</sup>

The second type of spine deformity is the Scheuermann disease. In case of this disease the spine has a normal curvature in the frontal plain, but the kyphosis could be rounder than at healthy people, or a kyphosis will develop near the groin on the spine. It is hard to discover, while it is often mistaken with simple negligent posture, and it remains without treatment. In general, shapes of vertebrae change on the inner side of spine, they are shorter and the collagen combination is changed in the endplates, so the cartilage rift become tight between vertebrae. Sometimes Schmorl lumps could be found. It means that a piece from cartilage disc go under the border plates. It is not an important alteration, however medicals take it for a sure symptom of the disease.

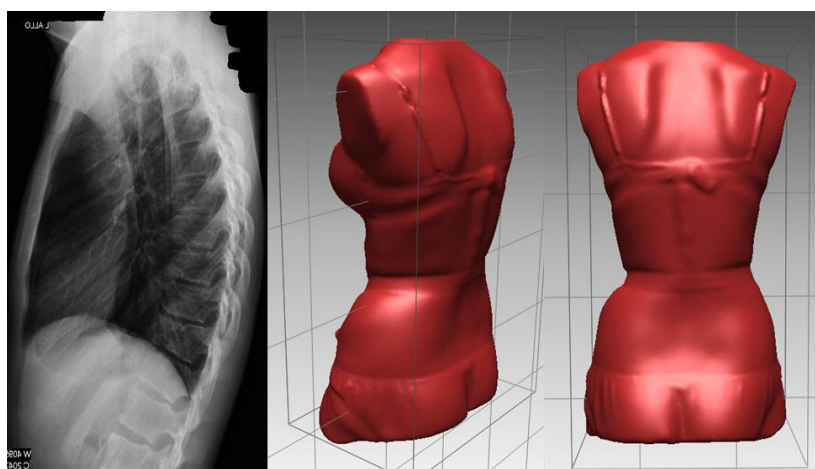


Figure 1. 0

### 3. Treatment of The Spinal Deformations

There are more alternatives for the treatment, but it's important to take the condition of the disease into consideration.

Under 20 Cobb degree physiotherapy is recommended. It is built up from very special exercises, muscles are strengthen asymmetrically, so they could stand the weed curvatures in the normal position. A few special exercises can be learned and have to be practiced 5 to 7 times a week to get better.



Between 20 and 50 Cobbs it's very important to use a brace<sup>4,5</sup> combined with Schroth physiotherapy. The brace is a rigid device. It puts pressure on the trunk to upright carriage.<sup>6-9</sup> Opposit of these it is very important to make moving areas, it's because of moving the trunk. It helps patients to use their own muscles, as they feel pain on pressurized areas, so they try to get in a position where they don't feel pain. It is important to do special exercises to strengthen the muscles. Doing other sports (swimming for example) while wearing brace could be also effective, as muscles of the spine get stronger asymmetrically, just like with physiotherapy.



*Figure 2. Cheneau brace*<sup>12</sup>

Above 50 degree Cobb spine surgery shall be needed. In case of a considerable deformity with large rotation the spine have to be stretched during weeks before the operation. Under the operation surgeon lay a metal device onto vertebrae and connect it with the spine. This device removes weed curvatures and keep the spine in a fixed position. It is only suggested in case of a very serious disease.

#### **4. Modeling**

Our technology changed a lot with the project's help. Modern scanning is used by modelling, and carving is also digitalized. It ensures more comfort for patients and technicians as well.

The patients have a conversation with the leader our technicians', Ferenc Marlok. The discussion gives us informations about the children, for example about their hobbies, sport activities. It all helps us to make the best, individual brace. Another very important reason is that children know that we deal with their personality.

According to the old technology modeling a brace was a long, dirty process, and it was very uncomfortable for young girl patients. Children had to take off almost all of their dress to let technicians put pen marks on their hips. Then they got a slim, transparent, stretch cotton T-shirt, named tube tricot. After orthopedic technician wound their trunk round with plaster bandage, they marked the hips before the plaster became solid. They cut this negative from the patient,

and produce the trunk model from plaster using that negative. Later this model was carved by technicians' hands. During this process the model was made flat to produce pressure areas, to produce moving areas the model had to be fatten by plaster. Around the finished model technician laid a warmed polyethylene sheet and it was tightened onto the model with vakuum. It became the final form of the brace. After the unnecessary parts were cut off, patient could get the individual device after last fitting and final formation.



*Figure 3. Plastering*

The first technical modernization was the digital modeling. Old, uncomfortable plastering is being followed by 3D scanning.

With the new technology patients have to take off their dress until underwear, then they have to step on a rounding podium. During rounding a 3D scanner takes photographs of their bodies. The frequency is 2 frames per seconds. This table turns round 360 ° in 40-50 seconds, so it can take pictures from many sides. In this way information is enough for the program to produce a 3D model of the patient. There are some sponge disc markers used to point at some important bones. These are the hip bones, to point at the base of the brace. In addition the 7th neck vertebra, vertex of both sholuder-blades, intersection of the spine and the line between the marked shoulder-blades, spina iliaca posterios superiors, and endpoints of clavículas near the arms.

Markers help us to compare the X-ray photographs and the 3D models. With this we can find out the real degrees of the curvatures, because it is an important problem, that X-ray assistants stand patients in the right posture, so the spine problem seems lighter, than it is in real.

To produce a brace, first step after scanning is to duplicate the original scan. So we can look the original conditions during the production. After that the unnecessary parts have to be cut off. The final model is a trunk without arms and legs, it's base line is under the hips. The rumpled, crushed parts have to be made smoother, for example borderlines of underwear. This step is important by milling the model.

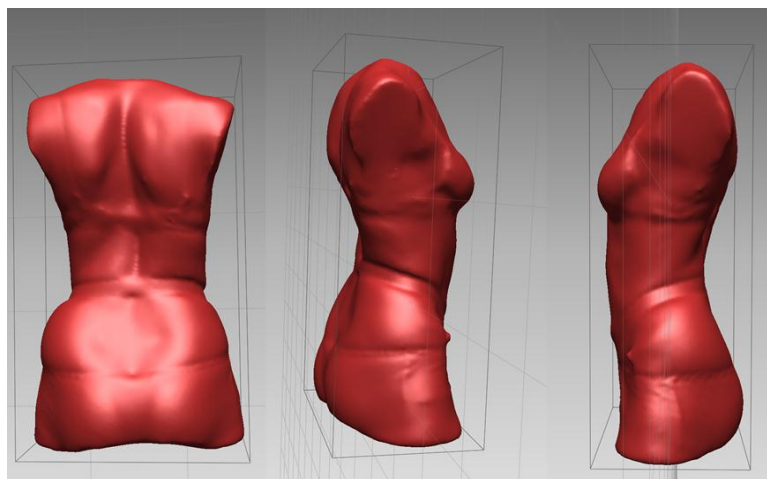


Figure 4. Scanned trunk

## 5. Transformation Using Imageware Software

The Imageware program<sup>10</sup> can transform the scanned 3D point cloud. An .STL Binary file have to be opened from the program, so we get the original scanned point cloud. We have to produce horizontal slides, then the vertical axis has to be defined. After that the program helps us to lay a skin on the cloud. The model is ready to use it in Rapidform XOR software.

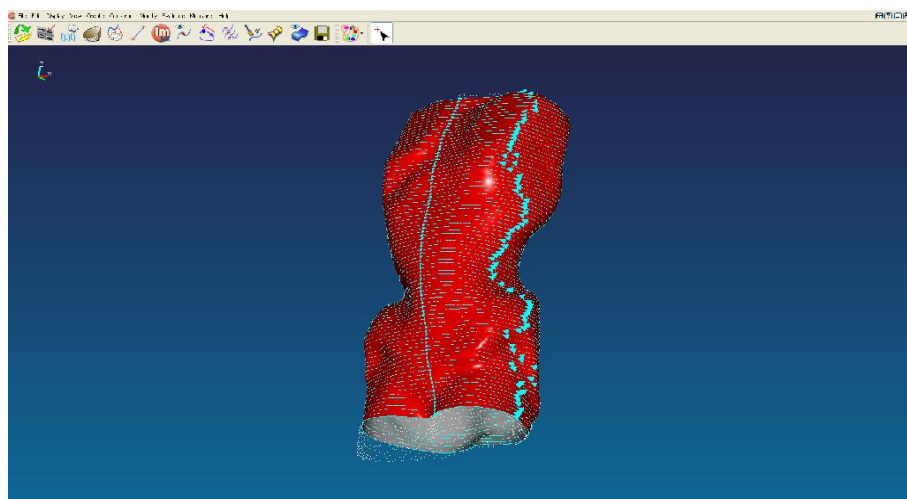


Figure 5. Point cloud after using Imageware

## 6. Digital carving

To develop the final form of the brace orthopedic technicians' experience and knowledge is needed. The model is imported to the RapidformXOR<sup>11</sup> software, then digital hewing is started. By hewing pressure and movig areas have to be produced to push the spine in the normal

position. First step is also duplication to keep the original conditions, then the model will be digitally fatten and reduce to make the necessary areas. The final model can be compared with the original next to or on each other to show the visible differences. By symmetrical models we can work on a half model first, than we can mirror it to the other side. It can be useful to carve Gschwand braces for patients with Scauermann disease.

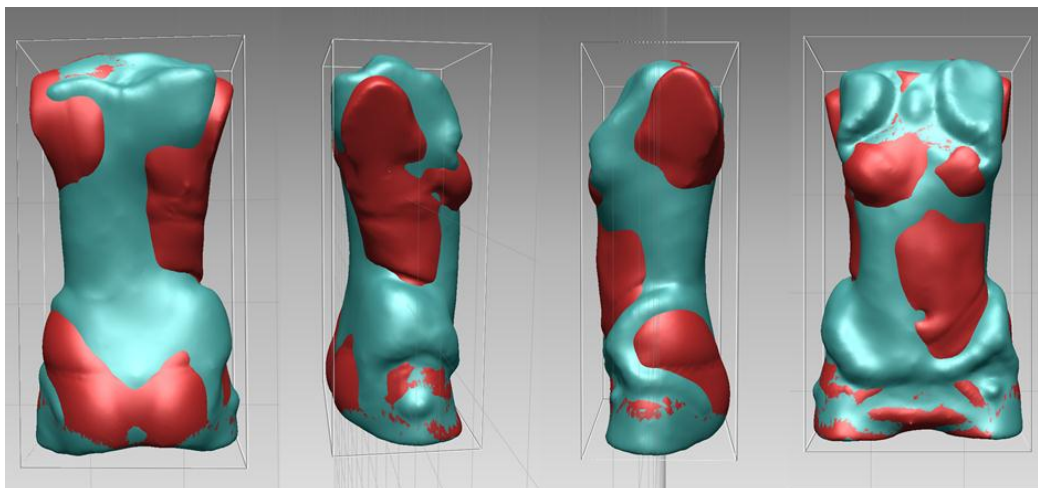


Figure 6. – The carved model (blue) imposed on the original scan (red)

## 7. Final Form

The next step is to create a millfile in the NX software. We have to create a new model with the name of the patient, then patient's digitally carved model will be imported. The opened model have to be prepared for milling. A line is needed to be moved out 250 mm on the shoulder-side. On the other end of the model the line have to be moved out only 10 mm. After that we can start to create a millfile. The system of co-ordinates has to be placed in the milling body. The program generates the milling courses. It is possible to change the generated courses, but is not recommended. The file now can be saved and sent to the milling machine.

The final file is forwarded to a CNC milling machine - with closed work area. It can produce the 1:1 proportion model of the carved trunk model. This body is made from foam (density 10-12 kg/m<sup>3</sup>). After milling it can be perfected by our technicians with plaster. The final body has to be placed on a stand and plastic rods also have to be sticked on the right areas for stiffen the sholuders. A large PE sheet will be warmed to 60 degrees to make it formable but not fluid. This sheet is rounded over the body by technicians and is strengthened using vakuum. After firming the unnecessary parts have to be cut off from the rigid PE trunk model. The brace is ready, but during the planned handing over it will be perfectly formed for the patient's body. Technicians always try to satisfy every demand according to their best knowledge, as device has to be quite comfortable. It has to be wearable more than 20 hour a day.

## REFERENCES

1. <http://www.scolinea.hu/gerincferdules>
2. [www.gerincferdules.hu](http://www.gerincferdules.hu)
3. Orosz M. Az idiopathiás scoliosis konzervatív kezelése, *Gyermekgyógyászat* 2005;56( 6):651-7.
4. Chêneau J. Ein Weg zur richtigen Skoliosebehandlung. *Orth. Tech.*, 4, 222, 1990.
5. Chêneau J. Das „original” Chêneau-Skoliosen-Korsett. *Orth. Tech. Dortmund* 1997.
6. Cobb JR. Outline for study of scoliosis. *Am. Acad. Orthop. Surg.* 5, 1948:261-266.
7. Orosz M.: Az idiopathiás scoliosisról. *Mozgásterápia.* 1, 2000:3-8.
8. Orosz M., Marlok, F.: A Chêneau korzett. *Rehabilitáció.* 1, 1997:10-11.
9. Orosz M. Hibásan készített és alkalmazott Chêneukorzettek kudarca a strukturális scoliosis kezelésében. *Magyar Traumat.* 2, 200:83-90.
10. [www.iwsinc.com](http://www.iwsinc.com)
11. <http://www.rapidform.com>
12. [korzetteselet.blogspot.com](http://korzetteselet.blogspot.com)

## MECHANICAL BEHAVIOUR OF HEALTHY AND DAMAGED HUMAN ARTERIES AND VALIDATION OF PARAMETERS DERIVED FROM EXPERIMENTS

Brigitta Krisztina Tóth, Imre Bojtár

Budapest University of Technology and Economics Department of Structural Mechanics

[brigitta.totb@mail.bme.hu](mailto:brigitta.totb@mail.bme.hu)

---

### **Abstract**

Our research group aimed to develop a numerical model for the analysis of healthy and damaged human blood vessels (e.g. an aneurysm, an adverse vasodilatation) and to investigate the hyperelastic mechanical response of human brain arterial tissue. One of our tasks was to perform laboratory analysis on the specimens taken from the wall of the vessel, to calculate material model parameters for numerical models based on our measurements. Biaxial biomechanical characterization of living tissues – like the artery walls – provides important information about their *in vivo* behaviour. The aim of our research is to estimate stresses of the aneurysm wall and its parent artery, and to estimate the likelihood of a later aneurysm rupture, too. Laboratory measurements have been undertaken, we have taken the specimens of the vessel wall from human cerebral aneurysms and from control healthy artery carotis interna (both from surgery and cadavers), and then we investigated the biomechanical properties of samples in uniaxial and biaxial tensile tests. We attained for this by means of processing the values of the deformations and (Cauchy-)stresses arising from the wall. We verified the necessity of the parameters calculated from the laboratory measurements with finite element simulations performed on a real geometry aneurysm sack. From our study it may be concluded that there is a need for a constitutive model which describes the hyperelastic behavior of the human arterial wall. We demonstrated with numerical simulations that consideration for inhomogeneity in investigations of diseased segments of blood vessels has crucial importance. We proved that damage taking place in aneurysm-sacks is many times more presumable than in healthy material parent arterial segments.

**Keywords:** hyperelastic material properties, internal carotid artery, aneurysm, biaxial measurement, finite element modelling, coupled modelling

---

### **Introduction**

Since a few years we have been working in a research group, which aimed to develop a numerical model for the analysis of damaged human blood vessels, i.e. a model, which is hoped to once help medical doctors to judge whether a damaged section of the blood vessel (e.g. an aneurysm, an adverse vasodilatation) needs to be operated on, and if so, with what urgency.

Our task was to perform laboratory analysis on the specimens taken from the wall of the vessel, to calculate material model parameters for numerical models based on my measurements. We performed laboratory measurements on specimens of vessel wall in order to determine the strength properties of the vessel wall. Several members of staff at the Budapest University of Technology and Economics deal with the simulation of brain aneurysms (sack-like vasodilatations), which makes it important to learn the modified properties of such adverse vessel sections. Naturally, to make a comparison, for this purpose we have to know the material

properties of the healthy vessels as check data. One of our aims is to determine material properties of both the adverse and the healthy vessels, which can be applied to computational models. Measurements on the material properties was necessary because we have not found any database regarding such vessels. It is the case because in several countries measurements on human tissues are prohibited by the law, and the scarce data collected with difficulty in the literature come from animal experiments.

During the numerical modelling we took into consideration the material properties of our own measurements to describe the elastic behaviour the vessel wall, therefore we can consider the material properties of the elastic tube in the coupled models.

## Methods

Let us consider the mechanical material model which we can use for our intended mechanical analysis of the vessel wall. It is often assumed about polymer-like – live or lifeless – materials with inner microstructure that they do not change their elementary volume due to external mechanical influences, that is (in the case of homogeneous isotropic material) their bulk modulus is approximately infinite and their Poisson's ratio is 0.5. The material of the vessel wall can be considered of this kind.

Stresses in hyperelastic, rubber-like materials are obtained by derivation of a deformation energy function assumed as known. We determined material properties for the so-called Mooney–Rivlin model, which is one of the most widely used model in numerical software packages. The Mooney–Rivlin energy function applies deformation invariants and the condition. The model has variants with two, three, five, or more parameters, too. Let us consider the energy function related to the variants with two, three, and five parameters without much detail. In the case of five parameters, the Mooney–Rivlin deformation energy function<sup>1</sup> takes the form of

$$\Psi = c_1(I_1' - 3) + c_2(I_2' - 3) + c_3(I_1' - 3)^2 + c_4(I_1' - 3)(I_2' - 3) + c_5(I_2' - 3)^2, \quad (1)$$

where  $I_1'$  is the first deviatoric deformation invariant,  $I_2'$  is the second deviatoric deformation invariant,  $c_1, c_2, c_3, c_4, c_5$  are parameters characterizing the deviatoric deformation of the material. The three-parameter variant of the Mooney–Rivlin models differs from this only as it contains material constants  $c_1, c_2, c_4$  in the equation above, while the two-parameter variant contains  $c_1, c_2$  only.

It is essential for the numerical analysis of human artery walls to have at least an approximate knowledge on the material behaviour of the vessel wall. In order to reach this goal, laboratory measurements have been undertaken for several years in the Institute of Human Physiology and Clinical Experimental Research of the Semmelweis University. We joined this series of measurements, too. We have taken the specimens of the vessel wall from patients under operations, and from brain vessels extracted from cadavers (deceased patients), and then we have measured the stress-strain curves of the material of the vessel wall in one-dimensional and two-dimensional tensile tests.

We cut 3 mm wide lengthwise and circumferential stripes out of the brain arteries (vessels of type internal carotid artery) obtained from cadavers for the purposes of the uniaxial tests and 8-by-8

mm large square-shaped specimens parallel to the above directions for the biaxial tests. The specimens were gradually pulled by a device equipped with strain gauges (fixed at both ends for uniaxial tests and fixed at all four sides for the biaxial tests), while the pulling force was digitally recorded (Figure 1).

During the processing of the measurement data, we have considered the original position of the specimens in the artery, basically in order to examine the inhomogeneous and anisotropic character of the material behaviour as accurately as possible.

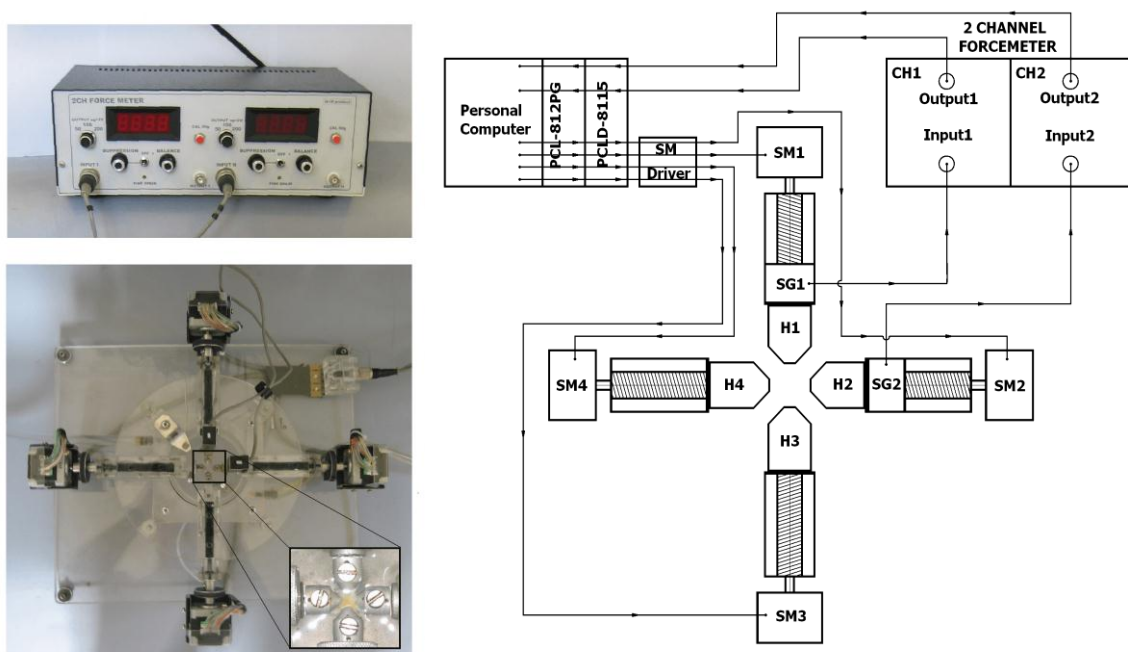


Figure 1. Biaxial laboratory measure device

(Institute of Human Physiology and Clinical Experimental Research, Semmelweis University)

The main parts of the biaxial device and the block chart are shown on the left and on the right, respectively. The specimen holders (H) are displayed with the two strain gauge (SG) attached. The two pairs of holders are placed perpendicular to each other. The output of the gauges is lead to a two-channel force measuring device, and the signals are transmitted to a PC by a multilab card. Displacements of the screws are actuated by 4 motors (SM), and the motions are transmitted to the PC by the multilab card and the SM control unit.

## Results and discussion

It is a common property of the curves obtained that the initial line with small elastic modulus is followed by a steeper curve with an elastic modulus multiple of the initial one. Dividing the curves in two parts approximately linear sections are obtained, hence separate moduli of elasticity can be determined for each section. We have evaluated the measurements on the 12 specimens of internal carotid artery and determined the piecewise moduli of elasticity. During these measurements we have calculated moduli of elasticity of lengthwise, circumferential, and square-shaped (for the biaxial tests) specimens for all artery sections, therefore we was able to evaluate a total of 46 valid measurement data.

By means of the stress-strain curves calculated from my measurements on internal carotid



arteries, we determined the hyperelastic Mooney–Rivlin material parameters required for the numerical analysis. By calculating the material properties we did not purely aim to provide data for our own research, but to make the foundations of a database which can be utilized by both medical doctors and engineers, and expanded in the future, too. Precisely for this purpose we have separately evaluated each specimen, and then tried to generalize the results. In the case of measurements on internal carotid artery used as a control group, we found the biaxial results particularly valuable. Plotting all curves obtained from biaxial measurements we can only deduce that a softer and a harder type of material can be distinguished. We fitted Mooney–Rivlin curves for all measurement series on internal carotid artery, and also on measurements we judged to be belonging to the softer and the harder types of material separately. For each measurement we considered the number of parameters (2, 3, or 5) in a way to get an acceptable approximation. The results are summarized in *Table 1* without details, together with the averaged maximal stresses and strains related to the first damaged states, which are regarded as failure.

|            | $c_1$ [Pa] | $c_2$ [Pa] | $c_3$ [Pa] | $c_4$ [Pa] | $c_5$ [Pa] | Max. stress [Pa] | Max. strain [m/m] |
|------------|------------|------------|------------|------------|------------|------------------|-------------------|
| ICA_all    | 4248       | -3946      |            | 22900      |            | 1592000±679000   | 0,8053±0,1650     |
| ICA_harder | 150900     | -136600    |            | 75490      |            | 2301000±1319000  | 0,6258±0,1176     |
| ICA_softer | 35700      | -30560     |            | 9998       |            | 1000000±488800   | 0,9550±0,2446     |

*Table 1.* Hyperelastic material model parameters obtained from averaging specimens of *internal carotid artery* (ICA), and the maximal stresses and strains related to the first irreversible damage.

Following our measurements on the walls of healthy arteries we dealt with the examination of aneurysms (adverse vasodilatations). As have mentioned before, we joined a series of measurements running for years at the Institute of Human Physiology and Clinical Experimental Research of the Semmelweis University. We took over the measurement series from Gábor Raffai, who performed measurements under the supervision of Emil Monos.<sup>2-4</sup> He cut stripes out of the aneurysms parallel to the imaginary axis (meridional) and perpendicular ring-like direction (circumferential) for the uniaxial tests. We have performed the procedure shown for the internal carotid artery now for the total of 91 uniaxial measurement results, too. During this we determined stress-strain curves, and determined for each specimen whether the 3-parameter or the 5-parameter variant of the Mooney–Rivlin model approximates the diagrams more precisely. Since we had a significantly larger amount of measurement data were at our disposal, we examined differences with respect to gender and orientation. We formed a total of 9 groups: all together, males and females separately, circumferential (perpendicular to the main axis of the aneurysm) and meridional (approximately in the main axis of the aneurysm) separately, and also the cases of circumferential female, circumferential male, meridional female, and meridional male. Unfortunately, the data were insufficient to distinguish on the basis of pathological history. Distinctly visible difference is observable after averaging samples from women and men. We found that samples from men are harder: they get damaged by lower strains but higher stresses. This symptom remains, if we examine women and men belonging to the circumferential class, as well as (but less characteristically) we do the same in the meridional class. We did not show significant deviation between classes circumferential and meridional. In *Table 2* we have summarized the Mooney–Rivlin material constants obtained by the grouping of aneurysms,

together with the averaged maximal stresses and strains related to the first damage regarded as failure.

|                 | $c_1$ [Pa] | $c_2$ [Pa] | $c_3$ [Pa] | $c_4$ [Pa] | $c_5$ [Pa] | Max. stress [Pa] | Max. strain [m/m] |
|-----------------|------------|------------|------------|------------|------------|------------------|-------------------|
| ANEURYSM all    | -168300    | 187800     |            | 196000     |            | 431500±69420     | 0,6834±0,0535     |
| ANEURYSM female | -101600    | 154200     |            | 118900     |            | 416200±68570     | 0,6995±0,0767     |
| ANEURYSM male   | -104200    | 148400     |            | 205300     |            | 524200±151300    | 0,5928±0,1154     |

Table 2. Hyperelastic material model parameters of *aneurysms* – obtained by averaging and grouping, and the maximal stresses and strains related to the first irreversible damage.

Our next task was to create the model of the blood and the vessel wall with multiple couplings. On the one hand, the fluid (i.e. the blood) and the particles carried in it (red blood cells) mutually influence one another (see previous section, also in the case of the rigid wall), and on the other hand, due to the pulsing of the blood plasma, the motion of the vessel wall encircling the lumen of the blood reacts on the flowing field. Thus the so-called multiply coupled ('back and forth') modelling is doubly present in the problem we analyse. During the modelling the two ends of the artery section were fixed for brevity, and the tube was surrounded by elastic embedding representing brain tissues.

We carried out numerical analysis of blood flow in vessels in the range of internal carotid artery because this is the range of which we possess material properties. We determined these properties from the vessel models created using the averaged material properties of our biaxial tests (see the first row in *Table 1*). We performed fluid dynamics simulations on the fluid contained in the lumen of the vessel as before, and a solid mechanics finite element analysis on the encircling vessel, and the two were coupled. In each time step the output of the fluid dynamics simulation in the tube with rigid wall was applied as loads on the encircling vessel wall of hyperelastic material. The displacements arising in that tube were applied then to the fluid field in the next time step in such a way that the fluid space was modified with those displacements. The input fluid flow and the particles representing the red blood cells were physiological realistic (concentration of 40-50%). We did not elaborate the effects of the elastic supports applied around the tube of the artery since this topic is investigated by another member of our department, Ferenc Nasztanovics.

Following the numerical simulations on the idealized geometry, we have performed simulations with finite element software package ANSYS 11.0 on real geometry as well – on a section of vessel containing a real brain aneurysm. The geometry and finite element mesh we used were obtained from *Ádám Ugron*, a member of the Department of Hydrodynamic Systems at BUTE, who deals with the simulations of fluid dynamical conditions of real brain aneurysms. Again in the numerical simulations we applied the hyperelastic material properties we gained from our laboratory measurements. We compared two cases. In the first case we applied the Mooney–Rivlin material parameters obtained by fitting a curve to the averaging of the healthy control arteries (internal carotid artery) to the entire vessel (including the aneurysm), see the first row in *Table 1*. In the second case the above mentioned parameters related to the general healthy arteries were exclusively applied to the parent arteries of the model and the aneurysm itself was modelled

with Mooney–Rivlin material parameters obtained from the averaged curves of measurements on the aneurysms, see the first row in *Table 2*). Since geometric dimensions of this real model were in direct correspondence with our idealized tube with diameter of 3 mm, the velocity of the blood was taken at a value of 0.35 m/s.

We found significant difference in stress values between the case of modelling the aneurysm with Mooney–Rivlin parameters of healthy vessels and the case of Mooney–Rivlin parameters of real aneurysms (see the von Mises stresses in *Figure 2* and also the principal stresses in *Table 3*).

|   | von Mises [Pa] | 1st pr. stress [Pa] | 2nd pr. stress [Pa] | 3rd pr. stress [Pa] |
|---|----------------|---------------------|---------------------|---------------------|
| Dilatation as healthy arteria carotis interna | 0,65           | 0,55                | 0,1                 | -0,4                |
| Dilatation as aneurysm                        | 6              | 4                   | 1,45                | -2,4                |

*Table 3.* Maximal stresses in the aneurysm bag (pr.=principal)

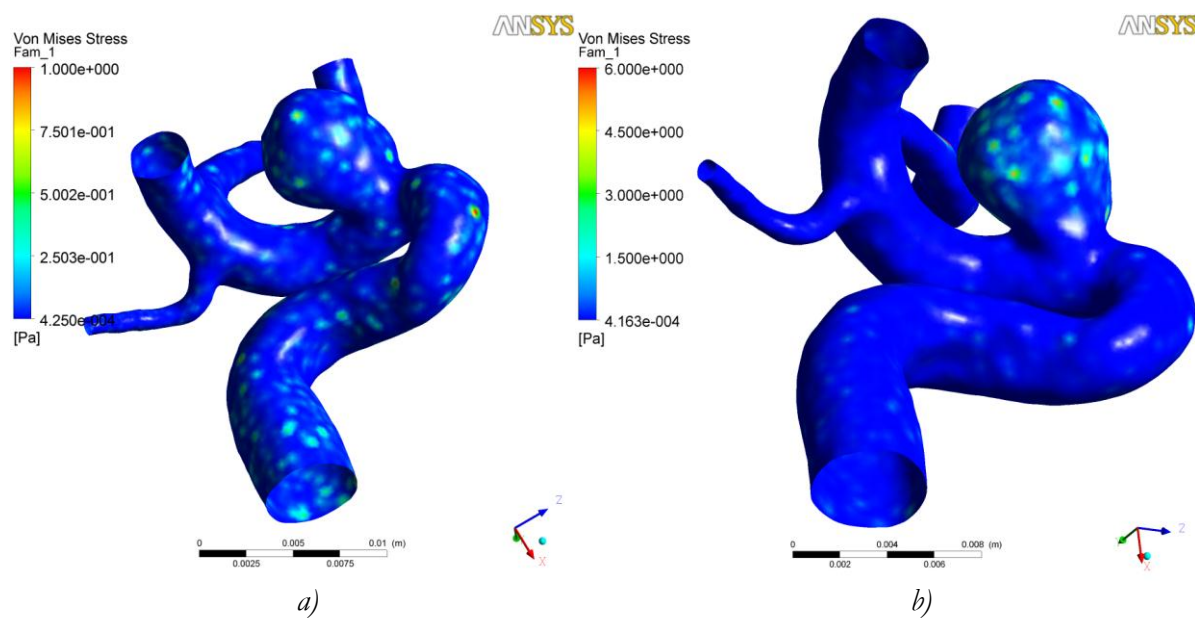


*Figure 2.* Von Mises stresses in an aneurysm with real geometry a) the entire vessel wall as internal carotid artery b) parent artery as internal carotid artery, and dilated section as aneurysm

## Conclusion

We performed uniaxial and biaxial stretching measurements on carotid interna type arteries obtained from interventions and from cadavers, by means of which we determined the characteristic stress-strain curves of the artery wall resulting from stretching force. On the basis of the stress-strain curves we developed the bilinear elastic and the more parametric hyperelastic Mooney–Rivlin constitutive material model of the artery wall for the period before damage. We created the basis of a database for medical purposes by performing the statistical investigation of the received results. In the direction of cutting-out we did not show significant deviation. Based

on the measurements we concluded that the type of artery under examination can be premordially characterized by a soft and a brittle material type. Our Mooney–Rivlin material parameters another data (maximal stresses and strains) obtained from arteries can be used as fundamental tools for further numerical examination of human arteries.

Based on the measurements we determined the characteristic stress-strain diagrams resulting from stretching forces of human cerebral aneurysms. Based upon these findings we developed the multi-parametric hyperelastic Mooney–Rivlin constitutive material model of this type of abnormal arterial wall related to the period before the damage. We created the basis of a medical database, and for each of the measurement data we determined whether the 3-parametric or the 5-parametric model is more suitable to describe. By performing the statistical investigation of the received results we established that characteristic divergences appear depending on the gender, however we did not find evident difference as a function of the cutting direction. We proved that the tissue samples obtained from males are more brittle in all sample categories: they deteriorate at shorter stretching and at higher values of stresses than the tissue samples of females.

We performed a numerical simulation of blood circulating in a real diseased arterial segment (including aneurysm) of dimension in the range of arteries of carotid interna type defined with Mooney–Rivlin material model with continuum based method by stationary flow. We proved that application of our material constants derived from the measurements performed on aneurysms yields significantly higher stresses compared to the application of material constants derived from the samples of healthy arteries of carotid interna type.

---

## REFERENCES

1. Holzapfel GA, Gasser TC, Ogden RW. A new constitutive framework for arterial wall mechanics and a comparative study of material modes. *Journal of Elasticity* 2000; 61:1-48.
2. Monos, E. Hemodinamics, biomechanics of the blood circulation, Semmelweis Kiadó, Budapest, 43 pages, 2004
3. Tóth M, Nádasy GyL, Nyáry I, Kerényi T, Orosz M, Molnárka Gy, Monos E. Sterically inhomogeneous viscoelastic behavior of human saccular cerebral aneurysms. *J.Vasc.Res.* 1998; 35:345-55.
4. Orosz M, Molnárka Gy, Nádasy GL, Raffai G, Kozmann G, Monos E. Validity of viscoelastic models of vessel wall, 64th An. Meeting of the Hung. Physiol. Soc.; Budapest, Hungary, 1997

***This work is connected to the scientific program of the "Development of quality-oriented and harmonized R+D+I strategy and functional model at BME" project. This project is supported by the New Hungary Development Plan (Project ID: TÁMOP-4.2.1/B-09/1/KMR-2010-0002).***

## THE TRUNK MODEL: A MULTI-SEGMENT APPROACH OF THE THORAX

Gábor Grósz, Beatrix Lauter, Gerlinde Lenaerts, Dóra Pákozdi, Katalin Vámos, Sándor Kiss, György Szóke, Tamás Terebessy

Department of Orthopaedics, Semmelweis University

[grgt85@gmail.com](mailto:grgt85@gmail.com)

---

### **Abstract**

3D motion analysis is a tool for evaluating gait and posture parameters in orthopaedic deformities. Spinal disorders are very common in paediatric orthopaedic practice. Recently used motion capture methods are not suitable for modeling the kinematics of the trunk segments. The aim of this study was to develop a kinematic model for the trunk that could be applied to measure segmental motions. In the present model the trunk was divided into three parts: the upper thorax, the lower thorax and the pelvis. 13 healthy volunteers were measured to calculate standard graphs for the segmental movements of the trunk. The distance of the C7-Th10 vertebrae, the sagittal- and frontal plane balance and the intersegmental rotation were evaluated. Results of this study present normative values of the trunk motion and highlight the flexibility of the thorax. Our trunk model provides possibility for segmental modeling the trunk in adolescence posture disorders such as scoliosis, Scheuermann's kyphosis and also in adult spinal diseases.

**Keywords:** Multi-segment model, Thorax, Gait Analysis, Scoliosis, Scheuermann's disease

---

### **1. Introduction**

Scoliosis and Scheuermann's disease are the most frequent orthopaedic deformities in the adolescence. The overall prevalence of scoliosis with curvature of more than  $10^\circ$  is 1.2% (3.5 times more frequent in girls), moreover the prevalence of curves exceeding  $20^\circ$  is 0.5%.<sup>1</sup> The frequency of Scheuermann's kyphosis is rather difficult to estimate, since different authors use variable criteria for the diagnosis. The prevalence varies from 3-8%.<sup>2-3</sup> Due to these two conditions thousands of teenagers need therapy. In both diseases the vertebral column is deformed, the shape and functions of the spine are altered.

Evaluation the rigidity of the deformed thoracic spine has utmost importance both for physiotherapy and for brace treatment. In the everyday clinical practice only manual methods exist to estimate the mobility of the thoracic spine. Functional X-ray tests are usually used to assess the possibility of correction only for planning surgery.<sup>4</sup>

Neither motion capture methods are suitable for assessing the 3D flexibility of the vertebral column for conservative therapy, because the commonly used gait models demonstrate the trunk as a single rigid body without any internal movements. The aim of our current study was to plan and develop a motion capture model which is able to describe the basic functional parameters of the spine during gait and to get information about the tilting and rotation movements of the upper part of the thorax compared to the lower part of the thorax.

## 2. Methods

Eleven healthy volunteers (mean age  $24 \pm 3.6$  years) were examined in the Gait Lab of Semmelweis University. Vicon PlugInGait FullBody model <sup>5</sup> was used for observing the range of motion of the lower limb joints. The trunk is represented as a single rigid body in the Vicon model. In our experimental setup the trunk was divided into three parts: the upper thorax, the lower thorax and the pelvis. The markers which were used for the model are shown in *Table 1*. Marker placement defines three axes. The C7 and CLAV markers for the axis of the upper thorax, the T10 and STRN markers for the axis of the lower thorax and the LASI, RASI, LPSI and RPSI markers for the sagittal midline axis of the pelvis. A simple axis allows assessing two dimensional movements. Therefore only tilting- and rotation of the segments can be measured. Tilting was determined as sagittal plane movements of the upper thorax to the lower thorax named on the trunk model as UPtoLOW tilt, movements of the upper thorax to the pelvis named on the trunk model as UptoPELV tilt, and movements of the lower thorax to the pelvis named on the trunk model as LOWtoPELV tilt. Similarly, rotation was determined as horizontal plane movements of the upper thorax to the lower thorax-, the upper thorax to the pelvis and the lower thorax to the pelvis and named on the trunk model as UPtoLOW rotation, UptoPELV rotation and LOWtoPELV rotation respectively. Although lateral bending movements are undetectable in this model, the benefit of this simple marker placement gives the possibility to use the model in corset wearing as well.

| Marker name | Position  | Segment     |
|-------------|---|-------------|
| C7          | 7 <sup>th</sup> cervical vertebra spinal process  | upper trunk |
| T10         | 10 <sup>th</sup> thoracal vertebra spinal process | lower trunk |
| CLAV        | proximal end of the sternum                       | upper trunk |
| STRN        | distal end of the sternum                         | lower trunk |
| LASI        | left anterior superior iliac spine                | pelvis      |
| RASI        | right anterior superior iliac spine               | pelvis      |
| LPSI        | left posterior superior iliac spine               | pelvis      |
| RPSI        | right posterior superior iliac spine              | pelvis      |

*Table 1.* Names and position of markers used in the trunk model

### 2.1 Upper thorax

#### 2.1.1 Anatomical definition

The upper part of the thorax is modelled with the axis defined by the segment between C7 and CLAV markers. The C7 marker is placed over the spinal process of the 7th cervical vertebra and the CLAV marker is placed over the jugular notch. The rigidity of this thoracic part is ensured by the first rib.

### **2.1.2 Technical frame**

Axis 1 is from C7 to CLAV. A horizontal supporting vector was set perpendicular to axis 1. Axis 2 is perpendicular to axis 1 and to the supporting vector.

## **2.2 Lower thorax**

### **2.2.1 Anatomical definition**

The Vicon FullBody model uses markers on the spinal process of the 10th thoracic vertebra and also on the xiphoid process of the sternum. The segment defined by these two markers assumed to move as a rigid body since the 10th pair of ribs provides bony connection between the two markers.

### **2.2.2. Technical frame**

Axis 1 is from T10 to STRN. A horizontal supporting vector was set perpendicular to axis 1. Axis 2 is perpendicular to axis 1 and to the supporting vector.

## **2.3 Pelvis**

### **2.3.1 Anatomical definition**

In conventional gait models the pelvis is usually demonstrated with markers on the iliac bones and on the sacrum.<sup>6,7,8</sup> We use markers placed over the anterior superior iliac spines and over the posterior superior iliac spines. Although the four markers would allow the 3D modelling of the pelvic movements, in our trunk model only the sagittal midline vector of the pelvis was considered.

### **2.3.2 Technical frame**

The sagittal midline vector of the pelvis was determined with the help of two virtual markers: one in the midpoint of LASI and RASI, named SILS, and one between LPSI and RPSI named SACR. The line defined by the two virtual markers is axis 1. A horizontal supporting vector was set perpendicular to axis 1. Axis 2 is perpendicular to axis 1 and to the supporting vector.

## **2.4 Additional calculations**

The perpendicular line to a vector in the horizontal plane is calculated by swapping the first and second coordinate and multiplying one of them by (-1). The third coordinate is 0 or a constant due to being parallel to the ground.

The model calculates the frontal- and sagittal balance of the spine too. The frontal balance describes the distance of the C7 marker from the virtual SACR marker on the horizontal line (frontal plane balance or clinically called decompensation)<sup>9</sup> The sagittal balance means the distance of the C7 marker from the virtual SACR marker on the sagittal line (sagittal balance).<sup>10</sup>

The distance between the C7 and Th10 markers was measured as well. The distance can model the upright position of thoracic spine, however aiming the inter subject comparability the parameter has to be normalised by the body height.

On the rotation graphs and also on the horizontal balance graphs the kinematic curves produced during the left step are presented in real values, however to ease the interpretation, the kinematic curves produced during the right step were multiplied by (-1) to allow the curves to run parallel.

### 3. Results

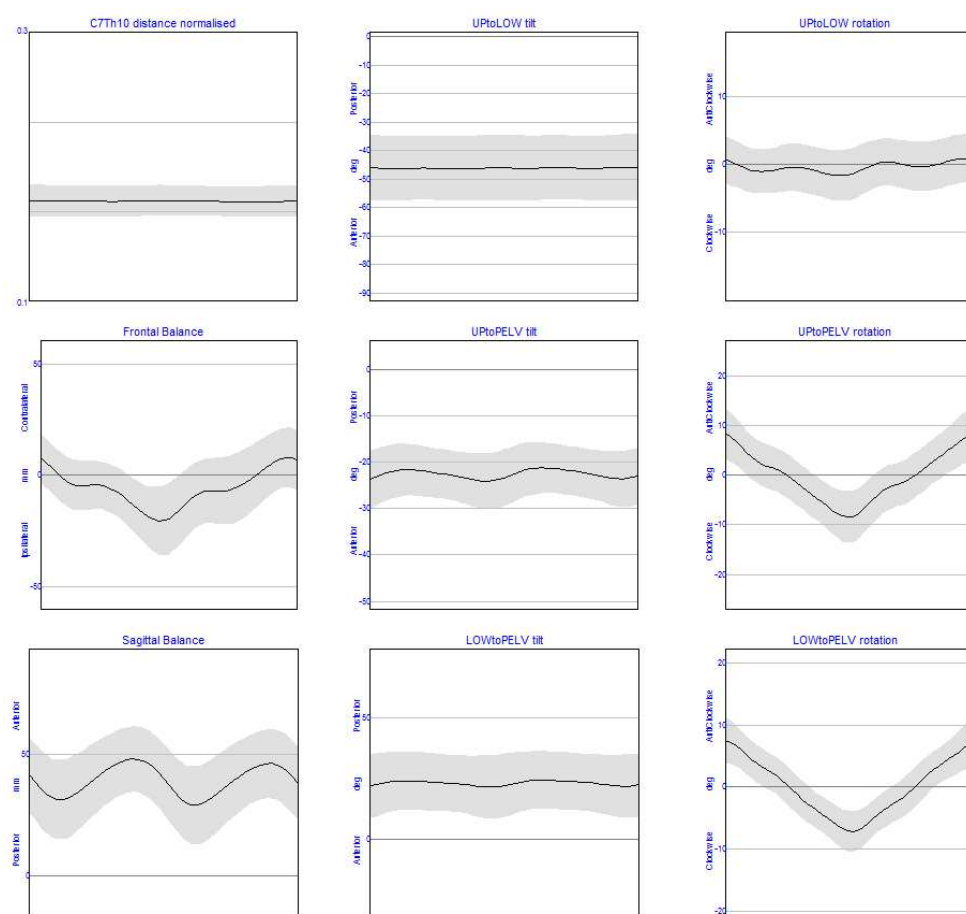


Figure 1. Averaged trunk segment angles and parameters from 11 healthy volunteers

A preliminary study has been carried out on the reliability on a model calculating the deformities of the trunk and movement of the spine during level walking. Based on the results of the eleven healthy volunteers the graphs of the trunk model are shown on *Figure 1*.



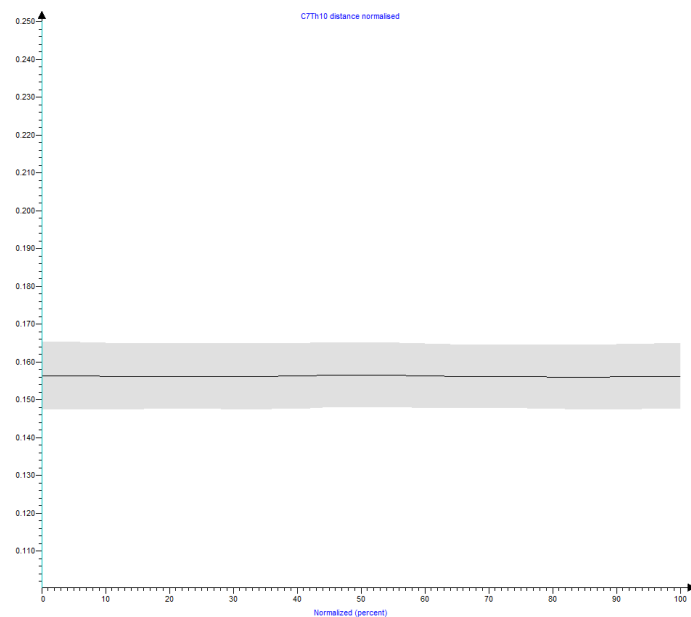


Figure 2. Normalised distance of the C7 and Th10 vertebra

The distance of the 7th cervical- and the 10th thoracic vertebra is a proper parameter to quantify the curvature of the spine, and is normalised by the height of the subject. Normalisation is necessary to compare the patients with different body height. Based on the results of the healthy volunteers the value of  $0.156 \pm 0,009$  is considered normal.

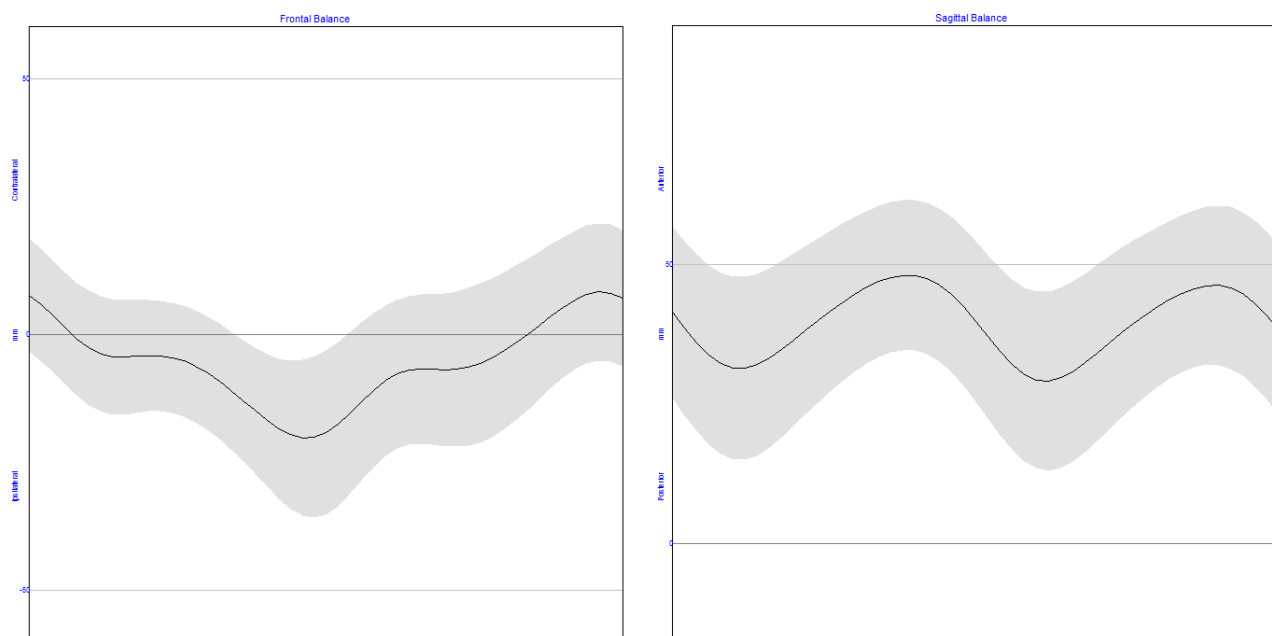


Figure 3. Frontal and sagittal balance of the spine

The frontal plane balance is oscillating with 1.5 cm amplitude around 5 mm decompensational offset. The peaks occur in midstance and in terminal swing. The offset can be explained by the

natural right convex curve of the spine. The sagittal balance can be described by a double bump shaped curve. The peaks occur in midstance and midswing. On the curve an average of 40 mm anterior imbalance is seen. The explanation for this phenomenon is that the sagittal balance was calculated with the distance of the C7 marker from the virtual SACR marker on the sagittal line, however sagittal balance means when C7 plumb line intersects the body of the first sacral vertebra. The virtual SACR marker is 3-5 cm posterior to the body of the first sacral vertebra.

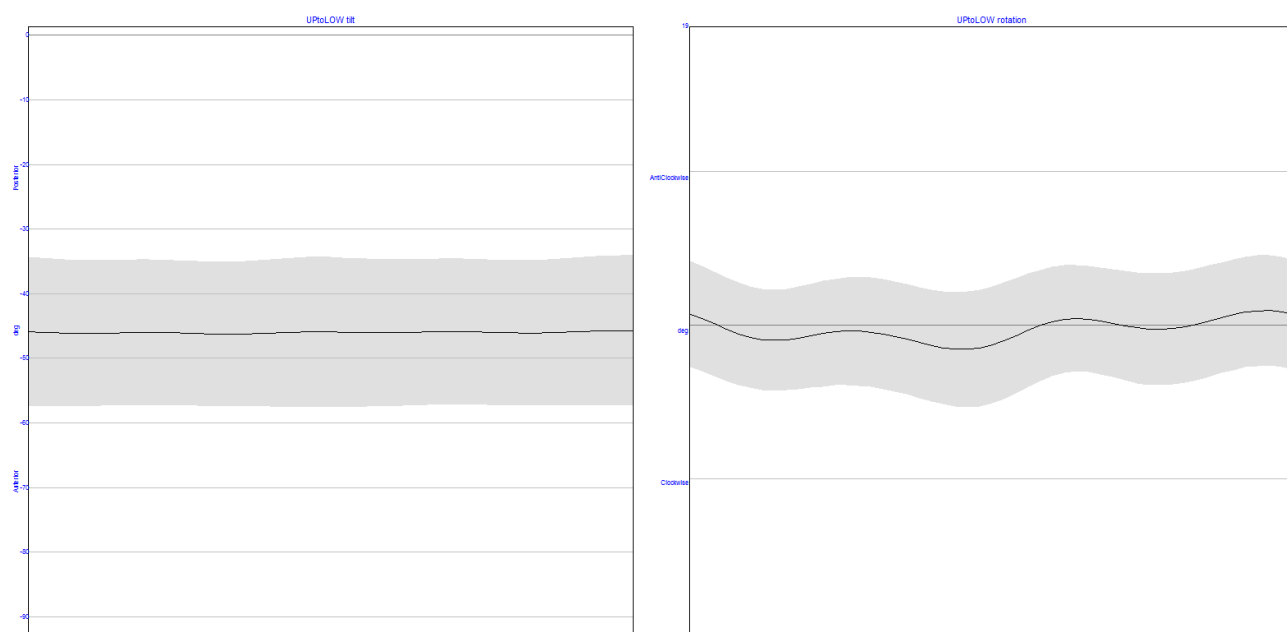


Figure 4. Upper trunk motion compared to lower trunk

As shown in *Figure 4*, the upper trunk movements compared to the lower trunk are minimal. An almost constant UptoLOW tilt can be observed and only a minimal clockwise rotation was measured in the upper trunk with respect to the lower trunk. The range of tilt is reduced to a value of less than  $1^\circ$  around  $46^\circ \pm 11,5$ , while the range of rotation is less than  $2,5^\circ$ . These observations are in good concordance with our expectations since the mild anticlockwise rotation of the lower trunk is caused by the physiological scoliosis of the healthy volunteers.

The motion of the upper and lower trunk compared to the pelvis is presented in *Figure 5*. The connection between the trunk segments and the pelvis is more flexible. The increased ROM is especially prominent in the coronal plane. UPtoPELV tilt and LOWtoPELV tilt show a double bump shaped curve with the peaks at loading response phase and at initial swing phase. Since initial swing phase corresponds with the loading response phase of the contralateral limb, the explanation of these peaks is the hip flexion and the sequel anterior pelvic tilt at loading response phase. UPtoPELV rotation and LOWtoPELV rotation curves are oscillating around zero degrees according to the alternating forward progression of the pelvis in stance phase of the gait cycle.

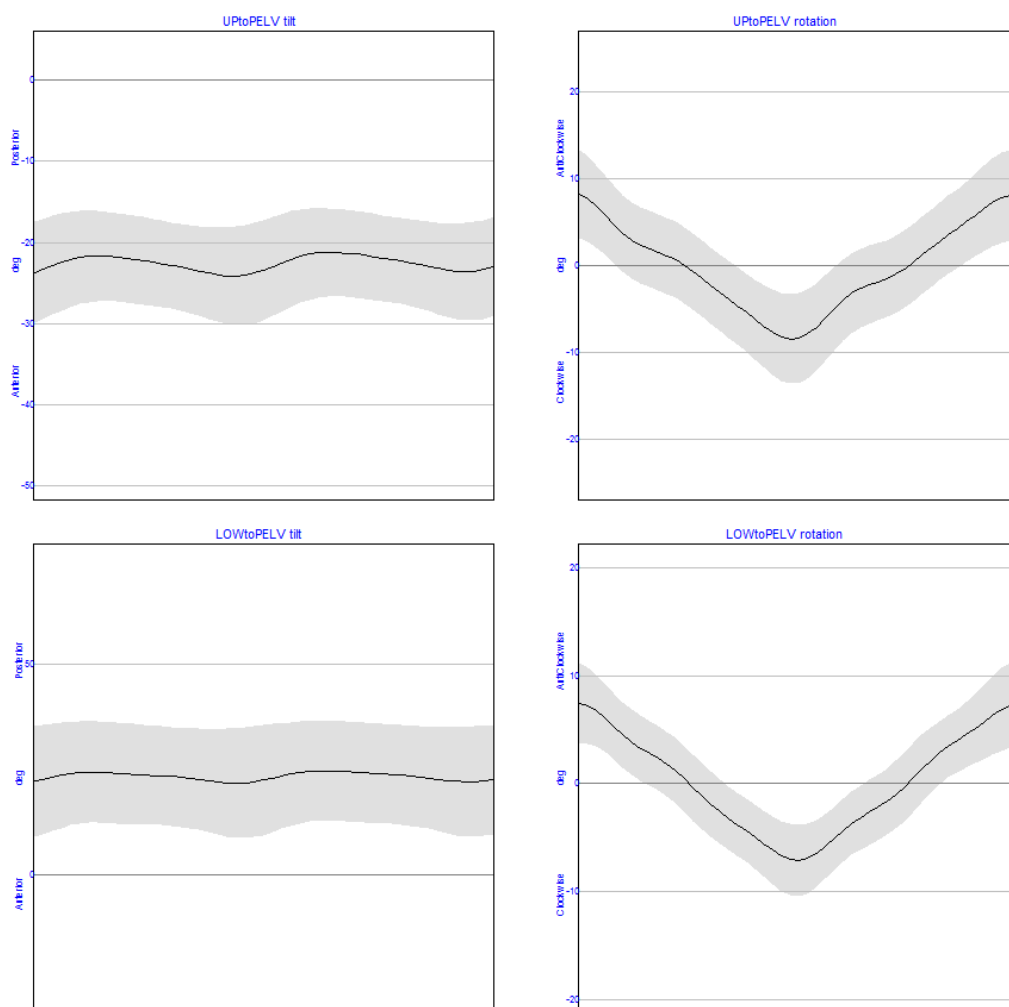


Figure 5. Upper and lower trunk motion compared to the pelvis

#### 4. Description

The model was planned for measuring the tilt and the rotation between the upper and lower segment of the thorax and also the movement of these two thoracic segments compared to the pelvis. The measured movements may model the thoracic torsion that can be observed in spinal deformities. Our results strengthen the theory that the thorax can be handled as a rigid body in the 3D motion capture measurements. Non-significant changes in tilting (UPToLOW tilt) and less than 2.5-degree-changes of rotation (UPToLOW rotation) can be observed between the two thoracic segments during the gait cycle. UPToLOW tilt gives information about the thoracic kyphosis. UPToLOW tilt and UPToLOW rotation together refer to the thoracic static torsion and appear as a positive or negative offset compared to the standard curves. According to our knowledge this is the only way for measuring thoracic torsion during gait.

The angles describing the movements between the upper thorax and the pelvis (UPToPELV tilt and UPToPELV rotation) refer to the posture of the trunk and to the movements of the pelvis compared to the thorax. The angles between the lower thorax and the pelvis provide information

about the position of the lumbar spine (lordosis) and about the static rotation of the lower thoracic spine (thoracic scoliosis).

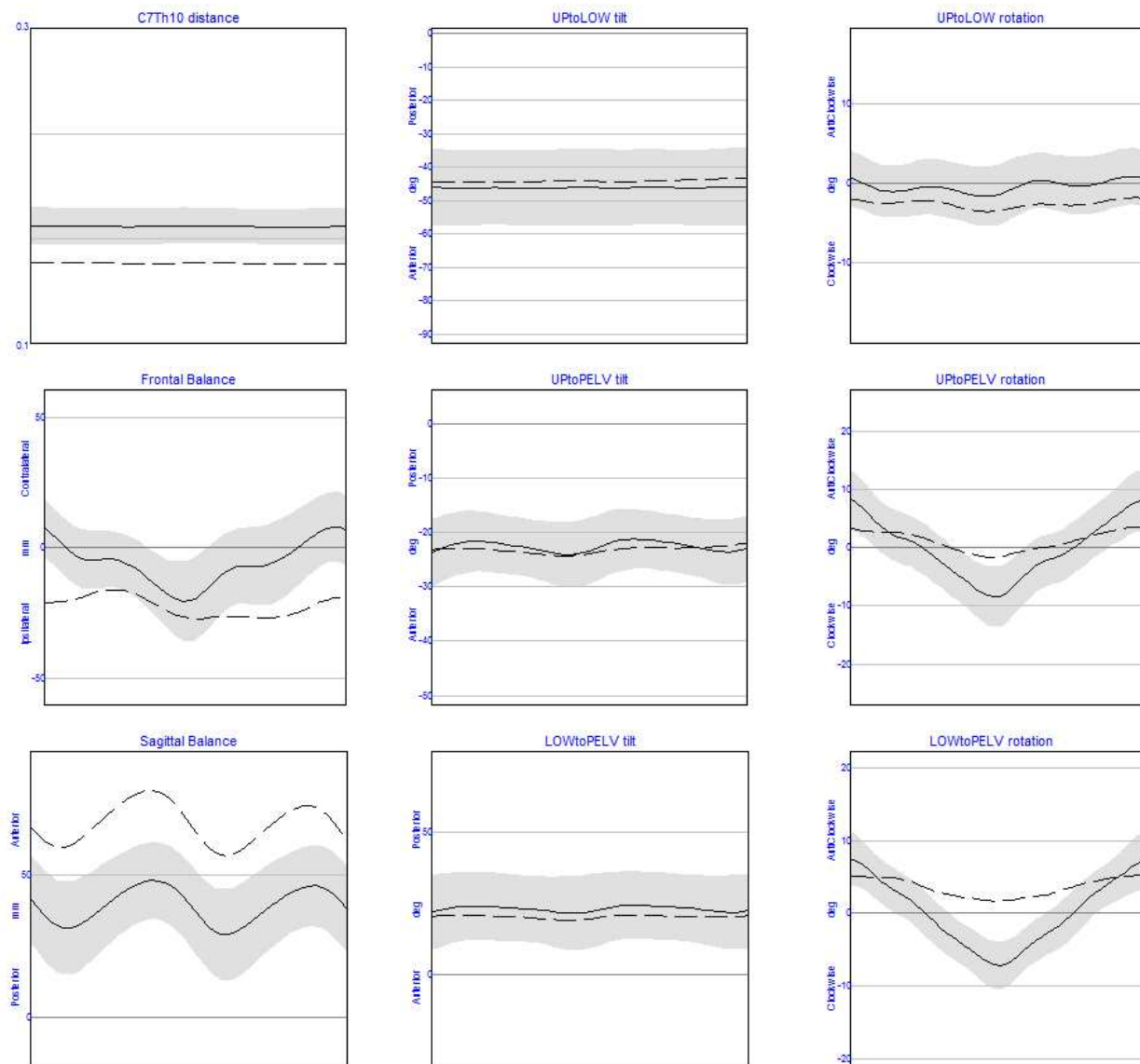


Figure 6. Trunk model results of a scoliotic patient compared to standard

As an example a 16 year old scoliotic patient (48 Cobb°, right convex dorsal – left convex lumbar) (Figure 6.) and a 15 year old patient with Scheuermann's disease (Figure 7.) was measured and processed with the Trunk Model. During the clinical measurement a 1 cm decompensation was observed. The difference in the frontal balance shows the change of this value during the gait cycle. On the sagittal balance graph a 25 mm anterior imbalance can be observed compared to the normal curve. All the 3 tilt graphs are within the standard range. The rotation graphs follow the normal curve with reduced amplitude in the segments compared to the pelvis and with the static offset caused by the rotation of the thoracic spine.

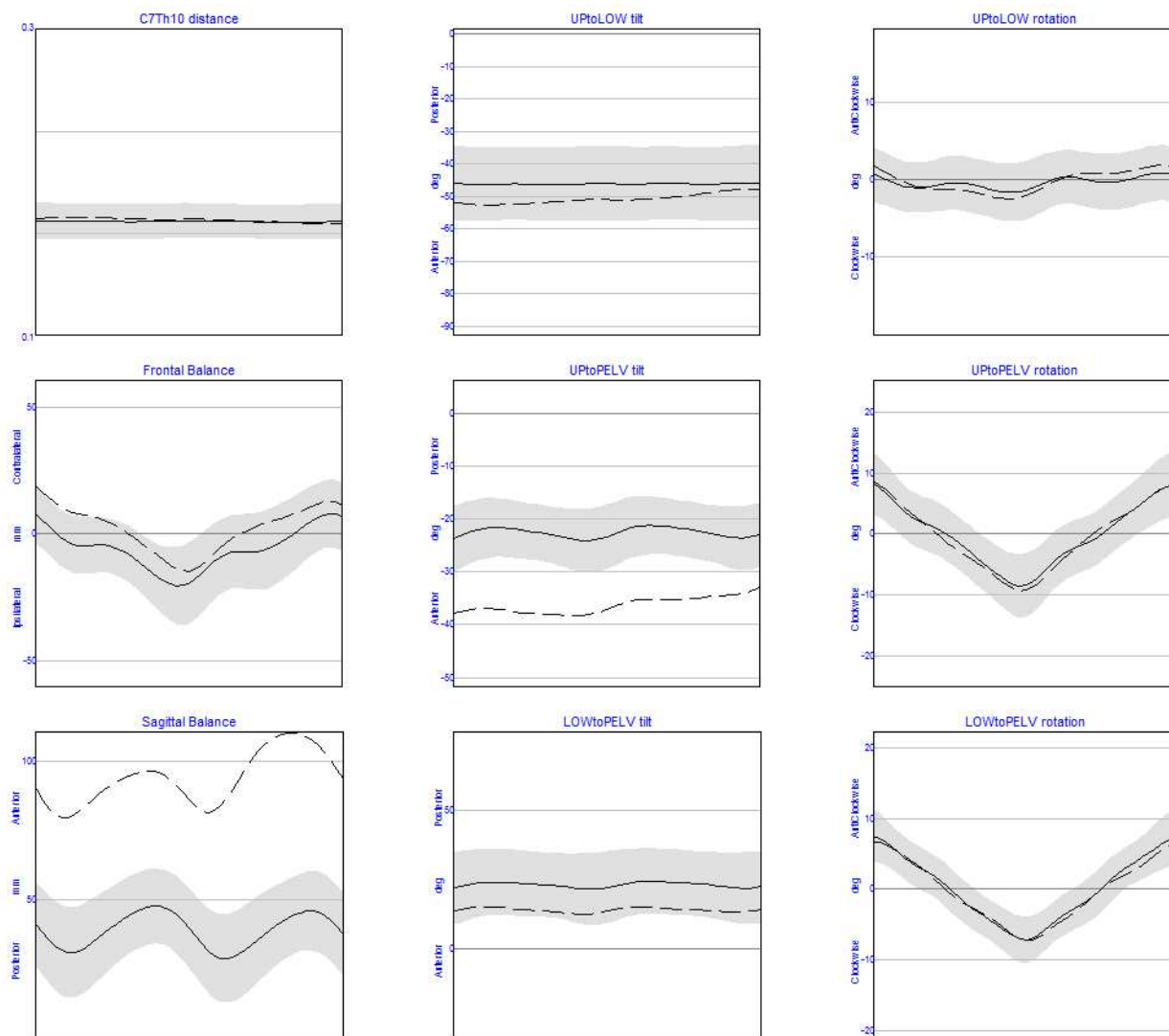


Figure 7. Trunk model results of a patient with Scheuermann's disease compared to standard.

In case of the patient with Scheuermann's disease the most prominent difference can be observed in the sagittal balance graph. Only a minimal gap can be seen in the frontal balance graph, while the rotation graphs overlap the normal curve. The anterior tilt which characterises the disease can be detected on the tilt graphs. The most prominent tilt can be observed in the UPToPELV tilt graph.

In our trunk model we use the original marker set of Vicon PlugInGait model, however extra markers may allow more accurate measurements. Additional marker may be positioned over the apical vertebra of a scoliotic curve showing the rotation of the thorax exactly at the point of the maximal vertebral rotation. Another possibility for further development of our model is to mark the Th12 vertebra which would show the complete thoracic kyphosis on the UPToLOW tilt graph.

## 5. Conclusion

Authors present a possible motion capture model for segmental modelling of the trunk. In the model tilting and rotational position, as well as movements of the upper- and lower part of the thorax and the pelvis are observed together with the frontal- and sagittal balance of the spine during gait. The possibility of applying the model is a subject for further investigations. Deformities under consideration are scoliosis, Scheuermann's disease, osteoporotic spine deformities and any other spinal or trunk disorders.

---

## REFERENCES

1. Bunnell WP, et al. Outcome of spinal screening. Spine (Phila Pa 1976) 1993 Sep 15;18(12):1572-80.
2. Scoles PV, Latimer BM, DigIovanni BF, Vargo E, Bauza S, Jellema LM, et al. Vertebral alterations in Scheuermann's kyphosis. Spine, 1991;16(5):509-15.
3. Frank Damborg, Vilhelm Engell, Mikkel Andersen, Kirsten Ohm Kyvik, Karsten Thomsen, et al. Prevalence, concordance, and heritability of Scheuermann kyphosis based on a study of twins. J Bone Joint Surg Am. 2006 Oct;88(10):2133-6 17015588.
4. Luk KD, Cheung KM, Lu DS, Leong JC., et al. Assessment of scoliosis correction in relation to flexibility using the fulcrum bending correction index. Spine (Phila Pa 1976) 1998 Nov 1;23(21):2303-7.
5. Vicon Oxford Metrics. Plug-In Gait Manual. Available from: URL: [http://www.irc-web.co.jp/vicon\\_web/news\\_bn/PIGManualver1.pdf](http://www.irc-web.co.jp/vicon_web/news_bn/PIGManualver1.pdf)
6. Kadaba MP, Ramakrishnan HK, Wootten ME, Gaine J, Gorton G, Cochran GV, et al. Repeatability of kinematic, kinetic, and electromyographic data in normal adult gait. J Orthop Res. 1989;7(6):849-60.
7. Kadaba MP, Ramakrishnan HK, Wootten ME, et al. Measurement of lower extremity kinematics during level walking. J Orthop Res. 1990 May;8(3):383-92.
8. Ounpuu S, Gage JR, Davis RB, et al. Three-dimensional lower extremity joint kinetics in normal pediatric gait. J Pediatr Orthop. 1991 May-Jun;11(3):341-9.
9. Negrini S, Negrini A, et al. Postural effects of symmetrical and asymmetrical loads on the spines of schoolchildren. Scoliosis. 2007 Jul 9;2:8.
10. Lazennec JY, Brusson A, Rousseau MA, et al. Hip-spine relations and sagittal balance clinical consequences. Eur Spine J. 2011 Sep;20 Suppl 5:686-98. doi: 10.1007/s00586-011-1937-9. Epub 2011 Jul 28.

***We acknowledge the generous support of NKTH – “Gerinőr2” project in funding this project. Also skilful assistance of the staff of the Paediatric Ward of Department of Orthopaedics at Semmelweis University is very well acknowledged.***

## BIOMECHANICAL EVALUATION OF TWO DIFFERENT VERTEBRAL INTERBODY DEVICES BY USING QCT-BASED CASE-SPECIFIC NONLINEAR FINITE ELEMENT MODELS: A PRELIMINARY REPORT

Péter Varga<sup>1</sup>, Péter Nédli<sup>2</sup>, Tibor Csákány<sup>3</sup>, Márta Kurutzné Kovács<sup>2</sup>, Péter Pál Varga<sup>3</sup>

<sup>1</sup>Julius Wolff Institute and Berlin-Brandenburg School for Regenerative Therapies, Charité - Universitätsmedizin Berlin, Germany

<sup>2</sup>Department of Structural Mechanics, Budapest University of Technology and Economics, Hungary

<sup>3</sup>National Center for Spinal Disorders, Budapest, Hungary

[peter.varga@charite.de](mailto:peter.varga@charite.de)

---

### Abstract

Interbody devices are widely used to replace the degenerated discs of the spine. For this purpose, a novel methodology uses cement instead of conventional spacers, which is hypothesized to provide smoother transition of forces, lower risk of bone tissue damage, thus smaller subsidence, reduced risk of further pathological deformations and other complications. This new treatment approach has been compared with the conventional method experimentally by mechanical loading of human vertebral motion segments treated with either of these. The present study aimed at complementing the that work with finite element analysis and, by performing in silico mechanical testing of QCT-based case specific models incorporating the elasto-plastic behavior of bone, providing better understanding of experimental results, in particular, the differences between the two sample groups equipped with the different spacer types. This report presents the applied numerical methodology as well as the first results, which are in line with the experimental ones. Besides providing deeper insight into the experimental outcomes, these models are expected to provide a basis for virtual parameter analysis studies, which may help to optimize the surgical procedure.

**Keywords:** vertebral spine, intervertebral disc degeneration, interbody device, motion segment, QCT, finite element analysis

---

### Introduction

In severe pathological cases of degenerated intervertebral discs surgical intervention is required to restore the original distance of the adjacent vertebrae and stabilize the spine. The most often applied solution is the fusion of adjacent vertebrae using graft material, which is in most cases combined with the application of interbody implants like metal or PEEK cages and spacers to provide mechanical stability and preserve the restored height. This approach leads to reduced range of motion but offers increased global stability of the spine and relieve low back pain. In the severe cases when the pathology of the intervertebral disc is accompanied by impaired bone competence e.g. in osteoporosis, application of the standard fixation approaches using interbody implants can be inadequate due to the reduced bone quality and the degeneration of the vertebral endplates and may lead to damage of the bone tissue at the interface via excessive subsidence of the spacer, yielding to further complications, pain, instability and potentially to the collapse of the

motion segment.<sup>1-4</sup> A novel method aims at circumventing the drawbacks of the conventional techniques by using cement spacers. In the frame of this approach bone cement is injected into the gap of the removed parts of the degenerated intervertebral disc and the remaining space is filled with graft material to foster fusion of the adjacent vertebrae.<sup>5-6</sup> The cement spacer accurately follows the actual contours of the endplates, provides larger contact surface and thus smoother transition of forces along the bone-cement interface. This technique is therefore believed to reduce stress concentrations and therefore the risk of bone tissue damage and extensive spacer subsidence leading to pathological deformations.

An *in vitro* experimental loading setup has recently been developed and utilized to obtain and compare the apparent mechanical properties of human spinal motion segments fixed with either a conventional or the cement spacer. Even though the mechanical testing represents the gold standard in assessing these properties and provides the ground truth, not all details can be obtained during the experiments and the investigation of all key influencing factors requires a large number of specimens. *In silico* approaches offer an alternative tool which can be efficiently used to complement or even replace experiments. Finite element models can be utilized to mimic the mechanical conditions and provide insight into the details of stress and strain fields in space and time. Such models may therefore help to better understand and correctly interpret the experimental results,<sup>7</sup> however, have first to be carefully validated against the real tests. Once validated, the models can be used to investigate the influence of certain factors like changes in the material properties or adjustment of the applied boundary conditions.

The goal of this study was to investigate and compare, by means of finite element analysis, the loading and damage profile of human motion segments stabilized with conventional and with cement spacers. In particular, we aimed at (i) generating case-specific finite element models based on CT images, (ii) validating these against the experimental results, (iii) using the details provided by the validated numerical analyses to better characterize and thus more accurately understand the observed differences between the two operation techniques and (iv) performing a sensitivity analysis to identify and optimize the major factors influencing the results to provide hints for enhancement of the surgical procedures. In this manuscript we report the preliminary results of steps (i-iii).

## **Methods**

Sixteen thoracic and lumbar spine motion segments, i.e. two adjacent vertebrae with the intervertebral disc were extracted from eight human cadaver spines. Donors were four female and four male with age ranging from 52 ys to 88 ys ( $70.6 \pm 13.9$  ys). All experiments were in line with the Hungarian legislative requirements and the ethical approval was granted by the Ethical Commission of the Semmelweis University, Budapest, Hungary. The samples were cleaned of surrounding soft tissues and stored frozen at  $-20$  °C until further processing. The superior and inferior parts of the segments were shallowly embedded in polymer plastic. The thickness of the embedding layers was closely 10 mm, but varied slightly due to the different sizes of the vertebrae and the fact that the volume of the resin was standardized. As the X-ray attenuation coefficient of the selected embedding resin was close to that of water, small glass beads were placed into the resin shortly before polymerization in order to mark the upper and lower surfaces of both embedding layers. Three to four beads were used for each surface. The planes of the inferior and



posterior resin layers were closely, but not completely parallel. A prepared and embedded specimen is shown in *Figure 1*.

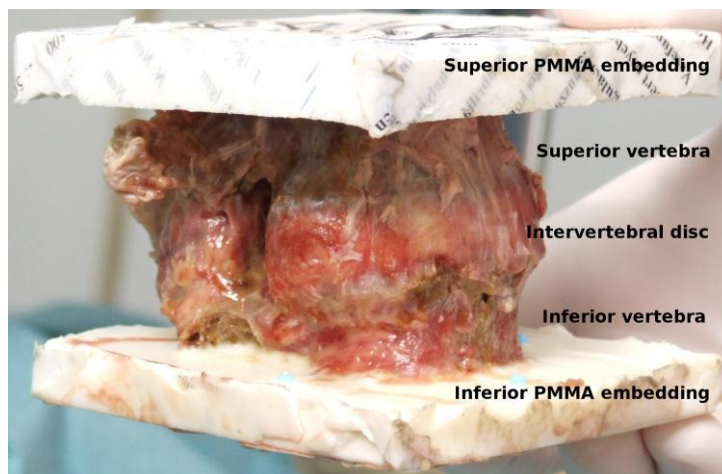


*Figure 1.* Human spinal motion segment specimen prepared for mechanical testing. The blue dots in the embedding layers are the glass beads.

Quantitative computed tomography (QCT) images of the motion segments were assessed by means of a conventional clinical instrument (Hitachi Presto, Hitachi Medical Corporation, Tokyo, Japan) according to the lumbar spine acquisition protocol. Scanning settings were 120 kVp energy, 150 mA current, 150 ms exposure time, 512x512 pixel matrix, 0.47 mm in-plane pixel size, 0.75 mm slice thickness. The samples were scanned in native state submerged in a water filled box to mimic the attenuation and scattering effects of soft tissues surrounding the vertebral spine *in vivo*.

Subsequently, the motion segments were operated with either a conventional method using a polyether ether ketone (PEEK) spacer, or the novel technique using polymethylmethacrylate (PMMA) cement. The motion segments were assigned randomly to the both groups. The posterior segments of the vertebrae were cropped on one side, a small window was cut on the annulus of the intervertebral disc and the nucleus removed. In case of the conventional method a commercial PEEK spacer was placed between the adjacent vertebral endplates. In the other case, PMMA cement was injected into the space left opened by the removed disc parts. To separate and elucidate the effect of bone quality, no posterior fixation instrumentation have been used. The graft material used in *in vivo* cases to fill the remaining gaps was not used here. Following the operation, the CT scans were repeated with the same settings described above. The CT images acquired before and after the cement injection process are shown in *Figure 2*.

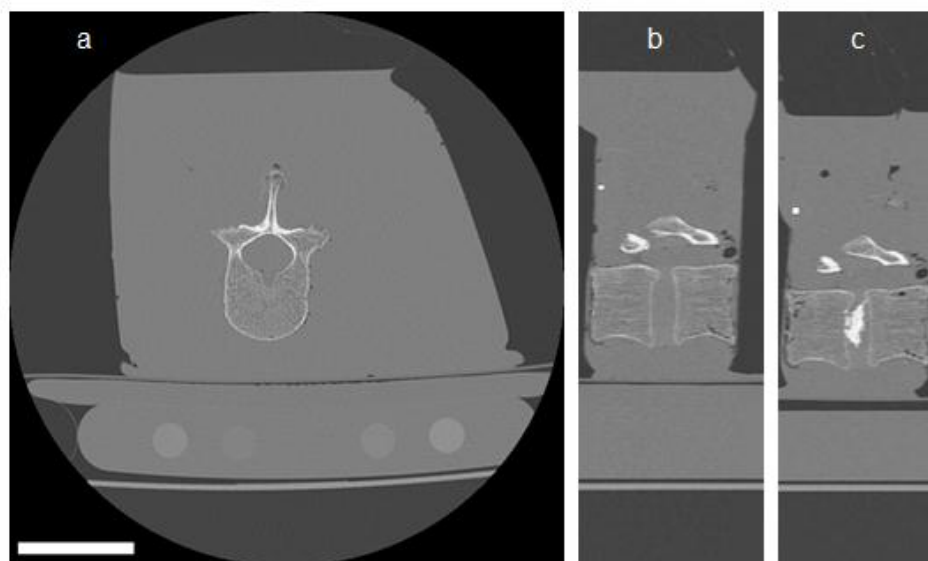


*Figure 2.* CT scans of a specimen of the cement spacer group. (a) Transverse CT slice showing one vertebral body of the motion segment in the water filled tank and the calibration phantom with five rods of different densities. White scale bar: 50 mm. (b) Mid-sagittal slice prior to operation with the intervertebral disc being intact. Note the glass bead marker of the embedding layer appearing as a bright dot. (c) Post operative mid-sagittal CT slice demonstrating the cement injected into the space of the removed nucleus between the adjacent vertebral bodies.

Destructive mechanical testing of the specimens were then performed by applying uniaxial compressive loading on the outer surfaces of the embedding layers by means of a servohydraulic testing device (Instron 8872, Instron, Norwood, USA). The samples were thawed at room temperature for 4-6 hours prior to testing. Loading rate of the displacement driven experiments was set to 5 mm/min to ensure quasi-static conditions, the displacement of the cross-head and the force in the load cell were recorded. The ultimate state was defined either as 20 % reduction in the resisting force or as 20 % total deformation. CT imaging was repeated after the tests with the aim to assess the final damage pattern. The test results of two specimens were not usable and thus these were excluded from further analyses.

The post-operative CT images were segmented by means of a semi-automated approach using the software tool ZibAmira (Zuse Institute Berlin, Germany) and the following compartments were separated: the cortical and trabecular bone volumes of both vertebral bodies, the articular cartilage layers at the joints of the vertebral posterior elements, the remnants of the annulus of the intervertebral disc as well as the PEEK or the bone cement spacer, respectively. The embedding layers were added as rectangular regions thickness and orientation of which were adjusted using the glass bead positions. Case-specific finite element meshes of each motion segment were then generated based on these images, all domains were meshed with linear tetrahedral elements using the CGAL library ([www.cgal.org](http://www.cgal.org)). Maximal cell size was set to 1.4 mm and the size of the tetrahedrons was adjusted to the local dimensions of the geometrical features (*Figure 3a*).

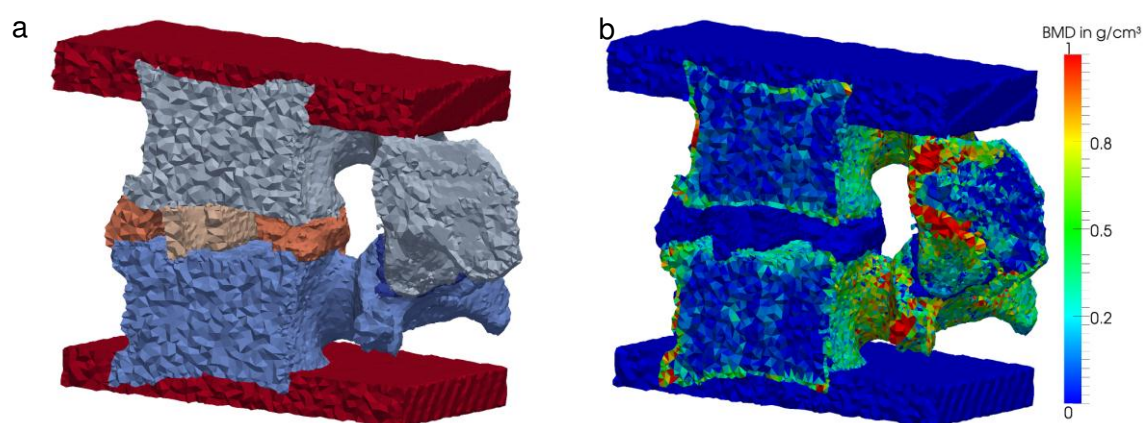


Figure 3. Finite element model of a motion segment stabilized with a PEEK spacer. Half of the model cropped by the mid-sagittal plane is made invisible to show the inner details. (a) The tetrahedral mesh with the different compartments (inferior vertebra, superior vertebra, articular cartilage, disc annulus, PEEK spacer, top and bottom embedding layers) distinguished by colors. (b) Average BMD in the bone elements as computed from the underlying QCT images. The non-bony parts are shown with 0 value (dark blue).

Material properties of the soft tissues, spacer, cement and embedding were assumed to be isotropic, homogeneous and linear elastic. For the two latter materials the elastic modulus was measured experimentally on small cylindrical samples. The properties of PEEK, articular cartilage and annulus were taken from literature. Bone was assumed to be a transversely isotropic, inhomogeneous and linear elasto-plastic material. For both the trabecular and cortical bone compartments the properties of the elements were scaled based on the CT images. Towards this end, the Hounsfield (HU) values were first converted into bone mineral density (BMD) units using the conversion rule assessed as the linear regression between the computed volumetric average HU value and the known mean mineral density of the five distinct rods of the calibration phantom appearing on each CT image (Figure 2a). The mean BMD value of each element was then determined using a custom written Matlab script (Matlab2009b, Mathworks Inc., Natick, USA) by identifying the image voxels centers of which fell within the element boundaries and taking the average density value of these (Figure 3b). The elements were categorized into 255 sets based on their mean densities. For each set, the elastic moduli and the yield strength were computed using experimentally established vertebra-specific relationships.<sup>8-9</sup> The applied material properties are summarized in Table 1.

| Material            | Type                  | Anisotropy             | Young's mod. in MPa      | Poisson's ratio |
|---------------------|-----------------------|------------------------|--------------------------|-----------------|
| Spacer (PEEK)       | Linear elastic        | Isotropic              | 4000                     | 0.4             |
| Bone cement         | Linear elastic        | Isotropic              | 10000                    | 0.3             |
| Embedding plastic   | Linear elastic        | Isotropic              | 700                      | 0.3             |
| Articular cartilage | Linear elastic        | Isotropic              | 5                        | 0.45            |
| Disc annulus        | Linear elastic        | Isotropic              | 10                       | 0.45            |
| Bone                | Linear elasto-plastic | Transversely isotropic | BMD-based <sup>8-9</sup> | 0.381 and 0.104 |

Table 1. Material properties used in the finite element models.

Boundary conditions were set to represent the mechanical tests. The lower plane of the inferior embedding layer as fully constrained. To approximate the loading, two distinct type of boundary conditions were used. In the first, more simplified case the uniaxial compressive displacement load was applied directly on the top surface of the upper embedding and a simple ramp scheme was used. In the second one, in order to better mimic the mechanical testing setup, an additional rectangular volume, parallel with the inferior embedding layer and representing the loading plate of the testing device, was included into the model and positioned above the superior embedding. Contact was defined between the upper surface of the superior embedding and the lower plane of the loading plate and the displacement load was applied on the upper surface of the loading plane along the direction of the plane normal. The embedding layers, bone cement and spacer were assumed to be rigidly bound to the bone surfaces.

The facet joints of the vertebrae were only approximately included into the models as the applied imaging modality could not capture the full level of details. In particular, the boundary and thickness of the articular cartilage layers could not be properly assessed. This joint was therefore simplified in the model, and as a simplified solution the cartilage layer was assumed to be very soft. A more proper approximation was targeted in a second approach, where cartilage layer was added only to one articular surface by defining a minimal constant gap between the outer surface of this cartilage layer and the articular bone surface and frictionless contact was defined between these both surfaces.

The nonlinear finite element simulations were performed in Abaqus v6.10 (SIMULIA, Dassault Systemes, Velizy-Villacoublay, France) and ANSYS v14.0 (ANSYS Inc., Southpointe, USA).

## Results

The results of the experimental tests are shown in details in the paper “Biomechanical evaluation of interbody devices by using mechanical compressive test: PEEK spacers versus PMMA cement osteoplasty” published in the same Proceedings Book. The processing of all simulation data is currently in progress and therefore we cannot present the complete set of results. Instead, we show and discuss the first outcomes of the finite element analyses.

The case-specific models allowed detailed evaluation of the initial position, orientation and contact conditions of the cement and PEEK spacers, which showed considerable variations among the specimens of both groups. The contact surface between the cement and the vertebral endplates were quantified based on the meshes and was found to be  $536.0 \pm 82.9$  mm<sup>2</sup> on average in three samples.

The force-displacement curves on the virtual mechanical tests were assessed by taking the summed nodal reaction forces extracted from the constrained surface of the inferior embedding layer and plotting this versus the applied displacement. *Figure 4a* shows the comparison of two specimens fixed with PEEK and cement spacers, respectively. The motion segment with cement spacer exhibits a larger initial stiffness, but a similar ultimate force as the one with the conventional spacer. The cement case have a more distinct yield point, while the PEEK spacer seems to cause a more continuously softening. All these are in line with the experimental

observations. A more through comparison of the simulation results with the experimental ones is in progress.

The effect of the boundary conditions is demonstrated in *Figure 4b*. The force-displacement curve of the models loaded through the stiff top plate exhibit an initial toe region, which resembles better the experimental results and is due to fact that during the first part of the loading the superior embedding progressively becomes more parallel with the inferior one. This is followed by a stiff part which corresponds to the shifted curve of the more simple loading situation. The differences between the two approaches to model the facet joint is in progress, the first results show that these do not have significant effect in the initial part of the loading process.

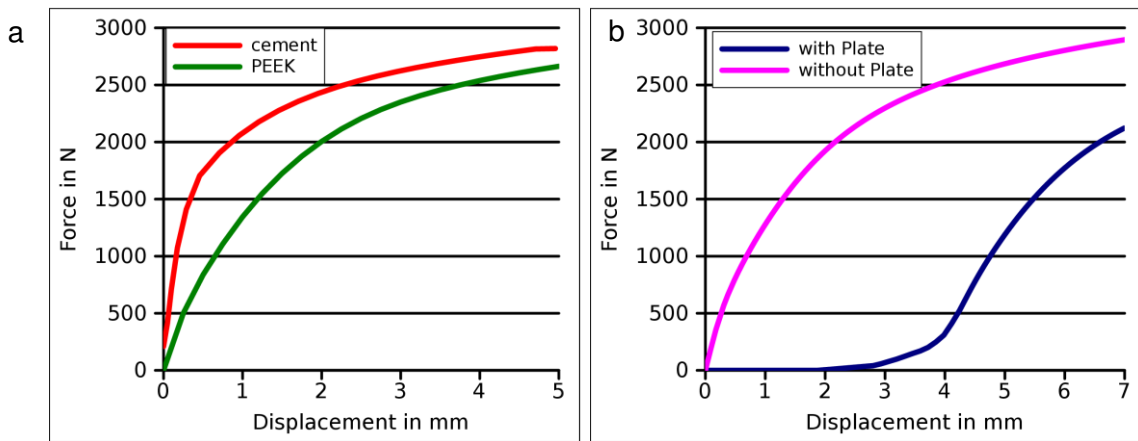


*Figure 4.* Force-displacement curves obtained from the finite element simulations. (a) Results of motion segments fixed with the cement and the PEEK spacer fixation. (b) Results of a motion segment fixed with PEEK spacer, loaded with either an additional plate (with plate) or directly through the embedding (without plate).

Contour plots of the plastic strains at each analysis step allowed to evaluate the initial location and evolution of damage zones within the bone compartments in course of the loading. The plastic deformation is more homogeneously distributed over a larger volume within the vertebral bodies (*Figure 5a*), while the conventional spacer, contacting the endplates on a relatively small area, causes a localized damage in both endplate and trabecular bone (*Figure 5b*).

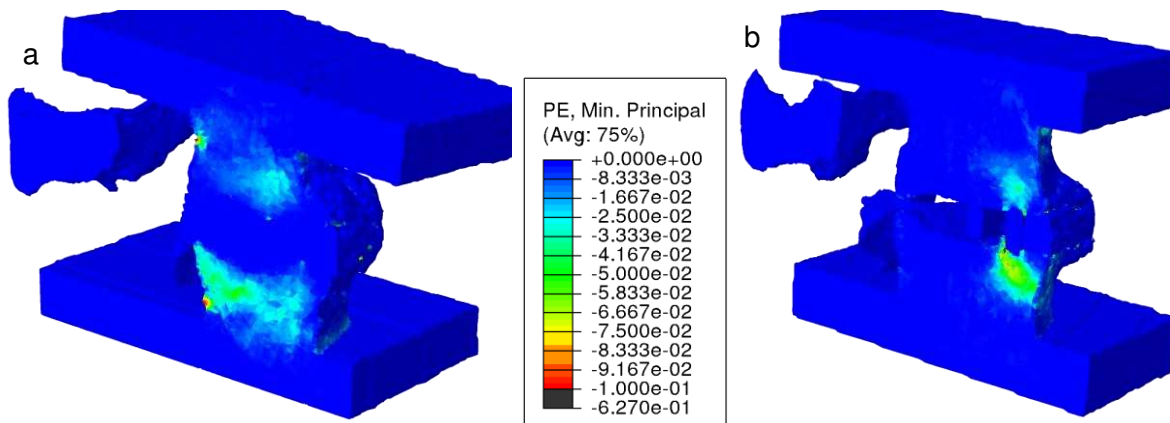


*Figure 5.* Plastic strains in the initial loading phase shown in a mid-sagittal cut plane of the finite element models of motion segments fixed with cement (a) and conventional spacer (b).

## Discussion

This paper presents the first results of a finite element simulation approach targeting the evaluation and comparison of the biomechanical properties of human vertebral motion segments fixed with two different interbody devices. Validation of the models with the quantitative results of the mechanical tests and the qualitative results of the post-experimental CT images is currently in progress.

The models seem to properly capture the softer behavior of the PEEK spacer case and the similar ultimate force of the both interbody devices. However, loading of the cement model produces a more distinct yield point, while the PEEK spacer appears to cause a more continuously softening, which is not fully in line with the experimental observations. The lack of the initial linear elastic response of the PEEK spacer models may be due to the inaccurate representation of the endplate, which may partially be due to the limited resolution of the QCT and the element sizes used to mesh this domain. Further, this may be attributed to the limitations of the applied material properties. All these details will have to be investigated with special care.

Despite these potential limitations, the preliminary plastic strain plots results reveal that, as expected, the cement spacer, offering a larger contact surface, efficiently reduces the stress concentrations at the bone-cement interface compared to the conventional spacer and thus leads to a more homogeneous distribution of plastic deformations. In fact, the conventional spacer seems to first perforate the endplate locally by shearing and the further loading involves only a rather small trabecular volume (*Figure 5a*). In turn, the larger cement bulk deforms the endplate as a whole in bending mode and therefore the plastic deformation accumulates first in the trabecular compartment rather than the endplate (*Figure 5b*). The endplate is thus subjected to smaller local stresses and a larger trabecular volume is involved into the resistance. These may be the reason for the higher initial stiffness of the cement spacer cases compared to the conventional ones, which exhibit an early reduction of stiffness. These differences can be crucial from a clinical point of view as the cement spacers, offering higher initial stiffness, may more efficiently inhibit excessive spacer subsidence and further complications. These early findings must be supported by the analysis of further specimens, however, are in line with the experimental results. Further, these results may help to understand the chronology of the damage processes, i.e. at which location the plastic zone was initiated and how it was propagating. Both models shown in *Figure 5* suggest the major damage to take place in the inferior vertebra. The important, but complex information carried by the spatial maps of plastic deformations will be compared at the ultimate state with the fracture patterns extracted from the post-experimental CT scans.

The available results allow to conclude also that the embedding has a significant effect in the mechanical behaviour of the segments. In particular, the plastic deformation seems to localize also at the cortex-embedding interface (*Figure 5a*). These boundary conditions were selected for the sake of the experimental tests and differ considerably from the physiological conditions and do not appropriately represent the in vivo case. Having the QCT-based case-specific models at hand will allow us to investigate the influence of selected parameters on the outcomes in particular, the effect of the embedding layers. Preliminary results indicate that removal of these layers alters the results significantly, non-embedded segments are softer and weaker. Moreover, the intact models can be generated from the CT images assessed prior to operation and the

differences in transmission of forces between the quasi-native anatomy and the post operative situation can be evaluated.

The models generated with the presented approach are suitable for the purposes of optimization aiming at defining the ideal positioning of the conventional spacers as well as the optimal location, volume and material properties of the cement spacers.

## **Conclusion**

The finite element simulations of human vertebral motion segments fixed with two distinct inter-body devices efficiently complement the mechanical tests and allow detailed investigation and better understanding of the experimental outcomes. Further, these models can be used to analyze and optimize the effect of different parameters like spacer location and material properties, which may help to improve the effectiveness and success of the surgical interventions and ultimately to reduce the occurrence of potential complications

---

## REFERENCES

1. Jost B, Cripton PA, Lund T, Oxland TR, Lippuner K, Jaeger Ph, Nolte LP. Compressive strength of interbody cages in the lumbar spine: the effect of cage shape, posterior instrumentation and bone density. *Eur Spine J* 1998; 7(2):132–41.
2. Lim TH, Kwon H, Jeon CH, XXXX Effect of endplate conditions and bone mineral density on the compressive strength of the graft-endplate interface in anterior cervical spine fusion. *Spine* 2001; 26(8):951–6.
3. Tan JS, Bailey CS, Dvorak MF, Fisher CG, Oxland TR. Interbody Device Shape and size are important to strengthen the vertebra–implant interface, *Spine* 2005; 30(6):638–44.
4. Oxland T, Lund T, Jost B, Cripton P, Lippuner K, Jaeger Ph, Nolte LP.. The relative importance of vertebral bone density and disc degeneration in spinal flexibility and interbody implant performance. *Spine* 1996;21:2558–69.
5. Csakany T, Varga PP. Discoplasty in Cases of Degenerative Spine with Complications of Osteoporosis, 52nd Congress of the Hungarian Orthopaedic Society and Section Meeting of the Hungarian Society of Arthroscopy, Szolnok, Hungary, 2009 June 25-27.
6. Csákány T, Rónai M, György ZM, Varga PP. Bone Cement as Intervertebral Spacer in Thoracolumbar Stabilization of Aging Spine - Radiological and Clinical Results, Global Spine Congress, Barcelona, Spain, 2011 March 23-26.
7. Polikeit A, Ferguson JS, Nolte LP, Orr TE. Factors influencing stresses in the lumbar spine after the insertion of intervertebral cages: finite element analysis. *Eur Spine J* 2003;12:413–20.
8. Kopperdahl DL, Morgan EF, Keaveny TM. Quantitative computed tomography estimates of the mechanical properties of human vertebral trabecular bone. *J Orthop Res* 2002;20:801–5.
9. Mirzaei M, Zeinali A, Razmjoo A, Nazemi M. On prediction of the strength levels and failure patterns of human vertebrae using quantitative computed tomography (QCT)-based finite element method. *J Biomech* 2009;42(11):1584-91.

*The authors gratefully acknowledge the Hungarian Scientific Research Found (Országos Tudományos Kutatási Alapprogramok, OTKA) for providing financial support in frame of*

*the grant K-075018. We thank Stefan Fröhlich for his contribution in the finite element modeling process.*



## DEVELOPMENT AND TEST RESULTS OF A SYSTEM FOR THE RECOVERY OF THE LOWER LIMBS

Peter Molnár, György Posgay, István Németh  
Metalektro Measuring Technique Ltd.  
[mpeter@metalektro.hu](mailto:mpeter@metalektro.hu)

---

### **Abstract**

According to medical research,<sup>1</sup> exertion of a certain level of loading to injured lower limbs is considered as important from the point of view of their recovery. Total unloading would decelerate coalescing of bones just like their permanent overloading. In order to avoid it, patients must be trained to walk with optimal load on lower limbs. A data logger with built-in load cell is designated both to sustain this process and to store data on load values exercised to limbs during recovery as well. The report below tells how this device was developed.

**Keywords:** load cell, lower limb, partial weight bearing, recovery, feedback, rehabilitation

---

### **Introduction**

An important condition for the recovery of the lower limbs is optimal loading distribution during walking. The goal of the development is to realize a system to train and control walking leading to limb loading prescribed by the physician. This article describes the development of the system measuring the loading of the lower limbs, criteria taken into account during development, the performed experiments, and the developed solutions. We review the patients who need rehabilitation and whose efficient recovery is assisted by the system.

### **Methods**

In course of rehabilitation related to lower limbs and walking it is necessary to know when and how much load the patient exposed the affected limbs or side to, what difference can be measured between the load of the healthy and rehabilitated limbs. An indispensable condition of the right recovery of the injured lower limb is partial release from load because full release may delay the setting (recovery) of the bone in the same way as overload<sup>1</sup>. During recovery the limbs are increasingly loaded up to 70% of full load, then the patient himself gets to full load at more or less suitable rate. Final goal of the rehabilitation of those with nervous system injury is to develop symmetrical walking and load therefore the patient must be urged to load the weaker limb to a greater extent. Similar is the case with patients walking long time with pain and load releasing devices. We can see that following the implantation of the prosthesis symmetrical limb loading is not restored<sup>4</sup> therefore symmetry of walking must be corrected through separate rehabilitation.

### **Current solution**

Training partial unloading is carried out by teaching the patient after he is standing to realize how much pain belongs to the desired load. It is usually carried out by a personal scale in hospital but the use of foot-board with force measurement possibility or instrumented treadmill are also

possible. This load is periodically controlled and new level of load is determined during control examination. The deficiency of the procedure is that the patient exerts load from memory, there is no continuous measurement and feedback on the right and wrong load. Data are not recorded to indicate to the physician how many steps the patient took under what load and whether kept the physician's advice.

## Goal

The goal is to develop force transducer-data collection-feedback device continuously usable during full recovery.<sup>2,3</sup> The force transducer shoe may continuously help the patient to learn and practice right limb loading. Thy physician and the physical therapist may set the next load level according to the improving condition of the patient on the basis of the unloaded data.

## Selection of force components characterizing the load of the lower limb

In course of normal walking only ground reaction force component is calculated during the measurement of lower limbs load because forces in the plane of the ground, in the direction of walking and perpendicular to it may take place only in case of significant acceleration like among professional football players. Among the occurring moments the torsion moment of the limb may be significant, but in case of patient requiring rehabilitation this value can be neglected because of slow, considered movement.

## Ground reaction force during normal walk

During normal walking there are more phases of movement of foot while contacted to the ground from heel strike while toe-off. The ground reaction force has two maximum points like peaks of heel and forefoot loading (*Figure 1*). It is suitable to measure the ground measuring force under the heel if the patient is able to walk in normal way. In that case the first peaks are measured and stored.

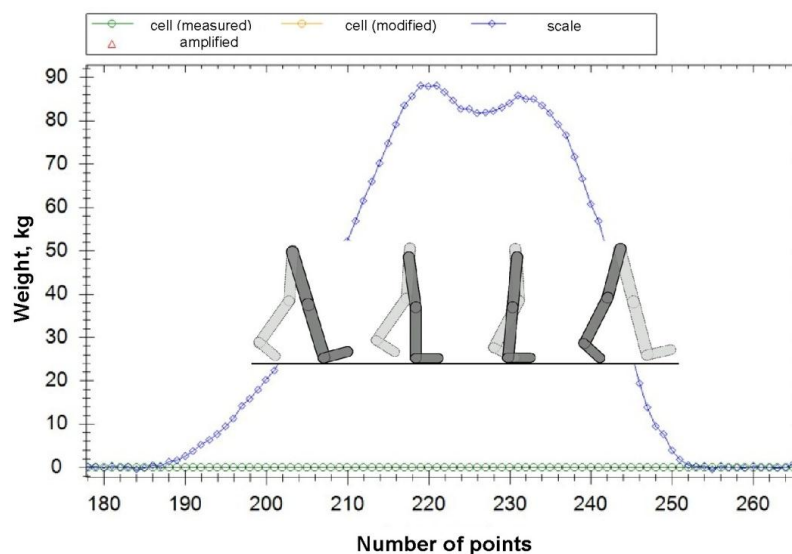


*Figure 1.* Walking phases and ground reaction force was recorded by scale platform (x axis – time with 50Hz sampling rate; y axis – load in kg)

If the patient is unable for rolling walk, does not load clearly his heel the action line of the maximum of the reaction force is shifted towards toes. The walking image of patients is measurable with a scale having big walking surface on which several steps can be taken. The shape of the force diagram can show that the walking image of the patient does not change therefore it is enough to measure reaction force on the heel. When measurement is started when force transducer shoe is adjusted to the patient, the extent of force shift can be set with the scale platform, in this way the measured values comply with the actual load. If the patient is unable to load his heel, forces must be measured on several points of the sole, on the heel, on the inner and outer sides of the first part of the foot, and on the big toe.

## **Results**

### **Development of suitable shoes**

Three criteria must be taken into account during the development of force transducer shoes: comfort, safety and accurate measurement results. Our experiments proved that comfortable force transmitting surfaces cannot be developed into flexible shoes between the force transducer and the sole because the roll of fat of the human sole and the flexible heel-sole of the shoes can cause great deformation during walking. The hard force transducer cell placed in the foot-shoe system on the one hand makes the use of shoes uncomfortable because of local pressure peaks; on the other hand flexible condition does not ensure that full load may be shifted to the force transducer cell because of the force components taken up by the flexible condition. Human sole cannot be made more rigid therefore a rigid pair of shoes was developed. Wooden sole clogs are comfortable and safe. Its wood frame is properly rigid, ensures comfortable force transducer surface and provides enough space for force transducer cell. The wooden frame of the clogs must have two parts: the upper part having contact with the foot and the lower part having contact with the ground. The lower and upper parts are connected with the force transducer cell or cells. Necessary measurement accuracy can be achieved with this development. Use of strap increases safety (*Figure 2*).



*Figure 2* Force transducer shoes on the scale platform

## Force measurement

### Force transducer sensor

As the first step of our development on the basis of literature and market research we decided to develop our own force transducer sensor and electronics since any device meeting the target is not available on the market. The following parameters were decided in the technical description: low consumption, thin construction, pressure directed load capacity, long term stability and accuracy, robust construction, usable up to 150 kg mass. We could not choose from insole-like pressure measuring sensors, which can be placed into shoes since everyday use would be unaffordable because of the high price and computer of high capacity and size to handle the great quantity of data is also necessary and it cannot be integrated into the shoes.

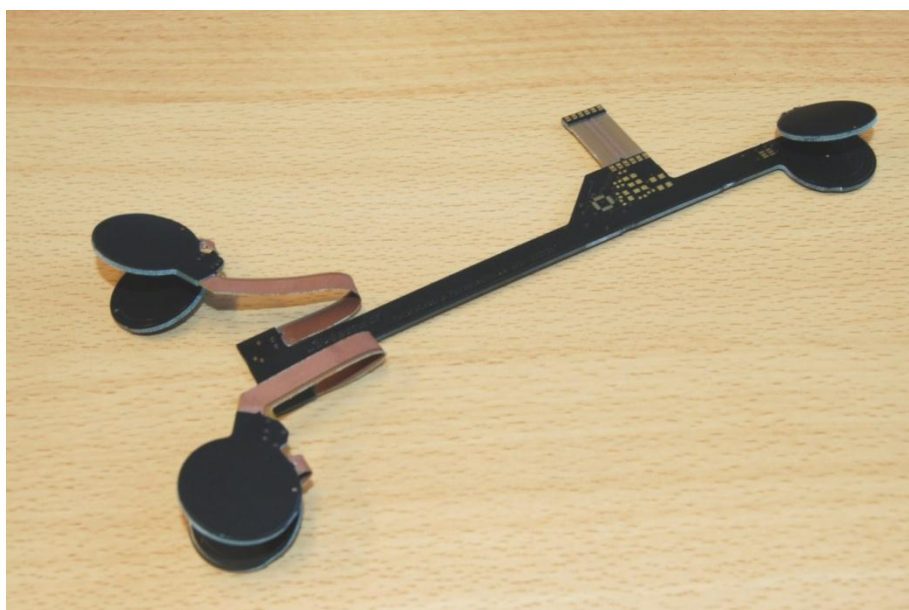


Figure 3. Electric board of system with three sensors

Therefore force measurement was reduced to measure one force only with optimum construction. Capacitive force transducer sensor was chosen (Figure 3). The “soul” of the capacitive sensor is dielectric and the spring element, which determine force shift, the force-electric signal characteristics and their dependencies on different conditions (temperature, humidity, etc.). Since sensors with these required characteristics are not available, we carried out our own development. We have developed a cell working with steel membrane; in that case dielectric is air, which is between measuring unit and spring element. The load bearing capacity of the cell with steel membrane, remaining deformation, and hysteresis were tested under laboratory conditions. The sizes of fitting parts taking part in springs and construction of their fitting surfaces were optimized, in this way hysteresis measurable during up load and release was reduced to minimum, the failure range of measurement fell within 2% (Figure 4). The disadvantage of the steel membrane cell is its weight and relatively high production cost because of several precision parts.

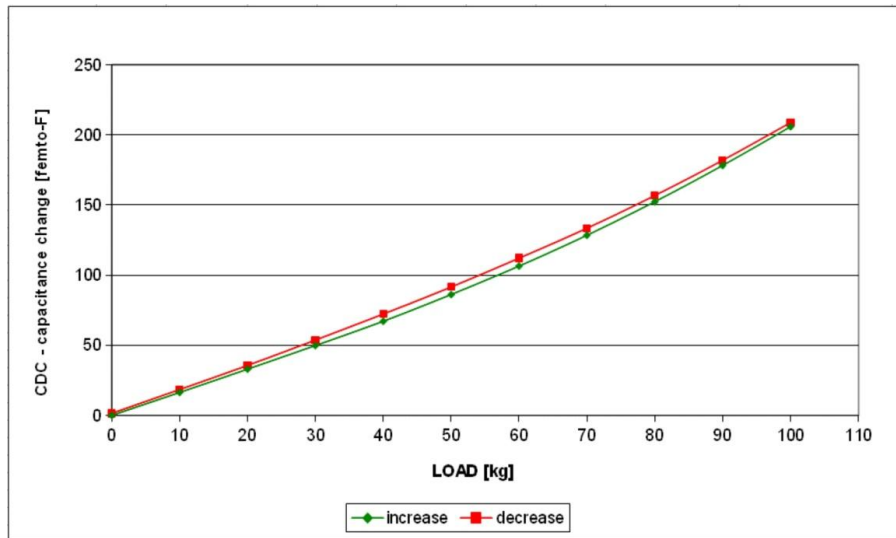


Figure 4. Hysteresis of steel spring

Capacitive force transducer using artificial rubber (silicone, polyurethane, PDMS) spring element was developed because of its simpler solution and lighter weight. In this sensor the artificial rubber spring is dielectric at the same time. On the basis of literature and market research several artificial rubber materials deemed suitable were chosen and the change of dielectric characteristics under pressure change, the change of force deformation functions under the effect of temperature, the limit load whose long term use does not cause remaining deformation in the artificial rubber were examined in laboratory.

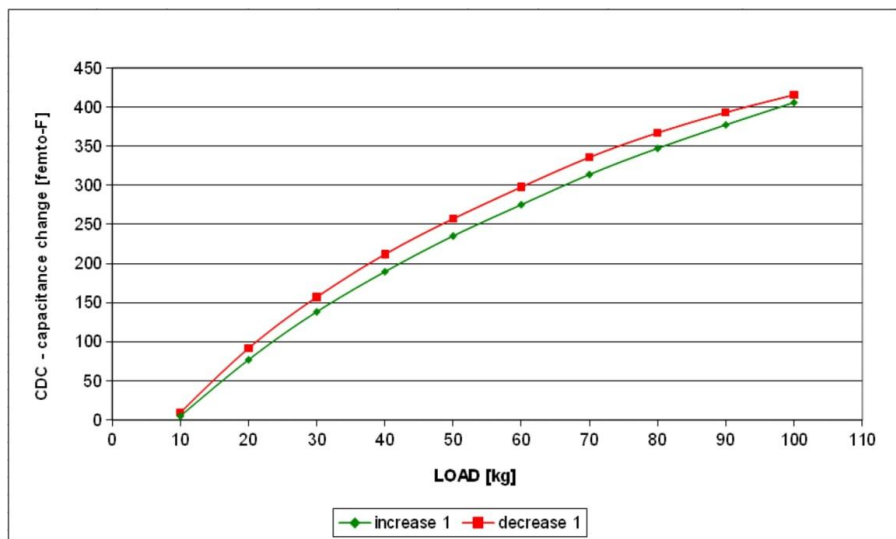


Figure 5. Hysteresis of PDMS spring

In addition we examined what geometric construction can minimize hysteresis typical of artificial rubber because of the relatively high inside friction of the material. The use of PDMS material could keep the 5 % failure range (Figure 5).

## Data processing

To determine the load peaks during walking with appropriate accuracy a data processing algorithm was developed for the dynamic measurements results based on force measurement with the frequency of 50/second. Continuous evaluation of the measurement data is necessary because the patients need feedback on each step. The evaluation algorithm working continuously during the measurement procedure is looking for maximum value or values during the given steps according to optimised parameters. We have to distinguish normal walking – when force decreases to zero – from the stamp and lounge, when the force does not decrease to zero between two maximum force values.

## Feedback

On the basis of the results of the evaluation algorithm the force transducer shoes give feedback to the patient, according to load levels determined to the given treatment period, which can be modified arbitrarily during the whole treatment period by the physical therapist or the physician. A proper procedure for the feedback can be the use of stimulus by sound, light and vibration. Tests have verified that the most efficient way is the sound signal is, because the mostly elderly people cannot listen to a lamp during walking, or have difficulties to interpret the vibration signal of the force transducer shoes.

The force transducer shoes themselves can give sound signal with their built beepers, but outer signal devices can improve the efficiency of the feedback, in case of hard of hearing patients. Two outer feedback instruments have been developed, with which the force transducer shoes are communicating on wireless channel. One of them is a sound signal attached on belt, it has its own power supply, loudspeaker and earphone (*Figure 6*), the other one is a watch which in addition to sound signals also shows measurement results on its display (*Figure 7*).



Figure 6. Use of wireless external feedback instrument with earphone



*Figure 7.* Use of wireless watch as feedback instrument

Two possibilities were developed for the way of feedback. On the one hand, based on the calculated maximum values the patient gets different sound signal after the step in case of load release or overload, it is called “punishing” feedback, because shoes beep only in case of error and with phase delay since maximum value is obtained only after finishing the step and sound signal can be started then. On the other hand “rewarding” sound signal, which gives different buzzer sound at the moment when the measured force value reaches the desired range, in this way indicates that the patient should not weigh on his foot to a greater extent since load is just right! The two feedbacks can be used simultaneously and separately, but clinical tests proved that elderly patients have difficulties to interpret three types of sound signals. “Personalization” procedure during measurement and data collection observes the efficiency of feedback, which is different person by person. It continuously modifies the feedback levels that the patient should remain in the load range defined by the physical therapist/physician.

### **Calibration of force measurement**

The relation between the value measured by the shoes and the value measured on the ground depends on the number of force transducer sensors, location in the shoes and the walk image of the patient, therefore the force measurement shoes must be set on force transducer platform by control measurement in case of all patients. A folding scale platform was constructed on which the patient can take several steps with only the affected foot on the surface, the other one and load releasing device are not (*Figure 8*). The measurement results of the scale platform along with the results of force transducer shoes appear in the application running on the joined computer. The measurement of the force transducer shoes can be corrected on the basis of the results (*Figure 9*). Simultaneously with the current article the construction of a force transducer treadmill, which is suitable for continuous measurement of the ground reaction of both feet is going on (*Figure 10*). The treadmill is equipped with load releasing elements and fall restricting pending

strap in this way it is not only suitable for the calibration of the force transducer shoes, but is also usable for rehabilitation therapy and examination. Joint measurement of the ground load of the two feet provides the physician accurate image about the asymmetrical walking of the patient.



Figure 8. Calibration of force transducer shoes on the scale platform

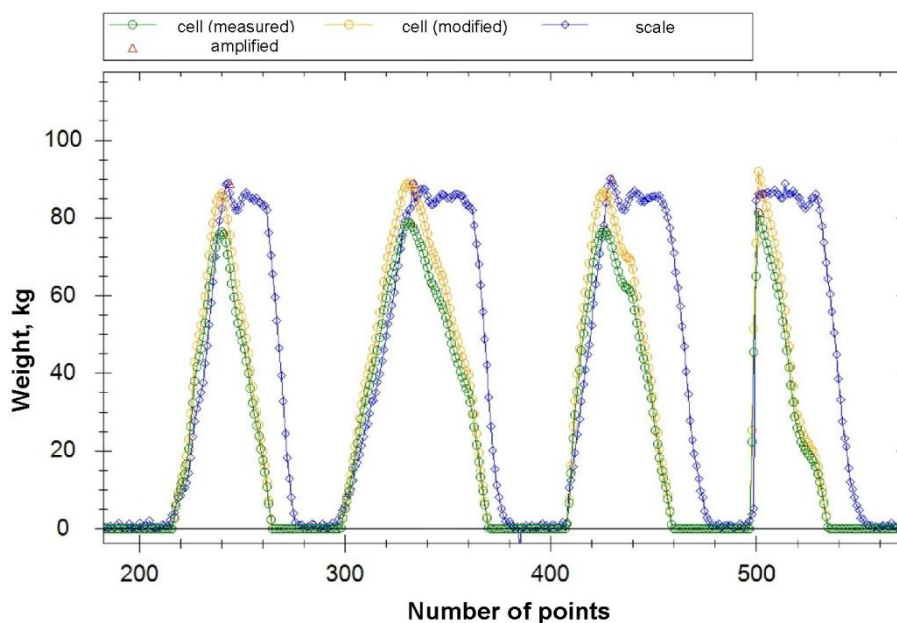


Figure 9. Results of calibration of force transducer shoes on the scale platform (green – shoes original; orange – shoes calibrated; blue – scale platform; x axis – time with 50Hz sampling rate; y axis – load)



## **Power supply**

The force transducer shoes must operate for at least 30 days safely with minimum handling. To this end there are three ways: battery and everyday charging, high capacity battery and self-charging system. Although several promising power supplies resulting from the force of steps during walking are published in periodicals, not one usable as real solution could be found. As final solution high capacity batteries were chosen, which are able to operate the force transducer shoes for at least 30 days even in cold weather. In addition to adequate power supply energy demand decreasing solutions were developed as the sleeping and measurement operation of electronics.



*Figure 10. 3D view of force transducer treadmill*

## **Software, data base**

Following the log in to the server new patients and walk improving devices can be entered, new treatments can be started and measurement results from treatments can be unloaded. All the data and measurements related to the treatment get to the server and in case of proper entitlement the entitled user can have access to all data from anywhere with the help of internet browser.

## **Elements of the realised system**

- force transducer data collecting-feedback shoes
- feedback instrument with wireless communication
- scale to train walking, to calibrate shoes
- treadmill to train walking, to calibrate shoes

- wireless communicator to PC for data movement between PC and scale, PC and treadmill, PC and shoes
- PC program
- server program

## Discussion

### Results of clinical tests

The clinical testing of the system is carried out with TUKEB license at three hospital departments. The clinical test was not finished when the manuscript was sent.

Results up to now:<sup>5</sup>

The system was tested on 10 healthy volunteers and 72 patients. The majority of patients in the test used the force transducer shoes following implantation of arthritis prostheses, the others after different fractures. The average age of the examined persons was 65 years, the average weight 76 kg. Test periods are traditional training of load release by physical therapist, the use of the device without feedback then with feedback.

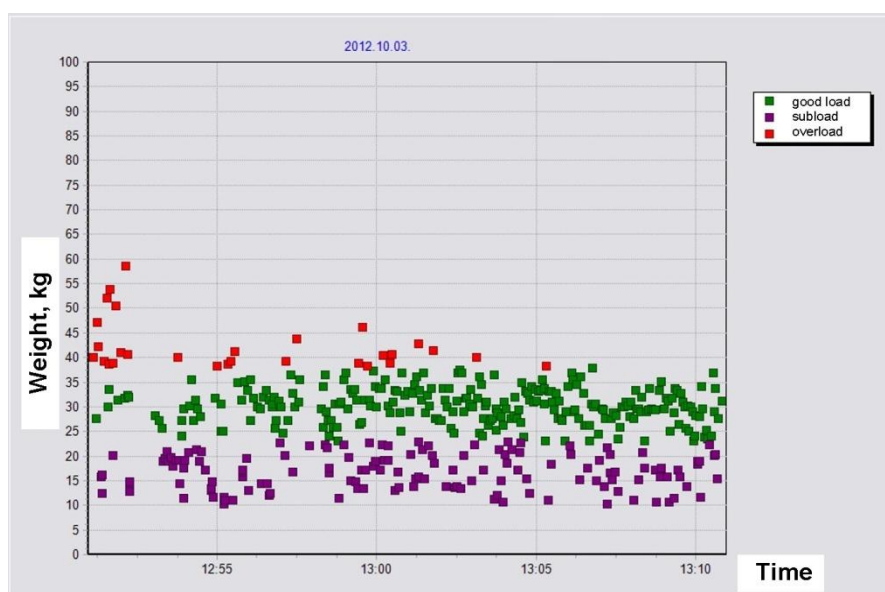


Figure 11. Measuring results in the data evaluation section of software (red – overload; green – load in the range; violet – load under the range)

On the basis of aggregate results we could conclude that the device must be used with feedback (sound signal, light signal or in vibrating mode). In this case the results showed 40 % reduction of overload in the clinical tests. Simultaneously with sending this article clinical tests are going on with patients affected by problems of the nervous system.

## **Possibilities for further development**

The Angel Heel slippers can be made suitable to measure also walk pattern, that is, the distance-time-angle parameters of walk, for the complex kinematic and dynamic examination of walking under natural conditions. These continuously wearable measurement- data collection systems can provide more accurate data than case by case control measurements since statistical mass of real results recorded under stress free environment can be obtained.

---

## **REFERENCES**

1. Pálkás J, Daróczy L, Pék Gy, Manó S, Csernátony Z. Electronic walking heel to train and control optimal load on lower limbs. In: Proceedings of the First Hungarian Conference on Biomechanics (Budapest, 11-12/06/04), 2004. p. 342-47., Budapest, Research Center of Biomechanics and BUTE ISBN 963 420 799 5
2. Molnár P, Németh I, Farkas L, Juhász T. Intelligent load cell as a new medical aid DAS 29 (29th Danubia-Adria Symposium), University of Belgrad Serbia, 2012. p. 70-71.
3. Molnár P, Németh I, Farkas L, Juhász T, Alsó végtag gyógyulását segítő Angel Heel készülék és rendszer. *Biomechanica Hungarica*, 2012 December p. 11-24.
4. Holnapy G, Kiss R. A csípőízületi protézis beültetés feltárásmódjának hatása a dinamikus egyensúlyozó képességre a posztoperatív időszak első hat hónapjában. *Biomechanica Hungarica*, 2012 December p. 25-30.
5. Hunya Zs, Manó S, Kósa V, Molnár P, Csuha Gy, Csernátony Z. Az alsó végtagi tehermentesítés betanítását segítő új típusú rehabilitációs segédeszköz, MOT-MTT 2013 accepted presentation A-0188

***Device development runs with contribution of the European Union and the co-financing by the European Social Fund. Identification number: GOP-1.1.1-09/1-2010-0183***

## ANODISATION OF MEDICAL GRADE TITANIUM

Bálint Katona<sup>1</sup>, Lilla Nádai<sup>1</sup>, Attila Terdik<sup>1</sup>, Eszter Bognár<sup>1,2</sup>

<sup>1</sup>Budapest University of Technology and Economics, Faculty of Mechanical Engineering, Department of Materials Science and Engineering

<sup>2</sup>MTA–BME Research Group for Composite Science and Technology

[katona@eik.bme.hu](mailto:katona@eik.bme.hu)

### Abstract

In recent years the number of titanium dental implants in use has significantly increased. At the same time bacterial infection of implants has become more common. The goal of our study was to develop a titanium-dioxide layer on the surface of titanium implant materials by anodisation with a view to impeding the attachment of contagious bacteria. In our experiments Grade 2 titanium and nanograin Grade 2 titanium discs were subjected to anodisation. We investigated the effect of voltage on the surface pattern of emerging titanium-dioxide. We examined the surfaces by reflected-light microscopy. We found that the value of the applied voltage and variation in grain size affected the thickness of the formed titanium-dioxide layer. These layers may promote or support desired forms of biological activity, such as cell attachment to integrate with bone.

**Keywords:** anodisation, titanium, Grade 2, nanograin, surface treatment

### 1. Introduction

Implant-associated infections have dramatically increased over the last decade in line with an unfortunate trend of growing resistance by bacteria to antibiotics. Bacterial infection can seriously compromise the success of an implant.<sup>1</sup> One way to reduce bacterial colonisation of an implant might be to subject it to a surface treatment that gives the implant surface a texture which is difficult to colonise. Perhaps paradoxically, we are therefore trying to achieve a surface which impedes one kind of cellular attachment (bacterial) and yet promotes another kind of cellular attachment (osseointegrative, supporting attachment by bone cells).

Anodisation is an electrolytic surface treatment. The work piece is connected into a circuit as an anode immersed in an anodising bath. A cathode is immersed in the bath as well, made from the same or different material as the work piece. The most common geometries of the cathodes are sheet or roll. After closure of the circuit electrons can flow (*Figure 1*).

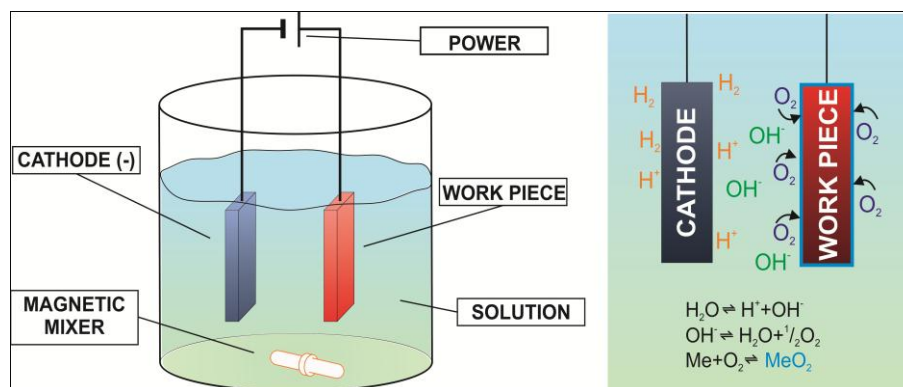


Figure 1. Schematic depiction of the anodisation experiment

Because of the voltage, oxygen is released from the anodising bath, which reacts with the work piece. A metal-oxide layer is created on the surface, the thickness of which depends on the applied voltage and to some extent duration of immersion.

Aside from time, the process is jointly determined by the applied voltage, the composition of the anodising bath and the material comprising the work piece. With anodisation, metals can be coated whose oxides adhere to their surfaces.<sup>2-5</sup>

Chen and his colleagues in their work examined titanium-dioxide films of 0.3  $\mu\text{m}$  thickness. Samples were mechanically polished and cleaned in acetone with ultrasonic cleaning equipment. Experiments were completed in a solution of 6 wt% hydrogen-fluoride. They used a cathode surface area of 9  $\text{cm}^2$  at a distance of 1 cm from the anode, and at voltages of 40, 60, 80 and 100 V, for durations of 2, 5 and 12 hours. They found that high hydrogen-fluoride concentration and voltage at 80 V are crucial for the formation of nanogrooves.<sup>6</sup>

Gong and his colleagues anodised pure titanium samples in 0.5 wt% hydrogen-fluoride mixture at 18°C for 20 minutes. They used magnetic mixing. It was found that nanotubular structures did not form if the applied voltage was more than 40 V. They found that under an applied voltage of 20 V nanotubes were formed which had average diameter 60 nm and length 250 nm.<sup>7</sup>

The colour of the formed oxide layer depends on its thickness. For titanium this ranges across a wide spectrum allowing us to infer the thickness of the formed titanium-dioxide layer from its colour.<sup>8</sup>

Puckett and his colleagues anodised films of pure (99.2 %) titanium. Before their experiments, the samples were chemically etched in a solution of hydrogen-fluoride and nitric acid to remove any surface contamination and the thin oxide layer. After this treatment the films were anodised in solution of 1.5 V/V% hydrogen-fluoride for 10 minutes at 20 V. They found that nanotubular-like titanium-dioxide structures were created on the surface. In another experiment they performed the anodization in a solution of 0.5 V/V% hydrogen-fluoride at 20 V for 1 minute. They found the surface had acquired nanotexture.<sup>9</sup>

Poznyak and colleagues anodised pure titanium samples with a titanium cathode. Before the experiment mechanical and chemical polishing were done in a warm hydrogen-fluoride and nitric acid solution. During anodisation, maximum current density was 10  $\text{mA}/\text{cm}^2$ , and maximum voltage was higher than 1000 V. The anodising bath they used was a mixture of nitric acid and distilled water. The depth of the created oxide layer was determined with Auger-spectroscopy, the phase composition was determined with X-ray diffraction, and the morphology of the surface was determined with scanning electron microscopy. They found that the density of the oxide layer was 3.2-3.9  $\text{g}/\text{cm}^3$ , which was 180 nm thick, containing 4 to 5% sulphur from the acid. The thicker oxide layer was rougher, and where  $d < 50$  nm then it was amorphous, whereas if  $d \approx 100$  nm then it was composed of anatase. If  $d \approx 300$  nm then the oxide layer contained both anatase and rutile<sup>10</sup>

In his research, Elias treated with a range of processes discs and dental implants made of one type of pure titanium. The etching pickle was a solution of nitric acid, hydrochloric acid and sulphuric acid. He found that chemically etched homogeneously rough surfaces were more biologically active in the osseointegrative sense. This facilitated the attachment of bone cells so the implants would support mechanical loading. The electrolytic solution for anodisation

contained calcium and phosphorus and he used micro-arc oxidation based on previous research.<sup>11</sup> He found that various treatments differently changed surface morphology and therefore the anodised samples needed greater torque to screw into bone than chemically etched implants.<sup>12</sup>

Gubicza and his colleagues in their research manufactured ultrafine-grained titanium with equal channel angular pressing, which known as ECAP technology and the combination of modern and conventional plastic deformation techniques. The formed grain size was 200-500 nm using ECAP and 50-300 nm using a combination of the ECAP, forging and drawing. They found that this material had increased yield stress (652 MPa) and increased dislocation density ( $24 \times 10^{14} \text{ m}^{-2}$ ).<sup>13-14</sup>

## 2. Methods and materials

In our experiments we used 13 mm-diameter titanium rods out of which we machined 2 mm-thick discs. We used two types of base material: pure titanium, known as Grade 2, and nanograin Grade 2 pure titanium. The latter is prepared using ECAP. The two materials vary only in grain size.

After making these discs we cut each disc into 4 identical quarters with a diamond disc cutter. The machining left burr and surface imperfections so we applied chemical etching to remove these. During treatment we used ultrasonic cleaning equipment. We used a mixture of 12 V/V% nitric acid, 9 V/V % hydrogen-fluoride, and distilled water. Based on our preliminary experiments the time of the chemical etching was chosen as 30 seconds. We kept the temperature at  $30 \pm 1^\circ\text{C}$ . The chemical etching successfully removed the burr and surface imperfections caused by machining and cutting.<sup>15</sup>

To further smooth surfaces we electropolished the chemically etched samples. We kept the temperature at  $30 \pm 1^\circ\text{C}$  during the process. We used 20 V and a 3-minute duration. After this we applied anodisation on the resulting work pieces.

We held samples with a clip of nickel-coated 316L austenitic stainless steel. This material transferred power to the sample. The clip did not touch the anodising bath. The cathode was a cylindrical mesh of 316L austenitic stainless steel.

Because the main criteria for the anodising bath were its oxygen and acidic properties we used a mixture of 0.1 V/V% hydrogen-fluoride and distilled water. We chose this concentration based on preliminary tests.

The applied voltages were between 10 and 200 V. The necessary voltages we created with a toroidal transformer. The exact value of the voltage in the circuit depends on the conductivity of the anodising solution and on the current limit. Over-high current density can cause problems so we limited this with a current limit, which stopped the voltage rising further during anodising. Exact values of the applied voltages of the samples are given in *Table 1*.

|              |    |    |    |    |    |    |    |    |    |     |     |     |     |     |     |     |     |     |     |     |
|--------------|----|----|----|----|----|----|----|----|----|-----|-----|-----|-----|-----|-----|-----|-----|-----|-----|-----|
| <b>Nr.</b>   | 1  | 2  | 3  | 4  | 5  | 6  | 7  | 8  | 9  | 10  | 11  | 12  | 13  | 14  | 15  | 16  | 17  | 18  | 19  | 20  |
| <b>U [V]</b> | 10 | 20 | 30 | 40 | 50 | 60 | 70 | 80 | 90 | 100 | 110 | 120 | 130 | 140 | 150 | 160 | 170 | 180 | 190 | 200 |

*Table 1.* The values of the anodising voltage of the samples

In preliminary anodising experiments we treated samples for durations of 1, 5 and 10 minutes and observed the formed oxide layer. We found this layer formed immediately so in the actual experiments we stopped when applied voltage reached the required value. During the process we used magnetic mixing with 150 rpm to keep the anodising solution in motion. The temperature of the anodising bath was  $20 \pm 1$  °C.

### 3. Results and discussion

We examined the formed surfaces with reflected-light microscopy. On images we can see that different voltage resulted in differently coloured titanium-dioxide layers (*Figures 2-3*). The colour is closely related to the thickness of the layer. *Figures 4-5* shows the reflected-light microscopy images of the anodised surfaces.

The two different types of base materials have the same chemical composition, they vary only in grain size. The grain size influences mechanical properties (e.g. tensile strength, hardness, dislocation density) as well as electrical properties (e.g. conductivity). On images we found that different grain sizes resulted in different oxide layer thicknesses at the same voltage value. We can conclude this from oxide colours, which closely track thickness.

On images we found local surface heterogeneities in titanium-dioxide layers. These are due to material defects, work piece shape, and uneven voltage distribution. The size of these heterogeneous areas stayed low at low applied voltages (10-100 V) but rise at higher voltages (100-200 V). This phenomenon held for both materials.

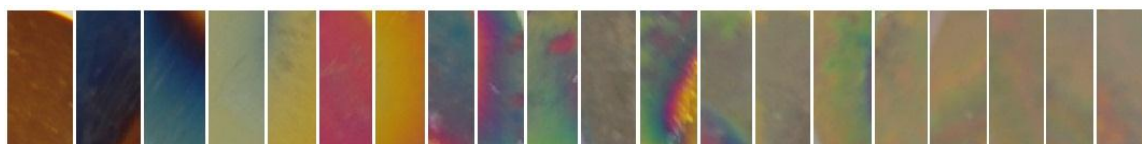


*Figure 2.* Sections of surfaces of the anodising Grade 2 titanium discs, with voltage changing from left to right from 10 to 200 V in 10 V increments



*Figure 3.* Sections of surfaces of the anodising nanograin Grade 2 titanium discs, with voltage changing from left to right from 10 to 200 V in 10 V increments

To observe possible nanostructures formed on the surface we have to use atomic-force microscopy. This gives higher-resolution images of the surface.

To observe the biological behaviour of these surfaces, bacteriological experiments were needed. Based on these we concluded that the formed titanium-dioxide layer can support osseointegration.

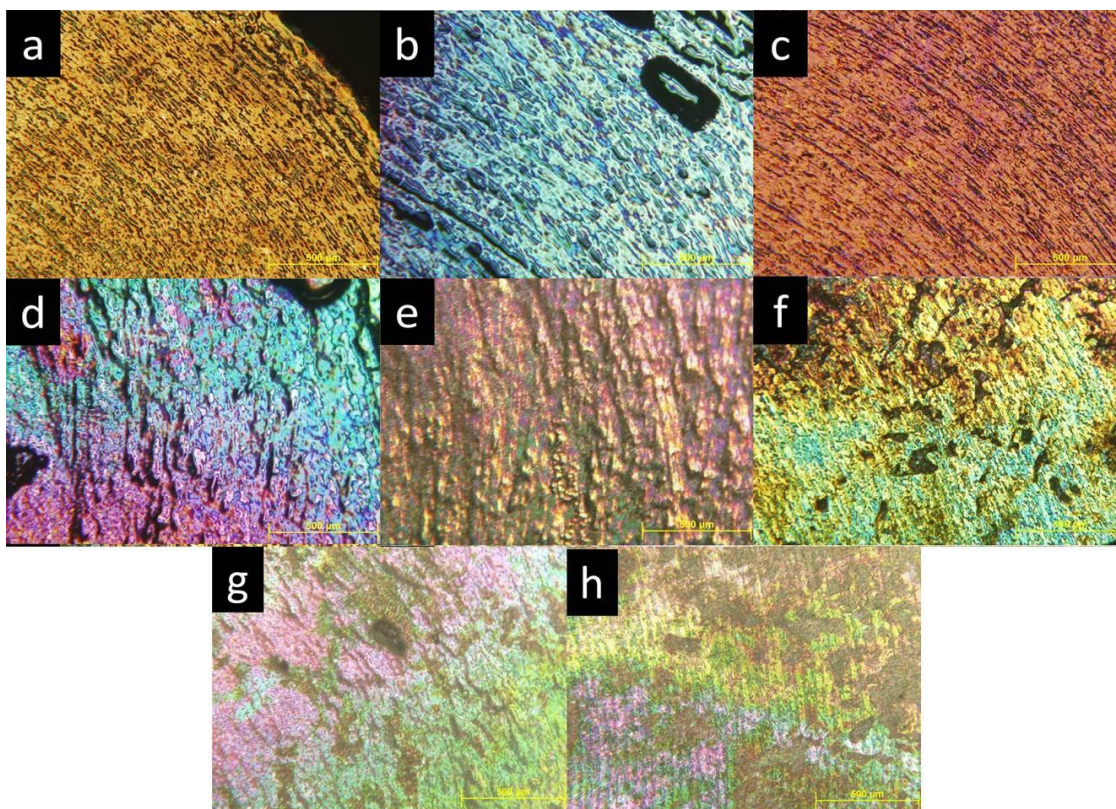


Figure 4. Reflected-light microscopy pictures of surfaces of the anodised Grade 2 titanium discs, 10 V (a), 30 V (b), 60 V (c), 90 V (d), 120 V (e), 150 V (f), 180 V (g), 200 V (h)

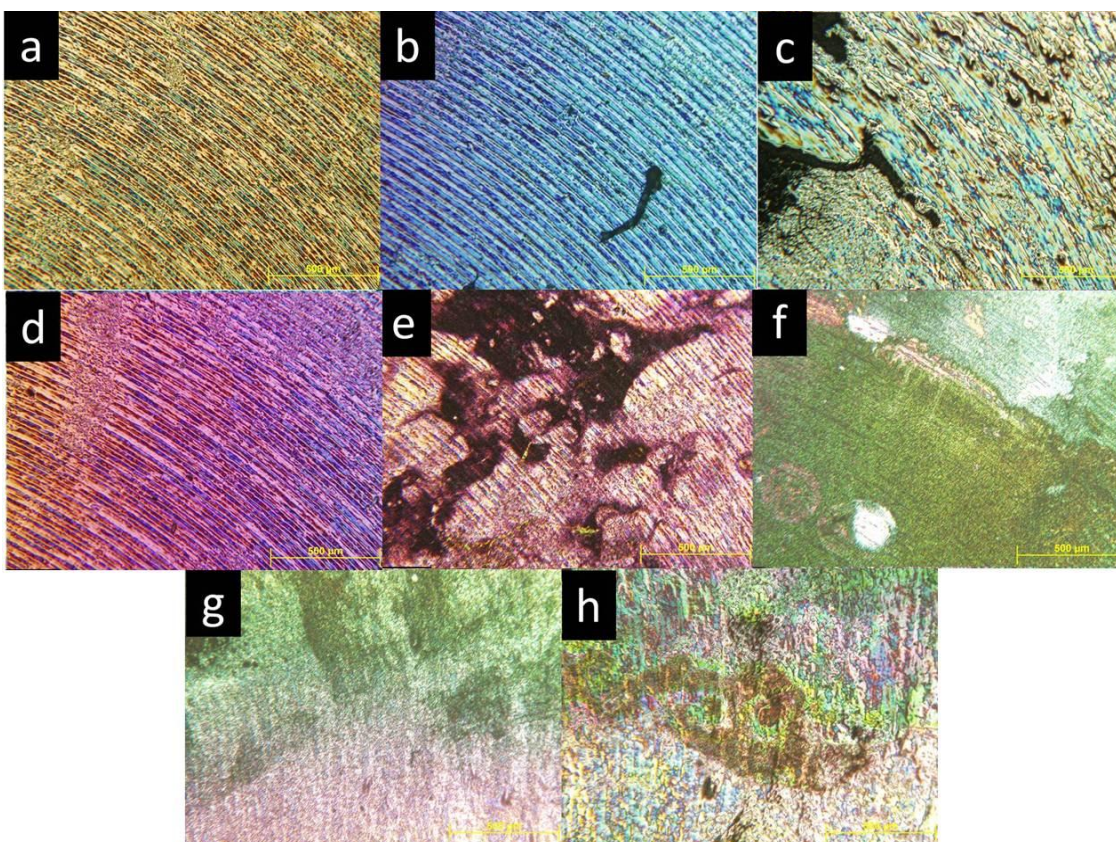


Figure 5. Reflected-light microscopy pictures of surfaces of the anodised nanograin Grade 2 titanium discs 10 V (a), 30 V (b), 60 V (c), 90 V (d), 120 V (e), 150 V (f), 180 V (g), 200 V (h)



## Conclusion

In our study we worked on disc segments of pure titanium, known as Grade 2 titanium, and nanograin Grade 2 pure titanium. Both materials can be used for medical implants. Before anodisation we treated the specimens with chemical etching and electropolishing. Chemical etching removed burrs and surface contamination, while electropolishing smoothed the surface.

For the anodising experiments applied voltages were between 10 and 200 V. The anodising bath was a mixture of 0.1 V/V% hydrogen-fluoride and distilled water and the temperature was 20 °C. During the process we used magnetic mixing.

Reflected-light microscopy images show that different voltages resulted in differently coloured titanium-dioxide layers, indicating varying thicknesses. On images we found that different grain sizes resulted in different oxide-layer thicknesses at the same voltage value. We found these layers contained local heterogeneities whose size increased with voltage.

Based on our experiments we can conclude that it is possible to create titanium-dioxide layers on the surface of pure titanium, and nanograin pure titanium. The thickness of the formed oxide layer depends mainly on the applied voltages and on the grain size.

---

## REFERENCES

1. Tanner A, Maiden MFJ, Lee K, Shulman LB, Weber HP. Dental Implant Infections. *Clinical Infectious Diseases*, 1997; 25(2):213–217, DOI: 10.1086/516243.
2. Yu X, Li Y, Wlodarski W, Kandasamy S, Kalantar-Zadeh K. Fabrication of nanostructured TiO<sub>2</sub> by anodization: A comparison between electrolytes and substrates. *Sensors and Actuators*, 2008;130(1):25–31, DOI:10.1016/j.snb.2007.07.076.
3. Macak JM, Tsuchiya H, Schmuki P. High-Aspect-Ratio TiO<sub>2</sub> Nanotubes by Anodization of Titanium. *Angewandte Chemie International Edition*, 2005;44(14):2100–2, DOI: 10.1002/anie.200462459.
4. Paulose M, Prakasam HE, Varghese OK, Peng L, Popat KC, Mor GK, Desai TA, Grimes CA. TiO<sub>2</sub> Nanotube Arrays of 1000 μm Length by Anodization of Titanium Foil: Phenol Red Diffusion. *The Journal of Physical Chemistry C*, 2007;111(41):14992–7, DOI: 10.1021/jp075258r.
5. Mor GK, Varghese OK, Paulose M, Grimes CA. Transparent Highly Ordered TiO<sub>2</sub> Nanotube Arrays via Anodization of Titanium Thin Films. *Advanced Functional Materials*, 2005;15(8):1291–6, DOI:10.1002/adfm.200500096
6. Chen Y, Wang XM, Lu SS, Zhang X. Formation of titanium oxide nanogrooves island arrays by anodization. *Electrochemistry Communications*, 2010;12(1):86–9.
7. Gong D, Grimes CA, Varghese OK, Wencong HU, Singh RS, Chen Z, Dickey EC. Titanium oxide nanotube arrays prepared by anodic oxidation. *Journal of Materials Research*, 2001;16(12):3331–4, DOI: 10.1557/JMR.2001.0457.
8. Diebold U. The surface science of titanium dioxide. *Surface Science Reports*, 2003;48(5–8):53–229, DOI: 10.1016/S0167-5729(02)00100-0.
9. Puckett SD, Taylor E, Raimondo T, Webster TJ. The relationship between the nanostructure of titanium surfaces and bacterial attachment, *Biomaterials*, 2010;31:706–713, DOI: 10.1016/j.biomaterials.2009.09.081.
10. Poznyak SK, Talapin DV, Kulak AI. Electrochemical oxidation of titanium by pulsed discharge in electrolyte. *Journal of Electroanalytical Chemistry*, 2005;579:299–310.

11. Li LH, Kong YM, Kim KW, Kim YW, Kim HE, Heo SJ, Koak JY. Improved biological performance of Ti implants due to surface modification by micro-arc oxidation. *Biomaterials*, 2004;25:2867-75.
12. Elias CN. Titanium dental implant surfaces. *Revista Matéria*, 2010;15:138-42.
13. Gubicza J, Fogarassy Zs, Krállics Gy, Lábár J, Törköly T. Microstructure and mechanical behavior of ultrafine-grained titanium. *Materials Science Forum*, 2008;589:99-104.
14. Krállics Gy, Malgin D, Raab GI, Alexandrov IV. Ultrafine Grained Materials III (eds). Proceedings of 2004 TMS Annual Meeting, Charlotte, North Carolina.
15. Nádai L, Katona B, Terdik A, Nagy P, Weszl M, Bognár E. Chemical etching and electropolishing of titanium. XVIII. FMTÜ, 2013:265-68, ISSN 2067-6 808.

*We would like to thank Liza Pelyhe, Torda Sélley, and Dávid Pammer for their contributions and for their help with the measurements. Special thanks for Miklós Weszl for his help and György Krállics for supplying the nanograin titanium rods. This work is connected to the scientific program of the "Development of quality-oriented and harmonized R+D+I strategy and functional model at BME" project. This project is supported by the New Hungary Development Plan (Project ID: TÁMOP-4.2.1/B-09/1/KMR-2010-0002).*

## INVESTIGATION OF METALLIC SURFACE AREA OF CORONARY STENTS

Dóra Károly<sup>1</sup>, Miksa Kovács<sup>1</sup>, Andrew Attila Terdik<sup>1</sup>, Eszter Bognár<sup>1,2</sup>

<sup>1</sup>Department of Materials Science and Engineering, Faculty of Mechanical Engineering, Budapest University of Technology and Economics

<sup>2</sup>MTA–BME Research Group for Composite Science and Technology

[karoly.dora@gmail.com](mailto:karoly.dora@gmail.com)

---

### Abstract

**OBJECTIVES:** Endovascular stents, such as coronary stents, are widely used for the treatment of narrowed or blocked blood vessels caused by plaque formation in the arteries. The narrowing of expanded blood vessels (restenosis) is perhaps the major complication associated with endovascular stent implantation that is believed to be caused by insufficient metallic surface area (MSA) in some stent designs. Our aim was to compare three examination methods which were developed at our department, to measure stent surface areas.

**METHODS:** The first method was manually performed using rotating equipment under a stereomicroscope. The second method, which has recently been developed, is an automated method using an integrated scanner and a rotating engine. Both methods aimed at converting the cylindrical stent into a flattened two-dimensional image in order to enable the measurement of stent surface area by imaging software. The third method is based on a calculation which uses various stent values such as diameter, length, and strut thickness. Each measurement process was tested on different types of stents.

**RESULTS:** Our findings showed that the methods gave similar results. The largest differences between the methods were speed and accuracy.

**CONCLUSIONS:** The results lead us to propose favouring the automated rotation method.

**Keywords:** coronary stent, metallic surface area (MSA), stent pattern, cell size, examination method

---

### 1. Introduction

In the European Union the commonest reason of death is diseases of the cardiovascular system, amongst which the most significant is coronary artery disease. The numbers are still increasing, so preventing this disease is a high priority in public health policy.<sup>1</sup>

Stent implantation is the primary method of angioplasty to treat atherosclerosis. A stent is a small mesh tube structure mounted on a balloon and delivered to the site of arterial narrowing by a catheter system. When the balloon is inflated, pressure expands the stent and causes its deformation plastically. After the deflation of the balloon and the removal of the catheter system, the newly expanded stent rigidly supports the arterial wall, alleviating the arterial narrowing. Therefore the artery is reopened to its full extent and blood flow to downstream tissues restored.<sup>2</sup> We prepared the following explanatory 3D models (*Figure 1*).

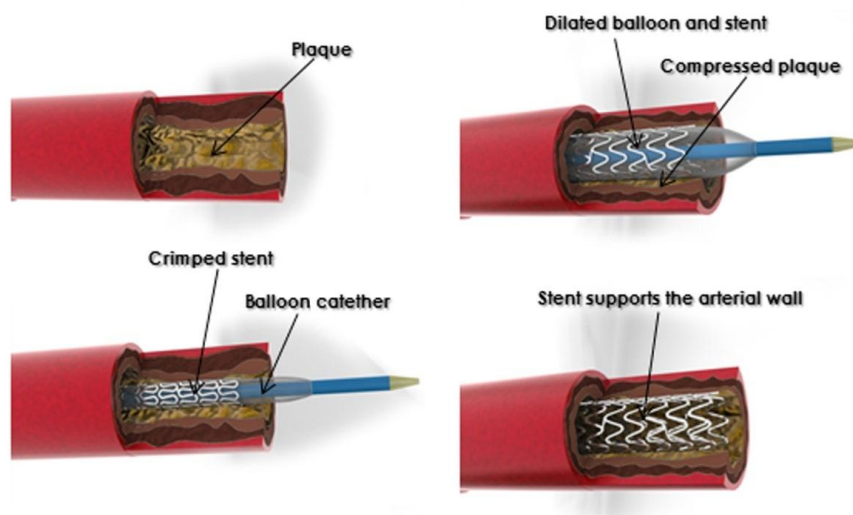


Figure 1. Stent dilating process

The narrowing of expanded blood vessels (restenosis) is perhaps the major complication associated with endovascular stent implantation. It is believed to be caused by inadequate MSA in stents.<sup>3</sup> The metallic surface area (MSA) of coronary stents is a ratio given as a percentage, of the stent's cylindrical surface to the covered surface of the blood vessel. For technical reasons too high a ratio is not recommended, because the contact area with the blood vessel wall is too large. In this case the risk of thrombus formation increases, increasing the risk of restenosis. On the other hand, too small a ratio can lead to mechanical problems.<sup>4</sup>

30-35% of all percutaneous coronary interventions involve small-diameter vessels of less than 3 mm. Small blood vessel size correlates with risk of restenosis after balloon angioplasty, as well as after stent placement. Stents deployed in small arteries have a higher metal-to-artery ratio; this may increase the risk of sub-acute thrombosis or restenosis. Various studies have shown that stent design, stent coating, and stent strut thickness may all influence event-free survival. Dedicated stents for small vessels with less metal (so a smaller metallic surface area), appropriate expansion properties and cell morphology, may further improve the results from stenting in this setting.<sup>5</sup>

Most studies related to stent surface focus on stent coatings. They are looking for a material, that meets mechanical requirements and generates an optimal biological response in the body. Because of this, knowing the exact size and geometry of the stent surface is very important. Furthermore, in the case of drug-eluting stents the stent pattern can also affect uniform dissolution.

In our work we looked at two experimental methods and a calculation to determine the MSA value and we compared their efficiency. All methods were developed at our department.

## 2. Methods and materials

In the study we investigated 4 coronary stents. (A) stent (Figure 2) and (B) stent (Figure 3) have the same geometry, but different size. (C1) stent (Figure 4) and (C2) stent (Figure 5) have the same geometry and size too. The stents were expanded at nominal pressure. The experimental methods are shown by the 3.0 x 8 mm, L605 CoCr (A) stent.

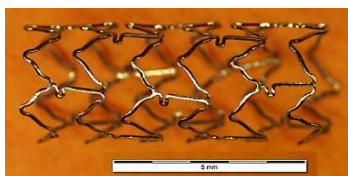


Figure 2. 3.0×8 mm stent (A)

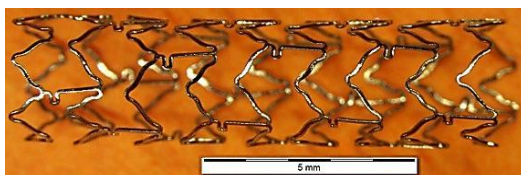


Figure 3. 3.0×12 mm stent (B)

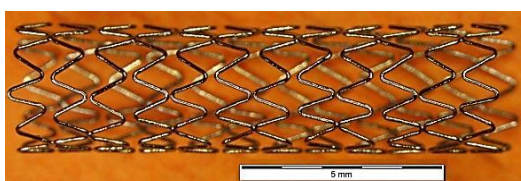


Figure 4. 3.0×12 mm stent (C1)

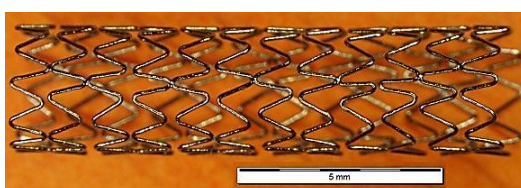


Figure 5. 3.0×12 mm stent (C2)

| Stent name | Diameter [mm] | Length [mm] | Mass [mg] | Density [g/cm <sup>3</sup> ] | Strut thickness [mm] | Nominal pressure [10 <sup>5</sup> Pa] | Material    |
|------------|---------------|-------------|-----------|------------------------------|----------------------|---------------------------------------|-------------|
| (A)        | 3.0           | 8           | 9.5       | 9.1                          | 0.085                | 9                                     | CoCr (L605) |
| (B)        | 3.0           | 12          | 11.2      | 9.1                          | 0.085                | 9                                     | CoCr (L605) |
| (C1)       | 3.0           | 12          | 17.7      | 9.1                          | 0.091                | 9                                     | CoCr (L605) |
| (C2)       | 3.0           | 12          | 17.7      | 9.1                          | 0.091                | 9                                     | CoCr (L605) |

Table 1. Data for the investigated stents

Table 1 shows the investigated stent systems' basic dimensions. Investigations were performed by stereo microscopy and a scanner. Surface areas were determined by evaluating the digital images with image analysis software. Evaluation was performed with JMicroVision measuring software. All measurements correspond to the MSZ EN ISO 25539-2 standard.<sup>6</sup>

## 2.1 The manual method

The first method was performed by manual stereo-microscopy. High-resolution digital images were taken of each segment of the stents' mantle. The pictures were taken with a stereo microscope fitted to a precision rotary unit. The stents were rotated by increments of 15° from the starting 0° position to 360°. The 24 pictures were then joined to each other, and examined with image analysis software.

## 2.2 The automatic method

The second method was done in an automated manner by a new configuration. The stents were pulled up to a shaft connected to a motor, so that the stents were rotating during the scanning process. In this case we get one whole picture of the stent pattern. The rotational speed and direction can be changed using the buttons of the control panel. Pictures were taken at a resolution of 4800 DPI. The Canon CanoScan LiDE 700F scanner that we used has a 9600 DPI resolution, so the images have far better quality than required.

Both (the first and the second) methods aimed at converting the cylindrical stent into a flattened 2 dimensional image in order to analyse the stent pattern with imaging software. With the stent pattern, the largest and the smallest cell area, and the maximum achievable cell diameter in them can be easily determined by an image analysis program. This feature is useful when another stent needs to be placed into a side branch of a vessel and the physician has to go through one of the stent cells with another stent or a balloon catheter.

## 2.3 The calculation

The third method is based on a calculation using various stent values such as stent diameter, length and strut thickness. If we imagine an ideal tube where we know the material (and thus density of the material), and set the outer diameter, length and wall thickness to be the same as the stent's, then by defining these features we can calculate the mass of the ideal tube which would have a 100% MSA value. We use the following formula (Equation 1):

$$m_{\text{tube}} \approx d \cdot \pi \cdot l \cdot s \cdot \rho, \quad (1)$$

where  $m_{\text{tube}}$ : mass of the tube,  $d$ : stent outer diameter,  $l$ : stent length,  $s$ : tube's wall thickness (so the strut thickness of the stent),  $\rho$ : density of the stent.

We get the metallic surface area (MSA) from the ratio of the stent mass ( $m_{\text{stent}}$ ) and the calculated mass of the ideal tube which has 100% MSA value (Equation 2).

$$\text{MSA} = \frac{m_{\text{stent}}}{m_{\text{tube}}} \cdot 100[\%] \quad (2)$$

To determine the strut thickness a slide was made from a normal (perpendicular) section of the struts. Given a large number of test samples, this significantly complicates the measurements. Also, this calculation only gives information about the MSA value and nothing about cell sizes.

### 3. Results

Our findings showed that the first and the second methods gave similar results (Figure 6). The third method gave a different MSA value for the (B), (C1) and (C2) stents. These are early estimates, but further studies will explore possible reasons for the difference.

The location of the largest and smallest cells are the same with the manual and the automatic method, except in the case of (C1) stent, where the location of the largest cell was different. Since the difference between the largest and the second largest cell was negligibly small, the error might be due to inappropriate joining of images.

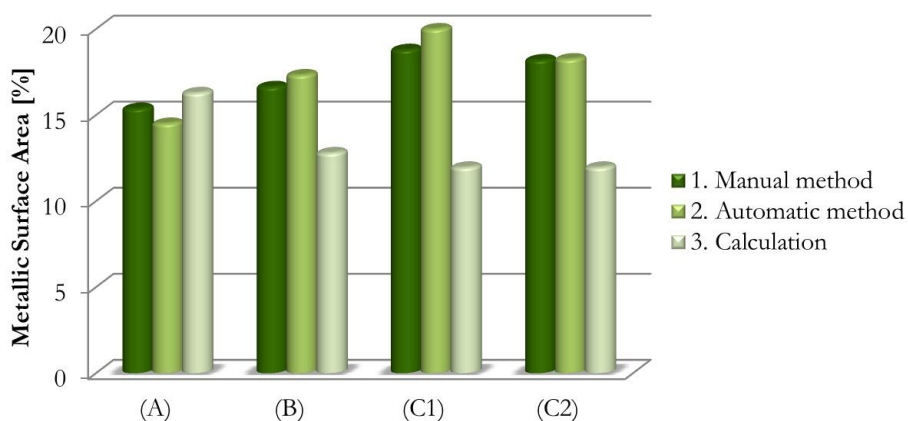


Figure 6. MSA values with the three methods

Figure 7 shows the stent pattern of stent (A) with the manual and the automatic method. The largest cell is yellow, the smallest cell is blue, and the circles with the maximum achievable diameter are red. Each stents' cells were counted; (A) has 12 cells, (B) has 15 cells, (C1) and (C2) both have 24 cells.

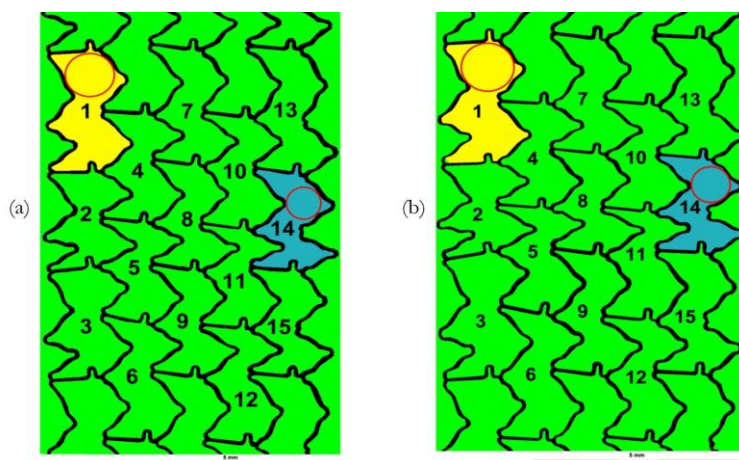


Figure 7. The evaluated stent pattern of stent (A) (a) with the manual method (b) with the automatic method

The metallic surface areas of all these stents are maximum 20%. This is appropriate for the re-formation of the intima cell layer. The measurement results are given with the following markings (Table 2):

- largest cell area (marked in yellow in Figure 7): ALC [mm<sup>2</sup>]
- maximum diameter of the circle in the largest cell (marked in red in Figure 7): DLC [mm]
- smallest cell area (marked in blue in Figure 7): ASC [mm<sup>2</sup>]
- maximum diameter of the circle in the smallest cell (marked in red in Figure 7): DSC [mm]
- average cell area: AAC [mm<sup>2</sup>]

| Stent       | Method   | MSA [%] | A <sub>LC</sub> [mm <sup>2</sup> ] | A <sub>SC</sub> [mm <sup>2</sup> ] | A <sub>A</sub> [mm <sup>2</sup> ] | D <sub>LC</sub> [mm] | D <sub>SC</sub> [mm] |
|-------------|----------|---------|------------------------------------|------------------------------------|-----------------------------------|----------------------|----------------------|
| <b>(A)</b>  | 1. Man.  | 15.38   | 4.12                               | 2.72                               | 3.33                              | 1.25                 | 0.89                 |
|             | 2. Auto. | 14.51   | 4.03                               | 2.70                               | 3.31                              | 1.25                 | 0.91                 |
|             | 3. Cal   | 16.29   |                                    |                                    |                                   |                      |                      |
| <b>(B)</b>  | 1. Man.  | 16.64   | 3.58                               | 2.41                               | 2.99                              | 1.08                 | 0.93                 |
|             | 2. Auto. | 17.33   | 3.62                               | 2.22                               | 2.94                              | 1.07                 | 0.89                 |
|             | 3. Cal   | 12.80   |                                    |                                    |                                   |                      |                      |
| <b>(C1)</b> | 1. Man.  | 18.80   | 3.88                               | 1.61                               | 3.14                              | 0.83                 | 0.68                 |
|             | 2. Auto. | 20.32   | 3.88                               | 1.77                               | 3.26                              | 0.86                 | 0.71                 |
|             | 3. Cal   | 11.96   |                                    |                                    |                                   |                      |                      |
| <b>(C2)</b> | 1. Man.  | 18.20   | 4.06                               | 1.70                               | 3.19                              | 0.81                 | 0.68                 |
|             | 2. Auto. | 18.25   | 4.04                               | 1.79                               | 3.25                              | 0.81                 | 0.69                 |
|             | 3. Cal   | 11.96   |                                    |                                    |                                   |                      |                      |

Table 2. The measurement results

#### 4. Discussion

The largest differences between the methods were speed and accuracy. Calculation was the quickest, but it gives just estimated results without cell sizes. Further studies will be taken to explore the accuracy of this method.

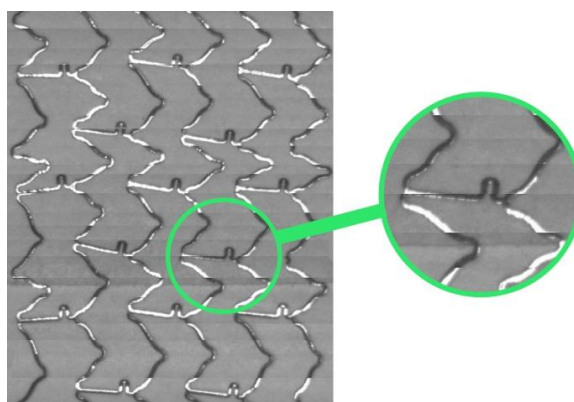
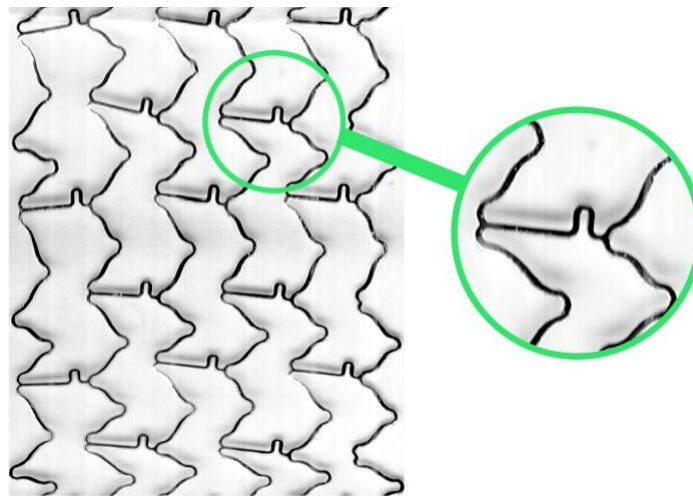


Figure 8. Stent (A) pattern with the manual method



The automatic method also needs less time (the difference is in hours), because the pictures did not need to be joined together. This is an important factor when the stent is too long to fit in the microscopic field. In that case separate images are taken of both ends of the stent, and then 48 images have to be joined up to create one big image. Resulting errors are multiplied during image editing, and time needed also increases.

In addition, *Figure 8* clearly shows that the struts reflect light in the microscope pictures of the metal stent surface. Bright and dark parts seem to have different strut widths which need to be corrected during evaluation. This both takes more time and causes inaccuracy. In contrast, reflective glare is eliminated in the images taken by scanner (*Figure 9*).



*Figure 9.* Stent (A) pattern with the automatic method

## 5. Conclusion

Some stent properties are important during implantation such as crossing profile or flexibility of the stent system, and others are important for the long-term effectiveness of the stent after implantation such as metallic surface area, the largest and the smallest cell sizes, and the maximum achievable cell diameter.

We used 3 methods to measure MSA values. These results favour the automatic method, which on the basis of this study seems to give the most information, most accurately, in the shortest time. The collected experience and results of this study provide a basis for further research. We plan to use the obtained image data to create a three-dimensional stent model and run finite-element simulations to predict mechanical properties of stents with given defined patterns.

## REFERENCES

1. Bertrand OF, et al, Biocompatibility Aspects of New Stent Technology. J Am Coll Cardiol, 1998;32: 562–71.
2. Ning L, Yuanxian G. Parametric Design Analysis and Shape Optimization of Coronary Arteries Stent Structure. 6th World Congresses of Structural and Multidisciplinary Optimization, Rio de Janeiro, 2005 May 30 – June 3.
3. Takács T, Bognár E, Dobránszky J. Az újraszűkülést befolyásoló paraméterek vizsgálata coronariastenteken. LAM 2010;20(3–4):227–233.
4. Ring Gy. Koszorúérsztentek és más endoprotézisek preklinikai vizsgálata. BME GPK PhD dissertation. Budapest, 2010.
5. Roguin A, Grenadier E. Stent-based percutaneous coronary interventions in small coronary arteries. Acute Card Care, 2006;8(2):70-4.
6. MSZ EN ISO 25539-2:2009 Cardiovascular implants. Endovascular devices. Part 2: Vascular stents (ISO 25539-2:2008)

*First we would like to thank János Dobránszky for valuable advice. Further we would like to thank the Department of Materials Science and Engineering and colleagues there for providing us with the environment and facilities to complete this project. Also, we would like to take this opportunity to thank Vascular Venture Ltd. for providing us with stents. This work is connected to the scientific program of the "Development of quality-oriented and harmonized R+D+I strategy and functional model at BME" project. This project is supported by the New Hungary Development Plan (Project ID: TÁMOP-4.2.1/B-09/1/KMR-2010-0002).*

## NOVEL MINIMAL INVASIVE SURGICAL TECHNIQUES FOR THE TREATMENT OF SEGMENTAL-LATERAL PATHOLOGIC LESIONS OF THE SPINE, PRESERVING THE DORSAL STABILIZING STRUCTURES

Zoltán Papp<sup>1</sup>, János Vajda<sup>1</sup>, Róbert Veres<sup>1</sup>, Péter Banczerowski<sup>1,2</sup>

<sup>1</sup>National Institute of Neurosurgery, Dept. of Spine Surgery, Budapest

<sup>2</sup>Semmelweis University, Faculty of Medicine, Dept. of Neurosurgery

[zolpapp@oiti.hu](mailto:zolpapp@oiti.hu)

---

### **Abstract**

**Objective:** Laminectomy, the commonly used dorsal approach for the surgical removal of most of the pathologic lesions, situated in the spinal canal and the neuroforamen destroying the dorsal stabilizing structures of the spinal column. Retraction and detachment of the longitudinal muscles, removal of the vertebral arches (laminectomy), and injury of the joint capsules and ligaments are responsible most of short and late-time complications. Among of these complications spinal deformities, segmental instability and permanent spinal pain are most often mentioned in the literature.

The main objective of the authors was to develop and evaluate the novel minimally invasive techniques suitable for exploring and treating different segmental-lateral pathologies, expanding to the neuroforamen or even paravertebrally, with preservation of the stability of the spine. One of the key issues of this article was to summarize these procedures, with evaluating the safety and efficacy in the routine spine surgery.

**Methods:** 153 patients were operated and followed up during 2000 to 2010 in our Institute with segmental lateral spinal pathologies. For the surgical treatment we used “Over-the-top” decompression, hemi-semi laminectomy, supraforaminal burr-hole, open-tunnel and paravertebral approaches alone or combined with each-other. The above mentioned surgical techniques are mostly our developments, or modifications of previously used surgical techniques.

**Results:** The new surgical procedures developed or modified by our team, are effective techniques for treating the spinal pathologies located in the spinal canal, neuroforamen or even the paravertebral space. The posterior stabilizing structures of the spine, as the vertebral laminae and the longitudinal musculature are mostly preserved. Leaving the longitudinal paraspinal musculature innervations intact, and with the preservation of the bone-muscle attachments and ligaments, the dynamic stability of the spine remains unchanged. Retaining the bony structures (vertebral arches) and the vertebral joints the static stability of the spinal column remain intact, the chance of developing the long-term spinal deformation is minimal.

During the follow up we performed static and dynamic X-ray, MR and CT scans, completed with neurological examinations to evaluate the progression of the illness, the neurological deficit and the actual state of the spinal column. With clinical use and evaluation of the various surgical approaches we determined the main indications and contraindications of the surgical procedures, highlighting the pit-falls and limitations.

**Conclusion:** The above mentioned minimally invasive surgical approaches are suitable for treating segmental – lateral spinal pathologies. . For the routine clinical use we organized the surgical techniques into a complete framework based on the location of the pathologic lesions.

**Keywords:** partial hemilaminectomy, dumbbell tumour, foraminotomy

---

## Introduction

The use of the classical laminectomy for dorsal approach to the pathologic lesions located in the spinal canal is widely used in spine surgery. Removal even of one vertebral arch, with detachment of the paravertebral muscles and uni- or bilateral destruction of the facet joints and ligaments are leading to the well-known short and long term complications. The most mentioned in the literatures are the persistent pain, spinal deformities, instability, even subluxation.<sup>7-8,10,21</sup> Several surgical techniques found in the literature to preserve the posterior structures, but most of them focused on multilevel spinal pathologies.<sup>4,6,9,11,12,18</sup>

One spinal segment consists of the two joining vertebrae with all of the ligaments and muscles connecting them to each-other. Our novel classification system for treatment of spinal disorders based on the intraspinal localization of pathologic lesions. Mainly, the lesions are localized in the spinal canal in segmental-lateral or axial-longitudinal situation. New minimal invasive spine surgery techniques have been developed with the goal to achieve better clinical outcomes, with the preservation of the dynamic and static stabilizing structures of the spinal column in treatment of the segmental-lateral pathologic lesions.<sup>8,9,11-12,17</sup>

The purpose of our retrospective study is to summarize the minimal invasive procedures with describing technical features, advantages, complications and clinical outcomes for treating segmental-lateral pathologies, located in the spinal canal, in the neuroforamen, or even paravertebrally.<sup>3,5,13,14-16</sup>

## Clinical Materials and Methods

Between 2000 and 2010 the authors performed 153 surgical procedures on patients with segmental-lateral pathologic lesions. Regarding to the minimal invasive surgical concept, every patients were operated with the following surgical techniques, thus are developed by our team, or modification of a previously used surgical technique.

### *Over-the-top decompression:*

Unilateral approach and short paravertebral muscle retraction performed, throughout a midline incision, on prone positioned patient. To achieve the sufficient decompression of the neural structures the medial part of the articular process, partially the upper and lower laminae arch, the base of spinous process, the ventral part of the interspinous ligament and the ligamentum flavum on both sides were removed. We operated 51 patients with one segment degenerative spinal canal stenosis.

### *Hemi-semi laminectomy:*

This approach also mentioned as partial hemilaminectomy.<sup>2,22</sup> The patient in prone position. The paraspinal muscles are dissected and retracted. The upper and lower arches of the laminae are drilled severally or in case of need altogether at the level of the lesion. The integrity of laminae remains intact. For wider surgical view, the base of spinous process may be removed. The interspinous ligaments are remained intact. 86 patients were operated during the evaluated time

period (2000-2010) with one to three segment “hemi-semi laminectomy“ technique. Histological distribution was as follows: 32 meningiomas, 27 neurinomas, 12 ependymomas, 3 arachnoideal cysts, 4 epidural haematomas, 5, epidural abscesses, 3 dural arterio-venous fistulas. (*Figure 1, Figure 2*)

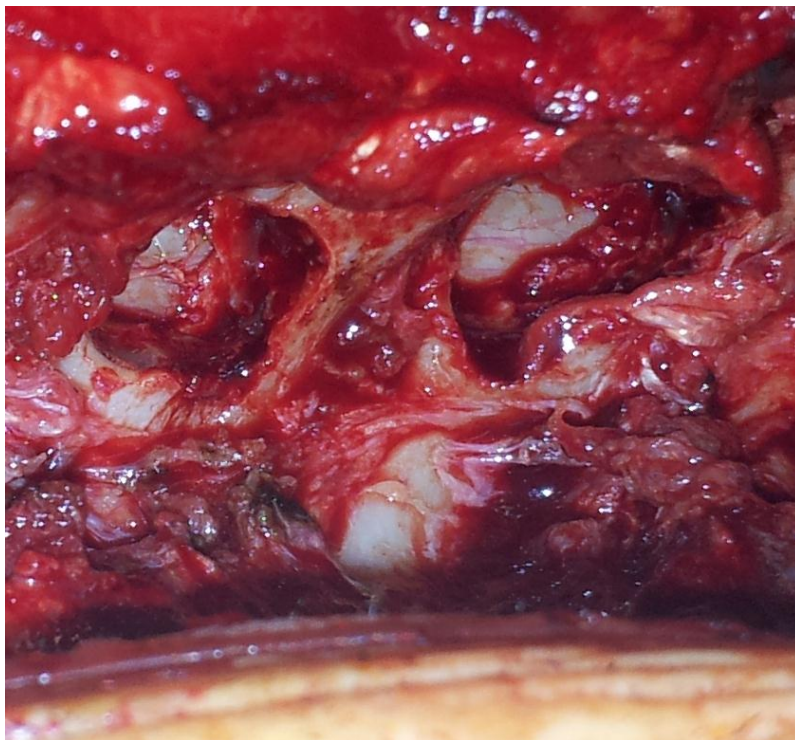


*Figure 1.* Intraoperative photograph showing two levels hemi-semi approach, on the thoracic spine, right side. The paraspinal muscles retracted on the right side, and the upper and lower arches of the laminae are drilled. The dura is not yet opened.

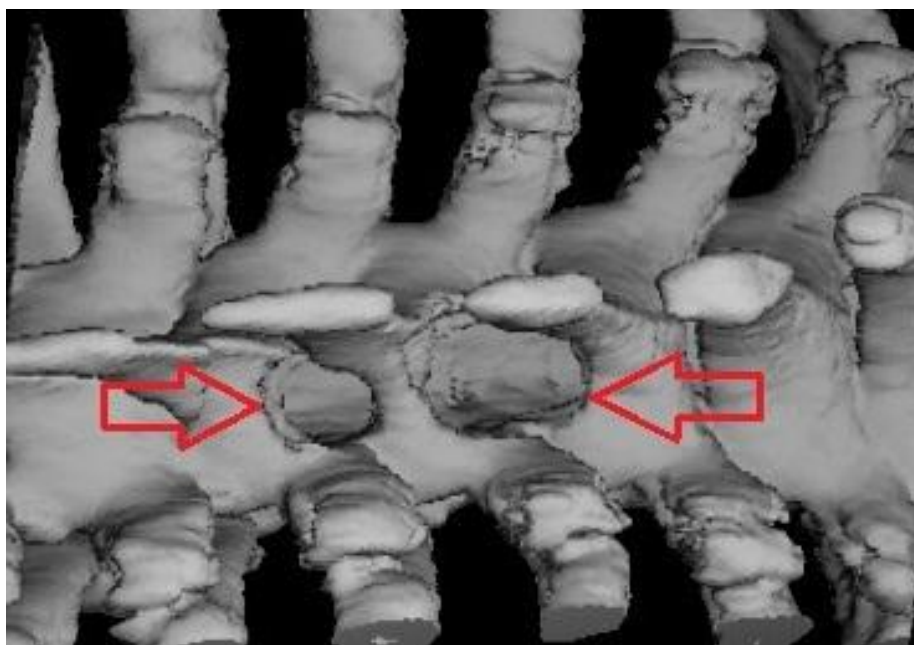


*Figure 2.* Postoperative three dimensional reconstructed computer tomographic image showing hemi-semi laminectomy approach and the fenestrated laminae on the thoracic spine.

*Supraforaminal burr-hole:*

This approach is suitable for the treatment of lesions extending to the neuroforamen. A hemi-semi laminectomy was done the above mentioned way, than the intervertebral foramen exposure was performed across the medial part of the facet joint with a high speed drill with the aim of sparing as much facet as possible. Throughout this 5-7mm wide burr-hole the removal of the intraforaminal part of the lesion was achieved. 7 patients were operated with neurinomas extending to the neuroforamen in the cervical spine. In 4 cases we removed schwannomas, and 3 cases neurofibromas. (Figure 3.)

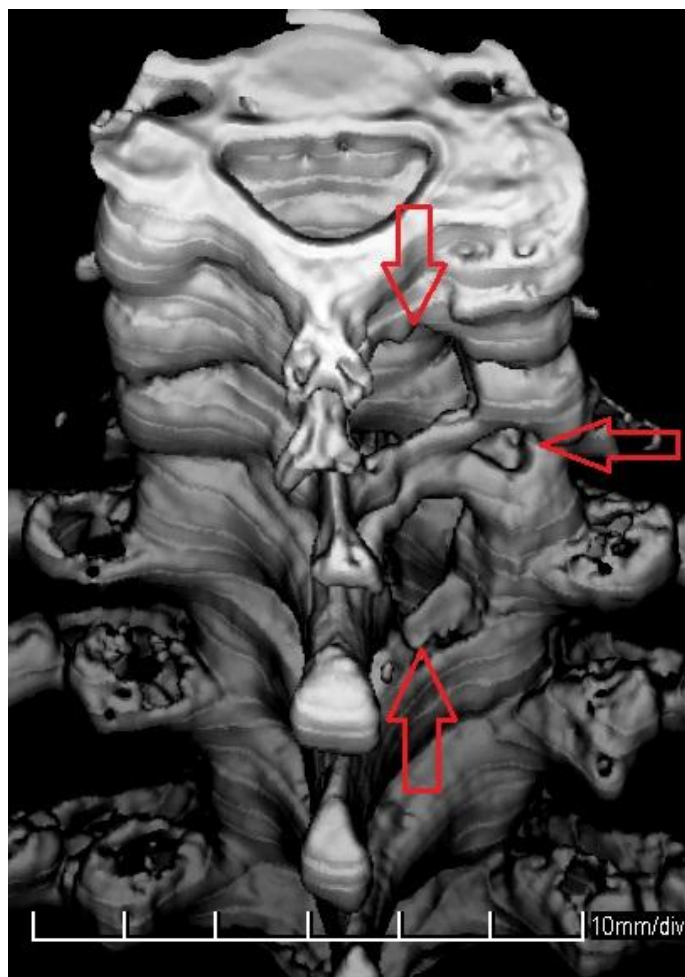


Figure 3. Postoperative three dimensional reconstructed computer tomographic image showing hemi-semi laminectomy with supraforaminal burr-hole approach on the cervical spine.

*Open-tunnel:*

This procedure consists of a hemi-semi laminectomy and the removal of the lateral part of the facet joints. With this approach, both end of the neuroforamen are opened, the tumor removal can be achieved, preserving the bony structures and facet joint as well. Patients are in prone position. After a midline or slightly parasagittal skin incision the paravertebral muscles were dissected and retracted as far as the lateral edge of the facet joints. At the level of the lesion a hemi-semi laminectomy was done. The intraforaminal components of the lesions are exposed from the inner side of the spinal canal through the hemi-semi laminectomy and from the outside made by the partial removal of the lateral part of the facet joint. The exit of the neuroforamen is

opened and tumor removal is possible from both ends of the opened „tunnel” with sparing the facet joints as much as possible. With this operative technique 6 patients were treated with schwannomas, while 3 with neurofibromas between 2000 and 2010. (Figure 4., Figure 5.)

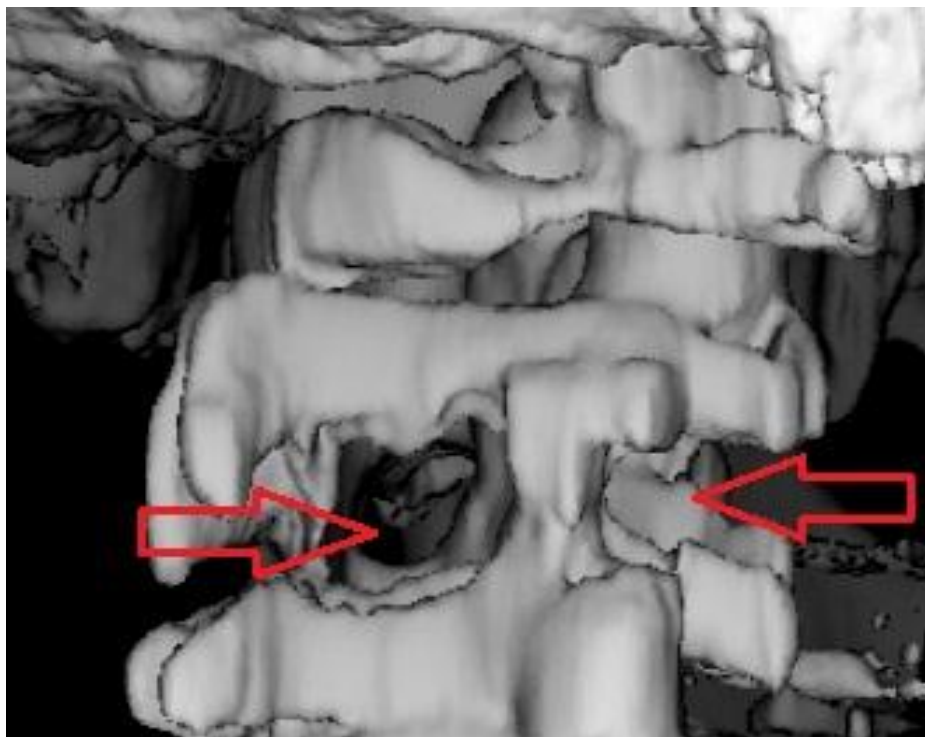


Figure 4. Postoperative three dimensional reconstructed computer tomographic image showing the open-tunnel approach at C2 level.

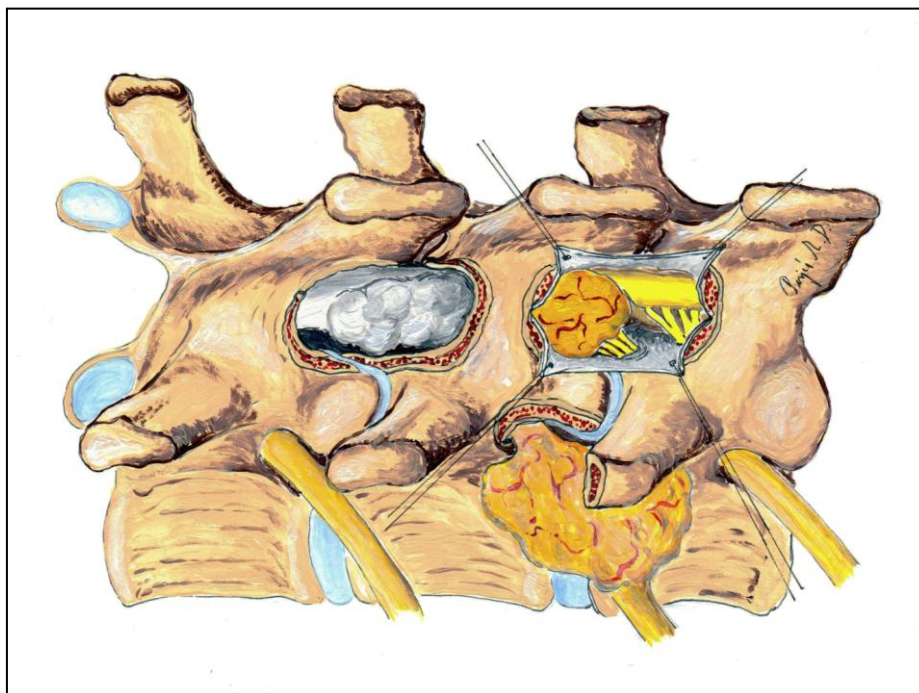


Figure 5. Schematic showing a thoracic dumbbell tumor and the “open-tunnel” approach. The inner part of the tumor removed during two level hemi-semi laminectomy approaches, while the paraspinal part resected directly. The neuroforamen opened at both end, and the remaining tumor was “pulled out”.

## **Results**

Postoperatively regular control examinations were done. On patients with degenerative spinal canal stenosis we performed CT and MR scans to verify the extent of the decompression of the neural structures. On tumor patients we did regular MR scans to follow the progression of lesion. Both patient group we performed static and dynamic X-ray examinations, to uncover the signs of segmental instability. All of the patients undergone neurological examinations regarding the initial symptoms as well.

All of the surgical approaches and procedures were sufficient to treat the selected pathologic lesions.

76% of the patients operated with “over-the-top” decompression technique have neurologic claudication symptoms eliminated, and the remaining 24% mentioned significant reduction. The low back pain was disappeared in 13%, reduced in 63%, and not changed in 24%. No sign of instability was detected.

Use of the hemi-semi laminectomy approach all of the pathologic lesions were removed completely.

All of the tumors, expanding to the neuroforamen were removed completely with combination of hemi-semi laminectomy and the supraforaminal burr-hole technique but one, because unseparable infiltration of the C6 nerve root. Instability in cervical spine flexion and extension did not occur during the follow up period.

The use of “open-tunnel” technique the extent of resection or neurological outcome was satisfactory. Regarding to the minimal invasive surgical approaches the skin incision and paraspinal muscle dissection was shorter, comparing to the “classic” dorsal surgical procedures. Early postoperative mobilization was allowed at every case. The average length of the hospital stay was 7.2 days (range 6-9 days).

No sign of spinal instability found during the follow-up period.

## **Discussion**

The most frequently used dorsal surgical approach for treatment of spinal lesions has been laminotomy until the last two decades. The surgical treatment of multilevel spinal pathologic lesion requires long, destructive approaches with multiple laminectomies and sacrifice of the attachments of the paraspinal muscles, the facet joints, and the ligaments. To avoid the postoperative complications various types of surgical techniques have been developed.<sup>6,9,12,15</sup> The main objective of these innovations to preserve and reconstruct the posterior spinal structures. Beyond the disadvantageous effect of the multilevel approaches the preservation of the anatomical and functional spinal segment is highlighted in the literature. For treating the segmental pathologic lesions also the laminectomy was the mostly used dorsal approach. Removal of one laminar arch with cutting the inter,- and supraspinosus ligaments, bilateral detachments of paraspinal muscles and destruction of facet joints are the most frequent cause of disturbance of the sagittal balance. Other important factor for development of long term complications is the segmental instability. The above mentioned irreversible changes accelerate



the ongoing degenerative procedures on the entire spinal column, advancing the long term symptoms and even neurological impairments.

The literature emphasizes the important role of the deep extensor muscles, especially in the neck. The multifidus and the semispinalis cervicis muscles act as dynamic stabilizers of the cervical spine together with the important static stabilizer structures, including the intervertebral discs, the vertebral arches, ligaments and intervertebral joint capsules. Once these muscles have been detached, it is impossible to reconstruct the complicated anatomy. The integrity of the nerves is also important because if they are injured (branches ramified from the dorsal ramus), preservation of the muscles becomes meaningless.<sup>20</sup>

According to the up-to-date biomechanical concepts new surgical approaches have been developed to avoid the short and long term complications of treatment the (one) segmental-lateral pathologic lesions.<sup>15,19,20</sup> All of these surgical procedures preserving the paraspinal muscle attachments and also the innervation of these muscles. The muscle retraction performed unilaterally, the contralateral side remain totally intact. Using the keyhole concept, the exploration of the spinal canal, and the neuroforamen needs only partial bone removal. The laminar arch remains intact at every approach. In consequence of this the various forces evoking in the course of spinal movements transmitted physiologically throughout the pedicles to the vertebral body. Due to the intervertebral facet joints and ligaments are not injured with these surgical techniques, the segmental stability does not affected.

With the above mentioned methods the operative field is restricted compared to laminectomy, but according to the keyhole principle, it is still enough under the operating microscope for the surgery of lesions located within the spinal canal, in the neuroforamen or paravertebrally.

Between 2000 and 2010 we operated 153 patients with segmental-lateral pathologic lesions with the newly developed or renewed minimal invasive surgical technique. During this period we determined the indications and limits of the procedures and arranged them into a framework based on the localization of the pathologic lesion. Based on our experience, these procedures are safe on all spinal segments (the cervical, thoracic, and lumbar spine) with an acceptable complication rate. Our novel, modified, minimally invasive technique enables surgeons to obtain a sufficient field for exploring different segmental-lateral spinal pathologies that require spinal canal decompression with preservation of the posterior structures of the spine and the attachments of the muscles.

## **Conclusion**

The minimally invasive surgical techniques for treating segmental-lateral pathologic lesions are safe and effective surgical procedures. The extent of resection are not affected by the newly developed approaches. The posterior dynamic and static stabilizing structures of the spine, as the vertebral laminae, the joint capsules, ligaments, and the longitudinal musculature are mostly preserved. Preservation of these structures helps to avoid the short and long term complications of the widely used laminectomy.

## REFERENCES

1. Brotchi. Intrinsic spinal cord tumor removal. *Neurosurg* 2002;50:1059-63.
2. Banczerowski P, Vajda J, Veres R. Removal of intraspinal space-occupying lesions through unilateral partial approach, the "hemi-semi laminectomy". *Clin Neurosci/Idegy Szle* 2008;61:114–22.
3. Cherqui A, Kim DH, Kim SH et al. Surgical approaches to paraspinal nerve sheath tumors. *Neurosurg Focus* 2007;22:E9
4. Chiou Sh-M, Eggert HR, Laborde G et al. Microsurgical unilateral approaches for spinal tumour surgery: Eight years experience in 256 primary operated patients. *Acta Neurochir* 1989;100:127–33.
5. Conti P, Pansini G, Mouchaty H et al. Spinal neurinomas: retrospective analysis and long-term outcome of 179 consecutively operated cases and review of the literature. *Surg Neurol* 2004;61:34 – 43.
6. Eggert HR, Scheremet R, Seeger W et al. Unilateral microsurgical approaches to extramedullary spinal tumours: Operative techniques and results. *Acta Neurochir* 1983;67:245–53.
7. Hosono N, Yonenobu K, Ono K. Neck and shoulder pain after laminoplasty. A noticeable complication. *Spine* 1996;21:1969-73.
8. Hukuda S, Ogata M, Mochizuki T, Shichikawa K. Laminectomy versus laminoplasty for cervical myelopathy: brief report. *J Bone Joint Surg (Br)* 1988;70:325-6.
9. Kato Y, Kaneko K, Kataoka H et al. Cervical hemilaminoplasty: technical note. *J Spinal Disord Tech* 2007;20:296–301.
10. Katsumi Y, Honma T, Nakamura T. Analysis of cervical instability resulting from laminectomies for removal of spinal cord tumour. *Spine* 1989;14:1171-6.
11. Kehrli P, Bergamaschi R, Maitrot D. Open-door laminoplasty in pediatric spinal neurosurgery. *Child Nerv Syst* 1996;12:551–2.
12. Koch-Wiewrodt D, Wagner W, Pernecky A. Unilateral multilevel interlaminar fenestration instead of laminectomy or hemilaminectomy: an alternative surgical approach to intraspinal space-occupying lesions. *J Neurosurg Spine* 2007;6:485–92.
13. Lot G, George B. Cervical neuromas with extradural components: surgical management in a series of 57 patients. *Neurosurgery* 1997;41:813–20.
14. MacCormick PC. Surgical management of dumbbell tumors of the cervical spine. *Neurosurg* 1996;38 :294–300.
15. Ogdena AT, Bresnahanb L, Smith JS, Natarajand R, Fesslerb RG. Biomechanical comparisons of traditional and minimally invasive intradural tumor exposures using finite element analysis. *Clinical Biomechanics* 2009;24:143-7.
16. Ozawa H, Kokubun S, Aizawa T et al. Spinal dumbbell tumors: an analysis of a series of 118 cases. *J Neurosurg Spine* 2007;7:587–93.
17. Sarioglu AC, Hanci M, Bozkus H et al. Unilateral hemilaminectomy for the removal of the spinal space-occupying lesions. *Minim Invas Neurosurg* 1997;40 :74 –7.
18. Shikata J, Yamamuro T, Shimizu K et al. Combined laminoplasty and posterolateral fusion for spinal canal surgery in children and adolescents. *Clin Orthop Related Res* 1990;259:92–9.
19. Raimondi AJ, Guterrez FA, Di Rocco C. Laminotomy and total reconstruction of the posterior arch for spinal canal surgery in childhood. *J Neurosurg* 1976;45:550-60.
20. Zhang J, Tsuzuki N, Hirabayashi S, Saiki K, Fujita K: Surgical anatomy of the nerves and muscles in the posterior cervical spine: A guide for avoiding inadvertent nerve injuries during the posterior approach. *Spine* 2003;28:1379–84.
21. Yasuoka S, Peterson HA, MacCarthy CS. Incidence of spinal column deformity after multilevel laminectomy in children and adults. *J Neurosurg* 1982;57:441-5.

22. Yasargil MG, Tranmer BI, Adamson TE et al. Unilateral partial hemilaminectomy for the removal extra- and intramedullary tumors and AVMs. In: Symon I, ed. *Advances and technical standards in neurosurgery*. Vol 18, Springer Verlag, Wien; 1991. p.113–32.

## FINITE ELEMENT ANALYSIS OF LONG-TIME AGING AND SUDDEN ACCIDENTAL DEGENERATION OF LUMBAR SPINE SEGMENTS IN COMPRESSION

Márta Kurutz<sup>1</sup>, László Oroszvály<sup>2</sup>

<sup>1</sup>Budapest University of Technology and Economics

<sup>2</sup>Knorr Bremse Hungaria Ltd

[kurutzm@eik.bme.hu](mailto:kurutzm@eik.bme.hu)

---

### Abstract

3D finite element analysis of long term aging and sudden accidental degeneration processes is presented for physiologic compression load. A systematic modeling and simulation is applied for analyzing the separated and mutual effect of certain material moduli of the components of lumbar motion segments on the mechanical behaviour and stability of the segment during the long time and sudden degeneration processes. It was concluded that due to their smallest stiffness the younger segments with light degeneration are the most vulnerable during both the long-time age-related and the sudden overload-related degeneration.

**Keywords:** finite element simulation, age-related degeneration, sudden accidental degeneration, lumbar motion segment, compressive stiffness

---

### Introduction

Numerical analyses are able to simulate biomechanical processes in their progress that are impossible to be followed experimentally, like spinal degeneration processes. Degeneration represents special and injurious changes in the structure, composition and function of spine or part of the spine, caused by aging or by certain accidental injurious effects, like a wrong movement or mechanical overloading.<sup>1</sup>

The age-related changes of spine start generally in the intervertebral discs; within the disc nucleus, altering markedly the mechanics of load transfer and spinal stability.<sup>2</sup> The age-related changes of the disc are manifested in loss of hydration, a drying and stiffening procedure in the texture of both nucleus and annulus.<sup>3</sup> Aging procedures are often accompanied by other kinds of degeneration: buckling, lesions, tears, fiber break in the annulus<sup>8,9</sup> or osteoporotic changes in the vertebral bone. However, some degeneration can happen suddenly, due to some traumatic effects causing disc prolapse, endplate disruption or osteoporotic vertebral fracture. These kinds of sudden degenerations can happen at any age.

Several recent studies conclude that instability of lumbar spine happens to the younger discs, and the stability restores with further aging.<sup>3-5</sup> Since sudden degenerations may also be dangerous in young age, further studies are necessary for understanding the biomechanical function of degeneration processes. Although FE modeling of lumbar spine focused recently to degenerations, there are no papers dealing with sudden degeneration processes. Some authors concluded that the nucleus underwent a transition from fluid-like to solid-like material during aging<sup>6,7</sup>, or classified the grades of aging degeneration as first stiffening of the nucleus then the whole disc.<sup>8</sup> Others<sup>4,9-10</sup> model aging degeneration by different loss of disc height and nucleus

---

compressibility, or other material properties. Others used poro-elastic FE models to simulate aging degeneration.<sup>11-14</sup> Most of these studies concluded that the highest risk of disc prolapse was found in mildly degenerated young discs, however there are no answer to the question why.

The goal of this study was to obtain numerical conclusions for the mechanical effects of the cases of (1) normal age-related changes and (2) sudden overload-related degenerations, moreover, (3) to answer the question why the mildly degenerated young segments are more vulnerable.

The paper aims to determine the separated and mutual effect of the main mechanical degeneration phenomena, the effect of gradual decrease of incompressibility of disc nucleus and the increase of stiffness of nucleus during age-related degeneration processes. The aim was also to determine the degenerative effects of short-term sudden compressive overload and to answer the question why are the younger spine segments more vulnerable.

## Methods

A 3D model of a typical lumbar segment L4-5 was created (*Figure 1a*) by using Pro/Engineer code. The geometry and tissue volumes were obtained by the anatomical measures of a typical lumbar segment.<sup>15,16</sup> Cortical and cancellous bone of vertebrae was separately modeled, including posterior bony elements and facet joints. The height of the disc was considered to decrease linearly from 10 to 6 mm for the five aging degeneration degrees. The endplates were divided into external bony and central cartilaginous part. Accordingly, the annulus matrix was divided into internal and external ring and three layers of annulus fibers; (*Figure 1b*).

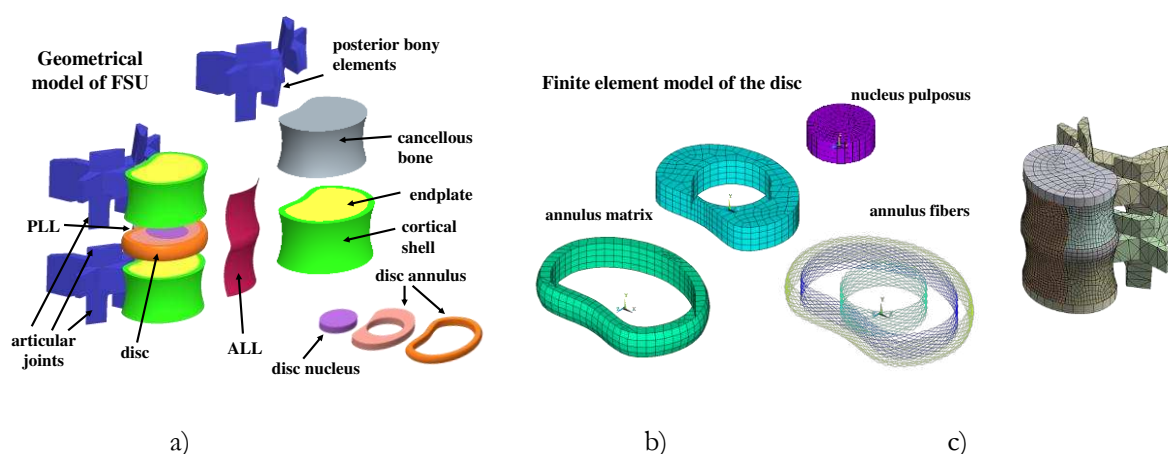


*Figure 1.* Geometric and finite element model of the lumbar segment

The FE mesh was generated by ANSYS Workbench and the connections between the several geometrical components were integrated to the FE model by ANSYS Classic (*Figure 1c*). The FE model consisted of solid, shell and bar elements. Annulus matrix, nucleus, cancellous bone, articular joints and different types of attachments were modeled by solid elements; cortical shells and endplates were modeled by shell elements. The compatibility between the adjacent solid and shell elements was guaranteed by contact elements. All ligaments were modeled by shell elements.

| Components of FSU                  | Young's mod<br>[MPa] | Poisson's<br>ratio |
|------------------------------------|----------------------|--------------------|
| vertebral cortical bone            | 12000                | 0,3                |
| posterior elements, facet          | 3500                 | 0,3                |
| vertebral cancellous bone          | 150                  | 0,3                |
| bony endplate                      | 12000                | 0,3                |
| cartilaginous endplate             | 100                  | 0,4                |
| nucleus                            | 1                    | 0,499              |
| annulus ground substance, internal | 4                    | 0,45               |
| annulus ground substance, external | 5                    | 0,40               |
| annulus fibers                     | 500/400/300*         | -                  |
| anterior longitudinal ligament     | 8**                  | 0,35               |
| posterior longitudinal ligament    | 10**                 | 0,35               |
| other ligaments                    | 5**                  | 0,35               |

\*external/middle/internal fibers, \*\*tension only

Table 1. Material moduli of the components of healthy FSU

Table 1 shows the material moduli of healthy FSU. For the bony elements and endplates, for both tension and compression, linear elastic isotropic materials were applied, based on the literature.<sup>4,5,17-19</sup> Annulus ground substance and nucleus were considered linear elastic for compression and bilinear elastic for tension. For the fluid-like healthy nucleus, the data of,<sup>20-23</sup> for the annulus matrix of<sup>15-16,24-25</sup> was considered. Collagen fibers of the annulus were considered as bilinear elastic isotropic tension-only material.<sup>26-29</sup> All the seven ligaments were integrated in the model with bilinear elastic tension-only materials of the literature again.

For the numerical simulation of age-related and sudden degeneration processes we developed a concise modeling system, seen in Table 2 containing five columns and five rows, consequently  $5 \times 5 = 25$  main blocks, named  $A_{ij}$ ,  $i, j = 1, 2, 3, 4, 5$ . Since the main characteristics of aging degeneration procedure of motion segments are the gradual loss of incompressibility of nucleus modeled by decreasing Poisson's ratio, and the gradual hardening of nucleus modeled by increasing Young's modulus, the main variables in Table 2 are the Young's modulus  $E$  of nucleus (in horizontal headings) and the Poisson's ratio  $\nu$  of nucleus (in vertical headings). Thus, horizontally the stiffening of nucleus and annulus matrix and the weakening of cancellous bone, endplates and annulus fibers are modeled during aging; and vertically the loss of nucleus fluidity is modeled. That is, horizontally (from left to right) the long-term age-related changes, while vertically (from up to down) the sudden degenerations could be modeled separately. Moreover, the five grades of age-related degeneration process are represented in the shadowed main diagonal blocks of Table 2 ( $A_{ij}$ ,  $i=j$ ), from the healthy (block  $A_{11}$ ) to the fully degenerated cases (block  $A_{55}$ ). Sudden degenerations were modeled by considering the actual grade of aging degeneration state in which the sudden overload happens. Based on Table 2 systematic numerical analysis could be done to analyze the separated and mutual effect of the material moduli.

| disc height | 10 mm       |                     |                |               | 9 mm        |                     |                |               | 8 mm       |                     |                |               | 7 mm     |                      |                |               | 6 mm     |                     |                |               |
|-------------|-------------|---------------------|----------------|---------------|-------------|---------------------|----------------|---------------|------------|---------------------|----------------|---------------|----------|----------------------|----------------|---------------|----------|---------------------|----------------|---------------|
| nucleus E   | 1 MPa       | annulus int/ext E/m | cart. bone E/m | end-plate E/m | 2 MPa       | annulus int/ext E/m | cart. bone E/m | end-plate E/m | 6 MPa      | annulus int/ext E/m | cart. bone E/m | end-plate E/m | 16 MPa   | annulus int/ext E/m  | cart. bone E/m | end-plate E/m | 36 MPa   | annulus int/ext E/m | cart. bone E/m | end-plate E/m |
| 0,499       | A11         | 4,6<br>0,45/0,40    | 150<br>0,3     | 100<br>0,4    | A12         | 4,5/6<br>0,44/0,39  | 125<br>0,3     | 80<br>0,4     | A13        | 6,5/9<br>0,43/0,38  | 100<br>0,3     | 60<br>0,4     | A14      | 11,5/17<br>0,42/0,37 | 75<br>0,3      | 40<br>0,4     | A15      | 20/29<br>0,41/0,36  | 50<br>0,3      | 20<br>0,4     |
| 0,475       | A21         | 4,6<br>0,45/0,40    | 150<br>0,3     | 100<br>0,4    | A22         | 4,5/6<br>0,44/0,39  | 125<br>0,3     | 80<br>0,4     | A23        | 6,5/9<br>0,43/0,38  | 100<br>0,3     | 60<br>0,4     | A24      | 11,5/17<br>0,42/0,37 | 75<br>0,3      | 40<br>0,4     | A25      | 20/29<br>0,41/0,36  | 50<br>0,3      | 20<br>0,4     |
| 0,450       | A31         | 4,6<br>0,45/0,40    | 150<br>0,3     | 100<br>0,4    | A32         | 4,5/6<br>0,44/0,39  | 125<br>0,3     | 80<br>0,4     | A33        | 6,5/9<br>0,43/0,38  | 100<br>0,3     | 60<br>0,4     | A34      | 11,5/17<br>0,42/0,37 | 75<br>0,3      | 40<br>0,4     | A35      | 20/29<br>0,41/0,36  | 50<br>0,3      | 20<br>0,4     |
| 0,425       | A41         | 4,6<br>0,45/0,40    | 150<br>0,3     | 100<br>0,4    | A42         | 4,5/6<br>0,44/0,39  | 125<br>0,3     | 80<br>0,4     | A43        | 6,5/9<br>0,43/0,38  | 100<br>0,3     | 60<br>0,4     | A44      | 11,5/17<br>0,42/0,37 | 75<br>0,3      | 40<br>0,4     | A45      | 20/29<br>0,41/0,36  | 50<br>0,3      | 20<br>0,4     |
| 0,400       | A51         | 4,6<br>0,45/0,40    | 150<br>0,3     | 100<br>0,4    | A52         | 4,5/6<br>0,44/0,39  | 125<br>0,3     | 80<br>0,4     | A53        | 6,5/9<br>0,43/0,38  | 100<br>0,3     | 60<br>0,4     | A54      | 11,5/17<br>0,42/0,37 | 75<br>0,3      | 40<br>0,4     | A55      | 20/29<br>0,41/0,36  | 50<br>0,3      | 20<br>0,4     |
| fibers      | 500/400/300 |                     |                |               | 250/200/150 |                     |                |               | 125/100/75 |                     |                |               | 63/50/38 |                      |                |               | 10/10/10 |                     |                |               |

Table 2. Systematic material modeling of age-related and sudden degenerations for numerical simulation of degeneration processes

For simulating age-related degeneration processes, 1000 N axial compression load was applied for all degeneration grades. For sudden traumatic degeneration processes, the 1000 N compression was increased to 5000 N.<sup>3</sup>

Our finite element models of healthy and degenerated FSU were validated both for compression and tension. Distribution of vertical compressive stresses in the mid-sagittal horizontal section of the disc, calculated for 2000 N compressive load for healthy and fully aging-degenerated FSU was compared to the experimental results of Adams et al.<sup>3</sup> obtained by stress profilometry for the same load. Degeneration caused vertical stress decrease in nucleus and internal annulus with high stress peaks in external annulus. Our numerical results were in good correspondence with the experiments of<sup>3,30-31</sup> For axial tension, the calculated elongations of discs were compared to the in vivo measured elongations of lumbar FSU model L3-S1 in<sup>32</sup> just after being suspended in water with 700 N body weight and 40 N extra weight in weightbath hydrotraction treatment.<sup>33</sup> The calculated elongations of healthy and degenerated lumbar FSUs were practically the same as measured by.<sup>32</sup>

## Results

Figure 2a shows the mean mid-sagittal compressive strains of disc elements that were smaller at the cartilaginous endplate supported middle of disc, in nucleus, and larger at the bony endplate supported edge of disc, in external annulus. Figure 2b shows the decreasing posterior, anterior and lateral disc bulging during aging. Figure 2c and 2d illustrate the central compressive strain of disc in terms of the separated effect of the gradual loss of incompressibility (Poisson's ratio) and gradual

stiffening (increasing Young's modulus) of nucleus. Their mutual effect can be seen in *Figure 2a* for nucleus, demonstrating that in the beginning period of aging, the effect of loss of nucleus incompressibility dominates, yielding maximum disc deformability in the second grade at mild degeneration, while later the effect of nucleus hardening dominates resulting significant decrease of deformations in further aging.

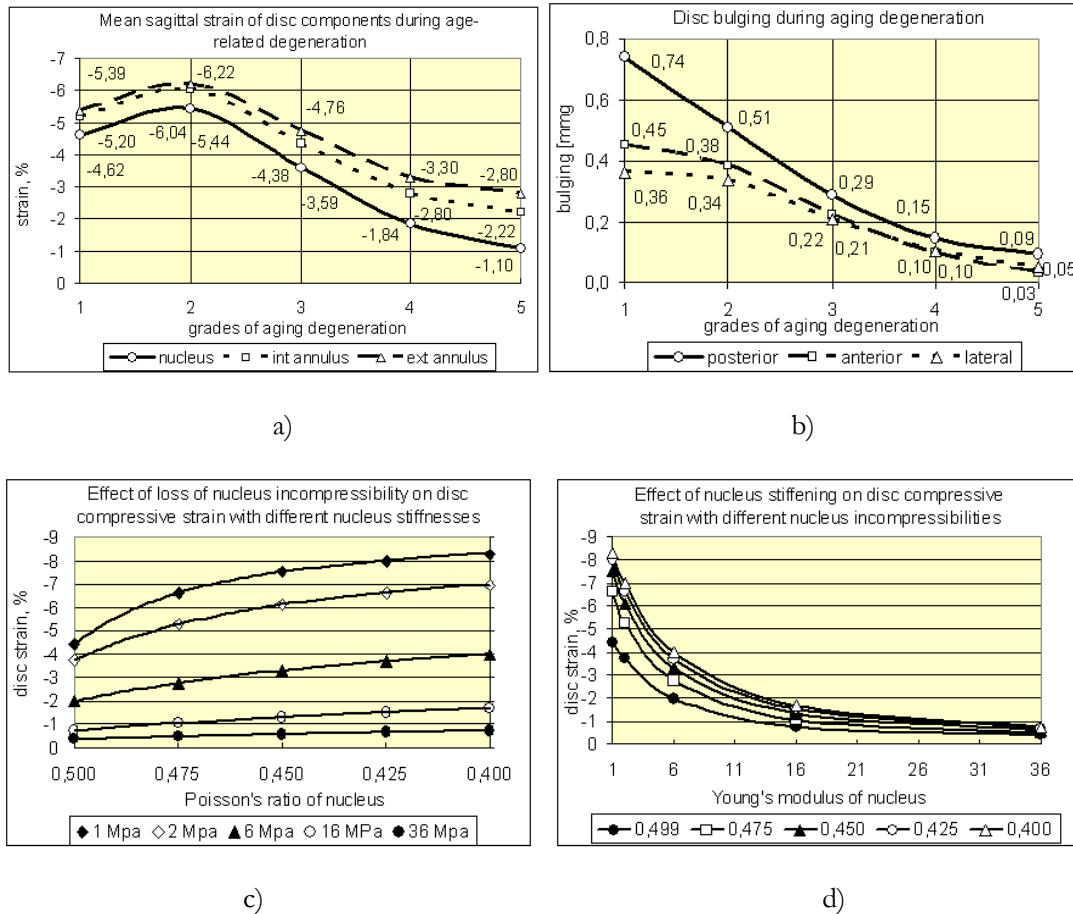


Figure 2. a) Mid-sagittal compressive strains of disc components and b) sagittal disc bulging during normal aging; The separated effect of c) the decrease of Poisson ratio of nucleus and d) the increase of Young's modulus of nucleus on the central compressive strain of disc during aging.

*Figure 3a* illustrates the mid-frontal vertical compressive stresses for the five aging grades. During aging, the gradual decrease of central and increase of external compressive stresses can be observed. *Figure 3b* shows the mean mid-frontal compressive stresses in the nucleus, internal and external annulus, demonstrating that the compressive load transfer moves from inside to outside the disc with aging. During the total aging process the stress decrease in the nucleus was 60%, in the internal annulus was 35%, however, in the external annulus 150% stress increase was observed. The separated effect of the decrease of Poisson ratio of nucleus (*Figure 3c*) and the increase of Young's modulus of nucleus (*Figure 3d*) on the vertical compressive stresses of nucleus demonstrated that in the beginning period of aging, the effect of loss of nucleus incompressibility dominated, causing rapid stress decrease in nucleus in the second grade, while



later the effect of nucleus hardening dominated resulting significant stress decrease during further aging.

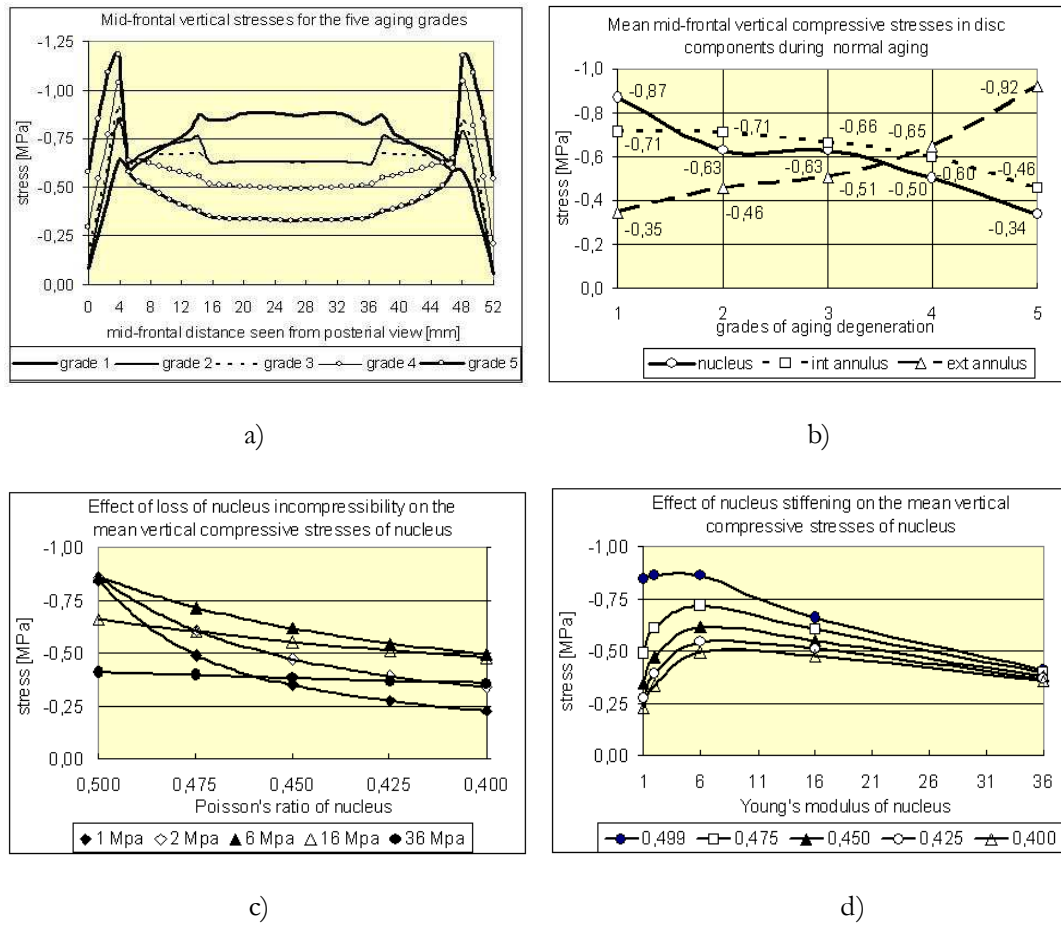


Figure 3. a) Mid-frontal distribution of vertical compressive stresses for the five aging degeneration grades; b) Change of the mean mid-frontal vertical compressive stresses of disc components during aging. The separated effect of c) decrease of Poisson ratio of nucleus and d) increase of Young's modulus of nucleus on the vertical compressive stresses of nucleus

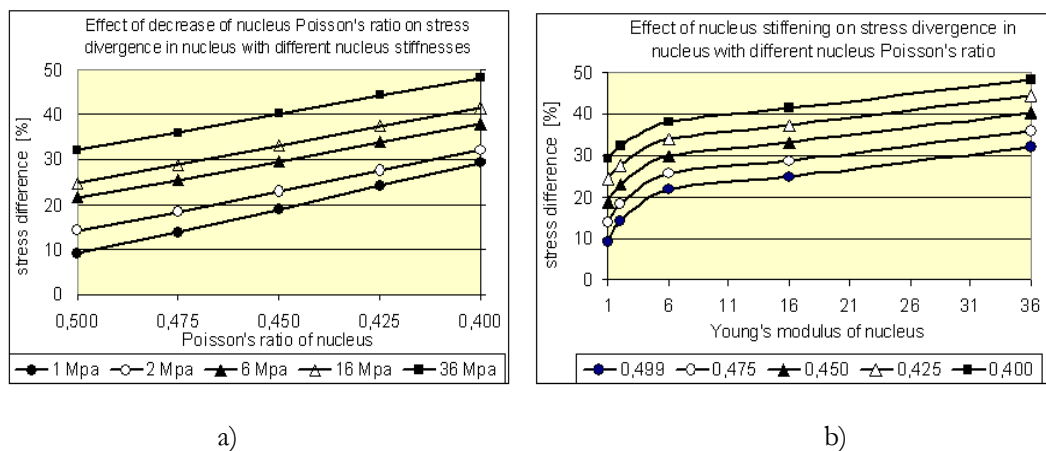


Figure 4. a) The separated effect of the a) loss of nucleus incompressibility and b) nucleus hardening on the stress divergence in nucleus

Figure 4a and 4b show the separated effect of the decrease of Poisson's ratio of nucleus and the increase of Young's modulus of nucleus on the stress divergence in nucleus. A healthy nucleus is in hydrostatic compression stress state, namely, the stresses in nucleus in different directions are equal. During the loss of hydrostatic stress state, the stresses start to diverge, that is, the difference among them starts to increase. Figure 4a and 4b demonstrates that the hydrostatic stress state needs fluid-like material with small Young's modulus.

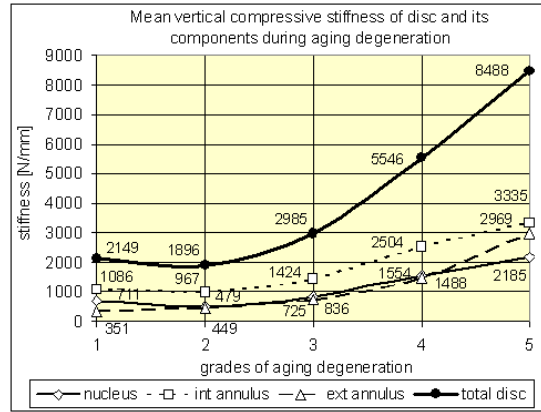


Figure 5. Change of compressive stiffness of disc components and total disc during aging degeneration

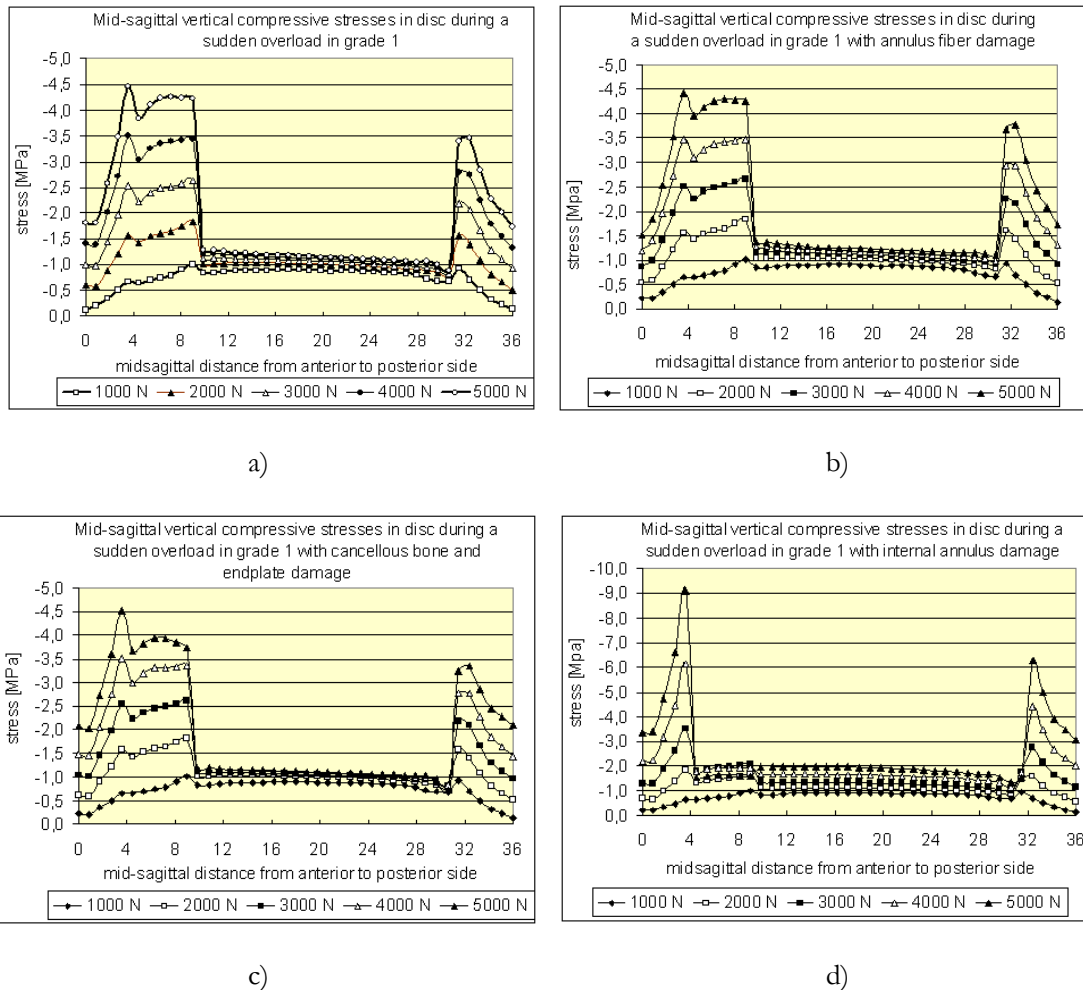


Figure 6. Sudden degeneration in grade 1 with a) sudden loss of nucleus incompressibility accompanied by b) annulus fiber damage, c) vertebral cancellous bone and endplate damage, d) internal annulus damage.

In *Figure 5* the change of vertical compressive stiffness of the disc and each of its components are seen during the age-related normal degeneration procedure. The stiffness of the total disc was about 2150, 1900, 3000, 5550 and 8500 N/mm in the five aging degeneration degree. It can be seen clearly that the minimum of compressive stiffness belongs to the early period of life, to the young adult age for all disc components and for the total disc.

The sudden degeneration in young age (in grade 1) was modeled by an accidental loss of hydrostatic stress state in nucleus due to a sudden overload when the nucleus quasi bursts out modeled by rapid decrease of Poisson's modulus of nucleus parallel to an accidental load increase from 1000 to 5000 N.

*Figure 6a* illustrates the mid-sagittal vertical compressive stress distribution in disc with sudden loss of nucleus incompressibility but all other organs are intact. In *Figure 6b* the nucleus damage is accompanied by annulus fiber damage, in *Figure 6c* by cancellous bone and endplate damage together, in *Figure 6d* by internal annulus buckling.

It can be seen that during the sudden overload with nucleus damage, the vertical compressive stresses did not change in the nucleus, however, in the annulus the stresses increased extremely, by 400%.

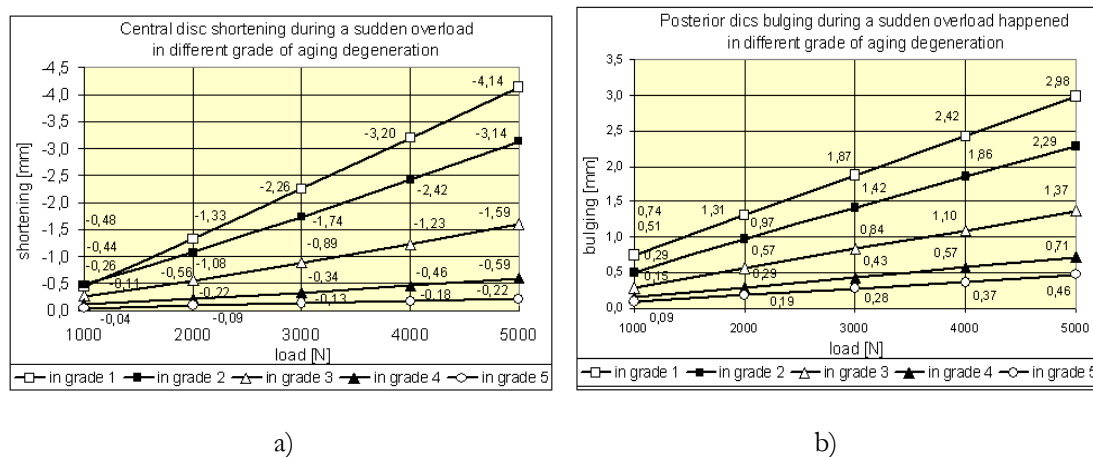
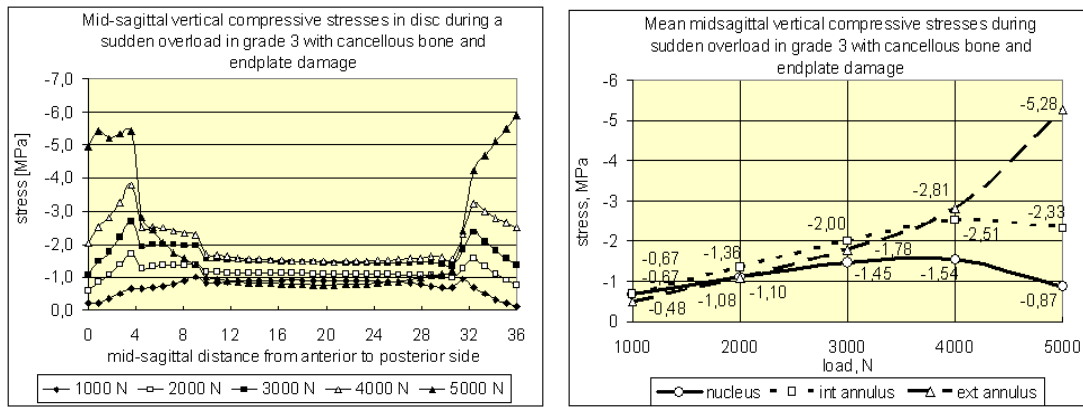


*Figure 7.* a) Central disc shortening and b) posterior disc bulging during a sudden overload for different grade of aging degeneration

In contrast to the aging degeneration, the overload-related degeneration can happen in any time, at any age. However, the consequence of it depends highly on the actual aging grade when it happened. In *Figure 7* the central disc shortening and the posterior disc bulging is illustrated in terms of the grades of normal aging degeneration when the accidental overload happened.

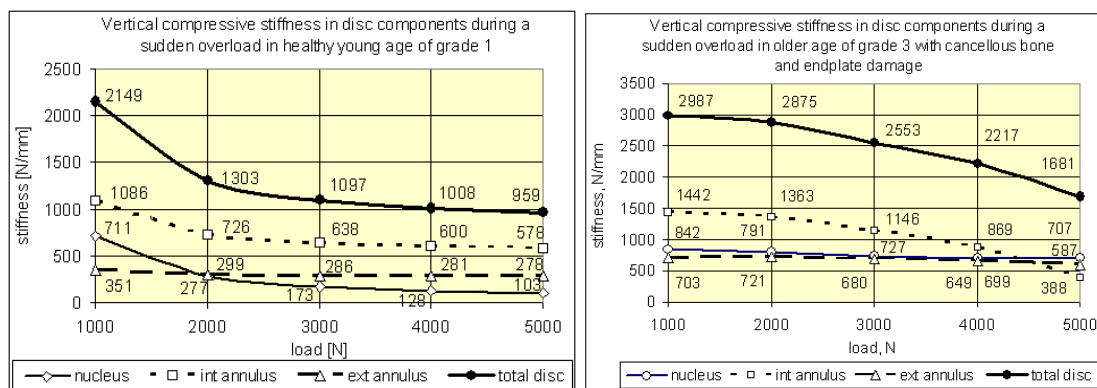
*Figure 8a* shows the mid-sagittal vertical compressive stress distribution in disc when the sudden overload happens in grade 3, in older age, accompanied by vertebral cancellous bone and endplate damage. In *Figure 8b* the stresses in disc components are illustrated during the sudden overload, demonstrating that due to the loss of load bearing capacity of cancellous bone, the load transfer through the vertebra and disc moves from inside to outside.



a)

b)

Figure 8. a) Mid-sagittal vertical compressive stress distribution in disc when the sudden overload happens in older age, in grade 3 with cancellous bone and endplate damage; b) the relating vertical compressive stresses



a)

b)

Figure 9. Stiffness loss of disc components during the sudden overload in the case of a) young age of grade 1 and b) older age of grade 3

Figure 9 shows the sudden stiffness loss of disc components during the sudden overload for grade 1 of young age and for grade 3 of older age. Observe that the stiffness decrease in young age starts from a lower level than in older age and consequently tends to a lower level. On the other hand, the gradient of fall of stiffness is more rapid in young age than in older age.

### Discussion and conclusion

By numerical simulation the separated effect of the two main factors of age-related disc degenerations, the gradual loss of incompressibility and the gradual increasing stiffness of nucleus can be modeled numerically by gradually decreasing Poisson's ratio and increasing Young's modulus of nucleus respectively.<sup>37</sup> In the first period of aging degeneration process the loss of incompressibility, later the stiffening of nucleus has the dominant effect on the deformability and stresses of disc (Figures 2 and 3). The reason of this phenomenon lays on the fact that the nucleus

is fluid-like only in young age, so it is obvious that the effect of loss of hydrostatics can be related to the first period of aging.<sup>6-7</sup>

During the aging degeneration the vertical load transfer moves from inside to outside, it tends to the external annulus (*Figure 3b*). Indeed, Adams et al.<sup>3,31</sup> obtained experimentally that the vertical compressive stress decreases in the nucleus and increases in the external annulus during aging degeneration.

The compressive stiffness of the whole disc is minimum in mildly degenerated state, and during further aging the stiffness of the disc strongly increases, leading to the risk of instability and injury in young age (*Figure 5*). Schmidt et al.<sup>14</sup> found that the disc prolapse initially increased for mildly degenerated state, and subsequently decreased for moderately and severely degenerated discs. Tang et al.<sup>9</sup> concluded that light degeneration of disc led to instability, while the stability restored with further degeneration. Adams et al.<sup>3</sup> found that lower lumbar discs which appeared to prolapse were non-degenerated of cadavers aged 40-50 years; severely degenerated discs could not be made to prolapse.

During sudden overload-related nucleus degeneration in young age, due to the sudden loss of nucleus incompressibility, the support of the internal annulus disappears, causing buckle in the annulus layers, thus, the load transfer moves dominantly to the external annulus (*Figure 6*) yielding strong increase in disc shortening and bulging, however, if the sudden overload happens in older age, these effects are smaller (*Figure 7*).

While during the age-related degeneration process the compressive stiffness of the disc increases, during the overload-related sudden process, the stiffness strongly decreases (*Figures 5 and 9*). Also in sudden degeneration the smallest stiffness belongs to the weakly degenerated state in young age since in this case the sudden stiffness loss starts at the smallest stiffness level. In older age, the sudden stiffness loss starts at a higher stiffness level (*Figure 9*). The gradient of sudden stiffness loss is also stronger in younger age.

We have proved by numerical analysis that younger segments are the most vulnerable during both long-time age-related and sudden overload-related degeneration. Several recent studies<sup>3-5,9-10</sup> concluded that light degeneration of disc in young age led to instability of lumbar spine, since the lightly degenerated discs had the smallest stiffness. These effects explain why are the young adults who suffer so frequently by low back pain problems.

---

## REFERENCES

1. Adams MA, Freeman BJ, Morrison HP, Nelson IW, Dolan P. Mechanical initiation of intervertebral disc degeneration, *Spine*, 2000;25(13):1625-36.
2. Ferguson SJ, Steffen T. Biomechanics of aging spine, *Eur.Spine J.* 203;12(2):97-103.
3. Adams MA, Bogduk N, Burton K, Dolan P. *The Biomechanics of Back Pain*, Churchill Livingstone, Edinburgh, London, New York, Oxford, Philadelphia, 2002 p. 238.
4. Rohlmann A, Zander T, Schmidt H, Wilke HJ, Bergmann G. Analysis of the influence of disc degeneration on the mechanical behaviour of a lumbar motion segment using the finite element method, *J. of Biomechanics*, 2006;39(13):2484-90.

5. Schmidt H, Heuer F, Simon U, Kettler A, Rohlmann A, Claes L, Wilke HJ. Application of a new calibration method for a three-dimensional finite element model of a human lumbar annulus fibrosus, *Clinical Biomechanics*, 2006;21(4):337-44.
6. Iatridis JC, Wedenbaum M, Setton LA, Mow VC. Is the nucleus pulposus a solid or a fluid? Mechanical behaviours of the nucleus pulposus of the human intervertebral disc, *Spine*, 1996;21(10): 1174-84.
7. Iatridis JC, Setton LA, Wedenbaum M, Mow VC. Alterations in the mechanical behavior of the human lumbar nucleus pulposus with degeneration and aging, *J. of Orthopaedic Research*, 1997;15(2):318-22.
8. Polikeit A, Nolte LP, Ferguson SJ. Simulated influence of osteoporosis and disc degeneration on the load transfer in a lumbar functional spinal unit, *J. of Biomechanics*, 2004;37(7):1061-9.
9. Tang XJ, Chen QX, Liu YS, Li FC. Analysis of lumbar disc degeneration using three-dimensional nonlinear finite element method, (Article in Chinese), *Zhonghua Yi Xue Za Zhi*, 2008;88(23):1634-8.
10. Schmidt H, Kettler A, Rohlmann A, Claes L, Wilke HJ. The risk of disc prolapses with complex loading in different degrees of disc degeneration - a finite element analysis, *Clinical Biomechanics*, 2007;22(9):988-98.
11. Schmidt H, Heuer F, Wilke HJ. Dependency of disc degeneration on shear and tensile strains between annular fiber layers for complex loads, *Medical Eng. Physics*, 2009;31(6):642-9.
12. Laible JP, Pflaster DS, Krag MH, Simon BR, Haugh LD. A poroelastic finite element model with application to the intervertebral disc. *Spine*, 1993;18(5):659-70.
13. Natarajan RN, Williams JR, Andersson GB. Modeling changes in intervertebral disc mechanics with degeneration, *J. of Bone and Joint Surgery Am.* 2006;88(4):36-40.
14. Schmidt H, Kettler A, Rohlmann A, Claes L, Wilke HJ. The risk of disc prolapses with complex loading in different degrees of disc degeneration - a finite element analysis, *Clinical Biomechanics*, 2007;22(9):988-98.
15. Denoziere G. Numerical modeling of ligamentous lumbar motion segment, Master thesis, Georgia Institute of Technology, 2004.
16. Panjabi MM, Oxland T, Takata K, Goel V, Duranceau J, Krag M. Articular facets of the human spine, quantitative three dimensional anatomy, *Spine*, 1993;18(10):1298-1310.
17. Denoziere G, Ku DN. Biomechanical comparison between fusion of two vertebrae and implantation of an artificial intervertebral disc, *J. of Biomechanics*, 2006;39(4):766-75.
18. Rohlmann A, Zander T, Schmidt H, Wilke HJ, Bergmann G. Analysis of the influence of disc degeneration on the mechanical behaviour of a lumbar motion segment using the finite element method, *J. of Biomechanics*, 2006;39(13):2484-90.
19. Schmidt H, Heuer F, Simon U, Kettler A, Rohlmann A, Claes L, Wilke HJ. Application of a new calibration method for a three-dimensional finite element model of a human lumbar annulus fibrosus, *Clinical Biomechanics*, 2006;21(4):337-44.
20. Rohlmann A, Bauer L, Zander T, Bergmann G, Wilke HJ. Determination of trunk muscle forces for flexion and extension by using a validated finite element model of the lumbar spine and measured in vivo data, *J. of Biomechanics*, 2006;39(6):981-9.
21. Noailly J, Wilke HJ, Planell JA, Lacroix D. How does the geometry affect the internal biomechanics of a lumbar spine bi-segment finite element model? Consequences on the validation process, *J. of Biomechanics*, 2007;40(11):2414-25.
22. Shirazi-Adl SA, Shrivastava SC, Ahmed AM. Stress analysis of the lumbar disc-body unit in compression. A three-dimensional nonlinear finite element study, *Spine*, 1984;9(2):120-34.
23. Shirazi-Adl A. Strain in fibers of a lumbar disc. Analysis of the role of lifting in producing disc prolapse, *Spine*, 1989;14(1):96-103.

24. Spilker RL, Jakobs DM, Schultz AB. Material constants for a finite element model of the intervertebral disc with a fibre composite annulus, J. of Biomechanical Eng. 1986;108(1):1-11.
25. Rao AA, Dumas GA. Influence of material properties on the mechanical behaviour of the L5-S1 intervertebral disc in compression: a nonlinear finite element study, J. of Biomedical Eng. 1991;13(2):139-51.
26. Goel VK, Kong W, Han JS, Weinstein JN, Gilbertson LG. A combined finite element and optimization investigation of lumbar spine mechanics with and without muscles. Spine, 1993;18(11):1531-41.
27. Lavaste F, Skalli W, Robin S, Roy-Camille R, Mazel C. Three-dimensional geometrical and mechanical modelling of lumbar spine, J. of Biomechanics, 1992;25(10):1153-64.
28. Zander T, Rohlmann A, Bergmann G. Influence of ligament stiffness on the mechanical behaviour of a functional spinal unit, J. of Biomechanics, 2004;37(7):1107-11.
29. Kurowski P, Kubo A. The relationship of degeneration of the intervertebral disc to mechanical loading conditions on lumbar vertebrae, Spine, 1986;11(7):726-31.
30. McNally DS, Adams MA. Internal intervertebral disc mechanics as revealed by stress profilometry, Spine, 1992;17(1):66-73.
31. Adams MA, McNally DS, Dolan P. Stress distributions inside intervertebral discs. The effects of age and degeneration. J. Bone Joint Surg. Br. 1996;78(6):965-72.
32. Kurutz M, Bene É, Lovas A. In vivo deformability of human lumbar spine segments in pure centric tension, measured during traction bath therapy, Acta of Bioengineering and Biomechanics, 2003;5(1):67-92.
33. Kurutz M, Bender T. Weightbath hydrotraction treatment – application, biomechanics and clinical effects, J. of Multidisciplinary Healthcare, 2010;(3):19-27.
34. Dolan P, Adams MA. Recent advances in lumbar spinal mechanics and their significance for modeling, Clinical Biomechanics., 2001;16(1):8-16.
35. Cassinelli E, Kang JD. Current understanding of lumbar disc degeneration, Operative techniques in orthopaedics, 2000;10(4):254-62.
36. Little JP, Adam CJ, Evans JH, Pettet GJ, Pearcy MJ. Nonlinear finite element analysis of annular lesions in the L4/5 intervertebral disc, J. of Biomechanics, 2007;40(12):2744-51.
37. Kurutz M, Oroszváry L. Finite element analysis of weightbath hydrotraction treatment of degenerated lumbar spine segments in elastic phase. J. of Biomechanics, 2010;43(1):433-41.

***The authors gratefully acknowledge the Hungarian Scientific Research Fund OTKA for providing financial support in the frame of the grant K-075018.***

## FINITE ELEMENT PARAMETER-ANALYSIS OF AGE-RELATED DEGENERATIONS OF COMPONENTS OF LUMBAR SPINE SEGMENTS IN COMPRESSION

Márta Kurutz<sup>1</sup>, László Oroszvány<sup>2</sup>

<sup>1</sup>Budapest University of Technology and Economics

<sup>2</sup>Knorr Bremse Hungaria Ltd

[kurutzm@eik.bme.hu](mailto:kurutzm@eik.bme.hu)

---

### **Abstract**

3D finite element parameter analysis of the degeneration-sensitivity of the material properties of the components of lumbar spinal motion segments is presented for physiologic compression load. The aim was to determine that material behaviour which dominantly determines the mechanical behaviour of the aging spine. Systematic numerical simulation was executed by using a finite element model validated by experimental results for both tension and compression. It was concluded that to keep the hydrostatic compression state of nucleus is the most important factor to maintain the stability of lumbar segments in the first period of aging process.

**Keywords:** finite element parameter analysis, lumbar motion segments, compression, material property, degeneration

---

### **Introduction**

Using numerical simulation we can find out how the stability of spinal motion segments is influenced by the healthy or degenerated state of each of its components, or rather the healthy or degenerated state of which of its components has the dominant effect on the degeneration or failure of the whole segment. At the same time, by numerical parameter-analysis we can determine that components the material moduli of which needs the most care and correctness to be collected for numerical analyses of spinal degeneration. In this study a systematic parameter-analysis is presented to determine the separated effect of each material parameter of the components of the lumbar spine segments on the mechanical behaviour and stability of the whole segment.

Degeneration represents special and injurious changes in the structure, composition and function of spine or part of the spine, caused by aging or by certain environmental external effects.<sup>1</sup> The age-related changes of spine start generally in the intervertebral discs; within the disc nucleus, altering markedly the mechanics of load transfer and spinal stability.<sup>2</sup> The age-related changes of the disc are manifested in loss of hydration, a drying and stiffening procedure in the texture of both nucleus and annulus.<sup>3</sup> Aging procedures are often accompanied by other kinds of degeneration: buckling, lesions, tears, fiber break in the annulus or osteoporotic changes in the vertebral bone.

The goal of this study was to obtain numerical conclusions for the separated mechanical effects of the material moduli of each components of the lumbar motion segment on the degeneration of the whole segment.



## Methods

For the numerical parameter-analysis, the finite element model of a typical lumbar motion segment was used that we developed earlier in ANSYS system,<sup>4</sup> representing five degeneration grade of aging. A 3D model of a typical lumbar segment L4-5 was created by using Pro/Engineer code. The geometry and tissue volumes were obtained by the anatomical measures of a typical lumbar segment.<sup>5,6</sup> Cortical and cancellous bone of vertebrae was separately modeled, including posterior bony elements and facet joints. The height of the disc was considered to decrease linearly from 10 to 6 mm for the five aging degeneration degrees. The endplates were divided into external bony and central cartilaginous part. Accordingly, the annulus matrix was divided into internal and external ring and three layers of annulus fibers.<sup>7</sup> The FE mesh was generated by ANSYS Workbench and the connections between the several geometrical components were integrated to the FE model by ANSYS Classic. The FE model consisted of solid, shell and bar elements. Annulus matrix, nucleus, cancellous bone, articular joints and different types of attachments were modeled by solid elements; cortical shells and endplates were modeled by shell elements. The compatibility between the adjacent solid and shell elements was guaranteed by contact elements. All ligaments were modeled by shell elements.

Table 1 shows the material moduli of healthy lumbar motion segment. For the bony elements and endplates, for both tension and compression, linear elastic isotropic materials were applied, based on the literature. Annulus ground substance and nucleus were considered linear elastic for compression and bilinear elastic for tension. Nucleus and annulus matrix were considered linear elastic. Collagen fibers of the annulus were considered as bilinear elastic isotropic tension-only material. All the seven ligaments were integrated in the model with bilinear elastic tension-only materials of the literature again.

| Components of FSU                  | Young's mod<br>[MPa] | Poisson's<br>ratio |
|------------------------------------|----------------------|--------------------|
| vertebral cortical bone            | 12000                | 0,3                |
| posterior elements, facet          | 3500                 | 0,3                |
| vertebral cancellous bone          | 150                  | 0,3                |
| bony endplate                      | 12000                | 0,3                |
| cartilaginous endplate             | 100                  | 0,4                |
| nucleus                            | 1                    | 0,499              |
| annulus ground substance, internal | 4                    | 0,45               |
| annulus ground substance, external | 5                    | 0,40               |
| annulus fibers                     | 500/400/300*         | -                  |
| anterior longitudinal ligament     | 8**                  | 0,35               |
| posterior longitudinal ligament    | 10**                 | 0,35               |
| other ligaments                    | 5**                  | 0,35               |

\*external/middle/internal fibers, \*\*tension only

Table 1. Material moduli of the components of healthy motion segment

Five grades of age-related degeneration process were introduced, seen in Table 2. Age-related normal degeneration processes of segment start generally in the nucleus. A healthy young nucleus is in hydrostatic compression state. During aging, the nucleus loses its incompressibility by changing gradually from fluid-like to solid material of increasing stiffness.<sup>8,9</sup> These kinds of

nucleus changes were modeled by decreasing Poisson's ratio with increasing Young's modulus, seen in *Table 2*. This behavior is generally accompanied by the stiffening process of the annulus. This procedure was modeled also by increasing Young's modulus with slightly decreasing Poisson's ratio, by distinguishing the internal capsular and the external ligamentous part of annulus, by considering the internal annulus to be weaker. The elastic moduli of annulus fibers were decreased during aging.

| Grades of aging degeneration*<br>(Young's mod/Poisson's ratio) | grade 1<br>(healthy) | grade 2     | grade 3    | grade 4   | grade 5<br>(fully deg.) |
|--|----------------------|-------------|------------|-----------|-------------------------|
| disc height [mm]   | 10                   | 9           | 8          | 7         | 6                       |
| nucleus  | 1/0.499              | 2/0.475     | 6/0.45     | 16/0.425  | 36/0.4                  |
| annulus matrix, internal ring                                  | 4/0.45               | 4,5/0.44    | 6,5/0.43   | 11,5/0.42 | 20/0.41                 |
| annulus matrix, external ring                                  | 5/0.40               | 6/0.39      | 9/0.38     | 17/0.37   | 29/0.36                 |
| cancellous bone  | 150/0.3              | 125/0.3     | 100/0.3    | 75/0.3    | 50/0.3                  |
| cartilaginous endplate   | 100/0.4              | 80/0.4      | 60/0.4     | 40/0.4    | 20/0.4                  |
| annulus fibers (ext/middle/int)                                | 500/400/300          | 250/200/150 | 125/100/75 | 63/50/38  | 10/10/10                |

\*Other bony elements are seen in *Table 1*

*Table 2.* Modeling of normal age-related changes of lumbar motion segment

In the parameter-analysis we assumed that all components of the motion segment are under normal degeneration according to the data of *Table 2* except for only one component that remains intact with the data of grade 1, with no degeneration. Then, the obtained mechanical results were compared to the case where all components are normally aging and degenerating. We have chosen this method where all components are normally aging only on does not, instead of the inverse unrealistic process where only one component would aging and all the others remain young. The reason was to follow a physiologically normal degeneration procedure to determine the component the healthy state of which would have a dominant effect on the stability of the whole motion segment.

The model was validated for both compression and tension. The compression behaviour was compared to the experimental results of Adams et al.<sup>3</sup> obtained by stress profilometry for 2000 N axial compressive load with endplate damage. For axial tension, the calculated elongations of discs were compared with in vivo measured elongations of lumbar FSU model L3-S1 in weightbath hydrotraction treatment.<sup>10,11</sup>

1000 N axial physiologic compression load was applied for all degeneration grades for all numerical simulations. The compression load was distributed along the superior and inferior surface of the upper and lower vertebra of FSU, by applying rigid load distributor plates at both surfaces.

## Results

*Figures 1-4* illustrate the stresses, strains and stiffnesses of the different parts of the disc for the age-related degeneration process when all components of the lumbar motion segment were under aging degenerated state characterized by the material moduli seen in *Table 2* except for the

nucleus, namely, its Young's modulus, its Poisson's ratio and both of them were separately kept on their initial healthy values of grade 1.

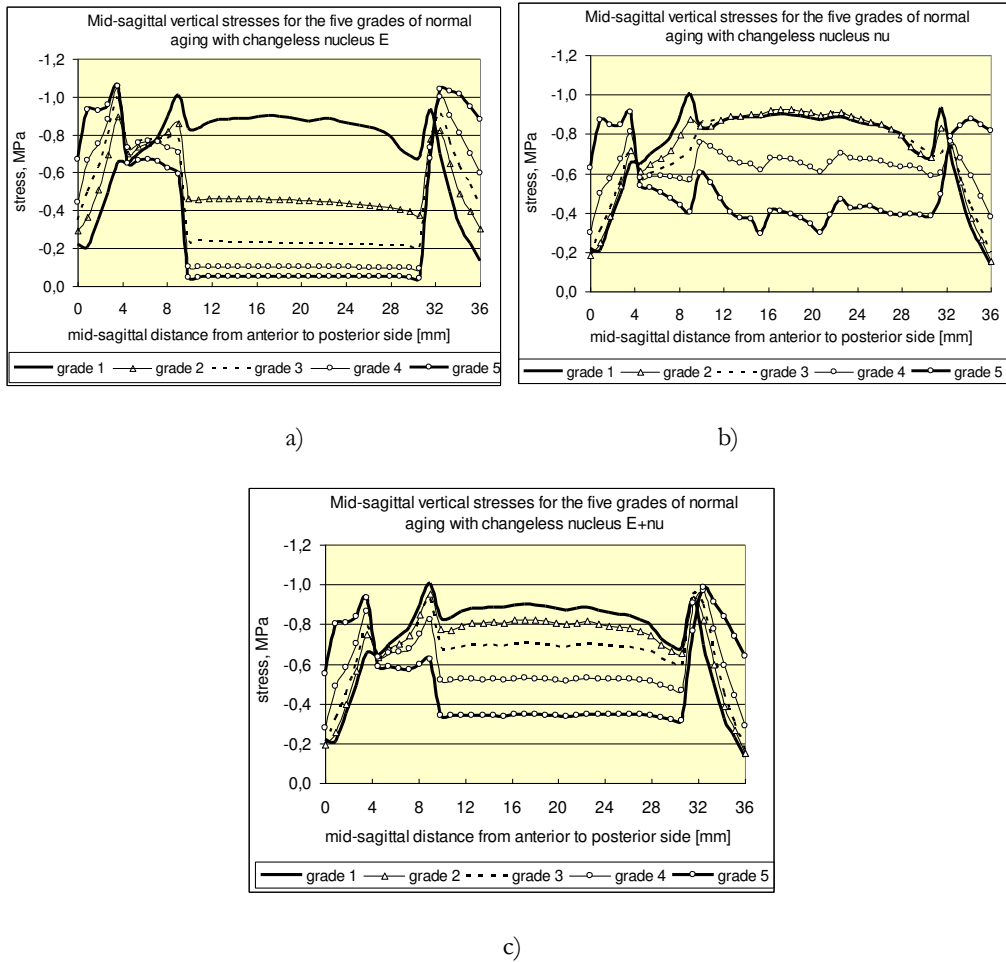


Figure 1. Mid-sagittal vertical stress distribution in the disc in the five grades of aging process while a) nucleus E, b) nucleus nu and c) nucleus E+nu keep their initial healthy values changeless

Figure 1 shows the mid-sagittal vertical compressive stress distribution in the disc from the anterior to the posterior end for the five aging degeneration grade. In Figure 1a the Young's modulus of nucleus kept its initial young value, in Figure 1b its Poisson's ratio remained changeless, while in Figure 1c both of them were changeless.

Figures 2a, 2b and 2c show the related change of mean mid-sagittal vertical compressive stresses in the disc nucleus, in the internal and external annulus, while Figure 2d shows the related posterior disc bulging during the five degeneration grade of the aging process. In Figures 3a and 3b the change of the internal and external compressive strains of disc can be seen, respectively. In Figures 4a, 4b and 4c the vertical compressive stiffness of the nucleus, internal and external annulus can be seen, respectively, while in Figure 4d the stiffness of the whole disc is illustrated.

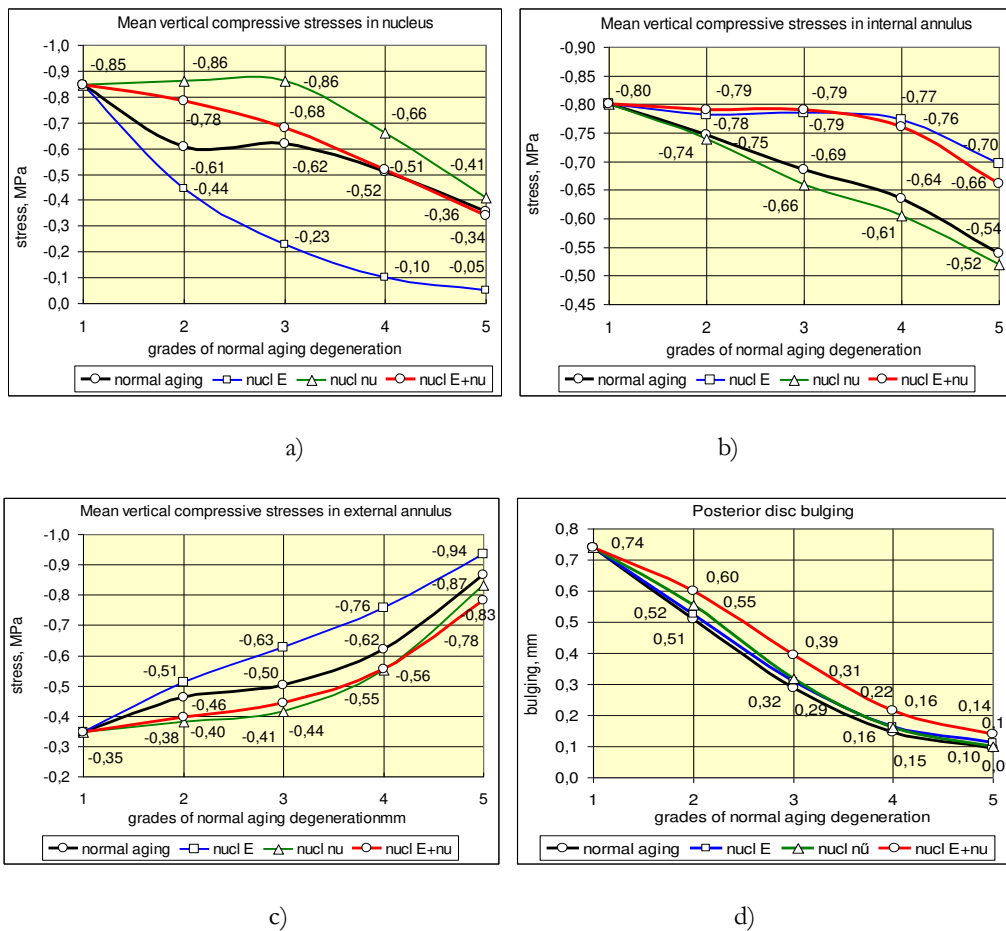


Figure 2. Mean vertical compressive stresses in a) nucleus, b) internal annulus, c) external annulus and d) posterior bulging for the cases of aging degeneration process while nucleus E, nu and E+nu keep their initial healthy values changeless

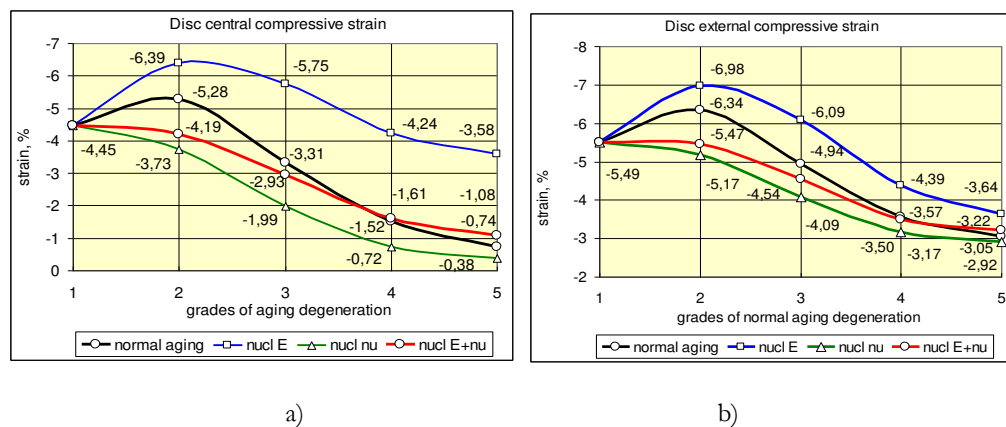


Figure 3: a) Central and b) external vertical compressive strains of disc for the cases of aging degeneration process if the nucleus E, nu and E+nu keep their initial healthy values changeless

When the Young's modulus of nucleus was kept separately on its initial small value ( $E=1$  MPa) during the aging of all other components (Table 2), the stresses in nucleus rapidly decreased (by 27%, in grade 2, by 63% in grade 3, Figure 2a), in the internal and external annulus rapidly increased (by 5-11% and 15-25% in grade 2 and 3, resp., Figures 2b and 2c). At the same time the central deformations in disc nucleus rapidly increased (by 21% in grade 2 and by 74% in grade 3,

Figure 3a), and the external deformations in annulus also increased (by 10% in grade 2 and by 23% in grade 3, Figure 3b), together with the increased posterior bulging (by 3% in grade 2 and by 7% in grade 3, Figure 2d). The most dangerous was the complete stiffness loss of nucleus (by 40% in grade 2 and by 79% in grade 3, Figure 4a) and the rapid stiffness loss of internal annulus (by 9% in grade 2 and by 20% in grade 3, Figure 4b) that led to the radical stiffness decrease of the whole disc (by 15% in grade 2 and by 33% in grade 3, Figure 4d).

Figure 1b illustrates that keeping the Poisson's ratio of nucleus on the fluid-like level ( $\nu=0,499$ ) with increasing solid-like Young's modulus of it was meaningless in grade 4 and grade 5 (Table 2), yielding chaotic zigzag lines on Figure 1b. However, with small Young's modulus, in grade 2 ( $E=2$  MPa) and 3 ( $E=6$  MPa) it means that the incompressibility of nucleus is kept, that increased the stresses in nucleus (by 40-42% in grade 2 and 3, Figure 2a), and unloaded the external annulus (by 17-18% in grade 2 and 3, Figure 2c). At the same time the central deformations of disc decreased (by 30 and 40% in grade 2 and 3, Figure 3a), and the external deformations also decreased (by 17-18% in grade 2 and 3, Figure 3b), with decrease of posterior bulging (by 9-10% in grade 2 and 3, Figure 2d). There was a rapid stiffness increase of nucleus (100% and 133% in grade 2 and 3, Figure 4a) and a large stiffness increase of internal annulus (29-31% in grade 2 and 3, Figure 4b) that led to the radical stiffness increase of the whole disc (by 41% and 54% in grade 2 and 3, Figure 4d).

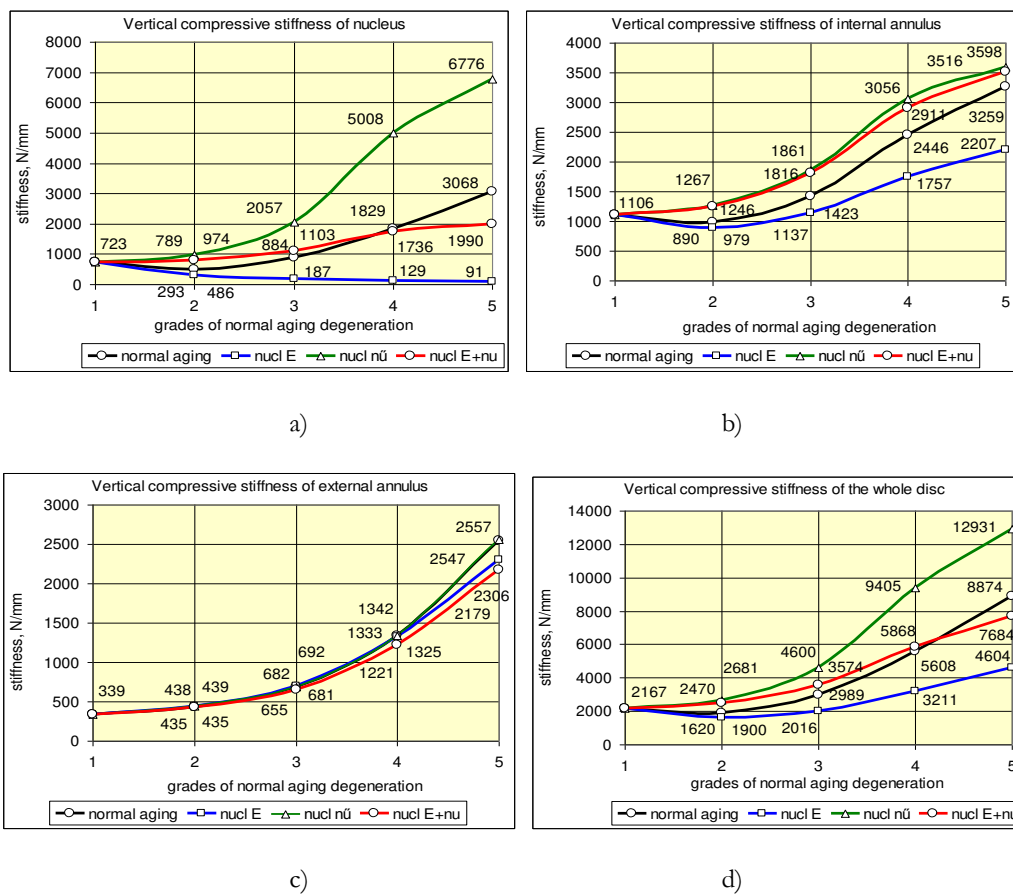
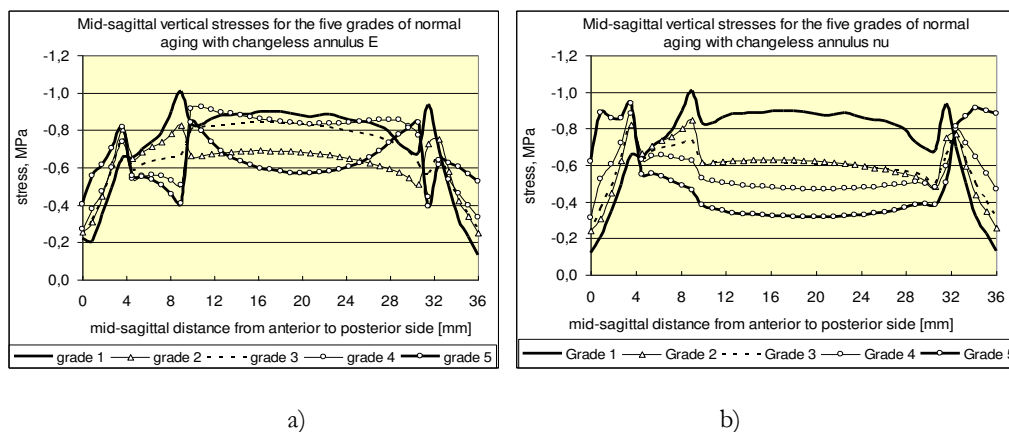


Figure 4. Vertical compressive stiffness of a) nucleus, b) internal and c) external annulus and d) the whole disc for the cases of aging degeneration process if the nucleus E, nu and E+nu keep their initial healthy values

Keeping the Young's modulus and Poisson's ratio of nucleus simultaneously on its young healthy level, the most radical effect was observed in the second grade of aging degeneration process, where the stresses in nucleus increased the most (by 29%, *Figure 2a*), the compressive strains in nucleus decreased the most (by 21%, *Figure 3a*), similarly to the external strains (by 14%, *Figure 3b*), and the stiffness of nucleus increased the most (by 62%, *Figure 4a*) yielding the largest increase of the whole disc also in grade 2 (by 30%, *Figure 4d*).

*Figures 5-8* illustrate the stresses, strains and stiffnesses of the different parts of the disc for the age-related degeneration process when all components of the lumbar motion segment were under normal aging degenerated state (*Table 2*) except for the annulus (internal and external together), namely, its Young's modulus, its Poisson's ratio and both of them were separately kept on their initial healthy values of grade 1.

*Figures 5a* and *5b* illustrate the mid-sagittal vertical stress distribution for the five grades of aging if the annulus Young's modulus and Poisson's ratio were kept changeless. The related mean vertical compressive stresses in nucleus, in internal and external annulus are seen in *Figures 6a, 6b* and *6c*, respectively, while the posterior bulging is seen in *Figure 6d*. The related central and external vertical compressive strains of the disc are illustrated in *Figures 7a* and *7b*, respectively. *Figures 8a, 8b, 8c* and *8d* show the vertical compressive stiffness of the nucleus, internal and external annulus, and the whole disc, respectively.



*Figure 5.* Mid-sagittal vertical stress distribution in the five grades of aging process when a) the Young's modulus, b) the Poisson's ratio of both the internal and external annulus are separately kept changeless

If the Young's moduli of internal and external annulus were kept on their initial values ( $E=4$  MPa and  $E=5$  MPa, respectively) during the gradual aging of all other components of the motion segment (*Table 2*), the stresses in the aging nucleus rapidly increased (by 7%, in grade 2, by 29% in grade 3, and by 68% in grade 4, *Figure 6a*); while both in the internal and external annulus decreased (by 8-13% in grade 3, *Figures 6b* and *6c*). At the same time the central deformations of disc rapidly increased (by 12% in grade 2 and by 43% in grade 3, *Figure 7a*), and the external deformations also increased (by 10% and 36% in grade 2 and 3, *Figure 7b*) in harmony with the posterior bulging increase (14% in grade 2 and 49% in grade 3, *Figure 6d*). There was a small decrease in the stiffness of nucleus (5-10% in grade 2 and 3, *Figure 8a*), but both in the internal and external annulus a considerable stiffness loss was observed (11% and 36% in grade 2 and 3, *Figures 8b* and *8c*) that led to the radical stiffness decrease of the whole disc (by 10% in grade 2 and by 27% in grade 3, *Figure 8d*).

It can be seen in *Figures 6, 7 and 8* that the Poisson's ratio of the internal and external annulus in itself has no significant effect on the stresses and deformations of the disc or on the stiffness of the disc components and the whole disc. If keeping simultaneously the Young's modulus and Poisson's ratio of internal and external annulus on their young healthy level, the effect was similar to the separated influence of Young's modulus of annulus in *Figures 6, 7 and 8*.

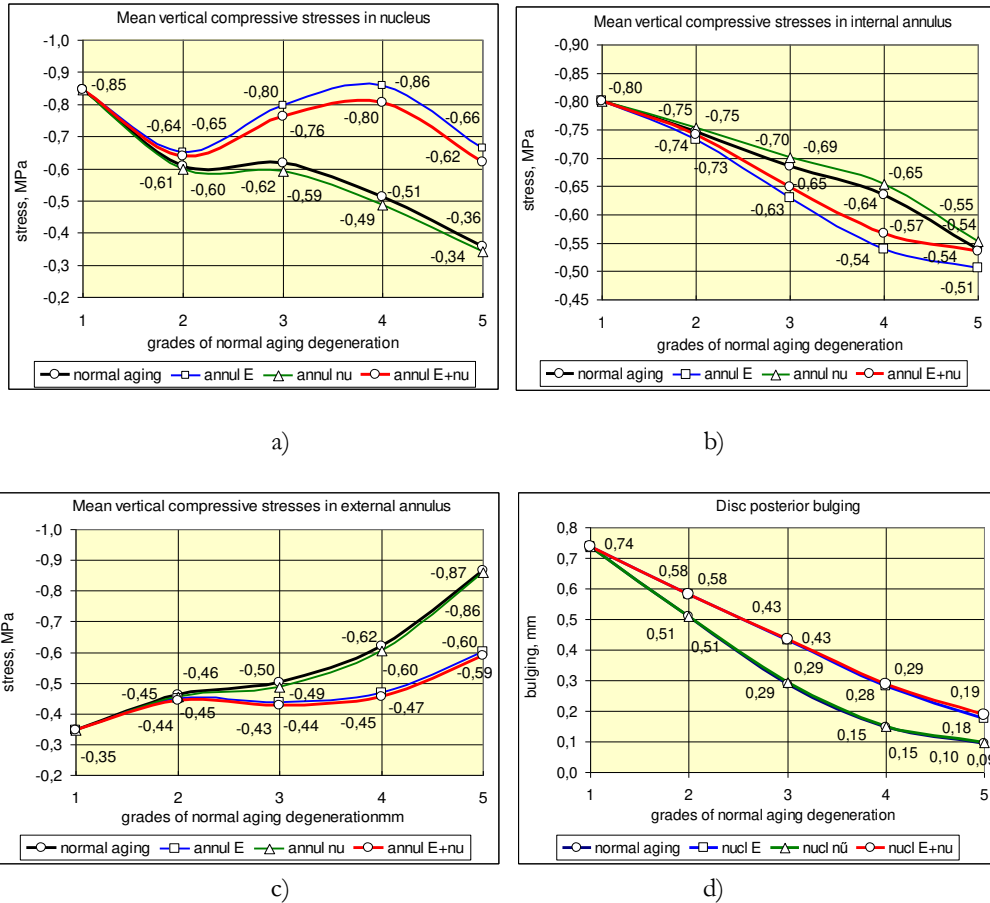


Figure 6. Mean vertical compressive stresses in a) nucleus, b) internal annulus, c) external annulus and d) posterior bulging for the cases of aging degeneration process when E, nu and E+nu of both the internal and external annulus are kept on their initial healthy values changeless

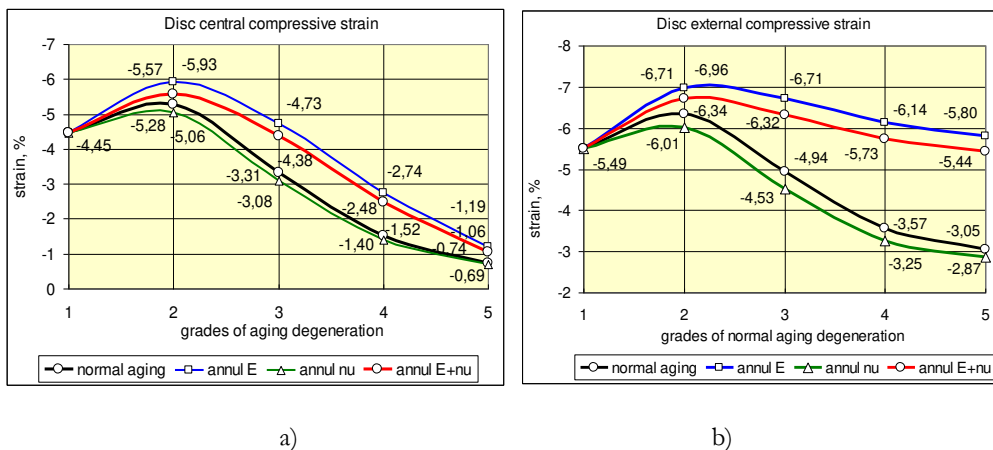


Figure 7. a) Central and b) external vertical compressive strains of disc in aging degeneration process if E, nu and E+nu of both the internal and external annulus are kept on their initial healthy values

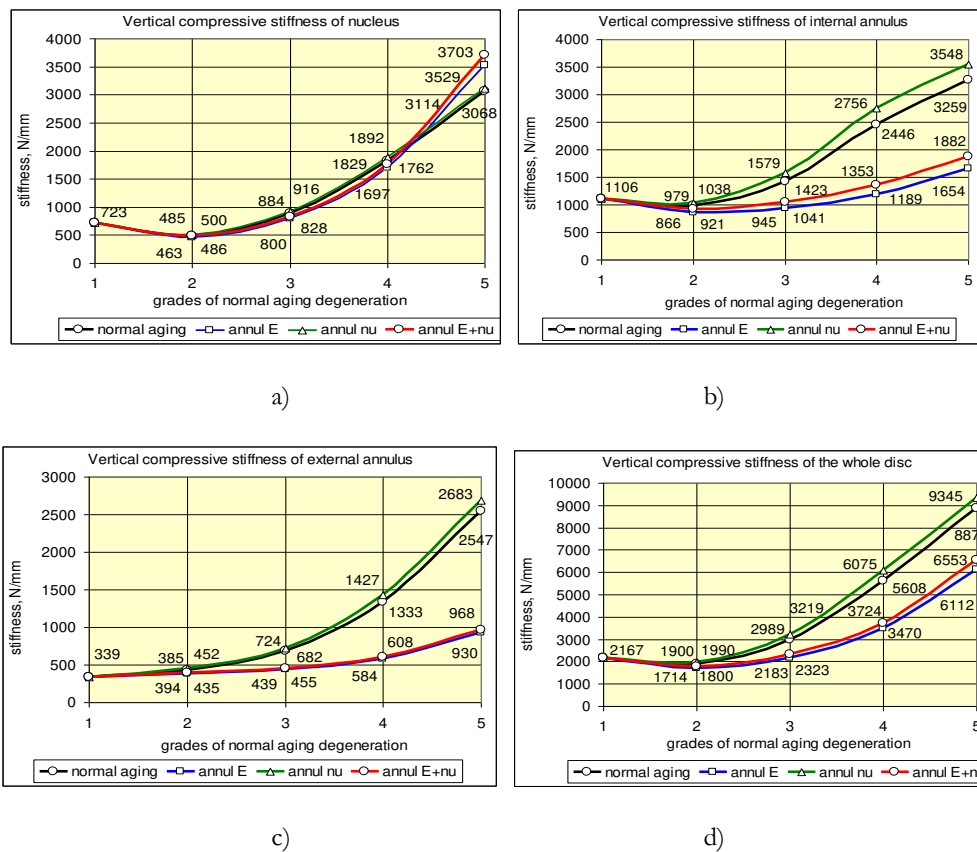


Figure 8. Vertical compressive stiffness of a) nucleus, b) internal and c) external annulus and d) the whole disc for the cases of aging degeneration process if E, nu and E+nu of both the internal and external annulus are kept on their initial healthy values changeless

Figures 9-11 illustrate the stresses, strains and stiffnesses of the different parts of the disc for the age-related degeneration process when all components of the lumbar motion segment were under normal aging degenerated state (Table 2) except for the vertebral cancellous bone and the cartilaginous endplate, when the Young's modulus of them were separately and together kept on their initial healthy values of grade 1.

In Figures 9a, 9b and 9c the change of the mean vertical compressive stresses in nucleus, internal and external annulus can be seen, respectively, while the posterior bulging is seen in Figure 9d during the five grades of aging degeneration. The related central and external vertical compressive strains of the disc are illustrated in Figures 10a and 10b, respectively. Figures 11a, 11b and 11c show the vertical compressive stiffness of the nucleus, the internal and external annulus, respectively, while in Figure 11d the stiffness of the whole disc can be seen for the grades of aging degeneration process.



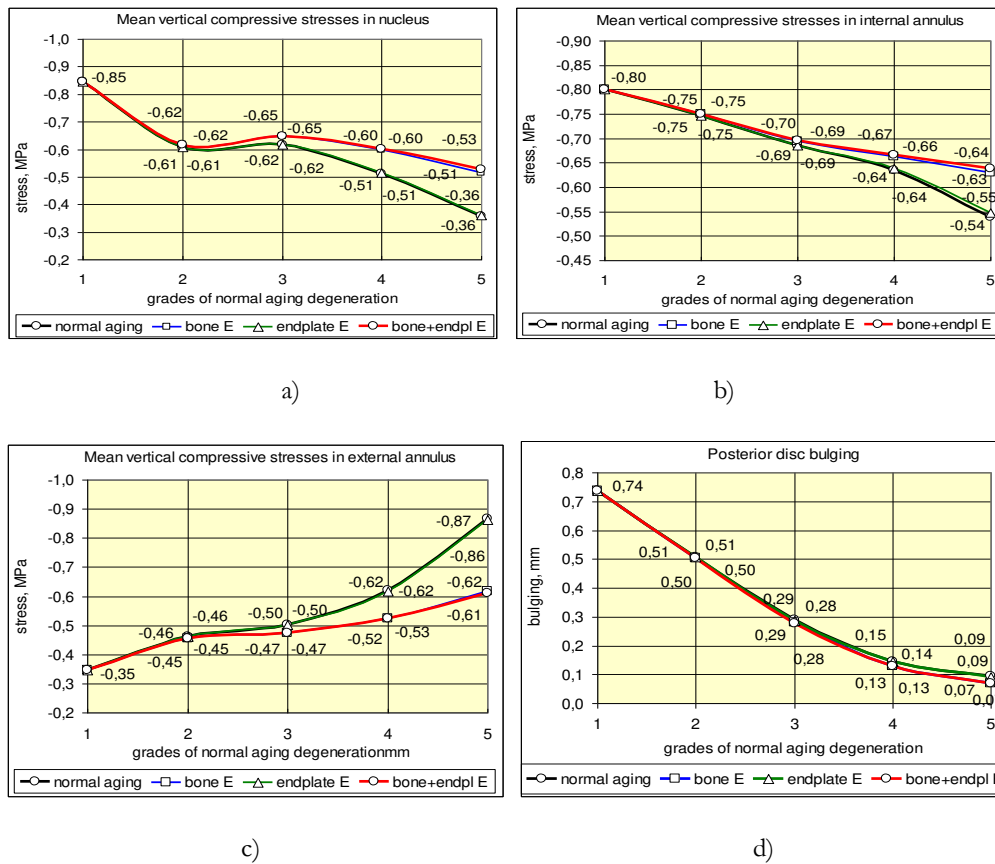


Figure 9. Mean vertical compressive stresses in a) nucleus, b) internal annulus and c) external annulus for the cases of aging degeneration process while the vertebral cancellous bone E, cartilaginous endplate E and bone + endplate E keep their initial healthy values changeless

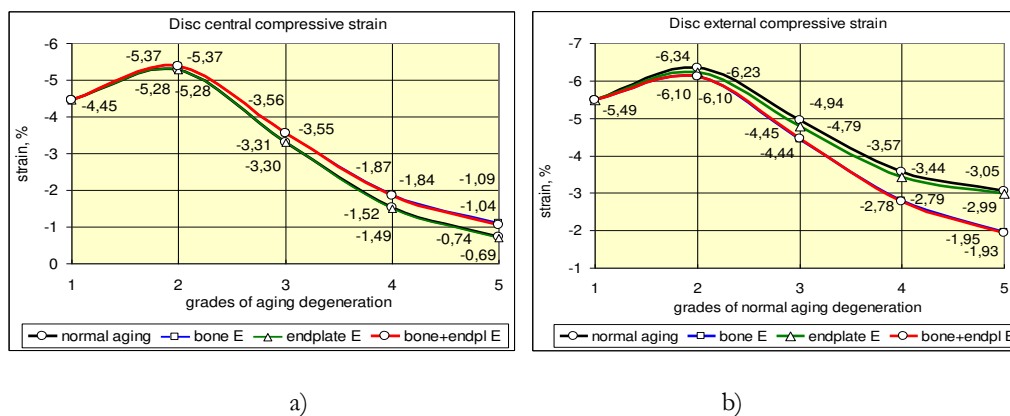
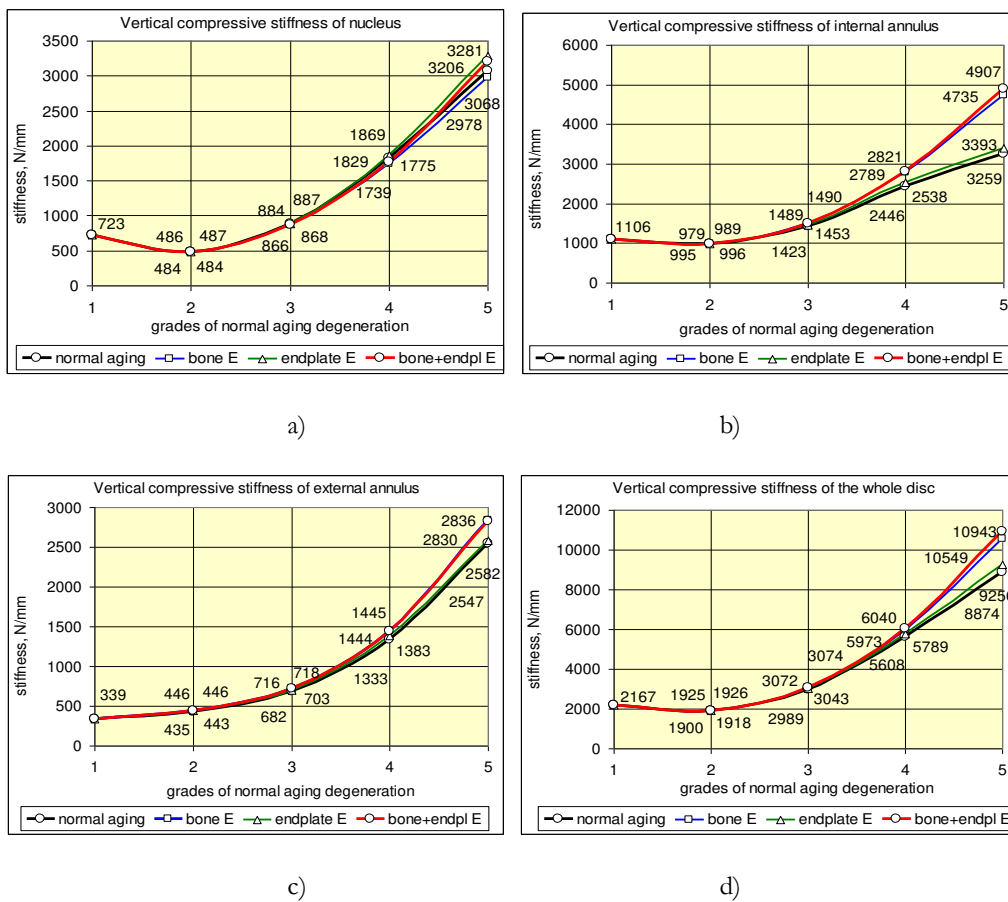


Figure 10. a) Central and b) external vertical compressive strains of disc for the cases of aging degeneration process if the vertebral cancellous bone E, cartilaginous endplate E and bone + endplate E keep their initial healthy values changeless

If the Young's modulus of the vertebral cancellous bone was kept on its original strong value ( $E=150$  MPa) while all other components were under gradual aging (Table 2), in the degeneration grade 2, 3 and 4 the stresses in the nucleus slightly increased (by 1%, 5%, 17%, Figure 9a), in the internal annulus also increased (by 0%, 1%, 4%, Figure 9b), while in the external annulus decreased

(by 1%, 5%, 15%, *Figure 9c*). At the same time the central deformations of disc increased (by 2%, 7%, 23%, *Figure 10a*), and the external deformations decreased (by 4%, 10%, 22%, *Figure 10b*) in harmony with the posterior bulging that also but slightly decreased (by 1%, 4%, 11%, *Figure 9d*). There was a small decrease in the stiffness of nucleus (0%, 2%, 5%, *Figure 11a*), and a small increase in the internal and external annulus (2-3%, 5%, 8-14%, *Figures 11b and 11c*) yielding only a small stiffness increase on the whole disc (1%, 3%, 7%, *Figure 11d*).

It can be seen in *Figures 9, 10 and 11* that the Young's modulus of endplate in itself has practically no effect on the stresses and deformations of the disc or on the stiffness of the disc components or that of the whole disc. If keeping simultaneously the Young's modulus of trabecular bone and endplate on the young healthy level, the effect was similar to the separated influence of the Young's modulus of bone, seen in *Figures 9, 10 and 11*.



*Figure 11.* Vertical compressive stiffness of a) nucleus, b) internal and c) external annulus and d) the whole disc for the cases of aging degeneration process if the vertebral cancellous bone E, cartilaginous endplate E and bone + endplate E keep their initial healthy values changeless

## Discussion and conclusion

Although the Young's modulus and the Poisson's ratio changes together during aging, by finite element numerical analysis the effect of them can be analyzed separately. It can be concluded that in the material modeling of spinal segments for numerical simulations, the Young's modulus and

Poisson's ratio of nucleus need special care since the mechanical behaviour of the components and the whole segment is very sensitive to these data.

It was demonstrated that a soft nucleus with lost hydrostatic state is very dangerous yielding the complete loss of load bearing capacity of nucleus. This happens when the young nucleus quasi burst out due to some traumatic or other accidental effect yielding extreme shortening and complete stiffness loss in nucleus (*Figures 3a and 4a*) and a large stiffness lost in the whole disc (*Figure 4d*) leading to the rapid overload and injury of the internal and external annulus (*Figures 2b and 2c*). Consequently, the most important is to keep the hydrostatic stress state in the young nucleus about the second degeneration degree, in the young adult age. Keeping the hydrostatic stress state in this age can increase the compression load bearing capacity of nucleus by 30-40% and the stiffness of the whole disc by 30%. The importance of keeping the incompressibility of nucleus in the first period of aging is supported by several authors<sup>3,12,13</sup> stating that light degeneration of disc led to instability, while the stability restored with further degeneration, since lightly degenerated discs had the smallest stiffness. Since the stiffness of young disc is influenced mainly by the state of nucleus, it is obvious that the effect of loss of hydrostatics is crucial in the starting period of aging process.<sup>8,9</sup>

The Poisson's ratio of annulus in itself has very small effect on the mechanics of disc, however, the effect of Young's modulus of annulus in itself and together with the Poisson's ratio is very important (*Figures 6, 7 and 8*). The stiffening of annulus during normal aging is useful, since it helps to maintain the stability of disc. Indeed,<sup>3,12,13</sup> concluded that after the instability in younger age the stability restored with further degeneration, since the stiffness increased during further degeneration.

The stiffness of the cartilaginous endplate in itself has also a very small influence, since it is supported by the vertebral cancellous bone, thus, the effect of it depends on the state of the bone (*Figures 9, 10 and 11*). We can say that the effect of the bone is important mainly for the elderly. In the first half of the aging process, the strong bone has a small effect equally on the stresses, deformations or stiffness. In the elderly, in grade 4 and 5, the strong bone increases the load transfer through the nucleus, and unloads the external annulus, it increases the central and decreases the external shortenings of disc by decreasing the bulging that can press the nerve roots causing load back problems (*Figures 9 and 10*). On the contrary, in the case of osteoporosis, the load transfer and the deformations move from inside to outside causing the overload of the external annulus, leading to strong bulging and injurious degeneration. However, the stiffness of disc is slightly influenced by the state of the bone.

By the separated analysis of the material moduli it can be concluded that to keep the hydrostatic stress state in the nucleus is crucial important in the first period of aging process. The loss of incompressibility of nucleus leads to the loss of load bearing capacity of nucleus and the injurious overload of the internal and external annulus. Osteoporosis moves the load transfer from the central to the external region that can lead to the breakdown of the cortical bone of vertebrae.

---

## REFERENCES

1. Adams MA, Freeman BJ, Morrison HP, Nelson IW, Dolan P. Mechanical initiation of intervertebral disc degeneration, *Spine*, 2000;25(13):1625-36.

2. Ferguson SJ, Steffen T. Biomechanics of aging spine, *Eur. Spine J.*, 2003;12(Suppl.2):97-103.
3. Adams MA, Bogduk N, Burton K, Dolan P. *The Biomechanics of Back Pain*, Churchill Livingstone, Edinburgh, London, New York, Oxford, Philadelphia, 2002. p. 238p.
4. Kurutz M, Oroszváry L. Finite element analysis of weightbath hydrotraction treatment of degenerated lumbar spine segments in elastic phase, *Journal of Biomechanics*, 2010;43(3):433-41.
5. Denoziere G. Numerical modeling of ligamentous lumbar motion segment, Master thesis, Georgia Institute of Technology, 2004.
6. Panjabi MM, Oxland T, Takata K, Goel V, Duranceau J, Krag M. Articular facets of the human spine, quantitative three dimensional anatomy, *Spine*, 1993;18(10):1298-1310.
7. Kurutz M, Oroszváry L. Finite Element Analysis of Long-Time Aging and Sudden Accidental Degeneration of Lumbar Spine Segments in Compression, *Biomechanica Hungarica*, 2013;VI(1):223-34.
8. Iatridis JC, Wedenbaum M, Setton LA, Mow VC. Is the nucleus pulposus a solid or a fluid? Mechanical behaviours of the nucleus pulposus of the human intervertebral disc, *Spine*, 1996;21(10):1174-84.
9. Iatridis JC, Setton LA, Wedenbaum M, Mow VC. Alterations in the mechanical behavior of the human lumbar nucleus pulposus with degeneration and aging. *J. of Orthopaedic Research*, 1997;15(2):318-22.
10. Kurutz M, Bender T. Weightbath hydrotraction treatment – application, biomechanics and clinical effects, *J. of Multidisciplinary Healthcare*, 2010;(3):19-27.
11. Kurutz M, Bene É, Lovas A. In vivo deformability of human lumbar spine segments in pure centric tension, measured during traction bath therapy, *Acta of Bioengineering and Biomechanics*, 2003;5(1):67-92.
12. Schmidt H, Kettler A, Rohlmann A, Claes L, Wilke HJ. The risk of disc prolapses with complex loading in different degrees of disc degeneration - a finite element analysis, *Clinical Biomechanics*, 2007;22(9):988-98.
13. Tang XJ, Chen QX, Liu YS, Li FC. Analysis of lumbar disc degeneration using three-dimensional nonlinear finite element method, (Article in Chinese), *Zhonghua Yi Xue Za Zhi*, 2008;88(23):1634-8.

***The authors gratefully acknowledge the Hungarian Scientific Research Fund OTKA for providing financial support in the frame of the grant K-075018.***

## FINITE ELEMENT ANALYSIS OF WEIGHTBATH HYDROTRACTION TREATMENT IN THE CASE OF OSTEOPOROSIS

Márta Kurutz<sup>1</sup>, László Oroszvály<sup>2</sup>

<sup>1</sup>Budapest University of Technology and Economics

<sup>2</sup>Knorr Bremse Hungaria Ltd

[kurutzm@eik.bme.hu](mailto:kurutzm@eik.bme.hu)

---

### **Abstract**

3D finite element analysis of the first elastic period of the weightbath hydrotraction treatment is presented to analyze the effect of osteoporosis during the traction procedure. A systematic parameter analysis of the material moduli of the aging spinal motion segment with osteoporotic bone was investigated. It was concluded that the osteoporosis in itself can not be a contraindicating factor of weightbath hydrotraction treatment. However, if applying extra weights, beside the quality of bone and the grade of osteoporosis, the age of patients, their body structure and body weight must be carefully considered as well.

**Keywords:** weightbath hydrotraction treatment, lumbar spinal motion segment, indirect and direct traction, elongation of disc, osteoporosis

---

### **Introduction**

A large percent of population is affected by low back pain, starting from the degeneration of lumbar spinal structures. In some cases, traction might be the effective treatment. Weightbath hydrotraction therapy (WHT) is a method of hydro- or balneotherapy where the patient is suspended in water, loaded by extra weights applied on certain points of the body, to stretch the different parts of the spinal column or lower limbs. The weightbath hydrotraction method, its indications, contraindications, and clinical effects, its application, equipment and the biomechanics of it were detailed in.<sup>1</sup> However, the question has not been answered yet that what is the relation between WHT and osteoporosis, or rather, is it possible to apply the treatment for strongly osteoporotic patients?

In this study a systematic parameter-analysis is used for the analysis of the mutual effect of the different material moduli of the components of the lumbar motion segment and the vertebral cancellous bone during the special loading conditions of the traction under the water.

Although finite element (FE) simulations are increasingly applied to examine the mechanical behaviour of healthy or degenerated spine or the effects of surgical treatments; as far as authors know, FE analyses of the weightbath-like underwater traction treatment can not be found in the literature except for<sup>2</sup> where 3D finite element models (FEM) of human lumbar functional spinal units (FSU) were used for the numerical analysis of weightbath hydrotraction therapy (WHT) in the case of healthy and degenerated lumbar spine. In this study the FE model developed in<sup>2</sup> has been extended to the analysis of WHT applied for osteoporotic lumbar spine.

## Methods

For the numerical analysis of the effect of WHT on osteoporotic spine, the FEM model that we developed earlier in ANSYS system<sup>2</sup> was used, representing five degeneration grade of aging. A 3D model of a typical lumbar segment L4-5 was created<sup>3,4</sup> by using Pro/Engineer code. Cortical and cancellous bone of vertebrae was separately modeled, including posterior bony elements and facet joints. The height of the disc was considered to decrease linearly from 10 to 6 mm for the five aging degeneration degrees. The endplates were divided into external bony and central cartilaginous part. Accordingly, the annulus matrix was divided into internal and external ring and three layers of annulus fibers. The FE mesh was generated by ANSYS Workbench and the connections between the several geometrical components were integrated to the FE model by ANSYS Classic. The FE model consisted of solid, shell and bar elements. Annulus matrix, nucleus, cancellous bone, articular joints and different types of attachments were modeled by solid elements; cortical shells and endplates were modeled by shell elements. The compatibility between the adjacent solid and shell elements was guaranteed by contact elements. All ligaments were modeled by shell elements.

| Components of FSU                  | Young's mod<br>[MPa] | Poisson's<br>ratio |
|------------------------------------|----------------------|--------------------|
| vertebral cortical bone            | 12000                | 0.3                |
| posterior elements, facet          | 3500                 | 0.3                |
| vertebral cancellous bone          | 150                  | 0.3                |
| bony endplate                      | 12000                | 0.3                |
| cartilaginous endplate             | 100                  | 0.4                |
| nucleus                            | 1                    | 0.499              |
| annulus ground substance, internal | 4                    | 0.45               |
| annulus ground substance, external | 5                    | 0.40               |
| annulus fibers                     | 500/400/300*         | -                  |
| anterior longitudinal ligament     | 8**                  | 0.35               |
| posterior longitudinal ligament    | 10**                 | 0.35               |
| other ligaments                    | 5**                  | 0.35               |

\*external/middle/internal fibers, \*\*tension only

Table 1. Material moduli of the components of healthy motion segment

Table 1 shows the material moduli of healthy lumbar motion segment. For the bony elements and endplates, for both tension and compression, linear elastic isotropic materials were applied, based on the literature. Annulus ground substance and nucleus were considered linear elastic for compression and bilinear elastic for tension. Nucleus and annulus matrix were considered linear elastic. Collagen fibers of the annulus were considered as bilinear elastic isotropic tension-only material. All the seven ligaments were integrated in the model with bilinear elastic tension-only materials of the literature again.

Five grades of age-related degeneration process were introduced, seen in Table 2 separately for compression and tension. Age-related normal degeneration processes of segment start generally in the nucleus. A healthy young nucleus is in hydrostatic compression state. During aging, the nucleus loses its incompressibility by changing gradually from fluid-like to solid material of increasing stiffness. These kinds of nucleus changes were modeled by decreasing Poisson's ratio

with increasing Young's modulus, seen in *Table 2*. This behavior is generally accompanied by the stiffening process of the annulus. This procedure was modeled also by increasing Young's modulus with slightly decreasing Poisson's ratio, by distinguishing the internal capsular and the external ligamentous part of annulus, by considering the internal annulus to be weaker. The elastic moduli of annulus fibers were decreased during aging.

| <b>Grades of aging degeneration*</b><br>(Young's mod/Poisson's ratio) | <b>grade 1</b><br>(healthy) | <b>grade 2</b> | <b>grade 3</b> | <b>grade 4</b> | <b>grade 5</b><br>(fully deg.) |
|---|-----------------------------|----------------|----------------|----------------|--------------------------------|
| disc height [mm]  | 10                          | 9              | 8              | 7              | 6                              |
| <b>For compression</b>  |                             |                |                |                |                                |
| nucleus   | 1/0.499                     | 2/0.475        | 6/0.45         | 16/0.425       | 36/0.4                         |
| annulus matrix, internal ring   | 4/0.45                      | 4.5/0.44       | 6.5/0.43       | 11.5/0.42      | 20/0.41                        |
| annulus matrix, external ring   | 5/0.40                      | 6/0.39         | 9/0.38         | 17/0.37        | 29/0.36                        |
| cancellous bone   | 150/0.3                     | 125/0.3        | 100/0.3        | 75/0.3         | 50/0.3                         |
| cartilaginous endplate  | 100/0.4                     | 80/0.4         | 60/0.4         | 40/0.4         | 20/0.4                         |
| annulus fibers (ext/middle/int)                                       | 500/400/300                 | 250/200/150    | 125/100/75     | 63/50/38       | 10/10/10                       |
| <b>For tension</b>  |                             |                |                |                |                                |
| nucleus   | 0.4/0.499                   | 1/0.475        | 1.6/0.45       | 2.2/0.425      | 2.8/0.4                        |
| annulus matrix, internal ring   | 0.4/0.45                    | 1/0.44         | 1.6/0.43       | 2.2/0.42       | 2.8/0.41                       |
| annulus matrix, external ring   | 0.5/0.40                    | 1.2/0.39       | 2/0.38         | 3/0.37         | 3.5/0.36                       |
| anterior longitudinal ligaments                                       | 8/0.45                      | 5/0.45         | 3/0.45         | 2/0.45         | 1/0.45                         |
| posterior longitudinal ligaments                                      | 10/0.45                     | 6.5/0.45       | 4/0.45         | 2/0.45         | 1/0.45                         |
| other ligaments   | 5/0.45                      | 5/0.45         | 3/0.45         | 2/0.45         | 1/0.45                         |

\*Other elements are seen in *Table 1*

*Table 2.* Modeling of age-related degeneration for compression and tension

For the annulus ground substance and for the nucleus were considered linear elastic material in compression, and bilinear elastic in traction. In the indirect phase of traction the compressive material moduli, in the direct phase of traction tensile Young's moduli of annulus matrix and nucleus were used, seen in *Table 2*. The compressive moduli were applied from the literature, the tensile moduli were determined by parameter identification based on the in vivo experiments made in traction bath.<sup>9-10</sup> For healthy nucleus we supposed fluid-like incompressible material both for tension and compression. For the nucleus fibers and spinal ligaments we supposed that during aging the fibers and ligaments elasticity decreases, that is, they are in more and more elongated state, instead of a gradual stiffening with a more rigid behaviour.

The traction forces occurring along the spine during WHT are detailed in.<sup>1</sup> During WHT, in the different parts of the spinal column different tensile forces may occur, depending (1) on the relative density of the human body and the water, (2) on the value and position of the applied extra weight loads, and first of all, (3) depending on the mode of suspension.

The classification of traction loads is based on the definition of traction elongation of segments. Since nobody knows the intact load- and deformationless state of segments and discs, a reference state must be chosen. In this way, elongation of segments is specified as an extension compared with the state of segments just before the traction bath treatment in normal upright standing

position. That is, zero elongation belongs to the compressed reference state of segments just before the treatment.

The traction loads are related to the same reference state, according to which there are two components of traction loads: (1) the indirect traction load, namely, the decompressive force consisting of the removal of the compressive preload of body weight and the removal of muscle forces that are partly or totally relaxed during the treatment; and (2) the direct traction load consisting of the active tensile force due to the buoyancy and the applied extra loads reduced by the buoyancy, as well. Consequently, the traction process in itself can also be divided into an indirect and a direct phase.

We applied exclusively cervical suspension in the water. In this case at the lumbar level the decompressive force is the weight of the upper body, that is about 58-60 % of the body weight,<sup>5</sup> completed by the muscle forces that are approximately the same as the upper body weight,<sup>6-7</sup> since the muscles are completely relaxed in water. Thus, the indirect traction load yields  $F_1 = 2 \cdot 0.6 \cdot G = 1.2G$ . The direct tensile force from the body weight and the extra load depend on the buoyancy,<sup>8</sup> namely, on the density  $\rho_b$  of the human body,  $\rho_w$  of the water and  $\rho_l$  of the lead material of extra loads. This way the direct tensile load from the body weight at the lumbar level is  $0.42G(1 - \rho_w/\rho_b) = 0.016G$  if  $\rho_b = 1040 \text{ kg/m}^3$  and  $\rho_w = 1000 \text{ kg/m}^3$ . This load is surprisingly small, so the idea of applying extra weights seems to be evident. The extra load from lead weights  $W$  yields  $W(1 - \rho_w/\rho_l) = 0.912W$  if  $\rho_l = 11350 \text{ kg/m}^3$ . Thus, finally the direct traction load yields  $F_2 = 0.016G + 0.912W$ . By supposing  $G = 700 \text{ N}$  body weight and  $W = 2 \cdot 20 = 40 \text{ N}$  extra loads, the indirect and direct traction loads yield 840 N and 47.7 N, respectively.

For the numerical simulation of WHT we applied a normal body weight of 700 N and 3x20 N extra lead weights applied on the ankles, thus the standard load were 850 N indirect and 50 N direct traction forces. The load was distributed along the superior and inferior surface of the upper and lower vertebra of the segment, by applying rigid load distributor plates on the surfaces. This load was acting during the 20 minutes long duration of the treatment.

WHT is a typical viscoelastic process with initial instant elastic and 20 minutes long creeping phases. Thus, the elongations can be divided to initial elastic and following creeping parts. In this study we analyze the osteoporotic relations in the initial elastic part of the treatment only. The creeping part depends on the damping characteristics of the components of the motion segment that was measured during the WHT treatment of patients by.<sup>11</sup>

In this study we assumed that all components of the motion segment are under normal degeneration according to the data of *Table 2* except for the cancellous bone and the endplate that remained intact with the data of grade 1. Then the elastic modulus of cancellous bone and the cartilaginous endplate was separately and simultaneously gradually decreased as seen in *Table 2* in which osteoporotic weakening was modeled. In the analysis the material moduli of the cortical bone were kept changeless. Then the obtained results, elongations and stresses in the components of disc and the disc contractions were compared.



Results

In the following the results are related to the instant beginning period of WHT, during which the behaviour of nucleus and annulus is bilinear elastic, namely, first the indirect load acts due to the remove of the upper body weight with the muscle forces, just after the direct traction load starts to act due to the buoyancy from the body and extra loads under the water.

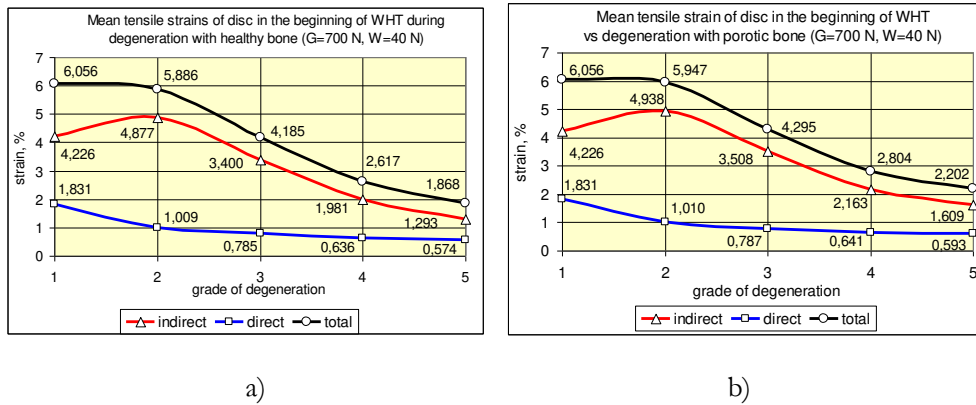


Figure 1. Mean indirect (from 850), direct (from 50N) and total (from 850+50N) tensile strains of the disc in the beginning of WHT for the grades of age-related degeneration process of lumbar motion segment with healthy (a) and osteoporotic (b) vertebral cancellous bone

Figure 1 illustrates the mean tensile strains of intervertebral disc from the indirect (850N), direct (50N) and total (850+50N) traction load the disc for a patient of 700N body weight with 2x20 N extra lead weight on the ankles in the grades of age-related degeneration process of segment with healthy (Figure 1a) and osteoporotic (Figure 1b) vertebral cancellous bone. Compared to the healthy case, the mean total strains of disc in osteoporotic case increased slightly, by 1, 3, 7 and 18% in grade 2, 3, 4 and 5 respectively.

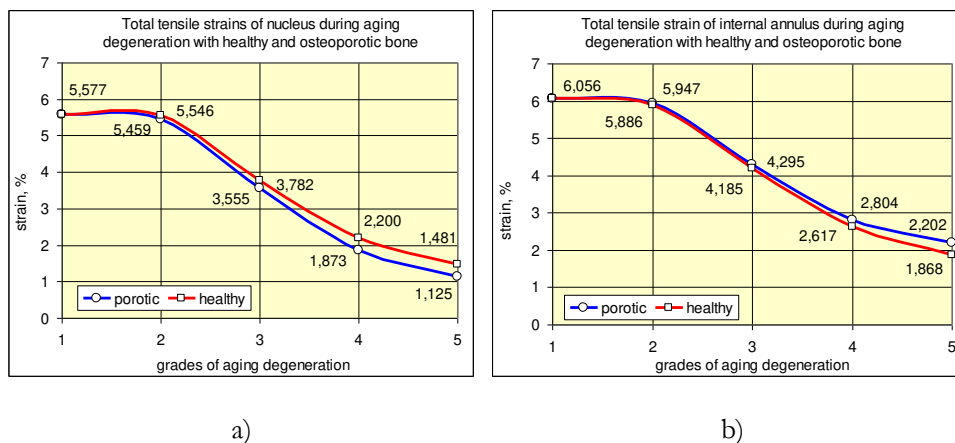


Figure 2. Total tensile strains (from 850+50N) of the disc nucleus (a) and external annulus (b) for a patient of 700N body weight with 2x20 N extra lead weights on ankles with healthy and osteoporotic cancellous bone in the beginning of WHT for the grades of degeneration process

However, the certain parts of the disc showed strongly different elongations and tensile strains, seen in Figure 2, where the total (indirect + direct) tensile strains of the disc nucleus and external

annulus can be seen. While in the nucleus the tensile strains decreased in osteoporotic case by 2, 6, 15 and 24%, in the external annulus the strains increased by 3, 10, 23 and 45%, for the aging grades 2, 3, 4 and 5, respectively. At the end of the elastic phase of WHT, in the elderly, in grade 3-5, the osteoporotic elongations and strains are 15-25% smaller in the middle of the disc and 25-45% larger in the edge of the disc.

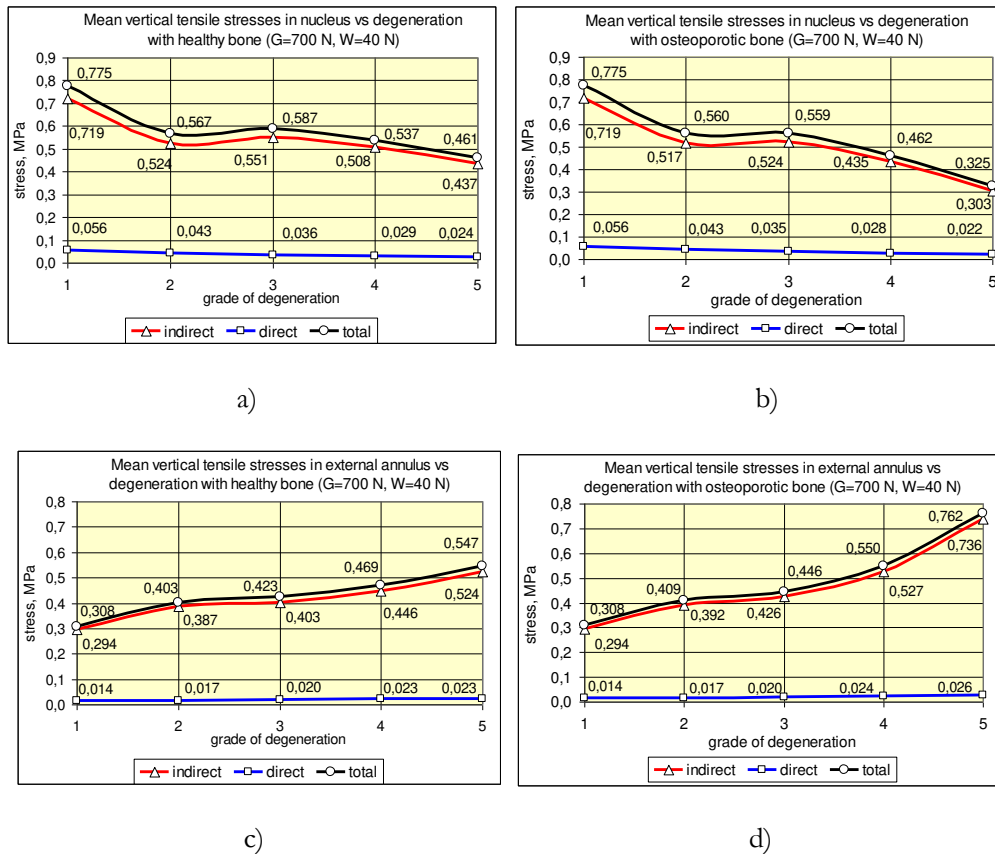


Figure 3. Mean indirect (for 850 N), direct (for 50N) and total (for 850+50N) tensile stresses in the nucleus with a) healthy and b) osteoporotic bone and in the external annulus with c) healthy and d) osteoporotic cancellous bone in the beginning of WHT for the grades of age-related degeneration process of lumbar motion segment

In Figure 3 the vertical tensile stresses in the nucleus (Figures 3a, 3b) and in the external annulus (Figures 3c, 3d) are illustrated from the indirect (850N), direct (50N) and total (850+50N) traction load in the grades of age-related degeneration process of segment with healthy (Figures 3a, 3c) and osteoporotic (Figures 3b, 3d) vertebral cancellous bone. Compared to the healthy bone case, in osteoporotic case the mean total tensile stresses in the nucleus decreased by 1, 5, 14 and 29%, while in the external annulus the stresses increased by 1, 5, 17 and 39% for the aging grades 2, 3, 4 and 5, respectively, as shown separately for the nucleus in Figure 4a and for the external annulus in Figure 4b. At the end of the elastic phase of WHT, in the elderly, in grade 3-5, the osteoporotic sagittal tensile stresses are 15-30% smaller in nucleus, but 20-40% larger in the external annulus.

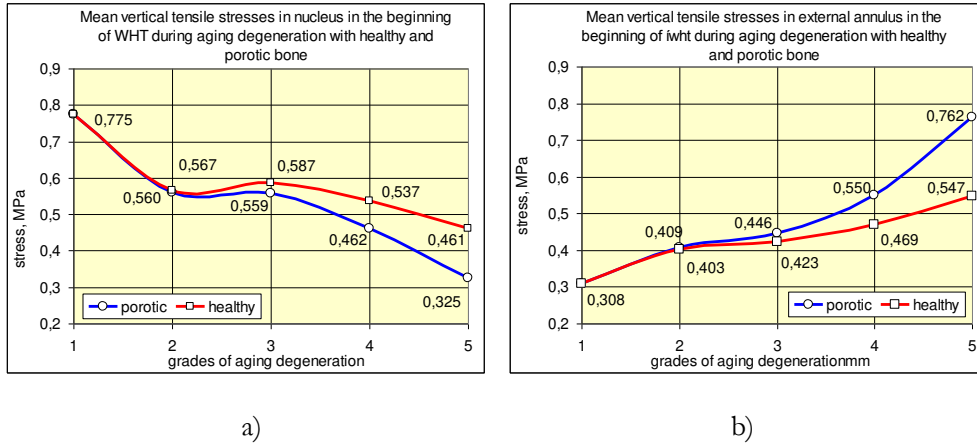


Fig. 4. Mean total vertical tensile stresses of the disc nucleus (a) and external annulus (b) with healthy and osteoporotic cancellous bone in the beginning of WHT for the grades of age-related degeneration process of lumbar motion segment

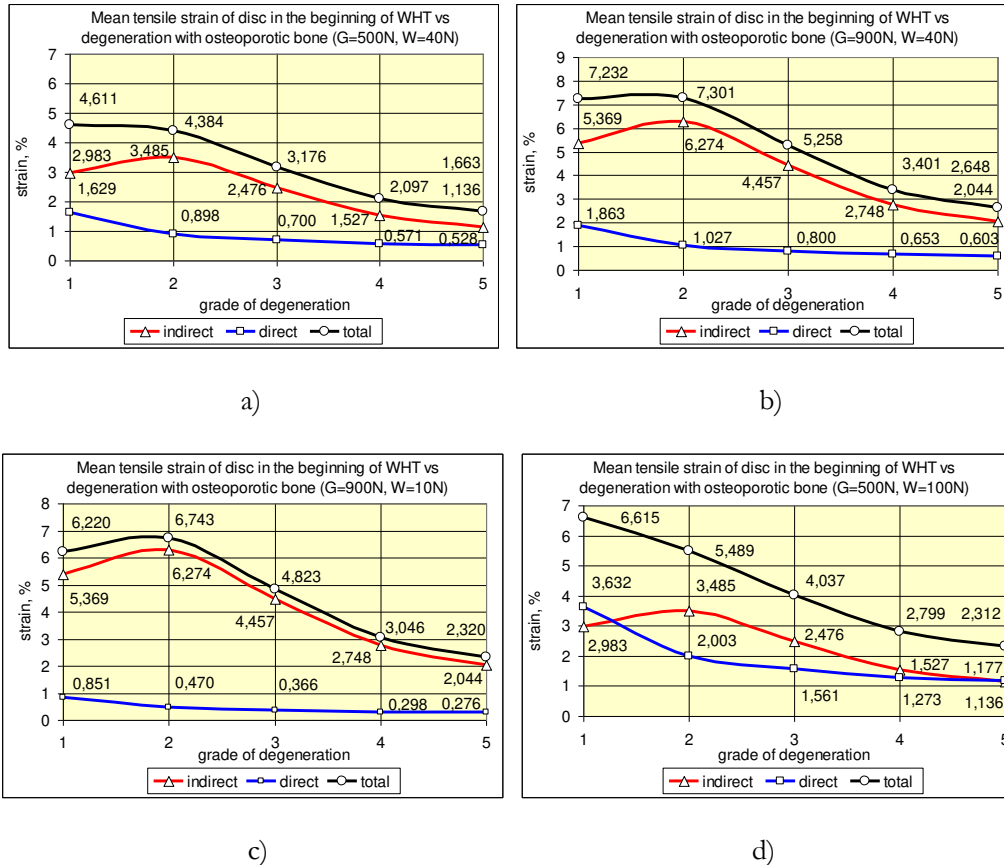
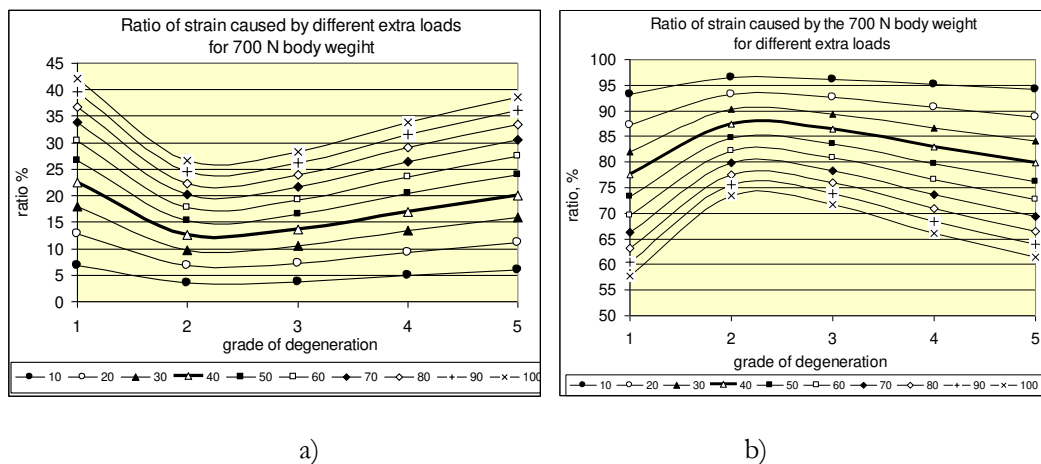


Figure 5. Mean indirect (for 850 N), direct (for 50N) and total (for 850+50N) tensile strains of the disc in the beginning of WHT for the grades of age-related degeneration process with osteoporotic cancellous bone, for the cases of different body weights G and applied extra loads W: a) G=500N , W=40N; b) G=900N, W=40N; c) G=900N, W=10N; d) G=500N, W= 100N

In the WHT the extra weight has a very important role in the traction effect. In *Figure 1b* the traction strains of disc were illustrated for the generally applied 2x20N extra weights for a osteoporotic patient of normal 700N body weight. In *Figures 5a* and *5b* the same extra lead weight was applied but for a small thin, and for a large corpulent equally osteoporotic patient of 500N and 900N body weight, respectively. While in the corpulent patient, the ratio of direct traction effect was only 10-18% of the total one, for the thin patient it was 18-30%. *Figures 5c* and *5d* show the extreme cases of the under-loaded (2x5N) corpulent patient with 3-5%, and the overloaded (2x50N) thin patient with 33-50% direct traction effect.

*Figure 6* summarizes the traction effect of extra weight loads for osteoporotic patients of normal body weight of 700N. The load was gradually increased by 2x5N load steps to 2x50N load. *Figure 6a* shows the ratio of traction effect caused by the extra loads, *Figure 6b* shows the ratio caused by the body weight. The heavy line among the curves related to the generally applied 2x20N extra weight. It can be seen that the extremum of all curves on both figures was located around the degeneration grade 2 of weakly degenerated young adult age.



*Figure 6.* The traction effect of the extra load for osteoporotic patient with 700N body weight: the ratio of tensile strain caused by the extra weight (a) and caused by the body weight (b) by increasing the extra load from 2x5N to 2x50N, increased proportional by 2x5N increments

Disc contraction is influenced by the external annulus elongation that increases in the case of osteoporosis. Disc contraction of a normal 700N body weight with 2x20N extra weights increased by 5-25% for osteoporotic elderly.

## Discussion and conclusion

Based on the numerical analysis, we can state that the load bearing zone in the disc moves from inside to outside. In the case of healthy trabecular bone the support of the nucleus both in tension and compression is strong, thus, in traction, higher central deformations occur. As the resistance of the bone decreases due to osteoporosis mainly in the middle domain of vertebrae, the deformations of the nucleus decrease and that of the external annulus increase. For healthy trabecular bone the middle of the disc shows the higher elongations, for osteoporotic bone the external regions give the larger elongations.

In agreement with earlier results of spinal degeneration analyses<sup>2,12</sup> the age-related deformability is maximum in the young adults in grade 2, as seen in the case of traction bath treatment as well (*Figure 1*). This yields that the traction effect of the extra loads is also minimum around grade 2, for weakly degenerated young adults (*Figure 6a*), in line with the maximum traction effect of body weight in the same age (*Figure 6b*).

By taking into account that the in vivo measured elongations in WHT for osteoporotic elderly over 60 years with 2x20N extra load was in the elastic phase of WHT about 0,23 mm that increased during the 20 minutes long viscoelastic phase of the treatment to about 0,55 mm detailed in,<sup>9-11</sup> we can conclude that the osteoporosis in itself can not contraindicate the weightbath hydrotraction treatment. This result is supported by the present numerical analysis, as well. However, if applying extra weights, beside the quality of bone, the grade of osteoporosis, the body structure and body weight, together with the age of patients must be carefully analyzed, by means of the result seen above.

---

## REFERENCES

1. Kurutz M, Bender T. Weightbath hydrotraction treatment – application, biomechanics and clinical effects, *J. of Multidisciplinary Healthcare*, 2010;(3):19-27.
2. Kurutz M, Oroszváry L. Finite element analysis of weightbath hydrotraction treatment of degenerated lumbar spine segments in elastic phase. *J. of Biomechanics*, 2010;43(1):433-41.
3. Denoziere, G. Numerical modeling of ligamentous lumbar motion segment, Master thesis, Georgia Institute of Technology, 2004.
4. Panjabi MM, Oxland T, Takata K, Goel V, Duranceau J, Krag M. Articular facets of the human spine, quantitative three dimensional anatomy, *Spine*, 1993;18(10):1298-1310.
5. Langrana NA, Edwards WT, Sharma M. Biomechanical analyses of loads on the lumbar spine, In: Eds. Wiesel, S.W., Weinstein, J.N., Herkowitz, H., Dvorak, J., Bell, G., *The Lumbar Spine*, W.B. Saunders Company, Biomechanics, 1996;1(4):163-81.
6. Nachemson AL, Disc pressure measurements, *Spine*, 1981;6(1):93-7.
7. Sato K, Kikuchi S, Yonezawa T. In vivo intradiscal pressure measurement in healthy individuals and in patients with ongoing back problems, *Spine*, 1999;24(23):2468-74.
8. Bene É, Kurutz M. Weight-bath and its biomechanics, (in Hungarian), *Orvosi Hetilap*, 1993;134(21): 1123-29.
9. Kurutz M, Bene É, Lovas A. In vivo deformability of human lumbar spine segments in pure centric tension, measured during traction bath therapy, *Acta of Bioengineering and Biomechanics*, 2003;5(1):67-92.
10. Kurutz M. Age-sensitivity of time-related in vivo deformability of human lumbar motion segments and discs in pure centric tension, *Journal of Biomechanics*, 2006;39(1):147-57.
11. Kurutz M. In vivo age- and sex-related creep of human lumbar motion segments and discs in pure centric tension, *Journal of Biomechanics*, 2006;39(7):1180-90.
12. Kurutz M, Oroszváry L. Finite Element Analysis of Long-Time Aging and Sudden Accidental Degeneration of Lumbar Spine Segments in Compression, *Biomechanica Hungarica*, 2013;VI(1):223-34.

*The authors gratefully acknowledge the Hungarian Scientific Research Fund OTKA for providing financial support in the frame of the grant K-075018.*

## BIOMECHANICAL EVALUATION OF INTERBODY DEVICES BY USING MECHANICAL COMPRESSIVE TEST: PEEK SPACERS VERSUS PMMA CEMENT SPACERS

Márta Kurutz<sup>1</sup>, Tibor Csákány<sup>2</sup>, Péter Varga<sup>3</sup>, Péter Pál Varga<sup>2</sup>

<sup>1</sup>Budapest University of Technology and Economics

<sup>2</sup>National Center for Spinal Disorders

<sup>3</sup>Julius Wolff Institute and Berlin-Brandenburg School for Regenerative Therapies, Charité - Universitätsmedizin

[kurutzm@eik.bme.hu](mailto:kurutzm@eik.bme.hu)

---

### Abstract

If spine degenerations are accompanied by osteoporosis, the traditional PEEK spacers can strongly subside into the irregularly deformed endplates and vertebrae following surgical stabilization. To avoid implant subsidence, a new technique is developed where bone cement is applied as interbody device along the vertebra-implant interface. In this study, the mechanical comparison of the traditional PEEK and the new PMMA cement spacers are presented based on uniaxial compression tests. It was concluded that in osteoporotic spine the cement spacers provide better contact along the irregularly deformed endplates, and stronger vertebra-implant interface leading to enhanced stability of lumbar interbody fixation. In the case of PMMA cages, the failure deformation of segments is almost the half of that of the PEEK spacers, while the stiffness of them is more than two times larger. In strongly osteoporotic cases, a more evenly distributed cement pattern results in smaller stress concentrations and greater strength which may decrease the risk of subsidence.

**Keywords:** interbody devices, PEEK spacer, PMMA bone cement spacer, vertebra-implant interface, device subsidence, failure load, stiffness

---

### Introduction

During surgical stabilization of spine the degeneration of the disc is often accompanied by osteoporosis of vertebrae. In this case inserting the interbody devices, the traditional spacers into the intervertebral space is very difficult due to the irregularly deformed, weakened osteoporotic endplates of vertebrae, moreover, implant subsidence reduces the strength of the joint and yield further complications.<sup>1-5</sup> To avoid implant subsidence, the strength of the vertebra-device interface must be increased. According to a new method developed in the National Center for Spinal Disorders in Budapest, instead of traditional spacers, bone cement is applied as interbody device at a certain part of the removed disc, while the other part of the removed disc is filled up by bone graft.<sup>6-7</sup> The benefit of the new method of using PMMA cement spacers is the larger and more perfect contact between the cement and the irregular surfaces of the endplates, obtaining a more even load transfer along the vertebra-implant interface and decreasing the extreme stress distribution and stress peaks due to the subsidence or penetration of the traditional spacers into the osteoporotic vertebrae.

A better understanding the reason of interbody device subsidence is necessary in order to avoid the problem effectively.<sup>5</sup> The goal of this work is to compare the mechanical characteristics:

---

strength, stiffness and deformability of lumbar motion segments stabilized by traditional PEEK and PMMA cement spacers (without posterior instrumentation), by using uniaxial compression tests. Parallel, we have developed the quantitative computed tomography QCT-based patient-specific nonlinear finite element models of each test specimen to analyze the vertebra-implant interface and the elastic-plastic damage process of the vertebral internal cancellous bone, local and global failure of the motion segment. The results of this part of research and the comparison of the results of mechanical tests and numerical simulations are detailed in other papers.

## Methods

The specimens were prepared in the National Center for Spinal Disorders in Budapest, and the compression tests were executed in the laboratory of the Biomechanical Research Centre of the Budapest University of Technology and Economics.

To analyze the mechanical behaviour of the bone-spacer interface and the cancellous bone inside the vertebrae, posterior instrumentation screw structures have not been applied for the specimens.<sup>1</sup> For traditional spacer, the polyether ether ketone (PEEK) thermoplastic spacers, while for cement spacer the polymethylmethacrylate (PMMA) bone cement spacers were applied, equally without posterior instrumentation.<sup>1</sup>

At present, for the specimens 16 cadaveric lumbar motion segments were extracted from 8 human lumbar spines (spine/level/gender/age/BMI/): A/L1-4/M/63/24,5/; B/L1-4/M/52/27,1/; C/L1-4/F/79/24,2/; D/L1-4/M/64/24,5/; E/L1-4/F/88/28,6/; F/L1-4/F/88/24,2/; G/L1-4/F/75/24,7/; H/L1-4/M/56/24,7/ that were scanned with dual energy X-ray absorptiometry (DEXA) to obtain bone mineral density (BMD), T-score and Z-score.

The 16 motion segments were divided into 2 groups: (1) fixation with PEEK spacers and (2) fixation with PMMA cement cages. In the PMMA group, all possible free places of the intervertebral space were filled in by the injected cement. No further filling material or bone debris was used for the present experiments. The specimens of both groups were embedded parallel by equally about 10 mm thick PMMA plastic discs around the inferior and superior endplates of the inferior and superior vertebrae, respectively.

Then the specimens were scanned individually with a high-resolution quantitative computed tomography (QCT) system (Hitachi Presto, Hitachi Medical Corporation, Tokyo, Japan) to provide 3D density maps of the specimens and bone quality. Vertebral heights, central and subcortical cross sectional areas, central and subcortical CT grey values were measured on QCT images. The CT scanning was performed for each specimen three times, before and after operation of segments and after the mechanical test. Since the PMMA embedding of specimens were transparent in CT, to distinguish correctly the bone and embedding, the upper and lower surfaces of embeddings were marked by glass pearls. The specimens were stored at -200C and were thawed at room temperature 4-6 hours before testing.

*Table 1a* illustrates the data of patients and pre-operated specimens, *Table 1b* the data of bone quality of specimens.



| Cage type   | Specimen | Age (yrs)   | Sex | BMI (kg/m <sup>2</sup> ) | Height (mm) |             | Cross Sectional Area (mm <sup>2</sup> ) |                  |                  |                  |
|-------------|----------|-------------|-----|--------------------------|-------------|-------------|---|------------------|------------------|------------------|
|             |          |             |     |                          | superior    | inferior    | superior central                        | superior subcort | inferior central | inferior subcort |
| <b>PMMA</b> |          |             |     |                          |             |             |   |                  |                  |                  |
| PMMA-1      | G/L1-2   | 75          | F   | 31.2                     | 22.40       | 23.90       | 724                                     | 1011             | 715              | 1115             |
| PMMA-2      | B/L3-4   | 52          | M   | 27.1                     | 26.70       | 27.55       | 896                                     | 1178             | 1002             | 1238             |
| PMMA-3      | A/L1-2   | 63          | M   | 24.5                     | 24.70       | 24.95       | 651                                     | 952              | 690              | 978              |
| PMMA-4      | B/L1-2   | 52          | M   | 27.1                     | 26.35       | 26.20       | 683                                     | 871              | 712              | 896              |
| PMMA-5      | F/L1-2   | 88          | F   | 24.2                     | 26.10       | 26.70       | 814                                     | 1053             | 877              | 1133             |
| PMMA-6      | F/L3-4   | 88          | F   | 24.2                     | 28.80       | 28.65       | 907                                     | 1174             | 981              | 1219             |
| <b>mean</b> |          | <b>69.7</b> |     | <b>26.4</b>              | <b>25.8</b> | <b>26.3</b> | <b>779</b>                              | <b>1040</b>      | <b>830</b>       | <b>1097</b>      |
| <b>SD</b>   |          | <b>16.5</b> |     | <b>2.73</b>              | <b>2.1</b>  | <b>1.7</b>  | <b>109</b>                              | <b>122</b>       | <b>142</b>       | <b>135</b>       |
| <b>PEEK</b> |          |             |     |                          |             |             |   |                  |                  |                  |
| PEEK-1      | C/L3-4   | 79          | F   | 24.2                     | 26.60       | 26.90       | 1071                                    | 1304             | 1145             | 1569             |
| PEEK-2      | H/L1-2   | 56          | M   | 24.7                     | 28.50       | 30.10       | 1049                                    | 1573             | 1181             | 1564             |
| PEEK-3      | H/L3-4   | 56          | M   | 24.7                     | 28.60       | 29.25       | 1349                                    | 1796             | 1344             | 1728             |
| PEEK-4      | D/L1-2   | 64          | M   | 24.5                     | 28.73       | 28.50       | 1086                                    | 1366             | 1152             | 1475             |
| PEEK-5      | D/L3-4   | 64          | M   | 24.5                     | 28.00       | 26.40       | 1224                                    | 1587             | 1283             | 1549             |
| PEEK-6      | E/L1-2   | 88          | F   | 28.6                     | 24.91       | 25.71       | 825                                     | 1005             | 929              | 1127             |
| <b>mean</b> |          | <b>67.8</b> |     | <b>25.2</b>              | <b>27.6</b> | <b>27.8</b> | <b>1101</b>                             | <b>1439</b>      | <b>1172</b>      | <b>1502</b>      |
| <b>SD</b>   |          | <b>13.0</b> |     | <b>1.68</b>              | <b>1.5</b>  | <b>1.7</b>  | <b>177</b>                              | <b>275</b>       | <b>143</b>       | <b>201</b>       |

Table 1a: Data of patients and geometry of pre-operated specimens

| Cage type    | Specimen | BMD (g/cm <sup>2</sup> ) |              | T-score     |             | CT-grey          |                      |                  |                      |  |
|--------------|----------|--------------------------|--------------|-------------|-------------|------------------|----------------------|------------------|----------------------|--|
|              |          | superior                 | inferior     | superior    | inferior    | superior central | superior subcortical | inferior central | inferior subcortical |  |
| <b>PMMA</b>  |          |                          |              |             |             |                  |                      |                  |                      |  |
| PMMA-1       | G/L1-2   | 0.606                    | 0.620        | -4.4        | -4.8        | 76               | 123                  | 85               | 94                   |  |
| PMMA-2       | B/L3-4   | 0.975                    | 0.934        | -2.2        | -2.6        | 196              | 171                  | 186              | 120                  |  |
| PMMA-3       | A/L1-2   | 0.789                    | 0.828        | -3.1        | -3.4        | 137              | 157                  | 90               | 132                  |  |
| PMMA-4       | B/L1-2   | 0.764                    | 0.900        | -3.3        | -2.8        | 141              | 183                  | 133              | 149                  |  |
| PMMA-5       | F/L1-2   | 0.620                    | 0.659        | -4.3        | -4.5        | 73               | 107                  | 70               | 102                  |  |
| PMMA-6       | F/L3-4   | 0.721                    | 0.768        | -4.0        | -3.6        | 106              | 136                  | 105              | 96                   |  |
| <b>mean/</b> |          | <b>0.746</b>             | <b>0.785</b> | <b>-3.6</b> | <b>-3.6</b> | <b>122</b>       | <b>146</b>           | <b>112</b>       | <b>116</b>           |  |
| <b>SD</b>    |          | <b>0.135</b>             | <b>0.127</b> | <b>0.8</b>  | <b>0.9</b>  | <b>47</b>        | <b>29</b>            | <b>42</b>        | <b>22</b>            |  |
| <b>PEEK</b>  |          |                          |              |             |             |                  |                      |                  |                      |  |
| PEEK-1       | C/L3-4   | 0.676                    | 0.670        | -4.4        | -4.4        | 50               | 78                   | 29               | 94                   |  |
| PEEK-2       | H/L1-2   | 0.834                    | 0.919        | -2.7        | -2.7        | 117              | 174                  | 104              | 166                  |  |
| PEEK-3       | H/L3-4   | 0.892                    | 0.863        | -2.9        | -3.1        | 141              | 219                  | 152              | 194                  |  |
| PEEK-4       | D/L1-2   | 0.828                    | 0.828        | -3.4        | -3.4        | 109              | 110                  | 80               | 109                  |  |
| PEEK-5       | D/L3-4   | 0.913                    | 0.888        | -2.7        | -2.9        | 79               | 134                  | 86               | 101                  |  |
| PEEK-6       | E/L1-2   | 0.751                    | 0.827        | -3.2        | -3.1        | 107              | 124                  | 84               | 123                  |  |
| <b>mean</b>  |          | <b>0.816</b>             | <b>0.833</b> | <b>-3.2</b> | <b>-3.3</b> | <b>101</b>       | <b>140</b>           | <b>89</b>        | <b>131</b>           |  |
| <b>SD</b>    |          | <b>0.089</b>             | <b>0.087</b> | <b>0.6</b>  | <b>0.6</b>  | <b>32</b>        | <b>50</b>            | <b>40</b>        | <b>40</b>            |  |

Table 1b: Bone quality data of pre-operated specimens

The compressive mechanical test was executed by using a servohydraulic universal testing machine (Instron 8870 series). Axial compressive displacement load was applied at a rate of 0.5 mm/min speed, to the limit of 20% decrease of the compressive force or 20% of compressive strain of the specimen. Axial compressive force and displacement were measured and the relating force-displacement curve was plotted. Failure loads, failure displacements and structural stiffnesses were extracted from the load-displacement curves. Failure load was the maximum load before the gradient of the curve changed from positive to negative, whereas stiffness was the slope of the linear portion of the load-displacement curve before failure occurred. Failure stresses were calculated along the central and subcortical cross sections of both the superior and inferior vertebrae, dividing the failure load by the relating cross sectional area of vertebra.

At present, the results of the mechanical tests is based on 2x6 specimens from the 2x8 ones, since the load-deflection curve of two specimens from both groups were invaluable.

## Results

In *Figure 1* the typical load-displacement curves of specimens stabilized by PEEK and PMMA cement cages are illustrated, while the relating numerical results are seen in *Table 2a* and *2b*.

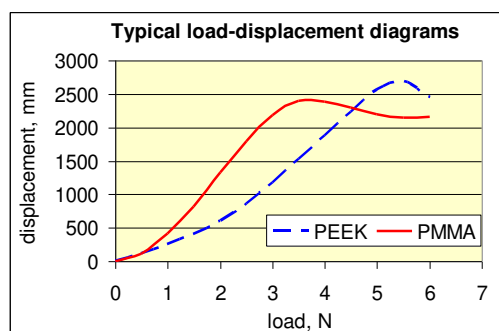


*Figure 1.* Typical load-displacement diagram of segments with PEEK and PMMA cement spacers

The mean failure load, elastic stiffness, failure displacement and failure stresses of specimens with PEEK and PMMA cement cages can be seen in *Figure 2*. Compressive failure load was not significantly affected by the cage types ( $P > 0.3$ ); it was 9% smaller in PMMA group in average (*Figure 2a*). On the contrary, compressive stiffness of segments was significantly affected by fixation devices ( $P < 0.002$ ): it was nearly two and a half times larger (247%) in the PMMA group than in the PEEK group (*Figure 2b*). Failure displacements, the shortening of segments in the PMMA group were only the half of that of the PEEK group ( $P < 0.0002$ , *Figure 2c*). Central and subcortical failure stresses of upper and lower vertebrae in PMMA group were equally about 25-28% higher ( $P < 0.004$ ) since the related central areas of vertebrae were about 27-29% smaller in this group. In contrast to the PMMA group, the standard deviation of all mechanical parameters (compared to the mean values) was definitely larger in the PEEK group, indicating the higher uncertainty and vulnerability of this kind of fixation. Central and subcortical failure stresses of upper and lower vertebrae in PMMA group were equally about 25-28% higher since the related central areas were about 27-29% smaller in this group.

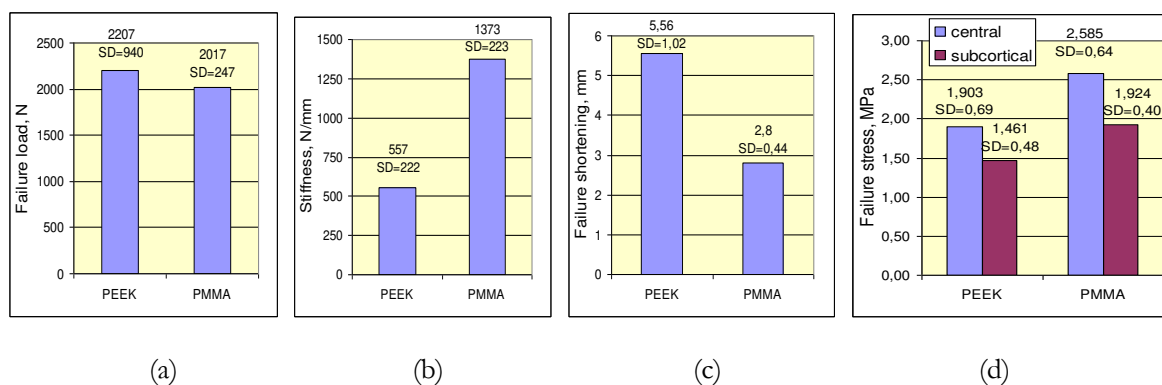


Figure 2. Mean failure load (a), stiffness (b), failure displacements (c) and failure stresses (d) of segments with PEEK and PMMA cement cages

| Type of spacers | Sample | Failure load (N) | Stiffness (N/mm) | Failure deform. (mm) | Type of spacers | Sample | Failure load (N) | Stiffness (N/mm) | Failure deform. (mm) |
|-----------------|--------|------------------|------------------|----------------------|-----------------|--------|------------------|------------------|----------------------|
| <b>PMMA</b>     |        |                  |                  | <b>PEEK</b>          |                 |        |                  |                  |                      |
| PMMA-1          | G/L1-2 | 2013             | 1460             | 2.52                 | PEEK-1          | C/L3-4 | 1400             | 350              | 5.70                 |
| PMMA-2          | B/L3-4 | 1630             | 1250             | 2.68                 | PEEK-2          | H/L1-2 | 2933             | 770              | 5.00                 |
| PMMA-3          | A/L1-2 | 2398             | 1050             | 3.57                 | PEEK-3          | H/L3-4 | 3368             | 760              | 6.86                 |
| PMMA-4          | B/L1-2 | 1975             | 1410             | 2.70                 | PEEK-4          | D/L1-2 | 2687             | 745              | 5.35                 |
| PMMA-5          | F/L1-2 | 1984             | 1350             | 3.00                 | PEEK-5          | D/L3-4 | 1893             | 390              | 6.42                 |
| PMMA-6          | F/L3-4 | 2100             | 1720             | 2.33                 | PEEK-6          | E/L1-2 | 958              | 325              | 4.00                 |
| <b>mean</b>     |        | <b>2017</b>      | <b>1373</b>      | <b>2.80</b>          | <b>mean</b>     |        | <b>2207</b>      | <b>557</b>       | <b>5.56</b>          |
| <b>SD</b>       |        | <b>247</b>       | <b>223</b>       | <b>0.44</b>          | <b>SD</b>       |        | <b>940</b>       | <b>222</b>       | <b>1.02</b>          |

Table 2a. Failure load, stiffness and failure shortening of segments with PMMA and PEEK spacers

| Type of Spacers | Sample | Stresses central superior (MPa) | Stresses central inferior (MPa) | Stresses subcort. superior (MPa) | Stresses subcort. inferior (MPa) | Type of Spacers | Sample | Stresses central superior (MPa) | Stresses central inferior (MPa) | Stresses subcort. superior (MPa) | Stresses subcort. inferior (MPa) |
|-----------------|--------|---------------------------------|---------------------------------|----------------------------------|----------------------------------|-----------------|--------|---------------------------------|---------------------------------|----------------------------------|----------------------------------|
| <b>PMMA</b>     |        |                                 |                                 |                                  |                                  | <b>PEEK</b>     |        |                                 |                                 |                                  |                                  |
| PMMA-1          | G/L1-2 | 2,780                           | 2,815                           | 1,991                            | 1,805                            | PEEK-1          | C/L3-4 | 1,307                           | 1,223                           | 1,074                            | 0,892                            |
| PMMA-2          | B/L3-4 | 1,819                           | 1,627                           | 1,384                            | 1,317                            | PEEK-2          | H/L1-2 | 2,796                           | 2,483                           | 1,865                            | 1,875                            |
| PMMA-3          | A/L1-2 | 3,684                           | 3,475                           | 2,519                            | 2,452                            | PEEK-3          | H/L3-4 | 2,497                           | 2,506                           | 1,875                            | 1,949                            |
| PMMA-4          | B/L1-2 | 2,892                           | 2,774                           | 2,268                            | 2,204                            | PEEK-4          | D/L1-2 | 2,474                           | 2,332                           | 1,967                            | 1,822                            |
| PMMA-5          | F/L1-2 | 2,437                           | 2,262                           | 1,884                            | 1,751                            | PEEK-5          | D/L3-4 | 1,547                           | 1,475                           | 1,193                            | 1,222                            |
| PMMA-6          | F/L3-4 | 2,315                           | 2,141                           | 1,789                            | 1,723                            | PEEK-6          | E/L1-2 | 1,161                           | 1,031                           | 0,953                            | 0,850                            |
| <b>mean</b>     |        | <b>2,673</b>                    | <b>2,559</b>                    | <b>1,975</b>                     | <b>1,865</b>                     | <b>mean</b>     |        | <b>1,964</b>                    | <b>1,842</b>                    | <b>1,488</b>                     | <b>1,435</b>                     |
| <b>SD</b>       |        | <b>0,58</b>                     | <b>0,60</b>                     | <b>0,36</b>                      | <b>0,37</b>                      | <b>SD</b>       |        | <b>0,71</b>                     | <b>0,67</b>                     | <b>0,46</b>                      | <b>0,51</b>                      |

Table 2b. Failure stresses in central and subcortical level of vertebrae of segments with PMMA and PEEK spacers

Correlation between failure load and bone quality can be seen in *Figure 3*. Correlation of the superior and inferior vertebrae for PMMA and PEEK spacers are shown in *Table 3*. Surprisingly, while the failure load of PEEK spacers showed a good positive correlation with the bone quality, mainly with CT grey ( $R=0,75$ ), and less with BMD ( $R=0,59$ ), the PMMA cement specimens showed a poor negative correlation (about  $R=-0,40$ ), as seen in *Figures 3a* and *3b*.

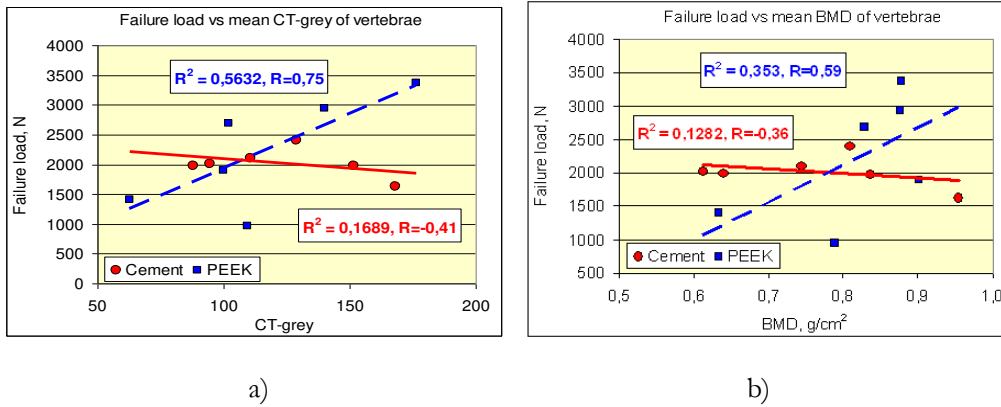


Figure 3. Failure load versus a) mean CT-grey and b) mean BMD of vertebrae

| Failure load | CT-grey          |                  |                  |                  |              |              |       | BMD      |          |       |
|--------------|------------------|------------------|------------------|------------------|--------------|--------------|-------|----------|----------|-------|
|              | central superior | central inferior | subcort superior | subcort inferior | central mean | subcort mean | mean  | superior | inferior | mean  |
| PMMA         | -0.40            | -0.71            | -0.18            | -0.08            | -0.56        | -0.07        | -0.41 | -0.42    | -0.27    | -0.36 |
| PEEK         | 0.69             | 0.72             | 0.74             | 0.73             | 0.72         | 0.75         | 0.75  | 0.65     | 0.53     | 0.59  |

Table 3. Correlation between failure load and bone quality of superior and inferior vertebrae for PMMA and PEEK spacers

However, the failure deformability, the shortening of specimens had practically no correlation with the bone quality at all, neither in the PEEK and nor in the PMMA group, as shown in *Figure 4*. Correlation between failure deformability and bone quality of the superior and inferior vertebrae for PMMA and PEEK spacers can be seen in *Table 4*.

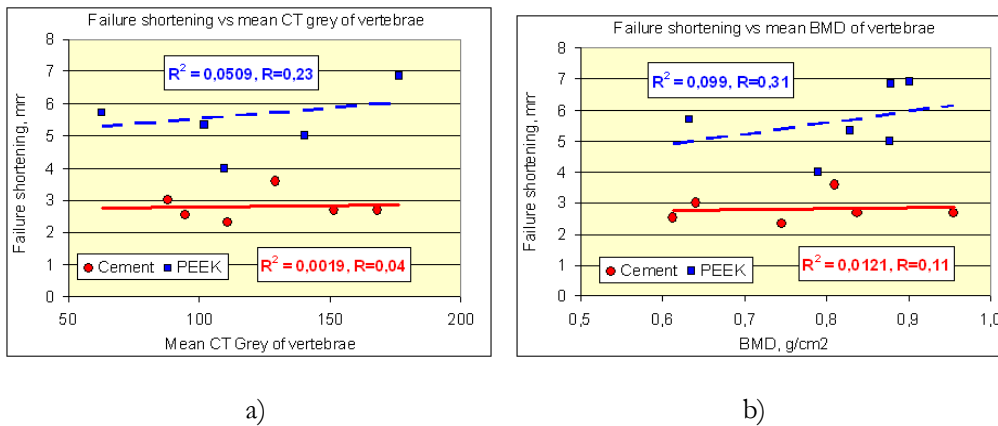


Figure 4. Failure shortening versus a) mean CT-grey and b) mean BMD

| Failure deformation | CT-grey          |                  |                  |                  |              |              |      | BMD      |          |      |
|---------------------|------------------|------------------|------------------|------------------|--------------|--------------|------|----------|----------|------|
|                     | central superior | central inferior | subcort superior | subcort inferior | central mean | subcort mean | mean | superior | inferior | mean |
| PMMA                | 0.11             | -0.28            | 0.08             | 0.44             | -0.07        | 0.24         | 0.04 | 0.10     | 0.12     | 0.11 |
| PEEK                | -0.03            | 0.32             | 0.35             | 0.15             | 0.17         | 0.26         | 0.23 | 0.60     | 0.11     | 0.31 |

Table 4. Correlation between failure shortening and bone quality of superior and inferior vertebrae for PMMA and PEEK spacers

Nevertheless, similar to the failure load was the behaviour of the elastic stiffness that showed a considerable positive correlation with both CT grey ( $R=0,69$ ) and BMD ( $0,53$ ) in PEEK group, and a small negative correlation ( $R=-0,35$  and  $R=-0,36$ ) in PMMA group (Figure 5a,b). Correlation of elastic stiffness with bone quality of the superior and inferior vertebrae for PMMA and PEEK spacers can be seen in Table 5.

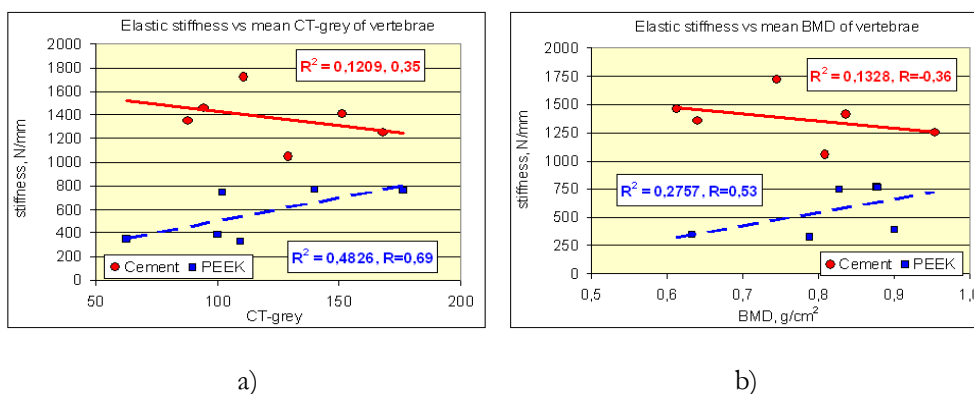


Figure 5. Elastic stiffness versus a) mean CT-grey and b) mean BMD

| Elastic stiffness | CT-grey          |                  |                  |                  |              |              |       | BMD      |          |       |
|-------------------|------------------|------------------|------------------|------------------|--------------|--------------|-------|----------|----------|-------|
|                   | central superior | central inferior | subcort superior | subcort inferior | central mean | subcort mean | mean  | superior | inferior | mean  |
| PMMA              | -0.42            | -0.11            | -0.30            | -0.53            | -0.28        | -0.41        | -0.36 | -0.39    | -0.32    | -0.36 |
| PEEK              | 0.73             | 0.64             | 0.64             | 0.69             | 0.70         | 0.75         | 0.69  | 0.52     | 0.51     | 0.53  |

Table 5. Correlation between elastic stiffness and bone quality of superior and inferior vertebrae for PMMA and PEEK spacers

Also similar was the behaviour of the central and subcortical compressive stresses both in the superior and inferior vertebra in PEEK group, having a considerable positive correlation with both CT grey (mean  $R=0,69$ ) and BMD (mean  $R=0,57$ ), seen in Figure 6a and Table 6. However, in the PMMA group, in the central region a small negative, while in the subcortical region a small positive correlation was with CT grey (mean  $R=-0,40$  and  $R=0,33$  resp.), and equally a small negative correlation was in both region with BMD (mean  $R=-0,21$ ) (Figure 5b).

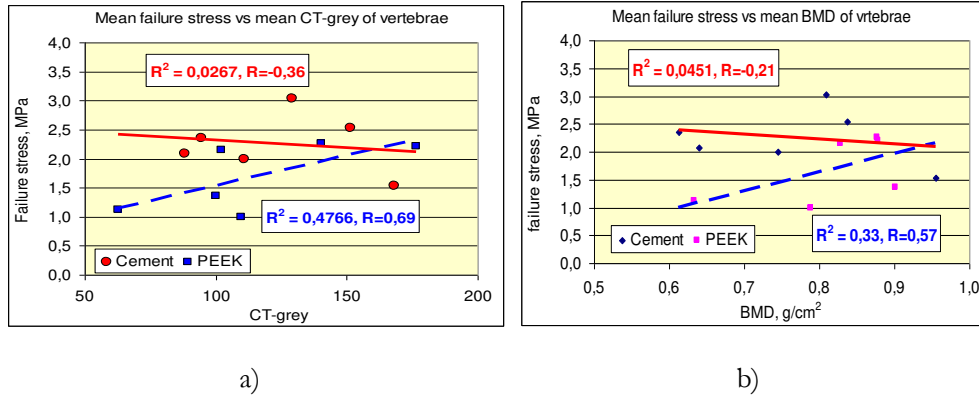


Figure 6. Mean central failure stresses versus a) mean CT-grey and b) mean BMD

| Failure stresses | CT-grey          |                  |                  |                  |              |              |       | BMD          |              |       |
|------------------|------------------|------------------|------------------|------------------|--------------|--------------|-------|--------------|--------------|-------|
|                  | central superior | central inferior | subcort superior | subcort inferior | central mean | subcort mean | mean  | central mean | subcort mean | mean  |
| PMMA             | -0.22            | -0.56            | 0.12             | 0.55             | -0.40        | 0.33         | -0.36 | -0.24        | -0.16        | -0.21 |
| PEEK             | 0.68             | 0.67             | 0.56             | 0.69             | 0.68         | 0.65         | 0.69  | 0.57         | 0.58         | 0.57  |

Table 6. Correlation between failure stresses and bone quality of superior and inferior vertebrae for PMMA and PEEK spacers

As seen in Figures 7a and 7b, between the failure load and the central and subcortical cross sectional areas of vertebrae there was a strong positive correlation ( $R=0,71$  and  $R=0,81$ , respectively) for the PEEK group, mainly for the subcortical areas, both for the superior and inferior vertebra; while in PMMA group there was a modest negative correlation, better for central ( $R=-0,59$ ) than for the subcortical areas ( $-0,48$ ).

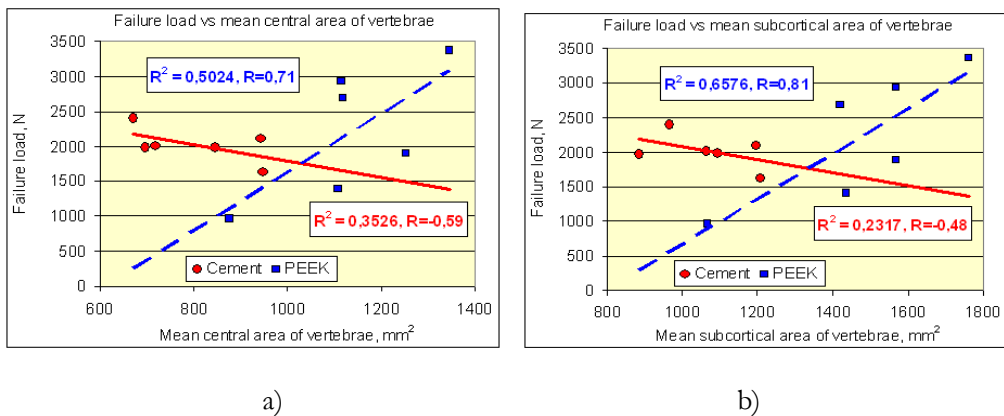


Figure 7. Failure load versus a) central and b) subcortical cross section area of vertebrae

Similarly, between the failure shortening and vertebral areas a strong positive correlation was found for the PEEK group, mainly for the central ( $R=0,95$ ) than for the subcortical areas ( $R=0,84$ ); however, the PMMA group attested a modest negative correlation ( $R=-0,52$  and  $R=-0,47$ ), seen in Figures 8a and 8b, respectively.

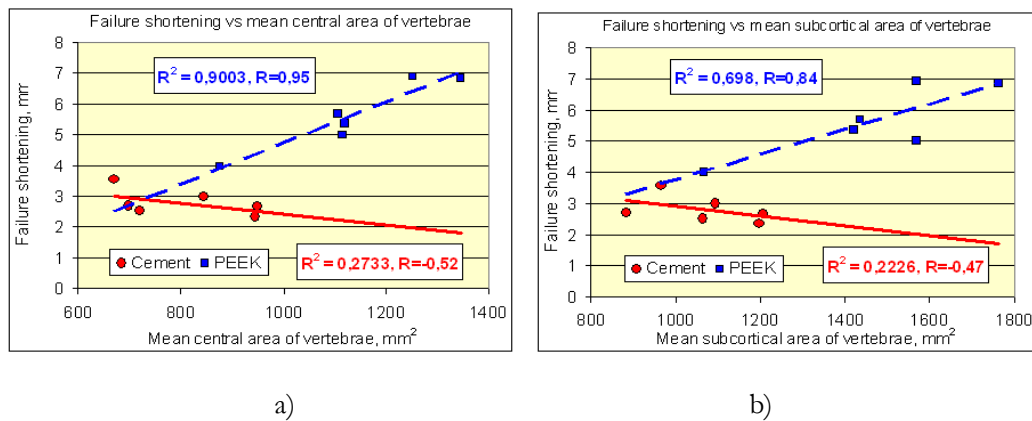


Figure 8. Failure shortening versus a) central and b) subcortical cross section area of vertebrae

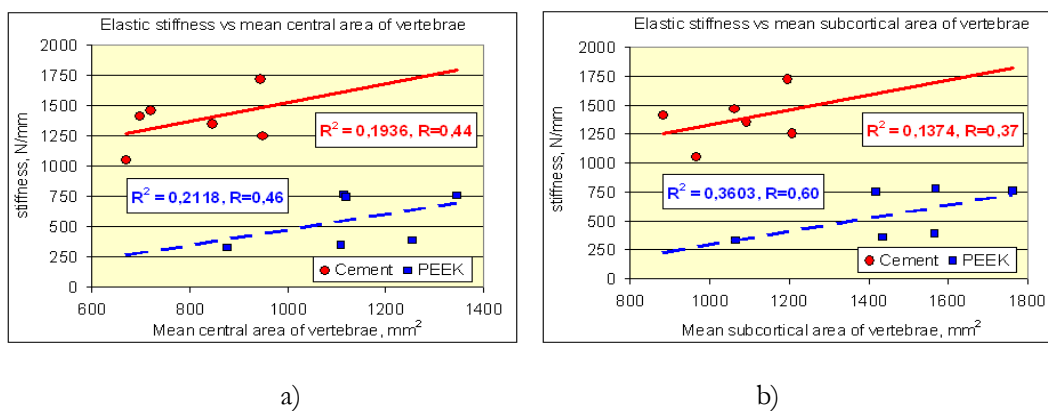


Figure 9. Elastic stiffness versus a) central and b) subcortical cross section area of vertebrae

Between the elastic stiffness and the central cross sectional areas of vertebrae a modest positive correlation was observed for both type of cages (about  $R=0,45$ ), however, with the subcortical areas the PEEK spacers showed a better correlation ( $R=0,60$ ) than the PMMA spacers ( $R=0,37$ ) as seen in Figures 9a and 9b.

## Discussion

In this work novel PMMA cement cages were compared with standard PEEK spacers using axial compressive test. The specimens were stabilized without instrumentation. Jost et al.<sup>1</sup> proved by using mechanical compressive tests for comparing several interbody cages that the posterior instrumentation has no significant effect on the load bearing of stabilized segments.

The average failure loads of 2017 N and 2207 N for PMMA and PEEK cages in this study (Table 2) were comparable to the values reported in previous literature,<sup>5,8-10</sup> however, there are considerable differences in the failure loads obtained by different embedding methods of the specimens. The average segmental stiffness of 557 N/mm of group of PEEK spacers and the higher stiffness of 1373 N/mm in group of novel PMMA cement spacers compared well with the values reported in.<sup>5,8,10</sup> The average failure displacements of 5,56 mm of PEEK group and 2.80 mm of PMMA group are in the ranges reported in.<sup>1,10</sup>

Surprisingly, the load bearing capacity of segments is inversely proportional with the bone quality of vertebrae in the case of PMMA cages, mainly centrally, while the load bearing of PEEK spacers is strongly related to the bone quality, mainly subcortically (*Figure 3* and *Table 3*). In the latter case the reason is that the contact of PEEK spacers needs strong subcortical bone due to the concentrated force-like load transfer along the vertebra–device interface, since in order to avoid implant subsidence or, equivalently, to obtain higher load bearing, the strength of the vertebra–device interface must exceed the applied loads. Previous experimental results of compressive test<sup>10</sup> suggest that the local trabecular structure beneath the endplate is an important component in the use of mesh cage. According to,<sup>5</sup> interbody device subsidence results from failure at the bone–implant interface rather than failure of the implant in itself. Similarly, higher failure loads have been reported for higher bone densities.<sup>1,10</sup> Unfortunately, even the strong interface is missing particularly in osteoporotic patients. In an osteoporotic spine, the same stability cannot be expected from the mesh cage as in a normal spine.<sup>10</sup> Several reports suggest that the stability of the cage in reconstructive surgery can not be guaranteed for strongly osteoporotic spine.<sup>1-2,5,6,10</sup> In<sup>13</sup> most of the fiber mesh implants subsided into the vertebral cancellous bone at compressive failure, suggesting that significant osteoporosis may be a contraindication for posterior lumbar interbody fusion.<sup>10</sup>

However, by injecting PMMA cement into the intervertebral space, the cement can penetrate into the gaps of osteoporotic vertebral bone providing a smooth, perfect and strong vertebra–device interface yielding higher strength, load bearing and stiffness with smaller subsidence providing stability of the motion segment. This fact is proved in<sup>14</sup> where vertebroplasty with PMMA and CaP cement was compared for healthy and osteoporotic vertebrae by axial compressive test. The main conclusion was that the strength and stiffness of vertebrae was inversely correlated to the bone mineral density. The lower the initial BMD was, the more pronounced the augmentation effect was. Both type of cement augmentation reliably and significantly raised the stiffness and maximal tolerable force until failure in osteoporotic vertebral bodies. In non-porotic specimens, no significant increase was achieved. This may be the reason of the inverse correlation between failure load and bone quality of PEEK and PMMA spacers (*Figure 3*), but not only for the failure load but for the compressive stiffness and central compressive stresses as well (*Figures 5* and *6*).

Similarly to the load bearing, while in the PEEK group the stiffness is proportionate to the bone quality, in the PMMA group the weaker bone provides larger stiffness (*Figure 5* and *Table 5*). Even for this, however, it seems to be surprising that the segmental shortenings are practically independent of bone quality in both groups (*Figure 4* and *Table 4*). For PMMA group it can be acceptable since in this group the dominant factor is the cement penetration into the weaker bone, moreover, the shortening of segment depends also on the position of more or less irregularly formed cement cage. In PEEK group the reason may be the local failure, the knife-effect of the edge of the spacer. The mode of trabecular failure could be a shear failure of horizontal struts under the edge of the spacer that yields buckling of relating longer vertical columns due to the loss of horizontal supports.<sup>5</sup> This local zone of trabecular failure leads to the larger implant subsidence independently on the global bone quality.

Similarly to the bone quality, mainly contrasted are the relations of PEEK and PMMA devices with the vertebral cross sectional areas. While the failure load of PEEK group is strongly



proportionate with the vertebral areas, the behaviour of the PMMA group shows an inverse relationship (*Figure 7*). Perhaps this fact is influenced also by the 30% difference of vertebral areas between the two groups. While in PMMA group the mean central and subcortical areas are 804 and 1137mm<sup>2</sup>, in the PEEK groups they are 1068 and 1470 mm<sup>2</sup>, respectively (*Table 1a*), thus in PEEK group the areas are larger. However, the reason of the contrasting behaviour lies not on the areal differences, better on the different vertebra–device interface contact and structure<sup>5</sup> and the different elastic-plastic behaviour between the two groups.

Strong positive correlation is between the cross sectional area and the deformability of PEEK group, while in PMMA group it is modestly negative (*Figure 8*). It is well known in mechanics that in the case of a homogeneous bar under compressive load, the cross sectional area is a part of the resistance against deformation. This is the case for the PMMA spacers, where the load transfer along the vertebra–device interface forms distributed load, consequently, the deformation is inversely proportionate to the vertebral area. The degree of correlation depends on the ratio of the total area and the contacting area between cement and vertebra. On the contrary, for PEEK spacers, the reason of the strong positive correlation is that the load transfer forms a quasi concentrated load along the vertebra–device interface. Consequently, the mechanical problem along the vertebra–device interface is not a simple compression one any more, better a bending problem. In this case, the mechanical fact for bent structures is manifested that a larger structure of the same material gives larger deformations for the same load, since the length of a bar or a plate are proportionate to the deformations but not to the resistance. If the load acts perfectly concentrated, this effect is even stronger. This leads to highly larger cage subsidence into the adjacent vertebrae for larger vertebral areas and endplates for PEEK spacers.

Surprisingly, similar tendency of correlation was found between the failure load and the vertebral areas in both groups (*Figure 7*). Previously we assumed for PMMA cement group, that the load bearing would be proportionate to the vertebral area. However, this is not the case. The modest negative correlation comes from the above detailed effect of concentrated-like load transfer along the vertebra–device interface. Namely, the failure load depends on the ratio of contacting cement area and total vertebral area, that is, on the extension of contact area between cement and endplates. If the cement covers the total endplate area, the behaviour of the vertebral-cement interface belongs to the pure compression problem. However, if the cement area covers only a part of the vertebral area, the load transfer along the interface moves from the distributed to the concentrated type load, consequently, the problem tends to the bending problems of larger subsidence. Since the cement/vertebra areal ratio is larger for smaller vertebrae resulting in higher load bearing, and inversely, that is why the failure load decreases with increasing vertebral area for an approximately constant contact area of cement cage. This fact was proved by compressive test in<sup>5</sup> by concluding that a relative larger indenter surface area on the same cross-sectional area of vertebra resulted in higher failure loads, or inversely, the same indenter area on larger vertebral area yields smaller failure loads. In<sup>11</sup> 50-80%, in<sup>12</sup> 30-40% of vertebral body cross sectional area must be covered by the interbody device to prevent subsidence for moderate physiologic loads.

To explain the strong positive correlation of PEEK spacers between the load bearing and vertebral area is more complicated. First we checked the correlation between the bone quality and the vertebral area. Between CT-grey and vertebral area we have found no correlation at all,

neither for superior and nor for inferior vertebrae, neither centrally and nor subcortically. Only a modest positive correlation ( $R=0,51$ ) has been found between the BMD and the superior vertebral areas, both centrally ( $R=0,49$ ) and subcortically ( $R=0,52$ ). This has only a small part in the positive correlation between the load bearing and the vertebral areas. The real reason can be that the plastification with limited stresses and load bearing is localized into a small zone closed to the edges of PEEK spacer, while on the other large volume of vertebral bone the behaviour is still elastic with increasing stresses and load bearing. This fact can be seen in the typical load-displacement diagram of PEEK spacers, where the failure occurs just after the end of the elastic behaviour, without any longer plastification part of curve (*Figure 1*). Thus, the larger vertebral area of elastic zone provides higher failure load.

The relation between the elastic stiffnesses and the vertebral areas shows a modest positive correlation for both types of intervertebral devices, in line with the relations of failure loads and deformations detailed above. Since the elastic stiffness is practically the quotient of the elastic load and deformation, the modest correlation seem to be acceptable for PEEK spacers, where the failure happens soon after the elastic zone, without any longer global plastic zone, seen in the typical load-displacement diagram (*Figure 1*). However, in the case of PMMA cement cages there is a longer plastic zone before and after the failure, indicating global plastification, when the end of the elastic stiffness zone is farther from the failure. Global plastification needs larger volume. This is the reason that while the correlation of vertebral areas with both the failure load and failure deformations was modestly negative, for the elastic stiffness it was modestly positive for cement cages.

## Conclusion

In line with previous studies, we concluded that the better contact between the shapes of device and bone is the clue to prevent complications coming from device subsidence. In osteoporotic spine instead of traditional PEEK spacers, PMMA cement spacers provide better contact and stronger vertebra-implant interface leading to enhanced stability of lumbar interbody fixation. In the case of PMMA cages, the failure deformation of segments is almost the half of that of the PEEK spacers, while the stiffness of them is two and a half times larger. The reason is the strong subsidence of PEEK spacers into the adjacent vertebrae. The weaker the vertebral bone is the larger subsidence occurs, in contrast to the cement spacers, where the bone quality has practically no importance. Moreover, we concluded that in strongly osteoporotic cases, the cement spacer provides larger strength. The nearly three times greater stiffness of cement spacers documented that the more perfect and smooth contact between the cement and endplate surface can prevent the extreme subsidence and disadvantageous stress distribution of lumbar interbody fixation. A more evenly distributed cement pattern results in greater increases in stiffness and induces smaller stress concentrations around the spacer, which may decrease the risk of subsidence.

In his study the novel PMMA cement cages and the standard PEEK spacers were compared with respect to severely osteoporotic cases, by using uniaxial compressive test. The current study indicates that the novel method, using PMMA cement spacers results in improved vertebra-device interface properties in particular for osteoporotic patients. Thus, we can conclude that the reason of the mainly contradictory behaviour of the PEEK and PMMA spacers lies on the

different vertebra–device interface and on the local and global plastification that will be soon introduced elsewhere, based on the relating CT- and specimen-specific finite element simulations.

---

## REFERENCES

1. Jost B, Cripton PA, Lund T, et al. Compressive strength of interbody cages in the lumbar spine: the effect of cage shape, posterior instrumentation and bone density. *Eur Spine J*, 1998;7(2):132–41.
2. Lim TH, Kwon H, Jeon CH, et al. Effect of endplate conditions and bone mineral density on the compressive strength of the graft-endplate interface in anterior cervical spine fusion. *Spine*, 2001;26(8):951–6.
3. Steffen T, Tsantrizos A, Aebi M. Effect of implant design and endplate preparation on the compressive strength of interbody fusion constructs. *Spine*, 2000;25(9):1077–84.
4. Grant JP, Oxland TR, Dvorak MF, et al. The effects of bone density and disc degeneration on the structural property distributions in the lower lumbar vertebral endplates. *J Orthop Res*, 2002;20(5):1115–20.
5. Tan JS, Bailey CS, Dvorak MF, Fisher CG, Oxland TR. Interbody Device Shape and size are important to strengthen the vertebra–implant interface, *Spine*, 2005;30(6):638–44.
6. Csakany T, Varga PP. Discoplasty in Cases of Degenerative Spine with Complications of Osteoporosis, *52nd Congress of the Hungarian Orthopaedic Society and Section Meeting of the Hungarian Society of Arthroscopy*, Szolnok, Hungary, 2009 June 25-27.
7. Csákány T, Rónai M, György ZM, Varga PP. Bone Cement as Intervertebral Spacer in Thoracolumbar Stabilization of Aging Spine - Radiological and Clinical Results, *Global Spine Congress*, Barcelona, Spain, 2011 March 23-26.
8. Au AG, Aiyangar AK, Anderson PA, Ploeg H-L. A New Bone Surrogate Model for Testing Interbody Device Subsidence, *Spine*, 2011;36(16):1289–96.
9. Hollowell JP, Vollmer DG, Wilson CR, Pintar FA, Yoganandan N. Biomechanical analysis of thoracolumbar interbody constructs. How important is the endplate? *Spine*, 1996;21(9):1032–6.
10. Hasegawa K, Abe M, Washio T, Hara T. An experimental study on the interface strength between titanium mesh cage and vertebra in reference to vertebral bone mineral density. *Spine*, 2001;26(8): 957–63.
11. Closkey RF, Parsons JR, Lee KC, Blacksin MF, Zimmermann MC. Mechanics of interbody spinal fusion. Analysis of critical bone graft area. *Spine*, 1993;18:1011–15.
12. Gill K. Introduction to interbody fusion. In: *Lin, M.P., Gill, K. (eds): Lumbar interbody fusion*. Rockville, Aspen, Maryland, 1989 p. 3–7.
13. Hoshijima K, Nightingale RW, Yu JR, Richardson WJ, Harper KD, Yamamoto H, Myers BS. Strength and stability of posterior lumbar interbody fusion: Comparison of titanium fiber mesh implant and tricortical bone graft. *Spine*, 1997;22(11):1181–8.
14. Heini PF, Berlemann U, Kaufmann M, Lippuner K, Fankhauser C, van Landuyt P. Augmentation of mechanical properties in osteoporotic vertebral bones - a biomechanical investigation of vertebroplasty efficacy with different bone cements. *Eur Spine J*. 2001;10(2):164-71.

***The authors gratefully acknowledge the Hungarian Scientific Research Fund OTKA for providing financial support in the frame of the grant K-075018. The authors are grateful to Lajos Borbás and Gábor Szabó for their help in laboratory experiments.***

## NUMERICAL SIMULATION OF BLOOD FLOW IN LARGE VESSELS DURING THROMBUS FORMATION

Gábor Závodszy, György Paál

Budapest University of Technology and Economics, Department of Hydrodynamic Systems

[zavodszy@hds.bme.hu](mailto:zavodszy@hds.bme.hu)

---

### **Abstract**

The thrombus formation in vessels is a very complex cascade process that is, amongst many other factors, dependent on the local blood flow characteristics. With the progressing formation, the geometry, and with it the flow pattern changes continuously. In addition to this, the adhesion, activation, and aggregation of the thrombocytes are heavily influenced by certain properties of the flow, most importantly by the emerging local shear forces. In the current work, the formation of a thrombus has been simulated using a simplified model of blood coagulation inside an artificial vessel section. While the employed blood coagulation model has heavily reduced the number of degrees of freedom compared to the real in-vivo bio-chemical processes, it is still capable of successfully reproducing several vital properties of a thrombus qualitatively.

---

### **Introduction**

The hemostasis is a critical mechanism in the self-defense of our body. This is a natural response of the cardiovascular system that prevents undesirable blood loss in case of vascular injury. The blood coagulation is an important step during the hemostasis. It is a very complex cascade process driven by several factors that can both promote and inhibit it. The main steps include the aggregation and the binding of the platelets that are dependent on the local flow properties. Simulating this phenomenon is a challenging task as one has to make several appropriately chosen approximations. Anand et al. reviewed<sup>1</sup> some of the interacting mechanisms regarding clot formation in flowing blood, and even though they deal with a narrower collection of participating processes, they are still numerous. Nesbitt et al. provided<sup>2</sup> some more insight into the thrombus formation by emphasizing the strong coupling with the hemodynamic properties. According to their experimental work, platelet aggregation is influenced by emerging shear forces as platelet adhesion favors low-shear zones. Several other authors recorded the ongoing process of thrombus formation: Celi et al. recorded<sup>3</sup> the thrombus formation in the microcirculation of a living mouse using widefield video-microscopy. This process has also been recorded using several reagents to highlight the concentration of the main components of the formation.<sup>4-5</sup>

There are several works aiming at simulating thrombus formation numerically, but most of them cover only portions of the whole process.<sup>6-10</sup> They try to solve the complex problem by approaching it either from the biochemical side and compute the reactions and the densities of the reagents, but fail to couple these equations with the changing flow field, or from the kinetic side, which usually lacks the appropriate handling of platelet concentrations. The platelet concentration profile inside vessels is an important factor, which is far from being constant in either venous or arterial vessels.<sup>11</sup> A lot of numerical models have been developed in the past decade in order to calculate the platelet concentration profile.<sup>12-14</sup> Their main findings are that the

margination effect of platelets is mainly caused by the finite size effect of both the smaller platelets and the significantly larger red blood cells (RBC). The rolling motion of the larger RBCs pushes the platelets to the sides of the flow channel. This drift force that acts upon platelets in blood flow seems to be proportional with the average local flow velocity. To prove this interaction between platelets and RBCs, Mountrakis et al. simulated 15 particle collisions in blood flow using the immersed boundary method.

## Methods

During the simulations blood coagulation made the geometry change in time. For this reason, in our simulations a two-dimensional lattice Boltzmann based fluid solver was used on a  $D_2Q_9$  lattice. This method has a clear advantage in handling complex and changing geometries over the more conventional finite-volume solvers. The theoretical bases of this method were laid down by Bhatnagar, Gross and Krook (BGK)<sup>16</sup>, and were later developed to the level of general usability for fluid flows by Quian et al<sup>17</sup>. We employed the so-called multiple-relaxation-time lattice Boltzmann model<sup>18</sup>, which provides increased numerical stability compared to the widely used BGK model.

The platelets immersed in the blood flow were simulated as a passive scalar concentration field coupled with the velocity field of the flow capable of advection and diffusion. The passive attribute means that the platelet distribution has no influence on the blood flow. This approximation is supported by the fact that the usual volumetric ratio of the platelets in blood is under 1%. The advection-diffusion of these platelets was also handled by the LBM method. When the velocity is prescribed by an already given velocity field (like in this case by the blood flow), the equilibrium function (from the original function<sup>17</sup>) of the scalar field reduces to the following:

$$f_i^{eq} = \omega \rho (1 + 3 \vec{e}_i \cdot \vec{u}) \quad (1)$$

where  $\omega$  is the relaxation frequency,  $\vec{e}_i$  is the  $i$ -th discretized velocity direction,  $\vec{u}$  is the local velocity of the blood flow, and  $\rho$  is the platelet concentration that can be computed analogously to fluid density:

$$\rho = \sum_{i=1}^9 f_i \quad (2)$$

where  $f_i$  is the particle distribution along the  $i$ -th discretized velocity on the lattice. The diffusion coefficient  $D$  then analogous to the numerical viscosity:

$$D = \frac{1}{3} (\tau - \frac{1}{2}) \quad (3)$$

where  $\tau = \frac{1}{\omega}$  is the relaxation time for the equilibrium function. The rolling motion of the RBCs is mainly caused by the emerging shear forces in the fluid. To simulate the marginating effect, we prescribe a virtual force  $\vec{F}_M$  that acts upon the density of the platelets. This force actually accounts for the finite size effects of the platelets and RBCs. The drift force acting on real platelets always drives platelets out from the main flow, to the sides of the vessel. It is a required behavior, as this causes increased platelet concentration in the vicinity of vessel walls where any

injury can possibly occur. This  $\vec{F}_M$  force points to the direction of the local largest shear stress decrease (in other words, to the direction of the smallest, most negative shear stress gradient). Its magnitude is proportional to the magnitude of the shear stress emerging in this specified direction. The proportionality ratio will require a proper parameter study later, although in the current work, it takes the value of one. Using this drift force, two simple channel flows were simulated with Reynolds numbers that are typical in these smaller vessels. The vessel wall was taken as a smooth, no-slip, rigid wall. The results of the simulations were compared to the experimental results of Woldhuis et al.<sup>17</sup>

The first simple channel flow simulation used constant velocity inlet and constant pressure outlet boundaries. The Reynolds number was set to one that is a typical value in venules. The result of the simulation is summarized below in *Figure 1*.

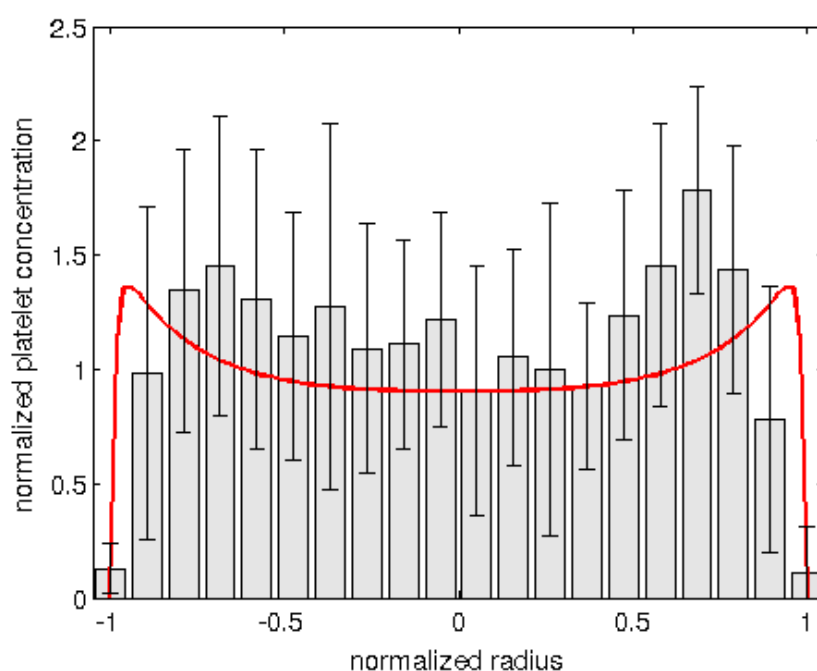


*Figure 1.* Normalized platelet concentration profile in a venule. The continuous red curve shows the results of the stationary simulation plotted over the experimental results of Woldhuis et al.<sup>19</sup> (Re=1)

The platelet concentration shows a good qualitative agreement with the experimental results. This numerical model had to be tested with pulsatile flow as well, in order to reinforce the statement of its validity. For this reason, the other simulation used a time-varying inlet velocity boundary condition. *Figure 2.* shows the inlet flow rate profile that essentially mimics the behavior of a real cardiac pressure wave.

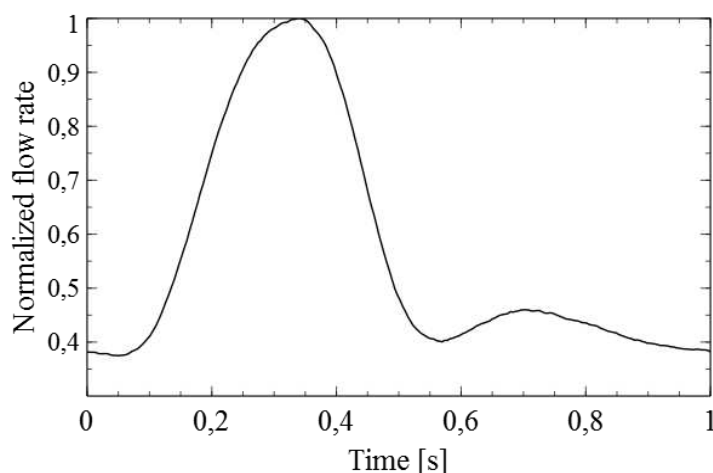


Figure 2. Normalized artificial flow rate curve that mimics the behavior of a real flow rate curve during a cardiac cycle.

The Reynolds number defined with the maximum of the possible inlet velocity was set to ten, which is a usual value for arterioles. The results of the simulation were also compared to the experimental results of the same authors in Figure 3. Again, good qualitative agreement has been found. The biggest deviation between the simulation and experimental results can be found near the vessel walls, but it is still within the error bars.

The coagulation of blood is modeled with changing the type of a numerical element from fluid cell to wall cell. For the thrombus formation in our simulation, coagulation is only possible at sites next to vessel walls or next to rigid blood cells that have already come to stasis. All the fluid LBM cells next to a wall cell have been tracked, as these cells have the ability to turn into a wall cell themselves. When this happens, their fluid cell neighbors are added to the list of near-wall cells. Though platelet activation in reality is a complex cascade process, we only simulate one reagent, the adenosine diphosphate (ADP) concentration, that is in our simulation not coupled with the blood flow. This means that the ADP concentration is not influenced by the local flow properties directly. Coagulation at a numeric lattice site depends on the relation of three variables:

$$P_{coag} = \frac{\rho_{platelet} \rho_{ADP}}{\tau_{MAX}} \quad (4)$$

where the  $P_{coag}$  is a probability in the sense, that its value decides whether a fluid cell should come to stasis or not, based on the local platelet concentration  $\rho_{platelet}$ , the local ADP concentration  $\rho_{ADP}$ , and the local maximum shear component of the stress tensor denoted by  $\tau_{MAX}$ . The level of  $P_{coag}$  that a numerical lattice has to reach for coagulation is an empirical parameter of the model for now. A later work should explore the deeper relation of these parameters.

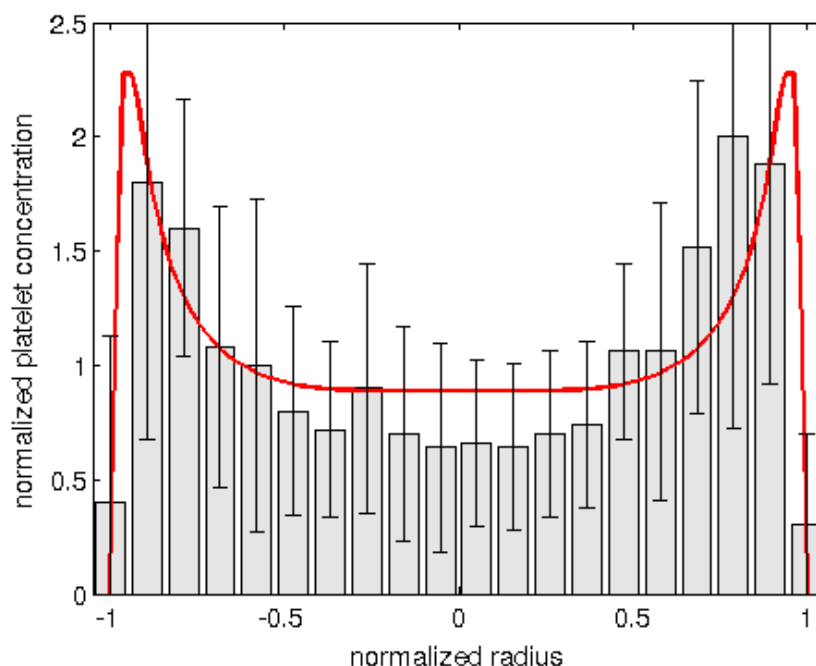


Figure 3. Time-averaged normalized platelet concentration profile in an arteriole. The continuous red curve shows the results of a transient simulation plotted over the experimental results of Woldhuis et al.<sup>19</sup> (Re=10)

There is one more component of the coagulation process. When a platelet is activated (or in our simulation when coagulation of a numerical lattice happens), it releases ADP that can initiate the activation of other platelets. In the simulations the ADP concentration decreases exponentially in space, so its release can be thought of as a nearly local ADP concentration increase. For coagulation, it is not enough to a single numerical lattice to have the appropriate values for one iteration, the parameters have to remain in the coagulation zone for a  $t_{window}$  time. This time was chosen to be  $t_{window} = 20 \text{ ms}$ , because this is the usual timeframe for ADP to activate a platelet. This also means that a newly registered near-wall lattice cannot turn into a wall cell sooner than  $20 \text{ ms}$ .

In Figure 4. a snapshot of a coagulation simulation is shown after six heartbeat cycles. The formation of the thrombus starts at an injury site. In in-vivo systems in case of vascular injury, a significant amount of ADP is released into the bloodstream from the injured vessel wall tissue. The injury site in this case was simulated by increasing the ADP concentration at a small amount of numerical lattices next to the vessel wall.



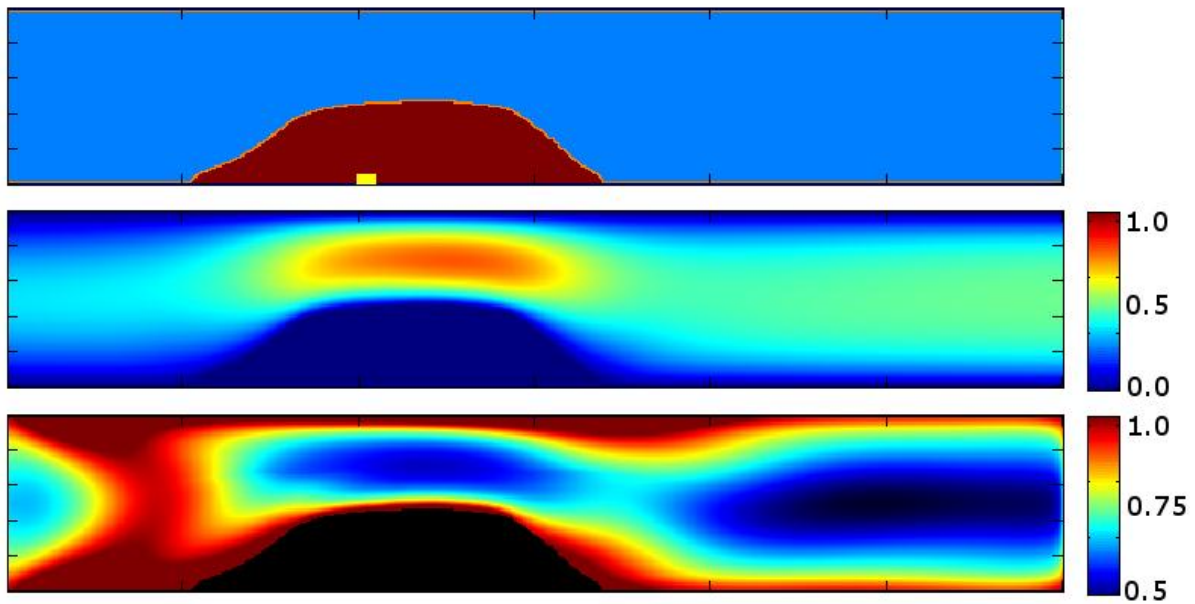


Figure 4. Typical result of a thrombus formation simulation at time instant of the end of a heartbeat cycle.

The flow direction is from the left to the right. The upper image shows the emerged geometry of the thrombus, with the place of vessel injury (yellow box at the bases of the thrombus). The middle image shows the current normalized velocity magnitudes (Reynolds number equals 10). The lower image shows the normalized platelet concentration at the same instant.

There are a few qualitative features of the calculated thrombus that worth mentioning. Firstly, as the thrombus begins to block the flow channel, the flow speed increases and that leads to larger emerging shear stresses that inhibit the process of the coagulation. This causes the relatively flat top of the thrombus. It is also noticeable that the thrombus growth is asymmetric to the site of injury; its growth is slower on the side facing the incoming bloodstream. This is again the result of the different shear stresses.

Two resulting thrombus geometries recorded at different times were compared to the videomicroscopy results of Nesbitt et al.<sup>11</sup> in Figure 5. The experimental results originate from an induced injury inside the arteriole of a living mouse. The exact form of the thrombus naturally depends on much more components that are taken into account in our simulation. Still, some qualitative features like effects of shear stresses can be studied with it.

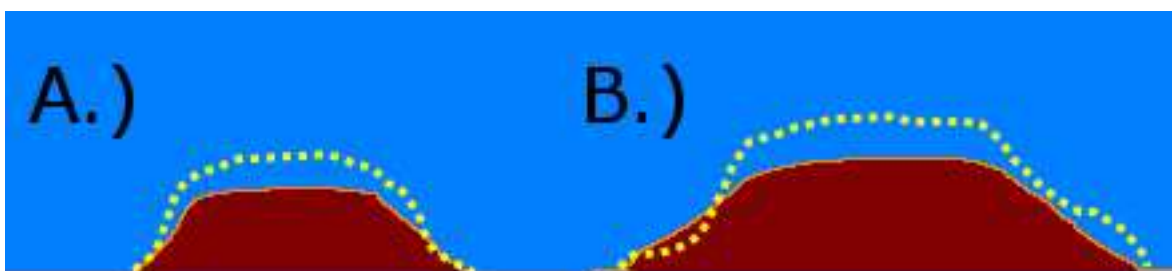


Figure 5. Geometry of the thrombus after A.) three and after B.) six heart beat cycles. The yellow dotted outline shows the geometry of the thrombus recorded with videomicroscopy by Nesbitt et al.<sup>2</sup>

## Conclusion

Simulation of blood coagulation is a heavily studied topic, with wide possibilities for applications. In this work a numerical model was presented that is computationally effective due to the large number of approximations. And though this model evidently has some shortcomings, like that in videomicroscopy records the outer layer of the thrombus is often not solid, and can dissolve easily in the flow and subside again later. In our model, however, the thrombus is handled as solid material, unable to dissolve. Also the effects of the several components of the coagulation cascade that was not taken into account. The model still seems to succeed in reproducing the major characteristics of an injury induced thrombus by only using a few components and coupling them to the flow properties. It should also be mentioned that due to the strongly simplified model, it might be capable of simulating other sediments in blood flows, like the deposition of fat particles on clinical devices. This possibility will drive the research to explore the limits of validity of such a simple coupled numerical model further.

---

## REFERENCES

1. Anand M, Rajagopal KR. A Model Incorporating some of the Mechanical and Biochemical Factors Underlying Clot Formation and Dissolution in Flowing Blood. *Journal of Theoretical Medicine* 5, 2003 p. 183-218.
2. Nesbitt W S, Westein E, Tovar-Lopez FJ, Tolouei E, Mitchell A, Fu J, Carberry J, Fouras A, Jackson S P. A shear gradient-dependent platelet aggregation mechanism drives thrombus formation. *Nature Medicine* 2009;15:665-73.
3. Celi A, Merrill-Skoloff G, Gross P, Falati S, Sim DS, Flaumenhaft R, Furie BC, Furie B. Thrombus formation: direct real-time observation and digital analysis of thrombus assembly in a living mouse by confocal and widefield intravital microscopy. *Journal of thrombosis and haemostasis JTH* 1, 2003 p. 60-68.
4. Falati S, Gross P, Merrill-Skoloff G, Furie B C, Furie B. Real-time in vivo imaging of platelets, tissue factor and fibrin during arterial thrombus formation in the mouse. *Nature Medicine* 8, 2002 p. 1175-81.
5. Furie B, Furie B C. In vivo thrombus formation. *Journal of thrombosis and haemostasis JTH* 5 2007;(1):12-7.
6. Alenitsyn AG, Kondratyev AS, Mikhailova I, Siddique I. Mathematical Modeling of Thrombus Growth in Microvessels. *Journal of Prime Research in Mathematics* 2008;4:195-205.
7. Harrison S E, Smith S M, Bernsdorf J, Hose D R, Lawford P V. Application and validation of the lattice Boltzmann method for modelling flow-related clotting. *Journal of Biomechanics* 40, 2007 p. 3023-8.
8. Wang W, King MR. Multiscale Modeling of Platelet Adhesion and Thrombus Growth. *Annals of Biomedical Engineering*, 2012 November 2012;40(11):2345-54.
9. Tamagawa M, Kaneda H, Hiramoto M, Nagahama S. Simulation of thrombus formation in shear flows using Lattice Boltzmann Method. *Artificial Organs* 33, 2009 p. 604-10.
10. Wang W, King MR. Multiscale Modeling of Platelet Adhesion and Thrombus Growth. *Annals of Biomedical Engineering* 2012.
11. Zhao H, Shaqfeh ESG. Numerical simulation of the margination of platelets in the microvasculature. Center of turbulence research, Stanford, Annual Research Briefs, 2010.

12. Jordan A, David T, Homer-Vanniasinkam S, Graham A, Walker P. The effects of margination and red cell augmented platelet diffusivity on platelet adhesion in complex flow. *Biorheology* 41, 2004. p. 641-53.
13. Tokarev AA, Butylin AA, Ermakova EA, Shnol EE, Panasenko GP, Ataulakhanov FI. Finite platelet size could be responsible for platelet margination effect. *Biophysical Journal* 101, 2011. p. 1835-43.
14. Zhao R, Kameneva MV, Antaki JF. Investigation of platelet margination phenomena at elevated shear stress. *Biorheology* 44, 2007. p. 161-77.
15. Mountrakis L, Lorenz E, Hoekstra AG. Where do the platelets go? A simulation study of fully resolved blood flow through aneurysmal vessels. *Interface Focus* 3: 20120089, Royal Society Publishing, 2012.
16. Bhatnagar PL, Gross EP, Krook M. A Model for Collision Processes in Gases. I. Small Amplitude Processes in Charged and Neutral One-Component Systems. *Physical Review* 94, 1954. p. 511-25.
17. Qian YH, D' Humières D, Lallemand P. Lattice BGK Models for Navier-Stokes Equation. *Europhysics Letters* 17, 1992. p. 479-84.
18. D'Humières D, Ginzburg I, Krafczyk M, Lallemand P, Luo L-S. Multiple-relaxation-time lattice Boltzmann models in three dimensions. *Philosophical Transactions of the Royal Society - Series A: Mathematical, Physical and Engineering Sciences* 360, 2002. p. 437-51.
19. Woldhuis B, Tangelder GJ, Slaaf DW, Reneman RS. Concentration profile of blood platelets differs in arterioles and venules. *American Journal of Physiology* . 1992. 262, H1217-H1223.

## EFFECT OF KAYAKING ON BALANCING ABILITY AFTER SUDDEN CHANGES IN DIRECTION

Árpád László Németh, Rita M. Kiss, Petra Aradi

Cooperation Research Center for Biomechanics

[nemetharpi89@gmail.com](mailto:nemetharpi89@gmail.com)

---

### **Abstract**

#### *Introduction*

Different sports influence the balancing ability variously. The aim of this study to examine the effect of kayaking on dynamical balancing ability after sudden changes in direction.

#### *Methods*

The investigation included 5 race-kayakists and 5 leisure-time sportsmen. Dynamical balancing ability have analyzed by the ultrasound-based sudden perturbation test (provocation test). A rigid platform have moved from its central position and fixed by a fastening unit. The rigid platform connected to a rigid frame by 4 or 8 steel springs of identical strength. The platform swings back into its original, resting position, stimulating sudden disturbances after releasing the fastening unit. The participant must balance and re-equilibrate as the plate moves. The motions of the rigid plate were recorded by an ultrasound-based system. From this motion the Lehr's damping ratio can be calculated and it characterizes the balancing ability of the investigated person.

#### *Results*

For the kayakist group, the average values of the Lehr's damping ratio determined were significantly bigger while standing on one limb and on both limbs compared to the parameters for the control group.

#### *Discussion*

A high level of complex coordination is required to regain equilibrium after a sudden change in direction. Sports activities can develop this ability. This investigation demonstrate that not only the traditional methods (a sudden stoppage from running, sudden setting in motion, jumping or changing in direction) but motion in a continuously moving media (in aqueous media) can also develop the balancing ability. During kayaking the media always changes; moreover, it often surges so persistent balancing is essential. The results draw attention to the fact that dynamic balancing ability can be developed by other than traditional methods.

**Keywords:** kayak, athletes, equilibrium ability after unidirectional sudden perturbation

---

### **1. Introduction**

The maintenance of balance is generally necessary during most motions, ranging from daily activities to more complex sport movements. The process of balancing can be realized if most parts of the body are in accordance. For example, we use more than 200 muscles of the 650 muscles of the body during walking.<sup>8,11</sup> Postural control is a complex function combining sensory input, centralized processing and neuromuscular responses.<sup>15</sup>

Most studies of postural control have focused on measuring balance during quiet standing. Postural balance has been characterized by different types of parameters such as COP (centre of pressure) or COM (centre of mass) posture and other parameters derived from studies on postural sway during standing.<sup>5,16-19</sup>

But static balance tests cannot sufficiently describe the maintenance of balance in daily activities (for example during walking).<sup>20</sup> During gait or when an external perturbation affects balance control, the risk of falling can occur.<sup>12</sup> There are studies that have analysed balance responses during walking on a walkway<sup>13</sup> and on a treadmill at a self-selected speed.<sup>6</sup> Few studies have examined the effect of sinusoidal moving platform translation on postural movement and stability.<sup>1-4</sup> These studies have examined the linear motion of body segments and the movement of COP or COM, and postural control and postural sway have been characterized by COP or COM parameters.<sup>20</sup>

A high level of complex coordination is required to regain equilibrium after a sudden impulse or a change in direction. This phenomenon often occurs in everyday life when one is hit or jerked while standing or walking.<sup>20</sup> These types of effects cannot be modelled using the traditional measurement methods.

Regaining the equilibrium after a sudden impulse or changes in direction can be measured using a provocation test. Balancing capacity can be characterized by the Lehr's damping ratio. Only a few research studies have been produced using this method up to the present. Two groups (a group of healthy young and healthy elderly participants) were examined, and then the results were compared. The reliability of the provocation test is demonstrated because the test was repeated with both patient groups after 7 weeks. There were no significant differences between the measurements. The other important result of this study is that the body mass of the investigated person does not influence the Lehr's damping ratio.<sup>7</sup>

The provocation test required the most complex balancing capacity. The above-mentioned studies did not deal with the effect of sports on balancing capacity. This study discusses the effect of kayaking on balancing capacity. A comparison is made between two groups of 5 people each; one of them consists of race-kayakists and the other group is a control group with non-sportsmen. Efficient balance control during kayaking is of primary importance. Therefore, kayaking is a suitable sport to explore the difference in balancing between sportsmen and non-sportsmen.

## 2. Methods

### 2.1 Participants

The investigation included 5 healthy leisure-time sportsmen, with similar physical abilities: they constituted the control group. The control group was compared with a group of 5 race-kayakists, signed racers of UTE Kayak-Canoe section. *Table 1* provides the demographic features of the participants.

| CONTROL GROUP    | Age (years) | Height (m)  | Mass (kg)   | BMI (kg/m <sup>2</sup> ) |
|------------------|-------------|-------------|-------------|--------------------------|
| Control 1        | 23          | 1.76        | 71          | 22.92                    |
| Control 2        | 23          | 1.76        | 75          | 24.21                    |
| Control 3        | 22          | 1.73        | 66          | 22.05                    |
| Control 4        | 21          | 1.83        | 68          | 20.31                    |
| Control 5        | 22          | 1.78        | 76          | 23.99                    |
| <b>Average</b>   | <b>22.2</b> | <b>1.77</b> | <b>71.2</b> | <b>22.70</b>             |
| <b>Deviation</b> | <b>0.84</b> | <b>0.04</b> | <b>4.32</b> | <b>1.59</b>              |
| Minimum          | 21          | 1.73        | 66          | 20.31                    |
| Maximum          | 23          | 1.83        | 76          | 24.21                    |
|                  |             |             |             |                          |
| KAYAKIST GROUP   | Age (years) | Height (m)  | Mass (kg)   | BMI (kg/m <sup>2</sup> ) |
| Kayakist 1       | 19          | 1.87        | 84          | 24.02                    |
| Kayakist 2       | 23          | 1.79        | 75          | 23.41                    |
| Kayakist 3       | 22          | 1.88        | 72          | 20.37                    |
| Kayakist 4       | 22          | 1.75        | 76          | 24.81                    |
| Kayakist 5       | 19          | 1.93        | 78          | 20.94                    |
| <b>Average</b>   | <b>21</b>   | <b>1.84</b> | <b>77</b>   | <b>22.71</b>             |
| <b>Deviation</b> | <b>1.87</b> | <b>0.07</b> | <b>4.47</b> | <b>1.95</b>              |
| Minimum          | 19          | 1.75        | 72          | 20.37                    |
| Maximum          | 23          | 1.93        | 84          | 24.82                    |

Table 1. Demographic data of subjects

There were no significant differences in age and height between the participants.

According to a physical examination performed before the test, the participants were not limited in their everyday motion and sports activities. Each participant's motion range, joint stability, axial position, muscular strength and muscular tension in the lower limbs were physiologically adequate.

Each participant was informed in writing about the risks and benefits of the study and given the opportunity to withdraw from the study at any time, and each of the participants provided signed consent. The study was authorized by the National Science and Research Ethics Committee (174/2005).

## 2.2. Methods

The effect of sudden impulse or changes in direction can be modelled using a commercially available PosturoMed device. The PosturoMed (Haider-Bioswing, Weiden, Germany) device, with its moveable and adjustable unstable therapy plates, is a widely used training and therapy device for neuron-orthopaedic rehabilitation, sport rehabilitation, and the prevention of sports injuries in Europe. It has a rigid platform (12 kg, 60 cm x 60 cm) (*Figure 1a*.) connected to a rigid frame by eight 15-cm steel springs of identical strength (*Figure 1b*).<sup>8,11</sup>

The displacement characteristic of the platform can be regulated by changing the number of working springs (4, 6 or 8). When the fastening unit (provocation unit) is locked the device can be fixed (*Figure 1c*). The plate can be moved from the central position in a wide range of translation (generally by 20 mm) and can be fixed in different positions by the fastening unit. By releasing the unit, the rigid plate can be set into motion. The platform swings back into its original, resting position, stimulating sudden disturbances. The participant must balance and re-equilibrate as the plate moves. In that case, the human body has to stop the oscillating platform, so the balancing ability of the investigated object is a damping element. The oscillating platform with the subject on it is a damped system. The short name for this test is provocation test.

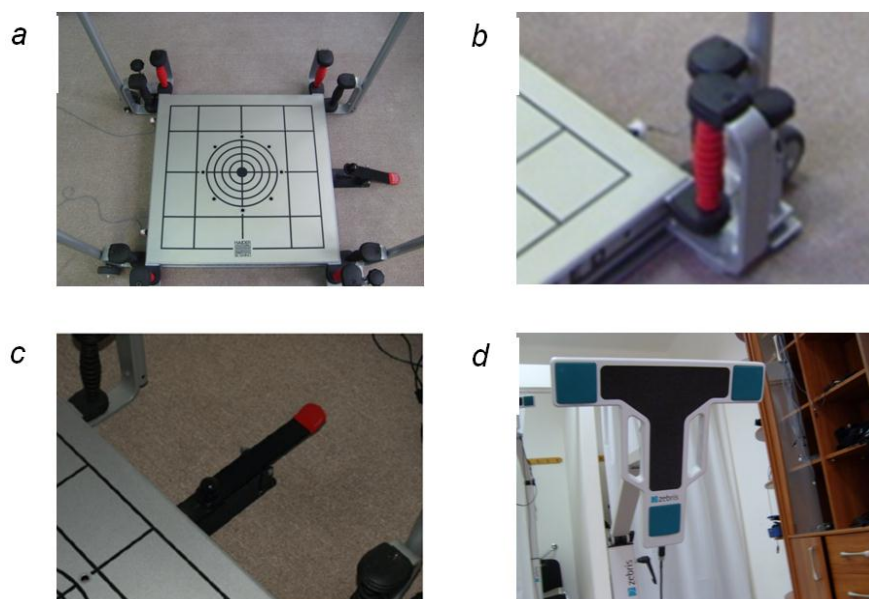


*Figure 1.* Measurement system components. (a) PosturoMed plate. (b) Steel spring. (c) Fastening unit. (d) Ultrasound-based measuring head.



*Figure 2.* Measurement arrangement. PosturoMed plate secured by springs of identical strength in different directions. Ultrasound-based measuring head located to the side of the object at 30 degrees.

In this study the test included four separate measurements: standing on both limbs, on the right and on the left limb and in a seated position (in a position similar to kayaking) (*Figures 3a, b, and c, d*).

During the test, the motions of the rigid plate were recorded by single, individual markers attached on the side of the plate. The spatial coordinates of the markers were measured using a ZEBRIS CMS10 (Zebris, Medizintechnik GmbH, Germany) computer-controlled, ultrasound-based motion analysis system (*Figure 1d*).<sup>8,11</sup> The measuring methods have been detailed in Kiss et al.<sup>10</sup> The ultrasound-based measuring head was located to the side of the object at 30 degrees (*Figure 2*), and the measuring frequency was 100 Hz. The accuracy of the measuring system is less than 1 mm. The tests were performed at the Biomechanical Laboratory of MÁV Hospital at Szolnok.

The participants were instructed that instead of watching their movement they should try to look straight ahead. Furthermore, they were instructed to balance with arm motion. They received no warnings that the plate would shift. If a participant did stumble or hold onto anything the trial was rejected.

The participants stood on the PosturoMed platform during the instructions to get acquainted with the unsteady platform. Before the measurement, an unrecorded trial was conducted to familiarize the participants with the procedure.

The participants were standing barefoot in the double-leg stance on the platform and during this time the platform was moved 20 mm in a medio-lateral direction towards the dominant side, and then locked by the fastening unit. After releasing the fastening unit the participants had to take up the standardized measuring position for 2 s, and manage to counterbalance the sudden disturbance using compensatory equilibrium reactions.

Each shift (double-leg stance, both single-leg stances and seated position) was repeated three times. The first measurement was carried out at double-leg stance, followed by measurement at dominant leg stance, then at non-dominant leg stance and finally while sitting.

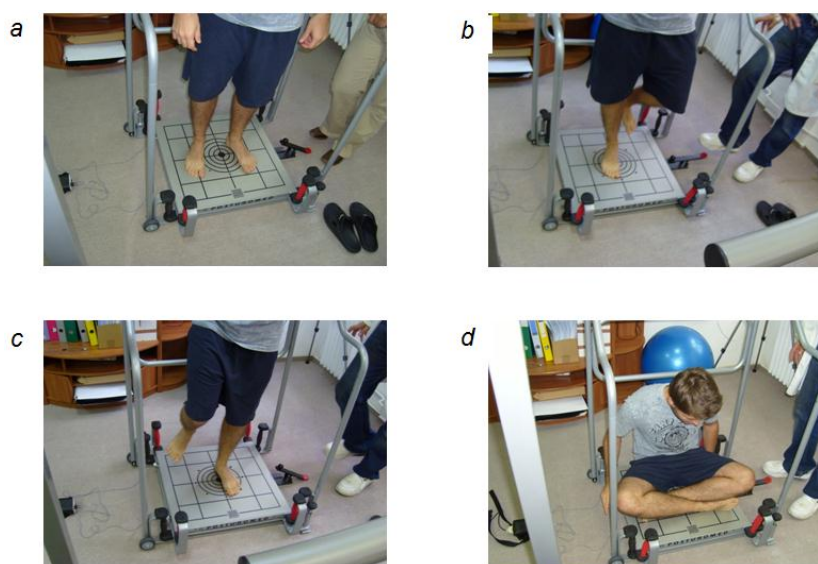


*Figure 3.* The four separate measurement positions. (a) Standing on both limbs. (b) Standing on the dominant limb. (c) Standing on the non-dominant limb. (d) Sitting stance.



There were 60 s rest intervals between measurements. The average values of successfully completed trials were taken as the value for each measuring position; a minimum of two successfully completed trials were required for each measuring position.

### 2.3 Assessment parameters<sup>8-9,10,12</sup>

The oscillating PosturoMed device with the participant on it is a damped system. The differential equation of the damped system is as follows (Figure 4).<sup>7-9,11</sup>

$$\ddot{x}(t) + \frac{k}{m}\dot{x}(t) + \frac{1}{mc}x(t) = 0 \quad (1)$$

where:  $m$  [kg=Ns<sup>2</sup>/m] is the mass of the participant and the platform,  
 $k$  [Ns/m] is the damping value,  
 $c$  [m/N] is the spring constant of the PosturoMed device.



Figure 4. Damping curve\_1. Lateral displacement of the measuring plate calculated from the spatial coordinates of the markers. The coordinate  $x$  is parallel to the direction of provocation and shows a damping curve.

From the above-mentioned damping curve the following parameters can be calculated:

- Average logarithmic decrement

During the test the logarithmic decrement is not exactly constant by reason of the many disturbing factors and because of the fact that the system is not closed. It is useful to determine the average logarithmic decrement – which is the average of the natural logarithm of the ratio of the amplitudes in an identical direction – for two periods separate in time (Figure 5):

$$\Lambda_i = \frac{1}{i-1} \ln \frac{K_1}{K_i} \quad (2)$$

where:  $K_1$  is the amplitude at moment  $t=t_1$ ,  
 $K_i$  is the amplitude at moment  $t=t_i$ .

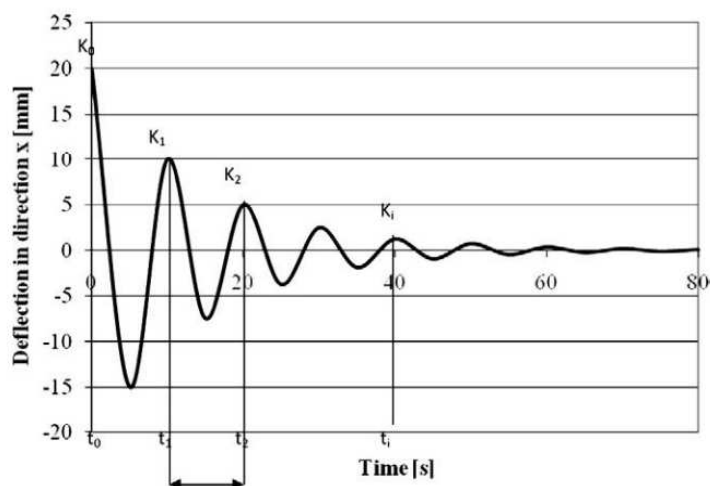


Figure 5. Damping curve\_2. Factors required to determine swing parameters ( $K_i$  is the amplitude at moment  $t=t_i$ ,  $T$  is the swing time). [8,9,11]

- The Lehr's damping ratio

Using the logarithmic decrement the Lehr's damping ratio can be calculated, which is the ratio of actual and critical damping:

$$D = \frac{\Lambda}{\sqrt{\Lambda^2 + 4\pi^2}} \quad (3)$$

If  $D > 1$ , the damping is too large, there will be no oscillating motion.

If  $D = 1$ , the system will have critical damping, and return to its equilibrium position.

If  $0 < D < 1$ , the motion is damped.

If  $D = 0$ , the result is undamped oscillation.

The measurement of balancing capacity in a static posture (standing, sitting) or during motion (walking, running) after a sudden perturbation such as a jump, sudden stop or sudden change in direction is a new, experimental method for motion analysis. The provocation test models the standing balance after a sudden change in direction. After a sudden perturbation the human posture manages to return to its original, stable state. The recovery of equilibrium depends on the balancing ability of the subject, which means that the muscles need to be activated to a certain extent. The functions of the muscles include producing force, controlling the body mass, and damping the oscillating plate. In this investigation the damping value was used to characterize the balancing ability.

If  $D = 1$  (critical damping), then the system returns to its stable position immediately without oscillation, which represents a perfect balancing ability. If  $D = 0$ , then the subject cannot damp the system. The Lehr's damping ratio ( $D$ ) characterizes the actual damping ability in the ratio of the perfect damping value. It can be stated that the Lehr's damping ratio characterizes the balancing ability. Furthermore, higher values of  $D$  means larger damping, so in this case the balancing ability is also better.

## 2.4 Statistical analysis

Lehr's damping ratios of the investigated groups were statistically analyzed using MS Excel Analysis Tool Pak Software.

The averages and standard deviations were calculated. The normality of the data distribution was assessed using the Kolmogorov-Smirnov test, and the uniformity of the standard deviations was assessed using an F-test.

The differences between the average values of identical parameters were determined by a one-sample t-test, applying a symmetrical critical range on the two-leg and right-leg, on the two-leg and left-leg and lastly on the dominant and opposite sides. In addition, a two-sample t-test applying a symmetrical critical range was conducted on the different groups. The significance level was  $p < 0,05$ .<sup>7,14</sup>

## 3. Results

Each volunteer managed to complete all four parts of the test; thus no exclusions occurred for incomplete results. The Lehr's damping ratio was between 0 and 1 so in all cases, the motion of the rigid plate was a damping movement. *Table 2* provides the results of the test.

For both groups, there was no significant difference between the average values of the Lehr's damping ratio determined while standing on both limbs compared to the parameters determined while standing on the dominant limb (control group:  $p=0.085786321$ , kayakist group:  $p=0.358633728$ ).

For both groups, the average values of the Lehr's damping ratio determined while standing on the non-dominant limb were significantly smaller compared to the parameters determined while standing on both limbs (control group:  $p=4.33692E-05$ , kayakist group:  $p=0.013274122$ ).

For the control group, the average values of the Lehr's damping ratio determined while standing on the non-dominant limb was significantly smaller compared to the parameters determined while standing on the dominant limb ( $p=0.018143081$ ).

For the kayakist group, there was no significant difference between the average values of the Lehr's damping ratio determined while standing on the non-dominant limb compared to the parameters determined while standing on the dominant limb ( $p=0.270511876$ ).

The average value of the Lehr's damping ratio determined while sitting was significantly smaller for the control group compared to the parameters for the kayakist group. ( $p_{\text{sitting}}=0.030894465$ )

### Average results

|                                | CONTROL GROUP | KAYAKIST GROUP |
|--------------------------------|---------------|----------------|
| standing on both limbs         | 0.058205168   | 0.054602563    |
| standing on dominant limb      | 0.046872176   | 0.048530459    |
| standing on non- dominant limb | 0.017101718   | 0.0346371      |
| sitting                        | 0.347739265   | 0.41046332     |

**Results of statistical analysis**

| <b>One-sample t-test</b>                                    | <b>CONTROL GROUP</b> | <b>KAYAKIST GROUP</b> |
|---|----------------------|-----------------------|
| standing on both limbs and standing on dominant limb        | 0.085786321          | 0.358633728           |
| standing on both limbs and standing on non-dominant limbs   | <b>4.33692E-05</b>   | <b>0.013274122</b>    |
| standing on dominant limb and standing on non-dominant limb | <b>0.018143081</b>   | 0.270511876           |

| <b>Two-sample t-test</b>       |                    |
|--------------------------------|--------------------|
| standing on both limbs         | 0.336123346        |
| standing on dominant limb      | 0.456813202        |
| standing on non- dominant limb | 0.218101272        |
| sitting                        | <b>0.030894465</b> |

Table 2. Lehr's damping ratio (D) calculated from the results of the provocation test (mean ±SD)

**4. Discussion**

To summarize the innovation of this study compared to former motion analysis, the following statements can be made. First of all, the dynamic balancing ability of active sportsmen was measured by a provocation test. The provocation test was formerly used to examine the effect of aging<sup>7</sup> and the effect of degree of hip osteoarthritis on balancing ability.<sup>9</sup> This study deals with the difference of balancing ability between healthy young people and sportsmen and the fact that sports can improve this ability. Furthermore, the other new element of the study was that the sportsmen were examined in a special posture. The kayakists were examined seated, which is a position they get accustomed to in the course of their everyday training.

The following observations can be stated by the comparison of the average Lehr's damping ratio of the two groups. The two groups performed approximately equally while the participants were standing on both limbs and on the dominant limb. The kayakist group had better results while standing on the non-dominant limb and while sitting. It is perceptible that the kayakist subjects possess similar Lehr's damping ratios for their dominant and non-dominant limbs, respectively, whereas the damping ratio of the non-dominant limbs of the members of the other group is three times worse than the damping ratio of their dominant limbs.

Regarding the results of comparisons within the same group, the Lehr's damping ratio calculated during standing on both limbs did not differ significantly from the value calculated during standing on the dominant limb for either of the groups. However, the results calculated during standing on both limbs did differ significantly from the calculated during standing on the non-dominant limb. In short, equilibrium after a sudden change in direction was similar when standing on both limbs and on the dominant limb, but it was decreased during standing on the non-dominant limb. Consequently it can be stated that in general, equilibrium ability after a

sudden change in direction is significantly influenced by the equilibrium ability of the dominant side.

Another new finding from the current research is that the Lehr's damping ratio calculated during standing on the non-dominant limb compared to the value calculated during standing on the dominant limb was significantly smaller in the control group but surprisingly, there was no significant difference in the kayakist group. The result of the control group was prospective and it confirms the findings of former research studies.<sup>7, 9</sup> However, it was not expected that there would be no significant difference between the equilibrium ability of the dominant and the non-dominant limb in the kayakist group. Therefore, there is no dependence on lateral dominance in case of the kayakists.

Regarding the results of comparisons between the different groups, the average value of the Lehr's damping ratio determined while sitting was significantly smaller for the control group compared to the parameters of the kayakist group. So it is reasonable to assume that the balancing ability of kayakists is significantly better in the special position they become accustomed to. Measurements while seated were unusual for the participants of the control group, but this special circumstance was not unknown for the kayakists because they grew familiar with it during their trainings.

A high level of complex coordination is required to regain equilibrium after a sudden change in direction. Sports activities can develop this ability. This investigation demonstrated that not only the traditional methods (a sudden stoppage from running, sudden setting in motion, jumping or changing in direction) but motion in a continuously moving media (in aqueous media) can also develop the balancing ability. During kayaking the media always changes; moreover, it often surges so persistent balancing is essential.

In summary, the results of the provocation test prove that unique balancing ability can be gained during motion in continuously changing, dynamic circumstances. The results draw attention to the fact that dynamic balancing ability can be developed by other than traditional methods.

---

## REFERENCES

1. Berger W, Discher M, Trippel M, Ibrahim IK, Dietz V. Developmental aspects of stance regulation, comprehension and adaption. *Experimental Brain Research* 1992;90:610-9.
2. Buchanan JJ, Horak FB. Emergence of postural pattern as a function of vision and translation frequency. *Journal of Neurophysiology* 1999;91:2325-39.
3. Corna S, Tarantola J, Nardone A, Giordano A, Schiepati M. Standing on a continuously moving platform: is body inertia counteracted or exploited? *Experimental Brain Research* 1999;124:331-41.
4. Dietz V, Trippel M, Ibrahim IK, Berger W. Human stance on a sinusoidally translating platform: balance control by feed forward and feedback mechanism. *Experimental Brain Research* 1993;93:356-62.
5. Donker SF, Roerding M, Greven AJ, Beek FJ. Regularity of centre of pressure trajectories depends on the amount of attention invested in postural control. *Experimental Brain Research* 2007;181:1-11.

6. Hof AL, Vermerris SM, Gjalterna WA. Balance responses to lateral perturbation in human treadmill walking. *Journal of Experimental Biology* 2010;213:2655-64.
7. Kiss RM. A new parameter for characterizing balancing ability on an unstable oscillatory platform. *Medical Engineering & Physics* 2011;33:1160-6.
8. Kiss RM. Biomechanics – Analysis of motion E-note for biomedical engineer students. Budapest: 2010. p. 153-8,227-43.
9. Kiss RM. Effect of the degree of hip osteoarthritis on equilibrium ability after sudden changes in direction. *Journal of Electromyography and Kinesiology* 2010;20:1052-7.
10. Kiss RM, Kocsis L, Knoll Zs. Joint kinematics and spatial temporal parameters of gait measured by an ultrasound based system. *Medical Engineering & Physics* 2004;26:611-20.
11. Kocsis L, Kiss RM, Illyés Á. Biomechanics of organs of locomotion. Budapest: TERC 2007. p. 138-40, 147-50,197-214.
12. Liu W, Kim SH, Long JT, Pohl PS, Duncan PW. Anticipatory postural adjustments and the latency of compensatory stepping reaction in humans. *Neuroscience Letters* 2003;336:1-4.
13. Majewski M, Bishoff-Ferrari HA, Gruneberg C, Dick W, Allum JHJ. Improvements in balance after total hip replacement. *The Journal of Bone and Joint Surgery British* 2005;87B:1337-43.
14. Nádori L, Derzsy B, Fábíán Gy, Osváth K, Rigler E, Zsidegh M. Measuring of sport ability. Budapest: Editor Sport 1989. p. 60-85.
15. Nashner LM. Computerized dynamic posturography. In: Goebek JA, editor. *Practical management of Dizzy patients*. Philadelphia: Lippicott Williams and Wilkins; 2001.
16. Newell KM, van Emmerik REA, Lee D, Sparague RL. On postural stability and variability. *Gait and posture* 1993. p. 1:225-30.
17. Prieto TY, Myklebust JB, Hoffmann RG, Lovett EG, Myklebust Bm. Measures of postural steadiness: differences between healthy young and elderly adults. *IEEE Transaction on Biomedical Engineering* 1996;43:956-66.
18. Riley MA, Balasubramaniam R, Turvay MT. Recurrence quantification analysis of postural fluctuation. *Gait and Posture* 1999;9:65-78.
19. Yamada N. Chaotic swaying of the upright posture. *Human Movement Science* 1995;14:711-36.
20. Winter DA. *ABC of balance during standing and walking*. Waterloo: Waterloo Biomechanics; 1995.

***Special thanks to Professor Kiss for her advice and help and to Petra Aradi MD PhD and Maria Takács MD for their assistance in completing the measurements. The authors gratefully acknowledge the Hungarian Scientific Research Fund OTKA for providing financial support in the frame of the grant K-083650.***

## DETERMINATION OF REFERENCE FUNCTION TO KNEE PROSTHESIS RATING

Gábor Katona<sup>1</sup>, Béla M. Csizmadia<sup>1</sup>, Kristóf Andrónyi<sup>2</sup>

<sup>1</sup>Szent István University, Faculty of Mechanical Engineering, Institute of Mechanics and Machinery

<sup>2</sup>Uzsoki Hospital, Department of orthopedic and traumatology

[katona.gabor@gek.szie.hu](mailto:katona.gabor@gek.szie.hu)

---

### Abstract

The knee joint is one of the most complicated joints in the human body. Fundamental knowledge about kinematics is essentially important in order to design knee prostheses which are functionally similar to the knee joint. In addition, the prosthesis should carry out similar kinematics, since only the geometrical resemblance is insufficient. As an initial step, an experimental apparatus, a test protocol and an evaluation method were developed which allows the investigation of the human knee joint kinematics. Based on the results of multiple experiments, a reference function was determined, which provides guidance on how the flexion-rotation function in the human knee joint can be described. The function also provides reference about the kinematics which should be defined in the design of prostheses, and to what extent does an arbitrary knee prosthesis follows the required kinematics. The definition of knee rotation is reported in this article.

**Keywords:** biomechanics, knee joint, rotation, flexion, kinematics, reference function

---

### Introduction

The goal of our research is to determine a kinematical and kinetical model of knee joint, which intends to help in the development of better prostheses. The movement of the knee joint can be investigated locally (sliding-rolling, etc.)<sup>1</sup> and globally (rotation, abduction, adduction, etc.)<sup>2</sup> The rotation has the most significant role in the knee joint motion from the above-mentioned knee movements. Our current aim is to describe the rotation of the human knee joint as a function of flexion. The reason for this is twofold. On the one hand, the knee joint kinematics can be characterized by this result, and on the other hand, it can be used to qualify and design knee prostheses. A suitable prosthesis has to be similar to a real knee joint regarding the carried out movements and not the geometry.

Kinematic analyzes presented by different authors show large deviation<sup>3-8</sup> (*Figure 1*). A mention must be made that several flexion-rotation functions of other authors – in accordance with reality – does not start from the origin. However, the starting point of the measured curves is transformed to the origin by most of the authors. Nevertheless, most of them do not indicate how this transformation is carried out. This problem will be further discussed in the article.

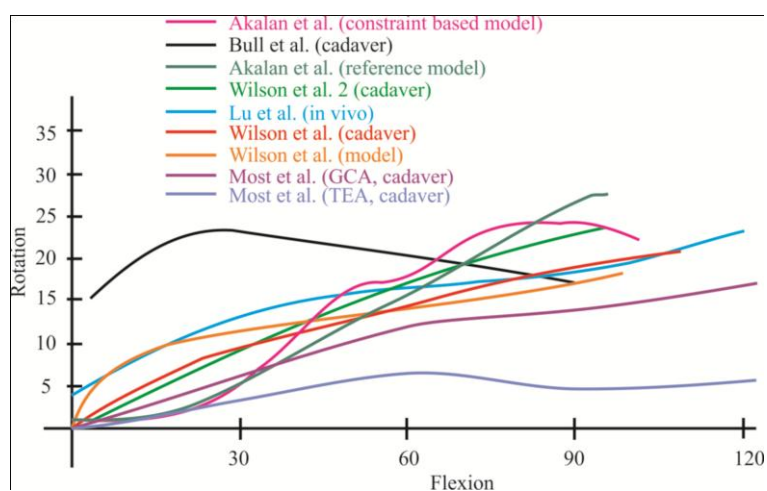


Figure 1. The results of different authors

Additional reasons for the differences between the curves are the followings: biological differences between the people, the applied experimental apparatus, the method of measurement and evaluation, different types of motion and at last the measurement error. The separation of these reasons is an important task in order to draw general conclusions. The diversity of apparatuses and the evaluation methods have significant role in the differences between the results. The upcoming errors can be significantly reduced by using simple apparatus for the experiments. For this reason, a novel, relatively simple experimental apparatus was developed by the Research Team. This apparatus helps the error analysis, the comparison of the measurements and ensures the unconstrained movement of the knee joint. One of the aims was to obtain precise and reproducible kinematical data possible about the knee joint motion.

General aim of the experimental apparatus design and construction was to carry out experiments on cadaver knee joints, in order to provide kinematic data to the knee prosthesis design. The apparatus was later further modified in a way that even prostheses can be clamped into the same apparatus, thus experiments under the same conditions can be carried out in order to compare the results of the measurements with the physiological joint kinematics. The usability of the cadaver knee joint as experimental model have only been studied by the default installation of the experimental apparatus in case of one motion type. This motion is the flexion of the tibia with a horizontally fixed femur.

The experimental apparatus is multifunctional, which is suitable for the determination of the cadaver knee kinematics and kinetics (Figure 2). It can be used in MR, in case of different type of loads and it is also suitable for testing knee prostheses. In the followings, only those parts of the apparatus will be shown which are needed regarding the investigation of the cadaver knee kinematics. The knee joint was resected with 10-15 cm parts of the femur and the tibia also. The joint is fixed to the apparatus with textile bakelite links (1) which are cemented into the medullary cavity. The link is cemented into the femur, while the femur itself is fixed to the base plate (2) of the apparatus, therefore the fixed femur is horizontally positioned. The loads acting on the joint are the weight load and the quadriceps muscle force in case of the studied motion type. The weight of the tibia was modeled with a concentrated force, which is connected to the tibia through a ball joint (3) screwed into the axis of the tibial link. The other force, the quadriceps



muscle force was modeled by rubber-muscle model (4). The suitability of this was proven earlier.<sup>9</sup> This muscle model is connected to the body of the apparatus via a load cell (5) and a spindle (6) for setting the knee position, and the muscle tension. The movement of the tibia is also realized by the spindle. The change of the tibial position relative to the extended position of the knee was determined by the Polaris<sup>10</sup> (Northern Digital Inc., Waterloo, Ontario, Canada) optical position measuring system after proper authentication. Two moving trackers were fixed to femur and the tibia. One of them was rigidly bolted to the fixed femur (7) and the other one was also rigidly bolted to the moving tibia. By this way they form a rigid body-system. The Polaris measuring system tracks the movement of the fixed trackers in the absolute coordinate system of the Polaris. During the experiment the tracker coordinate systems are rigidly fixed to the bones and they are continuously recorded by the Polaris. The position is described by six data: three coordinates of the origin in the absolute coordinate system and three angles which describes the position of the coordinate axes. These are the so-called Euler-angles.

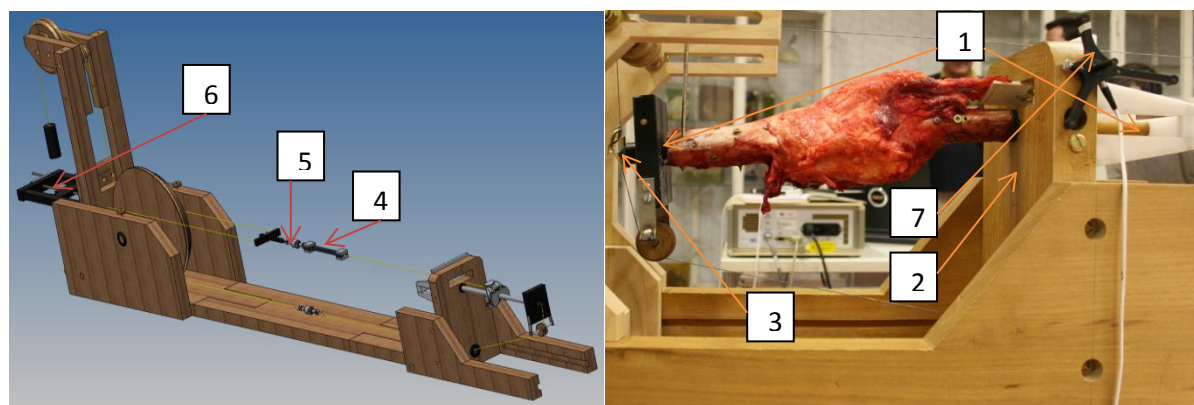


Figure 2. Cadaver knee test rig

### Method of experiments and evaluation

In our experiments, the knee joints were obtained from five subjects between 28-60 years of age. Experiments were performed on seven knee joints in order to create the reference function (TUKEB 165-1/2002). The condition of the knee joints were controlled after the experiments. All the used knee joints were in suitable, undamaged condition.

Analysis was performed using anatomical coordinate system fixed to the bones for the comparison of the measurements on different subjects. However, there was a fundamental problem in the evaluation, due to the missing anatomical points of the resected knee joint. Therefore, the anatomical points had to be recorded (Figure 4) on the whole body before the resection of the knee joint. These points are easily palpable on the tibia of the whole body, so their detection can be solved by a simple pointer tracker. The determination of the center point of the femoral head is more complex. It can be determined by measuring the coordinates of the motion tracker fixed to the femur during the circling motion of the femur. A mention must be made that these points generally move on a sphere. The center of the sphere, which is the center of the femoral head (fh), can be calculated (Figure 4) from the coordinates of the origin of the tracker coordinate system. The other two necessary points on the femur are the epicondylar

points. The described method was modified during the creation of the anatomical coordinate system. The centers of the femoral posterior condylar curves were used instead of the epicondylar points (Figure 3). The reason of this modification is also twofold. On the one hand, the epicondylar points are uninterpretable on prosthesis, and on the other hand, the accuracy of the epicondylar points' determination is much smaller than the accuracy of the determination of the posterior condylar curves' centers.<sup>11</sup> Anatomical coordinate system defined by the VAKHUM project was fitted to the recorded anatomical points<sup>12</sup> (Figure 4). Since the knee joint was fixed into the apparatus in resected state, the possibility of the transformation of resected anatomical points needed to be ensured. For this reason, the position of the secured markers, both in the femur and the tibia, were recorded. After these measurements the joint, which was fixed in the apparatus, was resected. The position of the anatomical points and the markers were recorded in the apparatus as well. In the following steps, continuous measurements were performed after the determination of the discrete points in order to determine the kinematics (flexion-rotation). The above-mentioned measurements were carried out in 3 repetitions per joint. These repetitions gave provided the same results, therefore the measurements are acceptably repeatable.<sup>13</sup>

The flexion-rotation data was determined by transformations using the transformation matrices. The matrices were generated from the positions of the anatomical points, the markers, and the current positions of the trackers. These transformation matrices can be generated from the data measured by the Polaris as well. These processes were carried out on basis of the Grood-Suntay's angle definition.<sup>14</sup> The results can be drawn as the function of flexion.

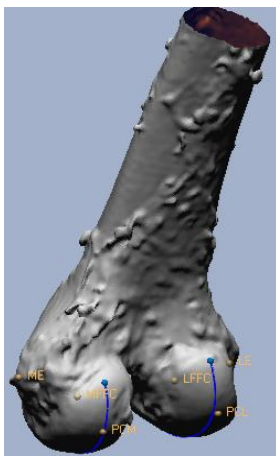


Figure 3. Anatomical points on the femur

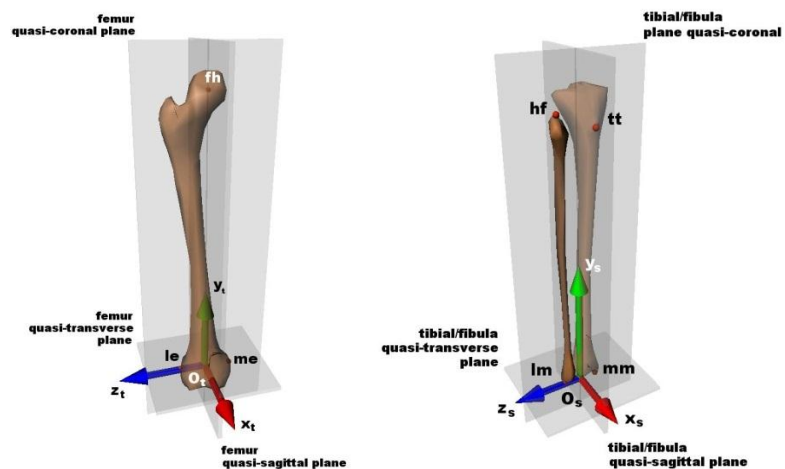


Figure 4. The anatomical coordinate system of the femur and the tibia

The literature suggests that during knee flexion the movement can be divided into two parts. The first 20-30° section of the flexion is the section the screw-home motion,<sup>13</sup> where the kinematics is governed mainly by the geometry. After this section the motion is continuously passing through to active functional arc<sup>13</sup> where the movements of knee joint is controlled by the muscle forces collectively. Accordingly, tri-linear functions were fitted to the rotation-flexion data. The first section of motion extends between 0° and 25° of flexion angle. This is the section of screw-home motion. The boundary of the following two segments (at about 50° of flexion angle) can be

interpreted from *Figure 5*. The second section of the flexion extends between 25° and 50°. This is a transitional section to unconstrained motion. The range over 50° of flexion is the range of unconstrained motion, where the motion may be governed by the muscle forces.

The schematic diagram of the approximate functions can be seen on *Figure 5*. The fitting was based on the principle of least squares. The parameters of the fitted functions can be calculated from equation 1 to 9.

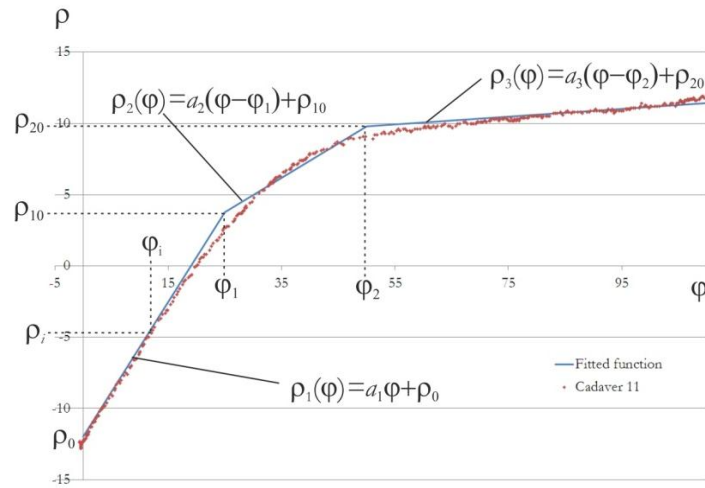


Figure 5. The trilinear function fitted to the measurement data on knee no. 7

First section: 0-25° flexion

$$a_1 = \frac{\sum_{i=1}^{n_1} \rho_i \cdot \varphi_i}{\sum_{i=1}^{n_1} \varphi_i^2} \quad (1)$$

$$\rho_0 = \frac{\sum_{i=1}^{n_1} \rho_i \sum_{i=1}^{n_1} \varphi_i^2 - \sum_{i=1}^{n_1} \varphi_i \sum_{i=1}^{n_1} \rho_i \varphi_i}{n_1 \sum_{i=1}^{n_1} \varphi_i^2 - \left( \sum_{i=1}^{n_1} \varphi_i \right)^2} \quad (2)$$

$$\rho_1(\varphi) = \rho_0 + a_1 \cdot \varphi \quad (3)$$

Second section: 25-50° flexion

$$a_2 = \frac{\sum_{i=n_1+1}^{n_2} \rho_i \cdot (\varphi_i - \varphi_1) - \rho_{10} \sum_{i=n_1+1}^{n_2} (\varphi_i - \varphi_1)}{\sum_{i=n_1+1}^{n_2} (\varphi_i - \varphi_1)^2} \quad (4)$$

$$\rho_{10} = a_1 \cdot \varphi_1 + \rho_0 \quad (5)$$

$$\rho_2(\varphi) = \rho_{10} + a_2 \cdot (\varphi - \varphi_1) \quad (6)$$

Third section: over 50° flexion

$$a_3 = \frac{\sum_{i=n_2+1}^{n_3} \rho_i \cdot (\varphi_i - \varphi_2) - \rho_{20} \sum_{i=n_2+1}^{n_3} (\varphi_i - \varphi_2)}{\sum_{i=n_2+1}^{n_3} (\varphi_i - \varphi_2)^2} \quad (7)$$

$$\rho_{20} = a_2 \cdot (\varphi_2 - \varphi_1) + \rho_{10} \quad (8)$$

$$\rho_3(\varphi) = \rho_{20} + a_3 \cdot (\varphi - \varphi_2) \quad (9)$$

where

$i$ : the sample of the measured data

$\varphi$ : flexion

$\rho$ : rotation

$a_1$ ;  $a_2$ ;  $a_3$ : the gradient of the fitting functions on the first, second and third sections

$\rho_0$ : the intersection of the fitting linear function along the first section

$\rho_1$ : the value of the rotation at the boundary of the first and second sections

$\rho_2$ : the value of the rotation at the boundary of the second and third sections

$\varphi_1$ : the value of the flexion at the boundary of the first and second sections ( $\varphi_1=25^\circ$ )

$\varphi_2$ : the value of the flexion at the boundary of the second and third sections ( $\varphi_2=50^\circ$ )

$n_1$ ;  $n_2$ ;  $n_3$ : the number of measured data on the first, second and third sections

Most of the authors treat the rotation as zero in the totally extended position (*Figure 1*). For the sake of the comparability, both the own measurement results and the fitting functions need to be transformed to zero.

If the points of the anatomical coordinate-system remain unchanged, then the degree of rotation is specified by the position of the malleolus points on the tibia. The two additional points which are needed for the tibial coordinate-system have virtually no effect on the curves, only the position of the longitudinal axis is determined by them. These points are close to each other and relatively far from the ankles, therefore the effect of changing in the range of the recording accuracy is minimal. If the positions of the malleolus points are changed then the curves shift parallel (*Figure 6*).

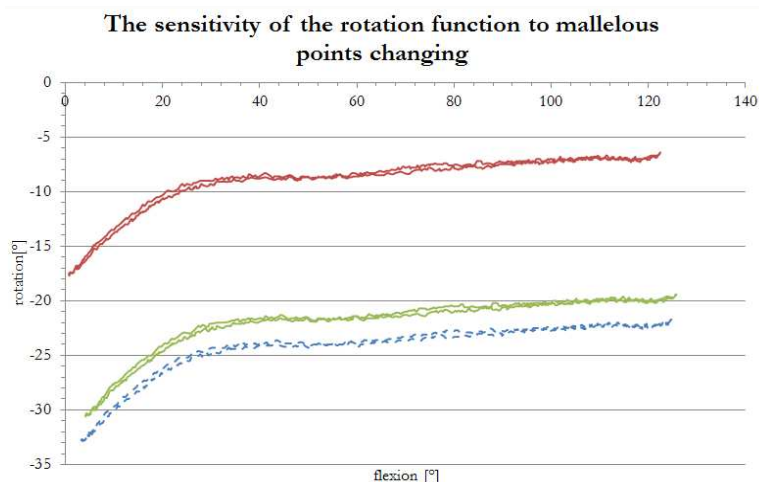


Figure 6. The sensitivity of the rotation function in case of knee no. 3

This phenomenon is interpreted as follows: according to the interpretation of Grood & Suntay, the rotation is a so-called third angle, which describes how the coordinate-system of the tibia is rotated relative to the longitudinal axis of the femur.

Based on these above-mentioned reasons, the fitted rotation-flexion functions can be shifted parallel towards the rotation into the origin (Figure 7). If the measurement results begin from non-zero flexion, the rotation value of zero flexion is determined by the intersection of the fitted functions. With this method, the starting points of the measured rotation-flexion curves can be transformed to the origin.

### Results

The functions fitted on experimental data (involving seven knee joints) are shown on Figure 7 after the transformation described above. These curves are drawn with thin line. The coefficients of the functions are included in Table 1. The reference function is obtained by averaging these functions, which is essential in the design of prostheses and in their qualification. The coefficients of the reference function are included in Table 2.

| $j$ | $a_{1j}$ | $a_{2j}$ | $a_{3j}$ | $\rho_{0j}$ [°] | $\rho_{10j}$ [°] | $\rho_{20j}$ [°] |
|-----|----------|----------|----------|-----------------|------------------|------------------|
| 1   | 0,48     | 0,058    | 0,101    | -24,2           | -12,1            | -10,6            |
| 2   | 0,42     | 0,094    | 0,048    | -14,1           | -3,5             | -1,1             |
| 3   | 0,38     | 0,029    | 0,028    | -18,3           | -8,7             | -7,9             |
| 4   | 0,47     | 0,123    | 0,047    | -28,7           | -16,8            | -13,7            |
| 5   | 0,24     | 0,020    | -0,032   | -13,4           | -7,4             | -6,8             |
| 6   | 0,61     | 0,088    | -0,025   | -11,6           | 3,6              | 5,9              |
| 7   | 0,63     | 0,240    | 0,02723  | -11,9           | 3,7              | 9,7              |

Table 1. The coefficients of the fitted functions

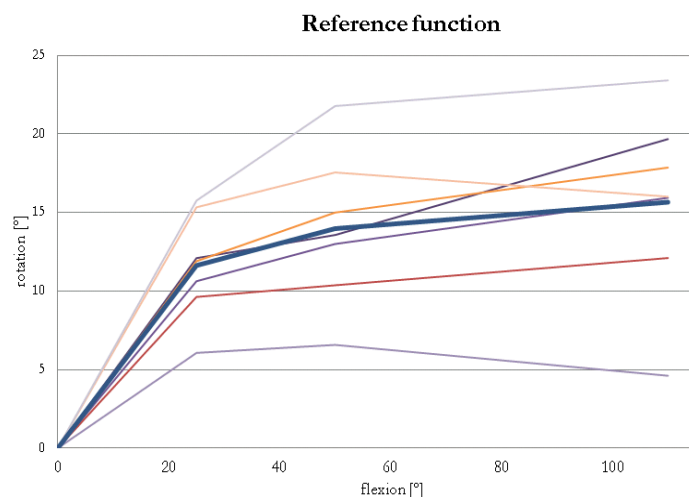


Figure 7. Reference function from the seven fitted and transformed linear functions

|                           | $a_1$       | $a_2$        | $a_3$        | $\rho_0$ [°] | $\rho_{10}$ [°] | $\rho_{20}$ [°] |
|---------------------------|-------------|--------------|--------------|--------------|-----------------|-----------------|
| <b>Reference function</b> | <b>0,46</b> | <b>0,093</b> | <b>0,028</b> | <b>0</b>     | <b>11,6</b>     | <b>13,9</b>     |

Table 2. The coefficients of the reference function

## Discussion, Conclusion

Overall as new results we can present:

- an earlier designed experimental apparatus,
- a protocol for determining the anatomical coordinate system,
- determination of a tri-linear rotation-flexion function which approximates the measured data and can be specified in segments,
- a function based on a large number of experiments, which describes the change of rotation on an average human knee joint.

The results can be utilized in prosthetic design in a way, that the rotation carried out by the prosthesis should approximate this function.

## REFERENCES

1. Fekete G, De Baets P, Wahab MA, Csizmadia BM, Katona G, Vanegas-Useche LV, Solanilla JA. Sliding-rolling ratio during deep squat with regard to different knee prostheses. Acta Polytechnica Hungarica 2012;9(5):5-24.
2. Baldwin MA, Clary C, Maletsky LP, Rullkoetter PJ. Verification of predicted specimen-specific natural and implanted patellofemoral kinematics during simulated deep knee bend. Journal of Biomechanics 2009;42(14):2341-8.
3. Wilson DR, Feikes JD, Zavatsky AB, O'Connor JJ. The components of passive knee movement are coupled to flexion angle. Journal of Biomechanics 2000;33:465-73.

4. Bull AMJ, Kessler O, Alam M, Amis AA. Changes in Knee Kinematics Reflect the Articular Geometry after Arthroplast. *Clinical Orthopaedics and Related Research* 2008;466:2491–9.
5. Most E, Axe J, Rubash H, Li G. Sensitivity of the knee joint kinematics calculation to selection of flexion axes. *Journal of Biomechanics* 2004;37:1743-8.
6. Akalan NE, Ozkan M, Temelli Y. Three-dimensional knee model: Constrained by isometric ligament bundles and experimentally obtained tibio-femoral contacts. *Journal of Biomechanics* 2008;41:890–6.
7. Wilson DR, Feikes JD, O'Connor JJ. Ligaments and articular contact guide passive knee flexion. *Journal of Biomechanics* 1998;31:1127-36.
8. Tung-Wu L, Tsung-Yuan T, Mei-Ying K, Horng-Chaung H, Hao-Ling C. In vivo three-dimensional kinematics of the normal knee during active extension under unloaded and loaded conditions using single-plane fluoroscopy. *Medical Engineering & Physics* 2008;30:1004–12.
9. Csizmadia B, Katona G. Some result of the motion analysis executed on experimental model of the knee. In: A. Tőrőková editor. *Proceedings of 23rd Danubia-Adria Symposium on Experimental Methods in Solid Mechanics*; 2006. Sept. 26-29; Zilina, Slovak Republic. Zilina: EDIS, 2006. p. 145-6.
10. NDI, <http://www.ndigital.com/medical/polarisfamily-techspecs.php>
11. Donald Eckhoff MD, Craig Hogan MD, Laura DiMatteo MD, Mitch Robinson MD, Bach J. Difference Between the Epicondylar and Cylindrical Axis of the Knee. *Clinical Orthopaedics and Related Research* 2007;461:238–44.
12. Hilal I, Van Sint Jan S, Leardini A, Della Croce U. D3.2. Technical Report on Data Collection Procedure ANNEX I. 20. p. In: *Virtual Animation of the Kinematics of the Human for Industrial, Educational and Research Purposes*. Information Societies Technology Programme. 2002.
13. Katona G, Csizmadia BM, Bíró I, Andrónyi K, Krakovits G. Motion analysis of human cadaver knee-joints using anatomical coordinate system. *Biomechanica Hungarica* 2010;3(1):93-100.
14. Grood ES, Suntay WJ. A joint coordinate system for the clinical description of 3-dimensional motions - application to the knee. *Journal of Biomechanical Engineering-Transactions of the Asme* 1983; 105(2):136-44.
15. Freeman MAR. How the knee moves. *Current Orthopaedics* 2001;15(6):444-50.

***The research was supported by the TÁMOP-4.2.2.B-10/1-2010-0011 „Development of a complex educational assistance/support system for talented students and prospective researchers at the Szent István University” project.***

## DEVELOPMENT OF ADHESION TEST FOR COATED MEDICAL DEVICE

Torda László Sélley<sup>1</sup>, Andrew Attila Terdik<sup>1</sup>, Eszter Bognár<sup>1,2</sup>

<sup>1</sup>Department of Materials Science and Engineering, Faculty of Mechanical Engineering, Budapest University of Technology and Economics

<sup>2</sup>MTA–BME Research Group for Composite Science and Technology

[torda90@gmail.com](mailto:torda90@gmail.com)

---

### Abstract

High biocompatibility is a basic requirement in medical technology. Polymer coatings can radically improve medical device biocompatibility, especially for surfaces like stainless steel. Adhesion is an important quality in a coating, and this was our rationale for developing a polymer adhesion testing protocol. We compared two biocompatible polymers, polyurethane (PUR) and poly-(DL-lactic-co-glycolic acid) (PDLG). Polymer layers were created on surface-treated stainless steel. The properties of different layers were compared. Adhesion of the coatings was characterised by concentration of coating solution, rate of the contacted surface and surface roughness of the carriers. PUR showed better adhesion under our test conditions.

**Keywords:** adhesion, biocompatible polymer, coating, PUR, PLGA

---

### 1. Introduction

Coatings are widely applied in the field of medical technology. Implants, surgical instruments and other medical devices can be provided with coatings.<sup>1</sup> Coatings can improve some surface properties such as biocompatibility, and this is especially the case with polymer coatings.<sup>2</sup> Polymer coatings generally make devices more bio – and haemocompatible, as well as more corrosion-resistant. Polymer coatings are also able to store and release active agents such as drugs. Another important property is adhesion to the carrier. Applied coatings are thin films with a micro-meter scale thickness.<sup>3</sup> There is a wide variety of existing adhesion measurements, like bending, capitation, impact test, etc.<sup>4</sup> Scratch tests and AFM for adhesion testing are used for measuring thin layer/carrier interaction like polymer coatings.<sup>5-7</sup> Scratch tests are impractical and slow, especially if we want to examine layers we are developing ourselves. In this paper we test the adhesion of two kinds of polymers using a method we developed.<sup>8-9</sup> We further developed the method considering the size of the contacting areas. For a carrier we chose stainless steel, a commonly used raw material in biomedical devices. Stainless steel 304 is used where high corrosion resistance, good formability, strength, manufacturing precision, reliability and hygiene are of particular importance.<sup>10</sup>

One polymer we tested as a coating was PUR. PUR is gathering pace as a coating in medical devices. Polyurethanes offer very high strength, high flexibility and proven impact resistance.<sup>11</sup>

The other polymer we tested was PDLG. It has been successful as a biodegradable polymer because it undergoes hydrolysis in the body to produce the original monomers, lactic acid and glycolic acid. These two monomers are easily broken down in the body without toxic effects, so this polymer is also biocompatible.<sup>12-13</sup>

---



Layers were made by dip-coating. This is the commonest and easiest technique for creating a continuous layer.<sup>14</sup> We created a polymer layer on a surface-treated 304 type stainless steel carrier and compared the properties of different coatings. Adhesion of the coatings were characterised by concentration of coating solution, area of contact, and carrier surface roughness.

## **2. Methods**

### **2.1 Carrier sheets**

During our examinations we used two sorts of coating carriers, 0.3×10×50mm (narrower) and 0.3×20×50 mm (broader) 304 type stainless steel sheets. Sheets were prepared by laser cutting. Sheets were surface-treated to improve their surface properties.

### **2.2 Surface treatment**

First we removed the burr and surface damage from laser cutting. Hydrochloric acid (36 wt %), nitric acid (65 wt %) and water in a 3:1:9 mixture was used as an etching solution. Sheets were etched in the mixture for 60 minutes in an ultrasonic cleaning vat. Then sheets were electropolished in order to improve surface properties and to reduce roughness. Phosphoric acid (85 wt %) sulphuric acid (98 wt %) and water in a 3:6:1 mixture with 20g/L glycerol was used as the electrolyte. For electropolishing we applied 0.01A/mm<sup>2</sup> current density at room temperature (~25°C) for 180, 210, and 240 seconds.

### **2.3 Surface roughness**

We measured the surface roughness of the surface-treated stainless steel sheets. Based on preliminary tests we wanted to observe the connection of surface roughness to adhesion in both kinds of polymer. A Talysurf CLI 2000 scanning-topography measurement instrument was used to determine the surface-treated sheets' surface roughness. Needle speed was 50 μm / second, geometry of the needle was 90°. A 4 to 4.75 mm area was examined on every 3-3 sample.

### **2.4 Applied polymers**

During our experiments we used two types of biocompatible polymers. The applied PUR composition was methylene diphenyl 2, 4'-diisocyanate (MDI), methylene diphenyl 4, 4'-diisocyanate butanediol, polytetrahydrofuran.<sup>15</sup> It is a non-biodegradable polymer, T<sub>g</sub> = 40 °C.

We applied PURAC PURASORB PDLG 5010 DL-lactic acid / glycolic acid 50:50 copolymer (PDLG). It is a biocompatible and biodegradable polymer, ρ = 1.24 kg/L density, IV = 1.04 dL/g inherent viscosity, MW = 104 kDa molecular weight, T<sub>g</sub> = 42 °C.

### **2.5 Creating the coating**

1, 2, and 3 wt% concentration solutions were made from the polymers. PDLG was dissolved in acetone, and PUR was dissolved in tetrahydrofuran. Stainless steel sheets were put into the solutions for 3 seconds then they were removed from the solutions at a speed of 5 mm per

second. We created one-layer coatings at room temperature.

## 2.6 Adhesion test

Each freshly coated sample was stacked to overlap part of another same-size steel sheet. Pairs of parallel sheets in flat-face contact were left to dry for one day in a constant air stream. Stuck-together samples were then pulled in opposite directions within the carrier-sheet plane (*Figure 1*).

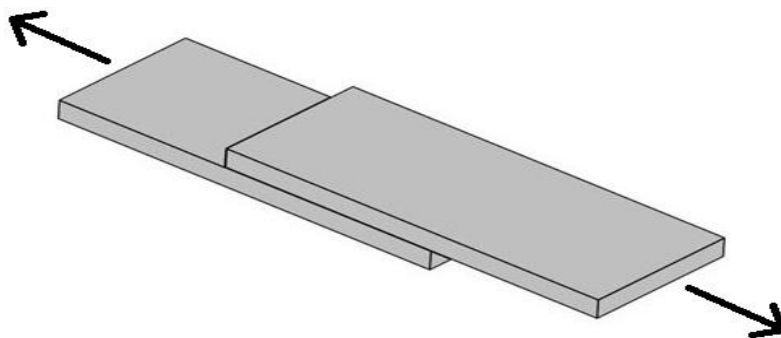


*Figure 1.* Schematic figure of each two-sheet sample as left to dry. Same-size surface-treated steel sheets were flat-face stacked like this after coating. In later tests we pulled the sheets in the two directions shown here by arrows

We varied the contact area from 10 mm×10 mm to 10 mm×20 mm with the narrower sheets, and from 20 mm×10 mm to 20 mm×20 mm with the broader sheets (*Figure 2*).

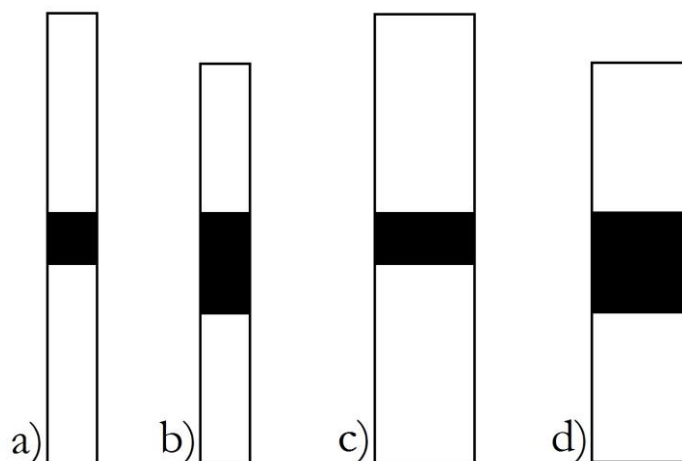


*Figure 2.* Schematic figure of each overlap area between pairs of adhering sheets a) 10 mm×10 mm narrower b) 10 mm×20 mm narrower c) 20 mm×10 mm broader d) 20 mm×20 mm broader.

During the separation by sliding, force (N) was measured as a function of displacement (mm). Motion was set at 4 mm per minute in every case. From the maximum values we got from experiments we deduced the relationship between the coating and the stainless steel sheet carrier. An Instron type 5965 tensile machine was used.

### 3. Results

We measured the surface roughness of the carriers, and the adhesion of polymer coatings from different solutions on various surface-treated and size carriers.

#### 3.1 Surface roughness

Sheet surface texture was compared to electropolishing time. No other parameters varied. Average surface roughness ( $R_a$ ) fell with increased electropolishing time. Higher roughness peaks are broken down by this surface treatment. Rough surfaces can adhere better. *Figure 3* shows the test results and *Table 1* average surface roughness ( $R_a$ ).

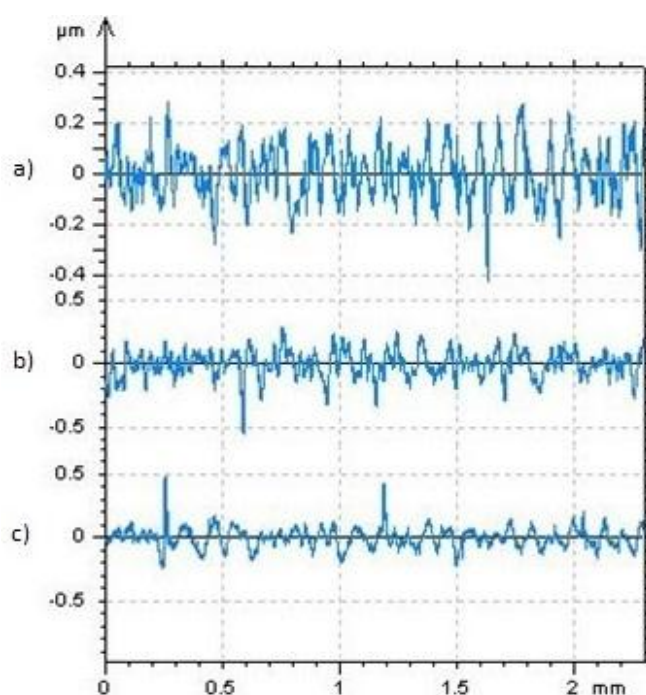


*Figure 3.* Electropolished stainless steel sheet surface roughness tests at a)  $t = 180$  sec, b)  $t = 210$  sec, c)  $t = 240$  sec

| Electropolishing time (s) | 180                 | 210                 | 240                 |
|---------------------------|---------------------|---------------------|---------------------|
| $R_a$ ( $\mu\text{m}$ )   | $0.1063 \pm 0.0332$ | $0.0913 \pm 0.0078$ | $0.0899 \pm 0,0312$ |

*Table 1.* Treated stainless steel sheets' surface roughness. More time spent electropolishing gave a smoother surface

#### 3.2 Adhesion of coating

All the coating types were tested three times with this method. *Figure 4* shows a typical tensile diagram similar to that for other samples. From these kinds of diagrams we took the maximums.

Averages of each three measurement were counted. Averages were divided the appropriate contacted areas. Adhesion was characterized with a unified comparable unit ( $\text{N}/\text{mm}^2$ ).

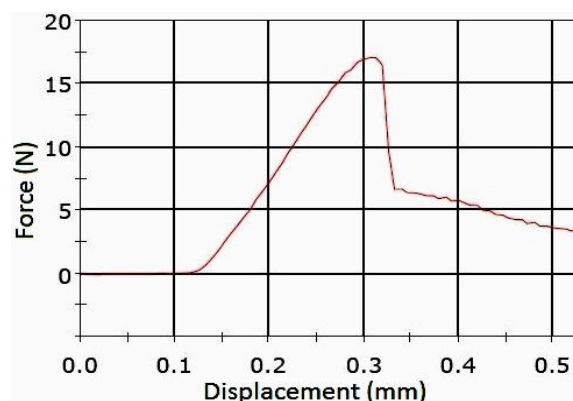


Figure 4. One sample's adhesion test

During our experiments it was found that measurements with broader samples were less accurate (Figure 5). If a sheet's surface is not completely flat, the surfaces are not in close contact. The uneven roughness of the sample may have occurred during sample preparation. This phenomenon creates inaccuracies in the measurements. The narrower ones caused no measuring problems. This can be observed on the narrower  $200 \text{ mm}^2$  samples.

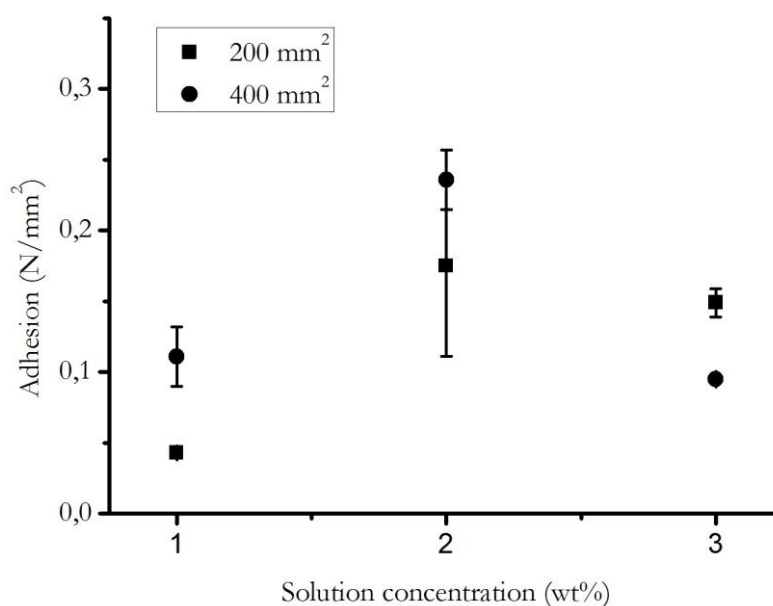


Fig. 5. Adhesion test results of the PUR coating on broader sheets. Imperfectly flat surfaces led to inaccuracies

Based on our previous experiments, we expected adhesion to worsen with increased electropolishing time. This statement was true in one case, the 1 wt% PDLG solution coatings (Figure 6). So in coatings made from less polymer the determining factor is steel-sheet surface roughness after electropolishing and before polymer coating. Higher average roughness provides better adhesion.

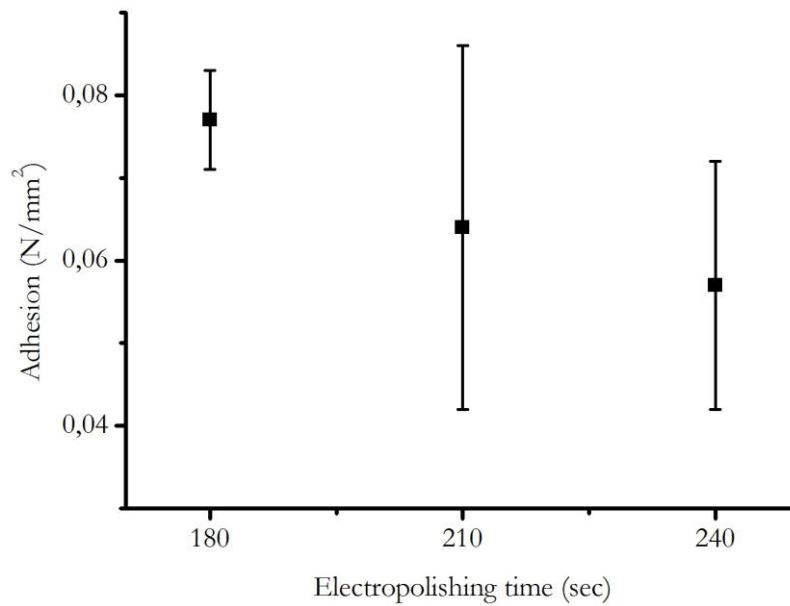


Fig. 6. Adhesion test results for the coating made from 1 wt% PDLG, area in contact 100 mm<sup>2</sup>. The smoother surface created by electropolishing caused weaker adhesion

Increasing polymer solution concentrations increased adhesion. With more continuous coating polymer-metal interaction become stronger. It can be observed in both polymers, PDLG and PUR. Figure 7 shows that under the same conditions, PUR has better adhesion than PDLG.

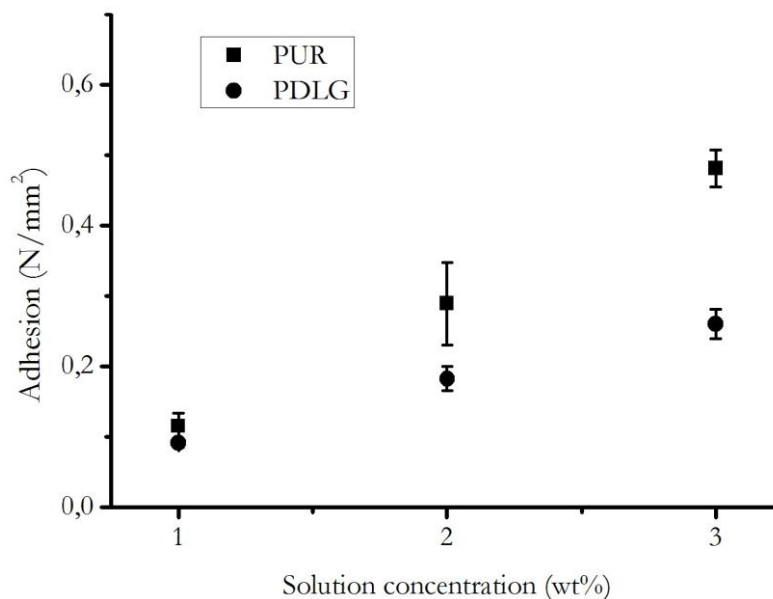


Figure 7. Comparing PUR and PDLG coating adhesion to solution concentration. Contact area was 100 mm<sup>2</sup>, sheets were electropolished for 180 sec. PUR had better adhesion than PDLG

#### 4. Conclusion

We developed a systematic method to examine coating layers' strength of adhesion. We anticipate using it to classify and compare future coatings.

During our experiments we laid down biocompatible coatings onto stainless steel carrier sheets. We found that the technique we developed is appropriate if the area in contact is at least 100 mm<sup>2</sup> and the carrier surface is as plain as possible.

Furthermore we conclude that from the two studied polymers, the PUR has better adhesion on surface-treated stainless steel 304 type carrier.

---

## REFERENCES

1. Hildebrand HF, Blanchemain N, Mayer G, Chai F, Lefebvre M, Boschini F. Surface coatings for biological activation and functionalization of medical devices. In: Surface and Coatings Technology. EMRS 2005 Symposium K — Protective Coatings and Thin Films: 2005 May 31 – June 3: Strasbourg(FR) 2006;200(22–23):6318–24.
2. Mani G, Feldman MD, Patel D, Agrawal CM. Coronary stents: A materials perspective. *Biomaterials* 28 2007. p. 1689-1710.
3. Fang HW, Li KY, Su TL, Yang TCK, Chang JS, Lin PL, Chang WC. Dip coating assisted polylactic acid deposition on steel surface: Film thickness affected by drag force and gravity. *Material Letters* 2008;62(21-22):3739-41.
4. Ollendorf H, Schneider D. A comparative study of adhesion test methods for hard coatings. *Surface and Coatings Technology* 1999;113(1-2):86-102.
5. Cortés EV, Lorenzo MA, Jirsa JO, Wheat HG, Carrasquillo RL. Adhesion Testing of Epoxy Coating. Texas Department of Transportation: 1998 Sept.
6. Ozsváth P, Bognár E. Szentbevonatok tapadásának vizsgálata és fejlesztése. (Examination and investigation of stent coating's adhesion). *Anyagok világa* 2010. p. 1.
7. Litteken CS, Dauskardt RH. Adhesion of polymer thin-films and patterned lines. *International Journal of Fracture* 2003;119/120:475-85.
8. Sélley TL, Terdik A, Bognár E. Biológiailag lebomló polimerbevonatok tapadásának vizsgálata (Investigation of biodegradable polymer coatings' adhesion test). *Fiatal Műszakiak Tudományos Ülésszaka XVIII: 2013 March 21–22: Kolozsvár (RO)*
9. Sélley TL, Szilágyi A, Bognár E. Biodegradable Polymer coatings for stents. 29th Danubia – Adria – Symposium on Advances in Experimental Mechanics: 2012 Sept 26 – 29: Belgrade (SRB)
10. Newson T. Stainless Steel – A Family of Medical Device Materials. This article first appeared in *Business Briefing: Medical Device Manufacturing & Technology* 2002: London (UK).
11. Smith RW: New Developments and Trends in Medical-grade Adhesives. *Medical Device Manufacturing & Technology* 2004: London (UK)
12. Onuki Y, Bhardwaj U, Papadimitrakopoulos MPF, Burgess DJ. A Review of the Biocompatibility of Implantable Devices: Current Challenges to Overcome Foreign Body Response. *J Diabetes Sci Technol*. 2008 November;2(6):1003–15.
13. Anderson JM, Shive MS. Biodegradation and biocompatibility of PLA and PLGA microspheres. *Advanced Drug Delivery Reviews* 1997;28:5–24.
14. Raval A, Choubey A, Kotadia H, et al. Novel Biodegradable Polymeric Matrix Coated Cardiovascular Stent For Controlled Drug Delivery. *Trends Biomater. Artif. Organs* 2007;2:101-10.
15. Fejős D, Sütő P, Molnár K, Pukánszky B. PU/PBT keverékek vizsgálata esetleges orvosi alkalmazásra. (Examination of PU / PBT blends for possible medical applications). *Műanyag és Gumi* 2011;48(12): 446-9.

*This work is connected to the scientific programme of the "Development of quality-oriented and harmonized R+D+I strategy and functional model at BME" project. This project is supported by the New Hungary Development Plan (Project ID: TÁMOP-4.2.1/B-09/1/KMR-2010-0002).*

*The work reported in the paper has been developed in the framework of the project „Talent care and cultivation in the scientific workshops of BME" project. This project is supported by the grant TÁMOP-4.2.2.B-10/1--2010-0009.*

*Many thanks go to Esther Kooijman at PURAC, who provided the PDLG and Kinga Molnár, who provided the PUR we used.*

## BIOMECHANICAL EVALUATION OF VERTEBROPLASTY AND KYPHOPLASTY BY UNIAXIAL COMPRESSIVE TEST

Márta Kurutz<sup>1</sup>, Gábor Jakab<sup>2</sup>, Péter Varga<sup>3</sup>, Péter Pál Varga<sup>2</sup>

<sup>1</sup>Budapest University of Technology and Economics

<sup>2</sup>National Center for Spinal Disorders, Budapest

<sup>3</sup>Julius Wolff Institute and Berlin-Brandenburg School for Regenerative Therapies, Charité - Universitätsmedizin

[kurutzm@eik.bme.hu](mailto:kurutzm@eik.bme.hu)

---

### **Abstract**

In vertebroplasty, by injecting cement into the fractured osteoporotic vertebra, the cement can leak into the surrounding soft tissues. To avoid this injurious side-effect, in kyphoplasty a suitable place is previously prepared for the cement, by an inflated and removed balloon. In this study the biomechanical evaluation of vertebroplasty and kyphoplasty is presented by comparing the strength, stiffness and deformability of post-operated vertebrae by using uniaxial compressive mechanical test. As for conclusion, mechanical properties following vertebroplasty are more sensitive to initial bone density than after kyphoplasty, however, both techniques give practically the same failure load, vertebroplasty yields larger stiffness and smaller compressive deformability.

**Keywords:** vertebroplasty, kyphoplasty, mechanical compressive test, failure load, failure displacement, compressive stiffness

---

### **Introduction**

Percutaneous vertebroplasty and kyphoplasty are well-established minimally invasive treatments for compression fractures of osteoporotic vertebral bodies.<sup>1-7</sup> In vertebroplasty, bone cement is injected through a needle into the fractured osteoporotic cancellous bone of the vertebra. In this case, the cement can leak into the soft tissues and veins and neural foramen surrounding the vertebra, causing further complications. To avoid this side-effect, in kyphoplasty, a balloon is first inserted and inflated to expand the compressed vertebra to its height more or less, and to prepare the place for the cement to be injected. After removing the balloon, the cement is injected into its prepared place. The benefit of kyphoplasty besides preventing cement leakage is that the vertebra partly recovers its height before the bone hardens. Without these treatments, the fractures will eventually heal, but in their collapsed position.

In this study the biomechanical evaluation of vertebroplasty and kyphoplasty is presented by comparing the strength, stiffness and deformability of post-operated vertebrae by using uniaxial compressive mechanical test.

### **Methods**

The specimens were prepared in the National Center for Spinal Disorders in Budapest, and the compression tests were executed in the laboratory of the Biomechanical Research Centre of the Budapest University of Technology and Economics.



At present, for the specimens 44 lumbar vertebrae were extracted from 13 human female cadaveric lumbar spines (spine/level/gender/age): A/L1-L4/F/60; B/L1-L3/F/60; C/L1-L3/-/-; D/T12-L5F/51; E/L1-L4/F/57; F/L1-L4/F/95; G/L1-L4/-/-; H/L1-L4/F/80; I/L1-L4/F/70; J/L1-L5F/60; K/L1-L5/F/88, L/L1-L3/F/, M/L1-L2/F. The 44 vertebrae were divided into 3 groups: 7 native vertebrae (NV), 16 vertebrae for vertebroplasty (VP) and 21 vertebrae for kyphoplasty (KP). In the VP group a total volume of 6 ml of PMMA cement was injected, in 3-3 ml bipedicular way. Similarly, in the KP group, 3-3 ml PMMA cement was injected into the place of inflated and removed two balloons, yielding a total value of 6 ml, as well. Thus, the same amount of cement was injected into all VP and KP augmented vertebrae.

The VP and KP groups were further divided into two groups: 8 vertebra from VP group for thick embedding (VP1) group and 8 for thin embedding (VP2) group; 10 vertebra from KP group for thick embedding (KP1) group and 11 for thin embedding (KP2) group. The specimens of thick and thin embedding groups were embedded parallel to about 8,6 and 3,6 mm polymethylmethacrylate PMMA discs, respectively, around the inferior and superior endplates of vertebrae. The native vertebrae remained without embedding.

Both the pre- and post-operated specimens were scanned individually with a high-resolution quantitative computed tomography (QCT) system (Hitachi Presto, Hitachi Medical Corporation, Tokyo, Japan) to provide 3D density maps of the vertebral bodies. The samples were scanned in native state submerged in a water filled box. The PMMA embedding of specimens were transparent in CT to distinguish correctly the bone and embedding, so the bordering planes of embeddings were marked by glass pearls. Vertebral heights, central cross sectional areas, CT grey values were measured from QCT images. The CT scan was performed for each specimen after the mechanical test as well. The specimens were stored at -200C and were thawed at room temperature 4-6 hours before testing.

Table 1a and 1b illustrate the data of pre-operated specimens for the thick and thin embedded groups, respectively.

**Thick embedded groups (VP1 and KP1)**

| Specimen         | Sample | Age (yrs) | Sex | Height (mm) | Area (mm <sup>2</sup> ) | CT-grey | Specimen         | Sample | Age (yrs) | Sex | Height (mm) | Area (mm <sup>2</sup> ) | CT-grey |
|------------------|--------|-----------|-----|-------------|-------------------------|---------|------------------|--------|-----------|-----|-------------|-------------------------|---------|
| <b>VP1 group</b> |        |           |     |             |                         |         | <b>KP1 group</b> |        |           |     |             |                         |         |
| VP1/1            | A/L1   | 60        | F   | 26,89       | 1199                    | 201     | KP1/1            | A/L2   | 60        | F   | 26,81       | 1349                    | 192     |
| VP1/2            | A/L3   | 60        | F   | 27,10       | 1366                    | 193     | KP1/2            | A/L4   | 60        | F   | 26,96       | 1445                    | 161     |
| VP1/3            | B/L1   | 60        | F   | 30,25       | 1437                    | -       | KP1/3            | B/L2   | 60        | F   | 29,30       | 1426                    | -       |
| VP1/4            | B/L3   | 60        | F   | 26,84       | 1566                    | -       | KP1/4            | C/L1   | -         | -   | 30,55       | 1431                    | 134     |
| VP1/5            | C/L2   | -         | -   | 31,33       | 1562                    | 115     | KP1/5            | C/L3   | -         | -   | 31,65       | 1661                    | 136     |
| VP1/6            | D/L1   | 51        | F   | 27,79       | 1112                    | 174     | KP1/6            | D/T12  | 51        | F   | 26,99       | 1244                    | 164     |
| VP1/7            | D/L3   | 51        | F   | 27,58       | 1341                    | 114     | KP1/7            | D/L2   | 51        | F   | 27,42       | 1211                    | 126     |
| VP1/8            | D/L5   | 51        | F   | 26,18       | 1379                    | 162     | KP1/8            | D/L4   | 51        | F   | 27,65       | 1355                    | 141     |
| mean             |        | 56        |     | 28,00       | 1370                    | 131     | mean             |        | 56        |     | 28,42       | 1390                    | 151     |
| SD               |        | 4,8       |     | 1,82        | 159                     | 63      | SD               |        | 4,9       |     | 1,86        | 139                     | 23      |

Table 1a. Data of pre-operated specimens for the thick embedded groups

## Thin embedded groups (VP2 and KP2)

| Specimen  | Sample | Age (yrs) | Sex | Height (mm) | Area (mm <sup>2</sup> ) | CT-grey | Specimen  | Sample | Age (yrs) | Sex | Height (mm) | Area (mm <sup>2</sup> ) | CT-grey |
|-----------|--------|-----------|-----|-------------|-------------------------|---------|-----------|--------|-----------|-----|-------------|-------------------------|---------|
| VP2 group |        |           |     |             |                         |         | KP2 group |        |           |     |             |                         |         |
| VP2/1     | E/L1   | 57        | F   | 26,75       | 985                     | 143     | KP2/1     | E/L2   | 57        | F   | 28,41       | 977                     | 152     |
| VP2/2     | E/L3   | 57        | F   | 27,19       | 1113                    | 171     | KP2/2     | E/L4   | 57        | F   | 27,31       | 1078                    | 121     |
| VP2/3     | G/L2   | -         | F   | 27,81       | 1244                    | 99      | KP2/3     | G/L3   | -         | F   | 28,57       | 1390                    | 67      |
| VP2/4     | I/L1   | 70        | F   | 25,63       | 832                     | 183     | KP2/4     | I/L2   | 70        | F   | 27,59       | 959                     | 179     |
| VP2/5     | I/L3   | 70        | F   | 26,46       | 1000                    | 178     | KP2/5     | I/L4   | 70        | F   | 27,58       | 1235                    | 86      |
| VP2/6     | H/L2   | 80        | F   | 25,01       | 1200                    | 243     | KP2/6     | K/L1   | 88        | F   | 21,94       | 919                     | 138     |
| VP2/7     | J/L3   | 68        | F   | 28,99       | 1152                    | 158     | KP2/7     | H/L1   | 80        | F   | 25,14       | 1239                    | 147     |
| VP2/8     | J/L5   | 68        | F   | 29,09       | 1277                    | 191     | KP2/8     | J/L1   | 68        | F   | 25,85       | 973                     | 166     |
| VP2/9     | F/L2   | 95        | F   | 25,55       | 921                     | 88      | KP2/9     | J/L4   | 68        | F   | 30,39       | 1319                    | 146     |
| VP2/10    | F/L4   | 95        | F   | 26,17       | 1045                    | 43      | KP2/10    | F/L2   | 95        | F   | 24,68       | 787                     | 67      |
|           |        |           |     |             |                         |         | KP2/11    | F/L4   | 95        | F   | 25,43       | 951                     | 72      |
| mean      |        | 73        |     | 26,87       | 1077                    | 150     | mean      |        | 75        |     | 26,63       | 1075                    | 122     |
| SD        |        | 14        |     | 1,41        | 145                     | 58      | SD        |        | 14        |     | 2,31        | 192                     | 42      |

Table 1b. Data of pre-operated specimens for the thin embedded groups

The compressive mechanical test was executed by using a servohydraulic testing machine (Instron 8870 series). Axial compressive displacement load was applied at a rate of 5mm/min speed, to the limit of 20% decrease of the compressive force or 20% of compressive strain of the specimen. Axial compressive force and displacement were measured and the relating force-displacement curve was plotted. Failure load (N), failure displacement (mm) and structural stiffness (N/mm) were extracted from the load-displacement curves. Failure load was the maximum load before the gradient of the curve changed from positive to negative, whereas stiffness was the slope of the linear portion of the load-displacement curve before failure occurred. Dividing the failure displacements by the original heights of the vertebrae, failure strains were also calculated. Based on the elastic stiffness, Young's moduli of augmented vertebrae were obtained as well.

## Results

Table 2a, 2b and 2c illustrate the values of failure load, elastic stiffness, Young's modulus, failure displacements (height losses) and failure strains extracted and calculated from the load-displacement diagrams obtained from the mechanical compressive tests, for the native vertebrae and for the thick and thin embedded groups, respectively. Mean failure load, stiffness and failure height loss of groups with thick and thin embeddings are seen in Figure 1.

Compressive failure load was practically not affected by the augmentation types, it was not significantly different for VP and KP groups in thick ( $P=0.40$ ) and thin ( $P=0.31$ ) embedded groups; it was only about 8% smaller in thin embedded groups for KP vertebrae, compared to the VP ones (Figure 1a). Compared to the native vertebrae without embedding, the failure load was significantly, 76-78% ( $P=0.002$ ) higher in thick, but only 21-11% ( $P=0.088$ ) higher in thin embedded groups, for VP and KP vertebrae, respectively.

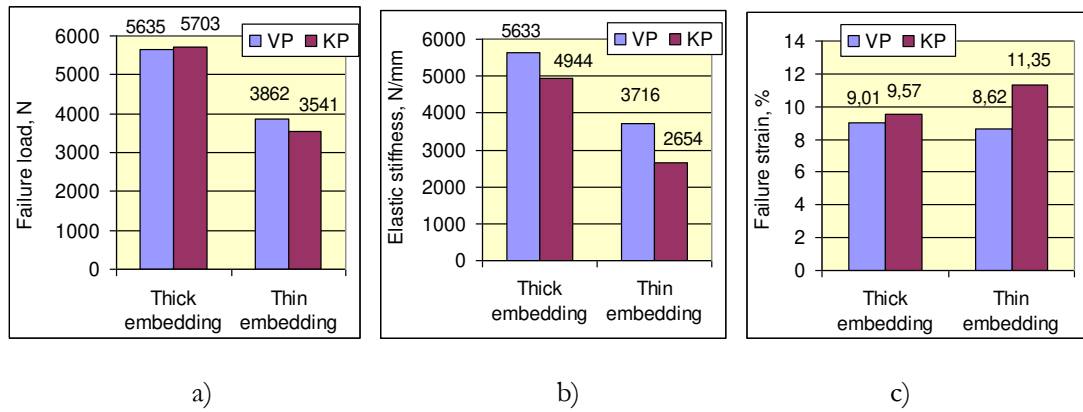


Figure 1: Mean failure load (a), stiffness (b) and failure height loss (c) of VP and KP groups with thick (VP1, KP1) and thin (VP2, KP2) embeddings

**Native vertebrae (NV group)**

| Specimen        | Sample | Sex | Height (mm)  | Area (mm <sup>2</sup> ) | Failure load (N) | Stiffness (N/mm) | Young mod (MPa) | Failure short. (mm) | Failure strain % |
|-----------------|--------|-----|--------------|-------------------------|------------------|------------------|-----------------|---------------------|------------------|
| <b>NV group</b> |        |     |              |                         |                  |                  |                 |                     |                  |
| NV/1            | L/L1   | F   | 27,5         | 908                     | 2210             | 750              | 23              | 5,00                | 18,18            |
| NV /2           | L/L3   | F   | 30,5         | 1320                    | 2548             | 779              | 18              | 4,69                | 15,38            |
| NV /3           | G/L4   | -   | 28,0         | 1134                    | 2986             | 656              | 16              | 5,66                | 20,21            |
| NV /4           | G/L1   | -   | 20,0         | 962                     | 3140             | 1056             | 22              | 6,04                | 30,20            |
| NV /5           | M/L1   | F   | 24,0         | 855                     | 3483             | 915              | 26              | 7,35                | 30,63            |
| NV /6           | M/L2   | F   | 26,0         | 908                     | 4711             | 1031             | 30              | 7,94                | 30,54            |
| NV /7           | L/L2   | F   | 30,0         | 1015                    | 3293             | 759              | 22              | 7,72                | 25,73            |
| <b>mean</b>     |        |     | <b>26,57</b> | <b>1370</b>             | <b>3196</b>      | <b>849</b>       | <b>22</b>       | <b>6,34</b>         | <b>24,41</b>     |
| <b>SD</b>       |        |     | <b>3,66</b>  | <b>163</b>              | <b>799</b>       | <b>153</b>       | <b>4</b>        | <b>1,33</b>         | <b>6,45</b>      |

Table 2a. Mechanical parameters of native vertebrae

**Thick embedded groups (VP1 and KP1)**

| Specimen         | Failure load (N) | Stiffness (N/mm) | Young mod (MPa) | Failure short. (mm) | Failure strain % | Specimen         | Failure load (N) | Stiffness (N/mm) | Young mod (MPa) | Failure short. (mm) | Failure strain % |
|------------------|------------------|------------------|-----------------|---------------------|------------------|------------------|------------------|------------------|-----------------|---------------------|------------------|
| <b>VP1 group</b> |                  |                  |                 |                     |                  | <b>KP1 group</b> |                  |                  |                 |                     |                  |
| VP1/1            | 5300             | 6818             | 153             | 1,61                | 5,99             | KP1/1            | 5449             | 4854             | 96              | 2,08                | 7,76             |
| VP1/2            | 5688             | 7692             | 153             | 1,59                | 5,87             | KP1/2            | 5022             | 4000             | 75              | 2,62                | 9,72             |
| VP1/3            | 4263             | 6849             | 144             | 1,43                | 4,73             | KP1/3            | 4546             | 5556             | 114             | 2,09                | 7,13             |
| VP1/4            | 7846             | 8046             | 138             | 2,97                | 11,07            | KP1/4            | 6403             | 4630             | 99              | 4,50                | 14,73            |
| VP1/5            | 5887             | 5000             | 100             | 3,77                | 12,03            | KP1/5            | 6786             | 6329             | 121             | 2,74                | 8,66             |
| VP1/6            | 4132             | 3419             | 85              | 1,90                | 6,84             | KP1/6            | 4197             | 4040             | 88              | 2,20                | 8,15             |
| VP1/7            | 6393             | 3593             | 74              | 3,75                | 13,60            | KP1/7            | 6951             | 5185             | 117             | 2,91                | 10,61            |
| VP1/8            | 5573             | 3650             | 69              | 3,13                | 11,96            | KP1/8            | 6270             | 4959             | 101             | 2,70                | 9,76             |
| <b>mean</b>      | <b>5635</b>      | <b>5633</b>      | <b>115</b>      | <b>2,52</b>         | <b>9,01</b>      | <b>mean</b>      | <b>5703</b>      | <b>4944</b>      | <b>101</b>      | <b>2,73</b>         | <b>9,57</b>      |
| <b>SD</b>        | <b>1182</b>      | <b>1940</b>      | <b>36</b>       | <b>0,99</b>         | <b>3,49</b>      | <b>SD</b>        | <b>1047</b>      | <b>771</b>       | <b>16</b>       | <b>0,78</b>         | <b>2,39</b>      |

Table 2b. Mechanical parameters of specimens in the thick embedded groups

## Thin embedded groups (VP2 and KP2)

| Specimen         | Failure load (N) | Stiffness (N/mm) | Young mod (MPa) | Failure short. (mm) | Failure strain % | Specimen         | Failure load (N) | Stiffness (N/mm) | Young mod (MPa) | Failure short. (mm) | Failure strain % |
|------------------|------------------|------------------|-----------------|---------------------|------------------|------------------|------------------|------------------|-----------------|---------------------|------------------|
| <b>VP2 group</b> |                  |                  |                 |                     |                  | <b>KP2 group</b> |                  |                  |                 |                     |                  |
| VP2/1            | 2400             | 2609             | 71              | 2,45                | 9,16             | KP2/1            | 3480             | 1676             | 49              | 4,82                | 16,97            |
| VP2/2            | 4595             | 4255             | 104             | 2,44                | 8,97             | KP2/2            | 3380             | 3614             | 92              | 2,08                | 7,62             |
| VP2/3            | 3884             | 2752             | 62              | 2,78                | 10,00            | KP2/3            | 4033             | 2985             | 61              | 3,64                | 12,74            |
| VP2/4            | 3537             | 3846             | 118             | 1,84                | 7,18             | KP2/4            | 3583             | 2419             | 70              | 3,49                | 12,65            |
| VP2/5            | 4000             | 4255             | 113             | 2,24                | 8,47             | KP2/5            | 3767             | 2222             | 50              | 3,51                | 12,73            |
| VP2/6            | 6944             | 4778             | 100             | 3,53                | 14,11            | KP2/6            | 3261             | 2222             | 53              | 2,88                | 13,13            |
| VP2/7            | 3889             | 3571             | 90              | 2,16                | 7,45             | KP2/7            | 6593             | 4380             | 89              | 3,19                | 12,69            |
| VP2/8            | 4444             | 6154             | 140             | 1,49                | 5,12             | KP2/8            | 2832             | 2569             | 68              | 2,69                | 10,41            |
| VP2/9            | 2009             | 2632             | 73              | 1,47                | 5,75             | KP2/9            | 2738             | 2391             | 55              | 2,26                | 7,44             |
| VP2/10           | 2913             | 2308             | 58              | 2,61                | 9,97             | KP2/10           | 2194             | 2410             | 76              | 2,00                | 8,10             |
|                  |                  |                  |                 |                     |                  | KP2/11           | 3091             | 2308             | 62              | 2,64                | 10,38            |
| <b>mean</b>      | <b>3862</b>      | <b>3716</b>      | <b>93</b>       | <b>2,30</b>         | <b>8,62</b>      | <b>mean</b>      | <b>3541</b>      | <b>2654</b>      | <b>66</b>       | <b>3,02</b>         | <b>11,35</b>     |
| <b>SD</b>        | <b>1373</b>      | <b>1202</b>      | <b>27</b>       | <b>0,62</b>         | <b>2,54</b>      | <b>SD</b>        | <b>1135</b>      | <b>752</b>       | <b>15</b>       | <b>0,83</b>         | <b>2,89</b>      |

Table 2c. Mechanical parameters of specimens in the thin embedded groups

Compressive stiffness for KP treatment was 12% smaller in thick ( $P=0.18$ ) and 29% smaller in thin ( $P=0.02$ ) embedded groups, compared to the VP one (*Figure 1b*). Compared to the native vertebrae where the stiffness was very low, in the thick embedded group it was 5,6-4,8 times higher ( $P<0.00001$ ) and in the thin embedded group 2,1-3,4 times higher ( $P<0.0001$ ), for VP and KP vertebrae, respectively. Similar difference and ratio was observed in Young's moduli of augmented vertebrae compared to the native ones.

Compressive vertebral height loss related to the original height, namely, the compressive strain was 6% larger in the thick ( $P=0.35$ ) and 32% larger in thin ( $P=0.018$ ) embedded groups for KP than for VP augmentation (*Figure 1c*). Related to the native vertebrae the strain was significantly smaller, by 63-61% in the thick and by 65-58% in the thin embedded groups for VP ( $P<0.00001$ ) and KP ( $P<0.001$ ) vertebrae, respectively.

However, the embedding thickness significantly affected most of the mechanical results. The failure load of the thin embedded groups was 32 % smaller for VP ( $P=0.018$ ) and 38% smaller for KP ( $P=0.0016$ ) vertebrae compared to the thick embedded groups (*Figure 1a*). Elastic stiffness of the thin embedded groups was 34% smaller for VP ( $P=0.031$ ) and 46% smaller for KP ( $P=0.0006$ ) vertebrae compared to the thick<sup>21</sup> embedded groups (*Figure 1b*). However, failure strain of the thin embedded groups was only 4 % smaller for VP ( $P=0.45$ ) but 19% larger for KP vertebrae ( $P=0.021$ ), compared to the thick embedded groups (*Figure 1c*).

Correlation between the failure load and the bone quality of thick and thin embedded VP and KP vertebrae can be seen in *Figure 2*. Surprisingly, while the failure load of VP2 vertebrae showed a good positive correlation with CT grey ( $R=0,75$ ), VP1 in thin embedded group had a small negative correlation ( $R=-0,32$ ). KP vertebrae had no correlation at all, neither in thick and nor in thin embedding.

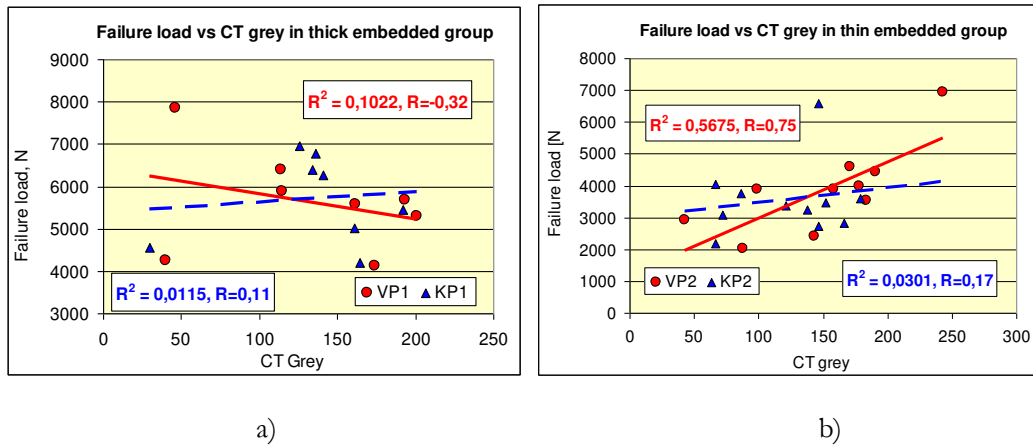


Figure 2: Failure load versus CT-grey of VP and KP groups in a) thick and b) thin embeddings

Correlation between the elastic stiffness and the bone quality of thick and thin embedded VP and KP vertebrae can be seen in Figure 3. Surprisingly, while the stiffness of VP2 vertebrae showed a good positive correlation with CT grey ( $R=0,80$ ), VP1 in thin embedded group had practically no correlation ( $R=-0,25$ ), similar to the KP vertebrae both in thick and thin embedded groups.

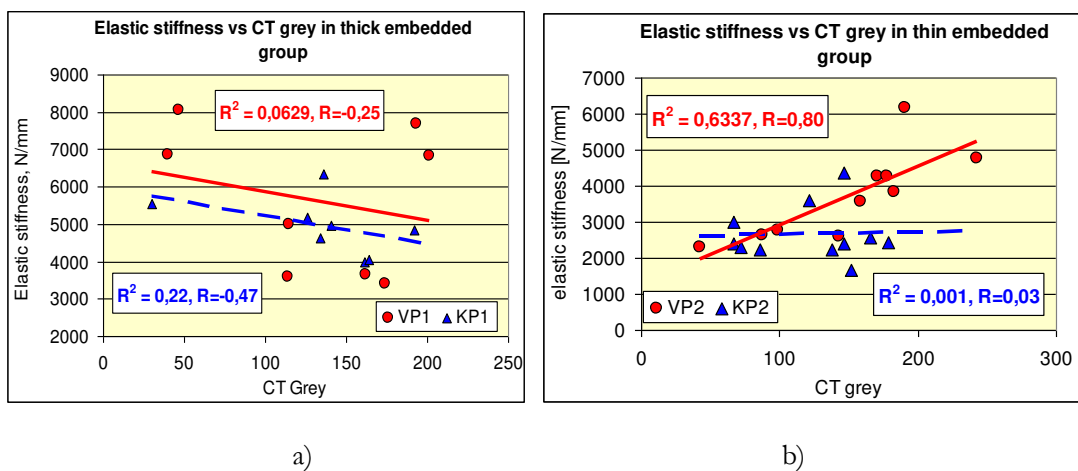


Figure 3: Elastic stiffness versus CT-grey of VP and KP groups in a) thick and b) thin embeddings

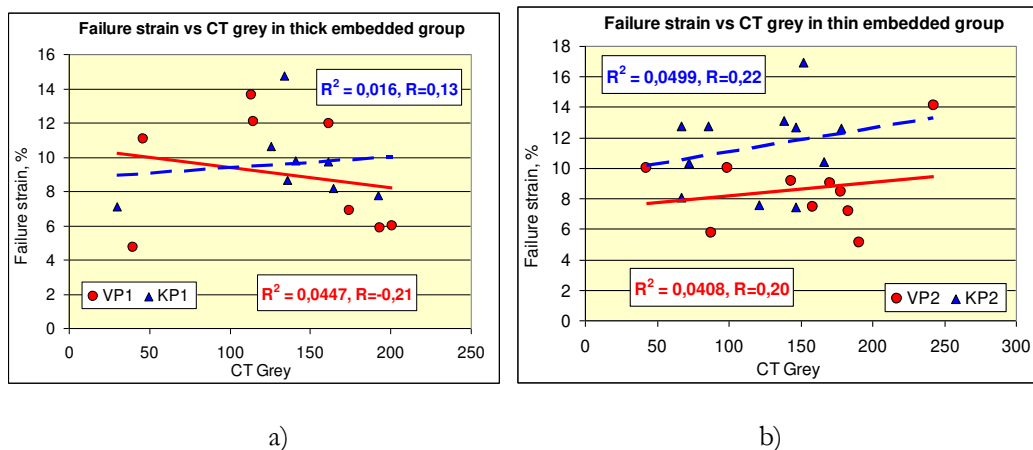
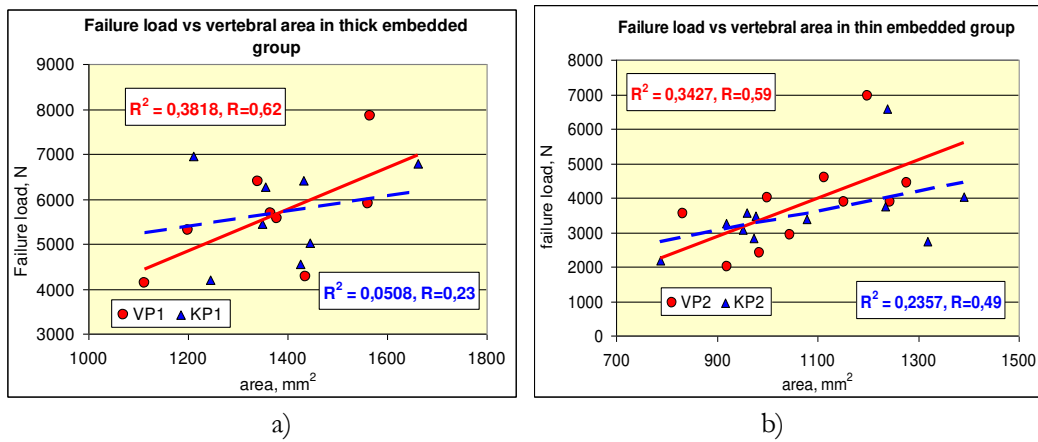


Figure 4: Failure shortening versus CT-grey of VP and KP groups in a) thick and b) thin embeddings

Correlation between the failure strain and the bone quality of thick and thin embedded VP and KP vertebrae can be seen in *Figure 4*. Practically, both VP and KP vertebrae had no correlation, neither in thick and nor in thin embedded groups.



*Figure 5:* Failure load versus vertebral area of VP and KP groups in a) thick and b) thin embeddings

Correlation between the failure load and the cross sectional area of vertebrae of thick and thin embedded VP and KP vertebrae can be seen in *Figure 5*. While the VP vertebrae show a modest positive correlation in both the thick and thin embedded groups ( $R=0,69$  and  $R=0,59$ , respectively), KP vertebrae had a little positive correlation in thin embedded groups ( $R=0,49$ ).

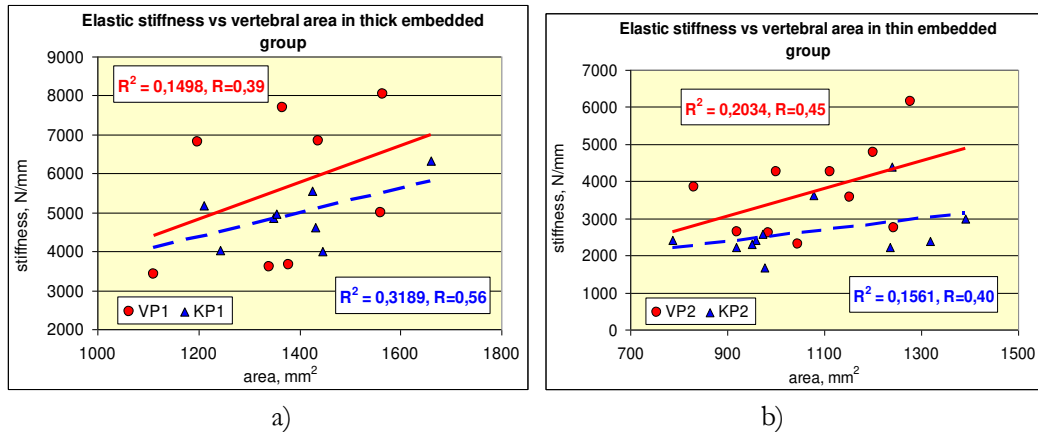


*Figure 6:* Elastic stiffness versus vertebral area of VP and KP groups in a) thick and b) thin embeddings

Correlation between the elastic stiffness and the cross sectional area of vertebrae of thick and thin embedded VP and KP vertebrae can be seen in *Figure 6*. Both VP and KP vertebrae show a modest positive correlation in both the thick and thin embedded groups.

Correlation between the failure strains and the cross sectional area of vertebrae of thick and thin embedded VP and KP vertebrae can be seen in *Figure 7*. While the VP vertebrae show a little positive correlation in the thick embedded groups ( $R=0,43$ ), KP vertebrae had practically no correlation, neither in thick and nor in thin embedded groups.

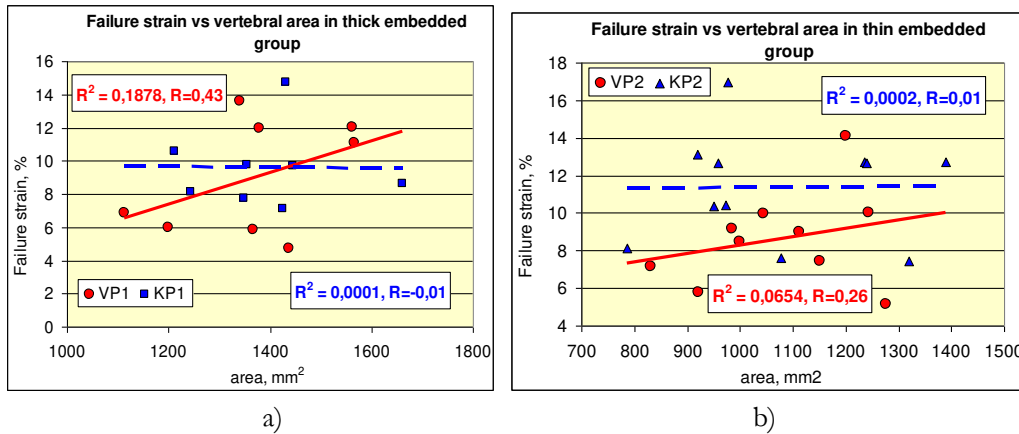


Figure 7: Failure strain versus vertebral area of VP and KP groups in a) thick and b) thin embeddings

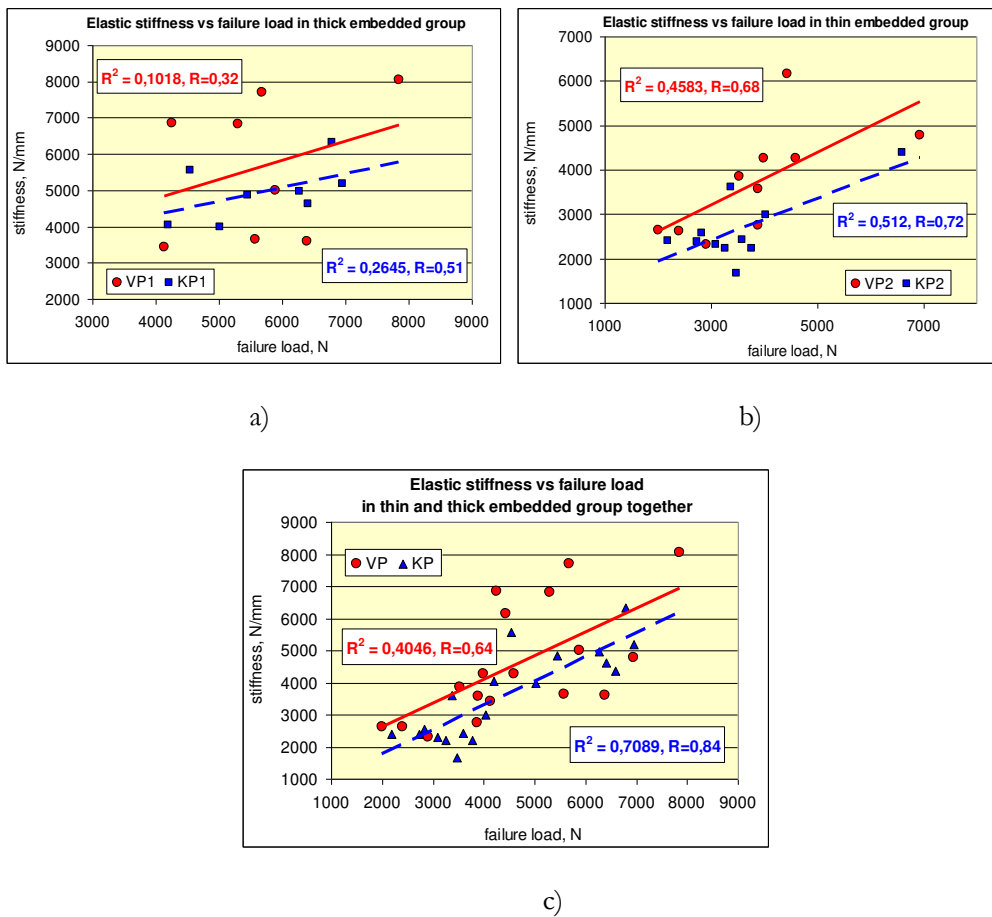


Figure 8: Elastic stiffness vs failure load in a) thick, b) thin and c) thick and thin embedded groups

Correlation between the elastic stiffness and failure load of vertebrae of thick and thin embedded VP and KP vertebrae can be seen in *Figures 8a* and *8b*, for the unified thick and thin embedded groups in *Figure 8c*. In the thin embedded group both VP2 ( $R=0.68$ ) and KP2 ( $R=0.72$ ), vertebrae had higher correlation between stiffness and failure load than in the thick embedded group VP1 ( $R=0.32$ ) and KP1 ( $R=0.51$ ) groups. KP vertebrae had higher correlation in both the thick and thin or in the unified thick and thin embedded group ( $R=0.84$ ) than VP vertebrae ( $R=0.64$ ).

The effect of embedding thickness on the failure load, elastic stiffness and failure shortening can be seen in *Figure 9*. In accordance with *Figure 1* all the three mechanical parameters are more or less sensitive to the embedding of experimental specimens, mainly the failure load and the stiffness of KP vertebrae, but the least the deformability.

## Discussion

All augmentation results highly depended on the embedding thickness. We can state that the thin embedding makes the specimens more sensitive than the thick one to the differences between the mechanical results of VP and KP vertebrae, as shown in *Figures 1* and *8*. Compared to the native vertebrae without embedding, the failure load was about 80% higher in the thick and only 10-20% higher in thin embedded group. Since the thin embedding is closer to the anatomic situation, we can accept the values of thin embedded group as numerical results, however, the tendencies can be confirmed by the results of thick embedded group.

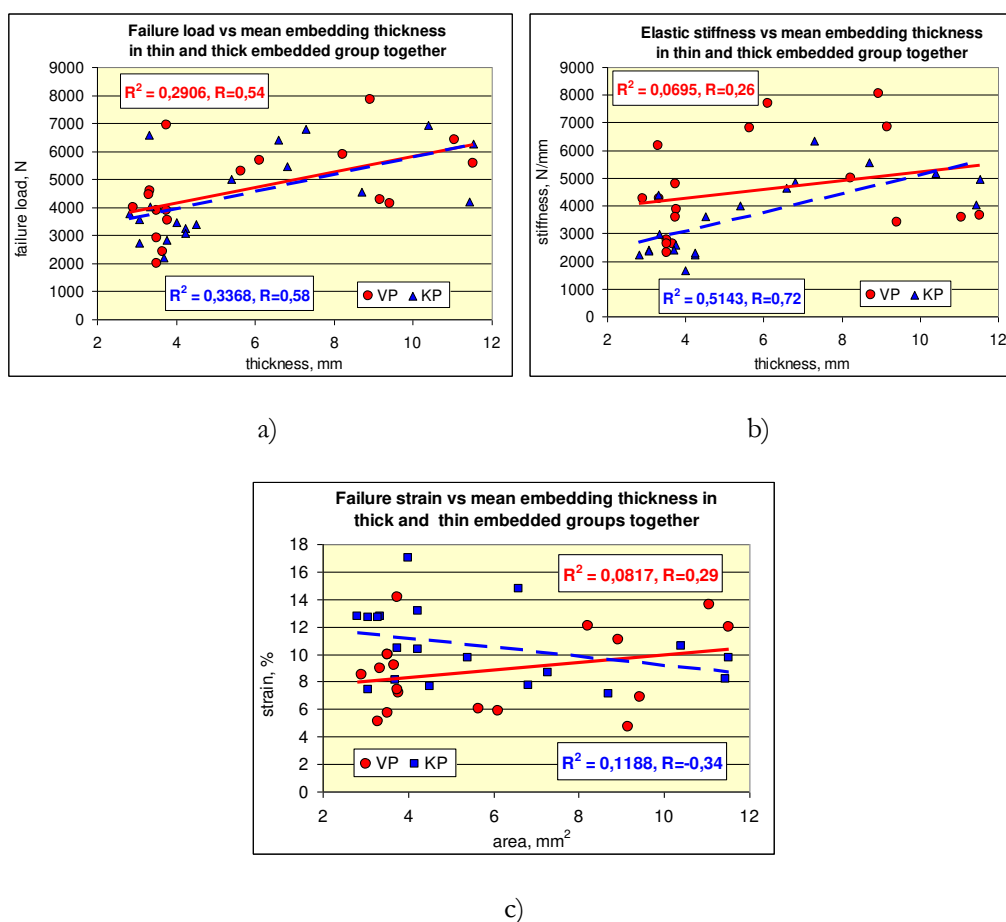


Figure 9: Effect of embedding thickness on the a) failure load, b) elastic stiffness and c) failure strain of VP and KP vertebrae

Compressive failure loads of VP and KP vertebrae were practically equal within each embedding group. The similar values of ultimate loads of VP1 and KP1 vertebrae just like to VP2 and KP2 vertebrae in this study are in agreement with the conclusion of21 that restoration of mechanical properties following PMMA cement augmentation was not significantly different for



vertebroplasty and kyphoplasty. However, there were considerable differences in the stiffnesses within each embedding groups. The reason may be the less uniform or non-smooth load distribution and load transfer inside the vertebral body that increases the deformability and decreases the stiffness of vertebrae.

We conclude that due to VP and KP augmentation, the failure load and the stiffness equally increases. Failure load and stiffness are in a significant correlation with each other ( $P=0.012$ ), mainly for the KP groups (0.0002), in particular in the thin embedded group ( $P=0.002$ ). The increase of the average failure load and stiffness of both VP and KP augmented vertebrae in this study were comparable with the results reported by<sup>9</sup> where compared to the native control vertebrae, a statistically significant increase in vertebral stiffness and failure load was observed by VP augmentation with PMMA cement. The statistical analysis of compressive mechanical tests<sup>10</sup> concluded that the failure load of vertebrae increased with prophylactic cement augmentation<sup>11</sup> and with cement augmentation of fractures<sup>9,12-18</sup>. Stiffness after fracture augmentation has been reported to increase<sup>9,15,17</sup> and to remain unchanged,<sup>14,18</sup> but even to reduce.<sup>12-13</sup>

As for the deformability of augmented vertebrae, under repetitive loading conditions<sup>19</sup> investigated the behavior of fractured osteoporotic vertebral bodies treated with either vertebroplasty or kyphoplasty. The authors concluded that vertebroplasty specimens had higher compression stiffness and smaller height reduction while kyphoplasty were initially taller, but because of a progressive loss of height during loading, the resulting constructs were shorter. Similar results were obtained in this study in the thin embedded group as the compressive strain loss of KP2 specimens was about 30% higher than that of the VP2 group. Comparing the effect of vertebroplasty and kyphoplasty for motion segments<sup>20</sup> concluded that the short-term mechanical effects of kyphoplasty were similar to those of vertebroplasty, with both procedures restoring stiffness, intradiscal pressure and spinal load sharing by a similar amount. Comparisons in<sup>21</sup> showed that the vertebral body heights were partially restored following both kyphoplasty and vertebroplasty, but most of this improvement was lost after creep loading. After the operation KP regained the height better than VP, but after the loading KP has more height loss.

Correlation of failure load and stiffness with the bone quality of thick and thin embedded VP and KP vertebrae shows uncertainty. The failure load of VP vertebrae showed a good positive correlation with CT grey values in thin and a weak negative correlation in thick embedding, while KP vertebrae had no correlation at all, neither in thick and nor in thin embedding. However,<sup>9</sup> concluded that the stiffness and load bearing were inversely correlated to the bone mineral density (BMD) values in osteoporotic vertebral bodies, where the lower the initial BMD was, the more pronounced the augmentation effect was.

The positive correlation of failure load and partly of stiffness with the vertebral cross sectional areas is acceptable since a larger vertebra can contain more augmentation material consequently it can hold larger load.

The failure load in this study depends equally on the embedding both for VP and KP specimens, demonstrating that the vertebral load bearing increases with increasing embedding thickness both for VP and KP specimens, and so does mainly the stiffness of KP vertebrae as well since the deformability of KP specimens decreases with increasing embedding thickness.

The ratio of strength, stiffness and height loss of the vertebral body in the above references has been reported to depend upon the type and volume of cement, bone mineral density, sex or age

of vertebrae, and experimental technique used. However, the influence of embedding type and thickness was not detailed in the mentioned studies; however, most of the experiments used embedded specimens that can determine the boundary conditions of the problem having a considerable influence on the experimentally obtained tissue properties,<sup>22-23,25</sup> in particular on the trabecular tissue properties that can be extremely sensitive to the end-effects. The influence of boundary conditions on the experimental bone tissue characteristics is analyzed by microCT voxel-based large-scale finite element models in.<sup>24,26</sup>

## Conclusion

In the present study two alternative vertebral augmentation techniques, vertebroplasty and balloon kyphoplasty were compared using axial compressive mechanical test. We can conclude that both techniques give practically the same failure load, vertebroplasty yields larger stiffness and smaller compressive deformability. Mechanical properties following VP are more sensitive to initial bone density than after KP. Embedding thickness affects the results considerably. The CT scans after the destructive tests will be analyzed in the near future.

---

## REFERENCES

1. Karlsson MK, Hasserijs R, Gerdhem P, Obrant KJ, Ohlin A. Vertebroplasty and kyphoplasty. New treatment strategies for fractures in the osteoporotic spine. *Acta Orthopaedica*, 2005;76(5):620–7.
2. Hulme PA, Krebs J, Ferguson SJ, Berlemann U. Vertebroplasty and Kyphoplasty: A Systematic Review of 69 Clinical Studies, *Spine*, 2006;31(17):1983-2001.
3. Taylor RS, Taylor RJ, Fritzell P. Balloon Kyphoplasty and Vertebroplasty for Vertebral Compression Fractures: A Comparative Systematic Review of Efficacy and Safety, *Spine*, 2006;31(23):2747-55.
4. Lavelle W, Carl A, Demers Lavelle E, Khaleel MA. Vertebroplasty and Kyphoplasty, *Anesthesiology Clinics*, 25, 2007. p. 913–28.
5. Taylor RS, Fritzell P, Taylor RJ. Balloon kyphoplasty in the management of vertebral compression fractures: an updated systematic review and meta-analysis, *Eur Spine J.*, 2007;16:1085–1100.
6. McGirt MJ, Parker SL, Wolinsky JP, Witham TF, Bydon A, Gokaslan ZL. Vertebroplasty and kyphoplasty for the treatment of vertebral compression fractures: an evidenced-based review of the literature, *The Spine Journal*, 2009;9(6):501-8.
7. Han S, Wan S, Ning L, Tong Y, Zhang J, Fan S. Percutaneous vertebroplasty versus balloon kyphoplasty for treatment of osteoporotic vertebral compression fracture: a meta-analysis of randomised and non-randomised controlled trials, *International Orthopaedics*, 2011;35:1349–58.
8. Schmidt R, Cakir B, Mattes T, Wegener M, Puhl W, Richter M. Cement leakage during vertebroplasty: an underestimated problem? *Eur. Spine J.*, 2005;14:466–73.
9. Heini PF, Berlemann U, Kaufmann M, Lippuner K, Fankhauser C, van Landuyt P. Augmentation of mechanical properties in osteoporotic vertebral bones - a biomechanical investigation of vertebroplasty efficacy with different bone cements. *Eur Spine J.* 2001;10(2):164-71.
10. Lieberman IH, Togawa D, Kayanja MM. Vertebroplasty and kyphoplasty: filler materials, *The Spine Journal* 2005;5:305–16.
11. Lim TH, Brebach GT, Renner SM, et al. Biomechanical evaluation of an injectable calcium phosphate cement for vertebroplasty. *Spine*, 2002;27:1297–302.

12. Belkoff SM, Mathis JM, Erbe EM, et al. Biomechanical evaluation of a new bone cement for use in vertebroplasty. *Spine*, 2000;25:1061–4.
13. Belkoff SM, Mathis JM, Deramond H, et al. An ex vivo biomechanical evaluation of a hydroxyapatite cement for use with kyphoplasty. *Am. J. Neuroradiol.*, 2001;22:1212–6.
14. Belkoff SM, Maroney M, Fenton DC, et al. An in vitro biomechanical evaluation of bone cements used in percutaneous vertebroplasty. *Bone*; 1999;25:23–6.
15. Belkoff SM, Mathis JM, Jasper LE, et al. The biomechanics of vertebroplasty: the effect of cement volume on mechanical behavior. *Spine*, 2001;26:1537–41.
16. Belkoff SM, Mathis JM, Jasper LE, et al. An ex vivo biomechanical evaluation of a hydroxyapatite cement for use with vertebroplasty. *Spine*, 2001;26:1542–6.
17. Molloy S, Mathis JM, Belkoff SM. The effect of vertebral body percentage fill on mechanical behavior during percutaneous vertebroplasty. *Spine*, 2003;28:1549–54.
18. Tohmeh AG, Mathis JM, Fenton DC, et al. Biomechanical efficacy of unipedicular versus bipedicular vertebroplasty for the management of osteoporotic compression fractures. *Spine*, 1999;24:1772–6.
19. Kim, M.J., Lindsey, D.P., Hannibal, M. Alamin, T.F., Vertebroplasty Versus Kyphoplasty: Biomechanical Behavior Under Repetitive Loading Conditions, *Spine*, 2006;31(18):2079-84.
20. Luo J, Adams MA, Dolan P. Vertebroplasty and Kyphoplasty Can Restore Normal Spine Mechanics following Osteoporotic Vertebral Fracture, *Journal of Osteoporosis*, Published online, 2010 p. 9.
21. Luo J, Bertram W, Sangar D, Adams MA, Annesley-Williams, D.J., Dolan, P., Is kyphoplasty better than vertebroplasty in restoring normal mechanical function to an injured spine?, *Bone*, 2010;46:1050–7.
22. Odgaard A, Linde F. The underestimation of Young's modulus in compressive testing of cancellous bone specimens. *Journal of Biomechanics*, 1991;24:691–8.
23. Keaveny TM, Borchers RE, Gibson LJ, Hayes WC. Theoretical analysis of the experimental artifact in trabecular bone compressive modulus, *Journal of Biomechanics*, 1993;26:599–607.
24. Jacobs CR, Davis BR, Rieger, CJ, Francis JJ, Saad M, Fyhrie DP. The impact of boundary conditions and mesh size on the accuracy of cancellous bone tissue modulus determination using large-scale finite-element modeling, *Journal of Biomechanics*, 1999;32(11), 1159–64.
25. Un K., Bevill G, Keaveny TM. The effects of side-artifacts on the elastic modulus of trabecular bone. *Journal of Biomechanics*, 2006;39:1955–63.
26. Bevill G, Eswaran SK, Farahmand F, Keaveny TM. The influence of boundary conditions and loading mode on high-resolution finite element-computed trabecular tissue properties, *Bone*, 2009;44:573-8.

***The authors gratefully acknowledge the Hungarian Scientific Research Fund OTKA for providing financial support in the frame of the grant K-075018. The authors are grateful to Lajos Borbás and Gábor Szabó for their help in laboratory experiments.***

## ANALYZING SPINAL DEFORMITIES BY SPATIAL DATA EXTRACTED FROM COMPUTER GENERATED MOIRÉ IMAGES

Attila Drajkó, Ádám J. Kocsis, Péter Tamás, Ákos Antal  
BUTE Department of Mechatronics, Optics, and Engineering Informatics  
[drajko.attila@schmidt-bender.hu](mailto:drajko.attila@schmidt-bender.hu)

---

### Abstract

Moiré measuring method is used widely throughout medical protocols, especially in the field of spinal diagnostics. In this article we will present an image processing method (written in National Instruments™ LabVIEW™ environment) to extract the height coordinates of a human back, by using the information provided by the moiré phenomenon formed on the surface. These data can be used to improve the accuracy of the two-dimensional deformation analysis (e.g. determination of Cobb Angle), or the relevance of three-dimensional aberrations (such as vertebral protrusions).

**Keywords:** moiré phenomenon, surface mapping, spinal diagnostics, image processing

---

### 1. Introduction

Moiré technique is a method widely used in various medical applications. In dental clinics, F.R. Wouters et al. used moiré phenomenon to examine gum swellings caused by dental implants.<sup>1</sup> Richard Smith et al. applied it in the improvement of the dimensional accuracy of tooth implants.<sup>2</sup> In plastic surgery, Sungyeon Ahn et al. developed a special grating to quantify the elasticity of human skin based on moiré strain analysis.<sup>3</sup> Tetsuo Kawara defined the topography of human cornea by forming the grating with a special fluid. He was able to reach a 5 µm of accuracy, and the method was useful in examining corneal deformities caused by cataract operations.<sup>4</sup>

The most common field where moiré technique is used in medical practice is orthopedics. In the United States, more and more school nurses uses it for spinal deformity screenings.<sup>15</sup> The main advantages are the relatively low cost, and the easy assembling of the measuring system (*Figure 1*), over and above the fast and simple interpretability. The moiré fringes formed on the human back allows the examiner to find the characteristic points of spine clearly.

In this paper, we are going to present an image processing method to determine the three-dimensional shape of the examined human back. At this point we note that this method can also be used on other surfaces, however further specifications are needed.

### 2. Methods

#### 2.1.1 Moiré technique

The moiré phenomenon can be readily observed by superimposing two periodic or quasi-periodic structures. When the two structures have the same or slightly different line spacing and their lines

are set approximately parallel, a new coarse pattern appears. This pattern is known as the moiré fringe pattern. The spacing and orientation of the moiré fringes depend on the spacing and orientation of the structures being overlapped whereas the visibility of fringes is related to the width of transparent or black lines with respect to the line spacing of the structures.<sup>5</sup> Moiré topographical methods can be distinguished as: the basic grating–shadow, the grating–projection, the grating–TV and the synthetic, computer generated grating methods.<sup>6-7</sup> Shadow moiré is a contour mapping technique that involves positioning a grating close to an object and observing its shadow on the object through the grating. Thus, the basic grating–shadow method offers the best accuracy and the simplest arrangement because the projected grating and the master grating are identical, so they have the highest degree of binding. The disadvantage of the shadow moiré technique is that the master grating must have similar size as the measured object.

This optical method is one of the most modern ways for measuring the spatial shape of the human body. The advantages are the simultaneity and the non-contact way of measuring, so it does not influence the analyzed body. Furthermore, information is obtained from all of the points of the analyzed surface at the same time. Its measurement applicability is wide.<sup>8-9,16-18</sup> This technique can also be used to determine deformation caused by pressure or by temperature change, in situations where measurement with mechanical processes cannot be carried out. It is also suitable to check dimensional accuracy of products made by mass production or in robotics.<sup>10-12</sup>

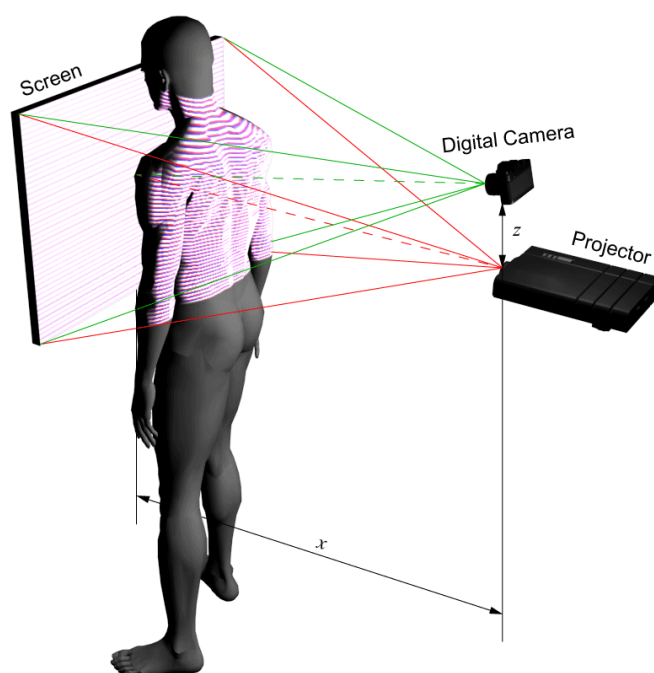


Figure 1. A classical moiré projection layout for human back examinations

In this research we used the color moiré technique to determine the directions of the surface. In 1980 A. Livnat, O. Kafri, and G. Erez defined and analyzed the so called “hill or valley” issue, caused by the ambiguity in the surface direction using the conventional black and white moiré gratings.<sup>13</sup> In 1992 K. Wenzel solved this problem by applying a bicolor projection grating.<sup>14</sup> The

color sequence formed by the moiré fringes defines the direction of the surface unequivocally. Figure 2 shows the advantage of this method, compared to the conventional moiré imaging.



Figure 2. The “hill or valley” issue, and its solution

### 2.1.2 The examined deformity: Idiopathic scoliosis

The origin of idiopathic scoliosis is unknown, and its emergence cannot be prevented. However with frequent screening, it can be easily identified, and with proper treatment it can be stopped, and corrected. By definition idiopathic scoliosis is an abnormal spatial curvature of the spine, which occurs before bone maturation, causing structural deformities. The spine curves in frontal plane, twists in horizontal plane, and becomes concave in sagittal plane. It can develop in any age, which significantly influences its severity. The vertebrae have a reduced mobility, and in some cases the spine cannot be straightened.

### 2.2 Simulation software

The following software had been written in National Instruments™ LabVIEW™ environment, based on its Vision Development module. The purpose of the application is the capability to simulate projection environments from near ideal to near realistic. The input is an 8 bit depth grayscale PNG heightmap that codes the height information as the intensity of its pixels. Using these data we can easily generate the three-dimensional surface we want to analyze. During the simulation, we were using central projection to create the deformed projection grating on the surface. This and the reference grating can also be parameterized arbitrarily. Consequently, the moiré effect is fully customizable. Figure 3 illustrates the user interface of the simulation software.

The following equation is used for calculating the color of the surface using central projection:

$$G_{p.y} = \frac{L_y - S_{p.y}}{L_z - S_{p.z}} \cdot (G_{p.z} - L_z) + L_y \quad (1)$$

Where  $S_{p.y}, S_{p.z}$  are the coordinates of the vertex of the analyzed surface, which the casted ray intersects,  $G_{p.y}, G_{p.z}$  are the coordinates of the intersection of the casted ray and the reference grating and  $L_y, L_z$  are the coordinates of the light source.

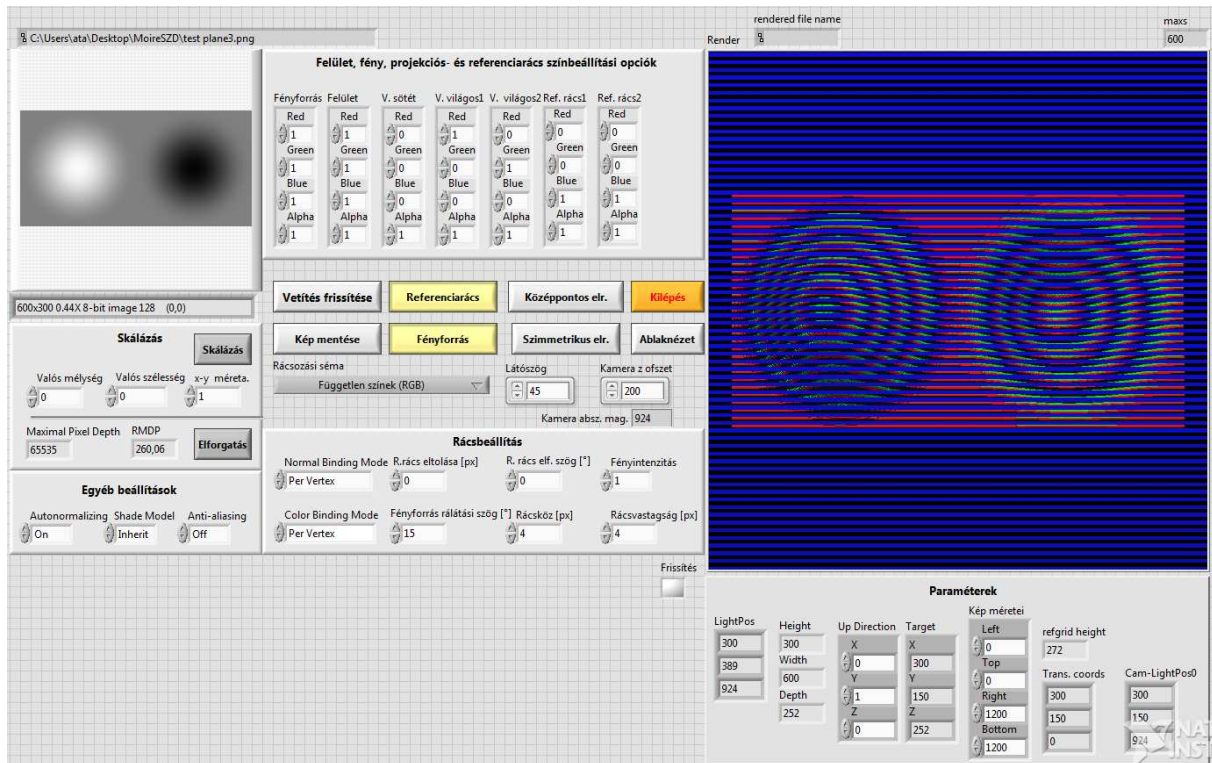


Figure 3. The user interface of the simulation software

Based on the experiments made with the software, we can conclude that the following parameters give the most characteristic and processable moiré effect (Figure 4):

- The optical axis of the digital camera is perpendicular to the screen, and intersects it at the central point.
- From top view, the axis of the camera and the projector are overlapped, and their distances from the screen are equal.
- On the side plane, the angle enclosed by these axes is 15-20°.

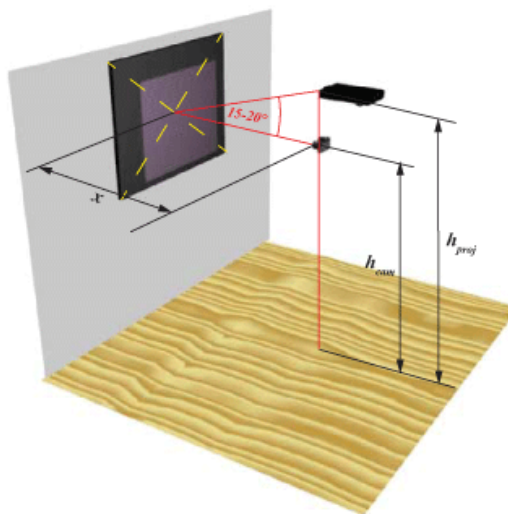


Figure 4. The optimal projection arrangement

Further experiments revealed that the projected grating should consist of red ( $R=255$ ,  $G=0$ ,  $B=0$ ) and green lines ( $R=0$ ,  $G=255$ ,  $B=0$ ), both with  $k$  width, and transparent lines with a width of  $2k$  in this order. The reference grating should be blue ( $R=0$ ,  $G=0$ ,  $B=255$ ) with  $2k$  period. The colour differences help the image processor, presented below, to separate the reference grating, from the projected.

### 3. Results

#### 3.1 Image processing

The cardinal issue of the image processing method is the precise separation and recognition of the moiré fringes. The usage of color grating helps us clearly identify the direction of the surface part covered by the fringe. As the grating is a periodical structure, we can separate it from the other parts of the image using Fast Fourier Transformation, and a low-pass filter. The next step we use, is a threshold method with automatic clustering setting, built in LabVIEW, to exclude the pixels which are not associated with the fringe. After these, we apply the pattern recognition algorithms in Vision Development module, to get numerical information from the fringes, like area, perimeter, number of holes, coordinate of the first pixel, etc. Finally, a pixel sampling algorithm in two lines starts at the widest part of each contour, between the lines of the reference grating. By this method, color sequence of the fringe is defined, from which, the direction of the surface part can be determined directly. This algorithm analyses each contour, thus the surface topology is ready to be calculated. *Figure 5* shows the user interface of the image processor.

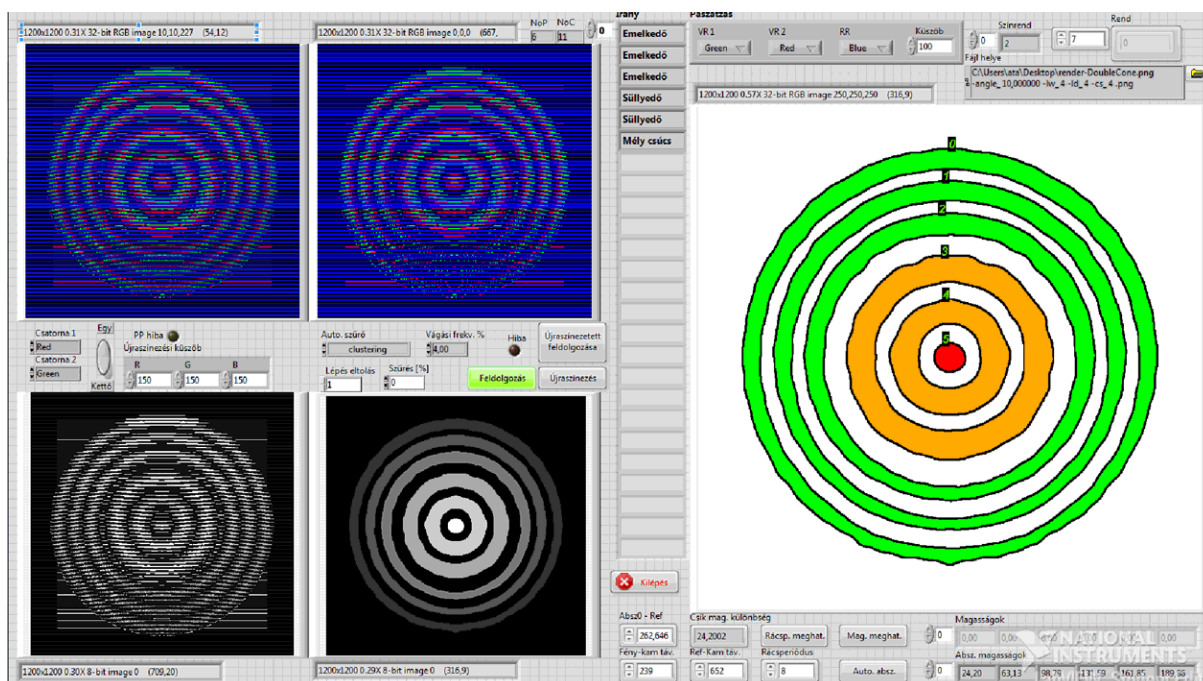


Figure 5. The user interface of the image processing software



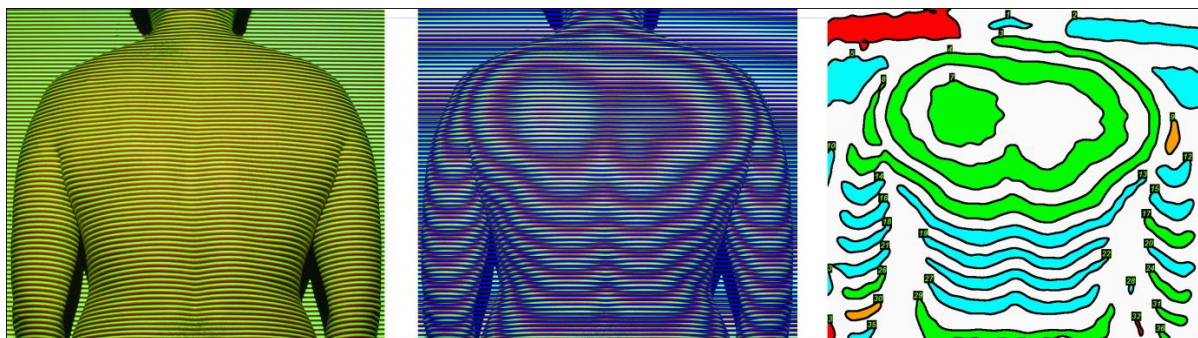


Figure 6. Phases of processing of human back

As Figure 6 shows, the presented algorithm separates the moiré fringes formed on the surface distinctly. Green areas represent rapidly raising surface parts, while cyan and orange parts have less or no climb respectively. This spatial data could be essential in evaluating vertebral deformities caused by scoliosis, not only on the plain of the surface, but in all direction.

#### 4. Conclusion

The presented image processing method is useful in evaluating spinal deformities based on moiré images. However its accuracy significantly depends on the measurement parameters, basic information about the vertebral deformity can be gained in all directions, thus a thorough examination could be prescribed if necessary. This method should be useful in automatic deformity evaluation as well. Using the spatial information a spline fitting algorithm would be able to restore the original surface. Nevertheless, in this case the amount of unnecessary information, caused by redundant fringes formed on the environment, have to be minimized. As previously mentioned, the software can also be applied in any surface mapping applications, although further specifications would be needed.

#### REFERENCES

1. Wouters FR, Jon-And C, Abramson N, Olsson L, Frithiof P-Ö. Soder and I. Dirtoft, Measurement of Gingival Swelling from Dental Casts by Generation of a Moire Pattern with Laser Light. J DENT RES 1988;67:1118, DOI: 0.1177/00220345880670081101
2. Smith R, Zaitoun H, Coxon T, Karmo M, Kaur G, Townsend G, Harris EF, Brook A. Defining new dental phenotypes using 3-D image analysis to enhance discrimination and insights into biological processes. Archives of Oral Biology – 2009 December;54(Suppl 1):118-25, DOI: 10.1016/j.archoralbio.2008.05.018)
3. Ahn S, Kim S, Lee H, Moon S, Chang, I. Correlation between a Cutometer® and quantitative evaluation using Moire topography in age-related skin elasticity. Skin Research and Technology, 2007;13:280–4. DOI: 10.1111/j.1600-0846.2007.00224.x
4. Kawara T. Corneal topography using moiré contour fringes, Appl. Opt. 1979;18,3675-8.
5. Patorski K, Kujawska M. Handbook of the moiré fringe technique, Elsevier Science Publishers, New York; 1993.

6. Windischbauer G. Survey on Applications of Moiré–Techniques in Medicine and Biology, in Optics in Biomedical Sciences, ed: G. von Bally, New York, Springer–Verlag: 1982. p. 244–9.
7. D’Acquisto L, Fratini A, Siddiolo M. A modified moiré technique for three–dimensional surface topography, Measurement Science and Technology, 2002;13(4):613–22.
8. Kamal SA. Determination of degree of correction of spinal deformity by moire topographs. In. Moire Fringe Topography and Spinal Deformity, Proceedings of the 2nd International Symposium, Gustav Fischer Verlag, Stuttgart, 1983. p. 117–26.
9. Neugebauer H. The different methods of measuring the curvature of scoliotic spine. In. Moire Fringe Topography and Spinal Deformity, Proceedings of the 2nd International Symposium, Gustav Fischer Verlag, Stuttgart, 1983. p. 17–26.
10. Dovica M. Komponenty a moduly mini- a mikromechanizmov. Monografi a. Edicia vedeckej a odbornej literatury SJF TU v Kosiciach, Typo Press, Kosice, 2002. p. 150.
11. Dovica M, Gmitterko A, Henriczyova T. Basic Study of the Mobile Minimechanism for Moving Inside the Tubes with Small Diameter. 16. Internationales Kolloqium Feinwerktechnik 1997. October 1–3.
12. Katuch P, Dovica M, Henriczyova T. Walking mini-robots with compliant body. Proceedings of the sixth conference on mechanical engineering, 2008. May 29–30. Budapest, I7, ISBN 963 420 947 8
13. Livnat A, Kafri O, Erez G. Hills and valleys analysis in optical mapping and its application to moiré contouring, Appl. Optics, 1980;19:3396–3400.
14. Wenzel K, Szines Moiré–Abra., Kép és Hangtechnika, 1992 November;38:33–64.
15. Adler NS, Csongradi J, Bleck EE. School Screening for Scoliosis—One Experience in California Using Clinical Examination and Moiré Photography, West J Med. 1984 November;141(5):631–3. PMID: PMC1011169.
16. Dovica M, Kelemenová T, Henriczyová T. Súradnicová metrológia, Košice : TU - 2012. p. 483. ISBN 978-80-553-1120-3.
17. Dovica M, Kelemenová T, Henriczyová T, Kertész T. Tréningové podklady pre Súradnicovú metrológiu, Košice : TU - 2012. p. 307. ISBN 978-80-553-1121-0.
18. Kelemenová T, Henriczyová T. Metrotomografia - nástroj na meranie rozmerov tvarovo zložitých súčiastok, In: AT&P Journal. Č. 9. 2009. p. 1–15. ISSN 1336-233X

***The authors would like to thank National Development Agency (NDA) of Hungarian Government for its support since this study has been carried out commonly as part of project GERINCO2 TECH\_08-A1/2-2008-0121. The work reported in the paper has been developed in the framework of the project „Talent care and cultivation in the scientific workshops of BME” project. This project is supported by the grant TÁMOP-4.2.2.B-10/1--2010-0009.***

## EXPERIMENTAL AND NUMERICAL ANALYSIS OF THE INFLUENCE OF EMBEDDING THICKNESS IN COMPRESSIVE MECHANICAL TESTING OF VERTEBRAL AUGMENTATION AND SPINAL INTERBODY FUSION

Márta Kurutz<sup>1</sup>, Péter Nédli<sup>1</sup>, Péter Varga<sup>2</sup>, Tibor Csákány<sup>3</sup>, Gábor Jakab<sup>3</sup>

<sup>1</sup>Budapest University of Technology and Economics

<sup>2</sup>Julius Wolff Institute and Berlin-Brandenburg School for Regenerative Therapies, Charité - Universitätsmedizin

<sup>3</sup>National Center for Spinal Disorders, Budapest

[kurutzm@eik.bme.hu](mailto:kurutzm@eik.bme.hu)

---

### Abstract

For in vitro mechanical testing of biomechanical objects the specimens must generally be embedded into a special material to obtain a stable position in the testing machine. However, the experimental boundary conditions may influence the results of the measurements. In this study the effect of embedding thickness on the mechanical properties of vertebrae treated by vertebroplasty and kyphoplasty and lumbar motion segments treated by interbody fusion with PEEK and PMMA cement spacers is analyzed by using compressive mechanical tests and QCT based specimen-specific finite element simulation.

**Keywords:** mechanical compressive test, embedding thickness, vertebroplasty, kyphoplasty, interbody fusion, specimen-specific finite-element method

---

### 1. Introduction

In vitro mechanical tests combined with computational methods are widely used for comprehensive analysis of spinal operation techniques. Mechanical testing of spinal specimens can be carefully well-prepared, however, to measure the mechanical characteristics and effective tissue moduli of the objects may have some uncertainties and additional errors due to the experimental boundary conditions, namely, due to the differences between model and experiment, in particular how the experimental boundary conditions are modelled.<sup>1</sup> Among others, material and embedding techniques highly influence the measured values, mainly for cellular structures. To determine the dependence of effective tissue properties on the applied boundary conditions and quantifying errors was investigated in<sup>1,2</sup> by using finite element method. According to our observations during comprehensive mechanical tests of augmented vertebrae and interbody fixation, changing the thickness of the embedding of specimens, the mechanical properties like failure loads, displacements and elastic stiffnesses can significantly change.

In this study the effect of embedding thickness on the mechanical properties of vertebrae treated by vertebroplasty and kyphoplasty and lumbar motion segments treated by interbody fusion with PEEK and PMMA cement spacers is analyzed by using compressive mechanical tests and QCT based specimen-specific finite element simulation.

## 2. Methods

The specimens were prepared in the National Center for Spinal Disorders in Budapest, and the compression tests were executed in the laboratory of the Biomechanical Research Centre of the Budapest University of Technology and Economics.

For the vertebral augmentation specimens 37 lumbar vertebrae were extracted from 11 human female cadaveric lumbar spines (spine/level/gender/age): A/L1-L4/F/60; B/L1-L3/F/60; C/L1-L3/-/-; D/T12-L5F/51; E/L1-L4/F/57; F/L1-L4/F/95; G/L1-L4/-/-; H/L1-L4/F/80; I/L1-L4/F/70; J/L1-L5F/60; K/L1-L5/F/88. The 37 vertebrae were divided into 2 groups: 16 vertebrae for vertebroplasty (VP) and 21 vertebrae for kyphoplasty (KP). In the VP group a total volume of 6 ml of PMMA cement was injected, in 3-3 ml bipedicular way. Similarly, in the KP group, 3-3 ml PMMA cement was injected into the place of inflated and removed two balloons, yielding a total value of 6 ml, as well. Thus, the same amount of cement was injected into all VP and KP augmented vertebrae. The VP and KP groups were further divided into two groups: 8 vertebra from VP group for thick embedding (VP1) group and 8 for thin embedding (VP2) group; 10 vertebra from KP group for thick embedding (KP1) group and 11 for thin embedding (KP2) group. The specimens of thick and thin embedding groups were embedded parallel to about 8,5 and 3,5 mm thick polymethylmethacrylate PMMA plastic discs, respectively, around the inferior and superior endplates of vertebrae. In *Table 1e 1a* and *1b* the embedding thickness data of thick and thin embedded groups are shown. The pre-operated detailed data of vertebrae can be seen in<sup>3</sup> published in the present proceedings book as well.

| Thick embedded groups (VP1 and KP1) |        |                  |                  |                  |        |                  |                  |
|-------------------------------------|--------|------------------|------------------|------------------|--------|------------------|------------------|
| Specimen                            | Sample | Superior         | Inferior         | Specimen         | Sample | Superior         | Inferior         |
|                                     |        | embedding        | embedding        |                  |        | embedding        | embedding        |
|                                     |        | thickness        | thickness        |                  |        | thickness        | thickness        |
|                                     |        | (mm)             | (mm)             |                  |        | (mm)             | (mm)             |
| <b>VP1 group</b>                    |        |                  |                  | <b>KP1 group</b> |        |                  |                  |
| VP1/1                               | A/L1   | 6.61             | 4.70             | KP1/1            | A/L2   | 7.52             | 6.11             |
| VP1/2                               | A/L3   | 4.70             | 7.52             | KP1/2            | A/L4   | 5.17             | 5.64             |
| VP1/3                               | B/L1   | 7.99             | 10.35            | KP1/3            | B/L2   | 8.46             | 8.93             |
| VP1/4                               | B/L3   | 10.82            | 7.05             | KP1/4            | C/L1   | 7.52             | 5.66             |
| VP1/5                               | C/L2   | 9.87             | 6.58             | KP1/5            | C/L3   | 7.53             | 7.05             |
| VP1/6                               | D/L1   | 6.11             | 4.23             | KP1/6            | D/T12  | 12.05            | 10.82            |
| VP1/7                               | D/L3   | 9.45             | 9.40             | KP1/7            | D/L2   | 10.44            | 10.34            |
| VP1/8                               | D/L5   | 11.29            | 10.82            | KP1/8            | D/L4   | 10.35            | 12.70            |
| <b>Mean/SD</b>                      |        | <b>8.89/2.19</b> | <b>7.84/2.42</b> | <b>Mean/SD</b>   |        | <b>8.63/2.19</b> | <b>8.41/2.69</b> |

*Table 1a.* Embedding thickness values of pre-operated specimens for the thick embedded groups

| Thin embedded groups (VP2 and KP2) |        |                  |                  |                  |        |                  |                  |
|------------------------------------|--------|------------------|------------------|------------------|--------|------------------|------------------|
| Specimen                           | Sample | Superior         | Inferior         | Specimen         | Sample | Superior         | Inferior         |
|                                    |        | embedding        | embedding        |                  |        | embedding        | embedding        |
|                                    |        | thickness        | thickness        |                  |        | thickness        | thickness        |
|                                    |        | (mm)             | (mm)             |                  |        | (mm)             | (mm)             |
| <b>VP2 group</b>                   |        |                  |                  | <b>KP2 group</b> |        |                  |                  |
| VP2/1                              | E/L1   | 3.33             | 4.00             | KP2/1            | E/L2   | 4.00             | 4.00             |
| VP2/2                              | E/L3   | 3.00             | 3.68             | KP2/2            | E/L4   | 5.00             | 4.00             |
| VP2/3                              | G/L2   | 3.33             | 3.72             | KP2/3            | G/L3   | 3.00             | 3.68             |
| VP2/4                              | I/L1   | 3.29             | 4.26             | KP2/4            | I/L2   | 3.29             | 2.82             |
| VP2/5                              | I/L3   | 2.40             | 3.42             | KP2/5            | I/L4   | 2.82             | 2.82             |
| VP2/6                              | H/L2   | 2.82             | 2.82             | KP2/6            | K/L1   | 4.70             | 3.76             |
| VP2/7                              | J/L3   | 4.70             | 2.82             | KP2/7            | H/L1   | 3.29             | 3.32             |
| VP2/8                              | J/L5   | 3.76             | 3.76             | KP2/8            | J/L1   | 4.23             | 3.29             |
| VP2/9                              | F/L2   | 3.29             | 3.32             | KP2/9            | J/L4   | 3.29             | 2.82             |
| VP2/10                             | F/L4   | 4.23             | 2.82             | KP2/10           | F/L2   | 4.26             | 3.12             |
|                                    |        |                  |                  | KP2/11           | F/L4   | 4.70             | 3.76             |
| <b>Mean/DS</b>                     |        | <b>3.40/0.64</b> | <b>3.49/0.50</b> | <b>Mean/SD</b>   |        | <b>3.87/0.76</b> | <b>3.40/0.47</b> |

Table 1b. Embedding thickness values of pre-operated specimens for the thin embedded groups

For the lumbar interbody fusion specimens 16 cadaveric lumbar motion segments were extracted from 8 human lumbar spines (spine/level/gender/age/BMI): A/L1-4/M/63/24.5/; B/L1-4/M/52/27.1/; C/L1-4/F/79/24.2/; D/L1-4/M/64/24.5/; E/L1-4/F/88/28.6/; F/L1-4/F/88/24.2/; G/L1-4/F/75/24.7/; H/L1-4/M/56/24.7/ that were scanned with dual energy X-ray absorptiometry (DEXA) to obtain bone mineral density (BMD), T-score and Z-score. The 16 motion segments were divided into 2 groups: 8 specimens with PEEK spacers and 8 with PMMA cement cages. In the PMMA group, all possible free places of the intervertebral space were filled in by the injected cement. No further filling material or bone debris was used for the present experiments. The specimens of both groups were embedded parallel by equally about 10 mm thick PMMA plastic discs around the inferior and superior endplates of the inferior and superior vertebrae, respectively. The pre-operated detailed data of the segments can be seen in<sup>4</sup> published in the present proceedings book as well.

Both the pre- and post-operated specimens were scanned individually with a high-resolution quantitative computed tomography (QCT) system (Hitachi Presto, Hitachi Medical Corporation, Tokyo, Japan) to provide 3D density maps of the vertebral bodies. The samples were scanned in native state submerged in a water filled box. The PMMA embedding of specimens were transparent in CT to distinguish correctly the bone and embedding, so the bordering planes of embeddings were marked by glass pearls. Vertebral heights, central cross sectional areas, CT grey values were measured from QCT images. The CT scan was performed for each specimen after the mechanical test as well. The specimens were stored at -200C and were thawed at room temperature 4-6 hours before testing.

Compressive mechanical testing of the specimens was performed by using a servohydraulic testing machine (Instron 8870, Norwood, USA). Axial compressive displacement load was applied at a rate of 5mm/min speed, to the limit of 20% decrease of the compressive force or

20% of compressive strain of the specimen. Axial compressive force and displacement were measured and the relating force-displacement curve was plotted. Failure load, failure displacement and structural stiffness were extracted from the load-displacement curves. Failure load was the maximum load before the gradient of the curve changed from positive to negative, whereas stiffness was the slope of the linear portion of the load-displacement curve before failure occurred. Dividing the failure displacements by the original heights, failure strains were also calculated for vertebra specimens.

At the same time, CT-based case-specific finite element models were constructed detailed in<sup>5</sup> published in the present proceedings book. The post-operative CT images were segmented by means of a semi-automated approach using the software tool ZibAmira (Zuse Institute Berlin, Germany). For the fixed motion segments the following volumes were distinguished: cortical and trabecular bone of both vertebral bodies, the articular cartilage layers at the joints of the posterior elements, the remnants of the disc annulus as well as the PEEK or the PMMA cement spacer, respectively. For the augmented vertebrae the following compartments were separated: cortical and trabecular bone volumes of vertebrae included the PMMA cement augmentation volume of vertebroplasty or kyphoplasty. The embedding layers were added as rectangular regions indicated by the glass bead positions.

The finite element meshes of each motion segment and augmented vertebra were then generated based on these images; all domains were meshed with linear tetrahedral elements using the CGAL library ([www.cgal.org](http://www.cgal.org)). Maximal cell size was set to 1.4 mm and the size of the tetrahedrons was adjusted to the local dimensions of the geometrical features. The finite element simulations were performed in Abaqus v6.10 (SIMULIA, Dassault Systemes, Velizy-Villacoublay, France) and ANSYS v14.0 (ANSYS Inc., Southpointe, USA).

Material properties of the soft tissues, spacer, cement and embedding were assumed to be isotropic, homogeneous and linear elastic. For the PMMA cement and plastic materials the elastic modulus was measured experimentally on small cylindrical samples. The properties of PEEK, articular cartilage and annulus were taken from the literature. Bone was assumed to be a transversely isotropic, inhomogeneous and linear elasto-plastic material. For both the trabecular and cortical bone compartments the properties of the elements were scaled based on the CT images by converting the Hounsfield (HU) values into bone mineral density (BMD) units, detailed in.<sup>5</sup> The elements were categorized into 255 sets based on their mean densities. For each set, the elastic moduli and the yield strength were computed using experimentally established vertebra-specific relationships<sup>8</sup> based on.<sup>6-7</sup> The material properties used in the finite element models are seen in *Table 1*.

| Material            | Type                  | Anisotropy             | Young's mod<br>[MPa] | Poisson's<br>ratio |
|---------------------|-----------------------|------------------------|----------------------|--------------------|
| bone                | linear elasto-plastic | transversely isotropic | BMD-based            | 0.381 and 0.104    |
| disc annulus        | linear elastic        | isotropic              | 10                   | 0.45               |
| articular cartilage | linear elastic        | isotropic              | 5                    | 0.45               |
| bone cement         | linear elastic        | isotropic              | 10000                | 0.3                |
| embedding plastic   | linear elastic        | isotropic              | 700                  | 0.3                |
| PEEK spacer         | linear elastic        | isotropic              | 4000                 | 0.4                |

*Table 2.* Material properties used in the finite element model

As for the boundary conditions of the model, the embedding layers, the augmentation cement, the PMMA bone cement and PEEK spacer were assumed to be rigidly bound to the bone surfaces. At present, as a first simplified solution the cartilage layer was assumed to be very soft. The lower plane of the inferior embedding layer was fully constrained. The displacement load was applied on the upper surface of the superior embedding along the direction of the plane normal.

In the finite element analysis of the effect of embedding thickness on the mechanical behaviour of the interbody fusion, we applied a slicing method. The original 10 mm thickness of the embedding was gradually made thinner by removing 2.5 mm thick slices from the embedding just to the total removal of it. These steps were made first parallel in the superior and the inferior embeddings, then separately. All these sliced versions were checked under inverse boundary conditions and loading, namely, first supported down and loaded from the top and later inversely.

In this paper, the effect of embedding thickness will be presented only for the mechanical tests of augmented vertebrae and for the finite element analysis of the plastic damage process of a single case of interbody fusion using PMMA cement spacer. The comparative analysis using both mechanical test and case-specific finite element simulation for both vertebral augmentation and interbody fusion is under progress.

### 3. Results

#### 3.1 The influence of the embedding thickness on the mechanical characteristics of vertebroplasty and kyphoplasty during compressive mechanical test

The results of the compressive mechanical tests, the values of the failure load and displacement and the elastic stiffness are detailed in<sup>3</sup> published in the present proceedings book. Here we cite the results relating to the embedding only. In *Figure 1* the mean failure load, stiffness and failure height loss of VP and KP groups are shown with thick and thin embeddings.

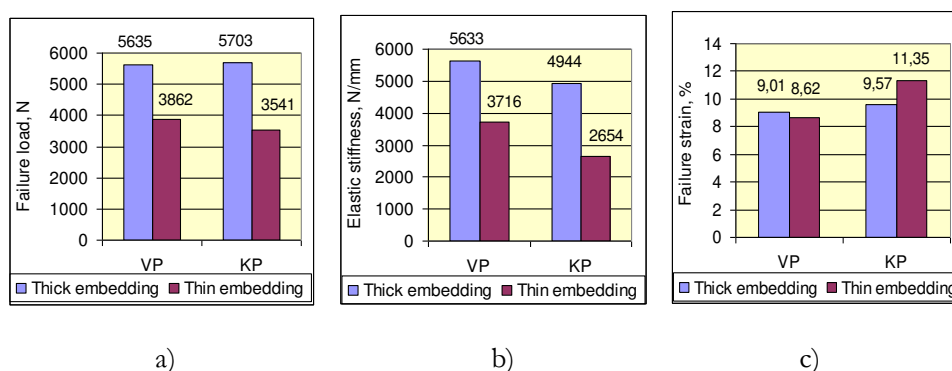


*Figure 1.* Mean failure load (a), stiffness (b) and failure height loss (c) of VP and KP groups with thick and thin embeddings

Compressive failure load was practically equal for VP and KP groups in thick ( $P=0.40$ ) embedded group and was about 8% smaller in thin embedded groups ( $P=0.31$ ) for KP vertebrae,

compared to the VP ones (Figure 1a). Compressive stiffness for KP treatment was 12% smaller in thick (P=0.18) and 29% smaller in thin (P=0.02) embedded groups, compared to the VP ones (Figure 1b). Compressive strain was 6% larger in the thick (P=0.35) and 32% larger in thin (P=0.018) embedded groups for KP than for VP augmentation (Figure 1c). The differences between the mechanical properties of VP and KP augmentation were significantly higher in the thin embedded group (P=0.04).

The embedding thickness significantly affected most of the mechanical results inside the augmentation type as well. The failure load of the thin embedded groups was 32 % smaller for VP (P=0.018) and 38% smaller for KP (P=0.0016) vertebrae compared to the thick embedded groups (Figure 1a). Elastic stiffness of the thin embedded groups was 34% smaller for VP (P=0.031) and 46% smaller for KP (P=0.0006) vertebrae compared to the thick embedded groups (Figure 1b). However, failure strain of the thin embedded groups was only 4 % smaller for VP (P=0.45) but 19% higher for KP vertebrae (P=0.021), compared to the thick embedded groups (Figure 1c).

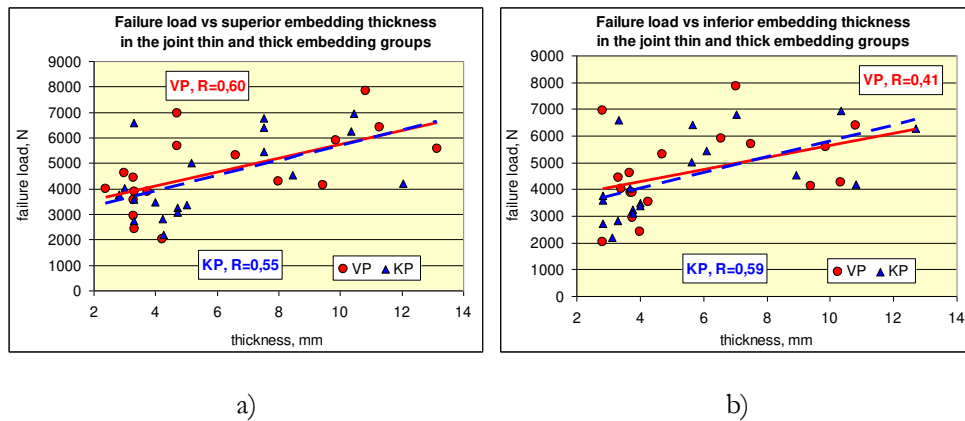


Figure 2. Failure load vs a) superior and b) inferior embedding thickness in VP and KP groups

| Failure load vs emb. thickness | VP1   | KP1   | VP2   | KP2   | VP   | KP   |
|--------------------------------|-------|-------|-------|-------|------|------|
| superior                       | 0.31  | -0.07 | 0.28  | -0.41 | 0.60 | 0.55 |
| inferior                       | -0.26 | -0.02 | -0.35 | 0.05  | 0.41 | 0.59 |
| mean                           | 0.07  | -0.04 | 0.03  | -0.26 | 0.54 | 0.58 |

Table 3. Correlation between failure load and superior, inferior and mean embedding thickness

Correlation between the failure load and the embedding thicknesses of thick and thin embedded VP and KP vertebrae can be seen in Figure 2 and Table 3. Evidently, while the failure load of both VP and KP vertebrae showed practically no correlation with the embedding thickness both in thick and thin embedded groups of small thickness differences, in the joint thick and thin embedded groups of radical thickness differences a good positive correlation was observed,



equally for the superior ( $R=0.60$ ,  $R=0.55$ ), inferior ( $R=0.41$ ,  $R=0.59$ ) and mean ( $R=0.54$ ,  $R=0.58$ ) embedding thicknesses, for VP and KP vertebrae, respectively.

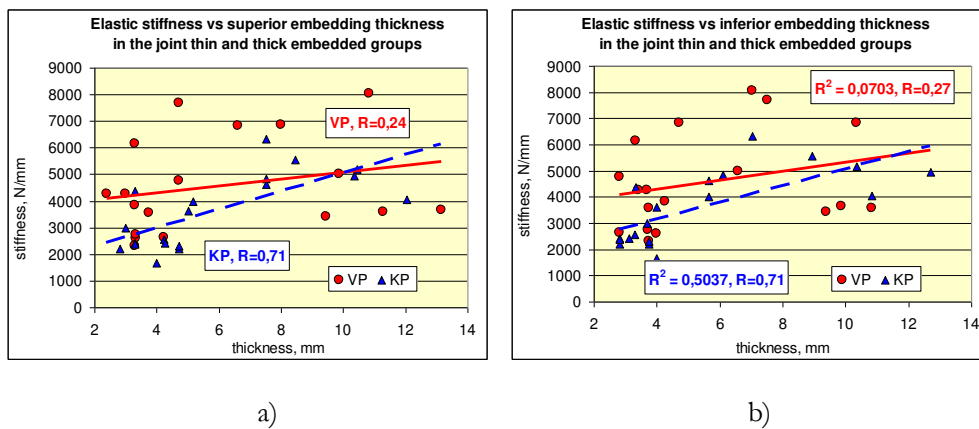


Figure 3. Elastic stiffness vs a) superior and b) inferior embedding thickness in VP and KP groups

| Stiffness vs emb. thickness | VP1   | KP1   | VP2   | KP2   | VP   | KP   |
|-----------------------------|-------|-------|-------|-------|------|------|
| superior                    | -0.62 | -0.05 | -0.04 | -0.06 | 0.24 | 0.71 |
| inferior                    | -0.55 | -0.03 | -0.28 | 0.08  | 0.27 | 0.71 |
| mean                        | -0.69 | 0.00  | -0.30 | 0.01  | 0.26 | 0.72 |

Table 4. Correlation between elastic stiffness and superior, inferior and mean embedding thickness

Correlation between the elastic stiffness and the embedding thicknesses of thick and thin embedded VP and KP vertebrae can be seen in Figure 3 and Table 4. While the stiffness of VP vertebrae showed a considerable negative correlation with the embedding thickness both in thick and thin embedded groups, in the joint thick and thin embedded groups of radical thickness differences a modest positive correlation was observed for the superior ( $R=0.24$ ), inferior ( $R=0.27$ ) and mean embeddings ( $R=0.26$ ). However, while the stiffness of KP vertebrae showed no correlation in separated thin and thick embedded groups, for the joint groups a strong positive correlation was observed equally for the superior ( $R=0.71$ ), inferior ( $R=0.71$ ) and mean ( $R=0.72$ ) embedding thicknesses

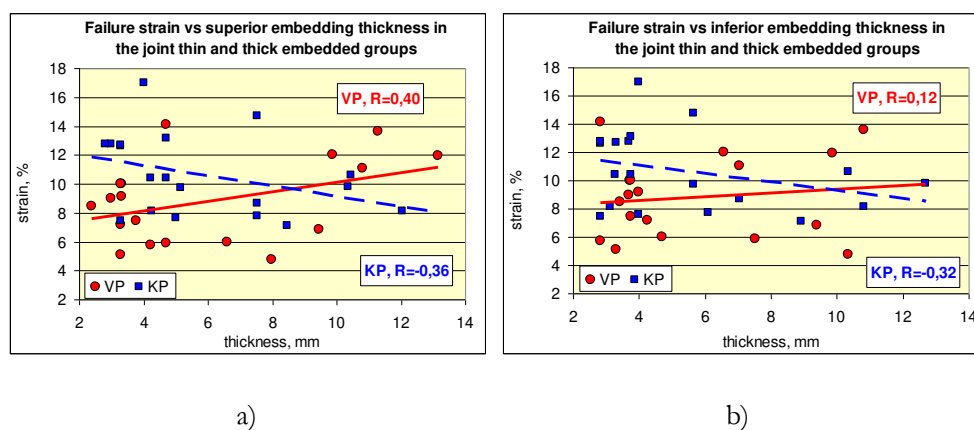


Figure 4. Failure strain vs a) superior and b) inferior embedding thickness in VP and KP groups

| Failure strain vs emb. thickness | VP1  | KP1   | VP2   | KP2   | VP   | KP    |
|----------------------------------|------|-------|-------|-------|------|-------|
| superior                         | 0.80 | -0.15 | 0.32  | -0.29 | 0.40 | -0.36 |
| inferior                         | 0.20 | -0.25 | -0.14 | 0.25  | 0.12 | -0.32 |
| mean                             | 0.63 | -0.21 | -0.09 | 0.25  | 0.29 | -0.34 |

Table 5. Correlation between failure strain and superior, inferior and mean embedding thickness

Correlation between the failure compressive strains and the embedding thicknesses of thick and thin embedded VP and KP vertebrae can be seen in *Figure 4* and *Table 5*. Surprisingly, the stiffness of VP vertebrae showed a considerable positive correlation with the embedding thickness in thick embedded groups, while there was no correlation in the thin embedded group, and in the joint thick and thin embedded groups a small negative correlation was shown. However, while the compressive strain of KP vertebrae showed no correlation in separated thin and thick embedded groups, for the joint groups a modest negative correlation was observed equally for the superior ( $R=-0.36$ ), inferior ( $R=-0.32$ ) and mean ( $R=-0.34$ ) embedding thicknesses.

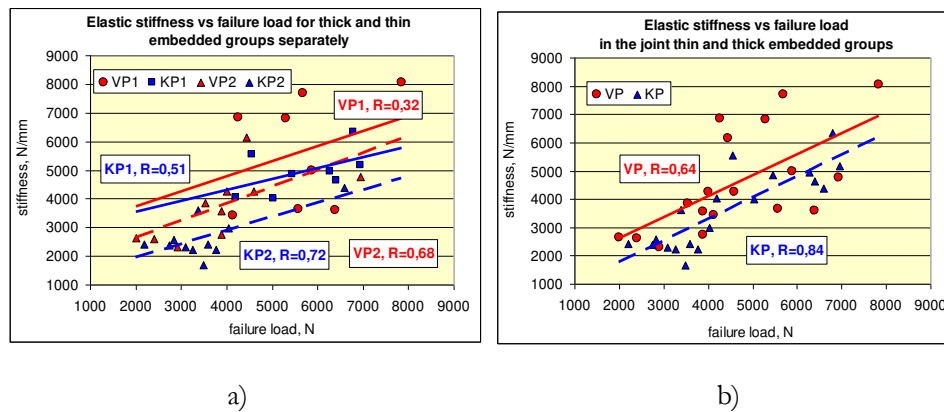


Figure 5. Elastic stiffness vs failure load of VP and KP vertebrae a) in thick and thin embedded groups separately and b) in the joint thin and thick embedded groups

Correlation between the elastic stiffness and failure load of thick and thin embedded VP and KP vertebrae can be seen in *Figures 5a* and *5b*, for the separated and unified thick and thin embedded groups, respectively. In the thin embedded group both VP2 ( $R=0.68$ ) and KP2 ( $R=0.72$ ) vertebrae had higher correlation between stiffness and failure load than in the thick embedded VP1 ( $R=0.32$ ) and KP1 ( $R=0.51$ ) groups. KP vertebrae had higher correlation in both the thick and thin or in the joined thick and thin embedded groups ( $R=0.84$ ) than VP vertebrae ( $R=0.64$ ).

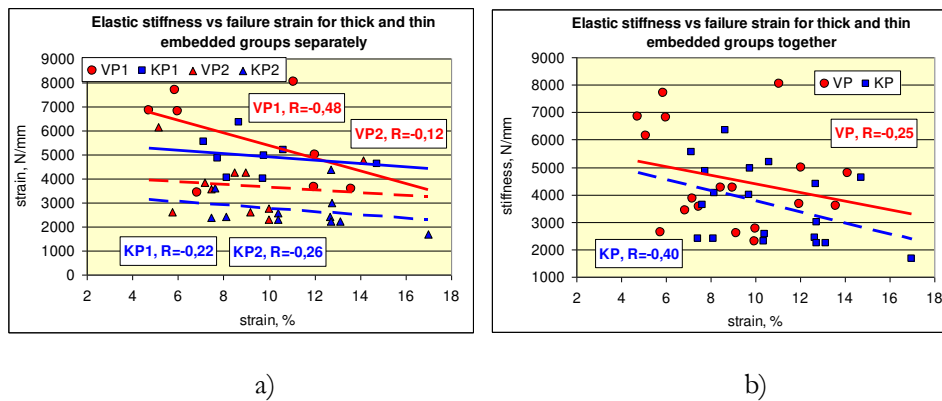


Figure 6. Elastic stiffness vs failure strain of VP and KP vertebrae a) in thick and thin embedded groups separately and b) in the joint thick and thin embedded groups

Correlation between the elastic stiffness and failure strain of thick and thin embedded VP and KP vertebrae can be seen in *Figures 6a* and *6b*, for the separated and unified thick and thin embedded groups, respectively. Evidently, all correlations are negative. VP1 vertebrae in the thick embedded group showed a modest negative correlation, all other vertebrae showed a small negative correlation, In the unified thick and thin embedded groups both VP ( $R=-0,25$ ) and KP ( $R=-0,40$ ) vertebrae had a modest negative correlation between the compressive strain and the embedding thickness.

### 3.2 The influence of the embedding thickness on the plastic damage process of a vertebral interbody device

The results of the compressive mechanical test applied for the segments of interbody fusion, the failure loads, failure displacements and elastic stiffnesses are detailed in<sup>4</sup>, and the related specimen-specific finite element method is presented in<sup>5</sup>. Here the analysis of the effect of embedding thickness by using case-specific finite element method was introduced for a single case of PMMA cement interbody device (PMMA-5 specimen in *Table 1a* and *1b* in<sup>4</sup>). The QCT-based finite element model of the specimen is seen in *Figure 7*.

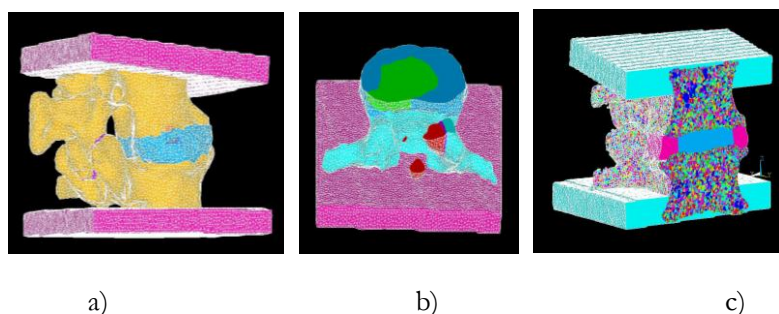
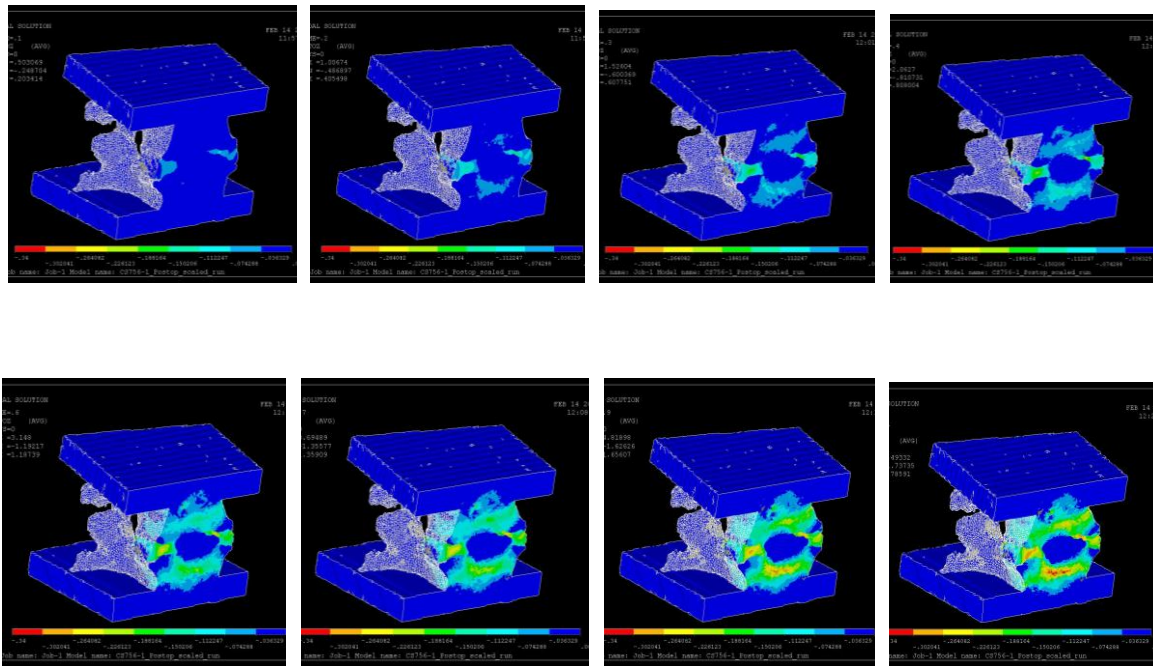


Figure 7. The QCT-based finite element model of the specimen of interbody fixation with PMMA cement interbody device (a); horizontal section through the disc with annulus remnant and cement spacer (b); and frontal section with the QCT- and BMD-based inhomogeneous cancellous and cortical bone (c)

In the numerical experiment, first the lower plane of the inferior embedding layer was fully constrained, and 5 mm compressive displacement load was applied in 10 time steps on the upper surface of the superior embedding along the direction of the plane normal. The steps of the gradual elastic-plastic stain evolution procedure of the specimen are shown in *Figure 8* for the original 10 mm thick superior and inferior embedding. As it was mentioned in the Method section for the embedding plastic material the elastic modulus was measured experimentally on small cylindrical samples and the obtained elastic modulus was used in the finite element analysis (*Table 2*). To avoid the effect of the embedding material, the loading procedure was performed by using a three times increased value for the embedding plastic, but the obtained load bearing and strain results were practically the same as seen in *Figure 8*.



*Figure 8.* Elastic-plastic damage procedure with the developing failure zones

Since the damage is represented by the plastification, in *Figure 9* the separated elastic and plastic strain zones are illustrated for the last step of loading procedure. Obviously, the maximal elastic strains occurred in the remnants of disc annulus while the maximal plastic strains developed in the trabecular bone, under the quasi rigid, non-deformable cement spacer. Thus, in the case of full 10 mm thick embedding, the damage zone started to develop just under the cement spacer, in the middle of the inferior vertebra, and the final failure zone situated at the same place.

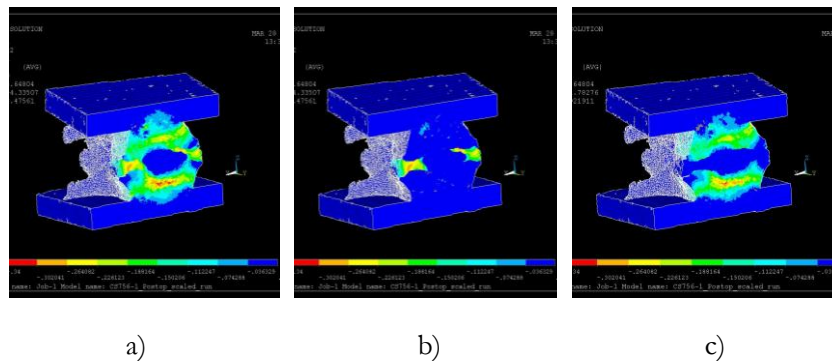


*Figure 9.* Total (a) and separated elastic (b) and plastic (c) strain zones in the final state of loading

For the slicing numerical experiment, the final location of the elastic-plastic strain zones of the last loading step is shown in *Figure 10*. Here the final elastic-plastic zones for the total thickness of 10 mm, then for 7.5, 5.0, 2.5 mm and finally for the total removing of the embedding is illustrated. The last picture in *Figure 10* shows the case of the inverse directional loading, with support on the top and displacement load on the bottom, acting upwards.

Since the damage can be represented by the evolution of plastic compressive strains during the loading, in *Figure 11* the relating separated plastic strains, that is, the damage zones are distinguished. By thinning gradually the embedding, the failure zone that started to develop in the middle of the inferior vertebra, just under the cement spacer, moved upwards, with the final position closed to the top of the superior vertebra.

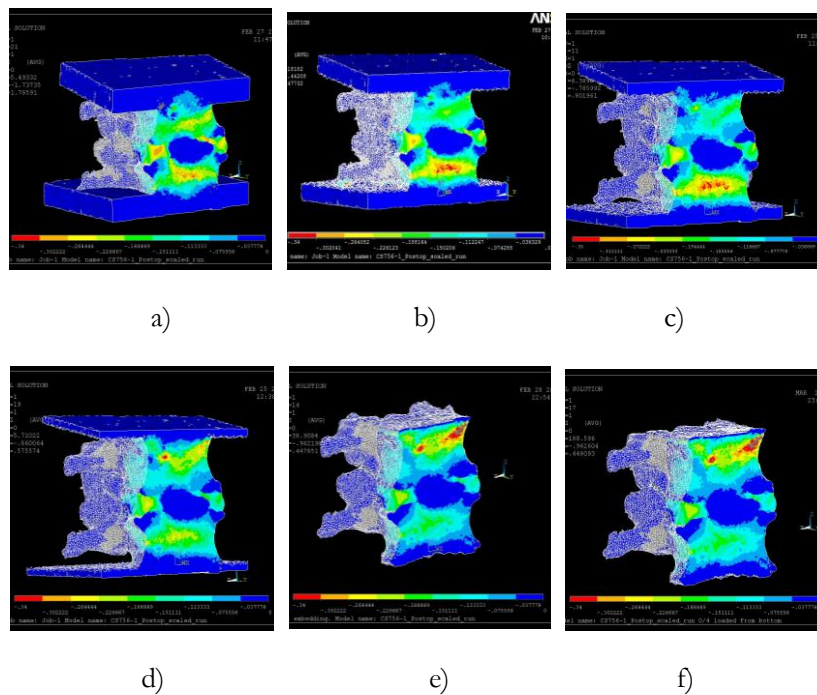


*Figure 10.* Final damage zones in the case of a) 10 mm, b) 7.5 mm, c) 5.0 mm, d) 2.5 mm and e) total remove of embedding, f) loaded upside down the case of total removed embedding

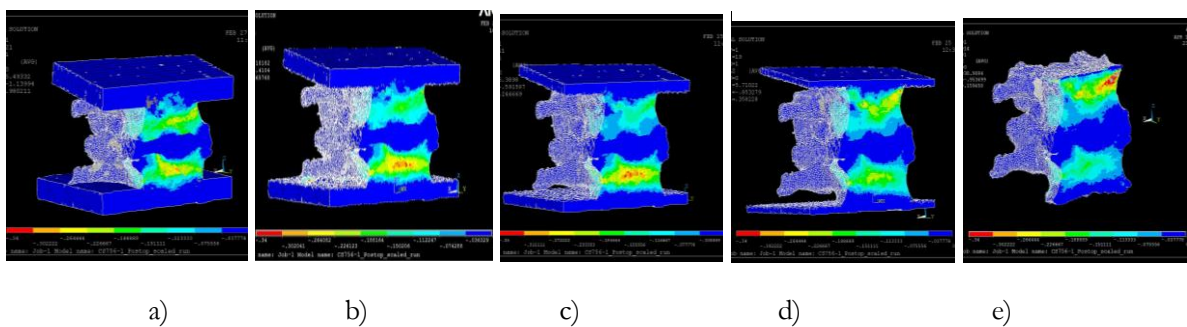


*Figure 11.* The separated plastic strain domains of the final damage zones in the case of a) 10 mm, b) 7.5 mm, c) 5.0 mm, d) 2.5 mm and e) total remove of embedding

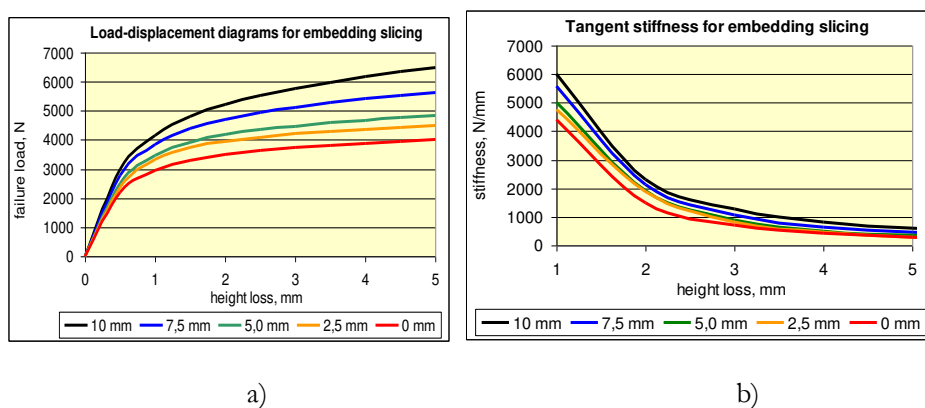


Figure 12. Load-displacement diagrams (a) and tangent stiffness (b) for different embedding thicknesses

In Figure 12 the load-displacement diagrams and the gradually decreasing tangent stiffnesses are shown for the slicing steps of embedding. By the total remove of embedding, the load bearing of the segment at the last loading step gradually decreased by about 40%, by 18, 14, 8 and 11% in each slice reduction step, subsequently, related to the previous value. The related stiffness decreased by 65% in 28, 33, 22 and 9% steps.

#### 4. Discussion and Conclusion

Mechanical results of vertebral augmentation highly depended on the embedding thickness. We can state that the thin embedding makes the specimens more sensitive to the differences between the mechanical results of VP and KP vertebrae than the thick one, as shown in Figure 1, namely, in thin embedding the differences in failure load, displacement and stiffness between VP and KP groups are larger. Compared to the native vertebrae without embedding in3, the failure load was about 80% higher in the thick and only 10-20% higher in thin embedded group. The embedding thickness significantly affected most of the mechanical results inside the augmentation type as well. The failure load and stiffness in the thin embedded groups was significantly smaller both VP and KP vertebrae compared to the thick embedded groups (Figures 1a, 1b).

The failure load is proportional with the embedding thicknesses equally for VP and KP vertebrae (Figure 2). However, this fact can be proved only in the joined thin and thick embedded groups. The reason is that the measured results are sensitive only to the larger thickness differences. However, the elastic stiffness only in the case of KP vertebrae is proportional with the embedding thicknesses, while the stiffness of VP vertebrae shows a great uncertainty in relation with the embedding thickness (Figure 3). The reason may be that due to the kyphoplasty a regular structure is formed that is partly supported by the embedding, while the stiffness of vertebroplasty is based mainly on the bone quality and structure. Indeed, as seen in,<sup>3</sup> there was higher bone quality in the thick embedded group than in the thin embedded one, so the correlation of the stiffness of VP vertebrae with bone quality was negative in thick and strongly positive in thin embedded group where the cement augmentation could fill in the osteoporotic

gaps. Similar regularity is found in the inverse proportionality between the failure compressive strains and the embedding thicknesses for KP vertebrae, and uncertainty for VP vertebrae (*Figure 4*). The reason may be the same as before.

Failure load and elastic stiffness are evidently proportional with each other. It is realized in both embedded groups, for both types of augmentation, however, better for the thin embedded group and better for KP vertebrae (*Figure 5*). The also evident inverse relationship between stiffness and deformability manifests itself better for KP augmentation again (*Figure 6*). The reason may be the clear and definite structure of kyphoplasty again, in comparison with the bone quality-dependent, irregularly distributed vertebroplasty. At the same time, in a comprehensive analysis the structural differences can better be distinguished in a thin embedded environment.

We can conclude that since the thin embedding is closer to the anatomic situation, the values of thin embedded group can be accepted as numerical results, however, the tendencies can be confirmed by the results of thick embedded group.

The specimen-specific finite element simulation of the failure process of the interbody fixation demonstrated a great influence of the embedding thickness on the mechanical characteristics. By means of the slicing method, beside the gradual decrease of the failure load and stiffness of specimens by slicing the embedding even thinner and thinner, the migration of the damage zones within the vertebral cancellous bone of the fixed segment could be presented. By the initial total embedding thickness the damage zone starts and develops under the cement spacer in the middle trabecular bone domain of the inferior vertebra. As the embedding become thinner and thinner, the position of the damage zone moves upwards, finally to the top of the upper vertebra (*Figure 11*). At the same time, the load bearing and stiffness of the segment gradually decreases (*Figure 12*). By applying the support and load in the inverse direction, the damage process and the numerical results are the same. The approximately 40% difference in the compressive strength between the 10 mm thick and no embedding is in agreement with the conclusion of 8 that the systematic underestimation error in the platens compression test can be in the range of 20-40%, however, for trabecular bone specimens, for end-artifact errors.

The damage inside the bone is manifested by plastic strains. In the case of no embedding with top loading, the damage starts in the upper region of the superior vertebra, closed to the loading region, according to the Saint-Venant principle. The reason may be the missing horizontal support at the ends of the specimens that – in the case of embedding – hinders the development of plastic strains. Theoretical analysis<sup>9</sup> of the experimental artifacts in the compressive tests of trabecular bone concludes that without friction at the interface between the test machine and the specimen always underestimates Young's modulus, thereby reducing the accuracy of the test. Similarly,<sup>1</sup> found that the assumption of a frictionless boundary condition in the parallel plate compression loading configuration was a significant source of error that could be overcome with the use of rigid end caps.

We can conclude that by evaluating the results of any mechanical tests, the thickness of the embedding must be considered, and when is possible, the results must be checked by case-specific finite element analysis.

## REFERENCES

1. Jacobs CR, Davis BR, Rieger CJ, Francis JJ, Saad M, Fyhrie DP. The impact of boundary conditions and mesh size on the accuracy of cancellous bone tissue modulus determination using large-scale finite-element modeling, *Journal of Biomechanics*, 1999;32(11):1159–64.
2. Bevill G, Eswaran SK, Farahmand F, Keaveny TM. The influence of boundary conditions and loading mode on high-resolution finite element-computed trabecular tissue properties, *Bone*, 2009;44:573-8.
3. Kurutz M, Jakab G, Varga P, Varga PP. Biomechanical evaluation of vertebroplasty and kyphoplasty by uniaxial compressive test, *Biomechanica Hungarica*, 2013;VI(1):311-22.
4. Kurutz M, Csákány T, Varga P, Varga PP. Biomechanical evaluation of interbody devices by uniaxial compressive test: PEEK spacers versus PMMA cement spacers, *Biomechanica Hungarica*, 2013;VI(1):259-71.
5. Varga P, Nédli P, Csákány T, Kurutz M, Varga PP. Biomechanical evaluation of two different vertebral interbody devices by using QCT-based case-specific nonlinear finite element models: A preliminary report, *Biomechanica Hungarica*, 2013;VI(1):175-84.
6. Kopperdahl DL, Morgan EF, Keaveny TM. Quantitative computed tomography estimates of the mechanical properties of human vertebral trabecular bone, *J Orthop Res*, 2002;20:801–5.
7. Mirzaei M, Zeinali A, Razmjoo A, Nazemi M. On prediction of the strength levels and failure patterns of human vertebrae using quantitative computed tomography (QCT)-based finite element method. *J Biomech*, 2009;42(11):1584-91.
8. Keaveny TM, Pinilla TP, Crawford RP, Kopperdahl DL, Lou A. Systematic and random errors in compression testing of trabecular bone, *J Orthop Res*, 1997;15:101–10.
9. Keaveny TM, Borchers RE, Gibson LJ, Hayes WC. Theoretical analysis of the experimental artifact in trabecular bone compressive modulus. *J Biomech*, 1993;26:599–607.

***The authors gratefully acknowledge the Hungarian Scientific Research Fund OTKA for providing financial support in the frame of the grant K-075018. The authors are grateful to Lajos Borbás and Gábor Szabó for their help in laboratory experiments.***